Sediment Provenance Constraints on West Antarctic Ice Sheet History

James William Barbour Marschalek

Imperial College London

The Grantham Institute for Climate Change and the Environment &
The Department of Earth Science and Engineering

Thesis submitted for the degree of Doctor of Philosophy (Ph.D.), 2022

Statement of Originality

I declare that the contents of this thesis are entirely my own work. Contributions of others are acknowledged at the beginnings of chapters or referenced appropriately.

James Marschalek

Copyright Statement

The copyright of this thesis rests with the author. Unless otherwise indicated, its contents are licensed under a Creative Commons Attribution-NonCommercial 4.0 International Licence (CC BY-NC). Under this licence, you may copy and redistribute the material in any medium or format. You may also create and distribute modified versions of the work. This is on the condition that: you credit the author and do not use it, or any derivative works, for a commercial purpose. When reusing or sharing this work, ensure you make the licence terms clear to others by naming the licence and linking to the licence text. Where a work has been adapted, you should indicate that the work has been changed and describe those changes. Please seek permission from the copyright holder for uses of this work that are not included in this licence or permitted under UK Copyright Law.

Acknowledgements

This thesis could not have come to fruition without the help of many people to whom I am very much indebted. Firstly, my supervisor team was unparalleled; being able to draw from their broad range of expertise and experience was fantastic. I could not ask for more from Tina van de Flierdt, who was always available when I needed her but equally happy to let me pursue ideas of my own. Her enthusiasm for our work always leaves me refreshed and inspired. I am also grateful to Martin Siegert for his guidance and support throughout my PhD. Many thanks are due to Ed Gasson for taking me on as a student during the pandemic. His ideas and regular chats have been greatly valued. I would also like to thank CD Hillenbrand for our excellent discussions. I am very grateful for his supervision during the NBP20-02 cruise.

I would like to thank the entire IODP Expedition 374 science party and the scientists and crew of the NBP20-02 cruise, without whom much of this thesis would not have been possible.

I am grateful to Barry Coles for his help and company down in the labs and Katharina Kreissing for her superb support of the lab group. The other MAGIC group members past and present made the PhD experience and I feel very lucky to have worked in such an excellent lab group.

Finally, I would like to thank my friends and family, but most of all Charlotte Michael, who put up with me staying late in the labs and is always there for me.

Thesis Abstract

The West Antarctic Ice Sheet (WAIS) is losing mass at an accelerating rate, and its inland-deepening bed slope means it holds the potential to cause rapid sea-level rise which would have wide-reaching societal consequences. To predict how the WAIS may respond in the future and plan appropriate mitigation and adaption strategies, it is useful to constrain its past response to changing environmental conditions. Studying Early Miocene sediments from the Ross Sea outer continental shelf reveals that they were sourced from West Antarctica, proving the WAIS could expand far across the continental shelf and contribute to sea-level change millions of years earlier than previously proven. Such qualitative information is highly valuable, but to help quantify such reconstructions, a computational framework to predict the sediment provenance signature of a given ice sheet configuration is developed. This helps pinpoint the extent of Pliocene ice sheet retreat in the Wilkes Subglacial Basin. Studies of WAIS sediment provenance are also limited by uncertainty regarding subglacial geology. Samples obtained from beneath the WAIS offer new insights into its bedrock's sediment provenance signature, as well as contributing to knowledge of how the WAIS entrains and transports sediments. Additionally, recent ice retreat has led to exposure of the first subaerial rock between two key outlets of the WAIS in the Amundsen Sea, which reveals the tectonic history of this rapidly changing region by defining the extent of crustal blocks and proving the existence of a hypothesised tectonic feature. Together, these projects advance knowledge of the history of the WAIS and provide the foundations for future studies of Antarctic sediment provenance. This will ultimately help constrain sea-level rise predictions.

Table of Contents

Abstract **4**

List of Figures **10**

List of Tables **15**

1. Introduction **16**
1.1. Why Study Antarctic Ice Sheet History? 17
1.2. The Cenozoic Evolution of Antarctica's Ice Sheets 19
1.3. Sediment Provenance as a tool for Investigating Ice Sheet History: Opportunities and Challenges 21
1.4. Provenance Tracing Techniques 23
1.4.1. Radiogenic Nd and Sr Isotopes 23
1.4.2. Zircon U-Pb Dating 24
1.5. Erosion Beneath Ice Sheets 24
1.6. Thesis Aims and Structure 26

2. A Large West Antarctic Ice Sheet Explains Early Neogene Sea Level Amplitude **29**
2.1. Introduction 31
2.2. IODP Site U1521 and Provenance Approach 33
2.3. Geological History of Antarctica 34
2.3.1. East Antarctica and the Transantarctic Mountains 34
2.3.2. Precambrian East Antarctica 35
2.3.3. The Ross Orogeny 36
2.3.4. Beacon Sedimentary Rocks and Ferrar Magmatites 37
2.3.5. West Antarctica 38
2.3.6. Cenozoic Volcanism 39
2.4. IODP Site U1521 Age Model 40
2.5. Neodymium and Strontium Isotopes in and around the Ross Sea 49
2.5.1. Terrestrial Rocks 50
2.5.2. Late Quaternary Tills and LGM Tills in Offshore Sediments 53
2.6. Methods 54
2.6.1. Neodymium and Strontium Isotopes 54
2.6.2. Detrital Zircon U-Pb Dating 56
2.6.3. Clast Petrography 56
2.6.4. Palynology 57
2.6.5. Hornblende $^{40}Ar/^{39Ar}$ Dating 59
2.6.6. Clay Mineralogy 59
2.6.7. X-Ray Fluorescence 60
2.7. Results 61
2.7.1. Radiogenic Isotopes at Site U1521 61

2.7.2. Clay Mineralogy *63*
2.7.3. Clast Petrography *66*
2.7.4. Palynology *68*
2.7.5. Zircon U-Pb Dating *70*
2.7.6. Hornblende $^{40}Ar/^{39}Ar$ Dating *72*
2.8. Discussion 74
2.8.1. Sediment Provenance of Sequence 2: Evidence for an Early Miocene WAIS *74*
2.8.2. Provenance Changes within Sequence 2 ..... *76*
2.8.3. Birth of a Marine-Based WAIS *78*
2.8.4. Ice Retreat during the Miocene Climatic Optimum *81*
2.9. Conclusions 82

3. Quantitative Interpretation of Antarctic Sediment Provenance Records 84
3.1. Introduction 87
3.2. Neodymium Isotope Map 88
3.2.1. Approach *88*
3.2.2. Regional Description of the Neodymium Isotope Map *94*
3.2.3. Data from Recent Seafloor Surface Sediments *101*
3.3. Debris Generation and Subglacial Transport 102
3.3.1. Ice Sheet Model and Erosion Rate *102*
3.3.2. Tracing the Generation and Subglacial Transport of Debris *103*
3.4. Detritus Transport in the Ocean 105
3.4.1. Iceberg Rafting *105*
3.4.2. Bottom Currents *114*
3.4.3. Gravitational Downslope Transport *118*
3.4.4. Relative Contribution of Transport Mechanisms *119*
3.5. Modelled Surface Sediment Signatures 120
3.6. Application to Smaller-than-present Palaeo Ice Sheets 128
3.6.1. Adaptions to Methods *128*
3.6.2. Comparison to IODP Site U1361 ..... *131*
3.6.3. Predicting the Provenance Signature of West Antarctic Ice Sheet Collapse *137*
3.7. Conclusions and Future Direction 139

4. Characterisation of the First Exposed Bedrock between Thwaites and Pine Island Glaciers 142
4.1. Introduction 145
4.2. Geological Setting 149
4.3. Field Observations 152
4.4. Methods 154
4.4.1. Sampling and Site Selection *154*
4.4.2. Radiogenic Nd and Sr Isotopes *155*
4.4.3. Zircon U-Pb Dating *156*

4.4.4. Zircon Hf Isotopes 157
4.4.5. (U-Th)/He Dating 158
4.4.6. Fission Track Dating 159
4.4.7. Major and Trace Element Geochemistry 160
4.5. Results 160
4.5.1. New Nd and Sr Isotope Provenance data from Seafloor Surface Sediments 160
4.5.2. Geo-/Thermo-Chronology of the Sif Island Granite 163
4.5.3. Neodymium and Strontium Isotope Composition of the Sif Island Granite 168
4.5.4. Major and Trace Element Composition of the Sif Island Granite 169
4.6. New Geological Constraints 170
4.6.1. Sediment Provenance: Thwaites Glacier 170
4.6.2. Sediment Provenance: Eastern Pine Island Bay and Pine Island Glacier 171
4.6.3. Comparisons to Surrounding Crustal Blocks 174
4.6.4. Thermal History and Structural Control of Pine Island Rift 175
4.7. Topographic Implications 177
4.8. Conclusions and Outlook 177

5. Constraining the Sediment Provenance Signature of West Antarctic Ice Sheet Collapse 179
5.1. Introduction 182
5.1.1. The Byrd Ice Core 182
5.1.2. Glacial Setting and Existing Analyses on the Byrd Ice Core Debris 183
5.1.3. Geology Beneath the WAIS 184
5.2. Methods 187
5.2.1. Core Sampling and Debris Recovered 187
5.2.2. Neodymium and Strontium Isotopes 190
5.2.3. Clay Mineralogy 191
5.2.4. $^{40}Ar/^{39}Ar$ Dating 191
5.2.5. SEM Imaging and Electron Microprobe Mineralogy 192
5.3. Results 192
5.3.1. Neodymium and Strontium Isotopes 192
5.3.2. Clay Mineralogy 195
5.3.3. SEM Imaging and Electron Microprobe Mineralogy 196
5.3.4. $^{40}Ar/^{39}Ar$ Dating and Pending Analyses 197
5.4. Discussion 198
5.4.1. Debris Provenance 198
5.4.2. Debris Endmember Contributions 199
5.4.3. Volcanic Material Beneath the WAIS 201
5.4.4. Kaolinite as a Sediment Provenance Tracer 202
5.4.5. Constraints on Offshore Nd and Sr Isotope Compositions 202
5.4.6. Rhyolite Clast 203

5.5. Conclusions and Future Work 204

6. New Insight into Ross Sea Sediment Provenance from Subglacial Sediments... 206
6.1. Introduction 208
6.2. Sample Sites 210
6.2.1. J9 210
6.2.2. Kamb Ice Stream Grounding Zone (KIS-GZ) 211
6.2.3. Hot Water Drill 2b (HWD-2b) 211
6.2.4. Whillans Grounding Zone (WGZ) 212
6.3. Methods 212
6.4. Results and Discussion 214
6.4.1. J9 215
6.4.2. KIS-GZ 216
6.4.3. HWD-2b 220
6.4.4. Whillans Grounding Zone 224
6.5. Concluding Remarks 225

7. Thesis Summary and Concluding Remarks 227
7.1. Thesis Summary 228
7.2. Future Study and Closing Remarks 230

Bibliography 232

Appendices 265

A.1. Chapter 2 Published Manuscript 266

A.2. Chapter 2 Supplementary Data Tables 289

A.3. Changes in Sediment Provenance at IODP Site U1521 during the Miocene Climatic Optimum 342

A.4. Nd and Sr Isotope Data for IODP Site U1522 347

A.5 Modelling Antarctic Erosion and Topographic development in the Early-Middle Miocene 350
A.5.1 Introduction 350
A.5.2 Adjustments to the Ice Sheet and Erosion Model 350
A.5.3 Results and Problems 351
A.5.4 Recommendations for Future Work 353

A.6 Provenance Tracing of the Last Glacial Maximum Ice Sheet 355
A.6.1 Introduction 355
A.6.2 West Antarctica and Antarctic Peninsula 356
A.6.3 George V Land Coast 356
A.6.4 Ross Sea and Victoria Land 357
A.6.5 Summary 358

A.7 BEAMISH Drilling - Foundation Ice Stream 359
A.7.1 Site and Geological Setting 359
A.7.2 Results and Discussion 360

Appendix References 361

List of Figures

		Page
1.1	Cartoon outlining the basic concepts of Marine Ice Sheet Instability and Marine Ice Cliff Instability	18
2.1	Location of IODP Site U1521 and the surrounding geology.	32
2.2	Compilation of zircon U-Pb ages from the Ross Sea sector.	35
2.3	Age model constraints below 75 mbsf at Site U1521.	41
2.4	Correlation of Site U1521 magnetostratigraphic tie points.	45
2.5	Kernel density estimate plots for literature measurements of rock ε_{Nd} compared to measurements on fine-grained Miocene detritus from Site U1521.	51
2.6	Map of approximate ε_{Nd} values in rocks and offshore sediments from around the Ross Sea embayment.	52
2.7	Selected provenance proxies from IODP Site U1521 compared to Early Miocene climate records.	61
2.8	IODP Site U1521 down-core clast and clay mineral distribution.	64
2.9	Kübler vs Esquevin index values for the IODP Site U1521 Sediments	65
2.10	Selected palynological counts compared to strontium and neodymium isotope data for IODP Site U1521	68
2.11	Site U1521 detrital zircon U-Pb age distributions.	71
2.12	Kernel density estimates for hornblende $^{40}Ar/^{39}Ar$ ages compared to zircon U-Pb ages younger than 1500 Ma.	73
2.13	Close up of the Site U1521 interval with a West Antarctic provenance.	76
3.1	Map of ε_{Nd} values used as an input for the provenance tracing and interpolated ε_{Nd} values offshore within 200 km of a surface sediment core location.	89
3.2	Locations mentioned in the main text displayed on BedMachine topography.	91
3.3	Example of the resolution of the high-resolution rock polygons from GeoMAP versus the simplified polygons used to construct the ε_{Nd} value map.	93
3.4	Ice flow lines and erosion rate map used to seed start locations.	103
3.5	Impact on root mean square error mismatch associated with random number generation and number of seed locations.	104

3.6 Heatmap of ocean surface velocity paths, which are assumed to approximate iceberg paths, and comparison to literature iceberg trajectory data. 107

3.7 Examples of different iceberg debris yield over time. 109

3.8 Effect of varying basal sediment thickness on the root mean square error of the match with surface sediment ε_{Nd} values. 110

3.9 Impact of assuming all debris is contained in a basal layer. 112

3.10 Monthly mean Antarctic sea ice extent from 1981-2010 plotted alongside the root mean square error fit between modelled monthly surface current ε_{Nd} value estimates and measured surface sediments. 113

3.11 Effect of varying the thickness of the layer with suspended sediment on the root mean square error match with surface sediment ε_{Nd} values. 116

3.12 Applied transport mechanisms for glacimarine detritus providing the closest match with interpolated surface sediment ε_{Nd} values around the Antarctic continental margin. 120

3.13 Simulated ε_{Nd} values around the West Antarctic margin including the absolute values and difference from the seafloor surface sediment data interpolation. 122

3.14 Comparison between observed and modelled ε_{Nd} values in seafloor surface sediments. 123

3.15 Results of an inverse distance weighting of predicted ε_{Nd} values from the ice sheet margin. 124

3.16 Close up of the Mertz Glacier Tongue (MGT) region imaged in June 1999 comparing observed sea ice trajectories and regions of mismatch between modelled and observed ε_{Nd} values. 128

3.17 IODP Site U1361 full ε_{Nd} record. 131

3.18 Relationship between modelled Antarctic ice volume and ε_{Nd} values at IODP Site U1361. 132

3.19 Source of icebergs crossing the longitude of IODP Site U1361 to the south of the site. 133

3.20 Modelled ice sheet extent and ε_{Nd} values for smaller and larger degrees of WSB retreat. 134

3.21 Impact of WAIS collapse on modelled ε_{Nd} values. 137

4.1 Location of Sif Island in the eastern Amundsen Sea Embayment relative to other rock exposures. 146

4.2 The exposure of Sif Island caused by a retreating ice front captured in LANDSAT imagery. 148

4.3 Field photographs of Sif Island. 152

4.4 Sif Island rock sample photographs. 153

4.5 Epsilon Nd and $^{87}Sr/^{86}Sr$ map of new seafloor surface samples compared to published samples. 161

4.6 Nd-Sr cross plot showing new samples compared to those already published. 162

4.7 Concordia diagrams for concordant grains. 164

4.8 Cathodoluminescence imaging of the 50 zircons analysed for U-Pb dating and ε_{Hf} analyses. 165

4.9 Sketch cooling history of Sif Island. 167

5.1 Location and surrounding geology of the Byrd ice core. 182

5.2 Images of the Byrd ice core basal ice and correlation to the original 1960s images. 187

5.3 Rhyolite porphyry cobble ~4-5 cm in diameter recovered from section 1406-C2. 188

5.4 Changes over depth in the ice column in Nd isotope ratios, Sr isotope ratios and smectite content. 193

5.5 Cross plot of Nd and Sr isotope compositions of the Byrd ice core debris compared to compiled literature data for West Antarctic rocks. 194

5.6 MEaSUREs velocity vectors over the Byrd ice core location and upper portion of Bindschadler Ice Stream. 196

5.7 Ice surface velocity and bed elevation near the Byrd ice core site. 198

6.1 Geological map of the Ross Sea region with new Ross Sea core sites. 209

6.2 Core photographs and x-ray scans of the four sediment cores. 210

6.3 Map of ε_{Nd} values around the Ross Sea with new subglacial sample data added. 214

6.4 Kernel density estimate for the KIS-GZ site and the upstream Kamb Ice Stream ('UpC') site. 216

6.5 Visual and x-ray images of the HWD-2b core, downcore variations in ε_{Nd} values, and results of ice sheet model particle tracking experiments. 221

A.2.1 Pictures of Transantarctic Mountain rock samples analysed for Nd and Sr isotope compositions. 322

A.3.1 Comparison of different proxies applied to Unit III, IODP Site U1521. 343

A.3.2 Site U1521 Unit III Nd-Sr crossplot 345

A.4.1 IODP Site U1522 Nd and Sr isotope data 347

A.5.1 Modelled and observed sediment volumes for different sectors of Antarctica at 14 Ma. 352

A.5.2 Modelled bed elevation and ice thickness at three-million-year intervals from 23-14 Ma. 353

A.6.1 Predicted ε_{Nd} values around the modelled LGM ice sheet with and without ice shelves 355

List of Tables

		Page
2.1	Age model tie points at Site U1521	42
2.2	Results of $^{87}Sr/^{86}Sr$ dating of shell fragments from Site U1521	48
2.3	Values used in the erosion rate calculation	79
3.1	Isotopic endmember assignment for central West Antarctica	98
3.2	Neodymium isotope data for new surface sediment samples in the Ross Sea	102
3.3	Parameters used in Chapter 3.	141
4.1	Neodymium and strontium isotope data for subglacial, NBP19-02 and NBP20-02 samples.	162
4.2	Sif Island U-Pb zircon data	166
4.3	Bulk rock neodymium and strontium isotope data for Sif Island	168
4.4	Zircon hafnium isotope data for sample SIA.	168
4.5	Selected major and trace element concentrations for the Sif Island granite	169
5.1	The length, position relative to the bed, ice mass, debris content and grain size fractions of the Byrd ice core samples.	189
5.2	Results of Nd and Sr isotope analyses on the fine grained (<75 μm) Byrd ice core debris.	192
5.3	Results of clay mineral composition from x-ray diffraction of the three sample depths.	195
5.4	Results of electron microprobe analysis of the 210-800 μm size fraction.	197
6.1	Neodymium and strontium isotope data collected at the new sub-ice sites.	215
6.2	Zircon U-Pb data for the KIS-GZ sample	218
A.2.1	*Clast data for IODP Expedition 374 Site U1521.*	289
A.2.2	Nd and Sr isotope data for IODP Expedition 374 Site U1521.	290
A.2.3	U-Pb zircon data for IODP Expedition 374 Site U1521	292
A.2.4	Data from Ar-Ar dating of hornblende grains from IODP Expedition 374 Site U1521.	311

A.2.5 Clay mineralogy data for IODP Expedition 374 Site U1521. 318

A.2.6 Dinocyct counts for IODP Expedition 374 Site U1521 319

A.2.7 Pollen and spore counts for IODP Expedition 374 Site U1521 321

A.2.8 Neodymium and Sr isotope data from new Transantarctic Mountain rock samples. 321

A.2.9 Literature compilation of terrestrial rock and sediment Nd and Sr isotope data. 324

A.3.1 Nd and Sr isotope data for IODP Expedition 374 Site U1521 Lithological Units I-III. 346

A.4.1 Nd and Sr isotope data for IODP Expedition 374 Site U1522. 349

A.7.1 Neodymium and strontium isotope data collected from the BEAMISH core 360

Chapter 1: Introduction



Folded debris-rich layers and melt layers (left) and debris frozen onto the base (right) of icebergs in Pine Island Bay. Photographed near Sif Island during the 2020 Nathaniel B Palmer NBP20-02 cruise.

1.1 Why Study Antarctic Ice Sheet History?

Antarctica contains approximately 90% of the world's ice, with the potential to raise global mean sea level by over 57 m if it melted entirely (Fretwell et al., 2013; Morlighem et al., 2020). Loss of this ice is accelerating, largely as a result of ocean warming, with Antarctica expected to be contributing approximately 0.5 cm a^{-1} to sea-level rise by 2100 (e.g. DeConto and Pollard, 2016; The IMBIE Team, 2018; Pörtner et al., 2019; Edwards et al., 2019; DeConto et al., 2021). Sea-level rise has the potential to create dramatic social and economic impacts on low lying cities and countries around the world (Hinkel et al., 2018). Predicting the likely rate and magnitude of Antarctica's ice mass loss is therefore of great societal importance. Model projections of future mass loss from Antarctica are, however, highly variable (e.g. Golledge et al., 2015; DeConto and Pollard, 2016; Edwards et al., 2019); a fuller understanding of glacial processes and ice-ocean-atmosphere interactions is required (Bakker et al., 2017).

Of particular concern are the West Antarctic Ice Sheet (WAIS) and areas of the East Antarctic Ice Sheet (EAIS) that are grounded below sea-level on slopes that deepen inland. This is because these parts of the ice sheets are in contact with relatively warm ocean waters which have the potential to initiate rapid mass loss through two hypothesised dynamical feedbacks: Marine Ice Sheet Instability (MISI; Weertman, 1974; Mercer, 1978) and Marine Ice Cliff Instability (MICI; Pollard et al., 2015; DeConto and Pollard, 2016) (Fig. 1.1). MISI is hypothesised to be triggered by a small retreat in the grounding zone onto a deeper bed. Essentially, this creates a higher vertical column of ice, promoting a greater flux of ice through the grounding zone. This leads to drawdown of ice from inland and thinning of the glacier, causing the grounding zone to retreat onto an even deeper bed as the edge becomes buoyant. This positive feedback continues, leading to rapid collapse of the ice sheet. MICI is a more controversial hypothesis (Edwards et al., 2019), largely as it has not been clearly observed in nature and is therefore difficult to accurately parameterise in models. MICI initiates as an ice shelf disintegrates due to surface melting and hydrofracturing. This removes the buttressing effect of the ice shelf, allowing ice cliffs greater than 100 m to form at the calving front. The mechanical properties of ice mean cliffs of this height are not structurally stable; thus, they collapse, revealing even higher cliffs behind them. This comprises another potential positive feedback process.

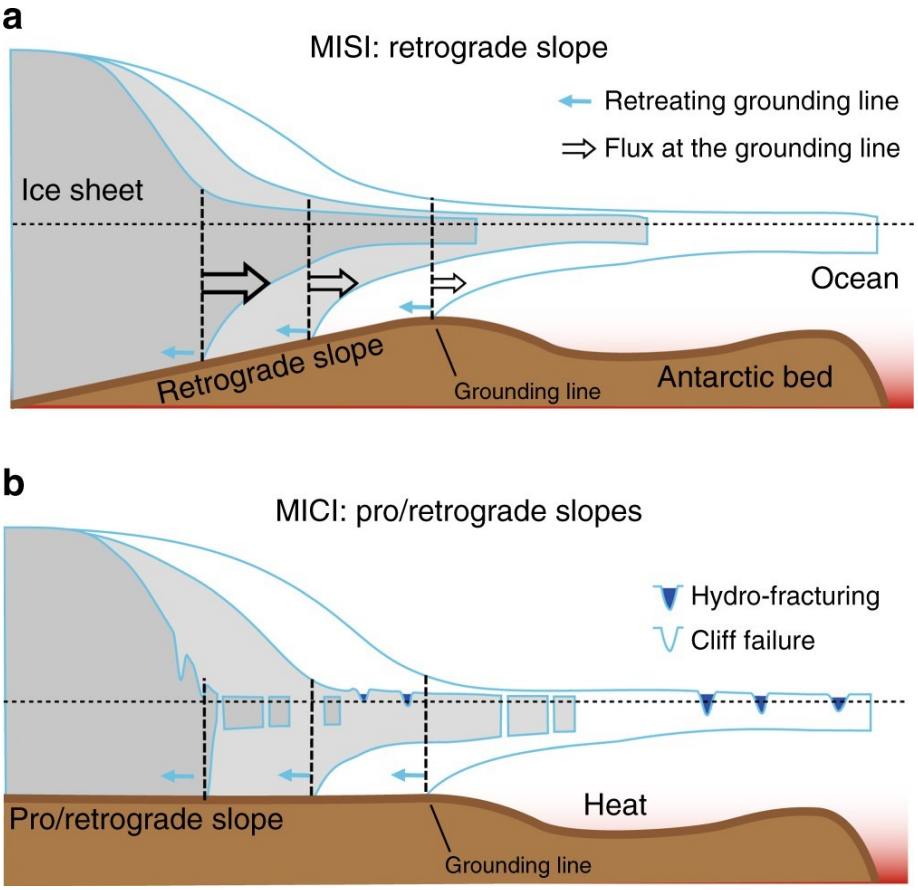


Figure 1.1. *Cartoon outlining the basic concepts of (a) Marine Ice Sheet Instability (MISI) and (b) Marine Ice Cliff Instability (MICI). From Pattyn (2018).*

Consequently, predicting how much ice will be lost from marine-based sectors of Antarctica and how fast this will occur over the coming decades and centuries is a major goal in the Antarctic research community (Scambos et al., 2017; Pattyn and Morlighem, 2020). A key avenue to addressing these uncertainties is reconstructing the past response of the ice sheets to different climatic thresholds. This can provide invaluable insight into the modern glacial system by revealing changes to ice sheet extent in response to environmental conditions both cooler and warmer than the present (e.g. Cook et al., 2013; Wilson et al., 2018; Marschalek et al., 2021). Such information can inform knowledge of modern processes and test ice-sheet model physics in climates well beyond the constraints of the instrumental record. Whilst far-field records have helped determine the global pattern of Cenozoic climate evolution (e.g. Zachos et al., 2001; 2008; Miller et al., 1991; 2020; Westerhold et al., 2020), ice-proximal records are necessary to resolve where ice was lost from and distinguish between ice volume and temperature impacts on the climate record. This thesis therefore focusses on sediment core records from close to (or within) the Antarctic continent, particularly the marine-based WAIS.

1.2 The Cenozoic Evolution of Antarctica's Ice Sheets

A brief overview of the current state of knowledge regarding how Antarctic's ice sheets have waxed and waned through the Cenozoic is provided below. A much more detailed history can be found in the recent edition of Antarctic Climate Evolution (Florindo et al., 2021).

Most of Antarctica was covered by temperate forest during the Cretaceous with no evidence for extensive ice coverage (Kennett and Barker, 1990; Klages et al., 2020). Conditions likely remained too warm for a continental-scale ice sheet throughout most of the Eocene (Pross et al., 2012; Galeotti et al., 2016). It is, however, possible there were at least some alpine glaciers present in high mountains in East Antarctica (Rose et al., 2013), which may have reached the ocean in the late Eocene (Gulick et al., 2017; Carter et al., 2017).

The first widespread evidence for major ice sheet growth did not occur until the Eocene-Oligocene boundary (e.g. Ehrmann and Mackensen, 1992; Escutia and Brinkhuis, 2014). The Eocene-Oligocene transition is accompanied by a large deep-water oxygen isotope excursion, attributed to global cooling and substantial ice-sheet growth in Antarctica (Zachos et al., 2008). Evidence for marine-terminating glaciers around East Antarctica is found through the Oligocene (33.9-23.8 Ma) (Galeotti et al., 2016; Kulhanek et al., 2019; Levy et al., 2019). However, drill core records from the Oligocene are somewhat sparse and often insufficient to distinguish the full extent of glaciation (Florindo et al., 2021). As well as an EAIS, glacial features in seismic data suggest there were likely West Antarctic marine-terminating glaciers in the Oligocene (Sorlien et al., 2007). Early West Antarctic glaciation would have been facilitated by a higher topography enhancing elevation/mass balance feedbacks (Wilson et al., 2013; Paxman et al., 2019a).

The beginning of the Miocene saw a major transient period of ice sheet growth and a drop in atmospheric CO_2 concentrations (Miller et al., 1991; Greenop et al., 2019). Relatively cold conditions characterised the rest of the Early Miocene, with ice sheet extent fluctuating in response to orbital forcing (Levy et al., 2019). The extent of these ice sheets is uncertain, with seismic data that is difficult to interpret (Pérez et al., 2021). Chapter 2 discusses new evidence constraining Early Miocene ice sheet history (Marschalek et al., 2021).

The end of the Early Miocene and earliest Middle Miocene (~17-14.5 Ma) comprises the Miocene Climatic Optimum (MCO), widely regarded as the warmest period since the Eocene (Shevenell et al., 2008). This saw a substantial loss of ice in Antarctica (Miller et al., 2020), and elevated atmospheric CO_2 concentrations compared to before and after the event (Rae et

al., 2021). Its warmth makes this period a potential proxy for future conditions in Antarctica. Retreat of the EAIS is recorded in the Ross Sea region (Levy et al., 2016). At ~14 Ma, the MCO was followed by a persistent cooling trend, known as the Middle Miocene Climate Transition. This saw the development of ice sheets extending into the ocean in both East and West Antarctica (De Santis et al., 1995; Lewis et al., 2008; Pierce et al., 2017), although ice cover may not have been complete at times, as indicated by pollen records (Sangiorgi et al., 2018).

Late Miocene (11.63-5.33 Ma) ice proximal records are rare, but low latitude records suggest repeated Antarctic glaciations (Miller et al., 1991). Kennett and Barker (1990) suggest this period may have seen the first advance of a large, marine-based WAIS, although Chapter 2 discusses evidence that this may have occurred much earlier. A further cooling trend at 7 to 5.4 Ma (Herbert et al., 2016) is reflected in evidence for cooler conditions in Antarctica (e.g. Larter et al., 1997; Rosenblume and Powell, 2019).

The Pliocene (5.33-2.58 Ma) provides a relatively recent period with climatic conditions comparable to those expected in the near future. Conditions were warmest in the early to middle Pliocene, when obliquity-paced oscillations of the Antarctic ice sheets occurred (Naish et al., 2009). Interglacial periods were characterised by retreated ice sheets (Cook et al., 2013) leading to high sea levels (Grant et al., 2019; Miller et al., 2020), reduced glacial meltwater in the ocean (McKay et al., 2009), and warm sea surface temperatures (Riesselman and Dunbar, 2013). Glacial periods saw ice sheet expansion to the edge of the continental shelf (Bart, 2001). A general cooling trend towards the end of the Pliocene is recorded in low latitude records (e.g. Zachos et al., 2008; Millar et al., 2020; Westerhold et al., 2020). The late Pliocene glacial period ice sheets were also characterised by relatively thick ice in the interior, partially offsetting retreat around the ice sheet margins (Yamane et al., 2015).

The Pleistocene saw the continuation of earth's climatic transition into an increasingly glacial state. Low latitude records of deep-sea temperature and ice volume begin to represent substantial Northern Hemisphere ice sheet fluctuations (Westerhold et al., 2020). A transition from obliquity-dominated to eccentricity-dominated pacing of glacial cycles, known as the Mid Pleistocene Transition, occurred at ~1.25-0.70 Ma (Maasch, 1988). A reduced Antarctic ice volume compared to the modern ice sheet is likely during the warmest Pleistocene interglacial periods, such as the Last Interglacial, with sea levels 6-9 m higher than today (Dutton et al., 2015). However, the Antarctic contribution to this sea-level rise is uncertain.

WAIS collapse in Pleistocene interglacials has yet to be confirmed (Hillenbrand et al., 2002), despite far-field records indicating that ice volume loss may have required this (Dutton et al., 2015). Furthermore, marine-based sectors of the EAIS may have retreated in warm interglacials (Wilson et al., 2018), but the extent of this retreat is subject to significant uncertainty (Golledge et al., 2021). The Antarctic contribution to periods of high sea level in the Pleistocene therefore remains a key focus of current research (Patterson et al., 2022).

Pleistocene glacial periods saw advance of ice to the edge of the continental shelf around most of Antarctica, best recorded for the Last Glacial Maximum (LGM; The RAISED consortium, 2014). Ice sheet behaviour since the LGM is well documented (see review by Siegert et al., 2021), but is beyond the scope of this thesis.

1.3 Sediment Provenance as a Tool for Investigating Ice Sheet History: Opportunities and Challenges

The Antarctic ice sheets' response to Cenozoic climate change and feedbacks between the ice sheets, climate and oceans are recorded in sediments deposited around the continent. One method of investigating Antarctica's past is tracing the provenance of marine sediments to their constituent rocks on land. This can be used to infer where an ice sheet was eroding, thus changes to ice flow and ice sheet extent. Identifying the rocks contributing to sediments deposited offshore of Antarctica benefits from the mixture of grain sizes present in glacial sediments, which allows for the application of various provenance techniques (Licht and Hemming, 2017). Different provenance proxies provide different and complimentary information on which rocks on the continent are present in marine samples; studies involving multiple provenance proxies can therefore offer more insight into past ice sheets and more robust conclusions (e.g. Cook et al., 2017; Licht and Hemming, 2017; Marschalek et al., 2021).

By understanding the fingerprint of the surrounding terrestrial geology, this information can be related to where the sediments were originally eroded from. This can in turn be used to infer where erosion was taking place at the time the sediments were deposited. As ice sheets typically erode more where ice is flowing more quickly, which is often the case closer to the grounding zone, sediment provenance changes offshore can suggest retreat of the ice sheet margin (e.g. Cook et al., 2013). In this way, tracing the provenance of glaciogenic sediments offers otherwise unobtainable insight into past ice flow patterns, advancing understanding of

ice sheet response to environmental change (Cook et al., 2013; Bertram et al., 2018; Wilson et al., 2018; Marschalek et al., 2021).

However, converting provenance interpretations from a sedimentary record into inferences about ice sheet flow as outlined above is never simple. There are a variety of complicating factors, including:

- **Iceberg rafting** – icebergs can travel in the clockwise-flowing Antarctic Circumpolar Current and anticlockwise-flowing Antarctic Coastal Current thousands of miles from where they calved. This can transport sediment far from its continental source region.
- **Uncertain geology** – >99% of Antarctica is covered by ice, meaning it is often difficult to constrain where a diagnostic rock type may be originating from. Sediment provenance around Antarctica is therefore by necessity an iterative process, revealing new information about the subglacial geology (e.g. Simões Pereira et al., 2018).
- **Uniform geology –** in some regions, geology can be uniform, or have extremely similar provenance characteristics. This fundamentally limits the resolution that can be obtained by studying provenance, although applying multiple proxies can minimise this effect (Licht and Hemming, 2017).
- **Preferential erosion of different rock types** – Ice does not erode evenly regardless of rock type, with geological factors controlling the erosion rate (Dühnforth et al., 2010; Iverson, 2012) and the onset of fast ice flow (Bell et al., 1998). Certain lithologies can therefore contribute preferentially to sediment provenance signatures.
- **Reworking** – Sediments deposited on the Antarctic continental margin are frequently removed and transported to more distal settings as ice sheets grow. This can lead to more homogenous sediment, reducing the amplitude of provenance fluctuations.
- **Processes of weathering, erosion, entrainment and transport beneath ice sheets -** Despite decades of intensive research, our understanding of how ice sheets erode subglacial bedrock remains poorly understood (Alley et al., 2019). Furthermore, changes to the basal conditions of the ice sheet, such as faster basal velocities, can influence where erosion is occurring, leading to provenance change without ice sheet margin retreat (Wilson et al., 2018; Golledge et al., 2021). This

results in difficulty converting changes to erosion recorded by sediment provenance reconstructions into changes to ice sheet form and flow.

These limitations do not lessen the valuable contributions of sediment provenance studies to understanding of past Antarctic glaciation; they are, however, necessary considerations when interpreting results. Chapter 3 attempts to account for some of these uncertainties to make more quantitative predictions of ice sheet volume, whilst Chapters 4, 5 and 6 aim to improve knowledge of uncertain subglacial geology beneath the WAIS.

1.4 Provenance Tracing Techniques

This thesis uses various methods to identify the source rocks comprising sediments offshore, including clay mineralogy, clast petrography, major and trace element geochemistry and $^{40}Ar/^{39}Ar$ dating of detrital hornblende grains. However, the principal methods employed (and measured personally) are the long-lived radiogenic isotope compositions of neodymium (Nd) and strontium (Sr), and uranium-lead (U-Pb) dating of detrital zircons. A very brief overview of these isotope systems is provided below.

1.4.1 Radiogenic Nd and Sr Isotopes

The decay of ^{147}Sm (Sm = samarium) to ^{143}Nd occurs with a half-life of 106 billion years and the decay of ^{87}Rb (Rb = rubidium) to ^{87}Sr has a half-life of 48.8 billion years. These long-lived radioactive decay systems can be utilised by isotope geochemists for a variety of applications. When extracted from the mantle, Nd and Rb preferentially enter the melt phase relative to the solid phase, which becomes enriched in Sm and Sr. Continental rocks formed from partial melts therefore have a lower Sm/Nd and higher Rb/Sr ratio than the mantle. The respective depletion and enrichment of these parent isotopes (^{147}Sm and ^{87}Rb) means that as they decay, continental rocks accumulate less ^{143}Nd and more ^{87}Sr over time compared to the mantle. Because elemental concentration can vary significantly, the accumulation of these radiogenic isotopes is measured relative to the stable isotopes ^{144}Nd and ^{86}Sr. As negligible fractionation of Sm and Nd are thought to have occurred during the Earth's formation, their relative abundances are assumed to be chondritic and are compared to the chondritic uniform reservoir (CHUR; Jacobsen and Wasserburg, 1980). The relatively low abundance of the parent isotope means the $^{143}Nd/^{144}Nd$ ratio of a continental rock will fall over time compared to the CHUR. In contrast, $^{87}Sr/^{86}Sr$ ratios are typically compared to the bulk silicate earth, and in a continental rock will rise over time relative to this due to ^{87}Rb enrichment. In this way,

the measured $^{143}Nd/^{144}Nd$ or $^{87}Sr/^{86}Sr$ ratio of a rock will broadly reflect both the initial composition of the partial melt and the time since separation from the mantle (Goldstein and Hemming, 2003). The $^{143}Nd/^{144}Nd$ ratio is typically reported in epsilon notation – i.e. relative to CHUR in parts per 10000:

$$\varepsilon_{Nd} = \left(\frac{(143_{Nd}/144_{Nd})_{sample}}{(143_{Nd}/144_{Nd})_{CHUR}} - 1\right) \times 10^4 \qquad (1.1)$$

1.4.2 Zircon U-Pb Dating

The U-(Th-)Pb dating method benefits from three radiogenic Pb isotopes: ^{206}Pb, ^{207}Pb and ^{208}Pb. These form from the radioactive decay of ^{238}U, ^{235}U and ^{232}Th, respectively. Whilst the Th-Pb system has useful applications, the U-Pb dating system is most widely used and is unique in that there are two parent-daughter pairs. These have different half-lives - 4.47 billion years for the decay of ^{238}U to ^{206}Pb and 0.71 billion years for the decay of ^{235}U to ^{207}Pb - giving different precision over different timescales. Furthermore, these two decay systems can be compared to check they give the same age, known as concordance. This provides an in-built test to ensure other complicating factors, such as metamorphism, have not influenced calculated ages. Zircon is an excellent mineral to apply the U-Pb method to as it incorporates U during crystal growth but rejects Pb. This means that any Pb present can be attributed to radioactive decay, although common Pb (i.e. primordial Pb in the crystal) can be corrected for and may be significant if the grain is particularly young with a low radiogenic Pb content (Andersen, 2002). Zircon grains are also very hard and resistant to weathering, meaning they can persist following erosion, even over multiple cycles of erosion and redeposition.

1.5 Erosion Beneath Ice Sheets

The methods described above can offer powerful insight into sediment provenance, which can be used to construct records documenting where erosion was occurring in the past. However, the location where most erosion was taking place does not translate directly to ice sheet extent. Although erosion rate is often assumed to scale with sliding velocity (e.g. Jamieson et al., 2008; Aitkin and Ursovec, 2021), which usually increases towards the ice sheet margin, various other factors such as climate and glacial thermal regime strongly affect erosion rates (Koppes et al., 2015). This means glaciers can erode at remarkable range of rates. Near pristine pre-glacial landscapes have been preserved for millions of years in the centre of the EAIS (Rose et al., 2013), whilst some of the most rapid erosion rates in nature – up to 10^{-1} m a^{-1} – have been observed in Alaska (Hallet et al., 1996). Combined with the

inaccessibility of the subglacial environment, this heterogeneity has resulted in the processes of glacial erosion being poorly understood despite the significant research effort into the subject (Alley et al., 2019). Erosive processes are nevertheless vital for converting sediment provenance information into interpretations of ice sheet behaviour; I therefore provide a very brief overview of erosion by ice sheets.

The lowest glacial erosion rates are found in regions where the bed is below pressure melting point. In these regions, there is no basal slip, so the ice is not transported away and there is no flowing water to remove detritus. Erosion rates are therefore extremely low in these parts of ice sheets, although potentially significant on geological timescales (Cuffey et al., 2000).

Far faster erosion can occur where there is basal slip and liquid water present at the ice sheet bed. Liquid water at the bed of the modern Antarctic ice sheet is primarily generated from the melting of basal ice. This water travels from areas of higher hydrostatic potential towards the ice sheet margin, sometimes uphill. Flow occurs through channelised networks, as well as through the till (Christofferson et al., 2014). Water is stored in subglacial lakes, which can episodically drain (Wingham et al., 2006). Primarily, the presence of liquid water allows the detritus generated to be moved away from the site and expose fresh bedrock, either entrained in basal ice sliding over the thawed bed or in subglacial streams (Alley et al., 2019). Removal of till is critical for the generation of new sediment, as where a mantle of till is present, this will deform and shield the underlying rock (Alley et al, 2019). Many modelling studies incorporate this effect into equations governing erosion (Pollard and DeConto, 2003; 2020; Golledge et al., 2013).

The requirement for liquid water at the ice-sediment interface to achieve erosion at faster rates of 10^{-4} to 10^{-2} m a^{-1} (Alley et al., 2019) demonstrates the importance of glacial thermal regime. Thermal regime in turn is influenced by climate and this effect is clear when comparing erosion rates in the Patagonian Andes (10^{-3} to 10^{-2} m a^{-1}) and the Antarctic Peninsula (10^{-4} to 10^{-5} m a^{-1}) (Koppes et al., 2015). Although effects such as surface meltwater penetration to the ice sheet bed are not relevant in present day Antarctica, warmer conditions in the past at times may well have resulted in surface melt. The potential for such processes should therefore be considered when studying past Antarctic ice sheets.

A factor often not considered when discussing glacial sedimentation and provenance is the height of detritus in the ice column (Licht and Hemming, 2017). This is a key control on how far debris is transported once it reaches an area of net melt, such as in an ice shelf cavity or in

an iceberg. Height of debris is controlled by the vertical motion within the ice column, in turn influenced by basal melt/freezing and changes to the local stress field (e.g. compression as tributaries converge, extension as ice accelerates). Shearing of basal ice can elevate basal debris, but water freezing onto the bed is perhaps most important (e.g. Christoffersen et al., 2010; Hooke et al., 2013). Furthermore, the transition zone between a thawed and frozen bed may be key for sediment entrainment, with repeated melting and freezing promoting debris entrainment (Winter et al., 2019). The height of debris in the ice column can also be persevered where there is low basal shear stress, such as in settings with deforming till, as new debris is unlikely to be generated leading to longer transport distances (Licht and Hemming, 2017). These complexities mean debris elevation in the ice column, thus sediment transport distances, are very difficult to predict (Hooke et al., 2013).

Despite the uncertainties regarding debris generation and transport beneath ice sheets, such processes are fundamentally linked to sediment provenance records and should be considered when making interpretations.

1.6 Thesis Aims and Structure

Determining the necessary emissions reductions and mitigation strategies to avoid serious societal perturbation from to anthropogenic climate change is dependent on accurately predicting future sea-level rise (Pörtner et al., 2019). Accelerating mass loss from the marine-based West Antarctic Ice Sheet (WAIS) has the potential for raising sea-level at rates and by amounts which would be disastrous for low-lying cities and nations (Hinkel et al., 2018).

This thesis aims to improve reconstructions of the West Antarctic Ice Sheet (WAIS) through geologic time, helping refine and test numerical models which are used to predict sea-level rise. This overall goal will be achieved through three routes:

1) Providing a new sediment provenance reconstruction from the Early Miocene, constraining the sea-level rise potential of the early WAIS (Chapter 2).
2) Pioneering a framework to help convert sediment provenance records into quantitative predictions of ice-sheet volume (Chapter 3).
3) Improving knowledge of the subglacial geology of West Antarctica, thus the likely provenance change resulting from WAIS collapse (Chapters 4, 5 and 6).

The main chapters comprising this thesis are summarised as follows:

Chapter 2 presents new sediment provenance records from International Ocean Discovery Program (IODP) Expedition 374 Site U1521. Provenance datasets include detrital Nd and Sr isotopes, zircon U-Pb dates, clast petrography, clay mineralogy and hornblende $^{40}Ar/^{39}Ar$ dates. These data are placed in an environmental context by developing an age model for the site and comparing the provenance data to palynological data and regional seismic stratigraphy. These datasets together show that a WAIS extending over much of the continental shelf existed in the Early Miocene, millions of years earlier than previously proven. This has important implications for the Cenozoic history of Antarctic glaciation and advances knowledge of the conditions required for a large WAIS to exist. Assuming relative sea-level change amplitude estimates are correct, a large volume WAIS in colder Early Miocene intervals would suggest that the warmest periods of the Miocene Climatic Optimum retained some ice on East Antarctica.

Chapter 3 develops the first framework for quantitatively estimating the sediment provenance signature expected for a modelled ice sheet configuration. The chapter focusses on the methods developed, which are first applied to the modern ice sheet. This allows the accuracy of the approach to be verified and parameters governing the marine transport of sediment to be calibrated to seafloor surface sediment measurements. The approach is then applied to selected palaeo ice-sheet model outputs to help match measured data offshore to likely ice sheet extent. This provenance tracing implies Pliocene records from the Wilkes Subglacial Basin record an ice-sheet retreat of up to 9.3 m sea-level equivalent total Antarctic ice volume.

Chapter 4 discusses data from new seafloor surface sediment samples collected from the Amundsen Sea Embayment, which help characterise the sediment provenance signature of Thwaites and Pine Island glaciers. The data reveal new information about the local geology and the spatial variability of Sr isotopes beneath Thwaites Glacier. The discovery of a new island between Thwaites and Pine Island glaciers elucidates the geological history of the bedrock in this previously unexposed region. The island shows geochemical characteristics similar to the Thurston Island and Antarctic Peninsula continental blocks and therefore represents the western-most exposure of this tectonic domain. The island also shows a different thermal history to island groups on the other side of Pine Island Bay, providing the first thermochronological evidence that Pine Island Glacier lies on a major structural feature. If representative of other nearby granites, the island may represent an isotopically novel endmember which can explain some of the isotopic variations seen in marine sediments.

Chapter 5 discusses insights into the subglacial geology of West Antarctica obtained from new analyses of subglacial debris from the Byrd ice core. Differences with depth in the ice column prove that the debris was entrained as the ice moved over different parts of the bed and not in a single freeze-on event. Sand grain textural analyses suggest the debris contains reworked sediments. The debris may record the basal ice travelling from an area richer in smectite and with thin sedimentary cover comprised of coarser grain-sizes to an area covered by fine-grained sediments derived from felsic protoliths. Clay mineralogy reveals a very high kaolinite content, implying pre-glacial sedimentary rocks are present nearby. A rhyolite porphyry clast dated to the Triassic provides a sample of the early Mesozoic rocks inferred to exist beneath the WAIS that were previously unanalysed. The Nd and Sr isotope data reveal that rocks with relatively high ε_{Nd} values and low $^{87}Sr/^{86}Sr$ exist beneath at least some of the ice sheet, which may provide an isotopic endmember with these characteristics that reaches marine sediments without the need for widespread Cenozoic volcanic rocks controversially hypothesised to exist beneath the WAIS. Together, these datasets help suggest the sediment provenance signature that might be expected if the ice-sheet margin was to retreat inland.

Chapter 6 presents data from four new sites beneath the Ross Ice Shelf, helping identify the signature of debris generated beneath different parts of the WAIS. Samples from near the grounding zones of Kamb and Whillans ice streams reveal the homogeneity of till beneath the lower trunks of these ice streams, suggesting either homogenous underlying geology or little generation of new till in their lower reaches. A seafloor surface sample from west of Kamb and Whillans ice streams (J9) reveals mixing of the detritus coming from each ice stream, likely recording their centennial cycles of stagnation and reactivation. Downcore samples from a core in the centre of the Ross Ice Shelf (HWD-2b) reveal substantial changes to sediment provenance over the record. The signature of the lowermost diamict does not match modelled ice flow line for the Last Glacial Maximum (LGM), suggesting that either the sediments record a later stage of deglaciation or that current numerical models do not accurately predict LGM ice flow in the centre of the Ross Ice Shelf.

Chapter 2. A Large West Antarctic Ice Sheet Explains Early Neogene Sea-Level Amplitude

This chapter is modified from the supplement and main text of: **Marschalek, J.W.,** Zurli, L., Talarico, F. van de Flierdt, T., Vermeesch, P. … & McKay, R.M. (2021). A large West Antarctic Ice Sheet explains early Neogene sea-level amplitude. *Nature* 600, 450–455. https://doi.org/10.1038/s41586-021-04148-0. This paper is attached as a supplement to this thesis (Section A.2). Modifications included integration of the supplement sections into relevant parts of the main text of the paper, including the supplementary methods. Furthermore, an extra figure (Fig. 2.9) and a small amount of additional discussion (particularly Section 2.8.4) was added.

Contributions: James Marschalek led the project, and the text was written with input from all of the contributors mentioned below. James Marschalek, Tina van de Flierdt and Rob M. McKay designed the project. James Marschalek and Tina van de Flierdt compared and interpreted the sediment provenance data. James Marschalek, Pieter Vermeesch and Andy Carter collected and processed the zircon U-Pb data. James Marschalek collected the Nd and Sr isotope data with assistance from Patric Simões Pereira, Katharina Kressing and Barry Coles. Luca Zurli, Franco Talarico and Matteo Perotti performed the clast identification and counts and interpreted these data. Francois Beny and Viviane Bout-Roumazeilles collected and helped interpret the clay mineral abundance data. Lara F. Pérez, Florence Colleoni and Laura De Santis calculated the sediment volume estimate. Francesca Sangiorgi, Joe Prebble and Christina Boshuis collected and interpreted the palynological data. Sidney R. Hemming analysed the hornblende grains for Ar-Ar dates. Tim E. van Peer, David Harwood, Nick B. Sullivan, Steve R. Meyers and Elizabeth M. Griffith helped define the age model for the site, which was compiled by Richard Levy and James Marschalek. Ed Gasson and Benjamin Keisling helped contextualise the data with respect to ice sheet modelling results. Denise K. Kulhanek provided the XRF data. Amelia E. Shevenell, Imogen Browne, Claus-Dieter Hillenbrand, Martin J. Siegert, Kathy J. Licht, Gerhard Kuhn and Justin E. Dodd provided input on specific technical aspects of the text.



A typical section of the Early Miocene diamict comprising the lower part of the IODP Site U1521 record.

Chapter Abstract

Early to Middle Miocene sea-level oscillations of approximately 40-60 m estimated from far-field records (Pekar and DeConto, 2006; Kominz et al., 2016; Miller et al., 2020) are interpreted to reflect the loss of virtually all East Antarctic ice during peak warmth (Miller et al., 2020). This contrasts with ice-sheet model experiments suggesting most terrestrial ice in East Antarctica was retained even during the warmest intervals of the Middle Miocene (Gasson et al., 2016; Paxman et al., 2020). Data and model outputs can be reconciled if a large West Antarctic Ice Sheet (WAIS) existed and expanded across most of the outer continental shelf during the Early Miocene, accounting for maximum ice-sheet volumes.

This chapter presents the earliest geological evidence proving large WAIS expansions occurred during the Early Miocene (~17.72-17.40 Ma). Geochemical and petrographic data show glacimarine sediments recovered at International Ocean Discovery Program (IODP) Site U1521 in the central Ross Sea derive from West Antarctica, requiring the presence of a WAIS covering most of the Ross Sea continental shelf. Seismic, lithological and palynological data reveal the intermittent proximity of grounded ice to Site U1521. The erosion rate calculated from this sediment package greatly exceeds the long-term mean, implying rapid erosion of West Antarctica. This interval therefore captures a key step in the genesis of a marine-based WAIS and a tipping point in Antarctic ice sheet evolution. The chapter also discusses the provenance of the other sediments present in the lower part of IODP Site U1521, which record the retreat of ice in the Miocene Climatic Optimum.

2.1 Introduction

Reconstructing past Antarctic ice sheet change informs predictions of the continent's contribution to future sea-level rise (Masson-Delmotte, 2013; Kennicutt et al., 2014). Since the 1970s, drilling efforts proximal to Antarctica have revealed the general Cenozoic evolution of Antarctic glaciation (Barrett, 1975; Kennett, 1977; Passchier and Krissek, 2008; Levy et al., 2016), but fundamental steps in the development of the ice sheets remain poorly constrained. One key uncertainty is the timing of West Antarctic Ice Sheet (WAIS) initiation and expansion across the outer continental shelf. Deep-sea benthic foraminifer oxygen isotope records and Antarctic abyssal plain sedimentary sequences suggested WAIS formation occurred in the Late Miocene or early Pliocene (Kennett and Barker, 1990; Zachos et al., 2001). However, drilling from the Antarctic margin (Hauptvogel and Passchier, 2012; Levy et al., 2016; 2019) and ice-sheet modelling studies (Gasson et al., 2016, Colleoni et al., 2018; Paxman et al., 2020) have raised the possibility that WAIS expansions into areas below sea-level could have occurred during the Early Miocene or earlier, facilitated by a subaerial West Antarctic topography (Wilson et al., 2012; Paxman et al., 2019a).

Without widespread WAIS expansions across the continental shelf in the Early Miocene, maximum ice volumes are low enough that global sea-level fluctuations of ~40-60 m estimated from far-field stratigraphic records (Kominz et al., 2016) and oxygen isotope-derived ice volume estimates (Pekar and DeConto, 2006; Miller et al., 2020) require the near complete loss of the East Antarctic Ice Sheet (EAIS) during the warmest Middle Miocene periods (Miller et al., 2020). Such an outcome is incompatible with current ice-sheet model outputs, which suggest retention of most terrestrial East Antarctic ice even during the warmest feasible Middle Miocene environmental conditions (Gasson et al., 2016). This is mainly due to hysteresis effects driven by height-mass balance feedbacks; once the ice sheet is present, parts of it can be retained in a climate warmer than that which would permit ice-sheet inception on an ice-free landscape (Gasson et al., 2016; Gasson and Keisling, 2020).

Marine sediments, deposited on the continental shelf of the Ross Sea, can reveal whether the WAIS expanded across the continental shelf during the Early Miocene. However, ice proximal geological records have been hampered by poor recovery, unconformities, and/or influence from East Antarctica (Barrett, 1975; Passchier and Krissek, 2008; Levy et al., 2016). Seismic data suggest that significant volumes of lower Miocene glacimarine sediment exist around the West Antarctic margin (Anderson and Bartek, 1992; DeSantis et al., 1995;

Gohl et al., 2013a; Pérez et al., 2021). However, seismic data require constraints from drilling to determine the age of the sediments, and to differentiate between detritus from continental-scale ice-sheet expansion and local ice caps on (paleo)topographic highs (Gohl et al., 2013a; Pérez et al., 2021). Consequently, WAIS grounding across the Ross Sea shelf is only clear in seismic data after the Middle Miocene Climate Transition (~14 Ma) (Bart, 2003; Chow and Bart, 2003); it remains uncertain whether there were earlier WAIS expansions across the Ross Sea shelf.

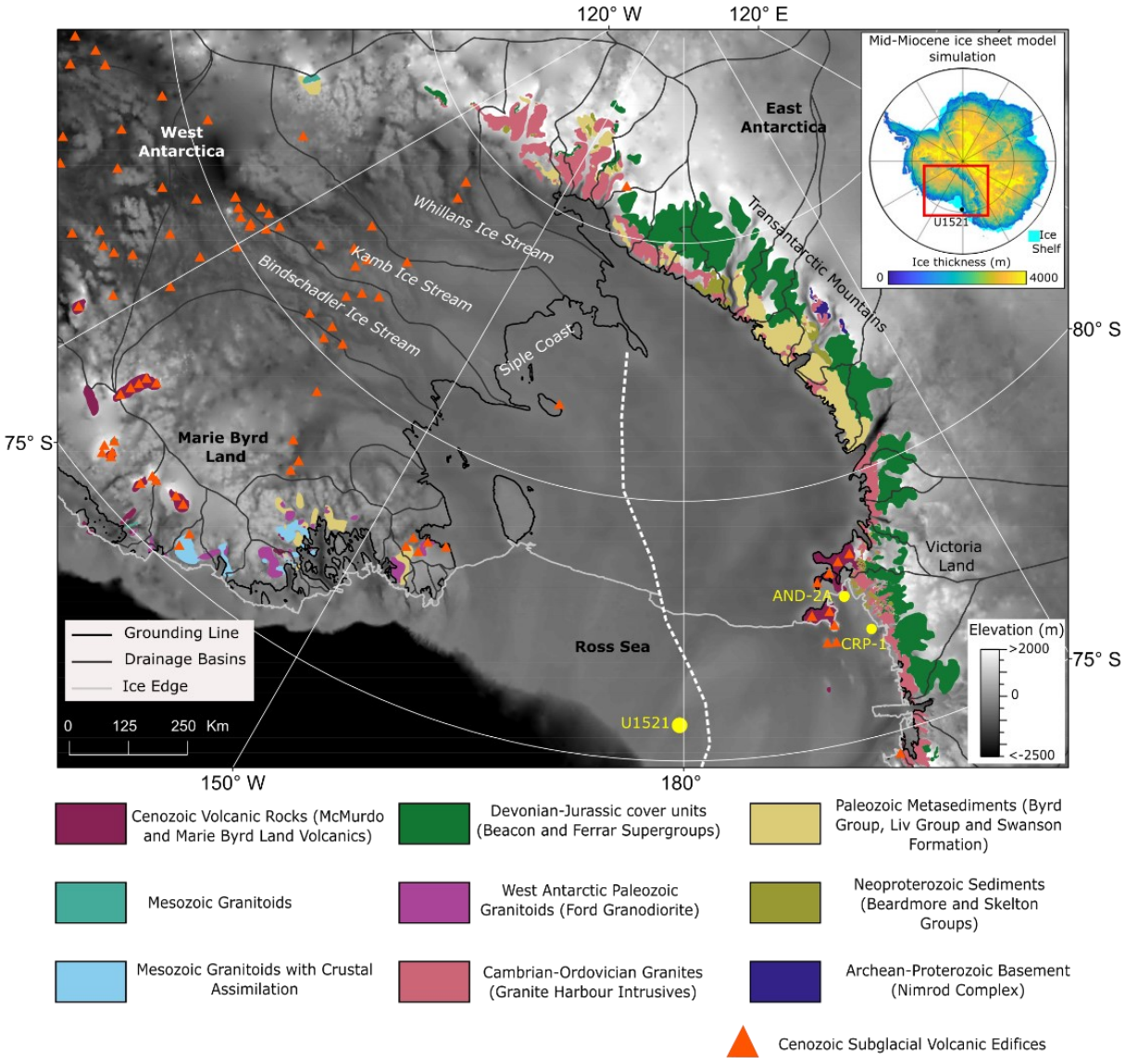


Figure 2.1. *Site U1521 location and surrounding geology. The outcropping regional geology (Cox et al., 2019) around the Ross Sea is overlain on the BedMachine Antarctica V1 modern bed topography (Morlighem et al., 2020). The MEaSUREs grounding line, ice sheet margin and basins are used (Rignot et al., 2013; Mouginot et al., 2017). IODP Site U1521 is located on the outer continental shelf of the central Ross Sea. Locations referenced in the text are*

labelled, including the ANDRILL 2A (AND-2A) and Cape Roberts Project 1 (CRP-1) drill sites. The white dashed line indicates the boundary between East and West Antarctic lithosphere (Tinto et al., 2019). Orange triangles show Cenozoic subglacial volcanic edifices detected based on morphological characteristics, gravity anomalies and magnetic anomalies (van Wyk de Vries et al., 2017). The inset shows an ice-sheet model simulation using a 'cold' climate ('cold' orbit and a climate with 280 ppm atmospheric CO_2 concentrations) and an estimated Middle Miocene topography (Gasson et al., 2016). Provenance indicators from Site U1521 Sequence 2 sediments are broadly consistent with an ice sheet similar to or exceeding the extent of this model output.

2.2 IODP Site U1521 and Provenance Approach

IODP Expedition 374 Site U1521 (75°41.0' S, 179°40.3' W; 562 m water depth) was drilled to 650.1 metres below sea floor (mbsf) in the Pennell Basin on the outer continental shelf of the Ross Sea (Fig. 2.1). The site was drilled in a region that ice-sheet models indicate is one of the last locations where ice grounds during glacial maxima, making it an ideal location to assess the timing of past WAIS expansions onto the outer continental shelf (Gasson et al., 2016; Colleoni et al., 2018; McKay et al., 2019). The sediments from the base of the borehole up to 209.17 mbsf are split into four chronostratigraphic sequences (1-4) which constitute an expanded lower Miocene section (~18 to ~16.3 Ma; Fig. 2.3) with 73% recovery. These sediments provide a unique window for detailed analysis of ice-sheet behaviour immediately before the onset of the Miocene Climate Optimum (MCO, ~17 Ma; Figs. 2.3, 2.7; Table 2.1).

Site U1521 sediments below 209.17 mbsf are predominantly muddy to sandy diamictites, often interbedded with thin laminae and beds of mudstone (McKay et al., 2019). Palynological counts on 23 samples revealed sparse palynomorphs in Sequences 1 and 4A, common reworked dinoflagellate cysts in Sequence 2, and evidence for high biological productivity in Sequence 3B (Fig. 2.10). These lithological and paleontological data from Sequences 1, 2, 3A and 4A indicate an ice-proximal glacimarine (and potentially subglacial) setting, while data from Sequence 3B suggest an ice-distal setting. Notably, the ~190 m thick succession of Sequence 2, containing a high proportion of reworked dinoflagellate cysts, was deposited rapidly (0.592 mm a^{-1}) within a ~317 kyr interval spanning ~17.72-17.40 Ma (Fig. 2.3).

Through comparison with terrestrial rock outcrops, the sediments recovered at Site U1521 were traced back to their source regions. A differing geological history of the rocks beneath

the EAIS and WAIS (Fig. 2.1; Section 2.3) gives the sediment eroded by each ice sheet a distinct geochemical, petrological and mineralogical composition, allowing expansions of the EAIS and WAIS to be distinguished. To avoid bias towards, or omission of, any lithologies, we applied multiple sediment provenance proxies (Licht and Hemmin, 2017). Specifically, we analysed the detrital fine fraction of 37 samples for neodymium (Nd) and strontium (Sr) isotope compositions (<63 μm) and 23 samples for clay mineralogy (<2 μm). Eight samples were also processed for U-Pb dating of detrital zircons (<300 μm) and five for $^{40}Ar/^{39}Ar$ dating of detrital hornblende grains (150-300 μm). Additionally, the petrological composition of 15,740 clasts >2 mm was identified down-core (Fig. 2.8).

2.3 Geological History of Antarctica

Interpretation of these provenance data requires an understanding of the petrology, age and geochemistry of potential source regions. A brief overview of the geology of the regions of Antarctica adjacent to the Ross Sea is therefore provided.

2.3.1 East Antarctica and the Transantarctic Mountains

Antarctica can be split broadly into Antarctica's two key tectonic provinces: East Antarctica, which has a history stretching back to the Archean (>2.75 Ga), and West Antarctica, which is largely Phanerozoic (<541 Ma) in age. More information can be found in recent reviews of West Antarctic (Jordan et al., 2020), East Antarctic (Boger et al., 2011) and Transantarctic Mountain (Goodge, 2020) geology, as well as references within these papers. To allow comparison between our new detrital zircon U-Pb and hornblende $^{40}Ar/^{39}Ar$ age data and the rocks present on land, published geochronological data are discussed (Fig. 2.2).

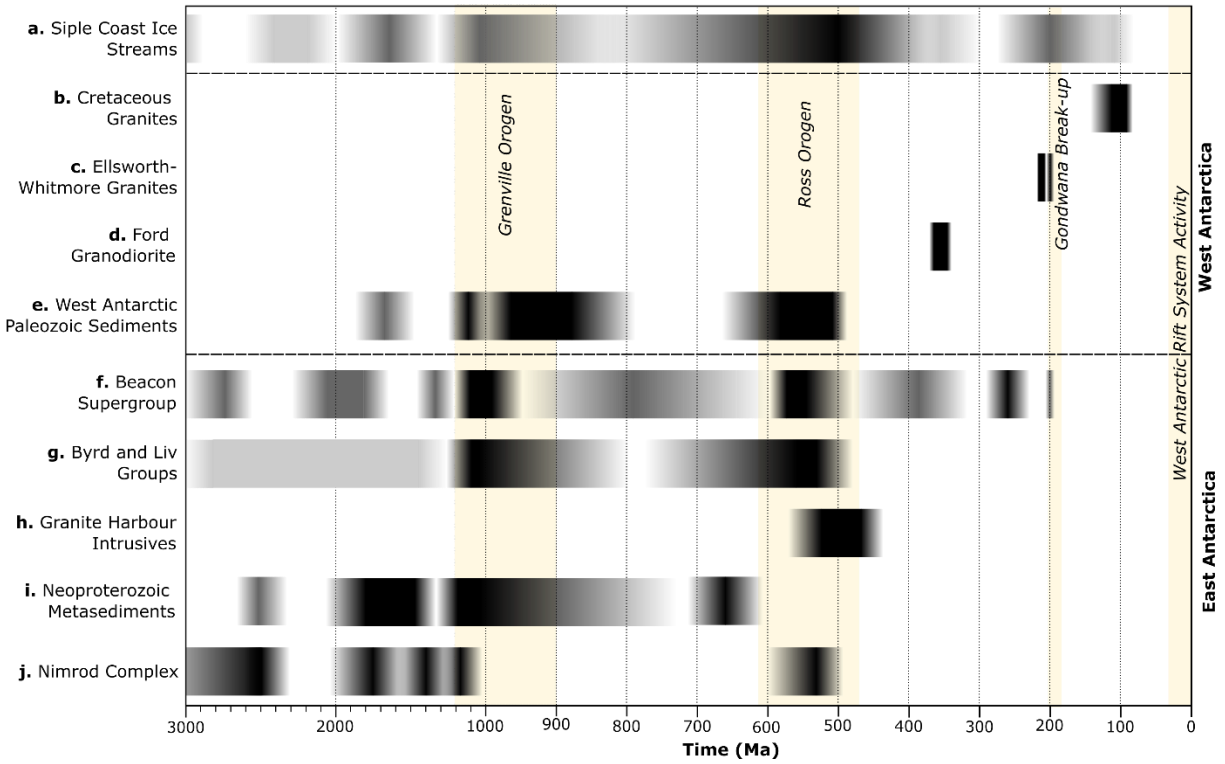


Figure 2.2 *Compilation of zircon U-Pb ages from the Ross Sea sector. Darker grey colours indicate more abundant ages and are qualitatively derived. References: (a) Licht et al. (2014); (b) Weaver et al. (1992), Mukasa and Dalziel (2000), Siddoway (2008), Korhonen et al. (2010); (c) Craddock et al. (2017); (d) Pankhurst et al. (1998), Korhonen et al. (2010); (e) Pankhurst et al. (1998), Flowerdew et al. (2007); (f) Elliot and Fanning (2008), Elliot et al. (2015); (g) Goodge et al. (2004), Paulsen et al. (2015) (and references within), Paulsen et al. (2018); (h) Goodge et al. (1993), Rowell et al. (1993), Van Schmus et al. (1995), Stump (1995), Encarnación, and Grunow (1996), Goodge et al. (2012), Paulsen et al. (2013), Martin et al. (2015); (i) Goodge et al. (2002), Stump et al. (2007), Cooper et al. (2011); (j) Goodge et al. (2001), Goodge and Fanning (2016).*

2.3.2 Precambrian East Antarctica

East Antarctica is composed of a mosaic of several Archean to Mesoproterozoic cratons joined by Neoproterozoic fold belts (Boger, 2011; Veevers and Saeed, 2011). Although nearly entirely covered by ice, these rocks contribute to the sediments deposited in the Ross Sea, as evidenced by detrital zircon U-Pb ages as old as 3.35 Ga (Fig. 2.2). These grains could be relict cores in magmatic crystals or could be reworked, as Archean to Proterozoic detrital zircons are common in most sedimentary rocks in the Transantarctic Mountains (Fig. 2.2). However, Archean and Proterozoic ages could also derive from primary erosion of rocks

in the interior of East Antarctica. Archean rocks outcrop as the high-grade metamorphic and igneous units of the Nimrod Group in the Miller and Geologists ranges of the central Transantarctic Mountains (Fig. 2.1) (Grindley et al., 1964; Goodge and Fanning, 1999).

Further Precambrian exposures include Neoproterozoic metasediments varying from low to high metamorphic grade, which outcrop along the strike of the modern Transantarctic Mountains (Laird, 1991; Goodge et al., 2004; Stump et al., 2007). These rocks include the Beardmore Group (comprising of the Cobham and inland Goldie formations) of the central Transantarctic Mountains and the Skelton Group of Southern Victoria Land (Goodge et al., 2002). Lithologically, these units are made up of quartzites, slates, paragneisses, impure marbles, calc-silicate schists and mica schists (Laird, 1991). In addition to these outcrops, Precambrian rocks are likely present beneath the ice inland of the Transantarctic Mountains. For instance, terranes of Grenville age (~1300-900 Ma) have been inferred by geophysical and detrital zircon data (Goodge et al., 2002; 2012; Goodge and Finn, 2010; Goodge and Fanning, 2010; Elliot et al., 2015). Zircons of Grenville age are reasonably common in younger meta-sedimentary (Neoproterozoic and Cambro-Ordovician) and sedimentary (Devonian-Jurassic) units (Fig. 2.2), as well as Ross Sea sediments (Fig. 2.11; Licht et al., 2014).

2.3.3 The Ross Orogeny

The Cambro-Ordovician Ross Orogeny was a period of continued tectonic activity from ~615 to 475 Ma linked to subduction along the Gondwanan margin (Goodge, 2020). This event caused metamorphism and widespread intrusion of calc-alkaline granitic batholiths known as the Granite Harbour Intrusive Complex along the entire length of the Transantarctic Mountains (Gunn and Warren, 1962; Rowell et al., 1993; Encarnación and Grunow, 1996; Goodge et al., 2012; Paulsen et al., 2013). In the southern Transantarctic Mountains, plutonism is associated with felsic volcanism (Van Schmus et al., 1995; Encarnación et al., 1999; Wareham et al., 2001). Ross Orogeny rocks are the main contributor to zircon populations in most Ross Sea sediments (Licht et al., 2014; Fig. 2.2; 2.11). Although the only known outcrops of intrusive bodies are younger than 550 Ma (Goodge et al., 2004; 2012; Paulsen et al., 2015), rocks deformed or emplaced during the Ross Orogeny likely extend for considerable distances beneath the East Antarctic Ice Sheet (Goodge and Finn, 2010; Goodge and Fanning, 2010; Elliot et al., 2015). Evidence for earlier (~615-550 Ma) intrusions includes a 590 Ma old glacially transported granitic pebble from the Nimrod Glacier (Goodge

et al., 2012), as well as abundant detrital zircons in the Beacon Supergroup sedimentary strata (Goodge et al., 2002; Flowerdew et al., 2007; Elliot and Fanning, 2008; Elsner et al., 2013; Elliot et al., 2016; 2017; Bader et al., 2017; Paulsen et al., 2017; Zurli et al., 2021) and many East Antarctic moraines (Licht and Palmer, 2013; Licht et al., 2014; Farmer and Licht, 2016; Welke et al., 2016; Bader et al., 2017).

The Ross Orogeny was accompanied by the deposition of sedimentary sequences along the Gondwanan margin. These sedimentary successions, locally associated with felsic volcanics, were affected by metamorphism soon after deposition (Laird, 1991; Wareham et al., 2001; Vogel et al., 2002; Goodge et al., 2004; Gootee and Stump, 2006; Paulsen et al., 2015; 2018). The Byrd Group and La Gorce Formation in the central and southern Transantarctic Mountains, respectively, record this Cambro-Ordovician deposition. The Byrd Group is represented by a platform carbonate, the Shackleton Limestone, cropping out between Byrd and Nimrod glaciers, and the siliciclastic Starshot Formation, made up of interbedded quartz dominated greywacke and dark pelite (Stump, 1995; Goodge et al., 2002; Goodge, 2020). The La Gorce Formation is lithologically comparable with the Starshot Formation (Goodge, 2020), and it is associated with the Liv Group, which consists of felsic porphyry and volcanoclastic rocks (Stump, 1995). Zircon U-Pb ages peak in both the Grenville and Ross orogens, with rare older grains in the Byrd Group (Fig. 2.2). Mica $^{40}Ar/^{39}Ar$ ages are limited to Ross Orogen grains (Goodge et al., 2004; Paulsen et al., 2015).

2.3.4 Beacon Sedimentary Rocks and Ferrar Magmatites

Following a prolonged period of erosion, the crystalline rocks described above were capped by 2.7-3.5 km of Beacon Supergroup sedimentary rocks deposited from the Devonian to the Early Jurassic (Barrett, 1991). These sedimentary strata are widespread along the Transantarctic Mountains, contain sedimentary facies and detrital compositions which vary widely over time, and likely extend far inland in some regions (Ferraccioli et al., 2009; Licht and Hemming, 2017; Welke et al., 2016; Paxman et al., 2019b; Fig. 2.1). By the latest early Jurassic, local explosive volcanism had become common across the Transantarctic Mountains, with thick breccia and ash beds occurring towards the top of the succession (Elliot, 1996; Elliot et al., 2016). Following this, crustal extension led to the Beacon Supergroup sedimentary rocks being intruded by the tholeiitic Ferrar large igneous province, adding approximately 1.5 km to the thickness of the sequence (Elliot and Fleming, 2004). Zircon U-Pb dating gives ages of 183-184 Ma for this event, which had a duration of less

than ~1 Myrs (Encarnación et al., 1996; Burgess et al., 2015). In the Ross Sea sector, the Ferrar Group is primarily comprised of intrusive dolerite sills and is the only exposed dolerite source for offshore sediments, implying dolerite clast abundance reflects the degree of Ferrar Group input to Ross Sea sediments (Fig. 2.7, 2.8). In addition, in Victoria Land and the central Transantarctic Mountains, large quantities of flood basalt were extruded onto the paleo-surface forming the up to 900 m thick Kirkpatrick Basalt (Elliot and Fleming, 2004). Ferrar Group rocks cropping out in the Transantarctic Mountains do not contain common zircon or hornblende grains large enough for dating when found in detrital offshore sediments (Cook et al., 2017).

2.3.5 West Antarctica

In contrast to the long history of East Antarctica, most of West Antarctica was formed between approximately 500 and 90 Ma in a convergent setting between Gondwana/East Antarctica and the Paleo-Pacific Ocean (Jordan et al., 2020). Grenville-age rocks are restricted to the Weddell Sea drainage basin (Jordan et al., 2020). However, rocks dating to the latter stages of the Ross Orogen are present in West Antarctica. These include early Palaeozoic metasediments found in the Ford Ranges of western Marie Byrd Land known as the Swanson Formation (Adams, 1986; Pankhurst et al., 1998). Temporal correlatives likely extend subglacially towards the Amundsen Sea and under much of West Antarctica (Siddoway, 2008). For instance, in the Whitmore Mountains, metamorphosed arkosic turbidite sequences are likely to be of similar age (Flowerdew et al., 2007). Zircon U-Pb age populations again have major peaks typical of the Ross and Grenville orogens, with rare older zircon ages. The Ross age peak is younger in the Whitmore Mountain sedimentary strata (~514 Ma; Flowerdew et al., 2007), but older in the Swanson Formation of the Ford Ranges (~550 Ma; Pankhurst et al., 1998; Yakymchuk et al., 2013; 2015).

In Marie Byrd Land, these metasedimentary rocks formed the country rock that was intruded by several pulses of Palaeozoic magmatic activity at 450-420 Ma, 375-310 Ma and 276 Ma (Korhonen et al., 2010; Pankhurst et al., 1998; Yakymchuk et al., 2013; 2015). These calc-alkaline granite and granodiorite plutons comprise the dominant outcrops in the Ford Ranges. Intrusion in West Antarctica linked to early extension during the Triassic is also likely based on detrital minerals (Licht et al., 2014; Perotti et al., 2017; Simões Pereira et al., 2018), although only a single ~200 Ma granite (the Mount Seelig Granite) outcrops in the Ross Sea catchment in the Whitmore Mountains (Craddock et al., 2017). Rocks of Triassic age may

therefore be more common beneath the West Antarctic Ice Sheet (WAIS) than exposures suggest (see Chapter 5).

Renewed magmatism and metamorphism in Marie Byrd Land occurred between approximately 128 and 94 Ma (Weaver et al., 1992; Mukasa and Dalziel, 2000; Siddoway, 2008; Korhonen et al., 2010). Outcrops of these granitoids extend from the Ford Ranges towards the Edward VII Peninsula and Ruppert and Hobbs coasts (Adams, 1987; Weaver et al., 1992; Mukasa and Dalziel, 2000). This Cretaceous activity was initially subduction-related but became rift-related following the beginning of crustal extension associated with the West Antarctic Rift System (Mukasa and Dalziel, 2000). Evidence for Cretaceous plutonism is not found in the Transantarctic Mountains; these zircon U-Pb ages are unique to West Antarctica (Licht et al., 2014). Subglacial till samples from three ice streams draining the Siple Coast region of the WAIS show Cretaceous zircons are only found beneath Kamb Ice Stream and ice streams located further east (Licht et al., 2014). This lack of distinctive West Antarctic ages and likely reworking of sediments originally shed from the Transantarctic Mountains means that detritus derived from the portion of the WAIS bordering the Transantarctic Mountains, such as Whillans Ice Stream, has an East Antarctic provenance (Fig. 2.11).

2.3.6 Cenozoic Volcanism

The development of volcanic centres in Marie Byrd Land and Victoria Land was linked to the development of the West Antarctic Rift System, with active volcanism continuing to the present day. Outcropping volcanoes are alkaline and largely basaltic in composition, although some felsic rocks are also present (LeMasurier et al., 1990). These can be broadly divided into the McMurdo Volcanic Group, found on the East Antarctic (western) side of the Ross Sea, and the Marie Byrd Land volcanic province on the West Antarctic (eastern) side. However, three more volcanoes erupted, probably subglacially, between 25 and 15 Ma further south in the Scott Glacier area (LeMasurier et al., 1990; Licht et al., 2018).

In Victoria Land, the McMurdo Volcanic Group is found along the flanks of the Transantarctic Mountains as well as offshore, with islands (Brodie, 1959) and numerous seamounts (Lawver et al., 2012) of volcanic origin. There is evidence for extrusive activity since the late Oligocene (Di Vincenzo et al., 2010), although outcropping rocks of Early Miocene age are limited to exposures at Mount Morning (Panter et al., 2018). Early Miocene exposures of the Marie Byrd Land volcanic province are well documented, with evidence of

activity since the late Eocene (McIntosh, 2000; LaMasurier and Rocchi, 2005; Rocchi et al., 2006). In Marie Byrd Land, early volcanism was largely basaltic and occurred further inland, moving to more felsic later volcanism that occurred in coastal regions (LeMasurier et al., 1990; LeMasurier, 2013). Magnetic anomalies suggest this province continues under the ice, with numerous subglacial volcanoes present (Behrendt et al., 1991; van Wyk de Vries et al., 2017; Fig. 2.1). All these Cenozoic volcanic rocks have extremely similar radiogenic Nd and Sr isotope ratios across the different regions (Table A.2.9).

2.4 IODP Site U1521 Age Model

A reliable age model is required to place the Site U1521 record in a global context. The age model for IODP Site U1521 uses magnetostratigraphy, biostratigraphy, cyclostratigraphy, $^{87}Sr/^{86}Sr$ dating of macrofossils, and $^{40}Ar/^{39}Ar$ ages of hornblende grains to correlate rock units to the Geomagnetic Polarity Timescale (GPTS; Ogg, 2020). Key events and tie points are summarized in Table 2.1 and illustrated in Figures 2.3 and 2.4. Biostratigraphic constraints include first and last appearance datums of diatoms. The maximum and minimum age range reported for these datums are derived from total and average ranges (Cody et al., 2008; Florindo et al., 2013) and hybrid range models derived from Constrained Optimization (CONOP) methods (Florindo et al., 2013; Crampton et al., 2016). Hybrid range model ages are used as primary constraints for our age model. This is because they best account for up section reworking of microfossil datums, which is common in glacial sedimentary environments, whilst recognising that major down section reworking is unlikely (partly because of the rarity of bioturbated intervals). They are marked by base of arrows in Figure 2.3 and mentioned in the text below. Biostratigraphic datums and magnetic polarity reversals provide tie points to construct lines of correlation (LOC) with the GPTS. The age model presented here includes the interval of West Antarctic sediment provenance (Sequence 2) and is described from the base of the borehole at 650 mbsf to 75 mbsf.

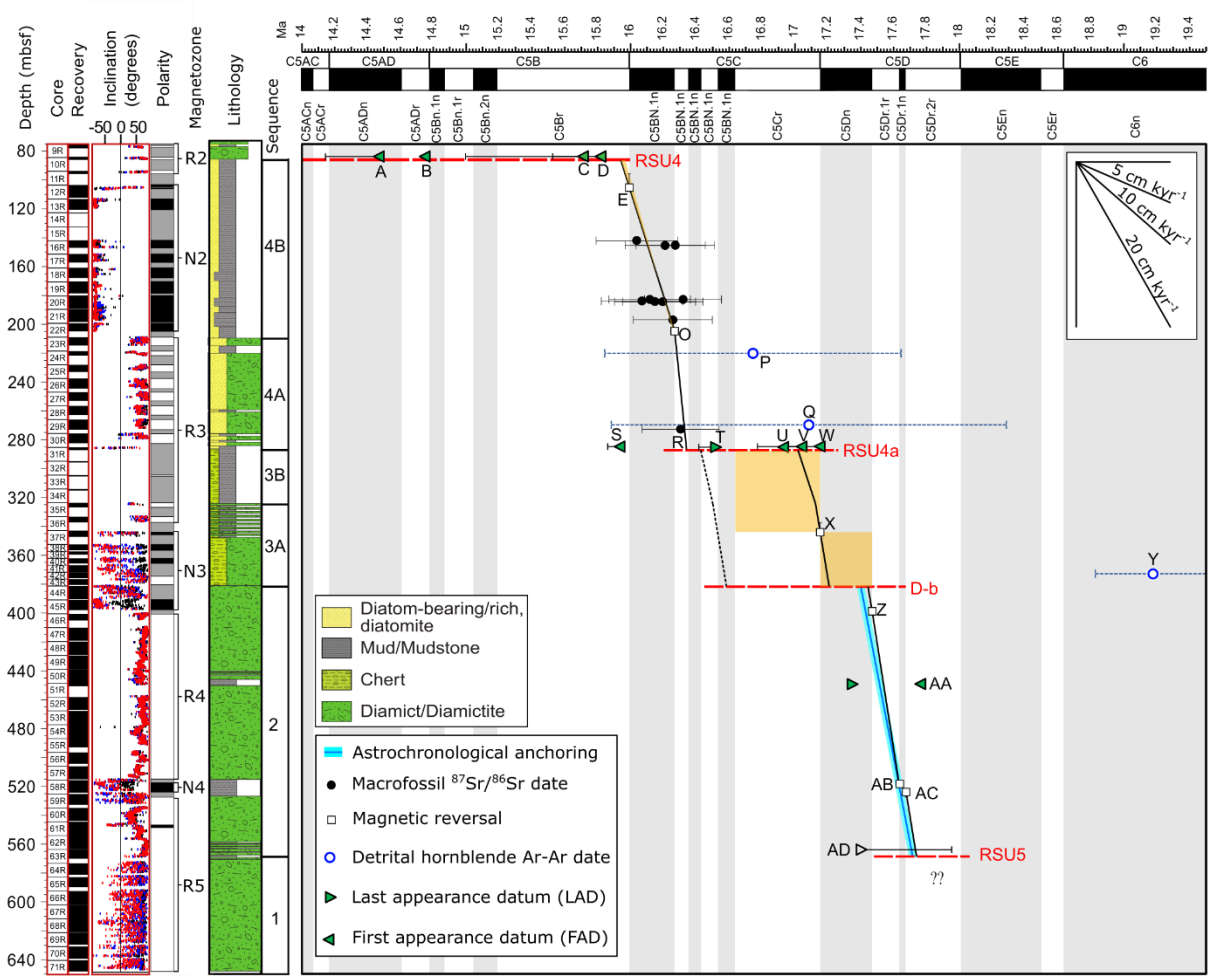


Figure 2.3. *Age model constraints below 75 mbsf at Site U1521. From left to right are: depth (metres below sea floor), core number, core recovery (black = recovered), inclination prior to and after 10 and 20 mT demagnetisation (black, blue and red points, successively), and corresponding polarity interpretations (black = normal, white = reversed, grey = no interpretation). Note that the polarity interpretations have been simplified compared to those in the cruise report (McKay et al., 2019), with small uncertainties related to core gaps removed. Note Site U1521 is in the Southern Hemisphere. The geomagnetic polarity timescale (Ogg, 2020) is shown across the top of the plot. The orange shaded regions indicate uncertainties in our age model and the dashed line marks an alternative line of correlation for Sequence 3. The blue line indicates the age model for Sequence 2 based on our astrochronological analyses, with the light blue shading indicating the ~20 kyr uncertainty associated with the phase relationship between clast abundances and obliquity. This astrochronological anchoring agrees closely with linear interpolations between magnetostratigraphic tie points (black line).*

Table 2.1. *Age model tie points at Site U1521. Reference numbers correspond to those in Marschalek et al. (2021): 11 = Levy et al., 2016; 23 = Pérez et al., 2021; 49 = Ogg, 2020, 88 = Cody et al., 2008; 89 = Florindo et al., 2013; 90 = Crampton et al., 2016; 93 = Farmer (2009).*

Depth (mbsf)	Depth Error	Event	Event Description	Type	Age (Ma)	Age Error	References	Notes
84.99	85.55	A	*Denticulopsis simonsenii*	FAD	14.48	14.14	89, 90	
84.99	85.72	B	*Denticulopsis hyalina*	FAD	14.76	14.73	89, 90	
84.99	85.55	C	*D. lauta*	FAD	15.72	14.99	89, 90	
84.99	85.55	D	*A. ingens*	FAD	15.83	15.52	89, 90	
85.34			RSU4	Unconformity	15.83-14.48		23	
105.9	± 0.4	E	C5Br/C5Cn.1n	MPR	15.994		49	
141.92		F	Shell Fragments	$^{87}Sr/^{86}Sr$ (Bivalve)	16.039	± 0.25		
145.135		G	Shell Fragments	$^{87}Sr/^{86}Sr$ (Bivalve)	16.211	± 0.24		
145.135		H	Shell Fragments	$^{87}Sr/^{86}Sr$ (Bivalve)	16.272	± 0.24		
182.7		I	Shell Fragments	$^{87}Sr/^{86}Sr$ (Bivalve)	16.117	± 0.25		
182.71		J	Shell Fragments	$^{87}Sr/^{86}Sr$ (Bivalve)	16.319	± 0.23		
183.825		K	Shell Fragments	$^{87}Sr/^{86}Sr$ (Bivalve)	16.071	± 0.25		
184.215		L	Shell Fragments	$^{87}Sr/^{86}Sr$ (Bivalve)	16.196	± 0.24		
184.215		M	Shell Fragments	$^{87}Sr/^{86}Sr$ (Bivalve)	16.149	± 0.25		
196.785		N	Shell Fragments	$^{87}Sr/^{86}Sr$ (Bivalve)	16.257	± 0.24		
207.0	± 2.0	O	C5Cn.1n/C5Cn.1r	MPR	16.261		49	
220.23	± 0.20	P	Hornblende grain (150-300 µm)	$^{40}Ar/^{39}Ar$ date	16.740	± 0.90		
270.03	± 0.20	Q	Hornblende grain (150-300 µm)	$^{40}Ar/^{39}Ar$ date	17.080	± 1.20		
272.65		R	Shell Fragments	$^{87}Sr/^{86}Sr$ (Bivalve)	16.304	± 0.23		
286.1	Opal CT	S	*N. grossepunctata*	FAD	15.94	15.87	89, 90	
286.1	Opal CT	T	*F. maleinterpretaria*	LAD	16.41	16.5	88, 89, 90	Incomplete
286.1	Opal CT	U	*S. cheethamii*	FAD	16.94	N/A	90	
286.1	Opal CT	V	*D. maccollumii*	FAD	17.05	16.77	89, 90	
286.1	Opal CT	W	*N .17 Schrader*	FAD	17.16	16.94	89, 90	
286.30			RSU4a	Unconformity	16.3 - 17		23	
341.0	± 3.6	X	C5Cr/C5Dn	MPR	17.154		49	
373.58	± 0.20	Y	Hornblende grain (150-300 µm)	$^{40}Ar/^{39}Ar$ date	19.17	± 0.35		Grain likely reworked
380.04			D-b	Unconformity	17.25 - 17.45		23	
398.85	± 1.65	Z	C5Dn/C5Dr.1r	MPR	17.466		49	
450.52	450.57	AA	*Thalassiosira sp. cf. T. bukryi*	Occurrence	17.7-17.4		89,93	
567.95			RSU5	Unconformity	18.6-17.8		11,23	

Biostratigraphic constraints through the interval from 650 mbsf to near the top of Sequence 3B (at ~286.1 mbsf) are sparse as the sediments are deeper than the Opal-CT transition and diatom preservation is relatively poor. The correlation of the four distinct magnetozones R5, N4, R4, and N3 to the GPTS is therefore primarily based on regional correlation of prominent seismic reflectors to other dated drill cores from the Ross Sea shelf, backed up by diatom biostratigraphic constraints. The section from 650 mbsf to 567.95 mbsf at Site U1521 (Sequence 1) is characterised by reversed magnetic polarity but offers no constraints which we can confidently use for correlating this reversed interval to the GPTS. However, robust age constraint for sediments at the base of Sequence 2 can be determined through regional correlation of Ross Sea Unconformity (RSU) 5 to other sites where chronostratigraphic data are available. RSU5 intersects Site U1521 at 567.95 mbsf (the base of Sequence 2) and is correlated across the Glomar Challenger Basin and tied to DSDP Site 273 at 282 mbsf (Pérez et al., 2021). The LAD of *T. praefraga* is observed at 309 mbsf in DSDP Site 273, which suggests that RSU5 is younger than 17.95 Ma at that site. RSU5 cannot be directly correlated into the western Ross Sea, but a major unconformity (U2) occurs in the AND-2A drill site at 774.94 mbsf and likely corresponds with RSU5 based on chronostratigraphy (Levy et al., 2016). Specifically, sediments that directly underlie U2 in AND-2A are characterised by a reversed magnetic polarity and are correlated to Chron C5Er (18.636 to 18.497 Ma) based on constraints that include $^{40}Ar/^{39}Ar$ dates of 18.82 ± 0.15 Ma on pumice clasts within a tuffaceous siltstone at 831.66 mbsf. The age of sediments that overlie U2 at the AND-2A drill site are constrained by the FAD of *T. praefraga* at 771.5 mbsf (<18.46 to 18.58 Ma), and a $^{40}Ar/^{39}Ar$ date of 18.04 ± 0.31 Ma on pumice clasts within a tuffaceous siltstone at 709.17 mbsf. These observations require correlation of the reversed magnetic polarity zone that characterise the sediments above U2 to Chron C5Dr.2r (18.007 to 17.676 Ma). All evidence presented above shows that between ~18.6 and ~17.8 Ma, a significant, regionally extensive, erosional event (or series of events) created surface RSU5/U2.

Sediments deposited on top of RSU5 at Site U1521 are characterised by reversed magnetic polarity. Based on the known age of RSU5 at DSDP Site 273 and U2 at AND-2A, we correlate the top of reversed magnetozone R5 in Site U1521 to Chron C5Dr.2r. This interpretation is consistent with the observation that *T. praefraga* is not present in a diatom-bearing sample at 563 mbsf, despite comprehensive searches for this species in this sample as well as diatom-bearing samples higher in Sequence 2. As *T. praefraga* is a small and compact diatom not prone to fragmentation which would likely be preserved in the observed diatom

assemblages, we are confident this absence is not a result of poor preservation below the Opal-CT transition. *T. praefraga* is a common species in upper Oligocene and lower Miocene sediments recovered from several sites across the Ross Sea, including Cape Roberts Project-2/2A, DSDP Site 273, and AND-2A (Scherer et al., 2000; Taviani et al., 2008; Levy et al., 2016). The total reported CONOP model-based age range for the LAD of *T. praefraga* is 17.95 to 16.82 Ma and the hybrid model range is 17.95 to 17.36 Ma (Cody et al., 2008; Florindo et al., 2013; Crampton et al., 2016). Consequently, we view the absence of *T. praefraga* as strong evidence that the sediments above 563 mbsf at Site U1521 are younger than 17.95 Ma.

We then correlate the magnetic polarity reversal (MPR) R5/N5 between 526.8 and 524 mbsf to C5Dr.1n/C5Dr.2r (17.676 Ma), the MPR N4/R4 between 517.2 and 515.1 mbsf to C5Dr.1r/C5Dr.1n (17.634 Ma), and the MPR R4/N3 between 400.5 and 397.2 mbsf to C5Dn/C5Dr.1r (17.466 Ma). We extend a line of correlation from this MPR to the top of Sequence 2, where it intersects with seismic surface D-b (Pérez et al., 2021). The correlation presented here by interpolating through these MPRs indicates sediments in Sequence 2 span the time interval from ~17.7-17.4 Ma. The occurrence of the diatom taxon *Thalassiosira* sp. cf. *T. bukryi* at 450.52 mbsf supports this correlation as the range reported for this taxon at ODP Site 744 is 17.7-17.4 Ma (Farmer, 2011; Florindo et al., 2013).

To refine the likely sedimentation rate and timespan of Sequence 2, a cyclostratigraphic analysis (Fig. 2.3) was conducted on clast abundance data (Fig. 2.8) spanning 568 to 380 mbsf. These data were analysed using TimeOpt (Meyers, 2015), which is a statistical optimization method for astronomical time scale construction and astrochronologic testing, executed by the *astrochron* package in R (Meyers, 2014) (function 'timeOpt'). Given a range of plausible sedimentation rates and a series of specified astronomical periodicities (for precession, obliquity, and eccentricity), TimeOpt identifies the age model that results in a time-series that best aligns with the predictions of Milankovitch theory. Specifically, two diagnostic attributes of the astronomical hypothesis are evaluated: the hierarchy of cyclic frequencies expected of Milankovitch Cycles, $r^2_{spectral}$, and the match between eccentricity cycles and the precession-band envelope, $r^2_{envelope}$ (Meyers, 2015, 2019). These two values (r^2_{power} and $r^2_{envelope}$) are multiplied to produce an r^2_{opt} value, which provides insight into the strength of a hypothesized astronomical signal at each evaluated sedimentation rate.

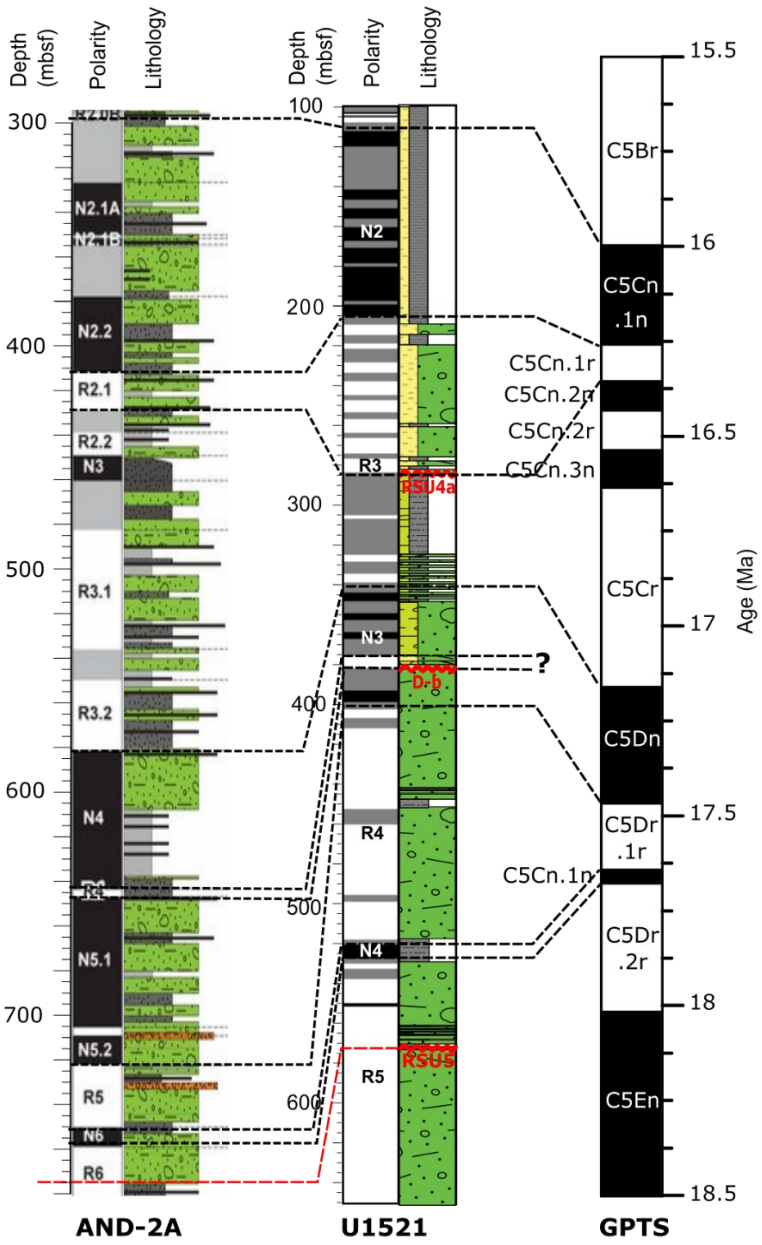


Figure 2.4. *Correlation of Site U1521 magnetostratigraphic tie points. Shown are correlations between the AND-2A record (Levy et al., 2016), Site U1521 (McKay et al., 2019) and the GPTS (Ogg, 2020).*

Assuming plausible average sedimentation rates between 40 cm kyr^{-1} and 65 cm kyr^{-1}, TimeOpt yields an optimal sedimentation rate of 59.2 cm kyr^{-1} for Sequence 2, with an r^2_{opt} of 0.396. To assess the statistical significance of the result, a Monte Carlo astrochronologic test is conducted to evaluate the null hypothesis that the observed variability in clast abundance arises entirely by stochastic processes, rather than astronomical forcing. The Monte Carlo simulations are generated using the function "timeOptSim", which creates a

large number of similar time-series of stochastic ("red") noise, to assess the probability that such datasets can produce an r^2_{opt} value comparable to the one generated by the clast abundance data (Meyers, 2015, 2019). This analysis yields a p-value of 0.005, indicating that the null hypothesis (i.e. the data is generated from a stochastic "red noise" process; specifically an AR1 process) can be rejected with a high degree of confidence. Given that the astrochronologically-estimated sedimentation rate is derived independently from the paleomagnetic data, their consistency is remarkable and provides strong evidence in support of an estimated duration of ~317 kyrs for Sequence 2 (Fig. 2.3; McKay et al., 2019).

While the 'floating' TimeOpt-derived astronomical time scale preserves information about elapsed time, it must be separately anchored to a specific numerical age. To do so, we use the 'slideCor' function in the *astrochron* package (Meyers, 2014); this is an automated approach to find the optimal anchoring of the floating TimeOpt-derived time scale to the theoretical astronomical solution of Laskar et al. (2004). Specifically, we have applied a Taner bandpass filter (Taner, 1992), isolating the periods between 60 ka and 27 ka for both the obliquity component of the astronomical solution (Laskar et al., 2004), and for the TimeOpt-derived floating astrochronology. The optimal match between the astronomical solution and floating astrochronology is identified using the squared Pearson correlation coefficient.

Independent biostratigraphic and magnetostratigraphic constraints mean we can restrict our 'slideCor' assessment to a feasible ~800 ka interval; our lower limit (17.950 Ma) is based on the absence of *T. praefraga* and the correlations of RSU5 described above, and our upper limit is based on the C5Cr/C5Dn MPR (17.154 Ma). Since the precise relationship between clast abundance and astronomical forcing is not known with certainty, any time-anchor for the astronomically calibrated section should be treated as having an uncertainty of at least a full obliquity cycle (~41 ka). Application of the slideCor function identifies two plausible regions of the astronomical solution for anchoring the Sequence 2 clast abundance data. The optimal match ($r^2 = 0.8497$) results in an astronomically calibrated section ranging from 17.601 Ma to 17.918 Ma (± 0.02 Ma). This would indicate that the interval is ~140-220 kyrs older than the age range suggested by the paleomagnetic interpretation, giving a very poor match with the measured polarities. However, a slightly less optimal match ($r^2 = 0.7704$) anchors the section to span 17.398 Ma to 17.715 Ma (± 0.02 Ma), which places it within ~40 kyrs of the paleomagnetic interpretation. This agreement of geochronological frameworks derived from paleomagnetism and astrochronology, which are broadly independent, provides strong support for this age model.

Uncertainties in the magnetostratigraphic age model, most notably for Subchrons C5Dr.1n and C5Dr.1r and Chron C5Dn, may account for some of the slight disagreement with the astrochronlogical approach described above. The available astronomically tuned durations of these (sub-)chrons agree within 10% (Billups et al., 2004; Kochhann et al., 2016). The small discrepancies in duration of (sub-)chrons originate from the astronomical tuning approach (carbon and oxygen isotopes tuned to eccentricity, tilt and precession at Site 1090 (Billups et al., 2004) and carbonate content to eccentricity only at Site U1336 (Kochhann et al., 2016)), as well as physical and palaeomagnetic recording processes such as bioturbation and the palaeomagnetic lock-in depth (Suganuma et al., 2010; 2011). Paleomagnetic measurement methods are discussed in detail in the cruise report (McKay et al., 2019).

We suggest 17.95-17.40 Ma as the absolute uncertainty of the timing of Sequence 2 deposition, based on the absence of *T. praefraga* (17.95 Ma) and occurrence of MPR C5Dn/C5Dr.1r (17.466 Ma) near the top of Sequence 2. However, more precise constraint on the duration of Sequence 2 deposition can be achieved based on the remarkable agreement of sedimentation rates based on the astronomical analysis of clast data and interpolation through magnetostratigraphic tie points, which suggest deposition occurred over ~317 kyrs. Combined with the close correlation between our astrochronological analyses and the timing of MPRs, we suggest a more precise interval for the deposition of Sequence 2, spanning ~17.72-17.40 ± 0.02 Ma. The ~20 kyr error represents uncertainty in the phase relationship between clast abundance and obliquity forcing. This range coincides closely with many independent records indicating ice-sheet growth, including a sea-level lowstand recorded on the New Jersey continental margin (~17.8-17.46 Ma) (Kominz et al., 2016), evidence for ice sheet growth in the AND-2A drill core sediments (~17.8-17.4 Ma) (Levy et al., 2016) and a peak in obliquity sensitivity (~17.8-17.5 Ma; Fig. 2.7) (Levy et al., 2019).

The age of Sequence 3A and 3B (324.20- 209.17 mbsf), bracketed by seismic surface D-b and regional unconformity RSU4a, is difficult to tightly constrain. Diatom preservation increases significantly in a sample at 286.1 mbsf at the base of Sequence 4A and the FADs of *Nitzschia sp. 17 Schrader*, *Synedropsis cheethamii*, and *Denticulopsis maccollumii* suggest sediments below this stratigraphic level are older than 17 Ma. The LAD of *F. maleinterpretaria* in this sample provides a minimum age constraint and suggests that the sediments below 286.1 Ma must be older than 16.41 Ma. These constraints require that the sediments between 344.6 and 286.3 mbsf, characterised by reversed polarity, correlate with either the Subchron C5Cn.2r or the base of Chron C5Cr. Correlation to the base of Chron

C5Cr is our favoured option as this would indicate that the interval of time missing across seismic surface D-b is relatively short, whereas regional unconformity RSU4a at the top of this unit records a hiatus of longer duration. The alternative interpretation is shown with a dashed line in Figure 2.3.

We constrain the slope of the LOC through Sequence 3B based on the sedimentation rate indicated for the diatom-bearing Sequence 4B as the sediments are similar, although affected by diagenesis in Sequence 3B. The sedimentation rate in Sequence 3A is assumed to be comparable to the Sequence 2 diamicts. We also acknowledge that the actual first appearance of the diatom taxa identified in the sample at 286.1 mbsf may have originally been deeper, but their presence has since been obscured by diagenesis. This would require that the LOC sit to the left (younger) of its current position. Therefore, we include an error box (orange box in Fig. 2.3) in our age model to show that the LOC could occur anywhere within this area depending on the amount of time missing across D-b and the sedimentation rate during deposition. We are confident that the MPR between 400.5 and 397.2 mbsf (N3/R3) is C5Dn/C5Dr.1r (17.466 Ma) based on constraints above and below this interval outlined above and place our LOC through the reversal. This LOC requires a time gap of ~ 180 kyrs across regional seismic surface D-b (Pérez et al., 2021) that separates Sequences 2 and 3.

Table 2.2. *Results of $^{87}Sr/^{86}Sr$ dating of shell fragments from Site U1521. Duplicates are aliquots of solid sample prepared and analysed independently.*

IODP Site	Core	Section	Top Offset (cm)	Bottom Offset (cm)	Midpoint depth (mbsf)	87Sr/86Sr normalized	2SEM (internal)	Timescale = GTS2020 McArthur et al. (2020) *mean age (Ma)*	error +/-	Trace Elements Sr/Ca ug/g	Mg/Ca ug/g	Na/Ca ug/g	Mn/Ca ug/g	Fe/Ca ug/g	Ba/Ca ug/g
U1521	16	1	10	14	141.920	0.708740	0.000006	16.039	0.25	3637					
U1521	16	3	102	105	145.135	0.708729	0.000006	16.211	0.24	6286	980	8436	32	529	2025
					145.135	0.708725	0.000007	16.272	0.24	7772	576	7377	27	334	2167
U1521	20	2	118	118	182.700	0.708735	0.000006	16.117	0.25	1697					
U1521	20	3	0	2	182.710	0.708722	0.000007	16.319	0.23	1535					
U1521	20	4	0	3	183.825	0.708738	0.000006	16.071	0.25	1612					
U1521	20	4	39	42	184.215	0.708730	0.000006	16.196	0.24	5041					
					184.215	0.708733	0.000006	16.149	0.25	5089					
U1521	21	5	119	122	196.785	0.708726	0.000006	16.257	0.24	3501	260	7641	58	45	682
U1521	29	6	46	48	272.650	0.708723	0.000005	16.304	0.23	5277	506	8110	94	384	2116

The relatively thin interval of reversed polarity within Chron C5Dn (at ca. 380 mbsf) is not identified in the current version of the GPTS (Fig. 2.4), but a similar short-duration reversed polarity event roughly halfway through Chron C5Dn is recorded in the AND-2A magnetostratigraphic record (Levy et al., 2016). Taking the palaeomagnetic uncertainties of ice-proximal sediments into account, we hypothesise that this rarely recorded reversed polarity event could be a genuine feature of the geomagnetic field that has not been detected in marine sediments due to signal smoothing at low sedimentation rates (Roberts and Winklhofer, 2004).

The age of sediments above RSU4a are very well constrained by diatom data, $^{87}Sr/^{86}Sr$ ages and magnetostratigraphy (Tables 2.1, 2.2). The LAD of *F. maleinterpretaria* indicates that the sediments above 286.1 mbsf must be younger than 16.41 Ma. An $^{87}Sr/^{86}Sr$ date on shell fragments at 272.65 mbsf indicates the interval with reversed polarity containing the fragments correlates with Subchron C5Cn.1r (16.351 to 16.261 Ma). This correlation means that the hybrid age model underestimates the maximum age of the FAD of *Nitzschia grossepunctata*, which occurs at 286.1 mbsf, and suggests the age indicated by the total range model age for this datum (16.23 Ma) is more likely. Together, these data indicate that the base of Sequence 4A dates to less than ~16.351 Ma. We correlate the MPR (R3/N2) between 209 and 205 mbsf to C5Cn.1n/C5Cn.1r (16.261 Ma). The sequence of well-dated shells through Sequence 4B allows us to correlate the sediments between 209 and 106.3 mbsf that are characterised by normal polarity with Subchron C5Cn.1n (16.261 to 15.994 Ma) and the MPR between 106.3 and 105.5 to C5Br/C5Cn.1n (15.994 Ma). The FADs of *Denticulopsis lauta*, *Actinocyclus ingens*, *Denticulopsis hyalina*, and *Denticulopsis simonsenii* at 84.99 mbsf indicate a major hiatus at this depth spanning from ~15.83 Ma to at least 14.48 Ma. This stratigraphic horizon correlates with RSU4, a major regional unconformity (Pérez et al., 2021).

2.5 Neodymium and Strontium Isotopes in and around the Ross Sea

Before interpreting results at IODP Site U1521, published radiogenic Nd and strontium Sr isotope data from terrestrial rock samples must be compiled and assessed. These can then be compared to marine sediments to identify the rock types likely supplying detritus to Site U1521. A full list of the data and references is provided in Table A.2.9. Errors on means are reported as two standard deviations. Figures focus on Nd isotope data, as these proved more diagnostic of sediment provenance shifts in the Ross Sea region.

2.5.1 Terrestrial Rocks

The long geological history of East Antarctica has resulted in its rocks with a wide range of isotopic compositions (Figs. 2.5, 2.6). Due to its age, the Nimrod Complex has an ε_{Nd} signature which is the least radiogenic (lowest) in the Ross Sea sector, and $^{87}Sr/^{86}Sr$ ratios are correspondingly radiogenic (high) (Table A.2.9). Isotopic analyses of the East Antarctic Neoproterozoic and Palaeozoic sedimentary rocks are varied, which is unsurprising given their diverse lithologies. Volcanic beds in the Liv Group have values spanning 4.3 to -7.6, and $^{87}Sr/^{86}Sr$ ratios spanning 0.705 to 0.778 (Wareham et al., 2001). However, these analyses are unlikely to be representative of the bulk composition; only volcanic rocks were sampled and not the siliciclastic and calcareous sedimentary strata that are also present, which we found to have ε_{Nd} values varying between -9.72 and -5.38 (Table A.2.9). In the central Transantarctic Mountains, Byrd Group samples have yielded ε_{Nd} values with a mean of -12.7 ± 4.2 (n = 9) and $^{87}Sr/^{86}Sr$ ratios of 0.745 ± 0.06 (n = 12). Older Beardmore and Skelton Group samples have similar mean ε_{Nd} values of -12.3 ± 7.7 (n = 19) and $^{87}Sr/^{86}Sr$ ratios of 0.741 ± 0.069 (n = 15).

Measured ε_{Nd} values for the Ross-age Granite Harbour Intrusive Complex vary significantly from -18.4 to -0.7 (n = 74). However, this variation is systematic (Fig. 2.6); differences are found between different plutons, reflecting the partial melting and assimilation of the different basement rocks present (Borg et al., 1990; Goodge et al., 2012). In general, it appears that more southerly Granite Harbour Intrusive Complex rocks are typically more radiogenic (ε_{Nd} = -3.1 to -1.1 in the Gabbro Hills; Borg et al., 1990) compared to more northerly ones (e.g. ε_{Nd} = -14.2 to -9.5 in Southern Victoria Land; Cox et al., 2000), with further variation perpendicular to the strike of the Transantarctic Mountains (Goodge et al., 2012). $^{87}Sr/^{86}Sr$ ratios vary more, even within regions, but broadly mirror these trends (Gunner, 1976).

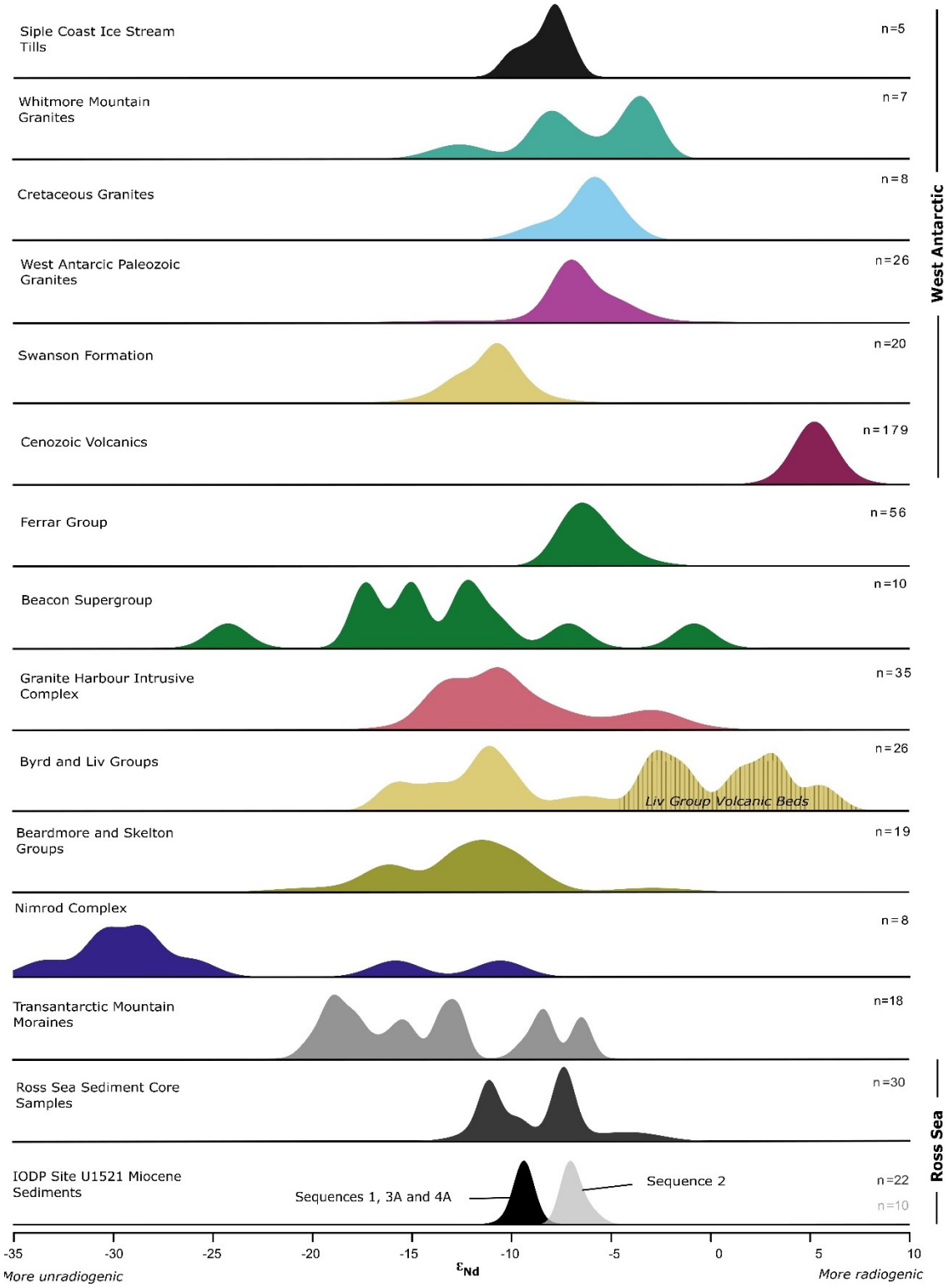


Figure 2.5. *Kernel density estimate plots for literature measurements of rock ε_{Nd} compared to measurements on fine-grained Miocene detritus from Site U1521. For references and a list of all the data, see Table A.2.9. The height of the curve indicates the density of measurements and n the total number of samples analysed. Colour scheme is identical to Figure 2.1, with sediments in grey.*

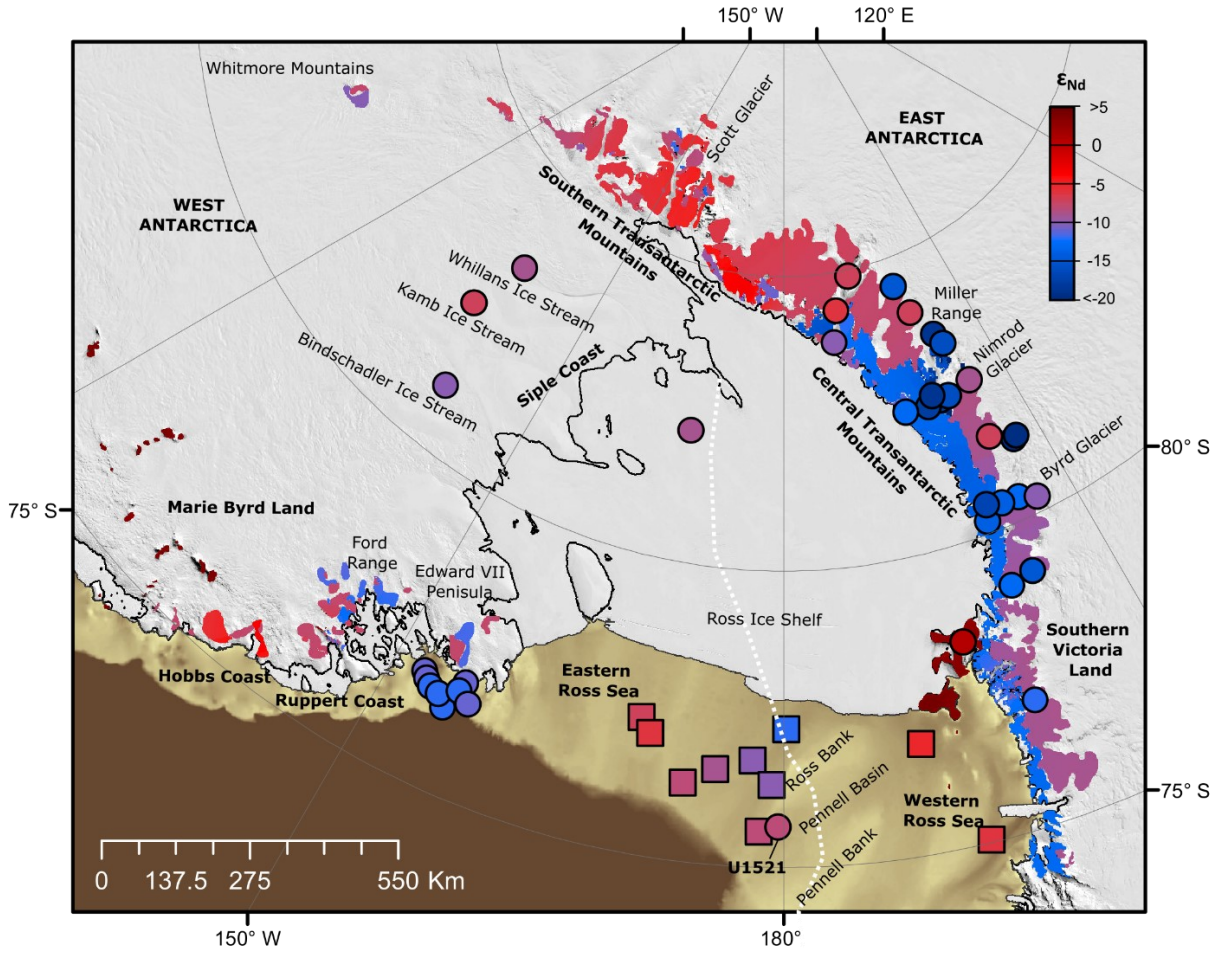


Figure 2.6. *Map of approximate ε_{Nd} values in rocks and offshore sediments from around the Ross Sea embayment. Epsilon Nd values are overlain on MODIS imagery (Haran et al., 2014) and the BedMachine Antarctica V1 modern bed topography (Morlighem et al., 2020), with the MEaSUREs grounding line and ice sheet margin shown (Rignot et al., 2013; Mouginot et al., 2017). The approximate boundary between West and East Antarctic lithosphere is shown using a white dashed line (Tinto et al., 2019). Modern/late Holocene and terrestrial till samples are represented by circles with the same colour bar (Farmer et al., 2006; Farmer and Licht, 2016; Simões Pereira et al., 2018). Although ice flow patterns have changed since their deposition, Last Glacial Maximum tills in offshore sediments are also plotted as squares to improve spatial coverage (Farmer et al., 2006). Individual samples and references are reported in Table A.2.9. The bedrock map was produced by Kriging between sample locations within a rock group (as defined in text and Table A.2.9), then masking to the outcrop area. Beacon and Ferrar Group (Fig. 2.1) rocks are often not differentiated in geological mapping, but are roughly equal volumetrically (Gann and Warren, 1962), with the uppermost Beacon Supergroup formations having a Ferrar-like isotopic signature (Elliot et al., 2016). We hence assume a 60% Ferrar, 40% Beacon mixture is representative.*

West Antarctica has a smaller range of radiogenic isotope ratios; most notably, there are no geological units with very unradiogenic ε_{Nd} values (Figs. 2.5, 2.6). However, many groups overlap with those in East Antarctica. The sedimentary rocks of the Swanson Formation have a mean ε_{Nd} value of -11.1 ± 3.0 (n = 19) and $^{87}Sr/^{86}Sr$ ratio of 0.735 ± 0.024 (n = 18), similar to the temporal equivalents in East Antarctica (Table A.2.9). The Palaeozoic intrusions into these sediments have ε_{Nd} values with a mean of -6.6 ± 4.8 (n = 26), and $^{87}Sr/^{86}Sr$ ratios (n = 22) cluster near a mean of 0.719 ± 0.022. The ~180-200 Ma intrusions in the Whitmore Mountains have ε_{Nd} values falling between -3.1 and -12.6 (mean = -6.6, n = 7) and $^{87}Sr/^{86}Sr$ ratios (n = 6) with a mean of 0.727 ± 0.030. Cretaceous granitic rocks have ε_{Nd} values ranging from -4.6 to -8.6, with a mean of -6.2 ± 2.8 (n = 8). $^{87}Sr/^{86}Sr$ ratios (n = 5) vary from 0.785 to 0.741 with a mean of 0.754 ± 0.037. Overall, a mixture of West Antarctic rocks would be expected to have more radiogenic values than a mixture of Transantarctic Mountain lithologies (Figs. 2.5, 2.6).

The range of Nd and Sr isotopic ratios in the Cenozoic rocks of the Marie Byrd Land volcanic province and McMurdo Volcanic Group is narrow and distinct from the older lithologies described above (Table A.2.9), with ε_{Nd} values from +7.3 to +2.8 (n = 179) and $^{87}Sr/^{86}Sr$ ratios from 0.702 to 0.705 (n = 224). Although geographically distant, the Marie Byrd Land and McMurdo volcanic provinces are isotopically extremely similar.

2.5.2 Late Quaternary Terrestrial Tills and LGM Tills in Offshore Sediments

Geologically young samples from moraines on land, subglacial tills and marine sediments can indicate subglacial distributions of rock types as they integrate the isotopic values of source rocks. This provides useful data for comparison with the provenance data from Site U1521. Samples taken from moraines in the Transantarctic Mountains tend to closely resemble nearby rock outcrops (Farmer and Licht, 2016), leading to ε_{Nd} values spanning the range of most rock types present (Figs. 2.5, 2.6). However, in Ross Sea marine and subglacial sediments, ε_{Nd} values are typically less varied as a greater degree of mixing has occurred. Neodymium and strontium isotope analyses on subglacial tills from the Siple Coast ice streams (n = 5) yielded ε_{Nd} values of -7.0 to -9.9 (Farmer et al., 2006). $^{87}Sr/^{86}Sr$ ratios were 0.731 beneath Whillans and Bindschadler ice streams and 0.720 beneath Kamb Ice Stream. Two samples from beneath the centre of the Ross Ice Shelf yielded a similar ε_{Nd} value (-8.2) and $^{87}Sr/^{86}Sr$ ratio (0.724) (Farmer et al., 2006).

In Ross Sea sediments from beyond the modern ice margin, ε_{Nd} values typically vary between approximately -11 and -5 (Figs. 2.5, 2.6); Farmer et al., 2006; Roy et al., 2007; Simões Pereira et al., 2018). More radiogenic values are found further east and west (Fig. 2.6); this pattern is mainly attributed to the influence of Cenozoic volcanic rocks in Marie Byrd Land and Victoria Land, respectively (Farmer and Licht, 2016). As they are highly radiogenic and typically have a high Nd concentration, only a small contribution to the sediments from these rocks can noticeably alter the sediment's isotopic composition. This control on spatial distributions of radiogenic isotope ratios means the abundance of these young rocks is likely to be a strong control on ε_{Nd} values at Site U1521, and responsible for the more radiogenic ε_{Nd} values in Sequence 2. Outcrops of these Cenozoic volcanic rocks in the vicinity of Site U1521 are limited, but, beneath the WAIS, subglacial volcanoes (Behrendt, 2013; Lough et al., 2013; van Wyk de Vries et al., 2017) and volcanic rocks (LeMasurier, 2013; Schroeder et al., 2014) are present and likely contributed to the subglacial tills deposited offshore (Fig. 2.1).

On the other hand, where these Cenozoic volcanic rocks are absent, the least radiogenic ε_{Nd} values of approximately -12 to -10 and highest $^{87}Sr/^{86}Sr$ ratios of approximately 0.720-0.725 are reached in Ross Sea tills (Farmer et al., 2006). These sediments must therefore represent a typical mixture of the rocks present in the central Transantarctic Mountains, consistent with the range of values seen in moraines and rock outcrops (Fig. 2.5).

2.6 Methods

Various methods were used to identify the provenance of the Site U1521 sediments and place these data in a paleoenvironmental context. These methods are described here.

2.6.1 Neodymium and Strontium Isotopes

Samples were disaggregated and wet sieved to isolate the <63 μm fraction, which was then dried at 60°C. This size fraction represents the bulk composition, as samarium and neodymium are incorporated in equal proportions into most rock-forming minerals, meaning grain-size sorting is not likely to impact results (Goldstein and Hemming, 2003; Garçon et al., 2013). However, the Rb-Sr system is subject to elemental fractionation during weathering and grain-size sorting, which can influence $^{87}Sr/^{86}Sr$ ratios (see Section 2.8.2). To remove authigenic Fe-Mn oxyhydroxide phases, samples were leached in a mixture of 0.05 M hydroxylamine hydrochloride, 15% acetic acid, and 0.03 M Ethylenediaminetetraacetic acid

(EDTA) at a pH of 4 (Gutjahr et al., 2007). A carbonate removal step was not included due to the very low carbonate content (McKay et al., 2019). Leached sediment was dried, homogenised, and 50 mg aliquots were digested on a hotplate in concentrated HF (2 mL), $HClO_4$ (0.8 mL) and HNO_3 (1 mL) for three to five days, with a subsequent 6 M HCl step. The Nd was isolated from the sample matrix using a cation exchange resin (AG50W-X8, 200-400 μm mesh) and HCl in increasing molarity, followed by a low molarity HCl Ln-Spec resin procedure (50–100 μm mesh). The sample matrix from the cation exchange step was dried down, taken up in HNO_3, then loaded onto Eichrom Sr Spec resin to wash down the matrix and elute the Sr (Simões Pereira et al., 2018).

Neodymium isotopes were measured in the MAGIC laboratories at Imperial College London on a Nu high resolution multi-collector inductively coupled plasma mass spectrometer (HR MC-ICP-MS). To account for instrumental mass bias, isotope ratios were corrected using an exponential law and a $^{146}Nd/^{144}Nd$ ratio of 0.7219. Although negligible, interference of ^{144}Sm on ^{144}Nd was corrected for. Bracketing standards were used to correct measured $^{143}Nd/^{144}Nd$ ratios to the commonly used JNdi-1 value of 0.512115 (Tanaka et al., 2000). USGS BCR-2 rock standard was processed alongside all samples and yielded $^{143}Nd/^{144}Nd$ ratios consistently within error of the published ratio of 0.512638 ± 0.000015 (Weis et al., 2006). Full procedural blanks for Nd ranged from 7 to 30 pg (n = 6). $^{143}Nd/^{144}Nd$ ratios are expressed using epsilon notation (ε_{Nd}), which denotes the deviation of a measured ratio from the modern Chondritic Uniform Reservoir (0.512638; Jacobsen and Wasserburg, 1980) in parts per 10,000.

Strontium isotopes were measured in the MAGIC laboratories at Imperial College London on a TIMS (Thermal Ionisation Mass Spectrometer). 10% of the sample was loaded in 1 μL of 6M HCl onto degassed tungsten filaments with 1 μL of $TaCl_5$ activator. The measured $^{87}Sr/^{86}Sr$ ratios were corrected for instrumental mass bias using an exponential law and an $^{88}Sr/^{86}Sr$ ratio of 8.375. Interference of ^{87}Rb was corrected for using an $^{87}Rb/^{85}Rb$ ratio of 0.386. Analyses of the NIST 987 standard reference material were completed every four unknowns, yielding a mean of 0.710290 ± 0.000041 (2SD, n = 36). Samples were corrected to the published value of 0.710252 ± 0.000013 (Weis et al., 2006). The relatively poor reproducibility for our NIST 987 runs was due to technical issues, but is still more than sufficient for interpreting sample results, which change in the 3rd to 4th decimal place. Accuracy of results was confirmed using rock standard USGS BCR-2, processed with every

batch of samples, which yielded $^{87}Sr/^{86}Sr$ ratios of 0.705010 ± 0.00029 (2SD, n = 18). This is well within error of the published ratio of 0.705013 ± 0.00010 (Weis et al., 2006).

2.6.2 Detrital Zircon U-Pb Dating

Zircon U-Pb dating was performed with the assistance of Pieter Vermeesch and Andy Carter (London Geochronology Centre). The sub-bottom depth midpoints of the nine samples are: A: 220.23, B: 270.03, C: 335.72, D: 373.58, E: 410.82, F: 487.40, G: 546.55, H: 588.00 and I: 642.21 mbsf. To ensure there were enough grains for statistical analysis, the above samples were taken over 40 cm intervals. Samples were disaggregated, dried and sieved at 300 µm. Zircons from the <300 µm fraction were concentrated using standard gravity settling and magnetic separation techniques. Samples were then mounted in resin, polished and analysed using an Agilent 7900 laser ablation inductively-coupled plasma mass spectrometer (LA-ICP-MS) with a 25-35 µm pit diameter in the London Geochronology Centre at University College London. Approximately 150 grains resembling zircons were randomly selected for analysis from each sample. Plešovice zircon (Sláma et al., 2008) was used as a primary standard to correct for instrumental mass bias and depth-dependent inter-element fractionation. Approximate U and Th concentrations were calculated by comparison with NIST 612 glass (Pearce et al., 1997).

Data reduction of the time-resolved mass spectrometer data was performed using GLITTER 4.5 (Griffin, 2008). Ages younger than 1100 Ma were calculated using the $^{206}Pb/^{238}U$ ratio whilst older grains used the $^{207}Pb/^{206}Pb$ ratio. Data were filtered to exclude non-zircons based on zirconium concentrations (>10^6 counts per second) and a -5/+15% discordance threshold was applied. This yielded at least 92 grains per sample, giving a 95% confidence that any age populations comprising more than 7% of the sample will be measured (Vermeesch, 2004). GJ1 zircon (Jackson et al., 2004) was used as a secondary standard to verify accuracy of the data. Repeat analyses using zircons with and without existing ablation pits were made to check sample reproducibility; these agreed within the uncertainties associated with random sampling. Final data were processed and visualised using the R package IsoplotR (Vermeesch, 2018a).

2.6.3 Clast Petrography

Clast identification was performed by Luca Zurli, Franco Talarico and Matteo Perotti (University of Siena). The gravel fraction (>2 mm) was characterized in continuum along the

core between 648.17 and 209.17 mbsf. Clasts exposed in the cut surface of the archive half core were measured, logged and described on the basis of macroscopic features (e.g. shape, colour, texture). Logging aimed to identify the distribution and variation of the gravel-size clasts along the core length. Clast logging followed the methods previously applied to the ANDRILL and Cape Roberts Project drill records from the Ross Sea. On the basis of macroscopic features, clasts were grouped into seven main lithological groups: igneous rocks, quartz fragments, dolerites, volcanic rocks, metamorphic rocks, sedimentary rocks and sedimentary intraclasts (Talarico and Sandroni, 1998; 2009; Talarico et al., 2000; Sandroni and Talarico, 2001). Data processing involved counting the occurrence of each lithological group over 10 cm core intervals and summarizing this for each core (Fig. 2.8). The total number of clasts was also summed for each metre interval (Fig. 2.8). To highlight the along-core variation in dolerite and volcanic clasts - two of the most indicative lithologies for provenance constraint - the number of these clasts was divided by the total number of clasts in each core (Fig. 2.8). A total of 73 pebble to cobble-sized clasts were sampled for petrographic analysis, of which the most representative of each lithological group were analysed using standard petrographic methods with polarized light microscopy.

2.6.4 Palynology

Sample processing was performed by Francesca Sangiorgi and Christina Boshuis at Utrecht University, following standard techniques of the Laboratory of Palaeobotany and Palynology. Joes Prebble (GNS Science) conducted the pollen identification. Samples were oven-dried and weighed (~15 g dry weight sediment each). One *Lycopodium clavatum* tablet with a known amount of marker spores was added for quantification of palynomorph abundances (Wood et al., 1996).

Samples were treated with 10% HCl (Hydrochloric acid) and cold 38% HF (Hydrofluoric acid), then sieved over a 10 µm mesh with occasional mild ultrasonic treatment. To avoid any potential processing-related preservation bias, no oxidation or acetolysis was carried out. The processed residue was transferred to microscope slides using glycerine jelly as a mounting medium, and 2 slides were analysed per sample at 400× magnification. Slides were examined for detailed marine palynomorphs (dinoflagellate cysts, acritarchs and other aquatic palynomorphs) and, at screening-level, terrestrial palynomorphs (pollen and spore) at Utrecht University. Subsequent detailed analysis of terrestrial palynomorphs on a sub-set of seven samples was undertaken at GNS Science. Of the 23 palynological samples analysed for

dinocysts, two contained <60 dinocysts (Sequence 1; 594.48 mbsf and Sequence 2; 567.75 mbsf) and one was almost barren (yielding only 12 *in situ* dinocysts, Sequence 3A; 374.9 mbsf). The almost barren sample is excluded from all plots. The two low abundance samples are included in our plots but require careful interpretation. Samples between 594.48 and 567.75 mbsf and below 594.48 mbsf (cores 65R, 67R, 69R and 71R) were also checked, but yielded few dinocyst specimens. Those present comprised of fragments of mostly reworked dinocysts.

Pollen and spore identification followed taxonomic compilations (Raine et al., 2011; Prebble 2016), augmented by key Antarctic literature (Truswell, 1983; Askin, 2000; Askin and Raine, 2000). For pollen and spores, scanning continued until an entire cover slide was completed, or a 100-count reached. Results are presented as specimens/gram, and percentage of all terrestrial palynomorphs. Dinocysts were identified based on a taxonomical index (Fensome and Williams, 2004) and informally and formally described species in the literature (Hannah et al., 2000; Hannah, 2006; Clowes et al., 2016; Bilj et al., 2018). Dinocyst percentages were calculated based on the total *in situ* dinocysts counted, excluding reworked specimens. The percentages of other palynomorph groups such as brackish and freshwater algae (*Cymatiosphaera* spp. and *Pediastrum* spp.) and reworked dinocysts were calculated using the total palynomorphs counted (Figs. 3.6, 3.9). *In situ* dinocyst and terrestrial palynomorph absolute abundance (specimens/g dry weight) and the absolute abundance of the other palynomorph groups were calculated by counting the amount of *Lycopodium clavatum* spores encountered, following the equation of Benninghoff (1962).

Protoperidinioid (P) dinocysts are mostly represented by the genera *Brigantedinium*, *Lejeunecysta*, and *Selenopemphix*. Gonyaulacoid (G) dinocysts mostly include *Batiacasphaera* spp., *Operculodinium* spp. and *Spiniferites* spp. Protoperidinioid cyst percentages (Heterotrophic % in Extended Data Fig. 2) and percentages of the most common species (*Brigantedinium* spp. *Lejeunecysta* spp., *Selenopemphix* spp. and *Selenopemphix antarctica*) were calculated to identify productivity trends and/or the presence of sea ice. P dinocysts are likely produced by heterotrophic dinoflagellates (Harland and Pudsey, 1999) and, at present, dominate the assemblages in Antarctic sediments in areas with high nutrients and/or (year-round) sea-ice cover. At present, samples in quasi perennial sea-ice covered areas are dominated by *Selenopemphix antarctica* (~75%), with abundant *Brigantedinium* spp. and rare occurrence of other species (Prebble et al., 2013; Zonneveld et al., 2013; Hartman et al., 2018). G cysts are generally produced by phototrophic dinoflagellates.

Operculodinium spp. is the most abundant, has species representatives among the extant cysts and has been selected to represent temperate-warm conditions. At present, it is almost exclusively found in temperate areas of the Southern Ocean north of the Subantarctic Front and never occurs in circum-Antarctic sediments south of the Polar Front (Prebble et al., 2013). In contrast, it is common to abundant in other Antarctic warm Miocene records (Warny et al., 2009; Sangiorgi et al., 2018). Reworked dinocysts include Eocene and Oligocene taxa (mostly *Vozzhennikovia* spp., but also few *Spinidinium* spp. and *Enneadocysta diktyostila*).

2.6.5 Hornblende $^{40}Ar/^{39}Ar$ Dating

Hornblende grains were picked from the magnetic separate of the samples prepared for U-Pb dating of zircons (150-300 μm size fraction). The samples were processed by Sidney Hemming. They were first co-irradiated with Fish Canyon sanidine (28.201 ± 0.046 Ma) (Kupier et al., 2008) for 8 hours in the CLICIT (Cadmium Lined In-Core Irradiation Tube) facility at Oregon State University reactor. Samples were loaded into planchettes, evacuated in a chamber with a ZnSe window, then heated with a CO_2 laser to release the gas. Samples were exposed to hot Zr-Al getters to remove reactive gases, and the inert gases were let into a VG5400 noble gas mass spectrometer and measured with peak hopping on an analogue multiplier in static vacuum mode. Backgrounds were corrected based on frequent measurements of blanks (~ every 4 unknowns) and mass discrimination was corrected based on measurements of air (~ every 12 unknowns). Corrections for nuclear interferences are based on reported measurements from the Berkeley Geochronology Lab (Renne, 1995). Analyses and data reduction were performed using MassSpec, a program written by Al Deino at the BGC. Errors are reported at 1 sigma.

2.6.6 Clay Mineralogy

Francois Beny and Viviane Bout-Roumazeilles performed the clay mineral analyses. Firstly, samples were decalcified using 0.1N HCl and deflocculated through repeated washing using pure water. To isolate the clay-size fraction (<2 μm), we employed differential settling according to Stoke's Law and then concentrated the sample using a centrifuge for 40 minutes at 3500 rotations per minute. An aliquot was then placed on glass slides, before X-ray diagrams were obtained using a Bruker D4Endeavor (standard 30 kV and 30 mA). Each sample was run between 2.49 and 32.5°2θ with a step size of 0.08°2θ (total of 369 steps) and

integration time of one second. Samples were run in three different ways: 1) air-dried, 2) glycolated (12 hours in ethylene glycol), and 3) heated at 490°C for 2 hours (Beny et al., 2020). The relative fraction of smectite, chlorite, illite and kaolinite is determined using the main X-ray diffraction peaks (layer and interlayer) on X-ray spectra according to their crystallographic characteristics (Brown and Brindley, 1984). Illite is readily identified using its main peak at 10 Å on all three runs. Smectite is characterized by a main peak at 14-15 Å on the air-dried samples that expands at 17 Å after ethylene glycol saturation and collapses at 10 Å with increasing heating. Kaolinite and chlorite both have a dominant peak at 7-7.2 Å, with pseudo-void deconvolution of the kaolinite/chlorite doublet at 3.54/3.58 Å required to distinguish between them. All measurements and semi-quantitative estimations are processed using the MacDiff software (Petschick, 2004). To distinguish between Fe/Mg-rich vs Al-rich illite, the Esquevin index was also employed (Esquevin, 1969), which corresponds to the ratio between the intensity of the peak of illite at 5 Å and at 10 Å (illite 5Å/10Å). The crystallinity of illite (i.e. Kübler index) was measured using the method of integral breadth (Petschick et al., 1996), with high crystallinity implying poorly crystallized mineral. This indicates the metamorphic grade of the source rocks.

2.6.7 X-Ray Fluorescence

XRF core scanning was conducted on Site U1521 cores using a 3rd generation Avaatech core scanner ("XRF2") at the IODP Gulf Coast Repository at Texas A&M University equipped with a 100 W rhodium side-window X-ray tube. Prior to scanning, cores were moved from cold storage to the lab to warm to room temperature for at least three hours to avoid condensation. Each section was prepared by scraping the core surface using either a glass microscope slide or a stainless steel spatula to remove the upper ~2 mm of sediment. The stainless steel spatula was used to avoid chipping glass onto the core surface when clasts were present. After scraping, the core surface was covered with 4 μm thick Ultralene film (SPEX Centriprep, Inc.) to protect the detector.

Each section was scanned at 1 cm (Core U1521A-4R to Section U1521A-21R-1), 2 cm (Cores U1521A-1R to 3R; Sections U1521A-1R-2 to 35R-2), or 4 to 5 cm (Section U1521A-35R-3 to Core 71R) resolution along the center of the core section using a 1.2 cm^2 illumination window set to 1 cm down-core and 1.2 cm cross-core. Three successive scans were performed on each core section using different excitation settings. The first scan was performed at 10 kV, 0.16 mA, and no filter with 6 s of live time to analyze for Al, Si, K, Ca,

Ti, and Fe. The second scan used 30 kV, 1.25 mA, and Pd-thick filter with 6 s of live time to analyze for Ni, Br, Rb, Sr, Zr, and Mo. The last scan was at 50 kV, 0.75 mA, and Cu filter with 10 s of live time to analyze for Ba. Raw X-ray spectra were processed using bAxil software (Brightspec), which uses a non-linear least squares method.

XRF data are archived in the IODP Laboratory Information Management System (LIMS): http://web.iodp.tamu.edu/LORE/.

2.7 Results

2.7.1 Radiogenic Isotopes at Site U1521

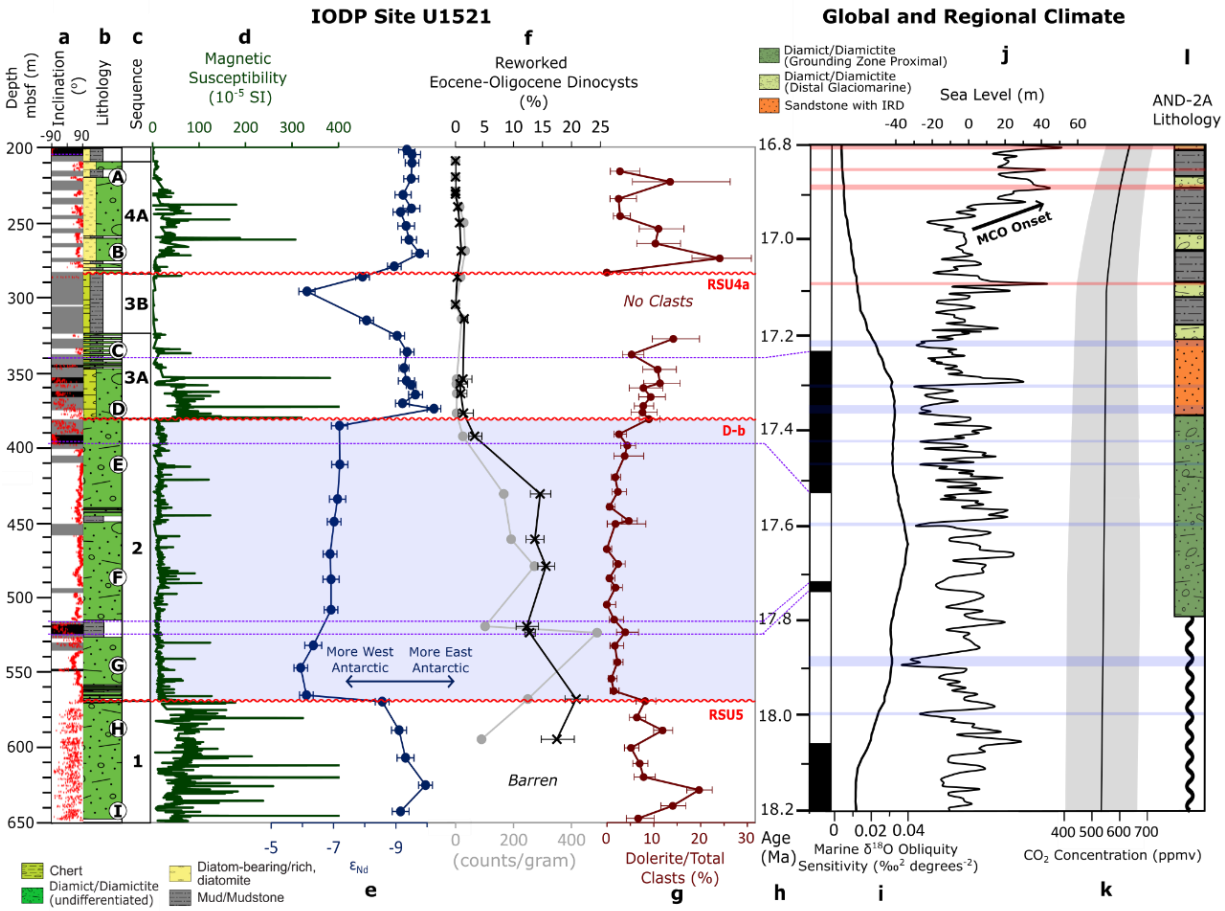


Figure 2.7*. Selected provenance proxies from IODP Site U1521 compared to Early Miocene climate records. The light blue shaded section (Sequence 2) highlights the interval with sediments of predominantly West Antarctic provenance. The depth of Ross Sea Unconformity (RSU) 4a and 5 and seismic surface D-b are indicated in red (Pérez et al., 2021). a) Site U1521 inclination data after 20 mT demagnetisation (red points) (McKay et al., 2019) and polarity interpretation (white = reverse polarity, black = normal polarity, grey = no*

interpretation). b) Site U1521 lithostratigraphy (McKay et al., 2019). c) Chronostratigraphic sequences. The circled letters between b) and c) mark the depths of the zircon U-Pb samples (Figure 2.11). d) Magnetic susceptibility measured on the whole core (McKay et al., 2019). e) Neodymium isotope signature of the fine fraction. Error bars are 2 S.D. external reproducibility, and the scale is reversed. f) Abundance of Eocene-Oligocene dinocysts as a percentage (black) and concentration (i.e., counts per gram sediment; grey). g) Dolerite clast abundance. Errors shown in f) and g) are 95% confidence intervals (Vermeesch, 2018b). Magnetostratigraphic tie points between the polarity interpretations from shipboard data (a; McKay et al., 2019) and geomagnetic polarity timescale (h; Ogg, 2020) are marked by purple dashed lines. i) Obliquity sensitivity, indicating the strength of obliquity in the $\delta^{18}O$ record relative to the theoretical strength of obliquity forcing. This has been interpreted as representing the presence of marine-based Antarctic ice (Levy et al., 2019). j) Sea-level record based on an oxygen isotope splice (Miller et al., 2020). Red and blue shaded intervals indicate pronounced sea-level highstands (>40 m) and lowstands (<-20 m), respectively. MCO = Miocene Climatic Optimum. k) CO_2 reconstruction with a LOESS smoothing (shaded region indicates 1 sigma error; Rae et al., 2021). l) Simplified lithological log from the AND-2A record, with diamictites differentiated based on a grounding-zone proximal vs distal glacimarine depositional setting (Levy et al., 2016; 2019).

At Site U1521, detrital ε_{Nd} values are consistently more radiogenic (less negative) in Sequence 2 compared to the sediments above and below (Fig. 2.7e), implying a contribution from a more radiogenic endmember. This endmember can be traced to beneath the WAIS; the ε_{Nd} values, ranging between -7.2 and -5.9, are in good agreement with measurements of Upper Quaternary diamicts from the eastern Ross Sea shelf, adjacent to West Antarctica (Farmer et al., 2006). Here, the radiogenic endmember is hypothesised to be the Cenozoic alkali volcanic rocks of Marie Byrd Land, West Antarctica (Fig. 2.5; Farmer et al., 2006). Subaerial outcrops of the Marie Byrd Land volcanic province are limited, but magnetic and gravity anomalies associated with subglacial cone-shaped structures indicate the presence of numerous subglacial volcanoes (Fig. 2.1; van Wyck de Vries et al., 2017). We hypothesize that the Marie Byrd Land volcanic province is the more radiogenic endmember in Sequence 2. Conversely, the less radiogenic (lower) ε_{Nd} values seen in Sequences 1, 3A and 4A reflect a mixture of lithologies present in the (East Antarctic) Transantarctic Mountains and fall within the range of Upper Quaternary Ross Sea (marine) tills of Transantarctic Mountain

provenance (Figs. 2.5, 2.6; Farmer et al., 2006; Farmer and Licht, 2016). These less radiogenic sediments also show higher and more variable magnetic susceptibility (Fig. 2.7; McKay et al., 2019). The patterns seen in the ε_{Nd} data are broadly mirrored by detrital Sr isotope compositions (Fig. 2.10).

2.7.2 Clay mineralogy

The relative abundance of different clay minerals can provide useful additional information on the provenance of fine-grained sediments around Antarctica (e.g. Ehrmann et al., 1992). At Site U1521, most samples are dominated by illite (44 ± 7%) and chlorite (30 ± 4%) (Fig. 2.8). These clay minerals are typical of physical weathering regimes, consistent with a glaciated margin (Fagel, 2007). The crystallographic properties of illite suggest it is derived from physical erosion of both biotite and muscovite from low pressure and low temperature metamorphic rocks. However, the composition of the illite is not the same in all the units, suggesting distinct sources of illite (Fig. 2.9). Consistent with a differing provenance to the other sequences, Sequence 2 is again distinct, with an illite end member that is characterised by a Kübler index higher than 0.3 and an Esquevin Index higher than 0.28 (Fig. 2.9). The other samples appear to have a different illite source, with a Kübler index between 0.17 and 0.25 and an Esquevin Index between 0.12 and 0.22, hinting at a metamorphic rock source in the Transantarctic Mountains. The Sequence 1 samples have the lowest Kübler index, implying a contribution from more high-grade metamorphic rocks (Fig. 2.9). Mixed-layer minerals represent 15% ± 6 of clay minerals at Site U1521 and are more abundant in Sequences 4A and 3A (18% ± 4) compared with Sequence 2 (9% ± 4) (Fig. 2.8). Around Antarctica, such mixed-layer minerals usually form through hydration of biotite (Kristoffersen et al., 2000), suggesting either enhanced chemical alteration or biotite-rich bedrocks.

Alongside these more abundant clay minerals, a small amount of kaolinite (1-7 %) is consistently present. Given that this mineral typically forms in warm and humid climates (Fagel, 2007), the kaolinite must be reworked from older strata. In this setting, a source from the Beacon Supergroup seems likely as this contains kaolinite (Ehrmann et al., 1992). However, kaolinite is also relatively abundant in modern to late Holocene sediments in parts of the Amundsen Sea shelf, where it has been suggested to originate from unknown pre-Oligocene sedimentary strata in subglacial basins in central West Antarctica, such as the Byrd Subglacial Basin and the Bentley Subglacial Trench (Hillenbrand et al., 2003; Ehrmann et al.,

2011; Simões Pereira et al., 2020; Klages, et al., 2020). The low abundance of kaolinite in Sequence 2 sediments at Site U1521, which have a West Antarctic provenance, therefore supports the hypothesis that the source of the kaolinite observed in the Amundsen Sea may be limited to the Amundsen Sea drainage sector of the WAIS – particularly the Thwaites Glacier catchment (Ehrmann et al., 2011; Simões Pereira et al., 2020).

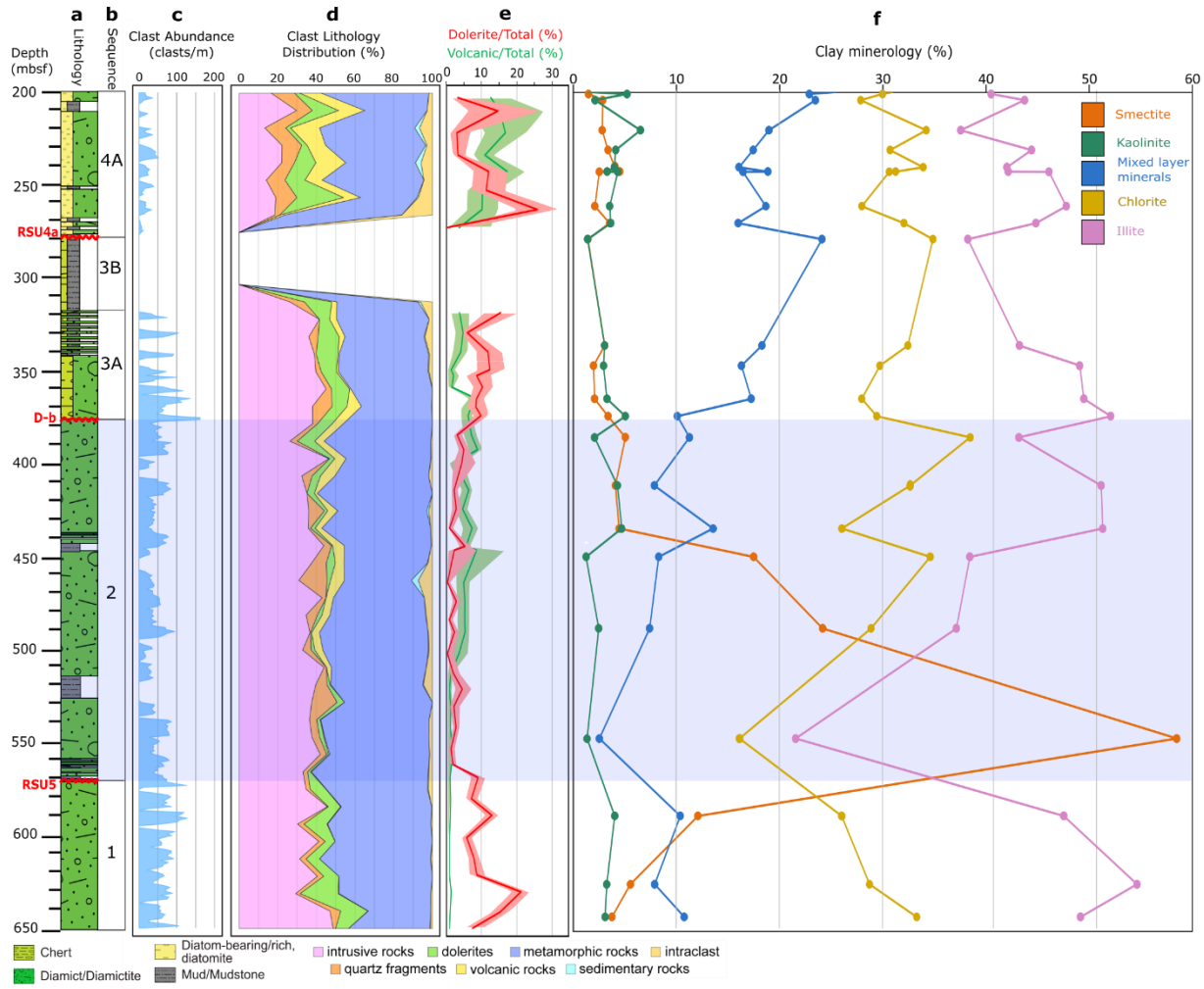


Figure 2.8. *Down-core clast and clay mineral distribution. The blue shaded area highlights Sequence 2, which is interpreted to consist of sediments with a West Antarctic provenance. a) Core lithology (see Figure 2.7 for key). b) Chronostratigraphic sequences. c) Clast abundance. d) Percentages of different clast lithologies. e) Ratio between dolerite and total number of clasts (red) and volcanic rocks and total number of clasts (green), with 95% confidence interval shown as pale shading (Vermeesch, 2018b). f) Clay mineral abundances.*

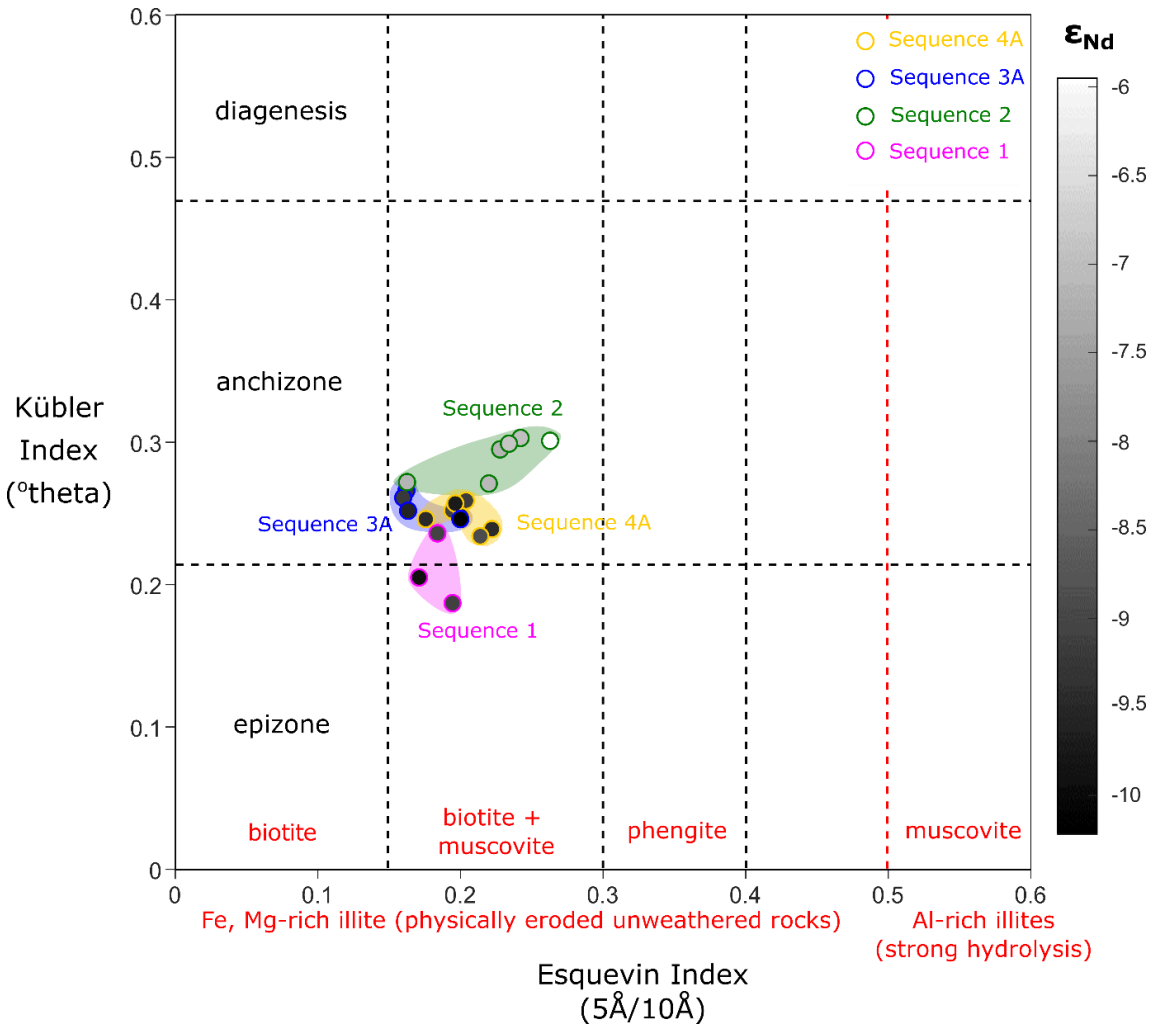


Figure 2.9. *Kübler vs Esquevin index values for the different sediments, with symbols coloured depending on their* ε_{Nd} *value and outlined depending on their stratigraphic position.*

Smectite is poorly crystallised and rare (<5%) throughout most of the section at Site U1521. The exception is Sequence 2, where the abundance of well-crystallised trioctahedral smectite reaches 58% towards the base. The 17Å/10Å ratio between smectite and illite diffraction intensities suggests this increase results from enhanced supply of smectite and not from decreased supply of illite and chlorite. We therefore infer an additional source of fine-grained detritus in this unit, which is likely basalt or volcanic material because smectite is generally considered a weathering product of these rock types (Fagel, 2007). This may point to a Marie Byrd Land volcanic province source. As the reworked dinocysts and diatoms indicate there were areas below sea level, some smectite may have formed through submarine weathering of these basaltic/volcanic rocks (halmyrolysis). The changes in smectite abundance throughout Sequence 2 are discussed in Section 2.8.2 below.

2.7.3 Clast Petrology

The petrology and relative abundance of clasts >2 mm offer valuable insight into potential sediment source regions. The abundance and petrology of all clasts exposed at the surface of the archive half was therefore macroscopically recorded continuously down-core at Site U1521. This was performed on all sections, but data for Sequence 3B are not available as it lacked clasts >2 mm. Clast abundance is variable through the record: Sequences 1 and 3A contain the greatest number, with fewer clasts observed in Sequence 2 (Fig. 2.8). This is most likely linked to the West Antarctic provenance of Sequence 2, as this was predominantly sourced from sedimentary strata in which gravel-sized and larger clasts are less likely to be preserved than sand, silt and clay particles. In contrast, subglacial erosion of crystalline bedrock is more likely to provide larger grains up to pebble to boulder size. Throughout the record, the most common clast type is meta-sedimentary - primarily meta-greywacke and meta-pelite. Igneous rocks, predominantly felsic granitoids, are the second most common clast type. Despite the relatively similar clast assemblage throughout the record, changes in the presence and abundance of certain rock types, such as volcanic rocks and dolerite (Fig. 2.8), provide useful constraints on provenance.

Sequence 1 contains high abundances of meta-greywacke clasts which can be traced to the Cambro-Ordovician meta-sedimentary sequences (Starshot Formation in the central Transantarctic Mountains and La Gorce Formation in the southern Transantarctic Mountains). Felsic granitoids, mainly grey granites, are likely derived from Granite Harbour Intrusive Complex plutons. Medium-grade schists and gneisses are sometimes present. Volcanic rocks are rare, whilst dolerite clasts, sourced from the Ferrar Group, are relatively common. Sedimentary rocks comprise less than 5% of the total amount but include some key lithologies such as limestones which are probably sourced from the Shackleton Limestone of the central Transantarctic Mountains. Clast lithologies in Sequence 1 are comparable with the outcropping geology of the Transantarctic Mountains; thus, a provenance from beneath the East Antarctic Ice Sheet is most likely. Most of those lithologies also outcrop in the southern Transantarctic Mountains, but the absence of felsic porphyries of the Liv Group is more compatible with a more northerly Transantarctic Mountain source.

Following Sequence 1, Sequence 2 shows a decrease in clast abundance linked to an increase in sedimentary intraclasts (Fig. 2.8). The main lithologies are (meta-)greywackes, (meta-)pelites and grey granitoids. A key feature is the sharp drop in the abundance of dolerite

clasts and the appearance of volcanic rock clasts in upper Sequence 2, which become more common than dolerite clasts (Fig. 2.8). The volcanic clasts are basaltic and occur in the granule fraction. A more detailed macroscopic identification is therefore not possible, but the Cenozoic subglacial volcanic edifices towards the eastern Ross Sea sector seem a likely source (Fig. 2.1). Meta-sedimentary lithologies may be derived from Cambro-Ordovician sequences (i.e. the Swanson Formation in Marie Byrd Land). Sequence 2 is also characterized by a scarcity of limestones and dolerites - lithologies confined to the Transantarctic Mountains.

Sequence 3A contains a clast assemblage resembling that of Sequence 1, with meta-sandstone, meta-pelites, grey granites, limestones, marbles and sandstones. Dolerite clasts reappear, whilst basalt clasts are less abundant; their presence compared to Sequence 1 may hint at some reworking of Sequence 2 strata in Sequence 3A. The granitoids are likely sourced from the Granite Harbour Intrusive Complex, while the meta-sedimentary clasts could originate from the Cambro-Ordovician sequences of the Transantarctic Mountains (i.e. Starshot and La Gorce formations). Limestones and carbonate conglomerates may have been sourced from the carbonate formations of the Byrd Group (i.e. Shackleton Limestone and Douglas Conglomerate), while a very mature quartz-arenite pebble could have been sourced from the Devonian formations of the Beacon Supergroup (Taylor Group). Dolerite clasts are more consistent with a Transantarctic Mountains than a West Antarctic source. The overall clast assemblage is most compatible with a source in the central Transantarctic Mountains.

Sequence 4A was poorly recovered and clasts are generally less abundant than in the underlying units, limiting the statistical robustness of the clast data. However, some general observations can be made. Meta-sedimentary clasts, sourced from the Cambro-Ordovician sequences, are more abundant than felsic intrusive igneous rocks of the Granite Harbour Intrusive Complex. Dolerite clasts are quite common (Figs. 2.7, 2.8), consistent with a Transantarctic Mountain provenance. The greater proportion of volcanic rock clasts in this sequence, which are likely to have more radiogenic ε_{Nd} values and less radiogenic $^{87}Sr/^{86}Sr$ ratios (Table A.2.9), is not evident in the isotopic data. Their apparent higher abundance may be a statistical artefact linked to the overall lower clast numbers rather than a real increase in volcanic clasts.

2.7.4 Palynology

Throughout Sequences 1 to 3A, the concentration of dinoflagellate cysts and other palynomorphs is low. These low concentrations are potentially due to dilution by a high supply of terrestrial detritus in an ice proximal (or subglacial) environment. Sequence 1 contains a high percentage of reworked dinoflagellates (17.5%; Figs. 2.7, 2.10), but this is a consequence of particularly low absolute concentration of dinocysts - possibly implying deposition in a subglacial environment - rather than a high number of reworked specimens. Reworked dinocysts are, however, common (13-21%, up to 489 per gram) in Sequence 2 (Fig. 2.10), suggesting Eocene to Oligocene sediments are being reworked. Alongside the data published here, three samples below 594.48 mbsf to the bottom of the hole were also scanned but were all (almost) barren of dinocysts. The few counted dinocysts (3-4 per slide, some fragments) were mostly reworked (*Vozzhennikovia*, fragments of *Deflandrea* and *Spinidinium*).

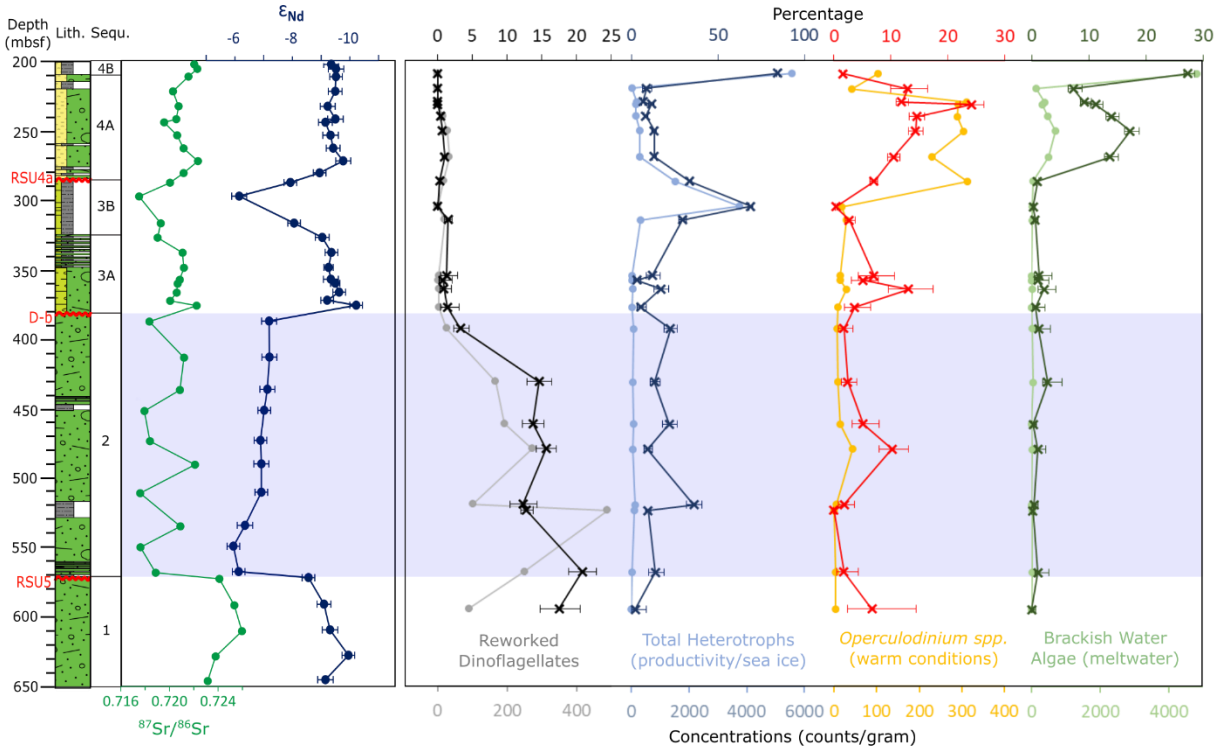


Figure 2.10. *Selected palynological counts compared to strontium and neodymium isotope data. Palynological data are reported as percentages (crosses) and counts/gram (circles). The blue shaded area represents Sequence 2, which is interpreted as consisting of sediments with a West Antarctic provenance. Error bars indicate a 95% confidence interval (Vermeesch, 2018b).*

In Sequence 3B, there is a sudden rise in the percentage (up to 69%) and absolute abundance of total heterotrophs, mostly in *Brigantedinium* spp. and *Lejeunecysta* spp. in approximately equal percentages and concentrations (Fig. 2.10). This may indicate an increase in biological productivity linked to a change to a more ice distal environment. Alternatively, the high heterotroph counts may indicate an increase in preservation, as heterotrophic dinocysts are more sensitive than phototrophic ones to oxidation and they prevail in anoxic/hypoxic bottom water environments (Zonneveld et al., 2007). We exclude the possibility that the assemblage in Sequence 3B represents an environment permanently covered by ice as the co-occurrence of these two genera has been previously linked to relatively cold conditions, with high productivity, sea-ice formation and melting in other Oligocene and Miocene Ross Sea sequences (Prebble et al., 2006; Clowes et al., 2016; Kulhanek et al., 2019). Also, in the modern ocean, *Lejeunecysta* spp. is never recorded under sea-ice; it is considered a temperate, coastal to neritic species, indicative of high productivity (Zonneveld et al., 2007).

Environmental conditions continue to change into Sequence 4A. *Operculodinium* spp., indicative of warmer conditions, and brackish water algae (mostly *Cymatiosphera* spp. with minor *Pediastrum* spp.), indicative of warmer and stratified water column conditions likely associated with meltwater (Feakins et al., 2012), are rare throughout much of the record but appear in Sequence 4A. Continued warming associated with high productivity is reflected in sharp rises in the concentrations of brackish water algae and heterotrophs at ~220 mbsf.

Overall, the marine palynology suggests a transition from ice-proximal sediments containing few palynomorphs (with reworked dinocysts in Sequence 2), to a warmer environment in Sequence 4A, especially in the uppermost sections. Sequence 3B is characterised by a combination of high productivity/high preservation conditions, with no notable indication of melting and stratification. This transition from an environment which is subglacial to ice proximal across the continental shelf (Sequence 1 and 2), then episodically ice-proximal (Sequence 3A to Sequence 4A), before becoming ice distal after ~16 Ma is consistent with interpretations of seismic facies (Pérez et al., 2021).

The miospore (spore-pollen) assemblage from Sequence 2 samples (479.24 mbsf and 567.78 mbsf) was very similar to that previously recovered from the Paleogene McMurdo Erratics (Askin, 2000). A wide diversity of *Nothofagidities* spp., and *Proteacidites* spp. forms were observed. Thus, we infer significant reworking from Eocene-early Oligoene sediments – consistent with dinoflagellate and diatom assemblages from the same unit. We observed no

evidence of Mesozoic reworking from these samples. Miospores in the two samples from Sequence 3A (354.56 mbsf, 377.25 mbsf) were sparse, and contained frequent inferred reworked Mesozoic grains. These inferred reworked specimens were generally poorly preserved with darkened exine. Three poorly preserved *Protohaploxypinus* spp. specimens, a distinctive component of the Permian Beacon Supergroup sediments (Kyle and Schopf, 1982), were noted in these samples. This is consistent with a Transantarctic Mountain provenance.

Pollen from near the Sequence 3B/4A boundary (286.02 mbsf) is fairly similar to the two samples from the overlying Sequence 4A. These are dominated by *Nothofagidites lachlaniae* complex, with persistent signs of likely Eocene reworking. However, evidence for Eocene reworking is less common than in Sequence 2 and there are more elements typical of Ross Sea Miocene deposits, for example *Coptospora*, and *Tricolpities* sp A., which are not seen in Sequence 2 (Askin and Raine, 2000; Kulhanek et al., 2019).

2.7.5 Zircon U-Pb Dating

Zircon U-Pb ages can offer important insights into specific source rocks. In the Transantarctic Mountains, Precambrian rocks were affected by the pervasive Ross Orogeny (615-470 Ma), which was accompanied by intrusive felsic magmatism (Goodge, 2020). Zircon age populations from Sequences 1, 3A and 4A show a strong peak towards the earlier part of the Ross Orogeny (595 to 535 Ma) and a 6 to 21% population of Archaean and Paleoproterozoic (>1600 Ma) zircon grains (Fig. 2.11). These features, together with a lack of grains younger than 250 Ma, resemble data from moraines in the Transantarctic Mountains (Licht et al., 2014; Licht and Palmer, 2016; Bader et al., 2017). Most samples plot between more coastal and more inland Transantarctic Mountain moraines (Fig. 2.11), consistent with mixing between these sediment sources as the glaciers traverse the mountain range.

Sequence 2 contains zircons with Cretaceous (~100 Ma) U-Pb ages (n = 16; Fig. 2.11a). Such ages are indicative of a West Antarctic provenance as they are presently only found beneath the modern Siple Coast ice streams, including Kamb Ice Stream and those closer to Marie Byrd Land (Licht et al., 2014; Perotti et al., 2017). The age spectra of samples from Sequence 2 share other features with data from the Siple Coast ice streams, including a broad Triassic (~240-190 Ma) age peak, few pre-Mesoproterozoic zircons (<5 % of grains) and a young (~515-505 Ma) Ross Orogeny peak (Fig. 2.11) (Licht et al., 2014).

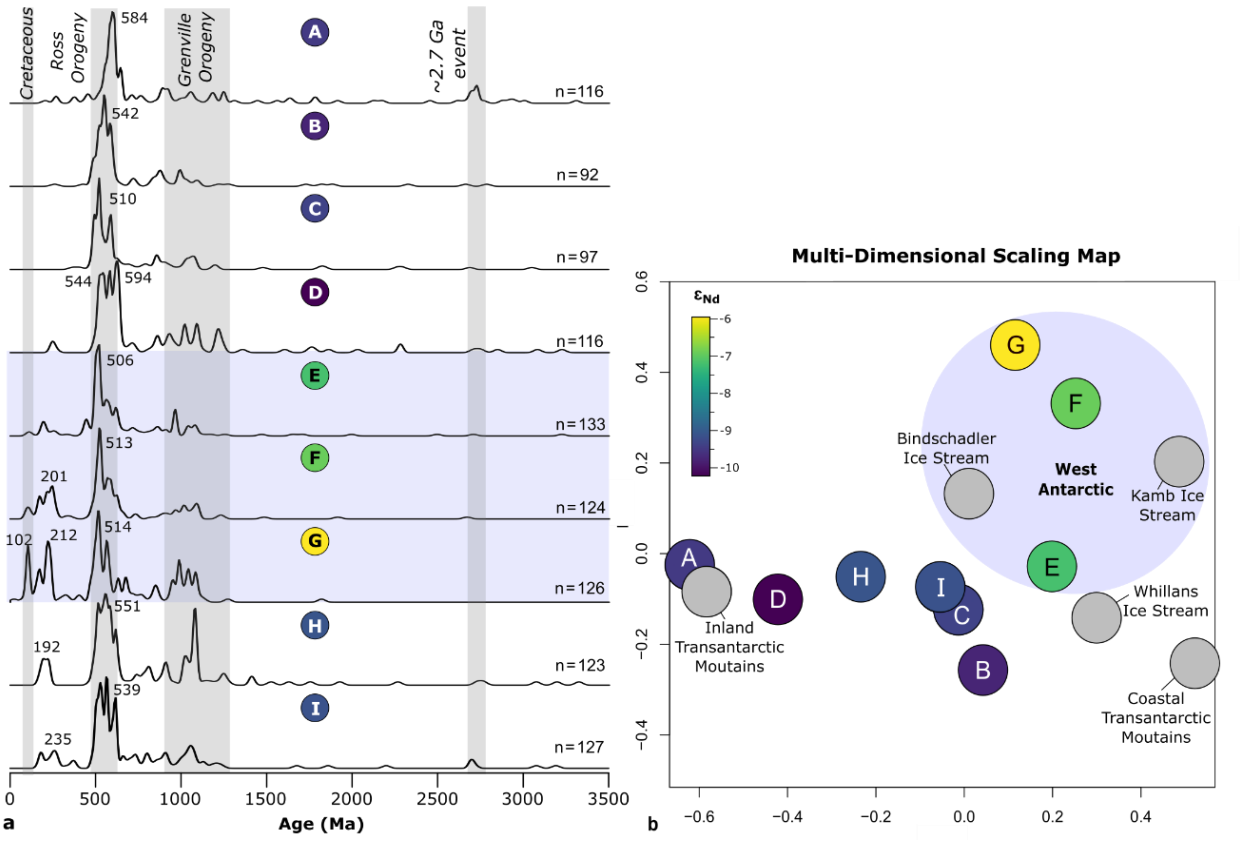


Figure 2.11. *Site U1521 detrital zircon U-Pb age distributions. a) Data displayed as kernel density estimates (KDEs). When present, large Ross Orogeny (~600-500 Ma), Triassic (~240-190 Ma) and Cretaceous (~100 Ma) age peaks are labelled numerically. The age ranges of the Ross Orogeny, Grenville Orogeny and a ~2.7 Ga event recorded in Ross Sea sedimentary strata are illustrated using grey-shaded bars. The sub-bottom depth midpoints of the samples A-I are shown in Figure 2.7 and listed in the methods section. b) Same data as in a), displayed as a multi-dimensional scaling (MDS) map calculated using the Kolmogorov–Smirnov statistic (Vermeesch, 2013). Stress (a measurement of the goodness of fit between the disparities and the fitted distances; Vermeesch, 2013) = 0.072. A MDS plot visualises the degree of similarity between samples, with the proximity of sample points reflecting their similarity. The axis scales are dimensionless and have no physical meaning. The colour of Site U1521 samples (A to I) corresponds their* ε_{Nd} *value. Previously published zircon U-Pb data from Kamb, Whillans and Bindschadler ice streams in West Antarctica, as well as Transantarctic Mountain moraines from inland and coastal regions, are shown in grey (Licht et al., 2014; Licht and Palmer, 2016; Bader et al., 2017). The KDEs and region of the MDS plot interpreted as having a West Antarctic provenance are shaded in light blue, consistent with the blue shading in panel a) and Figure 2.7. Note that although Whillans Ice Stream drains the WAIS, it is excluded from the blue shaded area due to its proximity to the*

Transantarctic Mountains (Figure 2.1), resulting in a subglacial sediment provenance signature indistinguishable from East Antarctic detritus (Licht et al., 2014).

2.7.6 Hornblende $^{40}Ar/^{39}Ar$ Dating

To complement the detrital zircon U-Pb dating, five of the samples taken from the magnetic separation step were also picked for detrital hornblende grains. The hornblende $^{40}Ar/^{39}Ar$ system has lower closure temperature (~500ºC; McDougall and Harrison, 1999) than the zircon U-Pb system (>900 ºC; Cherniak and Watson, 2001), giving ages which are younger and indicative of the last major tectonothermal event affecting the source rocks. Furthermore, hornblende is less prone to recycling in sedimentary rocks, and can therefore indicate whether a signal in the zircon U-Pb data is from primary erosion of crystalline rock or reworking of older sedimentary strata.

Features consistent between the $^{40}Ar/^{39}Ar$ dating and U-Pb dating include the main Ross Orogen peak, which is dominant in all samples. As expected given the higher closure temperature, the zircon U-Pb ages are consistently older (Fig. 2.12). Nevertheless, the age of the U-Pb Ross Orogen peak correlates well with the hornblende $^{40}Ar/^{39}Ar$ age peak. For instance, the oldest U-Pb Ross Orogen age peak is found in sample A (584 Ma), which also has the oldest $^{40}Ar/^{39}Ar$ age peak (516 Ma; Fig. 2.12). This observation is consistent with erosion of older rocks on the inland side of the Transantarctic Mountains. Further similarities include the Grenville-age grains present in all samples except Sequence 2. Thus, primary erosion of Grenville-age rocks did not contribute to the deposition of Sequence 2, consistent with the absence of these ages in the Ross Sea sector of West Antarctica (Jordan et al., 2020).

The biggest discrepancy between the two thermochronological datasets is the large population of hornblende grains in lower Sequence 4A (sample B) peaking at ~179 Ma; nearly a quarter of the grains have ages between 200 and 150 Ma (Fig. 3.11). This age is similar to that of Ferrar Group hornblende grains, which occur in some granophyres and pegmatites in Southern Victoria Land (Gunn and Warren, 1962; Morrison and Reay, 1995; Cox et al., 2012). However, the Ferrar Group is not usually hornblende-bearing (Cook et al., 2017). The source of these grains is therefore uncertain. One possibility is the existence of an unexposed subglacial coarse-grained rock associated with the Ferrar Group, such as the gabbroic, hornblende-bearing Dufek Intrusion in the Pensacola Mountains located to the south of the Weddell Sea embayment (Ford, 1976). Another possibility is that zircon grains are present but are too small to be intercepted during the heavy mineral separation.

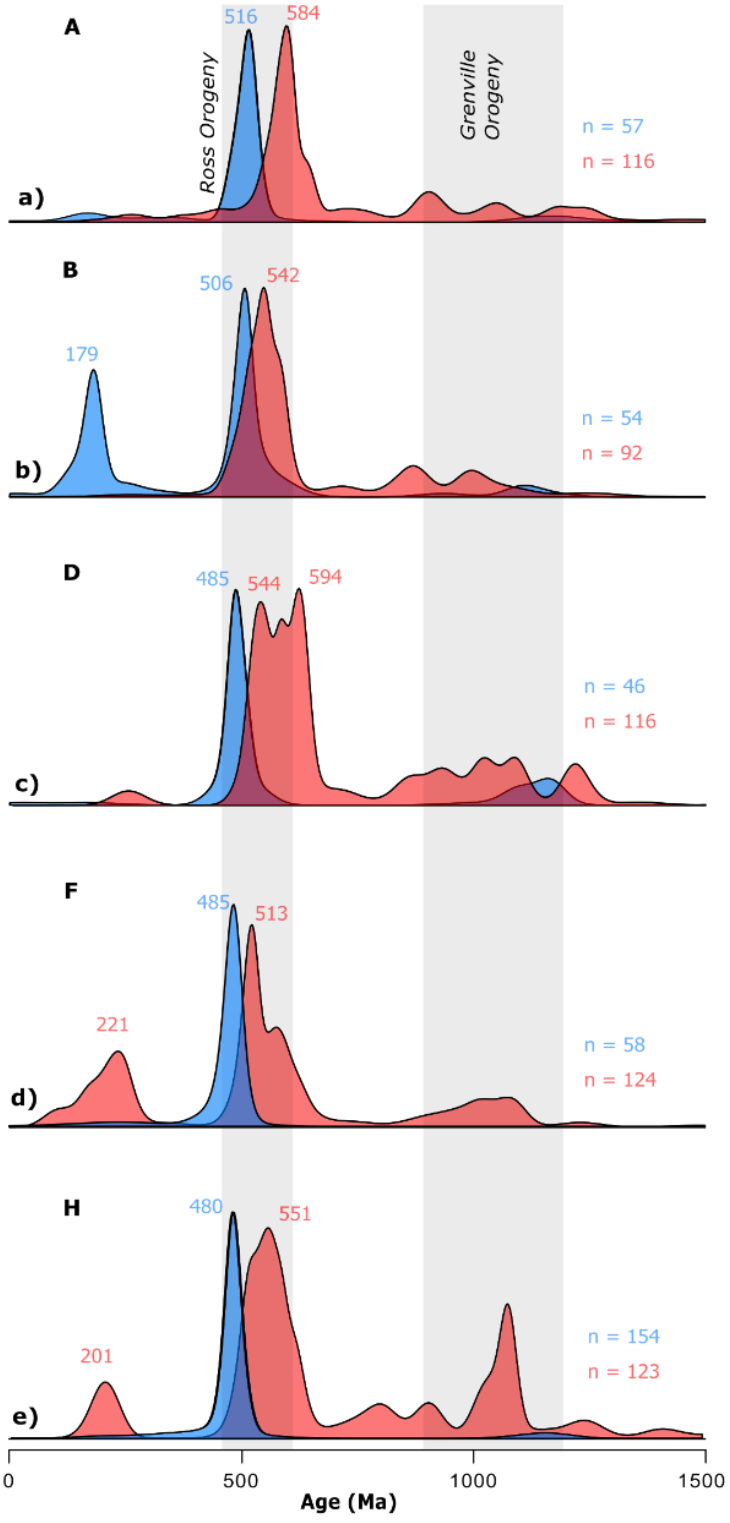


Figure 2.12. *Kernel density estimates for hornblende $^{40}Ar/^{39}Ar$ ages (blue) compared to zircon U-Pb ages younger than 1500 Ma (red). Bold letters correspond with those in Figure 2.11. The positions of major peaks and number of grains analysed are labelled in the corresponding colours. Stratigraphic position is shown in Figure 2.7.*

Alternatively, some rocks contributing to the lower Sequence 4A sample may have had older hornblende grains, common in the Granite Harbour Intrusive rocks, thermally reset (i.e. heated above ~500ºC) during the time of Ferrar large igneous province activity. This would explain the lack of ~180 Ma zircons dated using the U-Pb method, but abundance of hornblende grains of this age. An additional contrasting feature between the dating methods is the lack of ~200 Ma hornblende grains in the Sequence 1 and 2 hornblende samples (samples F and H), as this age is present in the zircon U-Pb age spectra. This may indicate reworking of the ~200 Ma zircons, or erosion of a very felsic (i.e. non-hornblende bearing) lithology.

2.8 Discussion

2.8.1 Sediment Provenance of Sequence 2: Evidence for an Early Miocene WAIS

All the datasets discussed above show that Sequence 2 has a distinct provenance signature compared to Sequences 1, 3A and 4A. The latter sequences all have zircon U-Pb ages consistent with sediment sourced from the Transantarctic Mountains including an older Ross Orogeny peak and more common Precambrian ages (Fig. 2.11). This is supported by ε_{Nd} values of ~-9 to -10 in these samples, consistent with this sediment source (Figs. 2.5, 2.6; Farmer et al., 2006). Clast lithologies also correlate with rocks in the Transantarctic Mountains, with lithologies including common felsic granitoids and meta-sediments alongside rarer limestones, marbles and sandstones (Fig. 2.8; Goodge, 2020). Although a relatively minor component, dolerite clasts are found throughout Sequences 1, 3A and 4A (Fig. 2.7g) and can be traced to the Jurassic Ferrar Group, which predominantly crops out in the Transantarctic Mountains (Fig. 2.1). Furthermore, rare *Protohaploxypinus* pollen, a distinctive component of the Permian Beacon Supergroup in the Transantarctic Mountains, are observed in Sequence 3A (Kyle and Schopf, 1982). Overall, the sediments comprising Site U1521 Sequences 1, 3A and 4A are predominantly sourced from erosion of the Transantarctic Mountains in East Antarctica.

In contrast, Sequence 2 is characterized by the highest ε_{Nd} values, likely due to a more radiogenic sediment source from the area beneath the modern WAIS. Samples with elevated ε_{Nd} values coincide with the presence of zircon U-Pb ages of ~100 Ma, which are diagnostic of a West Antarctic provenance (Fig. 2.11; Licht et al., 2014). Detrital hornblende $^{40}Ar/^{39}Ar$ ages from Sequence 2 further corroborate a West Antarctic provenance. Unlike zircon grains, which can survive multiple sedimentary cycles, hornblende grains are less resistant to

weathering. The absence of Grenvillian (~1100-900 Ma) ages in the Sequence 2 hornblende sample (Fig. 2.12) therefore suggests a West Antarctic provenance, as Grenville-age rocks are absent there (Jordan et al., 2020). The scarcity of Ferrar Group dolerite clasts, common in the Transantarctic Mountains, is also consistent with a West Antarctic provenance (Figs. 2.7; 2.8), as is a high proportion of smectite in the clay fraction at the bottom of Sequence 2 (≤58%; Fig. 2.8), with smectite percentages similar to Quaternary sediments in the eastern Ross Sea (Balshaw-Biddle, 1980). Additionally, Sequence 2 contains evidence for recycling of older marine detritus, most likely from the lower Cenozoic rift-fill strata that exist in the eastern Ross Sea region of the West Antarctic Rift System (De Santis et al., 1995). This is inferred from the dominance of reworked Eocene-Oligocene species in the diatom and spore-pollen assemblages (McKay et al., 2019), alongside the common (13-21%) reworked Eocene-Oligocene marine dinocysts, which are rare (<1.5%) in younger sediments (Fig. 2.10).

Further evidence for WAIS expansion can be found in seismic data, which can trace the sediment package deposited at Site U1521 between 17.72 and 17.40 Ma (Sequence 2) across the Ross Sea continental shelf (Pérez et al., 2021). The sediment package, which is thicker towards the eastern Ross Sea (i.e., West Antarctica), contains glacial features including widespread progradational wedges and high relief morainal banks (Anderson and Bartek, 1992; De Santis et al., 1995; Pérez et al., 2021). Coupled with the lithological and palynological evidence for ice proximity at Site U1521, this shows marine-terminating ice was present. Transport of large volumes of West Antarctic detritus as far west as the Pennell Basin in the central Ross Sea is evident in our provenance data, which, alongside common reworked marine microfossils, proves this marine-terminating ice derived from an Early Miocene WAIS which intermittently extended across most of the outer continental shelf.

Our data therefore reveal WAIS expansions across the Ross Sea continental shelf date back to at least 17.72 Ma, which is significantly earlier than previously suggested (Zachos et al., 2001; Kennett and Barker, 1990; Bart, 2003; Westerhold et al., 2020). Advance of the WAIS into marine-based areas (i.e., regions grounded mainly below sea level) at 17.72-17.40 Ma is supported by a corresponding period of high sensitivity of the marine $\delta^{18}O$ record to obliquity forcing (Fig. 2.7i). High obliquity sensitivity is considered a proxy for enhanced ice-sheet sensitivity to ocean dynamics and thus the presence of marine-based ice (Levy et al., 2019).

2.8.2 Provenance Changes within Sequence 2

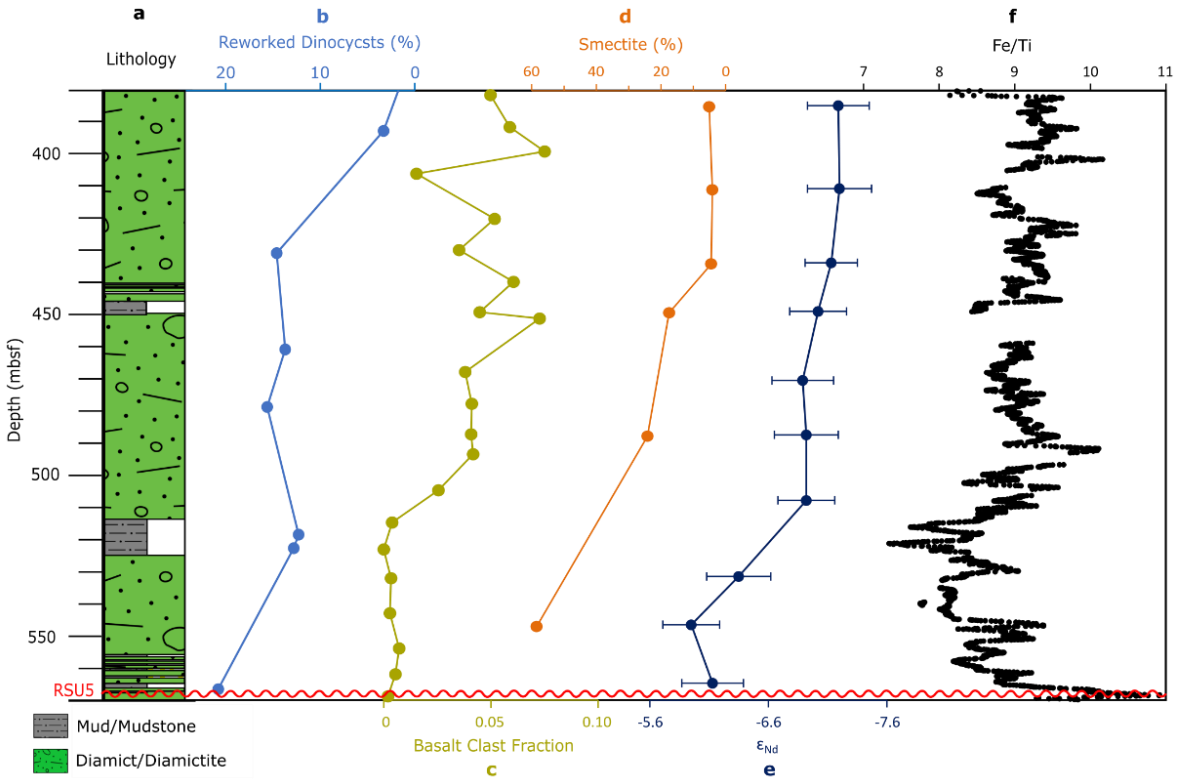


Figure 2.13. *Close up of the Site U1521 interval with a West Antarctic provenance. The stratigraphic log (a) is displayed alongside the percentage of reworked dinocysts (b), basalt clast fraction (c), relative abundance of smectite (d), Nd isotope data (e) and Fe/Ti ratios determined by X-ray fluorescence scanning (f).*

Beyond the identification of a West Antarctic provenance for Sequence 2 sediments, changes within the sequence allow further inferences about ice sheet development in this rapidly deposited interval. One notable trend is the slight decrease in ε_{Nd} values over time (Fig. 2.13e), which implies a decrease in the contribution of fine-grained detritus from the Marie Byrd Land volcanic province. Compared to other lithologies, the alkali basalts around the Ross Sea embayment are relatively rich in titanium (Goldich et al., 1975); thus, their decreased contribution to the sediments deposited at Site U1521 through time is consistent with an increase in the Fe/Ti ratio (Fig. 2.13f). Further evidence for provenance change within Sequence 2 is seen in the detrital zircon U-Pb data. These data show a decreasing Marie Byrd Land (West Antarctic) contribution over time, with the decreasing abundance of the indicative Cretaceous and late Triassic zircons up section suggesting a source closer to the Transantarctic Mountains (further south) for the younger sediments (Fig. 2.11). This also fits with the expectation that sediments sourced closer to Marie Byrd Land (further north) in

lower Sequence 2 will have a greater contribution from Cenozoic basalts, making the ε_{Nd} signature more radiogenic. We suggest the provenance changes observed within Sequence 2 can therefore be at least partially attributed to changes to ice sheet extent and dynamics.

Smectite abundance decreases upwards within Sequence 2 from 58% at the bottom to <10% at the top (Figs. 2.8; 2.13), with an excellent correlation between the smectite/illite ratio and ε_{Nd} ($R^2 = 0.997$). Smectite percentages similar to those identified in the lower Sequence 2 sediments are found east of 170° W in late Quaternary Ross Sea sediments (Balshaw-Biddle, 1980). This correlation suggests a source towards Marie Byrd Land and could be responsible for the high smectite content seen in lower Sequence 2. Smectite is a weathering product of basaltic and volcanic rocks and its formation is very slow beneath ice sheets (Rosenqvist, 1975; Tulaczyk et al., 1998). The smectite may therefore be derived from pre-glacial sediments (Fagel, 2007), in agreement with palynological data suggesting reworked Eocene-Oligocene detritus in Sequence 2.

Due to its derivation from volcanic rocks, a decreasing smectite content over time in Sequence 2 would be expected to correlate with a decrease in the fraction of basaltic source rocks (clasts) in the sediment. However, the abundance of gravel-sized volcanic clasts shows the opposite trend (Fig. 2.13). This anticorrelation between basalt clast abundance and smectite content can be explained if the sediments in lower Sequence 2 have undergone a higher degree of weathering and comminution.

We suggest that the lower Sequence 2 samples comprise a more weathered layer originally covering parts of West Antarctica. Basalt clasts are rare as they have typically been reduced in size to <2 mm, rendering them undetectable in the clast petrography. The weathered basaltic signal is, however, preserved in the <63 μm fraction, giving more radiogenic ε_{Nd} values and higher smectite percentages. At the time of the deposition of the material higher in Sequence 2, we infer that this weathered layer has been subglacially eroded, exposing the basalt bedrock beneath. This leads to an increase in the number of basaltic clasts in the coarser-grained size fraction at Site U1521, and a decrease in smectite contents and ε_{Nd} values in the fine fraction.

We acknowledge there are other potential explanations for the anticorrelation between basalt clasts and smectite contents but view these as much less likely. For instance, changes to ice sheet thickness could change the proportion of subaerial vs subglacial volcanism by exposing/burying volcanoes. Subglacial eruptions produce more subglacial water, which

would promote smectite formation. However, oxygen isotope data imply only minimal change to ice volumes during this interval (Fig. 2.7), suggesting that a decline of subglacial eruption products due to a thinning ice sheet is unlikely to explain the observed trends. We therefore view a progressive removal of weathered detritus as the most likely mechanism to explain the basalt clast/smectite abundance anticorrelation. A higher degree of weathering/comminution in the lower parts of Sequence 2 is also supported by the presence of only small, altered basalt clasts when these are present.

Further support for weathering influencing the provenance signature of the Sequence 2 sediments is found in the breakdown in the correlation between Nd and Sr isotope ratios. In the other sequences at Site U1521, measured Nd and Sr isotope ratios have a negative correlation (Fig. 2.10). This is because older/more evolved rocks typically have a higher $^{87}Sr/^{86}Sr$ and a lower ε_{Nd} signature compared to younger/less evolved rocks (Table A.2.9). The decoupling of these isotope systems in Sequence 2 likely results from the potential for fractionation of Rb and Sr. This can happen during weathering (Blum and Erel, 1997) due to the different atomic radii of the two elements and resulting affinities for entering the solution phase. Alternatively, fractionation can be dependent on grain size, as different minerals often have different Rb/Sr ratios (Eisenhauer et al., 1999). Coupled with the fact that certain minerals, such as clay minerals or biotite, are more likely to be present in the fine fraction of sediments, this can lead to variations in $^{87}Sr/^{86}Sr$ unrelated to sediment provenance. Grain size and/or weathering effects are therefore likely impacting the Sr isotope compositions of the Sequence 2 sediments, consistent with a more weathered sediment layer.

In summary, the anticorrelation between smectite and volcanic rocks suggests that lower in Sequence 2, basaltic bedrock was predominantly weathered to smectite and was thus largely confined to the finer grain size fractions. Over time, this more weathered regolith layer was removed, leading to erosion of progressively more pristine continental detritus containing more basalt clasts. Sequence 2 (17.72-17.40 Ma) could therefore record an advance of the WAIS over parts of West Antarctica which had not been covered by grounded ice for an extended period.

2.8.3 Birth of a Marine-Based WAIS

The mean erosion rate for the WAIS catchments draining to the Ross Sea between 17.72 and 17.40 Ma can be estimated using the volume of the corresponding seismic package east of Site U1521 (Pérez et al., 2021). The volume of sediment comprising Sequence 2 was

estimated based on seismic data for the Ross Sea continental shelf (Pérez et al., 2021). The isopach maps were developed by interpolating between available seismic reflection profiles (Pérez et al., 2021), giving a total volume of 175,526 ± 17,553 km^3. The 10% uncertainty accounts for uncertainty in seismic velocities, which vary from 1700-2700 ms^{-1} at Site U1521 based on tomography and 1970-2480 ms^{-1} based on down-hole measurements. As the provenance data suggest a West Antarctic sediment source for Site U1521 Sequence 2, we assume that all the sediments east of 180° and south of 73° are derived from West Antarctica. This is the vast majority (123,627 ± 12,550 km^3) of the sediment across the shelf. Our sediment volume estimate is conservative, as the top of Sequence 2 (surface D-b) has been truncated across much of the continental shelf by RSU4 (Pérez et al., 2021). Significant sediment volumes are also likely to be present beyond the edge of the seismic data from the continental rise. Any sediment beneath the modern Ross Ice Shelf is also unaccounted for, although this component is likely to be small.

Table 2.3. *Values used in the erosion rate calculation.*

	Median Erosion Estimate	Minimum Erosion Estimate	Maximum Erosion Estimate
Sediment Volume (km^3)	123,627	111,077	136,177
Mean Porosity	0.436	0.499	0.374
Terrigenous Fraction	0.95	0.9	1
Catchment Area (km^2)	759,640	911,569	607,712
Catchment Mean Erosion (m)	87.14	54.97	140.26
Duration (years)	317,416	337,416	297,416
Mean Erosion Rate ($mm\ yr^{-1}$)	0.275	0.163	0.472

To translate this sediment volume into an erosion rate, the approach and uncertainty range of Paxman et al. (2019a) was used to account for porosity and a small biogenic sediment component (Table 2.3). Using generic values in our porosity calculation is crude, with variation in the porosity of these Antarctic sediments likely to be significant (Niessen et al., 2013), but nevertheless sufficient for our order-of-magnitude estimate of erosion. It is reasonable to assume the major ice divides have remained in largely the same positions since the Early Miocene, as indicated by various modelling studies using reconstructed topographies (Gasson et al., 2016; Colleoni et al., 2018; Paxman et al., 2020). The size of the

eastern Ross Sea catchment (i.e. Ross Sea sector of the WAIS) was therefore assumed to be similar to the modern, with a 20% uncertainty. Some sediment in these units clearly contains reworked material; there are high concentrations of Eocene-Oligocene palynomorphs and diatoms. Although this means our erosion rate is not indicative of pure bedrock incision, it still represents a significant change to the topography and bathymetry of West Antarctica. The material removed likely exceeds our conservative estimate of ~87 m across the catchment. The 317,416 year duration is based on the cyclostratigraphic analyses described in the age model section, with a 20,000 year uncertainty.

The mean erosion rate of ~0.275 mm a^{-1} during this interval greatly exceeds the long-term mean rate of 0.012 mm a^{-1} calculated for this part of the WAIS between 23 and 14 Ma (Paxman et al., 2019a); even when the full uncertainty is taken into account (Table 2.3), it is still more than an order of magnitude higher. This highlights the 17.72 to 17.40 Ma interval as one of unusually rapid erosion, with erosion rates comparable to modern subpolar to temperate glacial catchments (Koppes et al., 2015). Transporting this large volume of subglacially eroded debris quickly to the WAIS margin required abundant meltwater at the ice sheet bed (Alley et al., 2019), as well as fast-flowing ice streams that extended into marine settings where broad deposition took place. Ocean temperatures must therefore have been sufficiently cool to permit the advance of marine-based ice, yet atmospheric conditions must have remained warm enough to provide sufficient precipitation to drive dynamic ice flow and enhanced basal erosion (Gasson et al., 2016).

Since most of West Antarctica, apart from Marie Byrd Land, was thermally subsiding throughout the Miocene (Paxman et al., 2019a), the high erosion rate at 17.72 to 17.40 Ma is unlikely to have been driven by tectonic uplift. The eroded sediments therefore reflect ice expansion and enhanced glacial incision of the terrestrial West Antarctic hinterland, plus infilling of the Ross Sea basins. This erosive event occurred at a time when topographic reconstructions indicate a transition from a terrestrial West Antarctic topography (23 Ma) to a largely submarine West Antarctic topography (14 Ma) (Paxman et al., 2019a). The timing and large volume of sediment deposited in Sequence 2 at Site U1521 suggests that the 17.72 to 17.40 Ma interval records a critical step in the transition of the WAIS from a largely terrestrial ice sheet to one that was primarily marine-based. This significant alteration to West Antarctic topography occurred just prior to major changes affecting the Antarctic cryosphere and global climate during the MCO (Levy et al., 2016; Miller et al., 2020). Subglacial erosion may therefore have driven changes in ice-sheet evolution and behaviour as, after ~17.40 Ma,

a greater submarine area in central West Antarctica would have made the mass-balance control of the WAIS more sensitive to external drivers such as sea level and oceanic forcing (Colleoni et al., 2018; Paxman et al., 2020). We propose that ice retreat at the onset of the MCO may be partially attributable to the crossing of this topographic tipping point and that Sequence 2 records the birth of a marine-based WAIS. This event dates to well before 14 Ma, the time slice at which topographic reconstructions first show a largely sub-marine West Antarctica (Paxman et al., 2019a).

2.8.4 Ice Retreat during the Miocene Climatic Optimum

Above Sequence 2, later changes to ice sheet extent can be inferred. Sequence 3B is dated to ~17.1- 17.0 Ma, just prior to the MCO (Fig. 2.3). The lack of clasts, poor recovery and difficulty in disaggregating the very compacted chert samples limited provenance data to radiogenic isotope analysis. Neodymium isotopes are relatively radiogenic, peaking at an ε_{Nd} value of -6.2 in the centre of the unit (Fig. 2.7). Although this value is similar to those in Sequence 2, the fine grain size and palynology of Sequence 3B suggest a very different depositional environment (Figs. 2.7, 2.10). A potential explanation for the observed ε_{Nd} composition of the Sequence 3B sediments is a decreased supply of clastic material due to a smaller, and thus more distal, ice sheet. In such a scenario, the developing volcanic centres in the McMurdo region could contribute a relatively greater proportion of detritus forming the sediments. The provenance may therefore result from a combination of Transantarctic Mountain and McMurdo Volcanic Group material, consistent with a terrestrial palynological assemblage similar to Sequence 4A. We hence suggest that similarly radiogenic ε_{Nd} values for Sequences 2 and 3B (Fig. 2.7) are coincidental, and, in fact, indicate a higher contribution from West Antarctica in Sequence 2, but an East Antarctic source in Sequence 3B.

Sequence 4A was deposited rapidly at approximately ~16.75 – 16.25 Ma (Fig. 2.3), placing it in the Miocene Climatic Optimum. The sequence is interpreted to have derived primarily from erosion of the Transantarctic Mountains in East Antarctica. This is evidenced by consistent ε_{Nd} values of ~-9, a lack of smectite, and the occurrence of dolerite clasts (Figs. 2.7, 2.8). However, more detailed changes within the sequence can be distinguished and may indicate retreat to erosion on the inland portions of the Transantarctic Mountains higher in Sequence 4A (Fig. 2.11). In the Transantarctic Mountains, the peak of the Ross Orogeny age populations in detrital zircons from moraines varies spatially (Licht and Palmer, 2013) and stratigraphically between different Beacon Supergroup formations (Elliot et al., 2017; Bader

et al., 2017). Zircons in modern moraines deposited by glaciers near their heads (i.e. before these glaciers traverse the Transantarctic Mountains) typically have an older (>~550 Ma) Ross Orogen age peak, whilst zircons from moraines deposited further downstream regions have a younger (~500 Ma) age peak (Licht and Farmer, 2016; Bader et al., 2017). The Ross Orogeny age peak in offshore sediments is therefore hypothesised to shift to older values if erosion in the Transantarctic Mountains was focussed further inland (Licht and Farmer, 2016). An old Ross Orogeny age peak is seen in the upper Sequence 4A zircon U-Pb sample (Fig. 2.11 sample A); this may indicate a retreat of the ice sheet margin leading to erosion further inland.

Further evidence for a retreated ice sheet is apparent in other datasets. Evidence for stratified and highly productive surface waters continues at the top of Sequence 4A (Fig. 2.10). This interpretation is supported by volume-based smear slides estimates of diatom content from Sequence 4A, which show an increase to >10% in the diamict and mudstone matrix. Mixed-layer minerals are more abundant in Sequence 4A (18% ± 4), suggesting either enhanced chemical alteration or biotite-rich bedrocks. We favour enhanced chemical alteration for this sequence, as this is consistent with the evidence for warming environmental conditions discussed above.

2.9 Conclusions

The data presented here document detailed Early Miocene sediment provenance shifts in the Ross Sea. Sediments deposited just prior to and during the MCO (Sequences 3B and 4A) record warmer paleoenvironmental conditions, with retreat of the glaciers traversing the Transantarctic Mountains leading to the focus of erosion shifting erosion of rocks further inland. Prior to this, rapid erosion of West Antarctic detritus led to the birth of a predominantly marine-based WAIS, with important implications for subsequent ice sheet sensitivity.

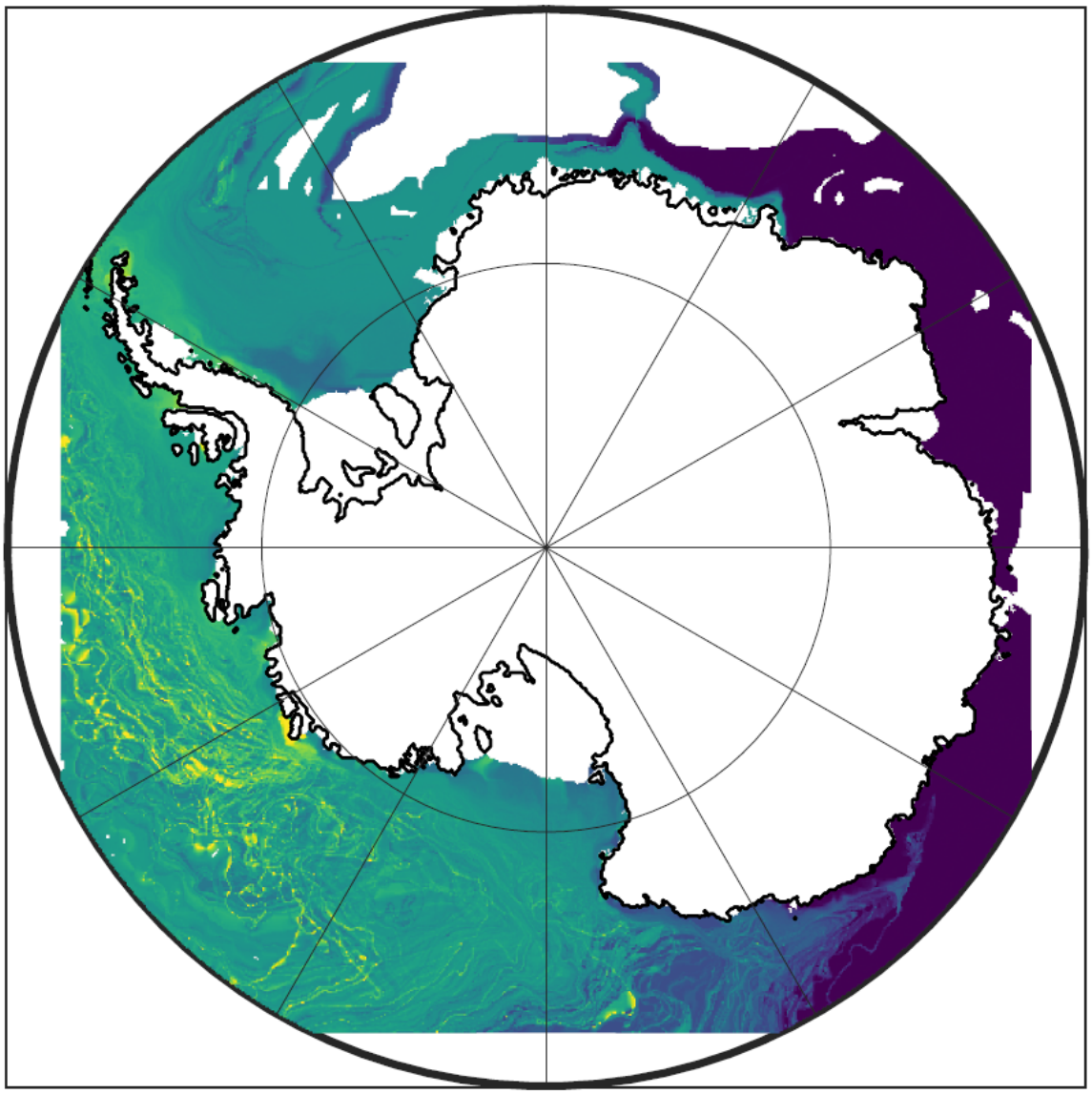
However, the chief finding is that grounded ice flowing from West Antarctica was close to Site U1521 towards the end of the Early Miocene. This result validates recent modelling studies suggesting that an ice sheet nucleating on a partially terrestrial West Antarctica could expand extensively into the marine realm under Early Miocene climatic and paleotopographic conditions (Gasson et al., 2016; Colleoni et al., 2018; Paxman et al., 2020). Our data are consistent with an ice extent similar to, or exceeding, the largest modelled Early to Middle Miocene Antarctic ice sheets (Fig. 2.1), containing ice volumes of approximately 80 m sea-

level equivalent (SLE) depending on the topographic reconstruction used (Gasson et al., 2016; Colleoni et al., 2018; Paxman et al., 2020). This expanded WAIS contained approximately 14-15 m SLE of ice, but also acted to buttress the EAIS resulting in significantly larger-than-present ice volumes (Gasson et al., 2016; Colleoni et al., 2018). These maximum ice volume constraints indicate that far-field sea-level amplitudes of ~40-60 m did not require the loss of nearly all terrestrial East Antarctic ice during subsequent warm periods during the MCO (Pekar and DeConto, 2006; Kominz et al., 2016; Miller et al., 2020), consistent with modelled EAIS hysteresis effects (Gasson et al., 2016). By providing the earliest conclusive evidence for a large marine-based WAIS, our data also dispel long-held inferences that a WAIS, able to significantly impact global eustacy and climate, was not present until the Middle or Late Miocene (Kennett and Barker, 1990; Zachos et al., 2001; Westerhold et al., 2020).

Relevant Appendix Sections – The published manuscript can be found in Appendix Section A.1. Data used to generate many of the figures shown are displayed in Appendix Section A.2. Data and discussion for lithological unit III (Sequence 4B) are found in Appendix Section A.3. Data and discussion regarding neighbouring IODP Expedition 374 Site U1522 are found in Appendix Section A.4.

Chapter 3. A Quantitative Approach to Interpreting Antarctic Sediment Provenance Records

James Marschalek designed and led the project with assistance from Ed Gasson. Guidance was also provided by Tina van de Flierdt, Martin Siegert and Claus-Dieter Hillenbrand. Ed Gasson re-ran the ice sheet model simulations to save additional outputs. Liam Holder provided new surface sediment ε_{Nd} data.



Tracing of Nd isotopes deposited at the ice sheet margin using modelled surface currents.

Chapter Summary

Ice sheet models offer excellent opportunities to examine the extent and drainage patterns of past ice sheets and make predictions regarding future Antarctic ice mass loss. Hypotheses regarding ice sheet response to different climates (e.g. Gasson et al., 2016), changes to bed topography (e.g. Colleoni et al., 2018), and changes to physical processes (e.g. DeConto and Pollard, 2016) can all be tested and visualised. Testing ice sheet models against real-world data from the sedimentary record improves model predictions of future ice sheet behaviour. However, interpretations of model outputs and palaeo data are rarely directly linked.

Provenance studies provide an excellent opportunity to do so. Tracing the origin of sediments deposited on the Antarctic continental margin to their continental source areas yields unique insights into the extent and flow dynamics of past ice sheets (e.g. Cook et al., 2013; Wilson et al., 2018; Marschalek et al., 2021). However, such marine sediment provenance studies are typically limited to qualitative interpretations as making quantitative statements is hindered by uncertainties regarding subglacial geology, processes of subglacial erosion, and entrainment and transport of detritus both by ice and in the ocean. Sediment provenance records can be used as a target for and compared to ice sheet modelling results to help overcome this limitation.

In this chapter, marine geochemical sediment provenance data are quantitively predicted using the output of numerical ice sheet modelling of modern and past ice sheets. The ice sheet model is used to infer the spatial pattern of erosion rates and to trace ice flow pathways. Beyond the ice sheet margin, simple approximations of modern detrital particle transport mechanisms produce a good agreement with marine surface sediments. We target West Antarctica and the eastern part of East Antarctica, where several sediment provenance records exist and the ice sheet is often marine-based, making it of particular relevance when predicting sea level rise. Although other parts of East Antarctica are also marine-based, compiling data here would require significant extra work and is therefore beyond the scope of this thesis.

Parameter calibration to the present day permits application of the approach to past ice sheet configurations. Applying the method to Pliocene simulations with varying degrees of Antarctic ice mass loss predicts the provenance signature of a collapsed West Antarctic Ice Sheet (WAIS) and Wilkes Subglacial Basin. The offshore ε_{Nd} values associated with WAIS collapse are likely to vary regionally and are sensitive to ocean currents in open seaways and

the uncertain geology near the margin of remaining ice caps. Progressive ice loss in the Wilkes Subglacial Basin leads to more radiogenic ε_{Nd} values offshore as more Ferrar Group rocks are eroded, but the trend reverses once the ice sheet retreats onto unradiogenic cratonic rocks to the south and west of the embayment. The sea level equivalent (SLE) ice sheet volume required for peak radiogenic values at Site U1361 is ~9.3 m lower than for the modern ice sheet.

The integration of Antarctic sediment provenance data with numerical modelling offers the opportunity for quantitative reconstructions of past ice sheets from offshore glacimarine sediments. It could also help target sites for drilling where the greatest changes to sediment provenance might be expected following ice sheet collapse. The methods presented are considered an initial 'proof of concept', highlighting the benefits of tracing sediment provenance numerically, rather than a final product. Potential refinements are mentioned throughout the chapter and would undoubtably lead to improved accuracy and even more useful results.

3.1. Introduction

Antarctic ice flow pathways and ice sheet extent in the geological past can be reconstructed using sediment provenance studies, which trace marine detrital sediments to their constituent source rocks on the continent (e.g. Ehrmann et al., 2011; Cook et al., 2013; Marschalek et al., 2021). Applying a broad suite of sediment provenance proxies such as radiogenic isotope compositions, mineral dating, clast/sand petrography and clay mineralogy can yield robust insights into broad-scale ice flow patterns and, from this, past ice sheet extents (e.g. Wilson et al., 2018; Licht and Hemming, 2017; Marschalek et al., 2021). However, conclusions about ice sheet extent and flow patterns drawn from such data are typically qualitative. This is because, when viewed in isolation, sediment provenance records can only predict where subglacial erosion was taking place, but often cannot distinguish between changes in ice extent, changes to subglacial conditions which influence erosion rates, or changes to glacimarine sediment transport processes (Golledge et al., 2021). Although such complexities are usually considered, interpretations of sediment provenance records are often limited to a 'nearest-neighbour' type approach, where changes in provenance are attributed to a simple advance/retreat of the ice sheet margin near to the core site (e.g. Cook et al., 2013). Numerical modelling offers the potential to make more quantitative estimates of the ice sheet state required to generate observed sediment provenance signatures by predicting the expected provenance of detritus at the ice sheet margin (Aitken and Ursovic, 2021).

The modern Antarctic ice sheets offer an excellent opportunity to study how till is moved beneath the ice, as properties such as surface velocities and ice thicknesses can be directly measured. Ice flow drainage pathways are therefore known with a high degree of confidence. These observational data can also be used to invert for parameters such as basal friction coefficients in numerical models, producing predictions of basal stresses (e.g. MacAyeal, 1992; Morlighem et al., 2013). These known variables make erosion rate estimates beneath the present-day ice sheet more reliable than those of past ice sheets, despite continuing difficulties predicting processes of erosion and entrainment of subglacial debris (Alley et al., 2019).

Offshore debris transport processes are another substantial source of uncertainty in glacimarine provenance records which can be more accurately simulated at the present day. The spatial distribution of provenance proxy measurements in marine sediments is far more complete in recent (i.e. late Holocene to modern) surface sediments than in older, more

difficult to date, sediments (e.g. Simões Pereira et al., 2018). Here, we make use of these available constraints to calibrate the results of sediment provenance modelling to the observed provenance of recent seafloor sediments. This yields information about Antarctica's subglacial geology and the debris transport processes acting at present. This calibrated model is then used to investigate Pliocene ice sheet model simulations.

The approach presented can readily be adapted for any sediment provenance tracer. We here choose detrital neodymium (Nd) isotopes due to the abundance of available data (e.g. Cook et al., 2013; Bertram et al., 2018; Simões Pereira, 2018; Wilson et al., 2018; Marschalek et al., 2021). The decay of ^{147}Sm to ^{143}Nd relative to the stable ^{144}Nd isotope gives rocks a ^{143}Nd/^{144}Nd signature which is a function of the time since the magma was separated from the mantle and the initial composition of the rock (Goldstein and Hemming, 2003). This ratio is typically reported in epsilon notation:

$$\varepsilon_{Nd} = \left(\frac{(^{143}Nd/^{144}Nd)_{sample}}{(^{143}Nd/^{144}Nd)_{CHUR}} - 1\right) \times 10^4 \qquad (3.1)$$

This means rock groups of different lithologies and ages can be differentiated based on their ε_{Nd} value. Neodymium isotopes are a powerful sediment provenance proxy as all rock-forming minerals incorporate Nd and Sm into their structure, meaning nearly all rock types will be accounted for and are integrated in the provenance signal. Furthermore, ε_{Nd} is generally unaffected by grain size sorting (Garçon et al., 2013) and the combined provenance signal is expressed simply, as a single number. This makes ε_{Nd} values ideal for tracing in a model.

Geographically, we examine the region offshore of West Antarctica and adjacent areas of East Antarctica (from approximately 60°W to 140°E; Fig. 3.1). This spans the location of most existing detrital Nd isotope provenance studies, and existing compilations of the ε_{Nd} values of continental rocks (Simões Pereira et al., 2018; Marschalek et al., 2021). Locations mentioned in the text are displayed in Figure 3.2.

3.2 Neodymium Isotope Map

3.2.1 Approach

To assign eroded detritus an ε_{Nd} value to compare to offshore records, the first requirement is a spatially continuous estimate of ε_{Nd} for the study area below grounded ice (Fig. 3.1). Constructing this map required the compilation of literature ε_{Nd} data for different rock types.

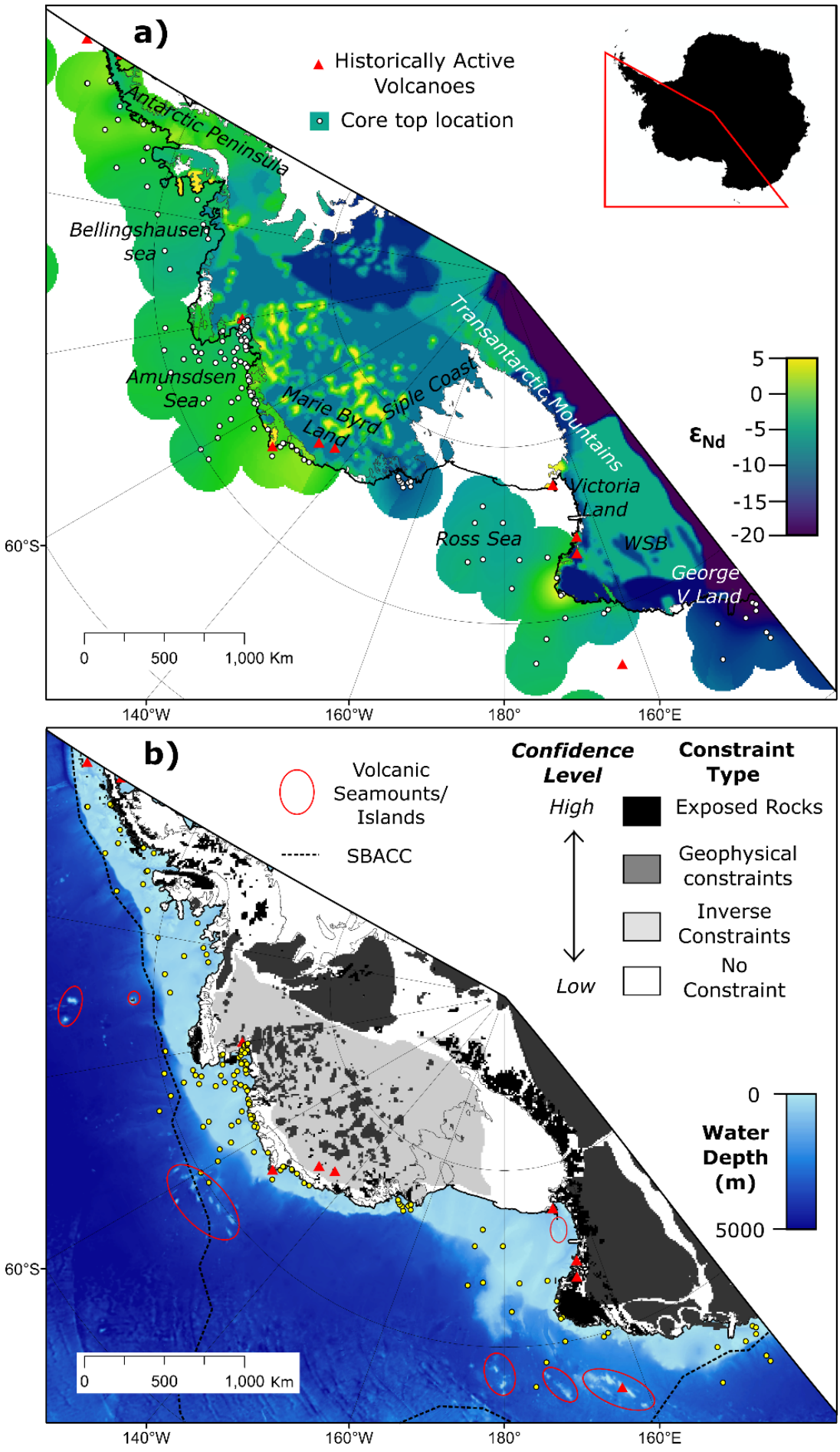

a)
Historically Active Volcanoes
Core top location
Antarctic Peninsula
Bellingshausen sea
Amunsdsen Sea
Marie Byrd Land
Siple Coast
Transantarctic Mountains
Victoria Land
Ross Sea
WSB
George V Land
5
0
-5
-10
-15
-20
εNd
0
500
1,000 Km
60°S
140°W
160°W
180°
160°E
b)
Volcanic Seamounts/ Islands
SBACC
Confidence Level
High
Low
Constraint Type
Exposed Rocks
Geophysical constraints
Inverse Constraints
No Constraint
0
Water Depth (m)
5000
0
500
1,000 Km
60°S
140°W
160°W
180°
160°E

Figure 3.1. *a) Map of ε_{Nd} values used as an input for the provenance tracing (inland) and interpolated ε_{Nd} values offshore within 200 km of a surface sediment core location. Seafloor surface sediment core locations are shown as white circles and volcanoes with observed activity are shown as red triangles (Patrick and Smellie, 2013). The MEaSUREs grounding line and ice extents are indicated using solid grey and black lines, respectively (Rignot et al., 2013; Mouginot et al., 2017). b) Uncertainty level of ε_{Nd} value estimate, displayed on BedMachine bathymetry (Morlighem et al., 2020). See definitions of the uncertainty levels in the main text. Volcanoes with reported subaerial eruptions in the historic record are shown in red (Patrick and Smellie, 2013), and seamounts and islands which are volcanic in origin (e.g. Lawver et al., 2013; Kipf et al., 2014) are circled in red. These features are displayed as they offer the potential for the addition of radiogenic detritus which is unaccounted for in our model. The Southern Boundary of the Antarctic Circumpolar Current (SBACC) is shown as a black dashed line (Orsi et al., 1995).*

This process was aided by an existing compilation of ε_{Nd} data from the Pacific sector of West Antarctica (Simões Pereira et al., 2018), extended to the Ross Sea sector (Marschalek et al., 2021). Where the rock sample location was not given in the original publication, coordinates were found by looking up the location name in the SCAR Antarctic Digital Database Map Viewer (https://www.add.scar.org/).

To convert the literature 'point data' into a continuous map, outcropping rocks were grouped. This was facilitated by the recent digital geological mapping of Antarctica from the SCAR GeoMAP project (Cox et al., 2019). To simplify this map, which comprised polygons at a resolution far beyond that required for this study, adjacent outcrops were grouped where subglacial continuity between exposures was deemed reasonable (see example in Fig. 3.3). For each major rock type, the point ε_{Nd} values were then interpolated and masked to the area of the simplified polygons. A resolution of 10 km was used, which is sufficient given the uncertainties resulting from the ice cover and matches the resolution used in the ice sheet model. These areas of exposed rock can be considered as having a high level of confidence in the final map, particularly when ε_{Nd} values for the rock group have been measured at numerous localities.

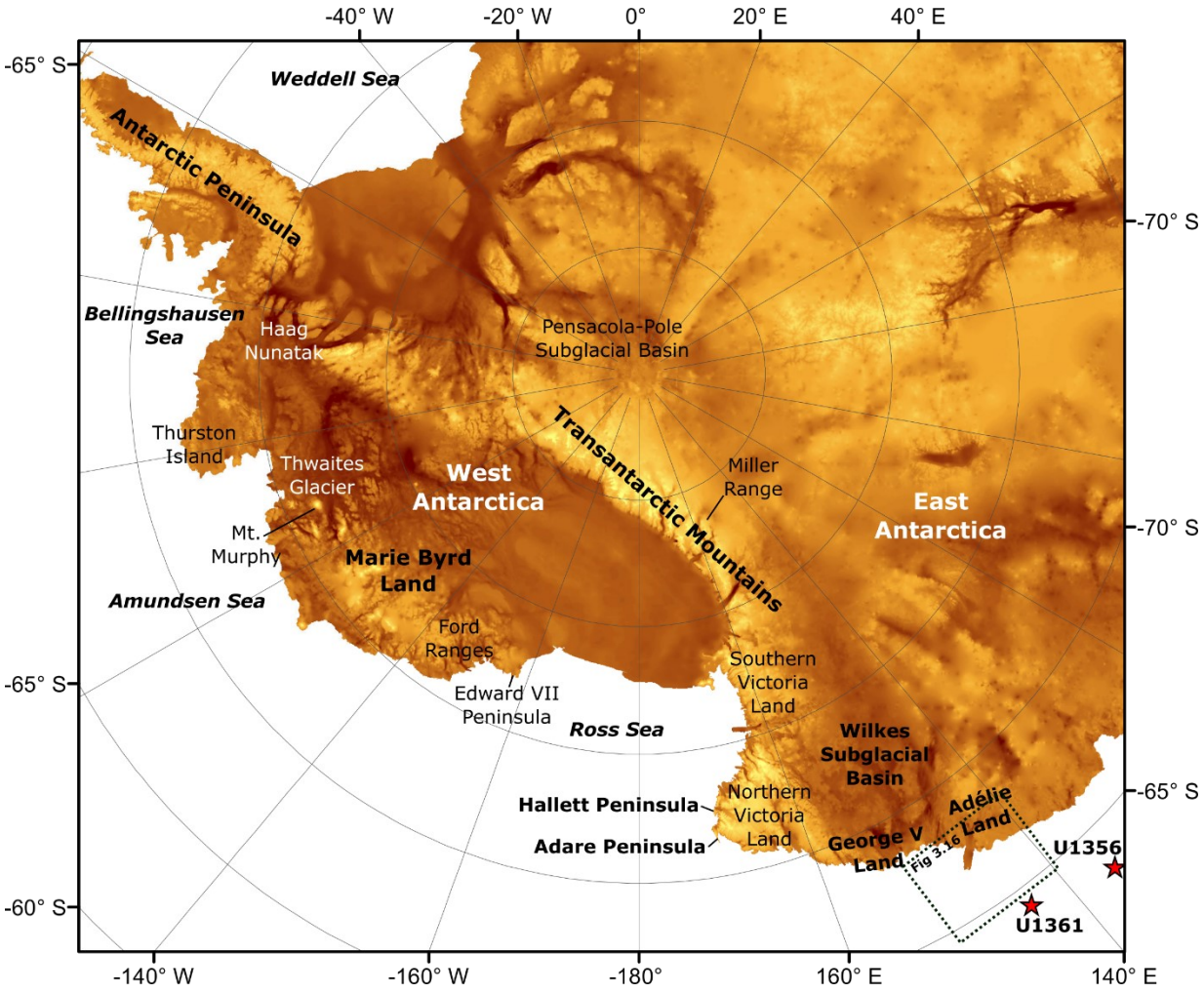


Figure 3.2 *Locations mentioned in the main text displayed on BedMachine topography (Morlighem et al., 2020). Position of Fig. 3.16 in Antarctica is shown using a dashed box.*

In contrast, most of the study area is covered by ice, making direct geological observations impossible. Pertinent airborne and on-ice geophysical studies (i.e. gravity, magnetic, subglacial geomorphology obtained by radar) were therefore used to inform ε_{Nd} values beneath the ice by making interpretations regarding the subglacial geology (e.g. Jordan et al., 2013a; Goodge and Finn, 2010; Studinger et al., 2006; van Wyk de Vries et al., 2017; Paxman et al., 2019b). In some regions, this approach can produce reasonably robust inferences. However, in other areas, relationships between exposed and subglacial geology are more obscure. Even in areas where geophysical constraints are good, some subglacial rocks may be hundreds of kilometres from the nearest comparable outcropping rocks. Consequently, using interpolation from the nearest outcrops to assign ε_{Nd} values, as described above for exposed rocks, could lead to bias towards only the geographically nearest measurement. Interpolation may therefore fail to reflect the true variability of the geology on land. To avoid this, areas

where ε_{Nd} was 'geophysically'-defined were uniformly assigned a mean ε_{Nd} value based on all suitable measurements of the rock type.

The sources used to determine the extent of subglacial geology and estimate ε_{Nd} values for each different rock group are discussed in detail below. To keep the initial offshore ε_{Nd} value estimate as independent as possible, an inverse approach was specifically avoided when constructing the ε_{Nd} map (i.e. using offshore values to predict onshore ones), except in a few locations where virtually no geophysical or geological data were available. A formal inversion for subglacial geochemistry, similar to that recently applied to fluvial provenance (Lipp et al., 2020), would undoubtably provide a much-improved match with modern observations as well as insights into subglacial geology to apply to simulations of past ice sheets. However, further development would be required to implement a formal inverse approach in a glacial setting, as additional information beyond a measurement near the ice sheet margin is required to give structure to interior ε_{Nd} values and avoid uniform values along a flow line.

To indicate the approximate uncertainty in the map produced, areas are classified with confidence levels (Fig. 3.1b):

1) Exposed rocks (high confidence; black) – exposed rock with ε_{Nd} measurements. The quantity and spatial distribution of ε_{Nd} measurements varies between rock types and, in some instances, sparse data meant that the number of data points used in the interpolation across a rock group was low.
2) Geophysical constraints (moderate confidence; dark grey) – areas with subglacial geology constrained by gravimetric/magnetic/geomorphological etc. data. Epsilon Nd values inferred for rock groups are based on the nearest equivalent exposures, but certain rock groups may be over- or under-represented, or ε_{Nd} values may be different away from measured rock outcrops.
3) Inverse/point constraints (low confidence; light grey) – areas with few direct constraints, limited to isolated subglacial samples. Epsilon Nd values are determined from these limited samples and surrounding rock exposures, loosely informed by offshore provenance data.
4) No estimate made (white) – these are without any rock type constraints, filled using Kriging.

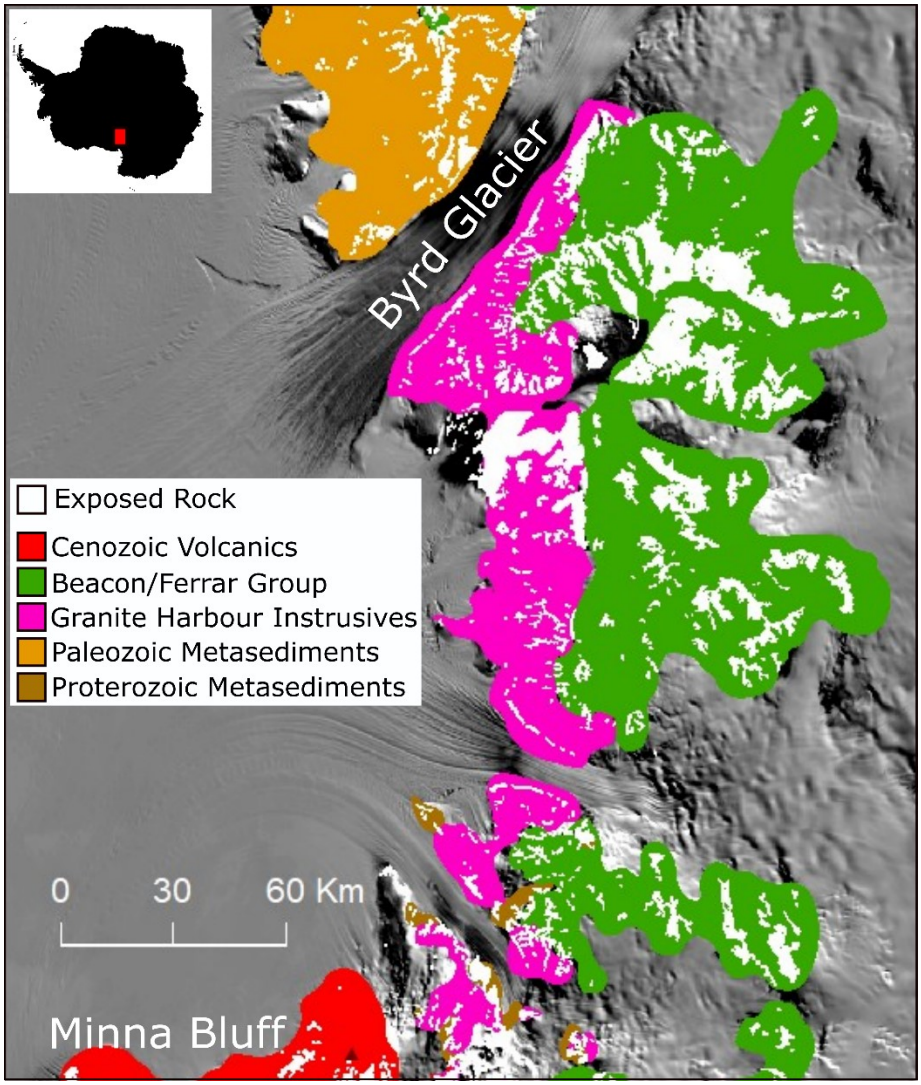


Figure 3.3 *Example of the resolution of the high-resolution rock polygons from GeoMAP (white; Cox et al., 2019) versus the simplified polygons used to construct the* ε_{Nd} *value map (coloured). The latter are sufficient at the >~10 km resolution of interest here. The region shown is a section of the Transantarctic Mountains between Byrd Glacier and Minna Bluff. The geology is overlain on MODIS imagery (Haran et al., 2014). The location within Antarctica is indicated in the upper left panel.*

Different rock types have different concentrations of Nd, meaning some rock types will contribute disproportionately to the ε_{Nd} values of subglacial detritus. This effect is not accounted for here due to the uncertainty in concentrations of different rock types, making quantitative assessments challenging. Assuming constant Nd concentration still yields useful results, but the inclusion of variable concentrations in future work would improve the accuracy of results. Any pre-glacial sedimentary strata, marine sediments deposited when the ice sheet was retreated, or subglacial till overlying bedrock at the base of grounded ice is also neglected, but subglacial mixing of detritus is somewhat accounted for in the interpolation between regions assigned ε_{Nd} values and assumptions of mean values of the surrounding rock types in some regions where sediments are likely present. These simplifications have the

effect of smoothing the bedrock ε_{Nd} values. Fully accounting for reworking of subglacial sediments would require a full integration of ε_{Nd} values in time-evolving model runs.

Some regions – particularly the interior of the WAIS towards Marie Byrd Land, the southernmost Transantarctic Mountains and the hinterland of the Bellingshausen Sea – lack even reliable geophysical constraints. In these regions, initial estimates were made by simply interpolating the map produced over the remaining gaps. However, this led to some obvious discrepancies between the ε_{Nd} values of rocks on land and nearby marine sediments. This effect was particularly pronounced in regions of West Antarctica, where geophysical bedrock studies typically focus on detecting relatively radiogenic subglacial igneous bodies. The lack of constraint on surrounding rock biases ε_{Nd} values. To account for this, most large areas of the study area with unassigned ε_{Nd} values were prescribed a value informed by sparse subglacial till samples (e.g. Farmer et al., 2006) and surrounding rock types, which markedly improved agreement with marine surface sediment ε_{Nd} values. As spatial variability in ε_{Nd} values is unknown in these regions, values were assumed to be uniform.

3.2.2 Regional Description of the Neodymium Isotope Map

I here present a region-by-region summary of the sources used to define the extent and Nd isotope composition of the bedrock of West Antarctica and adjacent areas of East Antarctica. A description of geological formations, lithologies and the tectonic framework of the study area is not relevant to this study and so is not discussed here. For recent reviews of East Antarctic, West Antarctic and Transantarctic Mountain geology, see Boger (2011), Jordan et al. (2020) and Goodge (2020), respectively. The geological background in Chapter 2 provides further information.

George V Land and the Wilkes Subglacial Basin

The extent of pre-Cambrian East Antarctic rock is mapped according to Goodge and Finn (2010), which is broadly consistent with ADMAP2 magnetic anomalies (Golynsky et al., 2018). The coastal extent of these pre-Cambrian rocks is based on interpretation of these data in Bertram et al. (2018). Limited measurements of this rock group give spatially variable ε_{Nd} values, spanning approximately -33 to -11 in the Miller Range of the central Transantarctic Mountains (Borg et al., 1990; Borg and DePaulo, 1994), -24 to -22 along the Adélie Land coast (Peucat et al., 1999), and -16 to -15 at the bed of the EPICA Dome C ice core (Delmonte et al., 2004). It is assumed a uniform ε_{Nd} value of -20 is reasonable given the

limited exposure of these rocks. Beyond the edge of the area studied, no attempt was made to compile literature ε_{Nd} values as erosion rates are low (e.g. Jamieson et al., 2010) and the Antarctic Coastal Current will carry any detritus reaching the coast westwards, out of the study area (e.g. Fig. 3.6). Rocks in other parts of Antarctica are thus unlikely to substantially impact the provenance signature of the regions studied offshore here, although some ice flowlines do cross beyond the study area shown in Fig. 3.1. Based on the assumptions described above, the rest of East Antarctica was also assigned a uniform ε_{Nd} value of -20.

Exposures of the late Neoproterozoic to Ordovician Wilson, Bowers and Robertson Bay Terranes are widespread throughout Northern Victoria Land. For these three respective rock groups, measured ε_{Nd} values range from -22.6 to -11.1 (Talarico et al., 1995; Henjes-Kunst and Schussler, 2003; Estrada et al., 2016), -19.9 to -10.5 (Tonarini and Rocchi, 1994; Henjes-Kunst and Schussler, 2003) and -15.6 to -12.3 (Henjes-Kunst and Schussler, 2003). However, most measurements cluster around a mean of approximately -14; this is applied as a uniform value for these groups.

Granite Harbour Intrusive rocks are exposed in Victoria Land and, although their ε_{Nd} values are allowed to vary spatially, these are relatively uniform, with a mean of ~-12 (Cox et al., 2000; Armienti et al., 1990; Dallai et al., 2003; Rocchi et al., 1998; 2009). These granitic rocks are also suggested to be present in the Wilkes Subglacial Basin, but the southern and northern extent and depth of these subglacial granitic bodies are subject to significant uncertainty (Ferraccioli et al., 2009).

The youngest rocks in the Wilkes Subglacial Basin are interpreted to be Ferrar Group dolerites and basalts, which intrude and overlay Beacon Supergroup siliciclastic rocks. The extent of these rock types beyond the very limited outcrops is suggested using previous interpretation of geophysical data in Bertram et al. (2018), with more southern limits mapped according to Jordan et al. (2013a). Jordan et al. (2013a) show a greater extent of Beacon/Ferrar Group rocks compared to the interpretations of Studinger et al. (2006) in Southern Victoria Land; we favour this more recent interpretation. Ferrar Group dolerites and basalts are isotopically well-constrained and consistent, with mean ε_{Nd} values of ~-6 (e.g. Elliot et al., 1999; Hergt et al., 1989; Molzahn et al., 1996). The ε_{Nd} values in Beacon Supergroup rocks are much more varied and sparsely measured, with mean values around -12 (Bertram, 2018; Fleming, 1995; Marschalek et al., 2021). Given that (i) the relative abundance of these rocks is uncertain but Ferrar sills are thought to be common through the

Wilkes Subglacial Basin (Ferracioli et al., 2009), (ii) concentrations of Nd are approximately twice as high in Ferrar Group rocks than Beacon Supergroup rocks (Bertram, 2018), and (iii) the uppermost Beacon Supergroup rocks have a Ferrar-like isotopic composition (Elliot et al., 2017), we assume an ε_{Nd} value of -7 is reasonable for a typical mixture of Beacon and Ferrar Group rocks.

Areas between the coast and Beacon/Ferrar Group rocks are assumed to be a mixture of Lower Palaeozoic rocks (i.e. Wilson Group, Bowers Group, Granite Harbour Intrusive and Robertson Bay Terranes), which are known to be present subglacially based on Miocene sediments from IODP Site U1359 (Pandey et al., 2017). Based on the most unradiogenic ε_{Nd} values measured in nearby seafloor surface sediments (~-15.5; Cook et al., 2013), this local endmember may be slightly more unradiogenic than the -14 to -12 described above; we therefore opt for -15 here. Sedimentary basins in the Wilkes Subglacial Basin (Frederick et al., 2016) are ignored, as it is assumed these would be comprised of mixtures of relatively local bedrock and are therefore accounted for using mean ε_{Nd} values for each rock type.

Southern Victoria Land and Transantarctic Mountains

The central Transantarctic Mountains provide some of the most extensive rock outcrops in Antarctica (Goodge, 2020). Neodymium isotope composition measurements are also plentiful for many rock types, making this a well-constrained region. We use the mapping of Cox et al. (2019) and isotopic data compiled and referenced in Marschalek et al. (2021) to produce the ε_{Nd} value map here. In the Transantarctic Mountains, there are outcrops of the pre-Cambrian and Beacon Supergroup/Ferrar Group rocks discussed above. Other rock types with ε_{Nd} measurements include the Neoproterozoic to early Paleozoic metasedimentary Skelton, Byrd, Beardmore and Liv groups (e.g. Borg et al., 1990; Borg and DePaulo, 1994; Cox et al., 2000; Goodge et al., 2008) and Palaeozoic Granite Harbour Intrusives (e.g. Goodge et al., 2012; Borg et al., 1990; Borg and DePaulo, 1994; Cox et al., 2000).

On the East Antarctic side of the southern Transantarctic Mountains, we extend the Ferrar Group and Beacon Supergroup into the Pensacola-Pole subglacial basin based on interpretations by Paxman et al. (2019b). The Precambrian East Antarctic craton, the extent of which is defined by Goodge and Finn (2010), is prescribed a ε_{Nd} value of -20 as described above. In the area between rock exposures in the southern Transantarctic Mountains and geophysical data around the South Pole, relatively little is known about the subglacial geology due to a lack of data; thus, the gap was initially simply interpolated across. However,

predicted ε_{Nd} values at the ice sheet margin for this portion of the Transantarctic Mountains were consistently too radiogenic (~-5) compared to recent ε_{Nd} values beneath Whillans Ice Stream (~-8 to -9) and in the Ross Sea (~-7 to -8) (Farmer et al., 2006; Marschalek et al., 2021). This may have been due to a bias towards exposures of the Granite Harbour Intrusive rocks, which have a mean ε_{Nd} value of -4.6 (n = 10) in this region (Borg et al., 1990; Borg and DePaulo, 1994). These are likely to be relatively resistant to erosion compared to the surrounding sedimentary rocks such as the Liv Group and Beacon Supergroup, meaning they may outcrop a disproportionate amount. There may also be bias towards exposure or measurement of more radiogenic beds in the Liv Group (e.g. Wareham et al., 2001).

To combat this bias, we applied a uniform ε_{Nd} value of -9 around rock outcrops, based on the limited measurements of Beardmore and Liv Group metasediments which likely comprise the bedrock between the Granite Harbour Intrusive batholiths (Marschalek et al., 2021). An ε_{Nd} value of -9 is also comparable to two measurements of the Beacon Supergroup in the southern Transantarctic Mountains (Marschalek et al., 2021).

To the north, the youngest rocks in this region are the Cenozoic McMurdo Volcanic Group in Victoria Land. These are heavily sampled and allowed to vary spatially in our map, but are generally consistent with a mean ε_{Nd} value of $+5.3 \pm 0.6$ (e.g. Avaido et al., 2015; Martin et al., 2013; Phillips et al., 2018).

Siple Coast and central West Antarctica

Ice cover is extensive and geophysical data are limited in the West Antarctic interior, making it difficult to constrain the sub-ice geology. However, till samples from beneath ice streams and in the Ross Sea provide some guidance to the likely subglacial lithologies (Farmer et al., 2006; Licht et al., 2014). Underlying much of this region are subglacial sedimentary basins, which range in age from the opening of the West Antarctic rift system in the mid-Cretaceous through to the Pliocene or Pleistocene (LeMasurier and Landis, 1996). Studies of sediment provenance suggest which rocks may be contributing (Farmer et al., 2006; Licht et al., 2014; Marschalek et al., 2021), including:

- A late plutonic phase of the Ross orogeny towards the Transantarctic Mountains (i.e. Granite Harbour Intrusives, see references above);
- Cretaceous to Triassic granitic rocks (e.g. Weaver et al., 1992; Craddock et al., 2017; Pankhurst et al., 1998);

- Palaeozoic (meta-)sedimentary rocks such as the Swanson Formation and equivalents in the Whitmore Mountains (e.g. Korhonen et al., 2010; Yakymchuk et al., 2015);
- Palaeozoic granitic rocks such as the Ford Granodiorite towards Marie Byrd Land (e.g. Weaver et al., 1992; Yakymchuk et al., 2015; Korhonen et al., 2010).

Potential mixtures of these lithologies in the sediments based on adjacent exposed rocks suggest an ε_{Nd} value of ~-10 (Table 3.1). This agrees well with the most unradiogenic sediments beneath the Siple Coast ice streams (Bindschalder Ice Stream), so is thought to be representative (Farmer et al., 2006). A uniform ε_{Nd} value of -10 was therefore applied across the entire West Antarctic interior. The magnitude and extent of contribution from Granite Harbour Intrusive rocks is difficult to constrain, but as these rocks have a mean ε_{Nd} value of ~-10 (Borg et al., 1990; Borg and DePaulo, 1994; Goodge et al., 2012), they may not influence the overall composition very much so are neglected (Table 3.1).

Table 3.1. *Endmember assignment for central West Antarctica. West Antarctic (W.A.) sediments refers to our approximation for all sediments likely to underlie the WAIS since the opening of the West Antarctic rift system, including pre-glacial sediments, marine sediments deposited in ice-free periods, and subglacial till. It is assumed the surrounding rock types forming the protoliths for these sediment types is likely to have remained relatively constant through the Cenozoic.*

Rock Group	Mean [Nd] (ppm)	Fraction	Mean ε_{Nd}
Palaeozoic (meta)sedimentary rocks	41	0.55	-11.3
Palaeozoic Granitoids	29	0.225	-6.8
Mesozoic Granitoids	12	0.225	-7.0
Mixture (W.A. sediments)	32	-	**-10.0**

It is very likely that some Cenozoic volcanic rocks also exist beneath the WAIS. The locations for these Cenozoic volcanic rocks were initially set based on exposed volcanoes, the volcano inventory of van Wyk de Wries et al. (2017) and the survey of Lundyk (2003). Preliminary investigation found they were required to reach sufficiently radiogenic ε_{Nd} values offshore, assuming surrounding rocks have values of -10 as described above. The existence of these volcanic rocks is subject to some uncertainty (Andrews and LeMasurier, 2021) and volcanic rocks comprise only a small fraction of gravel-sized detritus in the eastern Ross Sea, but it is possible these rocks have been physically weathered to finer grain sizes (Perotti et al., 2017).

Even when these potential volcanic rocks were included, ε_{Nd} values were not radiogenic enough to match observations. This may be linked to the uniform ε_{Nd} value of -10 applied for West Antarctic sediment. More radiogenic granitic rocks, potentially similar to the most radiogenic granitoids in the Ford Ranges (Korhonen et al., 2010) or on Thurston Island (Pankhurst et al., 1993), may be widespread in some areas beneath the WAIS, as unexposed Mesozoic-aged rocks are clearly present based on detrital zircon ages (Licht et al., 2014). However, without data to constrain the extent and isotopic composition of these rocks, we favour the addition of extra Cenozoic volcanic rocks to improve the match with observations. Behrendt (2013) correlated magnetic anomalies in the WAIS interior to subglacial late Cenozoic volcanic rocks. We assume that such rocks occur at sites with high magnetic anomalies based on the ADMAP-2 compilation (Golynski et al., 2018). Although this is a crude approach, new detailed mapping of possible volcanic material or more radiogenic granitic rocks beneath the WAIS is beyond the scope of this study. Indeed, understanding the mixture of rocks beneath the central WAIS would be greatly beneficial for future sediment provenance studies seeking to study WAIS collapse.

A uniform ε_{Nd} value of +5.3 was selected for these Cenozoic volcanic rocks based on the consistent isotopic signature of such rocks throughout Marie Byrd Land and Victoria Land (Avaido et al., 2015; Martin et al., 2013; Phillips et al., 2018; Futa and LeMasurier, 1983; Hart et al., 1995). Note, however, that the Kriging interpolation and 10 km resolution used means that small areas of volcanic material will not reach this value. This was an intentional effect to partially account for the uncertainty in the presence of these volcanoes.

Adjacent to the Edward VII Peninsula, where outcropping rocks are sparse, the model consistently predicted ε_{Nd} values that were too radiogenic in comparison with seafloor surface sediment values which reach a mean of -11.1 ± 0.4 ($n = 8$) (Simões Pereira et al., 2018; Carlson et al., 2021). This was likely a result of an underrepresentation of the Swanson Formation on the Edward VII Peninsula, as this rock group shows a close geochemical affinity with the glacimarine shelf sediments and may be widespread beneath the WAIS here (Simões Pereira et al., 2018). It was therefore assumed that the Swanson Formation, with an ε_{Nd} value of ~-12 (Korhonen et al., 2010; Yakymchuk et al., 2015), lies beneath most of the ice on the Edward VII Peninsula.

Amundsen and Bellingshausen Sea drainage sectors

Rock exposures around the Amundsen Sea embayment are particularly limited. Granites inferred to be present are assumed to be extensions of Mesozoic outcrops along this coast (Jordan pers. com.). Cenozoic volcanics are extended, largely under Thwaites Glacier, using interpretations of magnetic, gravimetric, and topographic data (Jordan pers. com.). Mafic rocks include gabbros of Cenozoic age (Simões Pereira et al., 2020; Jordan pers. com.), similar to Dorrell Rock near Mt. Murphy. The country rock surrounding these intrusions is assumed to be a mixture of typical West Antarctic rocks, assigned an ε_{Nd} value of -10 as described above.

A lack of rock outcrops and geophysical data translate to large uncertainties in the Bellingshausen Sea drainage sector of the WAIS (Fig. 3.1b). The Mesozoic granites and Antarctic Peninsular Volcanic Group present in the Antarctic Peninsula region are extended based on continuation of magnetic anomalies, but there are no outcrops to confirm this assumption is correct. Values are predominantly set to -10 as described above for the WAIS interior, assuming a similar mixture of rock types present. This matches with the ε_{Nd} values of sediments from beneath Pine Island Glacier ice shelf, which drains part of this region (Simões Pereira et al., 2020).

Antarctic Peninsula

Rocks are relatively well exposed along the Antarctic Peninsula, with lithological extrapolation between outcrops possible using geophysical data (Golynski et al., 2018) and geological maps (Burton-Johnson and Riley, 2015). The ε_{Nd} values of many rock types are, however, relatively poorly constrained (see the references within Simões Pereira et al., 2018 for available measured rock ε_{Nd} values). Fortunately, there is relatively little variation in Nd isotope compositions in this geologically young region, with ε_{Nd} values commonly between ~-6 to -2, although some rocks have values clustered around ~-10 to -8 and ~+1 to +3. (Simões Pereira et al., 2018). This relative lack of variation means uncertainty here is unlikely to substantially influence results.

Western Weddell Sea (West Antarctic side)

The extent of the Haag Nunataks block is taken from Jordan et al. (2020). It is possible this is overlain or intruded by a continuation of Jurassic volcanic/magmatic activity outcropping on

the Antarctic Peninsula. Furthermore, provenance data suggest that old (meta)sediments may be present on top of the Haag block as the mean ε_{Nd} value of ~-7.4 for these gneissic rocks (Storey et al., 1994) is more radiogenic than offshore of this part of the Ronne Ice Shelf (Williams, pers. comm.).

Most rocks around the Western Weddell Sea embayment are Cambrian-Permian sedimentary rocks, Cambrian volcanics or Mesozoic granites. Exposures are extended based on Jordan et al. (2013b), assuming outcrops are broadly representative of rocks present beneath the ice. The Cambrian volcanics and Mesozoic granites have been isotopically characterised, with respective mean ε_{Nd} values (±2SD) of -3.5 ± 4.3 (Curtis et al., 1999) and -6.6 ± 3.4 (Pankhurst et al., 1991; Borg and DePaulo, 1994; Craddock et al., 2017), but no known ε_{Nd} measurements of the widespread Cambrian-Permian sedimentary strata have been performed. It is therefore assumed an ε_{Nd} value of -13 is likely to be representative of these rocks, based on temporal equivalents in the southern Transantarctic Mountains such as the Byrd Group and non-volcanic beds of the Liv Group (Borg et al., 1990; Goodge et al., 2008; Marschalek et al., 2021). Measurements of offshore sediments agree with this hypothesis (Williams, pers. comm.). Beacon Supergroup and Ferrar Group outcrops in the Weddell Sea drainage sector follow the mapping of Paxman et al. (2019b) (see Transantarctic Mountain section). The extent of the Dufek intrusion (part of the Ferrar Group) is based on Ferris et al. (1998). Although we include this mapping, we do not include predictions for Weddell Sea offshore sediments in our results as these will be influenced by supply of debris from parts of East Antarctica which are located outside of our compilation area.

3.2.3 Data from Recent Seafloor Surface Sediments

To assess the accuracy of our sediment provenance tracing, comparison to measurements of ε_{Nd} in recent seabed surface sediments was conducted. These data were compiled from all known literature sources in our model domain (Walter et al., 2000; Roy et al., 2007; Pierce et al., 2011; Cook et al., 2013; Struve et al., 2017; Simões Pereira et al., 2018; Carlson et al., 2021). We also included new seafloor surface sediment ε_{Nd} data from the Ross Sea to improve spatial coverage in this area (Table 3.2).

Table 3.2. *Neodymium isotope data for new surface sediment samples in the Ross Sea. Non-IODP data were kindly provided by Liam Holder.*

Site	Sample depth	Latitude	Longitude	Water depth (m)	$^{143}Nd/^{144}Nd$	ε_{Nd}	± 2σ S.E.	± 2 S.D.
G837	Surface grab	-67.70	175.33	3430	0.512341	-5.80	0.000010	0.29
Procedural replicate					0.512358	-5.47	0.000011	0.27
Procedural replicate					0.512363	-5.37	0.000010	0.27
Procedural replicate					0.512339	-5.84	0.000010	0.29
A524	Surface grab	-73.33	187.20	3566	0.512336	-5.90	0.000008	0.29
A461	Surface grab	-73.53	171.37	564	0.512326	-6.08	0.000011	0.29
A452	Surface grab	-75.58	186.70	1253	0.512283	-6.92	0.000010	0.29
A523	Surface grab	-73.57	184.22	2762	0.512252	-7.53	0.000009	0.29
E194	Surface grab	-71.30	170.00	106	0.512921	5.51	0.000010	0.29
E196	Surface grab	-71.37	169.67	320	0.512864	4.41	0.000010	0.29
E183	Surface grab	-72.31	170.19	146	0.512855	4.23	0.000009	0.29
IODP U1521	4-6 cm	-75.68	-179.67	562	0.512243	-7.70	0.000009	0.26
IODP U1522	2-5 cm	-76.55	-174.76	558	0.512252	-7.53	0.000006	0.29

3.3 Debris Generation and Subglacial Transport

3.3.1 Ice Sheet Model and Erosion Rate

The ice sheet model simulations use a finite-difference numerical model with hybrid ice flow dynamics (Pollard and DeConto, 2012). Following the approach of Pollard and DeConto (2020), erosion rate (E) is calculated as proportional to the product of basal velocity (u_b) and basal shear stress (τ_b):

$$E = \tau_b u_b k \qquad (3.2)$$

The 'quarrying' coefficient k is a parameter dependant on properties including the erodibility of different rock types and other unaccounted for parameters. Here, a constant value of 5.1 x 10^{-10} was used for k as suggested by Pollard and DeConto (2020). As we are concerned only with relative, and not absolute, quantities of detritus, the value used will not impact results. Experiments were also performed with spatially variable k values for different sectors of Antarctica tuned to the quantity of marine sediment deposited on the Antarctic continental margin since 40 Ma (Pollard and DeConto, 2020). However, this yielded a worse match with seafloor surface sediment ε_{Nd} values than using a constant k, potentially because k values may not have remained constant over time so may not be representative of the modern ice sheet bed.

The approach presented here differs from the method used to predict sediment provenance from numerical modelling by Aitken and Urosevic (2021). Aitken and Urosevic (2021) used the squared basal velocity (capped at 600 m a^{-1}) as an erosion rate proxy, a 20 km resolution versus our 10 km one, and a Bayesian inference approach accounting for uncertain geological variation.

3.3.2 Tracing the Generation and Subglacial Transport of Detritus

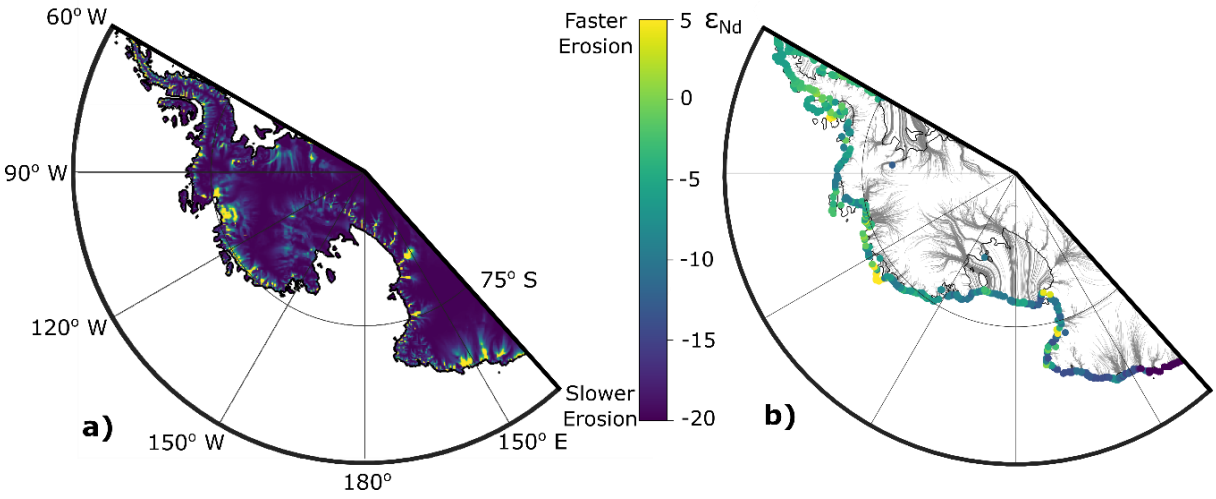


Figure 3.4. *a) Modelled erosion rate map used to seed start locations. Absolute erosion rates are not given as these are uncertain and not required to predict offshore provenance. b) Ice flow lines, with points at the end of each flow line coloured according to the* ε_{Nd} *value at the flow line start point.*

The provenance of the detritus reaching the ice sheet margin was modelled using the ice sheet model erosion rate. First, seed locations in the grounded portion of the ice sheet model grid were selected based on the erosion rate at the given location, with a given point proportionally more likely to be selected if the erosion rate was higher (Fig. 3.4a). This was performed by totalling the erosion rate value of all cells and calculating the fraction each cell represents of this total, then generating a random number and selecting a cell based on this probability. Following this, the flow path the detritus at each seed location took to the ice sheet margin was traced using the 'streamline' function in MATLAB. Using the basal velocity model output, this traced the flow paths of ice, and thus glaciogenic detritus, to the ice sheet margin (Fig. 3.4b). The end point location was then assigned the ε_{Nd} value of the source location. This was performed for 15,000 seed locations, which was considered a suitable compromise between computational time and accuracy (Fig. 3.5). To remove any

(minor) effects of random sampling in the subsequent optimisation and palaeo ice sheet applications, the default MATLAB random number stream was always reset.

Multiple streamlines typically ended at the same location on the ice sheet margin, reflecting particles incorporated at different points along a given flowline. Furthermore, as a seed location could be selected many times, a streamline may be repeated. To produce an ε_{Nd} value estimate at an ice sheet margin cell which reflects this uneven distribution along the ice flowline feeding into it, the mean values was taken. This approach does not account explicitly for detritus transport in subglacial hydrological networks, but these are unlikely to deviate significantly from ice flow vectors at the spatial scales of interest here.

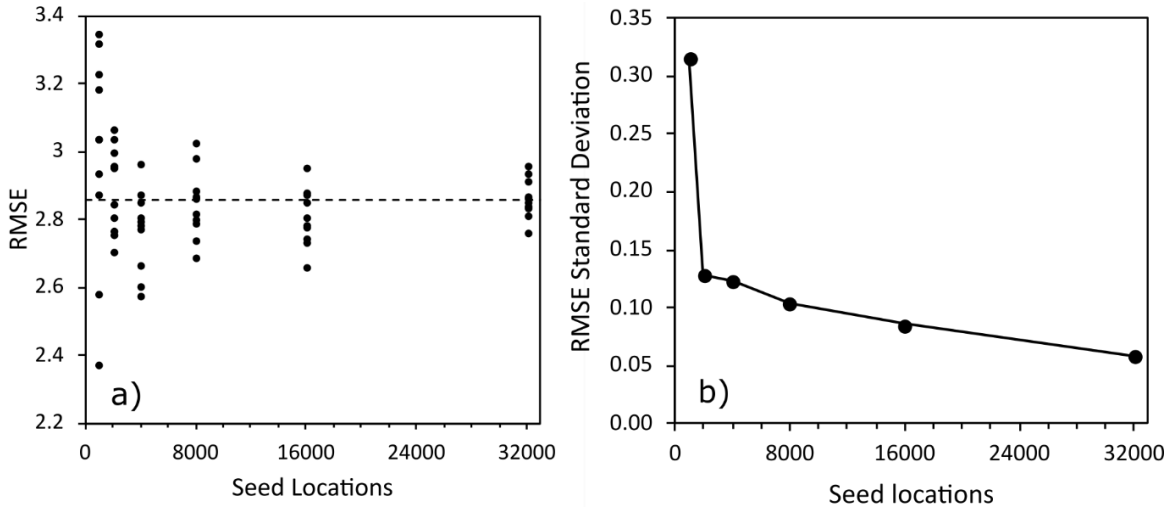


Figure 3.5. *Impact on root mean square error (RMSE) mismatch (i.e. mean of squared difference between seafloor surface sediment values and model results) associated with random number generation and number of seed locations. Note that only cells with a seafloor surface sediment measurement (points in Fig. 3.1) are used in calculations. a) RMSE of 10 runs with different random number sets at 1000, 2000, 4000, 8000, 16000 and 32000 seed locations. The horizontal dashed line indicates the overall mean of the 60 simulations. b) Standard deviation of the 10 runs for the different numbers of seed locations. Different random number sets were generated using the MATLAB 'rng shuffle' function, which uses the time to simulate randomness.*

By using a script external to the model code, this approach provides flexibility, with the opportunity to apply it to various existing model experiments. Our approach is not model-specific and could be applied to any ice sheet model output, providing key variables (bed elevation, basal shear stress and basal ice velocities with horizontal directional components) are saved.

3.4 Detritus Transport in the Ocean

Most sediment provenance records are from sites that are not located directly adjacent to the ice sheet margin. Transport of glaciogenic detritus in the ocean must therefore be considered. Here, methods of marine detritus transport are split into three key processes: iceberg rafting, bottom current transport, and gravitational downslope processes.

3.4.1 Iceberg Rafting

Iceberg rafted debris is one mechanism capable of long-distance transport of glaciogenic detritus in the ocean. Iceberg paths are a function of surface ocean current velocity, wind velocity and iceberg size, but surface current velocity dominates, particularly for large icebergs (Racow et al., 2017; Wagner et al., 2017). The ORAS5 ocean velocity reanalysis dataset (Zuo et al., 2019) was thus used to approximate the pathways icebergs would be expected to take. The dataset extends south to 80ºS, which reaches the coast in most locations except portions of the Ross and Weddell Seas. Simply interpolating available surface ocean velocities did not produce plausible flow directions near the ice sheet margin in the regions not covered by the reanalysis product. Consequently, the mean of the interpolated ocean velocity data and interpolated ice velocities beyond the ice sheet margin was used, after scaling the latter to the mean of local ocean velocities so they are a consistent order of magnitude.

A major simplification in our treatment of iceberg rafting of debris is our use of a constant debris load in all icebergs, which is discussed below. In reality, the glaciological setting will greatly influence this; icebergs from parts of the Antarctic Peninsula, for instance, typically have higher debris contents as outlet glaciers without large ice shelves are often present (Drewry and Cooper, 1981) and a relatively high number of rock outcrops when compared to other Antarctic regions causes these glaciers (and thus the icebergs calving from them) to transport englacial and supraglacial debris in addition to subglacial detritus. In contrast, many major glaciers further south bear only basal debris and flow into ice shelves, giving the opportunity for basal melting of most debris-laden ice by ocean water and subsequent calving of ‘clean’ icebergs (Smith et al., 2019). The reasoning for simplifications is discussed below, but we acknowledge that accounting for a variable debris load in icebergs would improve the accuracy of the results.

The ocean surface current velocities are then used as an input for the streamline function, with the seed locations set as the end point locations of the ice sheet provenance tracing component. An end point of multiple terrestrial streamlines is used as a start point for the equivalent number of times; i.e., if 10 ice streamlines end in a cell at the ice sheet margin, it is used to seed 10 marine streamlines. This weights the relative amounts of sediment offshore to areas with the greatest terrestrial sediment flux. Sea ice variability and weather patterns create substantial seasonal and interannual variations in iceberg pathways estimated from ocean surface current velocities. To account for this effect, the surface ocean component was run 324 times, once for each month in the ocean reanalysis data spanning 1993 to 2019 (25 years). Experiments on the number of months required showed using additional years improved the match between core top data and predictions, plateauing beyond ~20 years. Our iceberg pathways are broadly similar to observed iceberg tracks and studies focussing on iceberg modelling (Fig. 3.6). In addition, the spatial distribution of smaller icebergs observed from ships matches with the distribution we produce (Orheim et al., 2021). Trajectories are not consistent between ~90°E and ~60°W, outside of our study area, as the path of the Antarctic Coastal Current strays outside of our model domain at ~90°E (Fig. 3.6). A larger domain would therefore be required to study areas west of 90°E (e.g. iceberg alley).

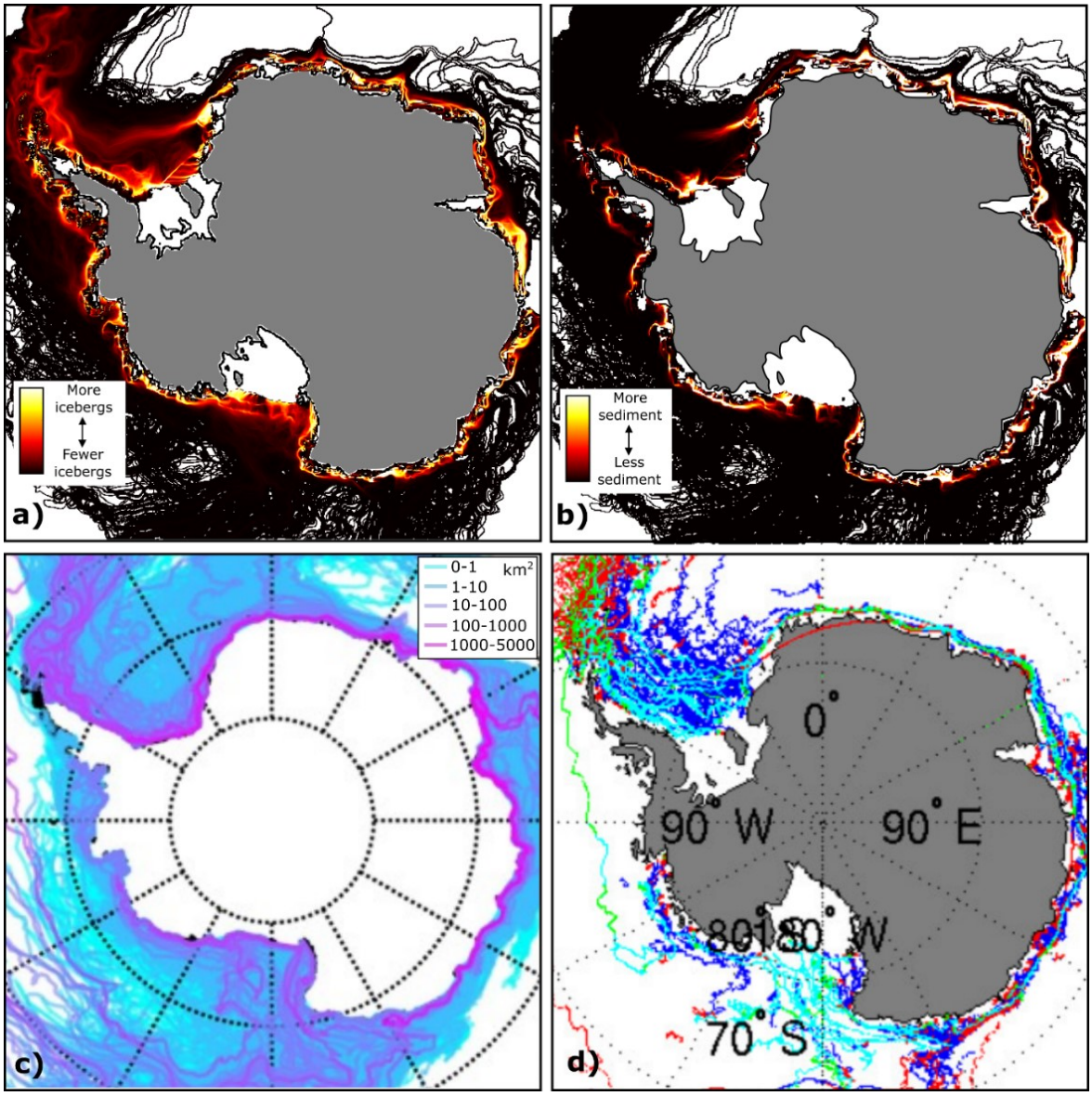


Figure 3.6. *a) Heatmap of ocean surface velocity paths, which are assumed to approximate iceberg paths. 'Hotter' colours have iceberg paths through them in more months. b) The relative quantity of iceberg-rafted sediment deposited by our representation of icebergs (unitless), showing higher debris loads closer to the iceberg source. c) Modelled iceberg trajectories accounting for additional influences such as wind velocities and sea ice (Rackow et al., 2017). Colours represent different size classes (0-1 km², 1-10 km², 10-100 km², 100-1000 km² and 1000-5000 km²). d) Observed trajectories of large (>5 km across) icebergs from the U.S. National Ice Centre and Brigham Young University (Stuart and Long, 2011), presented in Tournadre et al. (2016). Line colours correspond to trajectories: within sea ice after 2002 (blue), in open sea after 2002 (red), within sea ice before 2002 (light blue), and in open sea before 2002 (green). The broad pattern of iceberg movement we produce in (a) agrees well with modelled (c) and observed (d) iceberg trajectories in our study area.*

It is not realistic to assume that the volume of debris dropped by an iceberg remains constant over time. Transport of iceberg rafted debris (IBRD) over many hundreds of kilometres is possible (Dowdeswell et al., 1995), but typically transport is more local. This is because most debris is concentrated in the basal layers of the ice column, typically the lowermost 2-15 metres (Gow et al., 1979; Christoffersen et al., 2010; Shaw et al., 2011; Pettit et al., 2014). Ice sheet basal conditions, particularly melting/freezing rates, govern the thickness and nature of this basal sediment layer, meaning conditions at the ice sheet bed will strongly influence the thickness and distribution of debris-rich ice (Dowdeswell and Murray, 1990). Consequently, there are substantial variations in entrained sediment thickness around Antarctica even before the ice reaches the grounding zone.

Large proportions of frozen-on basal sediment or deforming subglacial till can be deposited near the grounding zone in sedimentary features such as a grounding-zone wedge (Batchelor and Dowdeswell, 2015). Moving seawards, a floating ice shelf, if present, will also influence the thickness of the sediment layer available at the calving line, with rain-out of englacial sediment governed by basal melt/freezing rates (Smith et al., 2019). Important influences include the size and morphology of the ice shelf (if present), the presence of pinning points which can allow freeze on of new sediment, and the amount of relatively warm ocean water reaching the base of the floating ice (Smith et al., 2019). These processes often lead to basal sediment being deposited, but debris near the base can also rise in the ice column if there is net freezing (Nicholls et al., 2012). Accounting for such complexities would improve the accuracy of our results but is beyond the scope of this study.

It is therefore assumed that nearly all sediment in the icebergs is contained in the layer of basal debris which is consistently 6 m thick at the calving line. The iceberg ocean melt rate (M_b) is assumed to be constant, and parameterised from the empirical equation of Russell-Head (1980):

$$M_b = 2.08 \times 10^{-7}(T_s + 1.8)^{1.5} \quad (3.3)$$

Sea surface temperatures (T_s) around Antarctica typically vary between approximately -2 and +2 (Locarnini et al., 2018); we simplify our melt rate parameterisation and assume T_s is consistently 0 ˚C. Temperatures vary seasonally and are likely to be cooler in the Antarctic Coastal Current and warmer further offshore in the Antarctic Circumpolar Current, but these complexities are not accounted for. The assumption of constant temperature gives a melt rate of ~0.04 m/day, which is consistent with observations of thinning beneath the fastest melting

ice shelves (Rignot et al., 2013; Depoorter et al., 2013). Such a melt rate implies a supply of basal debris from icebergs for ~138 days, broadly in line with estimates of sediment loss in studies with a more rigorous treatment of iceberg melt and sediment yield (Dowdeswell and Murray, 1990; Hopwood et al., 2019).

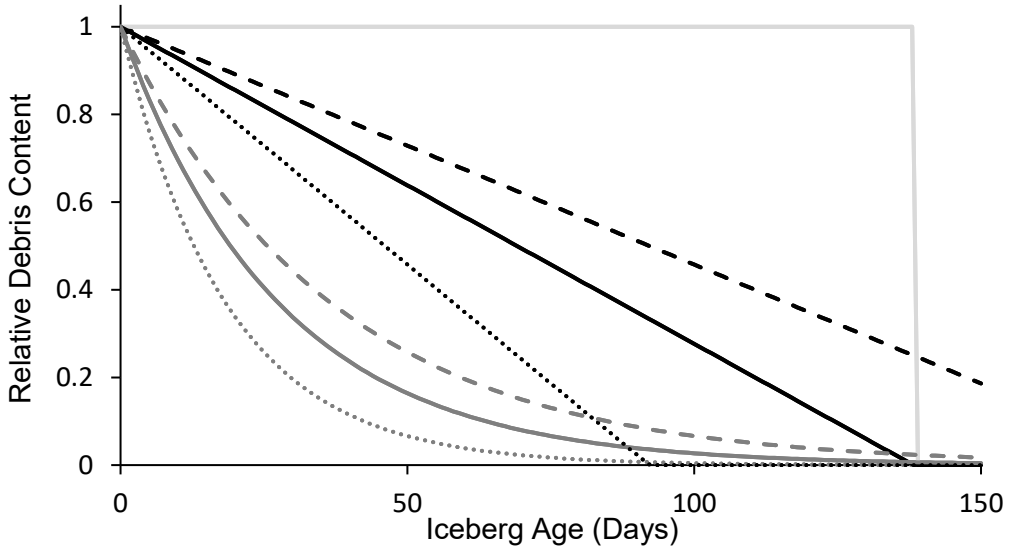


Figure 3.7. *Examples of different iceberg debris yield over time. Black lines indicate a linear relationship, dark grey an exponential decline and light grey a constant debris yield. 4, 6 and 8 m thick debris-rich ice layers are indicated by dotted, solid and dashed lines, respectively.*

The relative amount of sediment release over time from individual icebergs will depend on iceberg size, frequency of overturning and as such may be episodic (Drewry and Cooper, 1981; Dowdeswell, 1987; Dowdeswell and Murray, 1990). Empirical relationships between debris concentration and depth in the ice column have been formulated, showing a constant debris content for several meters followed by a sharp exponential decay (Yevteyev, 1959), but very few data are available to suggest how typical this relationship is around Antarctica (Drewry and Cooper, 1981). A linear relationship between sediment yield and height above the ice base is therefore viewed as representative on the longer spatial and temporal scales of interest here. From an initial debris content (D_0), the debris concentration in the basal ice (D) after t days of melting is given by:

$$D = D_0 - \frac{M_b t}{Z} \quad (3.4)$$

Where Z is the basal sediment thickness in metres. This is only valid while $M_b t < Z$, and as only relative amounts of sediment are relevant, $D_0 = 1$. Experiments were also performed

with an exponential decline in sediment yield and constant sediment yield, but these had little impact on the overall result (Fig. 3.7).

The thickness of basal debris is variable around Antarctica. However, as using a variable debris thickness would have added considerable complexity to the model, the basal debris thicknesses were instead tuned and our results compared with seafloor surface sediment data (Fig. 3.8). This gave a minimum in RMSE when using a basal debris thickness of 6-8 m. We opted for the lower end of this minimum as a thinner debris layer seems more plausible given the range of observed debris thicknesses (Gow et al., 1979; Christoffersen et al., 2010; Shaw et al., 2011; Pettit et al., 2014) and likelihood of this debris-rich layer thinning (or disappearing) due to sub-ice shelf melting in many parts of Antarctica (Smith et al., 2019). It should be noted that this value also reflects tuning for the iceberg melt rate, as described below.

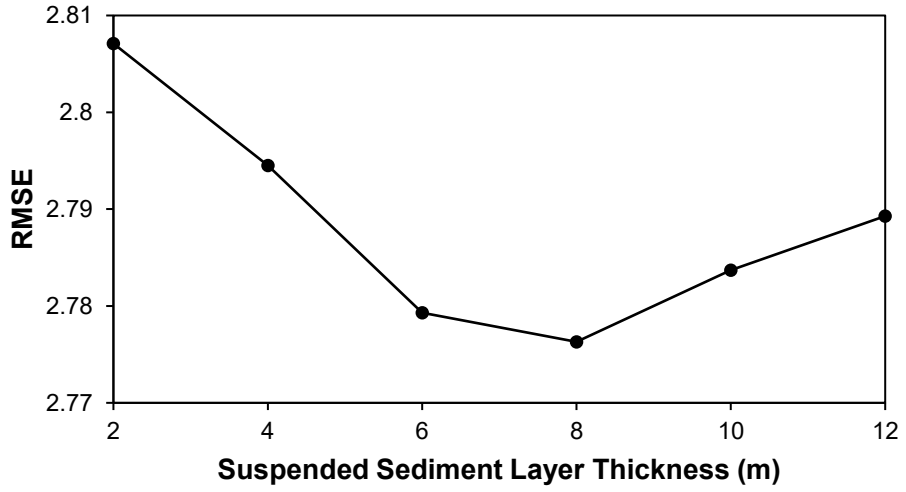


Figure 3.8. *Effect of varying basal sediment thickness on the RMSE of the match with surface sediment* ε_{Nd} *values.*

We note that the iceberg melt rate is highly sensitive to ocean temperature; a change from 0 ˚C to -0.7 ˚C more than halves the iceberg melt rate (Equation 3.3). The representation of iceberg debris loss is based on the melt rate divided by the sediment thickness (Equation 3.4). Consequently, the same change in debris concentration shed from the icebergs over time could be achieved if the melt rate was halved providing the basal debris thickness was also halved. For instance, 3 m debris-rich ice and ~-0.7 ˚C temperatures give the same result as 6 m debris-rich ice and 0 ˚C as the ice melts twice as fast. In this way, the mean basal sediment thickness tuned for (Fig. 3.8) equally reflects a tuned iceberg melt rate. Future efforts could use spatially variable iceberg melt rates; combined with a spatially variable estimate of basal

debris thickness at the ice sheet margin, this would provide a more accurate result without the need for tuning of these parameters.

As well as the thickness of the basal debris-rich ice layer, the relative concentration of debris will influence the amount lost from an iceberg. Little has been published regarding debris concentration versus depth in the ice column, and it can be assumed to vary significantly between localities depending on factors such as how the debris is incorporated (i.e. shearing and ice deformation vs. basal freeze on; Drewry and Cooper, 1981). To acknowledge these potential differences and investigate the sensitivity of our model to the distribution of basal debris, different relationships between basal debris concentration and depth were tested (Fig. 3.6). An exponential relationship is used:

$$D = D_0 \exp\left(-\lambda \frac{M_b t}{Z}\right) \qquad (3.5)$$

Where a decay coefficient $\lambda = 5$ was selected to rain-out basal debris for a length of time which agrees with more in-depth studies (e.g. Hopwood et al., 2019). Experiments were also performed with constant basal debris yield from the basal ice (i.e. $D = D_0$ while $M_b t < Z$). These changes to sediment distribution had only a very small impact on results. When compared to measured seafloor surface sediment ε_{Nd} values, an exponential relationship gave a RMSE of 2.80, 2.79 and 2.79 for 4, 6 and 8 m of basal debris, respectively, and a constant debris yield over 6 m of basal ice gave a RMSE of 2.78. These values are very similar to a linear debris decay (Fig. 3.8).

Supraglacial debris is rare, but occasionally present in Antarctica, and englacial debris above basal debris layers has been observed (Nicholls et al., 2012; Winters et al. 2019; Smith et al., 2019). To account for a small supraglacial/englacial debris load and observed and theoretical transport of IBRD for hundreds to thousands of kilometres offshore (Dowdeswell and Murray, 1990; Dowdeswell et al., 1995; Gil et al., 2009), it is assumed there is a very small, but finite, sediment yield for the entire iceberg track. This is set to 10^{-5} times the maximum debris load at the base of the ice column based on an assumption of a ~10% debris concentration in basal ice vs. ~0.001% higher in the ice column (Dowdeswell and Murray, 1990).

To produce an estimate of ε_{Nd} from iceberg rafting, the mean ε_{Nd} value of sediment at the ice sheet margin was applied along the iceberg paths, and weighted relative to the amount of sediment. This means debris from icebergs more proximal to their source location will dominate the ε_{Nd} signature, but where more local icebergs are absent, there is the potential for

far-travelled icebergs to influence ε_{Nd} values. After all pathways had been traced, the mean ε_{Nd} value was taken for each cell. Areas with no iceberg tracks over them, but within 40 km of an iceberg track, were filled using interpolation. This interpolation somewhat accounts for the potential for variations in ocean surface currents which are unresolved here. Furthermore, it is likely that over the decades to centuries integrated within most sediment samples of centimetre-scale thickness, there would be transport of icebergs over more of the sea floor than captured in the 25 years of data used here.

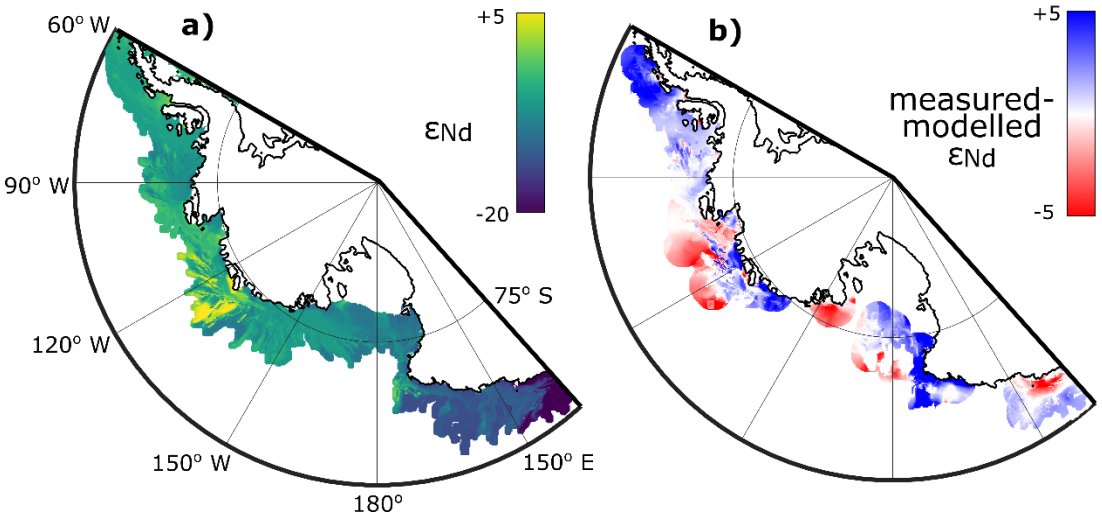


Figure 3.9. *Impact of assuming all debris is contained in a basal layer. a) The surface current (iceberg rafting) estimate, limited to coastal areas. b) Difference between the measured surface sediment and model best match estimate* ε_{Nd} *values. The discrepancy is larger than when an englacial sediment component is included (see Fig. 3.13).*

Including a very low minimum 'englacial' debris yield (i.e. debris above the basal ice) led to a noticeably better match with observations, suggesting that it is important to include a small contribution beyond a basal debris layer (Fig. 3.9). In addition to representing detritus higher in the ice column, this need to incorporate a baseline debris yield may also partially reflect the transport of very fine grained IBRD settling through the water column, which track ocean flow patterns. Once released from the ice, silt particles (on the order of 5-50 μm) with slower settling velocities will be transported horizontally as they sink down through the water column over periods of days to months, leading to potential transport distances of tens to thousands of kilometres, depending on grain size (Azetsu-Scott and Syvitski, 1999).

Fine-grained detritus can also derive from meltwater plumes rising from beneath the ice sheet. These can deposit sediment tens of kilometres from the grounding line and will track

ocean currents (Smith et al., 2019). Although they can travel at varying heights in the water column depending on the relative densities of the meltwater plume and ocean water masses, by using both surface and bottom current approximations, we assume their transport pathways are largely accounted for.

Sea ice conditions will impact iceberg movement and melt, leading to seasonal changes in surface current detritus transport. Grouping surface velocity data for each of the 12 months of the year over the 25-year dataset shows seasonal patterns in the fit between modelled and seafloor surface sediment ε_{Nd} values, and a possible relationship with sea ice extent (Fig. 3.10). Nevertheless, it seems using the surface velocity data for all the months equally weighted is the best option in lieu of more thorough treatment of seasonal processes and gives a good match with surface sediment ε_{Nd} values.

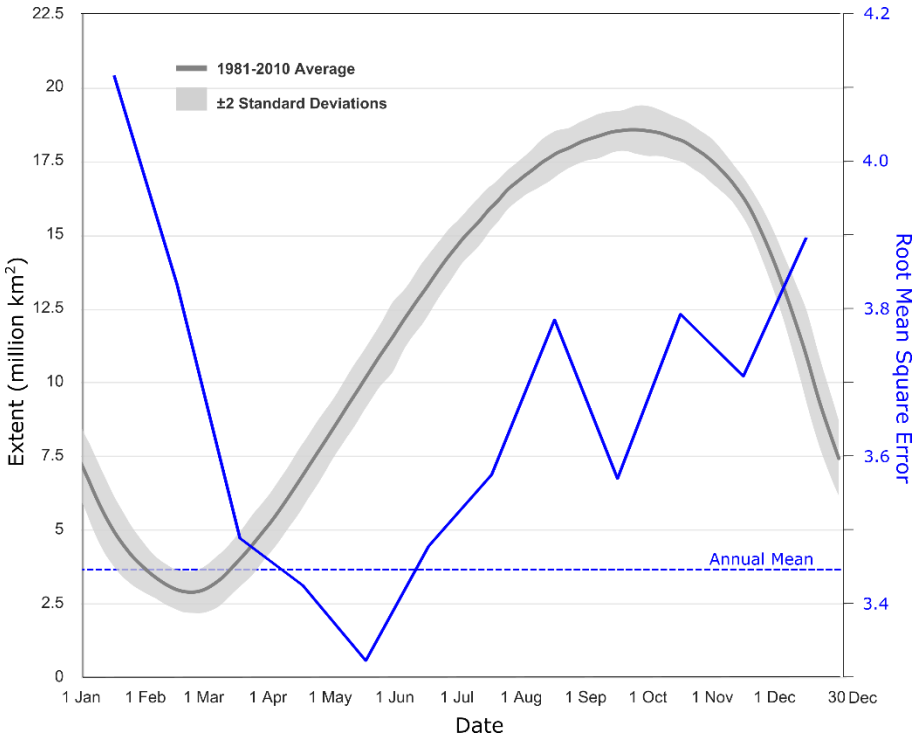


Figure 3.10. *Monthly mean Antarctic sea ice extent from 1981-2010 (greyscale; NSIDC, 2021). Plotted alongside the root mean square error fit between modelled monthly surface current (iceberg rafting)* ε_{Nd} *value estimates and measured surface sediments (blue). The horizontal blue dashed line indicates the results using surface velocity data from all months.*

The model suggests that it is iceberg trajectories in May, ~3 months after the sea ice minima, which impact the spatial distribution of IBRD most. This relationship may be linked to icebergs calving more frequently and escaping the vicinity of the calving zone more during sea ice minima. The three-month lag may be due to icebergs taking this long to move away

from the location they calved and reach core sites, many of which are located further offshore, where sea ice, which is forming most rapidly in May, locks them in position. To elucidate these processes further, sediment provenance estimates would have to be combined with detailed iceberg trajectory modelling, involving changing surface current velocities over time, plus seasonal variations in iceberg calving, sea ice and ocean temperatures.

3.4.2 Bottom Currents

Iceberg rafting, and the processes described above, are not responsible for all transport of glacimarine detritus. One key process operating especially on the continental rise is the transport and deposition of predominantly silt- and clay-sized detritus by bottom currents. These currents typically flow parallel to the continental slope where they can influence the movement of detrital particles already in suspension. Bottom currents do not only deposit sediments as "contourites" but can also erode and redistribute particles from the seabed surface if their velocities are sufficiently high. As well as the deeper ocean, bottom current speeds reach velocities sufficient to mobilise sediment on the continental shelf (Ha et al., 2014; Jenkins et al., 2018).

Bottom currents were defined as the deepest velocity in the ocean reanalysis product. Due to very sparse in-situ measurements, knowledge of bottom currents around the Antarctic margin is limited, but we suggest the ocean reanalysis product provides the best estimate available (Zuo et al., 2019). Detritus entrained in bottom currents is again routed using the MATLAB 'streamline' function. As ε_{Nd} values are generally measured on the <63 μm grain size fraction, it is assumed a current velocity of ~0.15 m/s is needed to start the resuspension and redistribution of some sediment particles (McCave and Hall, 2006; Gross and Williams, 1991). This threshold can vary significantly depending on properties such as the grain size and cohesivity of the sediment, but the 0.15 m/s approximation is assumed to be sufficient for our purposes.

The ocean reanalysis velocity data are unlikely to capture the full variability in bottom current behaviour, which includes significant changes to current speed and orientation on timescales as short as hours (e.g. Camerlenghi et al., 1997; Giorgetti et al., 2003). This poses the question as to whether the sediment record reflects predominantly an integrated mean of long-term bottom-current velocity variability, or whether it is dominated by episodes of peak current speed. Here, it is assumed the latter case applies and, to account for the temporal

variability in bottom current strength, peak flow velocities are assumed to be 2.5 times the monthly mean in the ocean reanalysis product. This relationship is based on measurements of bottom current strength at mooring sites around a contourite drift on the western Antarctic Peninsula continental rise (Camerlenghi et al., 1997; Giorgetti et al., 2003), which record peak velocities approximately two to three times greater than mean velocities. The bottom current speed record from the Antarctic Peninsula drift is also comparable with other bottom current records (Gross and Williams, 1991). It is therefore suggested that, in areas where mean flow velocity exceeds 0.06 m/s in the reanalysis product, the aforementioned 0.15 m/s threshold speed for the start of resuspension and winnowing is exceeded during times when currents are strongest. Consequently, all areas where bottom current velocities exceed 0.06 m/s are used as source locations for debris. Our approach is supported by the fact that the sortable silt mean size of seafloor surface sediment from another Antarctic Peninsula drift, recovered at a comparable water depth as the mooring measurements, suggests formation under a bottom current with a flow velocity matching the peak speed recorded in the mooring data (Hillenbrand et al., 2021).

As suspended particles will not be deposited uniformly over a given flow pathway, deposition over a streamline must be approximated. Although detailed modelling of bottom current erosion, transport and deposition is beyond the scope of this paper, an approximation produces a realistic exponential decay in suspended particle concentration (c) over time (t_s, seconds):

$$c = c_0 \exp\left(-\frac{p t_s v_s}{y}\right) \qquad (3.6)$$

Here, p is the probability of a particle sticking to the ocean floor, v_s is settling velocity, and y is the thickness of the layer with suspension load in metres (Einstein and Krone, 1962). As we are not concerned with absolute amounts of sediment, the initial particle concentration (c_0) can be neglected. A value of 3.3×10^{-4} m/s is used for the settling velocity, which is within the range expected for fine-grained detritus (Einstein and Krone, 1962; McCave, 2005). On the Antarctic margin, particles are often suspended in a nepheloid layer with a thickness on the order of ~10^2 – 10^3 m (e.g. Tucholke, 1977; Gilbert et al., 1998) instead of a layer with a clearly defined upper surface, making y a poorly constrained variable. Tuning this parameter to seafloor surface sediment ε_{Nd} data suggests 15 m provides an optimal fit (Fig. 3.11).

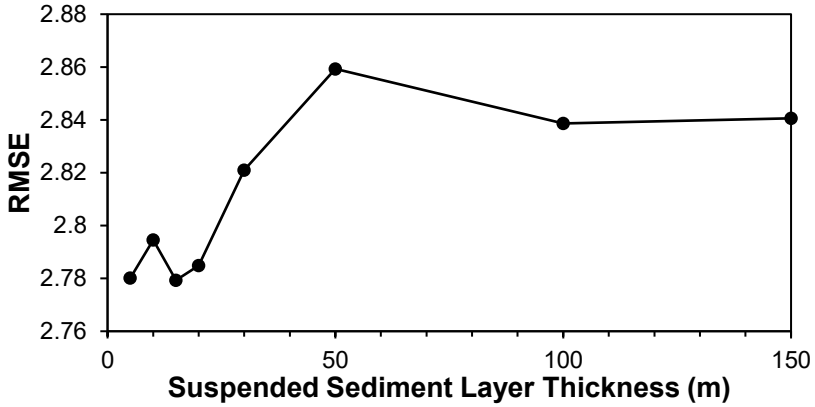


Figure 3.11. *Effect of varying the thickness of the layer with suspended sediment on the RMSE match with surface sediment ε_{Nd} values. Note that the magnitude of change is relatively small compared to the uncertainty associated with random seed location generation.*

Low suspended particle layer thicknesses (<5 m) lead to very short transport distances, which are unlikely to capture bottom current transport and instead resemble the surface current map used to initialise the bottom current flow paths. For longer transport distances, the large (100+ m) suspended layer thicknesses again show a better match with the provenance of recent seafloor surface sediments than intermediate thicknesses. This may be linked to these estimates having a longer detritus transport distance path and therefore estimated ε_{Nd} values with a larger spatial coverage. The lower RMSE may therefore be a result of having more mechanisms to choose from at more core sites, rather than a true improved match. Consequently, the RMSE minimum at a thickness of 15 m is favoured.

Although 15 m is substantially lower than the thickness of the nepheloid layer, we argue it is physically plausible given that nepheloid layer thicknesses have been measured in austral spring-summer, when the nepheloid layer probably contained large amounts of degrading biogenic matter (i.e. remnants of plankton blooms that took place just prior these measurements). Furthermore, suspended sediment concentrations are not uniform and are highest nearest the seafloor, and we are only concerned with bottom currents, which only comprise the lowermost part of the water column. Transmissometer data also suggest that suspended sediment concentrations increase markedly in the lower tens of metres of the water column (Gardner et al., 2020)

The probability of the particle sticking to the bed in Equation 3.6 (p) can be calculated from bottom shear stress, τ_w (N m^{-2}), using a critical depositional stress, τ_c (N m^{-2}):

$$p = 1 - \frac{\tau_w}{\tau_c} \qquad (3.7)$$

(Einstein and Krone 1962). τ_c is set to 0.08 N m^{-2}, in line with observed estimates for different classes of suspended sediment which vary between 0.05 and 0.1 N m^{-2} (Shi et al., 2015; Lumborg, 2005; McCave, 2008). In turn, τ_w can be approximated as a product of vertically averaged velocity ($\overline{U}$) and water density (ρ) using a quadratic law (Mofjeld, 1988; Garcia and Parker, 1993):

$$\tau_w = \rho C_d \overline{U}^2 \qquad (3.8)$$

At the deep water depths of interest here, the drag coefficient, C_d, can be estimated using:

$$C_d = \kappa^2 / [\log\left(\frac{H}{z_0}\right) - 1]^2 \qquad (3.9)$$

Where H is water depth and z_0 is the roughness length. Here we use 5x10^{-4} m for the roughness length, which is a reasonable approximation given that the drag coefficient is insensitive to small changes in this at large water depths (i.e. $H \gg z_0$) (Mofjeld, 1988). κ is the von Kármán constant, 0.41. This approximation yields a spatially-variable drag coefficient on the order of ~10^{-3}, which is a magnitude consistent with observations (Umlauf and Arenborg, 2009). The basal current velocity is assumed to be approximately equal to the depth-averaged velocity for simplicity.

To set the initial ε_{Nd} composition of detritus mobilised by bottom currents, we use the output from the surface current method. To account for any seasonal changes in bottom current velocity, we then iterate the current tracing for 24 months (2018-2019 ocean reanalysis product), using the output from the previous month to set the ε_{Nd} value of sediment eroded where possible. Similar to the surface current estimate, the results for detritus moved by bottom currents is interpolated for 40 km around pathways. This helps account for unresolved pathways, and for the fact that there is relatively little data to constrain modelled bottom current velocities in the ocean reanalysis product. Extending this interpolation distance gives a significantly better overall match with provenance data from the seabed surface sediments but, unlike the surface current estimate, there are fewer areas where bottom current remobilisation occurs. This means the improvement in the match with seafloor surface sediments is likely to be a consequence of having more mechanisms to choose from at some sites, rather than a more realistic result. Interpolating excessive distances from the modelled pathways will not represent the uncertainties described above, as in some areas bottom

current velocities are unlikely to exceed the required threshold for sediment remobilisation. 40 km was therefore selected as a compromise between the representation of some uncertainty in bottom currents, whilst retaining some areas where bottom current remobilisation is unrealistic.

This approach is by necessity a major simplification of the treatment of particle transport and sediment remobilisation by bottom currents. Nevertheless, the areas subject to sediment remobilisation are captured, plus the provenance of detritus reaching a given location through bottom current transport.

3.4.3 Gravitational Downslope Transport

Substantial volumes of glacimarine detritus can be moved through gravity-driven downslope processes such as turbidity currents, slumps and debris flows. To represent these transport mechanisms, the mean ε_{Nd} values from the surface and bottom current methods at all locations with a slope of >1° (Stow, 1994), mostly confined to the shelf break, are selected. These grid cells are used as start locations from which the direction of gravitational transport is calculated from by selecting the adjacent cell (including diagonals) with the lowest bed elevation. This next cell is set to the same ε_{Nd} value as the starting cell. This iterates until a cell is repeated (i.e. an upwards slope is reached). This method makes no attempt to account for travel distance along a gravitational transport pathway, but unlike ocean currents, such paths are unlikely to cross as the direction of travel will always be approximately perpendicular to the coast (on the shelf) or shelf break (on the upper continental slope). There is therefore no need to calculate the relative quantity of sediment.

Bathymetric features not resolved at our 10 km model resolution mean gravitational flows are likely to carry sediment beyond the constraints of the approximate gravity flow paths. The gravitational transport ε_{Nd} estimate is therefore interpolated at all locations beyond the shelf break. Theoretically, the relief on the continental shelf is often sufficient for gravity flows to redistribute sediment (e.g. Anderson et al., 1983; Hillenbrand et al., 2005). However, these processes are unlikely to transport significant amounts of sediment at the spatial scales (10's-100's km) considered here, and recent gravitational downslope deposits have only been identified locally on the very rugged, deep inner continental shelf (e.g., Smith et al., 2009). Thus, we do not interpolate the gravitational transport ε_{Nd} estimate on the continental shelf, defined as water depths >1200 m. Although this is depth threshold is significantly deeper than the true shelf break at ~500-600 m, using 1200 m avoids inclusion of most over-

deepened areas on the innermost shelf close the ice sheet margin, where interpolation should be avoided. Very few core sites exist on the upper continental slope, so using this depth threshold has little impact on results.

Turbidity currents flowing perpendicular to the shelf break can carry suspended sediment to locations where they are captured by bottom currents flowing parallel to the shelf break. To account for this interaction between gravitational downslope processes and bottom current transport, the output of the gravity flow method was iterated once with the bottom current method described above. This improves the match with observed surface sediment ε_{Nd} values. Although this approach does not explicitly represent sediment suspended by gravitational process which are then captured by bottom currents, using an iterative method accounts for particle transport both parallel and perpendicular to the shelf break in both the bottom current and gravitational ε_{Nd} value estimates.

3.4.4 Relative Contribution of Transport Mechanisms

A key challenge is apportioning the relative contribution of the three marine transport mechanisms described above around the Antarctic continental margin. In some settings, marine transport processes can be estimated given observations of geomorphological features (e.g., contourite drifts, channels eroded by turbidity currents), grain size parameters (e.g., content of coarse-grained ice-rafted debris, percentage and mean of sortable silt) and sedimentary structures (e.g., normally graded turbidites, winnowed layers of residual coarse-grained sediments). However, making these inferences requires bathymetric data and sediment cores, and it often remains difficult to determine the fraction of the sediment transported by different mechanisms.

This issue is addressed by predicting a map of the provenance (ε_{Nd}) signature of detritus transported by each of the three key transport mechanisms at all sites where they are likely to impact detritus transport. Which mechanism, or combination of mechanisms, produces the closest match with observed seafloor surface sediment ε_{Nd} values at a given core site is then calculated. Mixtures of transport mechanisms are permitted where the measured surface sediment value lies between the different mechanism estimates. Assigning one method to each grid cell is not physically accurate, as all marine transport mechanisms may interact at a given location, with bottom currents redistributing particles supplied by gravitational downslope processes or even reworking older sediments. Different mechanisms may also at some locations produce very similar ε_{Nd} values, which our approach does not account for.

However, the approach used will indicate where different transport mechanisms are dominant. A major strength of this approach is that it does not require an estimate of the absolute quantity of detritus transported by each mechanism, which is useful given that the rates of these processes are poorly constrained.

3.5 Modelled Surface Sediment Signatures

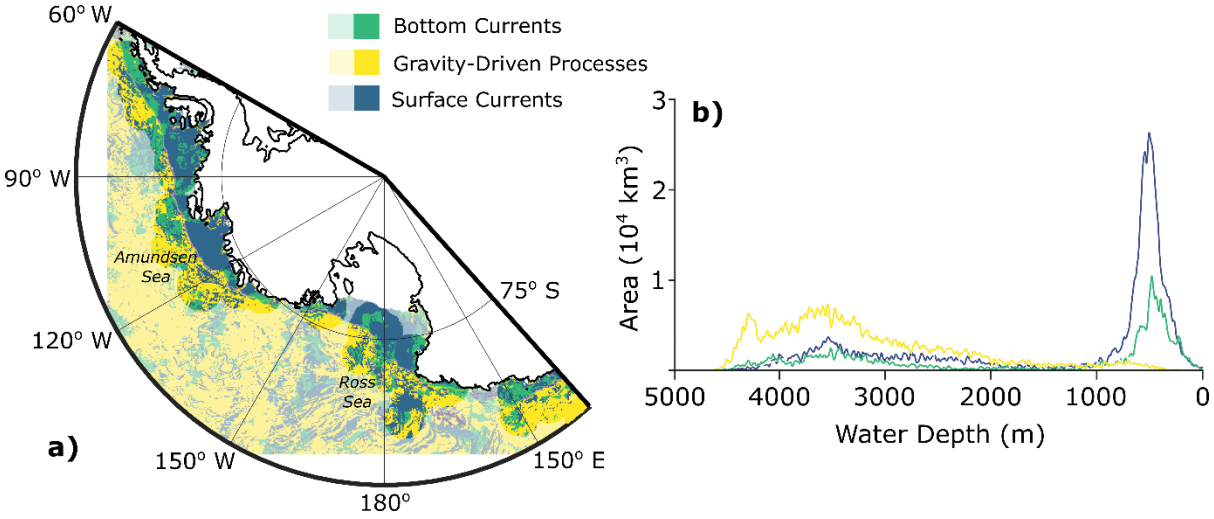


Figure 3.12. *a) Applied transport mechanisms for glacimarine detritus providing the closest match with interpolated surface sediment ε_{Nd} values around the Antarctic continental margin. Colours are darker within 200 km of sample constraints, and pale away from these constraints. Grey shades show where two or more methods predict an identical ε_{Nd} value. b) The same data plotted against water depth (spline through 10 m bins), showing dominance of surface current estimate on the shelf and gravity driven processes on the beyond the shelf break.*

Predicting the ε_{Nd} values of seafloor surface sediments on the Antarctic margin from each of the three mechanisms and comparing this to observations highlights that a single transport mechanism alone, such as iceberg rafting, cannot fully explain offshore sediment provenance. Each of the three mechanisms produces a close match with measured ε_{Nd} values in different areas (Fig. 3.12). On the continental shelf, the closest match between modelled and measured ε_{Nd} values is often provided by the surface current estimate. The shelf of the Amundsen Sea in particular appears to show a predominance of surface currents on sediment provenance, likely due to slow bottom current speeds in the ocean reanalysis product. The Ross Sea does, however, have some areas where bottom currents provide the closest match; these are concentrated around bathymetric highs, the Victoria Land coast, and parts of the outermost

shelf/uppermost slope. There may be some relationship with the pathways of Ross Sea Bottom Water export, although the spatial match is not perfect (Orsi and Wiederwohl, 2009). Beyond the continental shelf, gravitational downslope processes often provide the closest match to surface sediment ε_{Nd} values, suggesting sediment transport perpendicular to the shelf break is dominant further offshore. However, surface sediment constraints are virtually absent further from the continental slope, meaning predictions here have little constraint.

Near most surface sediment samples, we produce a close agreement between model results and measured data, with an overall root mean square error (RMSE) of 2.78. The prediction accounting for different transport processes matches 41% of surface sediment values within 1 epsilon unit and 77% within three epsilon units. The ε_{Nd} signals in past sediment provenance records off East Antarctica and in the Ross Sea exceed three epsilon units (e.g. Cook et al., 2013; Wilson et al., 2018; Marschalek et al., 2021), implying our predictions are sufficiently accurate at most sites to exceed the likely amplitude of change in ε_{Nd} values following a change to ice sheet flow pathways or erosion.

Broad spatial patterns in ε_{Nd} values and their match with measured surface sediments are generally consistent between the three transport mechanisms (Fig. 3.13). The surface current estimate is accurate in many areas closer to the coast, with an overall RMSE of 3.45 (Fig. 3.13a,b; Fig. 3.14a). Further offshore, however, individual surface current flow paths can be distinguished in the model ε_{Nd} output. At these locations, icebergs are less common, meaning our result often reflects a single iceberg trajectory rather than a mean of many flow paths as is the case closer to the continent. Although the Antarctic Circumpolar Current (ACC) is likely to have a strong, consistent imprint north of its southern boundary (SBACC; Fig 3.1), meaning there is a reduced need for multiple iceberg tracks over the same point, a greater density of flowlines than that achieved is still required to reduce the gaps between flow paths. The surface current method is therefore viewed as less reliable in the deep ocean, where a surface current record spanning several decades and/or at a higher resolution would likely be required to get a denser network of flow paths over these areas, adding significant computational cost. However, few sediment provenance records study these sediments, as mixing of detritus means provenance changes become increasingly diluted and hard to trace to specific source locations when far from the continental sediment source.

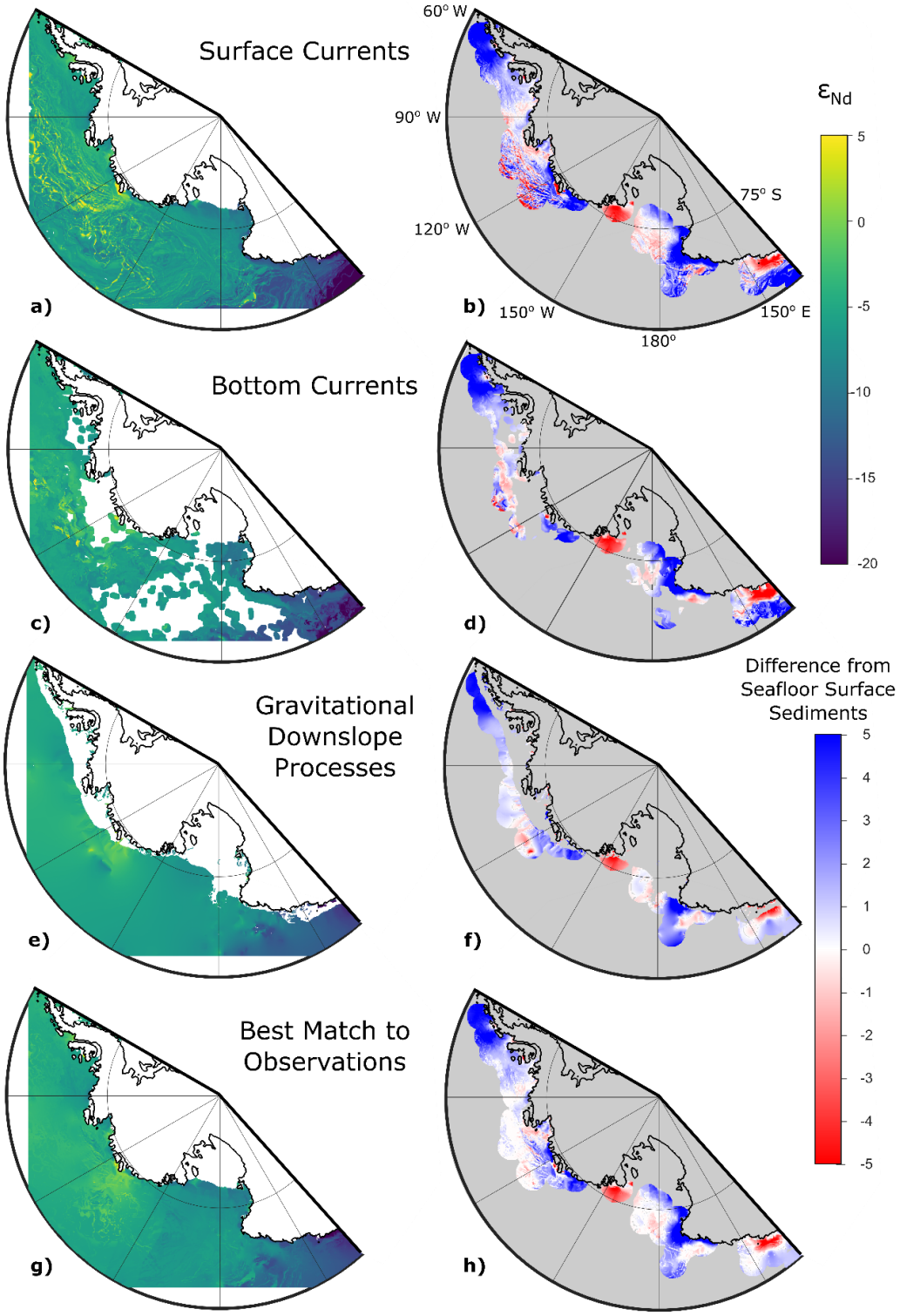


Figure 3.13. *Simulated ε_{Nd} values around the West Antarctic margin including the absolute values (a, c, e, g) and difference from the seafloor surface sediment data interpolation (b, d, f, h). The surface current (a & b), bottom current (c & d) and gravitational downslope (e & f) estimates are shown, as well as the result when the closest matching method (surface current, bottom current, gravitational) to the interpolated core top ε_{Nd} values is selected for each grid cell (g and h).*

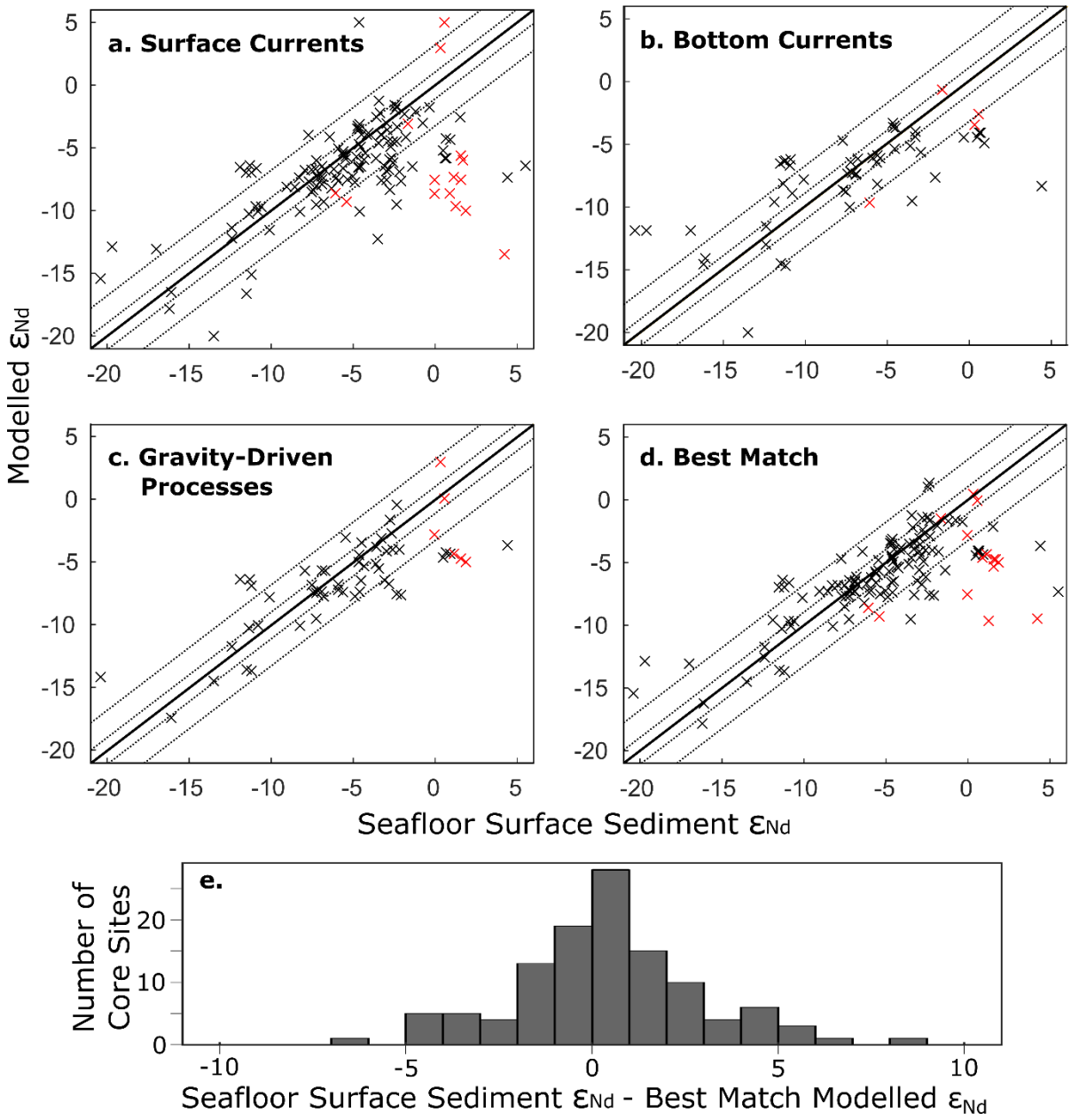


Figure 3.14. *Comparison between observed and modelled ε_{Nd} values in seafloor surface sediments. Results are shown for each sediment transport mechanism individually (a-c), plus selection of the nearest matching method (d). The solid 1:1 line is bracketed by dashed lines indicating 1 and 3 epsilon unit deviations. Red points are samples within 200 km of active volcanoes that are likely influenced by unaccounted for volcanic material with a high (~+5) ε_{Nd} value. The difference between seafloor surface sediments and the best match modelled ε_{Nd} values is also shown as a histogram (e).*

Although it also captures the same general patterns as the surface current ε_{Nd} estimate, the bottom current estimate deviates more from measured ε_{Nd} values, with a RMSE of 4.01 (Fig. 3.13c,d; 3.14b). This seems to be linked to a general smoothing of the ε_{Nd} signal, which is

consistent with this transport mechanism moving detritus that has already been mobilised or transported by a different mechanism, giving more potential for mixing. These results suggest bottom currents may dominate sediment provenance signals in relatively few areas, principally parts of the continental slope and rise where they interact with suspended sediment mobilised by downslope processes (Fig. 3.12).

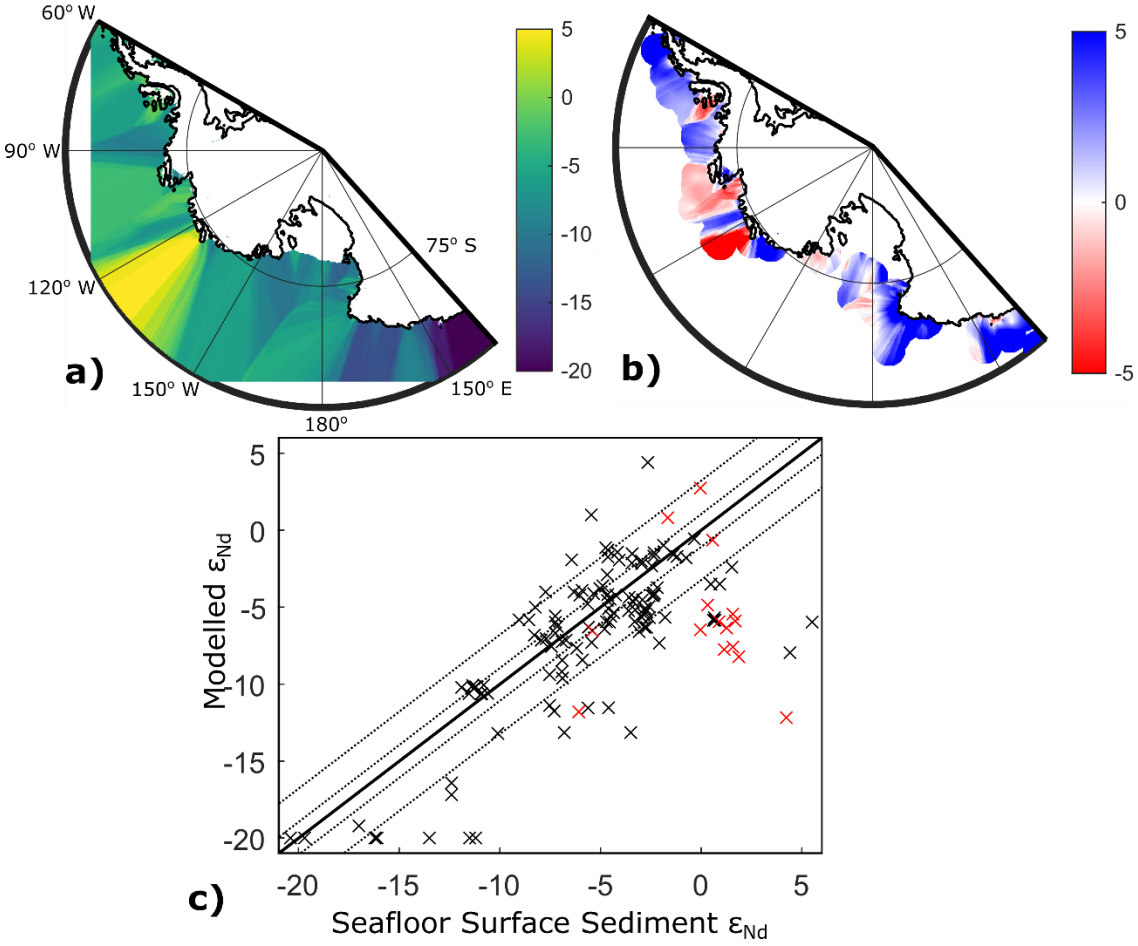


Figure 3.15. *Results of an inverse distance weighting of predicted ε_{Nd} values from the ice sheet margin, including a) the interpolated ε_{Nd} values and b) the difference from interpolated surface sediment ε_{Nd} values. c) Shows the scatter relationship between measured and modelled seafloor surface sediments.*

Our method results in a significantly closer match to sample sites than a simple inverse distance weighting interpolation from the detritus supplied to the ice sheet margin, which gives a RMSE of 3.51 (Fig. 3.15). This does not reflect transport of sediment parallel to the coast in ocean currents and therefore yields a worse match with surface sediment ε_{Nd} values.

The model indicates that beyond the continental shelf, it is likely that detritus moved by gravitational processes typically exceed detritus transport solely influenced by ocean currents

in areas with surface sediment constrains (i.e. the continental slope and rise). Overall, gravitational downslope processes give the closest match with observations, with an RMSE of 2.96 (Fig. 3.13e,f; 3.14c). Substantial model-data mismatch for the gravitational downslope mechanism is limited to sites with clear localised explanations, which are discussed in detail below. The good agreement between our model and seafloor surface samples beyond the shelf may also be partly explained by these sediments typically being reworked and integrated more, leading to less extreme ε_{Nd} values with variations more likely to be averaged out. The ability of our model to closely reproduce ε_{Nd} values on the lower continental slope and the continental rise may be linked to this smoothing of the ε_{Nd} signal. For instance, our input ε_{Nd} map (Fig. 3.1) uses a mean value for rock types or subglacial sediments in many areas, due to a lack of geological constraint. This means heterogeneity in source ε_{Nd} values are reflected more directly on the continental shelf but are less relevant further offshore.

As well as the areas further offshore where gravitational downslope processes dominate, the model-data match is particularly good, and nearly always deviates by less than one ε_{Nd} unit, in the central Ross Sea and the Bellingshausen Sea (Fig. 3.13). In these areas, the close match may be linked to the use of offshore data to produce the initial ε_{Nd} value map, but the results are nevertheless encouraging. The Amundsen Sea Embayment offers a dense offshore sample network to compare our results to (Simões Pereira et al., 2020). The modelled ε_{Nd} values do not resolve finer-scale features, but the match is good close to the terminus of both Pine Island and Thwaites glaciers and in the central Pine Island-Thwaites paleo-ice stream trough (Fig. 3.13). The prediction also captures the mixing of these distinct detritus further offshore (Simões Pereira et al., 2020).

Areas where the three transport mechanisms consistently predict ε_{Nd} values that are less radiogenic (lower) than those observed include the coast of Victoria Land, part of the Hobbs coast of Marie Byrd Land and towards the tip of the Antarctic Peninsula (Fig. 3.13). This mismatch is likely attributable to volcanoes in these areas that are either still active or have been active in the recent past (e.g., Dunbar et al., 2021; Patrick and Smellie, 2013) (Fig. 3.1), as Cenozoic volcanic material in West Antarctica and Victoria Land is highly radiogenic (~+5.3 ε_{Nd}) and has a high Nd concentration (Goldich et al., 1975; Aviado et al., 2015; Futa and LeMasurier, 1983; Hart et al., 1997). This explanation is supported by the observation that clay-sized detritus in sediments offshore from the volcanic South Shetland Islands, northern tip of the Antarctic Peninsula, has relatively high smectite contents, and this signal

has a strong imprint on continental rise sediments in the region (e.g., Hillenbrand and Ehrmann, 2005).

Our methods do not make any attempt to account for tephra erupted above the ice surface and carried offshore, either by winds or in layers within icebergs, which could be present in the surface sediments in areas close to and downwind of volcanoes and substantially influence ε_{Nd} values. Grain size distributions and visual observations near the McMurdo Ice Shelf suggest that seafloor surface sediments here are dominated by aeolian sediments, supporting this hypothesis (Atkins and Dunbar, 2009). These observations show where marine sediment provenance records using ε_{Nd} values are likely influenced by radiogenic volcanic material; Nd isotope data from these areas should be interpreted with caution. A slight bias towards more unradiogenic modelled ε_{Nd} values may be explained by neglecting the long-distance transport of such material (Fig. 3.14e).

Three sample sites adjacent to the Adare and Hallett peninsulas on the Northern Victoria Land coast recorded particularly radiogenic ε_{Nd} values (Table 3.2), not captured by our model results. Mineralogy and ε_{Nd} values of >+4 suggest the sediments are almost entirely formed of the late Cenozoic volcanic rock constituting these peninsulas. However, as they have not been volcanically active for at least ~2 million years (LeMasurier et al. 1990), we cannot attribute this discrepancy to tephra and instead suggest it is a limitation of our 10 km model resolution, which is not able to resolve such localised areas of a particular rock type (Fig. 3.1). If such sites close to the shore were of interest for sediment provenance tracing, a more localised, high resolution modelling approach should be pursued to yield more accurate results.

To visualise the locations of seafloor surface sediment samples which are in the vicinity of recently active volcanoes and therefore potentially influenced by significant volcanic deposition, sites within 200 km are highlighted in red in our scatter plots and excluded from our statistics (Fig. 3.14). Note that the exclusion of these sites does not imply that sediment provenance data here are not useful; instead, these areas are viewed as having the potential for unaccounted-for volcanic influences. One exception is the recent volcanic activity suggested in the Hudson Mountains near Pine Island Bay in the Amundsen Sea (Patrick and Smellie, 2013; Corr and Vaughan, 2008), which we do not use to exclude data. Any volcanic input to marine sediments is likely very local and minor given both the restricted geographical distribution of this tephra (Corr and Vaughan, 2008) and the large supply of non-volcanic glaciogenic detritus from the adjacent Pine Island and Thwaites glaciers.

Sediment could also reach sample sites from volcanic seamounts and islands (Fig. 3.1). These range in age from the early Cenozoic to recent and are found offshore of Marie Byrd Land (Kipf et al., 2014; Hagen et al., 1998; Prestvik and Duncan, 1991; Hagedorn et al., 2007), north of Victoria Land (Johnson et al., 1982) and in the western Ross Sea (Lawver et al., 2012; Rilling et al., 2009; Panter and Castillo, 2007). Radiogenic isotope compositions are similar to the aforementioned Cenozoic volcanic rocks (Kipf et al., 2014; Panter and Castillo, 2007; Prestvik and Duncan, 1991). These seamounts and islands are not accounted for in our ε_{Nd} estimate as the extent and magnitude of the influence of such features on seafloor sediment ε_{Nd} values is uncertain.

Offshore of the Wilkes Subglacial Basin and adjacent to the King Edward VII Peninsula, predicted ε_{Nd} values are more radiogenic (higher) than those measured in the seabed sediments (Fig. 3.13). A key factor influencing ε_{Nd} values in these regions is transport of relatively radiogenic detritus in the Antarctic Coastal Current, which in both these areas appears to be comprising a greater fraction of detritus in our model than in reality. This is a result of icebergs remaining closer to the coast in the simulation. In these areas, we suggest that the ocean reanalysis product may not be resolving local factors - such as local ocean currents and the presence of grounded icebergs and fast ice - which lead to more far-travelled icebergs carrying relatively radiogenic detritus being diverted north, away from the coast. Offshore from Wilkes Subglacial Basin, for example, high-resolution modelling of sea ice trajectories around Mertz Glacier area shows that icebergs from the east are deflected north (Marsland et al., 2004), allowing locally derived debris to be more dominant in the lee side of the “Promontory” (Orejola et al., 2014). This area of deflection matches remarkably well with the area where model results and observations differ (red area, Fig. 3.16). Similarly, a gyre offshore from King Edward VII Peninsula deflects icebergs, which drift within the Antarctic Coastal Current westwards along the Amundsen Sea shelf, to the north before injecting them into the eastward flowing Antarctic Circumpolar Current (Keys, 1990; Rackow et al., 2017). This implies that grounded bergs, sea ice and unresolved ocean currents are a key control on the provenance of sediment on the continental shelf in these regions and should be carefully considered when interpreting sediment provenance records.

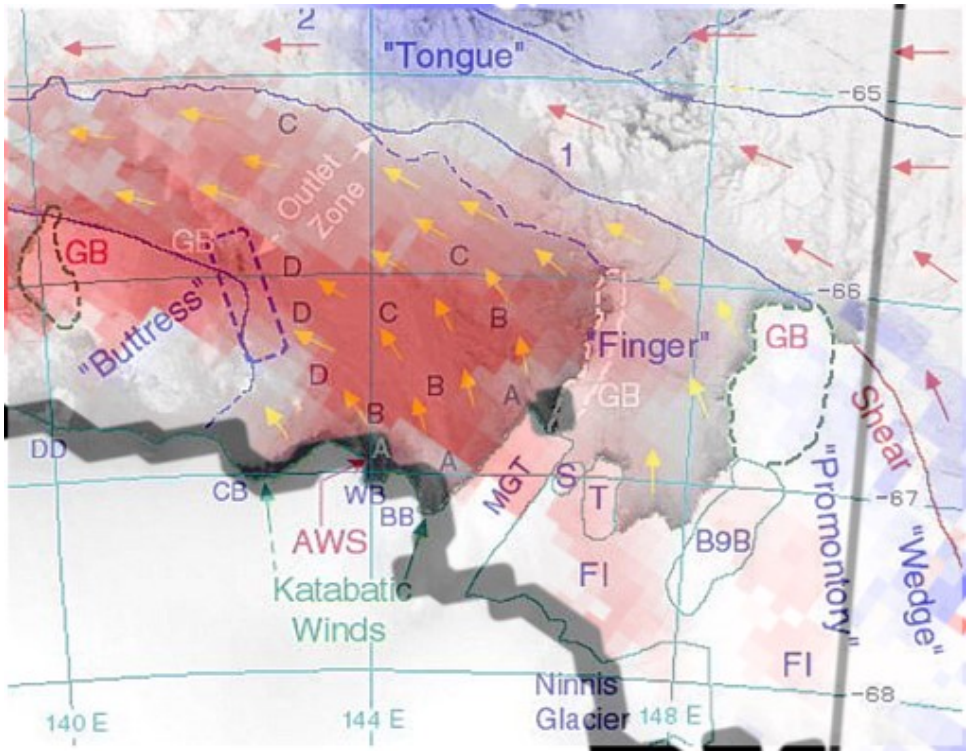


Figure 3.16 *Close up of the Mertz Glacier Tongue (MGT) region imaged in June 1999, adapted from Massom et al. (2001) and Marsland et al. (2004). Red-blue colours indicate the discrepancy between the modelled and core top ε_{Nd} values as in Fig. 3.13h. Overlain is a map of old (multi-year) and new sea ice trajectories (red and yellow arrows, respectively), which are deflected to the north due to "Promontory" of grounded bergs (GB), including iceberg B9B, and fast ice (FI). DD, Dumont d'UIrville; CB, Commonwealth Bay; WB, Watt Bay; BB, Buchanan Bay. S and T are individual grounded bergs.*

At some sites, disagreement observed may be linked to uncertain dating of seafloor surface sediments. Here, to achieve a good spatial coverage, we group all available measurements likely to be late Holocene in age, but difficulty in dating often carbonate-poor Antarctic sediments mean these may vary in age throughout the Holocene on a site-by-site basis.

3.6 Application to Smaller-than-present Palaeo Ice Sheets

3.6.1 Adaptions to methods

Processes such as subglacial erosion rates and detritus transport in the oceans have, until now, been considered only qualitatively when studying detrital sediment provenance records. Quantitative predictions of sediment provenance signals from past ice sheets have the potential to transform interpretation of such records; the sea-level change associated with a

provenance shift can be directly inferred. To construct an offshore ε_{Nd} estimate for past ice sheet states, we use an identical approach to that described for the modern ice sheet to predict the composition of the detritus at the ice sheet margin. Beyond the ice margin, the comparison between modelled and observed ε_{Nd} values of seafloor surface sediments described above produces a map illustrating which transport processes produce ε_{Nd} values most closely matching observations in different areas (Fig. 3.12). This is used to suggest which method may be dominant for past ice sheet configurations, predicting what ε_{Nd} values could be expected offshore.

Marine transport of glaciogenic detritus is clearly related to atmospheric and oceanic processes and thus will have changed in the past. However, we suggest that at the broad spatial scale studied here, changes to the dominance of different mechanisms may be sufficiently minor that useful predictions can still be made. For instance, the persistence of ice in East Antarctica and a degree of independence from climate means features such as the Antarctic Circumpolar Current and westerly winds driving an Antarctic Coastal Current are robust and will likely be present in all ice sheet configurations (Toyos et al., 2020; Weber et al., 2021). Although such features may slightly change their position or change in intensity, models of past climate and ocean currents lack sufficient resolution to resolve these currents at the required precision, implying that the use of modern data remains the best option. For instance, only high-resolution ocean reanalysis velocities in modern simulations resolve the Antarctic Coastal Current in enough detail to reproduce the realistic escape of icebergs from this current (Fig. 3.6). High resolution modelling of past oceans would improve the reconstruction of iceberg trajectories and consequently predictions of sediment provenance.

In addition, when applying the provenance tracing method to smaller-than-present ice sheets, using modern ocean velocities cannot always achieve sensible ocean current transport pathways. In particular, when marine-based areas of the Antarctic ice sheets, such as the majority of the WAIS, have collapsed, using interpolated modern ocean velocities does not give sensible flow trajectories. To give realistic ocean currents in areas with significant modelled reduction in ice extent, such as the WAIS interior, a Pliocene ocean model simulation from PlioMIP2 was used (Feng et al., 2020). However, important features such as the Antarctic Coastal Current are not resolved at sufficient resolution; we thus retain the use of the modern velocity data where these are available. Further changes include increasing the uniform ocean temperature to 2 ^{o}C instead of 0 ^{o}C, consistent with the amount of ocean warming used when modelling Pliocene ice sheets (DeConto and Pollard, 2016). Basal debris

will consequently not be transported as far from its source location by icebergs compared to today.

The Pliocene was the most recent time when atmospheric CO_2 concentrations were the same as today and high global sea-levels imply that large parts of Antarctica were free of grounded ice (Burke et al., 2018; Grant et al., 2019). The Pliocene is therefore of particular interest to paleoclimate studies and examined here. Uncertainty as to which sectors of the Antarctic ice sheets were lost or reduced in size means it is important to predict the sediment provenance change that might be expected given the collapse of marine-based sectors of the Antarctic ice sheets. These include the WAIS and Wilkes Subglacial Basin (WSB). The provenance tracing method was therefore applied to ice sheet model simulations of warm (interglacial) Pliocene intervals (Pollard and DeConto, 2009; DeConto and Pollard, 2016), and the results were compared to variations in ε_{Nd} from the sediment core record at IODP Site U1361 (Cook et al., 2013; 2017; Bertram et al., 2018; Fig. 3.17).

All ice sheet model simulations used show a collapsed WAIS with open seaways (Pollard and Deconot, 2009; DeConto and Pollard, 2016). Although no sediment provenance record from West Antarctica exists proving such a collapse, it has been inferred from the ANDRILL AND-1B drill core in the Ross Sea (Naish et al., 2009; McKay et al., 2012) and is a ubiquitous feature of most 'warm' Pliocene ice sheet models. In contrast to the WAIS collapse seen in all time slices, large differences are seen between the model simulations in the WSB, where the ice sheet is either largely intact (Pollard and DeConto, 2009) or partially retreated (DeConto and Pollard, 2016). These differences are predominantly a result of updates to the ice sheet model physics implemented between the studies. The climate forcing used is identical as the simulations used here were rerun in Gasson et al. (2016). The Pollard and DeConto (2009) simulation used is also a small part of much longer model timespan. Note that we do not seek to study a specific Pliocene time interval, but instead use these models as representative of different potential Pliocene ice extents.

3.6.2 Comparison to IODP Site U1361

International Ocean Discovery Program (IODP) Site U1361 off the Adélie Land coast contains a record of Antarctic ice sheet change during the Pliocene. Seafloor surface sediments at the site have a measured ε_{Nd} value of -11.5 (Cook et al., 2013), just over 2 epsilon units higher than our modelled prediction of -13.6 for the modern ice sheet configuration. The discrepancy with surface sediment data is likely linked to grounded icebergs and fast ice forcing surface currents carrying relatively radiogenic detritus further north towards this site compared to the currents used in the ocean model, as discussed above (Fig. 3.16). Provenance at Site U1361 is therefore clearly influenced by the presence or absence of icebergs and sea ice altering ocean circulation in this area. However, it is likely that warmer Southern Ocean waters during the Pliocene (e.g. McKay et al., 2012) would lead to fewer grounded icebergs and less sea ice in this area near Ninnis Glacier, which would reduce or remove the cause for the deflection of ocean currents (and thus glaciogenic debris) to the north. The relationship between ocean temperature and sea ice concentration/iceberg residence time on this specific part of the continental shelf would need further investigation to establish the importance of this effect on sediment provenance at Site U1361 under different climatic conditions.

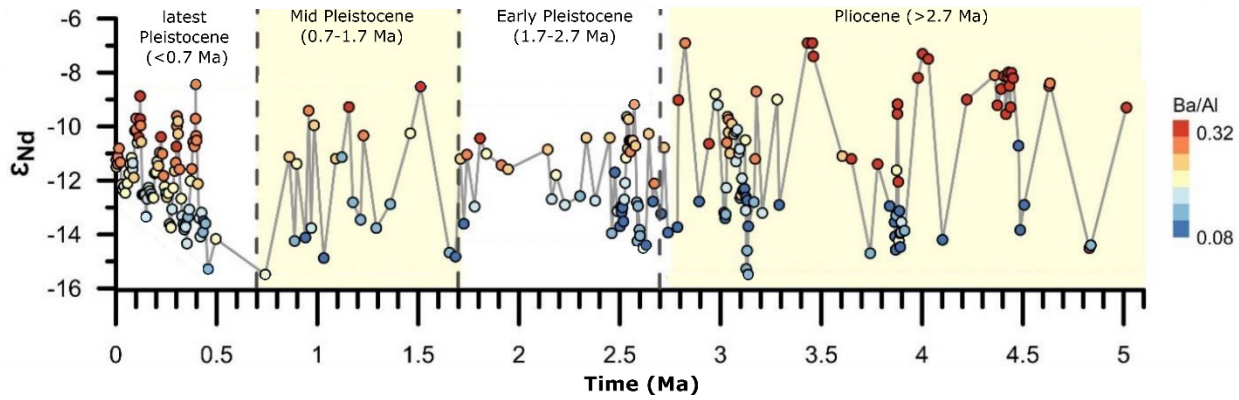


Figure 3.17. *IODP Site U1361 full ε_{Nd} record, including data from Cook et al. (2013), Cook et al. (2017), Bertram et al. (2018) and Wilson et al. (2018) and Bertram (2018). Sample points are coloured based on the Ba/Al ratio, where higher values (red) indicate warmer conditions and lower values (blue) cooler conditions. Key time intervals are separated using vertical dashed grey lines at 2.7, 1.7 and 0.7 Ma. Figure adapted from Bertram (2018).*

A further explanation for the discrepancy between our model and the seafloor surface sediment ε_{Nd} value at this site could be linked to the age constraints for the site, which only

reach as young as 6.678 ± 0.171 ka at 0.27-0.25 mbsf. The uppermost sample could thus be as old as mid-Holocene in age, when ice thicknesses and extent around Antarctica was often different to today (e.g. Johnson et al., 2019; Stutz et al., 2021). Thus, the Site U1361 seafloor surface sediment sample may not represent the present ice sheet and oceanographic signature.

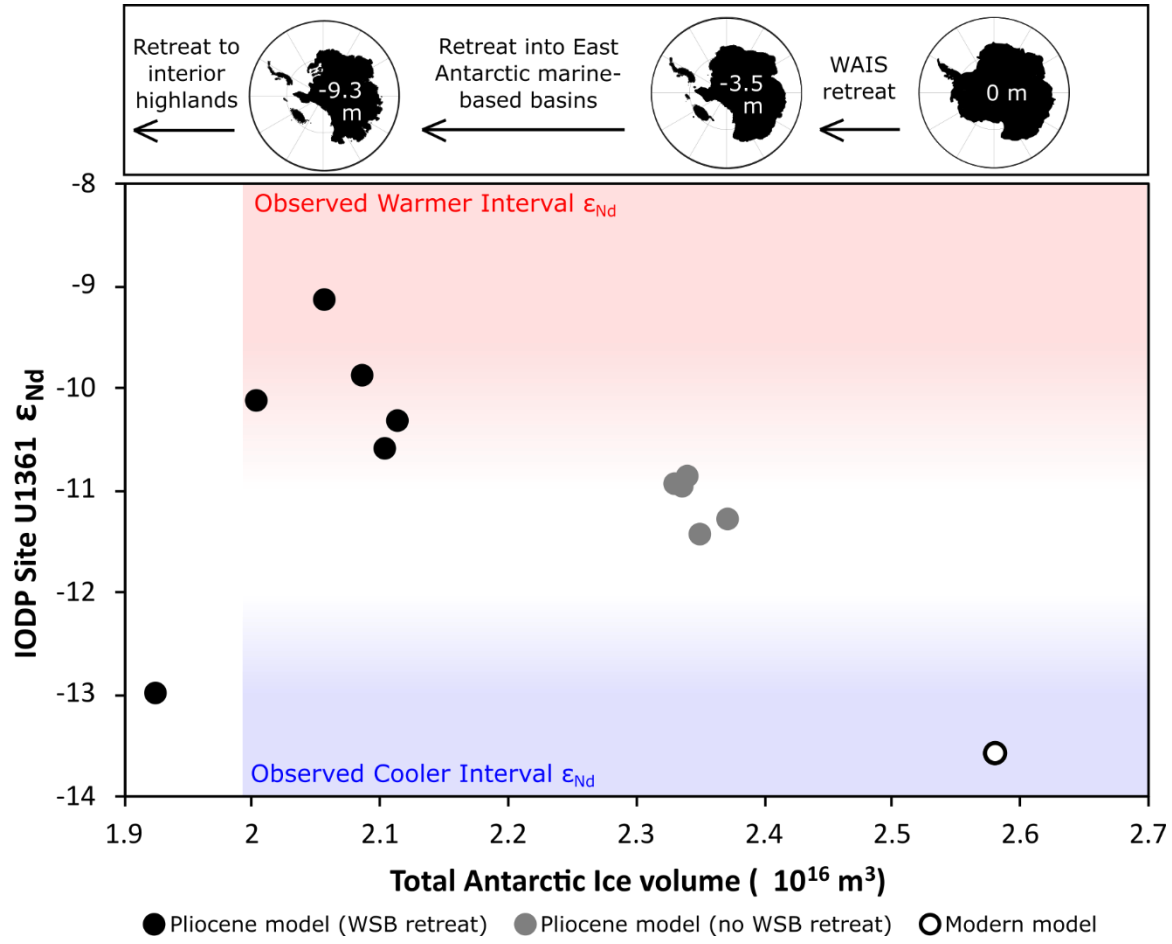


Figure 3.18. *Relationship between modelled Antarctic ice volume and ε_{Nd} values at IODP Site U1361. Ice sheet model time slices include the modern ice sheet (hollow black circle) and Pliocene ice sheets simulations with Wilkes Subglacial Basin (WSB) retreat (DeConto and Pollard, 2016; solid black circles) and without WSB retreat (Pollard and DeConto, 2009; solid grey circles). The red and blue shaded regions indicate the approximate range of ε_{Nd} values associated with warmer and cooler conditions in the U1361 record, respectively (Cook et al., 2013; 2017; Bertram et al., 2018). The ε_{Nd} value ranges indicated are representative the entire U1361 record rather than a specific time interval. Key ice sheet model ice extents and their sea level equivalent volumes relative to today are show in the upper panel, where black indicates ice cover.*

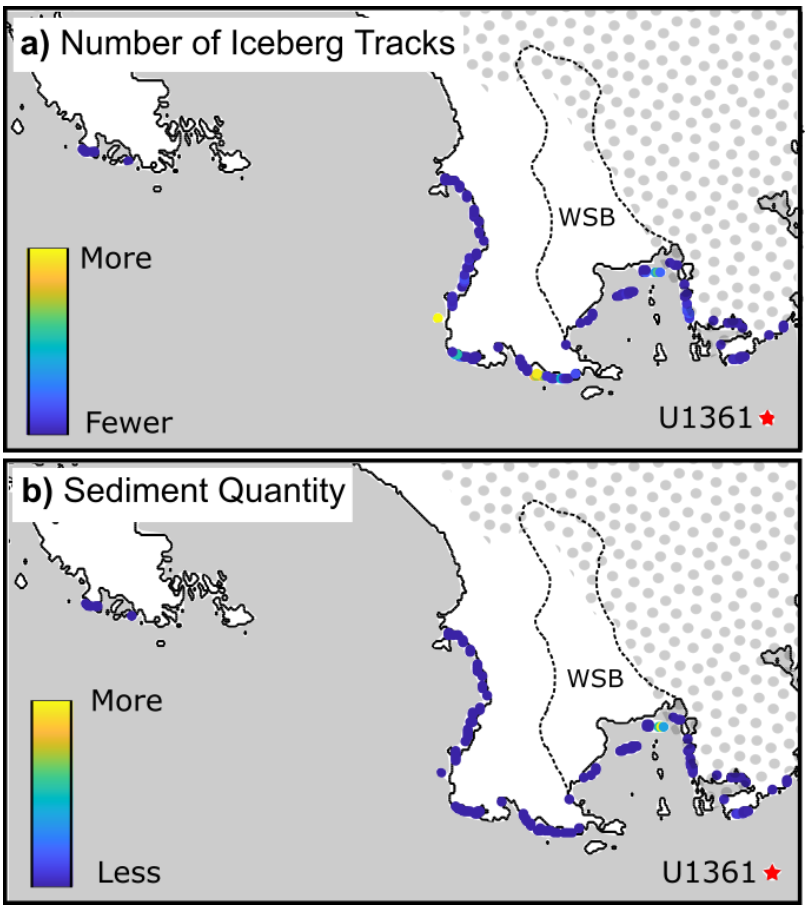


Figure 3.19. *Source of icebergs crossing the longitude of IODP Site U1361 (red star) to the south of the site. a) shows the number of icebergs sourced from each location, and b) the relative quantity of sediment sourced from each location. Both are dimensionless as only relative changes are of interest here. The stippled area shows the approximate extent of the Archaean to Paleoproterozoic Adélie Craton (Goodge and Finn, 2010), which is characterised by very unradiogenic (negative) Nd isotope compositions. The dashed line indicates the approximate extent of the Wilkes Subglacial Basin.*

Predicted ε_{Nd} values for Pliocene simulations with a collapsed WAIS but without a retreated WSB (Pollard and DeConto, 2009) give ε_{Nd} values of approximately -11.5 to -10.9 at IODP Site U1361, similar to values measured between intervals classed as warm or cool (Cook et al., 2013; 2017; Bertram et al., 2018; Fig. 3.17; 3.18). The rise to more radiogenic ε_{Nd} values than produced by the modern ice sheet could be attributed to faster ice flow and erosion further inland, allowing erosion of Ferrar Group material without substantial ice sheet retreat; this has been suggested for the Last Interglacial period (Wilson et al., 2018; Golledge et al., 2020). Westward transport of detritus from the Ross Sea and Marie Byrd Land may contribute partially to this ε_{Nd} shift, but tracing the source of debris reaching the core site (e.g.

Fig. 3.19) suggests the influence of this detritus is minor. Consequently, the model indicates a shift in erosion to areas further inland, but without a significant reduction in grounded ice extent, produces a rise in ε_{Nd} values, but is unlikely to achieve the magnitude of ε_{Nd} change documented by the intervals with the most radiogenic ε_{Nd} values at Site U1361.

Therefore, changes to ice velocity/erosion rates without significant ice sheet margin retreat are unlikely to achieve a shift to ε_{Nd} values of up to -8.4 at Site U1361 measured by Wilson et al. (2018), which they interpret as a signature of WSB retreat during the Last Interglacial. However, values of ~-10.4 during MIS 7 (Wilson et al., 2018) could be achieved without significant retreat of the WSB, suggesting WSB retreat is not ubiquitous during Pleistocene interglacials.

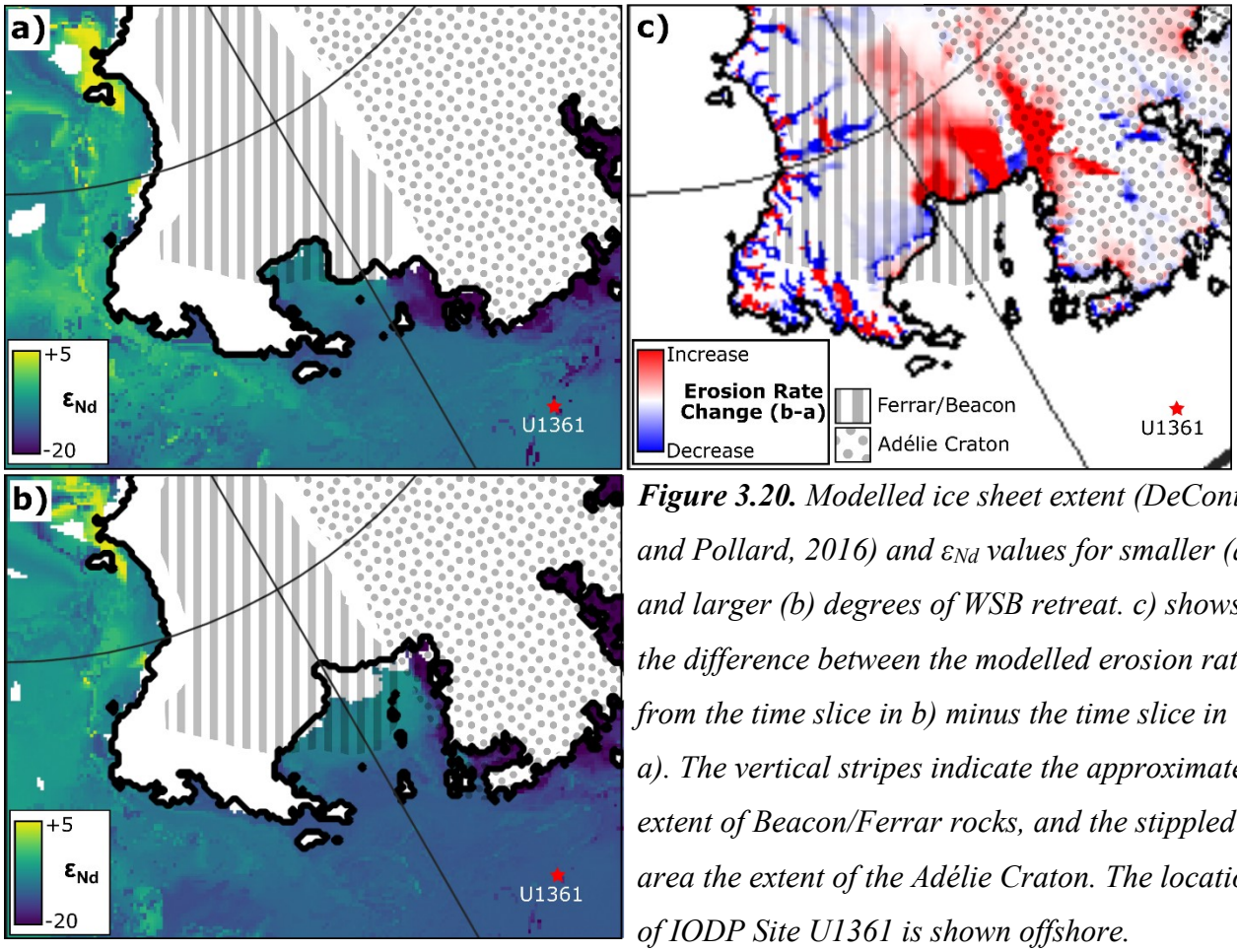


Figure 3.20. *Modelled ice sheet extent (DeConto and Pollard, 2016) and ε_{Nd} values for smaller (a) and larger (b) degrees of WSB retreat. c) shows the difference between the modelled erosion rate from the time slice in b) minus the time slice in a). The vertical stripes indicate the approximate extent of Beacon/Ferrar rocks, and the stippled area the extent of the Adélie Craton. The location of IODP Site U1361 is shown offshore.*

When there is retreat of the ice margin into the WSB, sediments deposited at Site U1361 show extreme ε_{Nd} values of up to -6.9 (Cook et al., 2013; 2017). However, many of the most radiogenic sediment intervals in other parts of the Plio-Pleistocene record at Site U1361 only reach -9.0 (Bertram et al., 2018) and -8.4 (Wilson et al., 2018) (Fig. 3.17). The simulations presented here approach these values by reaching ~-9.1 (Fig. 3.18) and thus the range

typically characterising Pliocene warm periods, given as >-11.0 (Bertram et al., 2018) or >-9.5 (Cook et al., 2013). Available ice sheet model time slices do not include a continuum of ice sheet states, so it is possible slightly more radiogenic ε_{Nd} values than those shown in Fig. 3.18 could be reached given slightly different ice sheet configurations.

Tracing the source of the detritus reaching a given site is theoretically possible using our approach but would be computationally demanding. Instead, to investigate the broad source regions likely to be contributing glaciogenic detritus to Site U1361, the model saves all surface sediment tracks crossing the approximate longitude range (143-145 ^{o}E) and south of the approximate latitude (64 ^{o}S) of the site. Using a range for the former captures the potential for downslope transport. This tracing reveals that there is consistently detritus reaching this region from Victoria Land north of Ross Island, and along much of the George V Land coast east of the site (Fig. 3.19). There is also a small contribution from the ice cap on Marie Byrd Land. Contributions from these distant sediment source regions is supported by $^{40}Ar/^{39}Ar$ dating of Pliocene hornblende grains at Site U1361 (Cook et al., 2017). Although more icebergs crossing the latitudinal transect are often sourced from Northern Victoria Land or the Oates Land coast (east of the WSB), the WSB is always the source of the largest fraction of sediment (Fig. 3.19). This tracing therefore supports geochemical inferences suggesting that the shift to more radiogenic ε_{Nd} values at Site U1361 when the ice sheet retreats is predominantly driven by erosion of the Ferrar Group, which is shed into the newly-created embayment on the George V Land coast (Fig. 3.20; Cook et al., 2013; Bertram et al., 2018).

Despite the overall dominance of Ferrar Group rocks at Site U1361, the detritus carried westward from Marie Byrd Land and Victoria Land in the Antarctic Coastal Current does constitute a small, but non-negligible, radiogenic component. A decrease in this far-travelled detritus might be expected given a higher iceberg melt rate in a warmer ocean, but Cook et al. (2017) note an increase in West Antarctic hornblende grains during warm intervals. This has been explained by a greatly enhanced iceberg production to overcome the warmer ocean temperatures (Cook et al., 2014; 2017). We offer another potential explanation for the observation of more far travel debris in warmer intervals, which could act in parallel to enhanced iceberg production. Cooler ocean temperatures, such as those at the present day, mean that far-travelled icebergs (i.e. from Marie Byrd Land, Victoria Land) have shed all their debris-rich basal ice by the time they reach Site U1361, whilst locally-derived icebergs (i.e. from the Wilkes Subglacial Basin) retain some basal debris, which dominates the

provenance signature. We tentatively suggest that, given warmer ocean temperatures, nearly all of the debris-rich basal ice layer melts from the icebergs before it reaches Site U1361, regardless of whether it is far travelled or more locally sourced. Englacial debris advected higher in the ice column from all source locations would therefore dominate the sediment deposited, giving a greater proportion of far-travelled debris. At Site U1361, this would be reflected in more radiogenic ε_{Nd} values in warmer intervals.

A key finding from our tracing is that a retreat of more than ~250 km into the southwestern part of the WSB causes ε_{Nd} values to decrease to more unradiogenic values (-13.0) than time slices when retreat is limited to the eastern part of the WSB (up to -9.1) (Fig. 3.18). Such an EAIS reduction occurs during the warmest simulated Pliocene time slices of DeConto and Pollard (2016). This decrease arises because when the ice sheet retreats far inland, it reaches areas on the southwestern side of the WSB underlain by the highly unradiogenic Archean to Proterozoic Adélie craton (Fig. 3.20; see also Pierce et al., 2017), the edge of which is clearly defined in magnetic surveys and shear wave velocity data (Ferracioli et al., 2009; Goodge and Finn, 2010). While the record at IODP Site U1361 does not reach beyond the late Miocene, IODP Site U1356 (Fig. 3.2) shows evidence for such a phenomenon from the Miocene, when ice sheet extent was, at times, even smaller than during the Pliocene. The baseline Nd isotope signature for such a retreated ice margin at Site U1356 is ~-16 to -14, whilst a shift towards more radiogenic values in middle Miocene times marks ice advances (i.e. northward expansion into the WSB eroding Ferrar and Beacon Group rocks with more radiogenic signatures (Pierce et al., 2017).

Overall, this non-linear relationship between ice sheet volume and ε_{Nd} values allows pinpointing of the extent of ice sheet retreat required to give a particular offshore provenance signature. The most radiogenic ε_{Nd} values in sediments at Site U1361 appear to be derived from an Antarctic ice sheet with a sea level equivalent volume of 48.6 m, ~9.3 m less than today (Morlighem et al., 2020). The lack of high Ba/Al samples with unradiogenic ε_{Nd} values throughout the U1361 Pliocene record (Fig. 3.17) implies the ice sheet did not retreat far enough to erode significant amounts of unradiogenic Adélie craton. This implies sea level highstands in the Pliocene may not have exceeded ~9.3 m above present.

3.6.3 Predicting the Provenance Signature of West Antarctic Ice Sheet Collapse

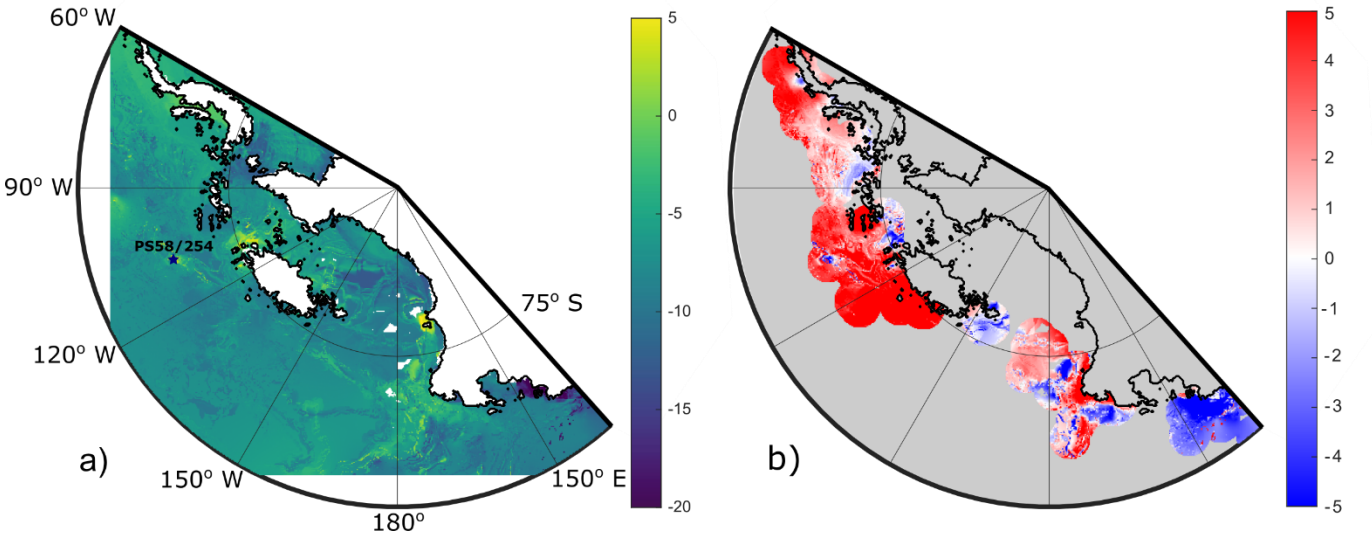


Figure 3.21 *Impact of WAIS collapse on modelled ε_{Nd} values. a) Absolute ε_{Nd} values and b) difference compared to seafloor surface sediment interpolation. The ice sheet model simulation is from DeConto and Pollard (2016), but similar distributions of ε_{Nd} values are seen along the Pacific coast of West Antarctica in all WAIS collapse scenarios.*

Along the Pacific West Antarctic margin, the collapse of the WAIS leads to consistent changes to sediment provenance in all model time slices. Before discussing these trends, it should be noted that ice velocities draining the part of the ice sheet remaining on Marie Byrd Land are relatively low in the ice cap's interior, giving a high sensitivity to bedrock ε_{Nd} values around the ice cap margin. Epsilon Nd values are highly uncertain here, translating to uncertainties in the magnitude of the provenance shift. Improved mapping of subglacial geology would reduce this uncertainty.

There are no published Pliocene sedimentary records to compare our results to, but we make some observations that could be compared to future downcore results from recent and upcoming drilling efforts to diagnose WAIS collapse:

1) **Ross Sea** - More radiogenic detritus is shed into the eastern Ross Sea (Fig. 3.21) than at present. Here, open ocean conditions on the southern side of Marie Byrd Land allow more radiogenic detritus to reach the eastern Ross Sea compared to times when there is a large WAIS present. Additionally, the ice margin retreats around the Edward VII Peninsula, where unradiogenic debris derived from the Swanson Formation metasedimentary rocks dominates the provenance signature of modern offshore sediments (Simões Pereira et al., 2018). Few icebergs travel through the

central Ross Sea, perhaps linked to the low-resolution Pliocene ocean model used, but it appears there may be a slight decrease in ε_{Nd} values here during a WAIS collapse. In the western Ross Sea, the direction of the ε_{Nd} value shift is sensitive to the trajectories of icebergs from Ross Island and the adjacent areas, which are dominated by rocks of the highly radiogenic McMurdo Volcanic province. Their enhanced erosion is the primary cause of deposition of sediments with more radiogenic ε_{Nd} values in the area.

2) **Bellingshausen Sea** – This region is relatively insensitive to WAIS collapse, but on the continental shelf, more radiogenic detritus is shed into the Bellingshausen Sea (Fig. 3.21). Here, erosion of detritus in basins inland that give relatively unradiogenic ε_{Nd} values (prescribed a value of -10) is reduced as there is no grounded ice there. This leads to sediment being predominantly sourced from the Antarctic Peninsula to the northeast and potentially the Thurston Island block to the west, where ε_{Nd} values are more radiogenic. Further offshore, the change is smaller but slightly skewed to more negative ε_{Nd} values. This may be linked to changes in erosion on the Antarctic Peninsula, as westward transport of this detritus is dominant here.
3) **Amundsen Sea** – When the WAIS is collapsed, this region receives less radiogenic detritus (Fig. 3.21). This could be attributed to a reduction in the contribution from radiogenic rocks from the West Antarctic interior, such as the Thwaites Glacier catchment (Simões Pereira et al., 2020). Open seaways through the West Antarctic interior would imply detritus can instead reach offshore locations from areas with more unradiogenic rocks, including the Ellsworth Mountains. A rise in ε_{Nd} values does occur near the coast in the western Amundsen Sea, which may be attributed to erosion of volcanic edifices, such as Mt Murphy, as these are known to have remained islands with glaciated summits during times of WAIS retreat.

Site PS58/254 (location in Fig. 3.21) provides only a Pleistocene ε_{Nd} record, but a Pliocene WAIS collapse is expected to have caused a similar provenance change and thus shift in ε_{Nd} values as a Pleistocene collapse. At this site, the model is sensitive to (sparse) iceberg flow paths, but a mean of all simulations with a collapsed WAIS predicts a ε_{Nd} value of -4.7 (n = 12), slightly less radiogenic than the surface sediment value of -3.0 (Simões Pereira, 2018). The direction of this shift is consistent with the sedimentary record spanning the last ~800 kyrs, which shows slightly (<1 epsilon unit) less radiogenic values during interglacial periods (Simões Pereira, 2018). The simulated magnitude of change is, however, greater than that measured. The record of Simões Pereira (2018) may therefore suggest full WAIS collapse did

not occur during the Pleistocene, although modelled ε_{Nd} values could be influenced by inaccurate representation of iceberg pathways when the ice sheet is collapsed. The modelling presented here highlights the relative insensitivity of detrital ε_{Nd} values to changes in ice sheet extent in the Amundsen Sea, where rock ε_{Nd} values are more homogenous than in the Ross Sea (Marschalek et al., 2021) and East Antarctica (e.g. Cook et al., 2013).

3.7 Conclusions and Future Direction

Tracing the provenance of glacimarine sediments using the results of an ice sheet model and simple approximations of offshore transport mechanisms can help refine the interpretations of geochemical sediment provenance data. Tighter coupling of numerical model simulations and provenance data offers the potential for the advancement of both fields; results of numerical modelling can be directly compared to real-world constraints, and interpretations of geochemical data can be tested and visualised. The approach presented here can also predict areas where the greatest provenance change might be expected given a change to the ice sheet, helping identify priority targets for future drilling campaigns.

The approach is particularly powerful beyond - but close to - the continental shelf, where it produces a close match when using a simulation of the modern ice sheet to predict ε_{Nd} values for seafloor surface sediments. This is likely because gravitational downslope processes dominate here, allowing greater integration of provenance signals and making our approach less reliant on precise mapping of uncertain subglacial geology. On the continental shelf, we are able to capture the general pattern of ε_{Nd} values seen around West Antarctica and the East Antarctic George V Land margin. Substantial model-data disagreement can readily be explained by specific regional factors not captured in the provenance tracing.

Applying the method to past ice sheet configurations gives new insights into existing sediment provenance records. At IODP Site U1361, offshore of the Wilkes Subglacial Basin (East Antarctica) the approach is able to capture nearly all of the variation in ε_{Nd} values seen in the sedimentary record. Changes to erosion and/or transport of detritus around the Antarctic Coastal Current without substantial ice sheet margin retreat in the WSB are unlikely to lead to the largest changes in sediment provenance recorded at the site, including those during the last interglacial (Wilson et al., 2018). During the most retreated ice sheet model scenarios, we predict a non-linear relationship between ε_{Nd} values and ice volume. If the western part of the WSB retreats more than ~250 km inland of its present position, erosion of the highly unradiogenic Adélie Craton increases substantially, leading to a

decrease in ε_{Nd} values offshore. Consequently, intervals where the most radiogenic ε_{Nd} values are reached during the Pliocene likely correspond to an Antarctic ice volume SLE ~9.3 m lower than today. As there is no evidence for a reversal in the relationship between ε_{Nd} values at Site U1361 and ice volume in the Pliocene (i.e. an unradiogenic value with a high Ba/Al; Fig. 3.17), the model suggests sea-level contributions from Pliocene Antarctica compared to the present day did not exceed ~10 m.

Improved knowledge of subglacial geology, particularly in much of West Antarctica, would improve the accuracy and potential for a numerical approach to give useful, accurate results. Future geophysical surveys, as well as drilling campaigns targeting subglacial sediments and especially bedrock, will reduce uncertainty in our ε_{Nd} map, thus predictions offshore. For past ice sheets, high resolution ocean modelling covering time intervals when the ice sheet had a very different extent compared to today would greatly improve our estimate by capturing the likely motion of icebergs in different climatic conditions. Additional insights into past ice sheet behaviour and useful comparisons with sediment core records could be achieved by focussing this approach on different parts of the Antarctic continent. Our method could also be adapted for numerous provenance proxies, each offering a different sensitivity to changes to erosion thus different precision in different regions and at different times in the past (Licht and Hemming, 2017). Such proxies include detrital mineral dating, major and trace element geochemistry, clay and heavy mineralogy, or clast petrography.

Table 3.3. *Parameters used in this chapter.*

Parameter	Symbol	Unit	Value (if constant)
'Quarrying' coefficient	k		5.1×10^{-10}
Iceberg basal melt rate	M_b	m/day	-
Ocean Temperature	T_s	^{o}C	0 (modern), 2 (Pliocene)
Debris yield	D	-	-
Time	t; t_s	days; seconds	-
Basal sediment thickness	Z	M	6
Sediment decay coefficient	λ	-	5
Relative suspended sediment concentration	c	-	-
Probability of particle sticking to bed	p	-	-
Settling velocity	v_s	m/s	3.3×10^{-3}
Suspended sediment layer thickness	y	m	15
Bottom shear stress	τ_w	Pascals	-
Critical depositional stress	τ_c	Pascals	0.08
Drag coefficient	C_d	-	-
Seawater density	ρ	kg/m^3	1025
Vertically averaged velocity	$\bar{U}$	m/s	-
von Kármán constant	κ	-	0.41
Roughness length	z_0	m	5×10^{-4}
Water depth	H	m	-
Slope to initiate gravitational downslope transport	-	Degrees	1

Relevant Appendix Sections – Appendix A.5 discusses coupled Miocene ice sheet and erosion modelling linked to this work. Section A.6 presents results from the application of the methods to the Last Glacial Maximum.

Chapter 4. Characterisation of the First Exposed Bedrock between Thwaites and Pine Island Glacier

James Marschalek measured the Nd and Sr isotopes and collated and interpreted all the data with guidance from Tina van de Flierdt and Claus-Dieter Hillenbrand. Stuart Thomson and Christine Siddoway collected and helped interpret the thermochronological (fission track and (U-Th)/He) data and zircon Hf isotope data. Pieter Vermeesch and Andy Carter helped measure the U-Pb zircon samples. Major and trace element data were provided by Sam Hammond, with the assistance of Liam Holder. Julia Wellner, Claus-Dieter Hillenbrand and various crew members of the *R.V. Nathaniel B Palmer* made it possible to circumnavigate and sample Sif Island, as well as collect the sediment cores studied. James Smith provided the Thwaites sub-ice-shelf samples.



Sif Island's tall ice cliffs with Thwaites Eastern Ice Shelf in the background. Photo credit: C.-D. Hillenbrand.

Chapter Summary

Thwaites and Pine Island glaciers comprise the 'weak underbelly' of the West Antarctic Ice Sheet (WAIS) and have long been recognised as the first areas where marine ice sheet instability may initiate (Hughes, 1981). Analysis of recent observational data indicate that such processes may have already begun (Joughin et al., 2014). Assessing the past response of these glaciers to different environmental conditions is key for understanding tipping points and placing modern processes in a long-term context. This can help determine the magnitude and rate of future WAIS collapse.

This chapter discusses the discovery of Sif Island during the "THwaites Offshore Research (THOR)" NBP20-02 cruise in 2020, following its exposure in the early 2010s as ice retreated from a coastal region of slow-flowing ice between Pine Island Glacier and Thwaites Glacier. To understand the tectonic development of this region and identify its provenance signature in marine sediments used to reconstruct past changes in the Amundsen Sea drainage sector of the WAIS, the petrography, geochemistry, and thermal history of the island is explored. These results are compared to seafloor surface sediment samples collected close to Thwaites and Pine Island glaciers during cruise NBP20-02 and cruise NBP19-02 in 2019, and from beneath the grounding zone of Thwaites Glacier and its Eastern Ice Shelf.

Sif Island was found to be formed of granite dating to ~178-173 Ma. It has a relatively radiogenic ε_{Nd} value (-3.88) and a comparatively radiogenic $^{87}Sr/^{86}Sr$ ratio (0.725175), which major and trace element analysis suggests is linked to a fractionated composition with a high Rb/Sr ratio. A suite of fission track and (U-Th)/He dates revealed the granite cooled rapidly after its emplacement to below the zircon fission track closure temperature at ~165 Ma. Later rapid uplift occurred at ~92-91 Ma. Seafloor surface sediment samples from close to Pine Island Glacier have ε_{Nd} values of ~-7 to -8 and $^{87}Sr/^{86}Sr$ ratios of ~0.724 to 0.728, in close agreement with previously published compositions of nearby samples (Simões Pereira et al., 2020). Sediments retrieved from the grounding zone of Thwaites Glacier reach ε_{Nd} values of up to ~-2.2, varying over a short spatial scale reflecting lateral advection of detritus from the east under the Eastern Ice Shelf.

However, both $^{87}Sr/^{86}Sr$ ratios and ε_{Nd} values in samples collected from below the Eastern Ice Shelf as well as Thwaites Glacier's grounding zone are unusually high rather than showing a typical anti-correlation between the Nd and Sr isotope ratios. This may be linked to the isotopic composition of Sif Island which, if representative of the surrounding rocks, has a

high $^{87}Sr/^{86}Sr$ ratio relative to its ε_{Nd} value and helps explain a lack of correlation between these isotope systems previously observed in some offshore down-core sediment samples (e.g. Simões Pereira, 2018). Sif Island also provides constraint on the provenance of glaciogenic detritus supplied by Pine Island Glacier, as it does not match the radiogenic Nd and Sr isotopic composition of the more evolved, unradiogenic granitic rocks assumed to constitute the bedrock substrate below most of Pine Island Glacier (Simões Pereira et al., 2020). These unexposed unradiogenic source rocks are isotopically dissimilar to Sif Island and therefore must be located further inland below Pine Island Glacier.

The age and geochemistry of the Sif Island granite shares many similarities with rocks exposed on Thurston Island and the Antarctic Peninsula. Therefore, Sif Island marks the most westerly outcrop of these Early-Middle Jurassic rocks. The zircon fission track age of the Sif Island granite (~165 Ma) contrasts with that of the rocks exposed on islands along the eastern coast of the Amundsen Sea Embayment (~100 Ma; Lindow et al., 2016), providing the first clear thermochronological evidence for a tectonic boundary beneath the trunk of Pine Island Glacier.

4.1. Introduction

The exposure of new islands in polar regions is a visually powerful symptom of a warming climate. These islands are separating due to major ice mass loss, resulting in the retreat of ice caps and ice sheets as well as local sea-level fall and isostatic uplift in surrounding coastal areas. This phenomenon has been observed through a combination of satellite imagery and ship-based expeditions several times in recent years throughout the polar regions (e.g. Ziaja and Ostafi, 2019; Hansen et al., 2022). During expedition NBP20-02 with RV/IB *Nathaniel B. Palmer* in 2020, which was conducted on behalf of the "THwaites Offshore Research (THOR)" project (https://thwaitesglacieroffshoreresearch.org/), a hitherto uncharted small island, named "Sif Island", was discovered in Pine Island Bay in the eastern Amundsen Sea Embayment at a latitude of -75.095 and longitude of -102.825. Subsequent analysis of satellite imagery revealed that Sif Island was separated during the early 2010s from slow-flowing ice draining between Thwaites Glacier and Pine Island Glacier into Pine Island Bay (Fig. 4.1; 4.2). The island is uniquely located in one of the most sensitive parts of the cryosphere, making understanding the behaviour of the ice sheet here crucial for predicting the magnitude and rate of future global sea-level rise from Antarctic Ice Sheet mass loss (Scambos et al., 2017; Pörtner et al., 2019). Thwaites and Pine Island glaciers drain about one third of the largely marine-based and inherently unstable West Antarctic Ice Sheet (WAIS) into the Amundsen Sea Embayment (Rignot et al., 2019). Alone, they have the potential to raise sea level by approximately 1.2 m (Morlighem et al., 2020). These two ice streams are of interest to society and scientist alike due to their observed recent thinning, flow acceleration and grounding line retreat (summarised in Scambos et al., 2017), which, due to an inland deepening bed slope, may reflect the early stages of runaway mass loss from this sector of the WAIS (Weertman, 1974; Thomas and Bentley, 1978; Hughes, 1981; Joughin et al., 2014; Rosier et al., 2021).

Revealing the history of these glaciers can help infer tipping points and provide data to test representations of physical mechanisms in numerical modelling. Paleo data can therefore improve predictions of how the WAIS may respond to current oceanic and climatic warming on centennial to millennial timescales. A powerful method for reconstructing past ice sheet change is the study of glacimarine sediment provenance, where shifts in the focus of erosion recorded in offshore sediments can be related to ice sheet extent (e.g. Marschalek et al., 2021). Such reconstructions rely on knowledge of subglacial geology which, for Thwaites

and Pine Island glaciers, is complicated by the near complete ice cover of their drainage basins.

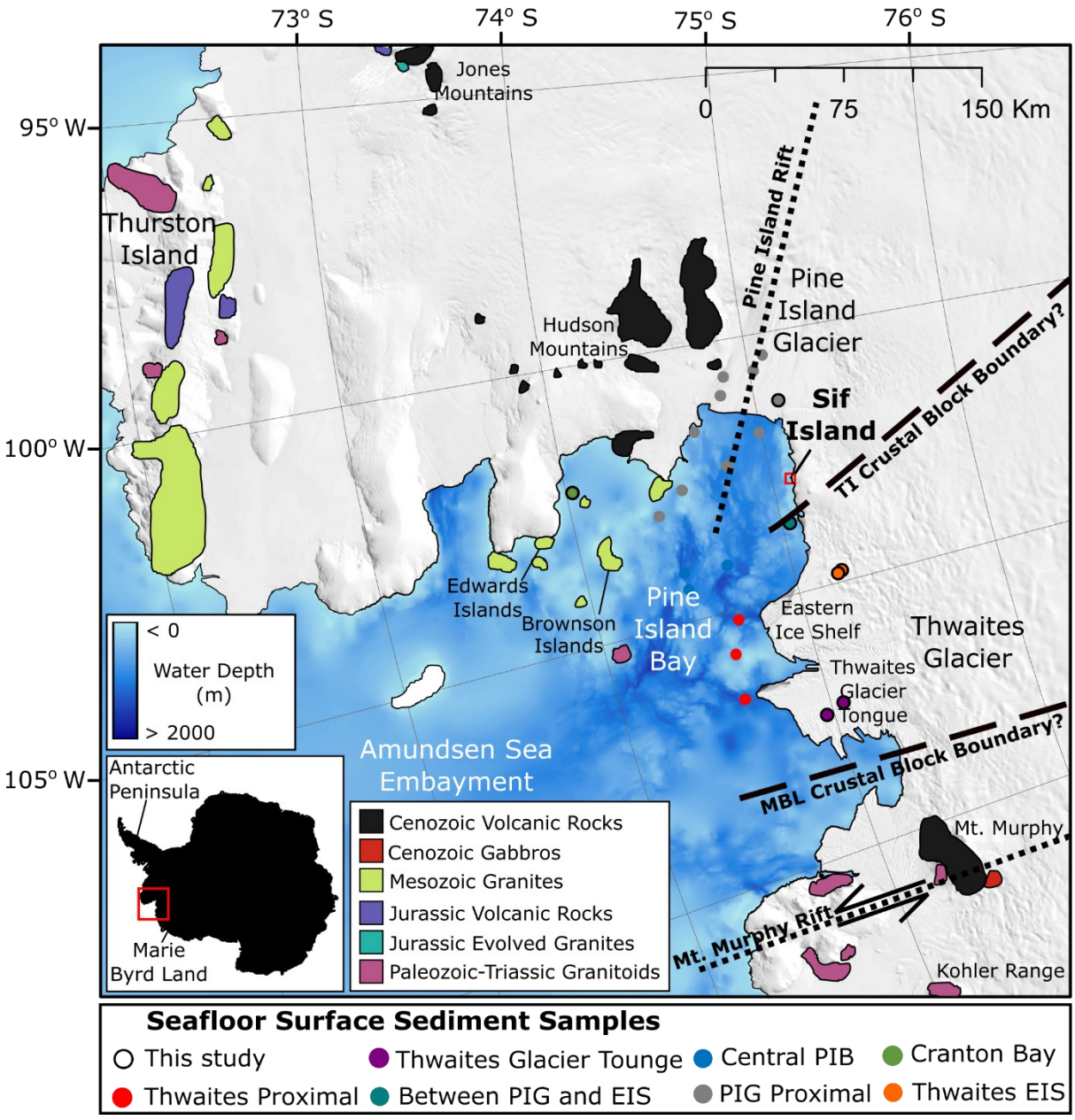


Figure 4.1. *Location of Sif Island in the eastern Amundsen Sea Embayment, relative to other rock exposures which are mapped based on Cox et al. (2019) and classified based on Simões Pereira et al. (2020). The location of the main map within Antarctica is shown in the bottom left insert (red box), and the position of Sif Island (corresponding to Figure 4.2) is indicated in the main map (red box). The approximate position of Pine Island Rift is based on Jordan et al. (2010) and that of Mt. Murphy Rift on Spiegel et al. (2016). The uncertain Thurston Island (TI) and Marie Byrd Land (MBL) crustal block boundaries are displayed following Zundel et al. (2019). Bathymetry shown is from BedMachine V1 (Morlighem et al., 2020) and Hogan et*

al. (2020). Ice sheet extent is from the MEaSUREs dataset (Mouginot et al., 2017; Rignot et al., 2013), so is inaccurate near rapidly changing calving fronts of Thwaites and Pine Island glaciers. On land, MODIS ice imagery is shown (Haran et al., 2014). Plotted as circles are seafloor surface sediment samples analysed for Nd and Sr isotope composition. Previous data from Simões Pereira et al. (2020) are displayed as coloured circles (see key in lower panel) alongside data new to this study (outlined in black).

This extensive cover by grounded ice and ice shelves means using the fingerprint of glacimarine detritus to reconstruct past ice sheet change has to be inverted; i.e., the provenance of seafloor surface sediments collected proximal to the modern ice margin is used to infer the subglacial geology. However, even this goal is difficult to achieve because of dense sea-ice cover in the Amundsen Sea Embayment throughout most of the year. Simões Pereira et al. (2020) reported data from a multi-proxy analytical approach on the provenance of seafloor surface sediments from the eastern Amundsen Sea Embayment, revealing that Thwaites and Pine Island glaciers supply glaciogenic detritus with distinctive fingerprints. The datasets included $^{40}Ar/^{39}Ar$ ages of iceberg rafted hornblende and biotite grains, radiogenic Nd and Sr isotope ratio compositions of fine-grained (<63 μm) detritus, clay mineral assemblages, and major and trace element compositions. The results showed that Pine Island Glacier is likely underlain by evolved granitoids of late Palaeozoic to Early Jurassic age, whereas Thwaites Glacier is likely underlain by Cretaceous igneous rocks, pre-Oligocene sedimentary strata, and Cenozoic gabbroic bodies (Simões Pereira et al., 2020). In this chapter, both Sif Island rock samples and new glacimarine and sub-ice sediment samples offer further refinements to knowledge of subglacial geology, which will ultimately help inform predictions of future ice mass loss.

The geological and tectonic development of this region can also be elucidated by analysing the composition of the bedrock exposed at Sif Island, and this can help understand how the large-scale modern bed morphology developed and influenced the ice drainage pattern in the Amundsen Sea sector of the WAIS. Major tectonic features are hypothesised to run throughout the Amundsen Sea Embayment and influence WAIS drainage (Gohl, 2012), including beneath Pine Island Rift and adjacent to Mt. Murphy on the western side of Thwaites Glacier (Jordan et al., 2010; Spiegel et al., 2016). Sif Island is the only subaerial rock outcrop between these two features (Fig. 4.1). The island is isolated from any other outcrops by at least 60 km in all directions and provides the only window into the previously unexposed bedrock between Thwaites and Pine Island glaciers. It is therefore perfectly

located to explore the subglacial geology of this region and shed light on one of the most poorly geologically characterised regions on earth.

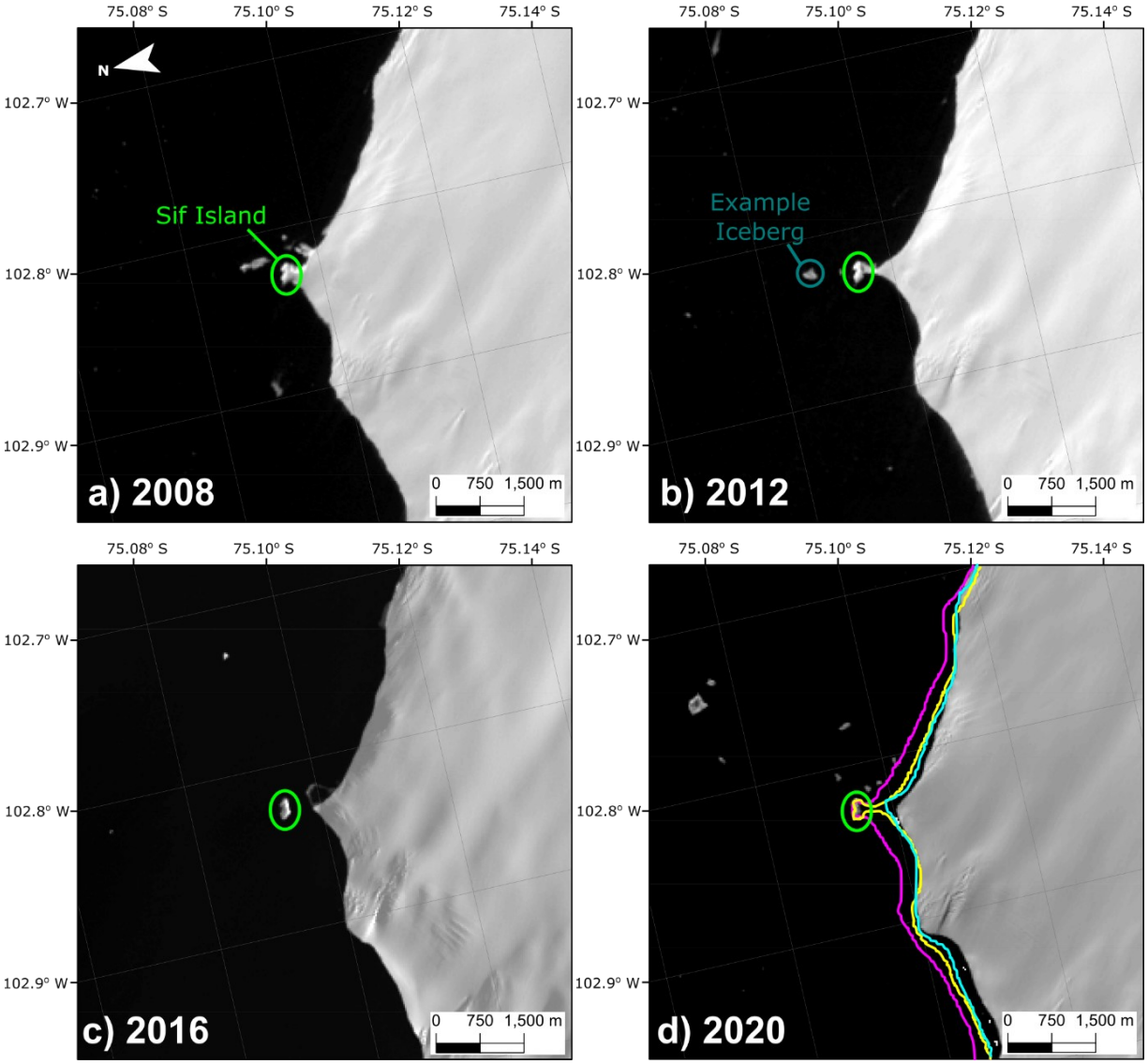


Figure 4.2. *The exposure of Sif Island caused by a retreating ice front captured in LANDSAT imagery from 23th Nov. 2008 (a, Landsat 7), 18th Nov. 2012 (b, Landsat 7), 11th Jan. 2016 (c, Landsat 8) and 26th Jan. 2020 (d, Landsat 8). Landsat OLI/TIRS imagery courtesy of the USGS. The ice margin retreated by approximately 500 m in the 12-year period. Panel d) shows previous ice extents in a)-c) as magenta, yellow and cyan lines, respectively. The position of Sif Island is circled in green, with an example iceberg circled in teal in panel b for comparison. The location of the map within Pine Island Bay is shown in Figure 4.1.*

We report new results helping characterise the hidden geology of the catchment areas of Pine Island Glacier and Thwaites Glacier. Sampling of Sif Island and marine sediments was conducted as part of the THOR project. The island was named in honour of the project after

the Norse goddess Sif, the wife of Thor. The THOR project is part of the wider International Thwaites Glacier Collaboration (ITGC) programme. This is a joint U.S. (National Science Foundation) and U.K. (Natural Environment Research council) initiative to substantially improve decadal and longer-term projections of ice loss and sea level rise originating from Thwaites Glacier (https://thwaitesglacier.org/).

4.2 Geological Setting

Sif Island is located in the eastern part of the Amundsen Sea Embayment, which lies at the junction between two major crustal blocks: the Marie Byrd Land (MBL) block and the Thurston Island block (Jordan et al., 2020). The region is therefore considered a major tectonic boundary (e.g. Gohl et al., 2007; 2013b; Jordan et al., 2010; 2020; Fig. 4.1). To the west of Sif Island, the geology of the MBL block can be broadly divided into an eastern (Amundsen) and western (Ross) province, with the Amundsen Province located closest to Sif Island (Pankhurst et al., 1998). The Thurston Island block to the east of the Amundsen Sea Embayment records a magmatic arc sequence since the Palaeozoic. It may have rotated by 180^{o} between the Late Jurassic and mid-Cretaceous and has a geological history similar to that of the Antarctic Peninsula block further east (Riley et al., 2017a). A brief overview of the main rock groups of the Thurston Island, Antarctic Peninsula and eastern MBL crustal blocks is provided.

Early Palaeozoic sedimentary rocks and metamorphosed magmatic events are recorded along the Pacific margin of West Antarctica (e.g. Adams, 1986; Pankhurst et al., 1998; Siddoway, 2008; Yakymchuk et al., 2015). However, intrusive rocks become more common in the Devonian and Carboniferous, particularly in westmost MBL, where they form the Ford Granodiorite (Pankhurst et al., 1998; Korhonen et al., 2010; Yakymchuk et al., 2015). Detrital hornblende and biotite grain $^{40}Ar/^{39}Ar$ ages of ~380 Ma and ~330-270 Ma are also recorded in glacimarine sediments sourced from Thwaites Glacier (Simões Pereira et al., 2020). Further north-east, rocks cropping out on Thurston Island also have mineral ages of ~349 Ma (Riley et al., 2017a) and ~309 Ma (Pankhurst et al., 1993), with detrital mineral ages from offshore sediments peaking at ~352 Ma (Simões Pereira et al., 2018). These Devonian-Carboniferous rocks comprise the oldest dated basement of the Thurston Island block. The Antarctic Peninsula also has a Palaeozoic metamorphic basement (e.g. Millar et al., 2002; Riley et al., 2012), which is overlain by Carboniferous to Triassic sedimentary rocks (Burton-Johnson and Riley, 2015).

The Kohler Range of eastern MBL contains evidence for Permian magmatism, spanning ~280-270 Ma (Pankhurst et al., 1998; Mukasa and Daziel, 2000). Further pulses of magmatism occurred during the Triassic on Thurston Island, where intrusive bodies date to 240-220 Ma (Riley et al., 2017a), and the Antarctic Peninsula, where Triassic magmatic rocks date to 236-220 Ma (Millar et al., 2002; Flowerdew et al., 2006; Riley et al., 2012; Bastias et al., 2021). Granitoids from the Jones Mountains, south of Thurston Island, were intruded at 198±2 Ma (Pankhurst et al., 1993). This granite is relatively evolved, with a higher crustal component indicated by unradiogenic ε_{Nd} values (Pankhurst et al., 1993). The Nd isotope composition of sub-ice shelf sediments from Pine Island Glacier (PIG) is similarly unradiogenic (low), with ε_{Nd} values of ~-8.5 (Simões Pereira et al., 2020). This supports other geochemical, thermochronological and petrographic data suggesting PIG is underlain by granitic bedrock which is largely Triassic to Early Jurassic in age (Lindow et al., 2016; Simões Pereira et al., 2018; 2020).

Evidence for late Early Jurassic magmatic activity in MBL is limited to a single inherited ~181 Ma zircon age (Korhonen et al., 2010). However, Thurston Island and the Antarctic Peninsula host various volcanic rocks of this age. Silicic tuffs on Thurston Island date to 182-181 Ma and may correspond to the rocks of the Chon Aike event along the Antarctic Peninsula (Riley et al., 2017b). This event saw felsic rocks emplaced and extruded in three phases: ~188-178 Ma (V1), 173-160 Ma (V2) and 157-145 Ma (V3) (Pankhurst et al., 2000; Bastias et al., 2021). The oldest phase is associated with the emplacement of the Ferrar and Karoo Large Igneous Provinces (LIPs) along the Transantarctic Mountains and in South Africa, respectively, although the Chon Aike province spans a greater duration and has also been associated with the subduction of Pacific lithosphere (see Bastias et al., 2021 and references therein). The V1 and V2 phases are found further to the south of the Antarctic Peninsula, close to the position of the proposed rotated Thurston Island block (Riley et al., 2017a). Extrusive rocks here are often known as the Antarctic Peninsula Volcanic Group.

Magmatism is recorded again on Thurston Island during the Late Jurassic (Pankhurst et al., 1993; Riley et al., 2017a). However, magmatism was not widespread along the paleo-Pacific margin until the mid-Cretaceous, when granitic batholiths were emplaced along this margin. Plutonism spanning ~128-94 Ma is common along the MBL coast (e.g. Adams 1987; Siddoway 2008), on Thurston Island (e.g. Pankhurst et al., 1993; Riley et al., 2017a) and on the Antarctic Peninsula (e.g. Leat et al., 1995; Burton-Johnson and Riley, 2015). These Cretaceous rocks are also common in the low-relief island groups in Pine Island Bay,

close to the location of Sif Island (Kipf et al., 2012; Mukasa and Dalziel, 2000; Pankhurst et al., 1993, 1998; Lindow et al., 2016; Zundel et al., 2019). Corresponding ages also dominate detrital mineral ages in glaciogenic detritus supplied by Thwaites Glacier, although they are notably rare in detritus shed from PIG (Simões Pereira et al., 2020).

Cretaceous magmatism is linked to the West Antarctic rift system, as significant extension began at this time (Siddoway, 2008). Extension continued into the Cenozoic, with Pine Island Bay inferred to be a branch of the West Antarctic rift system which was active in the early Cenozoic (Jordan et al., 2010; Gohl et al., 2013b; Spiegel et al., 2016). This rift branch, referred to as Pine Island Rift (Fig. 5.1), runs approximately perpendicular to the main rift axis (Lindow et al., 2016). Due to the lack of rock exposures, inferences regarding geological boundaries and structural features are based on and limited to geophysical data (e.g. Fig. 4.1). The Thurston Island crustal block boundary is sometimes suggested to follow Pine Island Rift (e.g. Jordan et al., 2020), whereas others put it close to Mount Murphy (e.g. Spiegel et al., 2016). Thus, whilst Pine Island Rift has been linked to Cenozoic West Antarctic rift system activity, it is uncertain whether it follows an older crustal block boundary or formed within the Thurston Island block largely because of Cenozoic West Antarctic rift system activity.

Cenozoic volcanic rocks are also common throughout West Antarctica. Around the eastern Amundsen Sea Embayment, these include the Hudson Mountains to the north of PIG and isolated volcanoes to the west of Thwaites Glacier, such as Mt. Murphy. This volcano marks the easternmost extent of the "Marie Byrd Land volcanic province", which is alkaline and largely basaltic in composition, although some felsic rocks are also present (LeMasurier and Thomson, 1990; LeMasurier, 2013). Cenozoic volcanic rocks likely continue beneath the ice sheet, inferred from magnetic anomalies, radar data and geochemical data (Behrendt et al., 1991; Corr and Vaughan, 2008; van Wyk de Vries et al., 2017; Simões Pereira et al., 2020). This volcanic - and potentially gabbroic plutonic (Simões Pereira et al., 2020) - activity is linked to a later phase of West Antarctic rift system activity (LeMasurier and Thomson, 1990).

4.3 Field Observations

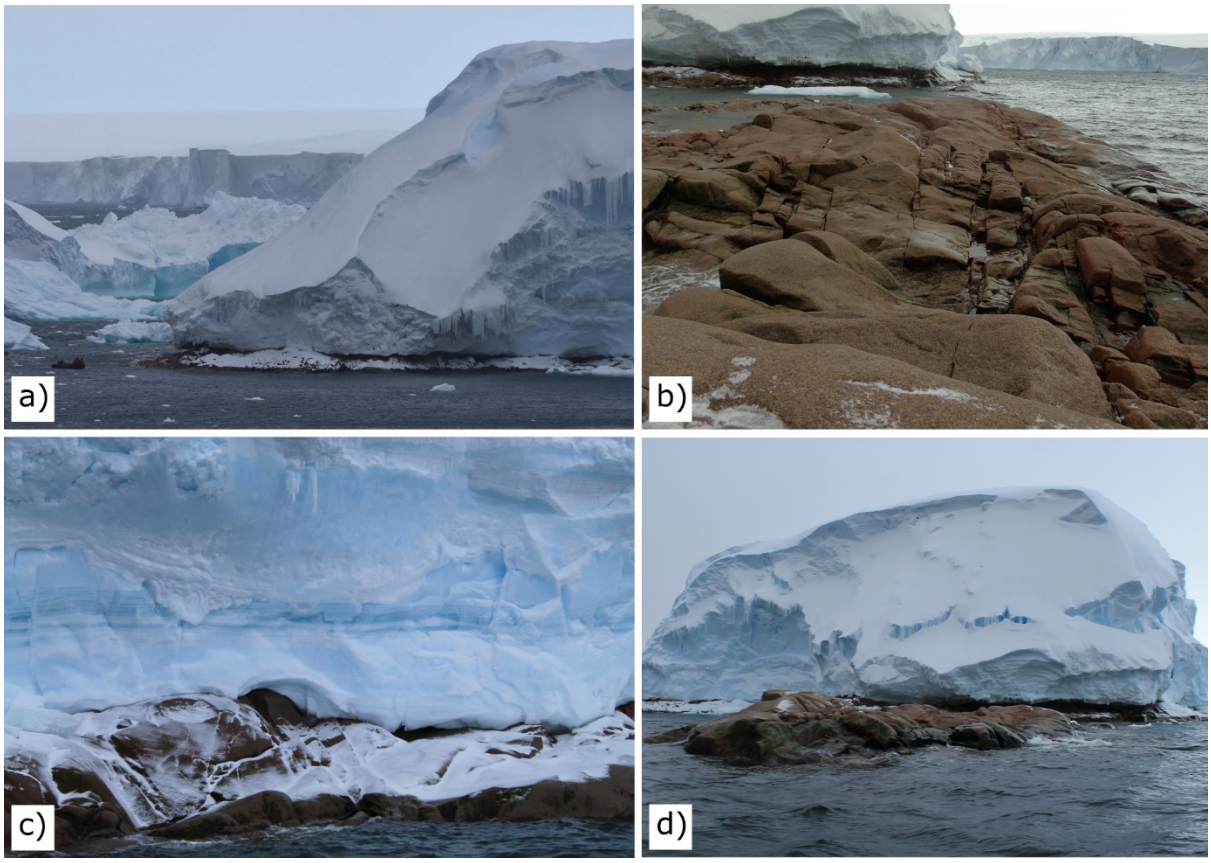


Figure 4.3. *Field photographs of Sif Island. a) The thick ice cover of the island (right), remaining after retreat of the ice margin, which is visible in the background. Grounded icebergs are present between the modern ice margin and the island (left), and a boat with geologists to the left of the island provides scale. b) Exposed rock at the sampling location, with the main island visible in the top left of the image. c) A typical section of the basal ice and rock exposure. Melt layers are visible in the ice. d) Sampling location with the main island in the background.*

To explore the previously unexposed geology between Thwaites and Pine Island glaciers, Sif Island was visited and circumnavigated shortly after its discovery during cruise NBP20-02 in early 2020. The island is approximately 350 m long and 120 m wide (Fig. 4.2). At the time of visiting, ~1-2 m of bedrock was exposed above the water line around the island perimeter (Fig. 4.3), although the tidal state was unknown. Above this bedrock, approximately 40-50 m thick ice covered almost the entire island. Although accumulation rates are high in Pine Island Bay relative to the Antarctic interior (Johnson et al., 2018), the substantial thickness of this ice, as well as the history of ice margin retreat documented in the satellite imagery (Fig.

4.2), suggests that this ice cover is a remnant of the adjacent ice sheet rather than the result of purely local snow accumulation. It is therefore likely to have been a remnant of either grounded slow-flowing ice or a minor ice rumple - i.e., part of an ice shelf that extended seaward from today's coast and was pinned on the island.

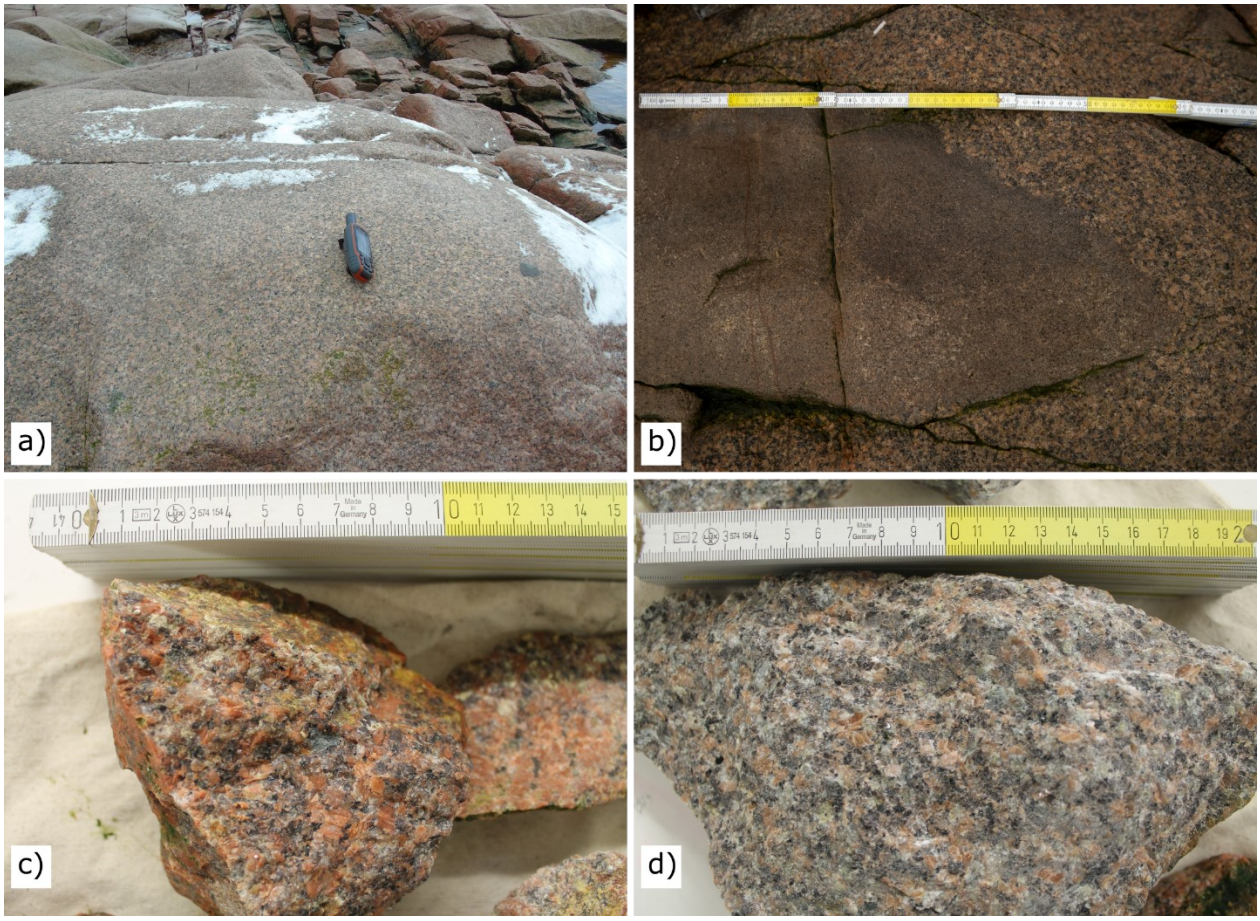


Figure 4.4. *a) Typical exposed bedrock surface. b) sharp contact between the coarse-grained granite forming the bulk of the outcrop and a finer grained granitic intrusion or xenolith c) Hand specimen of 'pinker' sample (e.g. SIA and SIC). d) Hand specimen of sample SIB, collected just below the exposure shown in panel a).*

Sampling was possible thanks to a small (~15-20 m diameter), ice-free rocky promontory approximately 30-40 m away from the main island (Fig. 4.3b and d). This rose to ~1 m above sea level at the time of visiting. The blocky, jointed pink granite appeared indistinguishable at an outcrop scale to all the rock visible around the perimeter of the main island (Fig. 4.3), so is thought to be representative. The granite is coarse-grained, pink and equigranular (Fig. 4.4). Exposed rock had a smooth surface, and neither erratic nor glacial surface features, such as striations, were observed, which may be consistent with the relatively thin ice frozen to the bed in this area (Fig. 4.3; 4.4). The bedrock composition and surface are consistent with

recent geophysical interpretation of the subglacial morphology beneath Thwaites Glacier, which shows regions thought to indicate a hard, crystalline bedrock (Muto et al., 2019).

4.4 Methods

4.4.1 Sampling and Sample Selection

Samples from Sif Island were obtained from different parts of the accessible outcrop and three samples with designated names SIA, SIB and SIC (SI = Sif Island) were analysed. Sample SIB is shown in Fig. 4.4d and was collected from the base of the exposure in Fig. 4.4a. Samples SIA and SIC were collected from just beyond the top of the exposure visible in Fig 4.4a, near the centre of the outcrop shown in Fig. 4.3b. As hand specimens, SIA and SIC resembled the sample in Fig. 4.4c.

All three rock samples were dated using the zircon U-Pb method. Fission track and (U-Th)/He dating, plus zircon Hf isotope analysis, were performed on sample SIA. For bulk rock geochemical and radiogenic Nd and Sr isotope analyses, ~230 g of sample SIB was powdered, ensuring the sample was not biased towards any particular mineral type. Agreement between replicates implies this powder was homogenous and representative of the bulk rock (Tables 4.2, 4.4).

Marine sediment cores were collected on cruises NBP19-02 in 2019 and NBP20-02 in 2020 (Fig. 4.1). The coring methods, sample depth intervals and locations are recorded in Table 4.5. Two additional sediment samples were obtained in early 2020 by drilling through the Thwaites Glacier upstream of the grounding zone and through its Eastern Ice Shelf downstream of the grounding zone. For the marine expeditions, the goal was to target areas close to the ice margin that had not been sampled previously (Fig. 4.5). Exceptional sea ice conditions and break-up of a large part of the Thwaites Glacier Tongue in early 2019 allowed ship-based coring far closer to Thwaites Glacier than has ever been possible (i.e. under the former glacier tongue). Furthermore, a large calving event from Pine Island Glacier in early 2020 permitted ship-based coring near to the sites of sub-ice-shelf cores collected in 2012/2013 (Smith et al., 2017). A seafloor surface sediment sample from close to Sif Island and a sample from Cranton Bay, where fast-ice cover had prevented coring before 2020, were also selected to improve existing knowledge of variations in the local geology around the eastern Amundsen Sea Embayment. All marine and subglacial samples were analysed for Nd and Sr isotopes.

4.4.2 Radiogenic Nd and Sr Isotopes

The sediment samples were prepared for Nd and Sr isotope measurements by sieving to isolate the <63 μm fraction, which is assumed to be representative of the bulk sediment. This fraction was leached in a mixture of 0.05 M hydroxylamine hydrochloride, 15% acetic acid, and 0.03 M EDTA at a pH of 4 (Gutjahr et al., 2007). A carbonate removal step was not included due to the very low carbonate content in surface sediments from the study area (e.g. Fig. 3A in Hauck et al., 2012). Leached sediment was dried, homogenised, and 50 mg aliquots were digested on a hotplate in concentrated HF, $HClO_4$, and HNO_3 for three to five days. Rock sample analyses were performed on 50 mg of the sample SIB rock powder, and the leaching step was skipped as this is only used for the removal of authigenic phases in marine sediments. All samples were processed alongside ~75 mg of USGS BCR-2 rock standard. The Nd was isolated from the sample matrix using a cation exchange resin (AG50W-X8, 200-400 μm mesh) and HCl in increasing molarity, followed by a low molarity HCl Ln-Spec resin procedure (50–100 μm mesh). The sample matrix from the cation exchange step was dried, taken up in HNO_3, then loaded onto Eichrom Sr Spec resin to wash down the matrix and elute the Sr (Simões Pereira et al., 2018).

Neodymium isotopes were measured in the MAGIC laboratories at Imperial College London on a Nu high resolution multi-collector inductively coupled plasma mass spectrometer (HR MC-ICP-MS). To account for instrumental mass bias, isotope ratios were corrected using an exponential law and a $^{146}Nd/^{144}Nd$ ratio of 0.7219. Although negligible, interference of ^{144}Sm on ^{144}Nd was corrected for. Bracketing standards were used to correct measured $^{143}Nd/^{144}Nd$ ratios to the commonly used JNdi-1 value of 0.512115 (Tanaka et al., 2000). USGS BCR-2 rock standard measurements yielded $^{143}Nd/^{144}Nd$ ratios consistently within error of the published ratio of 0.512638 ± 0.000015 (Weis et al., 2006). Full procedural blanks for Nd were 18 and 41 pg. $^{143}Nd/^{144}Nd$ ratios are expressed using epsilon notation (ε_{Nd}), which denotes the deviation of a measured ratio from the modern Chondritic Uniform Reservoir (0.512638) in parts per 10,000 (Jacobsen and Wasserburg, 1980).

Strontium isotopes were measured in the MAGIC laboratories at Imperial College London on a TIMS (Thermal Ionisation Mass Spectrometer). Samples were loaded in 1 μL of 6M HCl onto degassed tungsten filaments with 1 μL of $TaCl_5$ activator. The measured $^{87}Sr/^{86}Sr$ ratios were corrected for instrumental mass bias using an exponential law and an $^{88}Sr/^{86}Sr$ ratio of 8.375. Interference of ^{87}Rb was corrected for using an $^{87}Rb/^{85}Rb$ ratio of 0.386. Analyses of

the NIST 987 standard reference material were completed every four unknowns, yielding a mean of 0.710275 ± 0.000028 (2SD, n = 15). Samples were corrected to the published value of 0.710252 ± 0.000013 (Weis et al., 2006). The relatively poor reproducibility for our NIST 987 runs was due to technical issues, but is still more than sufficient for interpreting sample results, which change in the 3rd to 4th digit. Accuracy of results was confirmed using rock standard USGS BCR-2, processed with every batch of samples, which yielded $^{87}Sr/^{86}Sr$ ratios of 0.705003 ± 0.00018 (2SD, n = 6). This is within error of the published ratio of 0.705013 ± 0.00010 (Weis et al., 2006).

4.4.3 Zircon U-Pb Dating

Apatite and zircon grains for all the geochronological methods described below were concentrated using standard crushing, density separation and magnetic separation techniques. Zircon U-Pb analyses were performed by James Marschalek and Pieter Vermeesch at the London Geochronology Centre, University College London, and by Stuart Thomson at the Arizona LaserChron Center, University of Arizona.

At the London Geochronology Centre, the entire mineral separate was mounted in epoxy resin and 20 grains were analysed from two different rock samples (SIB and SIC). A New Wave NWR 193nm laser ablation system coupled to an Agilent 7700 ICP–MS was used. Plešovice zircon was used as a primary standard to correct for instrumental mass bias and depth-dependent inter-element fractionation (Sláma et al., 2008), whilst GJ1 zircon was used as a secondary standard to verify accuracy of the data (Jackson et al., 2004). Uranium and Th concentrations were estimated by comparison with NIST 612 glass (Pearce et al., 1997). Data reduction of the time-resolved mass spectrometer data was performed using GLITTER 4.5 (Griffin, 2008). Although the number of discordant ages was high for sample SIB, the GJ1 ages suggest the data are reliable.

Zircon U-Pb dating at the Arizona LaserChron Center (www.laserchron.org) used the methods of Gehrels et al. (2008), which are not discussed in detail here, applied to 50 zircon grains selected from a third hand specimen (SIA). Instrumentation comprised a Photon Machines Analyte G2 excimer laser equipped with HelEx ablation cell using a spot diameter of 20 microns, coupled to an Element2 HR ICPMS. Sri Lanka and FC-1 zircon crystals were used as the primary zircon standard reference material, and R33 zircon crystals used as secondary standard. Data reduction was performed in MATLAB® using the Arizona LaserChron Center AgeCalcML software. Detailed methods are available at

www.laserchron.org. Laser spot selection was conducted using colour cathodoluminescence (CL) images generated with a Hitachi 3400N SEM and a Gatan CL2 detector system (www.geoarizonasem.org).

All final data analysis and visualisation was performed using Isoplot-R (Vermeesch, 2018a). Discordant grains were filtered using the log ratio distance to the concordia composition (Vermeesch, 2021). Instead of applying a fixed threshold to select between the use of the $^{206}Pb/^{238}U$ ratio or $^{207}Pb/^{206}Pb$ ratio to calculate the age, a single-grain concordia age was calculated. Final ages were calculated as a weighted mean.

4.4.4 Zircon Hf Isotopes

Methods used for Hf isotope analyses are based on those in Cecil et al. (2011) and were conducted by Stuart Thomson at the Arizona Laserchron Centre, University of Arizona. Measurements were conducted using a Nu HR ICP-MS connected to a Photon Machines Analyte G2 excimer laser. 10 ppb solutions of JMC475 and a Spex Hf solution, then 10 ppb solutions containing Spex Hf, Yb, and Lu, were used to determine instrument settings. When all solutions yield $^{176}Hf/^{177}Hf$ of ~0.28216, instrument settings are optimized for laser ablation analyses and seven different standard zircons (Mud Tank, 91500, Temora, R33, FC52, Plešovice, and Sri Lanka) were analysed mounted in the same epoxy pucks. When precision and accuracy were acceptable (i.e. ≤1 unit of εHf at the 2σ level), unknowns were analysed using identical acquisition parameters.

Laser ablation pits with a diameter of 40 μm were placed on top of the U-Pb analysis pits, with CL images used to ensure that the ablation pits do not overlap multiple age domains or inclusions (Fig. 4.6). Each acquisition consisted of one 40-second integration on backgrounds (on peaks with no laser firing) followed by 60 one-second integrations with the laser firing. Using a typical laser fluence of ~5 J cm^{-2} and pulse rate of 7 hz, the ablation rate is ~0.8 microns per second. Each standard was analysed at the beginning and end of the sample run.

Isotope fractionation was accounted for using the method of Woodhead et al. (2004): βHf (mass fractionation factor in the exponential law) was determined from the measured $^{179}Hf/^{177}Hf$; βYb was determined from the measured $^{173}Yb/^{171}Yb$ (except for very low Yb signals); βLu was assumed to be the same as βYb. Ytterbium and Lu interferences were corrected by measurement of $^{176}Yb/^{171}Yb$ and $^{176}Lu/^{175}Lu$ (respectively), as advocated by

Woodhead et al. (2004). Stable isotope ratios used as reference were: $^{179}Hf/^{177}Hf$ =0.73250 (Patchett & Tatsumoto, 1980); $^{173}Yb/^{171}Yb$ = 1.132338 (Vervoort et al. 2004); $^{176}Yb/^{171}Yb$ =0.901691 (Vervoort et al., 2004; Amelin and Davis, 2005); $^{176}Lu/^{175}Lu$ = 0.02653 (Patchett, 1983). All corrections were done line-by-line. For very low Yb signals, βHf was used for fractionation correction of Yb isotope ratios. The corrected $^{176}Hf/^{177}Hf$ values were filtered for outliers (2-sigma filter), and the average and standard error was calculated from the resulting ~58 integrations.

The cut off for using βHf versus βYb was determined by monitoring the average offset of the standards from their known values, and the cut off was set at the minimum offset. This was achieved at ~6 mv of ^{171}Yb. The $^{176}Hf/^{177}Hf$ at time of crystallization was calculated from measurement of present-day $^{176}Hf/^{177}Hf$ and $^{176}Lu/^{177}Hf$, using the decay constant of ^{176}Lu ($\lambda = 1.867e^{-11}$) from Scherer et al. (2001) and Söderlund et al. (2004). No capability is provided for calculating Hf depleted mantle model ages because the $^{176}Hf/^{177}Hf$ and $^{176}Lu/^{177}Hf$ of the source material(s) from which the zircon crystallized is not known.

4.4.5 (U-Th)/He Dating

(U-Th)/He dating was conducted by Stuart Thomson at the Arizona Radiogenic Helium Dating Laboratory (ARDHL), University of Arizona. Zircon and apatite grains were examined under a polarizing stereo-microscope and selected for (U-Th)/He on the basis of grains size (>60 μm diameter), morphology, clarity, and lack of inclusions. Final grains were imaged, their dimensions measured, and then loaded into Nb packets. To measure He, aliquots were heated with a diode laser to ~1300 ˚C for 18-20 minutes for zircon, and to ~900 ˚C for four minutes for apatite. One or more gas re-extractions (lasing) for 20-21 minutes at higher temperatures were performed for zircon grains and no gas re-extracts were done for apatite grains. Extracted He was spiked with ^{3}He, purified using cryogenic and gettering methods, and measured with a quadrupole mass spectrometer. A known amount of ^{4}He was measured every 8th analysis to monitor instrument drift. Degassed apatite grains were retrieved, spiked with a ^{233}U-^{229}Th-^{147}Nd-^{42}Ca tracer, dissolved in HNO_3, and U, Th, Nd, and Ca isotopes were analyzed on an Element 2 high-resolution inductively-coupled plasma mass spectrometer (HR-ICP-MS). Following addition of a ^{233}U-^{229}Th spike, equilibration, and dissolution in HF in a Parr bomb, the U and Th isotopes of zircon aliquots were measured on an Element 2 HR-ICP-MS. Grain masses were used to calculate U, Th, Sm, and He

concentrations. For apatite grains, the mass was calculated from Ca measurements and stoichiometry following the protocols of Guenthner et al. (2016). For zircon grains, we report the dimensional mass calculated from grain length measurements and assumptions about morphology following the protocols of Hourigan et al. (2005). Durango apatite and Fish Canyon tuff zircon were used as standards to assess dissolution protocols and HR-ICP-MS analyses. Blank-corrected (U-Th-Sm)/He and (U-Th)/He ages were calculated with propagated analytical uncertainties from U, Th, Sm, and He measurements. Alpha-ejection corrections were applied using grain measurements and assuming apatite and zircon are unzoned with respect to U, Th, and Sm (Hourigan et al., 2005; Ketcham et al., 2011).

4.4.6 Fission Track Dating

Fission track dating was performed by Stuart Thomson at the Arizona Fission Track Laboratory, University of Arizona. Apatite grains were mounted in epoxy resin, polished with alumina powder, and spontaneous fission tracks revealed by etching with 5.5M HNO_3 at 21°C (±1 °C) for 20 (±0.5) seconds (Donelick et al., 2005). Zircon grains were mounted in PFA Teflon, diamond polished, and etched in an oven at 220°C using a KOH-NaOH eutectic melt (Gleadow et al., 1976) in a zirconium crucible for 3 to 9 hours. The optimum fission track etch time is dependent on age and radiation damage and was monitored by repeated etching and observation at 3-6 hour time intervals. Samples were analysed by the external detector method (Gleadow, 1981) using very low uranium, annealed muscovite mica detectors, and irradiated at the Oregon State University Triga Reactor, Corvallis, USA. The neutron fluence was monitored using European Institute for Reference Materials and Measurements (IRMM) uranium-dosed glasses IRMM 540R for apatite and IRMM 541 for zircon. After irradiation, induced fission tracks in the mica external detectors were revealed by etching with 48% HF at 20°C for 20 minutes. Spontaneous and induced fission track densities were counted using an Olympus BX61 microscope at 1250x magnification using an automated Kinetek Stage system. Apatite horizontal confined fission track lengths and D_{par} (mean fission-track etch pit diameter parallel to the crystallographic c-axis) values were measured using FTStage software, an attached drawing tube, and a digitizing tablet (supplied by Trevor Dumitru of Stanford University) calibrated against a stage micrometer. Central ages (Galbraith and Laslett, 1993; Galbraith, 2005) were calculated using the IUGS recommended zeta-calibration approach of Hurford and Green (1983). Apatite and zircon IRMM 540R and IRMM541 weighted mean zeta calibration factors of 343.1±8.7 and

116.0±0.3 respectively, were obtained by repeated calibration against internationally agreed age standards including Fish Canyon tuff and Durango apatite, and Fish Canyon tuff and Tardree rhyolite zircon, according to the recommendations of Hurford (1990).

4.4.7 Major and Trace Element Geochemistry

Approximately 50 mg of the powdered SIB sample was digested in a mixture of concentrated HNO_3, HF and $HClO_4$, with different samples digested for major and trace element analyses and isotopic analyses. Selected major and trace element analyses were performed by Liam Holder under the assistance of Samantha Hammond at the Open University using an Agilent 8800 ICP triple quadrupole mass spectrometer (see methods in Simões Pereira et al., 2018). An integrated collision reaction cell filled with either no gas, He, or O_2 removed interference ions. Oxide formation (CeO+/Ce+) was kept below 1.0% and 0.6% in no gas and He gas mode, respectively, and doubly charged species (Ce2+/Ce+) were kept below 1.5% and 1.0%, respectively. Detection limits of light trace elements were typically 2–50 ppt in solution, while mid to heavy trace elements (Rb-U) were ≤ 2 ppt. Measurements were compared to five USGS reference materials, and instrument drift corrected for using an internal standard. An overall precision for trace elements better than 5% and accuracy better than 10%, and major element precision and accuracy of ~5%, was indicated by BCR-2 standard measurements.

4.5 Results

4.5.1 New Nd and Sr Isotope Provenance data from Seafloor Surface Sediments

The two surface sediment samples upstream and downstream of the EIS grounding zone have ε_{Nd} values of -2.69 and -2.12 (orange circles in Fig. 4.5; Table 4.1), which are slightly more radiogenic than seafloor sediments further west. These more westerly samples from the former terminus of the Thwaites Glacier Tongue (purple circles in Fig. 4.5) have ε_{Nd} values of -3.30 and -2.73. The $^{87}Sr/^{86}Sr$ ratios of the EIS samples are ~0.713-0.714, compared to ~ 0.710-0.712 for the Thwaites Glacier Tongue samples (Fig. 4.6; Table 4.1). The marine sediment sample from Cranton Bay has a detrital ε_{Nd} value of -3.85 ± 0.25 and $^{87}Sr/^{86}Sr$ ratio of 0.709465 (Fig 4.5, 4.6; Table 4.1). The two samples from the southern PIG ice-shelf front and vicinity of Sif Island, respectively, have relatively unradiogenic ε_{Nd} values (-8.14 and -6.62) and radiogenic $^{87}Sr/^{86}Sr$ ratios (0.727888 and 0.723971) (Fig. 4.6; Table 4.1).

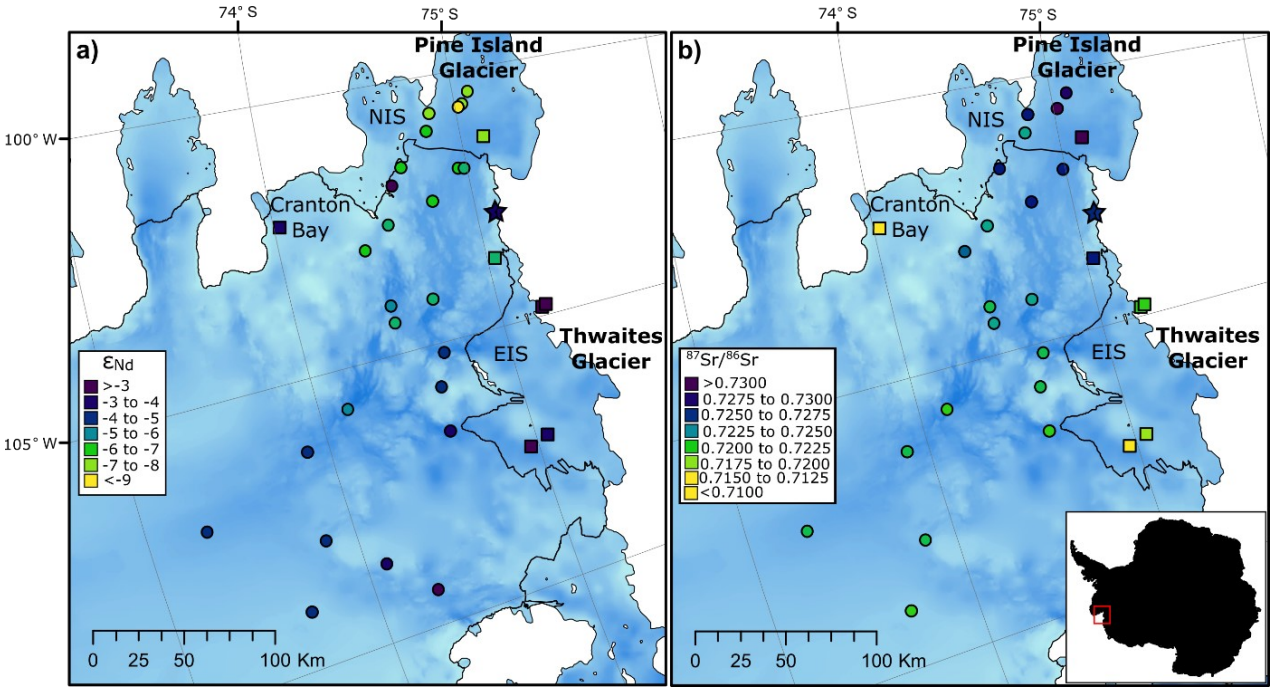


Figure 4.5. *a) Epsilon Nd and b) $^{87}Sr/^{86}Sr$ map of new seafloor surface samples (squares) compared to samples from Simões Pereira et al. (2020) (circles). The Sif Island Granite is plotted as a star. The location within Antarctica is indicated by red box in the lower right panel. Bathymetry shown is from BedMachine V1 (Morlighem et al., 2020) and Hogan et al. (2020). The MEaSUREs ice sheet extent and grounding lines are shown as thick and thin black lines respectively (Mouginot et al., 2017; Rignot et al., 2013). Note that the MEaSUREs data do not reflect recent major retreat of the ice shelves fringing Thwaites Glacier and Pine Island Glacier since ca. 2017. EIS = Thwaites Eastern Ice Shelf, NIS = Northern Ice Shelf (connected to Pine Island Glacier since ca. 2017).*

Table 4.1. *Neodymium and strontium isotope data for subglacial, NBP19-02 and NBP20-02 samples. Location acronyms include the Eastern Ice Shelf (EIS), Thwaites Glacier Tongue (TGT), Cranton Bay (CB) and southern Pine Island Bay (sPIB). EIS samples were collected downstream of the grounding zone (GZDS) and upstream of the grounding zone (GZUS) using a percussion corer. The shipboard samples were collected using a mega corer (MC) or a jumbo gravity corer (JGC).*

Site Name	Location	Depth Below Seafloor	Latitude	Longitude	$^{143}Nd/^{144}Nd$	2SE	ε_{Nd}	2SD	$^{87}Sr/^{86}Sr$	2SE
Thwaites EIS GZDS-LDCZ	EIS	Barrel Scrapings	-75.2072	-104.825	0.512500	0.000010	-2.69	0.23	0.713819	0.000007
Thwaites EIS GZUS-LDCZ	EIS	89.5 cm	-75.2288	-104.785	0.51253	0.000013	-2.12	0.25	0.713277	0.000007
NBP19-02 MC12	TGT	0-1 cm	-75.0579	-107.229	0.512469	0.000012	-3.30	0.27	0.711734	0.000009
NBP20-02 MC73	CB	0-1 cm	-74.0294	-102.228	0.512441	0.000009	-3.85	0.25	0.709465	0.000007
NBP20-02 MC66	sPIB	0-1 cm	-75.0382	-103.678	0.512299	0.000009	-6.62	0.21	0.723971	0.000009
NBP19-02 JGC10 1W	TGT	2-4 cm	-74.9604	-107.357	0.512498	0.000009	-2.73	0.25	0.709974	0.000008
Procedural replicate			As above		0.512490	0.000011	-2.88	0.21	0.709960	0.000008
NBP20-02 MC19	sPIB	0-1 cm	-75.1133	-101.335	0.512221	0.000012	-8.14	0.25	0.727888	0.000009

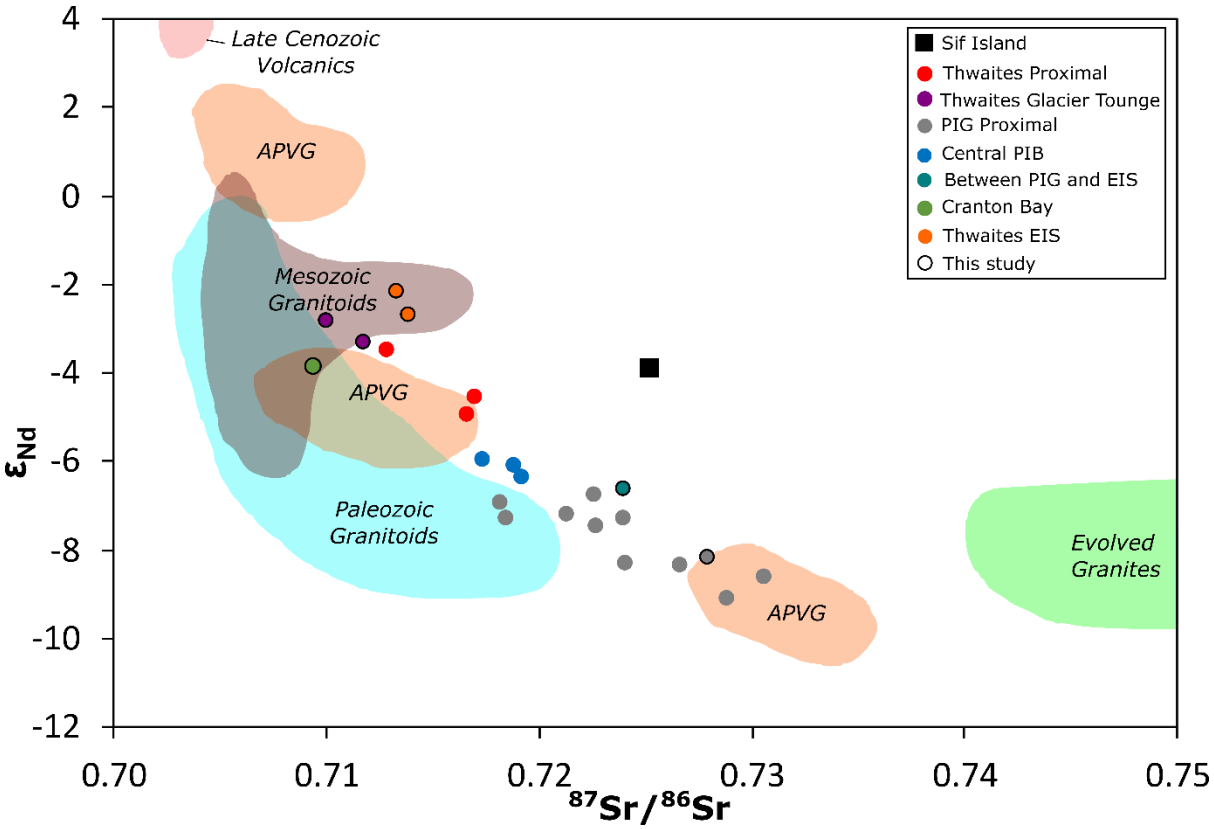


Figure 4.6. *Nd-Sr cross plot showing new samples (black outlines) compared to those published in Simões Pereira et al. (2020) (no outlines), with different fill colours marking samples from different geographical areas. PIG = Pine Island Glacier, PIB = Pine Island Bay, EIS = Eastern Ice Shelf. 'Thwaites proximal' samples displayed (red) are selected western PIB samples closest to Thwaites Glacier. Coloured polygons represent the typical isotopic range of different local rock types (APVG = Antarctic Peninsula Volcanic Group). Sif Island is plotted as a black square. Adapted from Simões Pereira et al. (2020).*

4.5.2 Geo-/Thermo-Chronology of the Sif Island Granite

Zircon U-Pb dating of samples SIA, SIB and SIC gave weighted mean crystallisation ages of 173.3 ± 1.0, 177.6 ± 1.4 and 174.0 ± 1.0 Ma, respectively (Fig. 4.7; Table 4.2). In addition, two concordant inherited cores from SIA were dated at 307.0 ± 4.5 and 379.5 ± 7.2 Ma (Fig. 4.8), implying partial melting of continental rocks of this age contributed to the melt.

Forty apatite grains and twenty zircon grains were analysed for fission track dating from sample SIA. Uranium concentrations were generally low, with relatively few tracks. The zircon fission track (ZFT) age was 165.5 ± 7.2 Ma, which is considerably older than ZFT ages from the islands north of Pine Island Rift, which range from 104.9 to 87.6 Ma (Lindow et al., 2016). Apatite fission track (AFT) ages gave a date of 91.7 ± 5.7 Ma, in broad agreement with AFT ages from islands north of Pine Island Rift which, although they span ~120 to 60 Ma, cluster around 90 Ma (Lindow et al., 2016). The Sif Island AFT age also resembles low elevation samples on Thurston Island (Zundel et al., 2019).

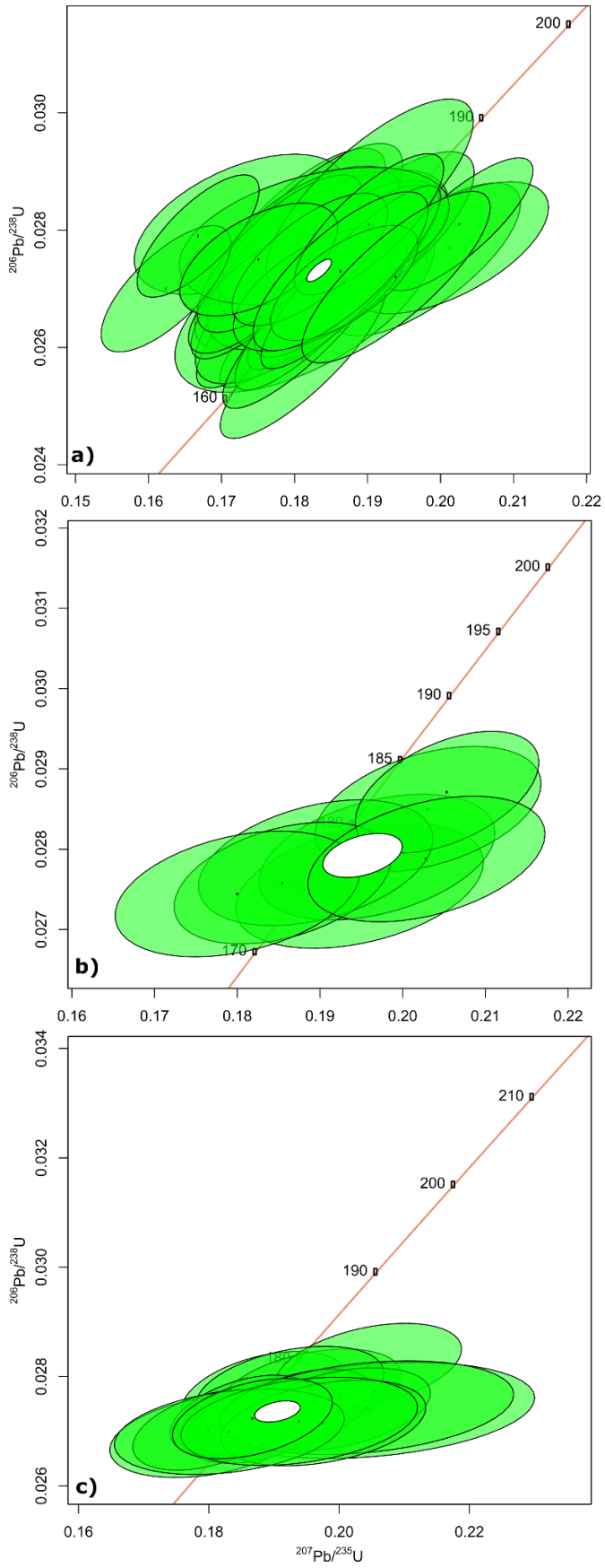


Figure 4.7. *Concordia diagrams for concordant grains. SIA (a, n = 42); SIB (b, n = 8); and SIC (c, n = 16).*



Figure 4.8. *Cathodoluminescence imaging of the 50 zircons analysed for U-Pb dating and ε_{Hf} analyses.*

With the exception of a single zircon (U-Th)/He age of 92.3 ± 1.3 Ma, zircon (U-Th)/He (ZHe) and apatite (U-Th)/He (AHe) ages were consistently older than the zircon U-Pb crystallization and fission track ages. This is likely to be a consequence of contamination from neighbouring U-rich grains adding parentless He to the grains. This hypothesis is supported by an anti-correlation between dates and effective uranium concentrations, plus high concentrations of tracks at the edges of grains consistent with 'bad neighbours' injecting parentless He. In apatite grains, zircon inclusions containing relatively high concentrations of uranium were also common, preventing useful AHe dating.

Table 4.2. *U-Pb zircon data. Samples highlighted in red are not used in age calculations as they are either discordant or inherited cores.*

Grain No.	U (ppm)	Th (ppm)	Th/U	238U/ 206Pb	±s.e.	207Pb/ 206Pb	±s.e.	207/235 Age	±s.e.	206/238 Age	±s.e.	207/206 Age	±s.e.	Concordia Age	±s.e.	Disc. (%)
Arizona Geochronology Centre – SIA																
1	220.0	121.7	0.55	36.41	0.7069	0.0529	0.0009	183.52	4.45	174.88	3.35	296.18	41.33	175.11	3.36	5.3
2	172.5	97.2	0.56	37.35	0.8939	0.0517	0.0009	169.27	6.25	170.49	4.02	152.18	75.16	170.44	4.01	-0.8
3	77.8	34.3	0.44	36.07	0.5992	0.0529	0.0012	186.23	4.66	176.14	2.88	316.18	49.37	176.16	2.89	6.1
4	157.6	69.6	0.44	36.42	0.8259	0.0507	0.0010	167.80	4.70	174.88	3.92	69.08	47.84	173.71	3.87	-4.5
5	1207.5	531.0	0.44	36.92	0.6779	0.0661	0.0018	210.45	6.33	172.37	3.13	661.45	59.60	170.41	3.13	22.0
6	643.6	231.4	0.36	37.75	0.6856	0.0500	0.0005	167.11	3.22	168.61	3.03	146.03	24.17	168.20	2.99	-1.0
7	114.2	45.1	0.40	35.70	0.7277	0.0487	0.0008	168.58	4.18	178.02	3.58	38.00	41.84	176.07	3.52	-6.0
8	513.3	167.5	0.33	37.59	0.7434	0.0495	0.0006	165.48	3.68	169.23	3.31	112.05	32.56	168.41	3.26	-2.5
9	155.8	101.1	0.65	38.76	0.8284	0.0515	0.0007	169.01	3.97	164.21	3.47	236.73	31.92	164.64	3.48	3.1
10	304.1	159.5	0.52	36.63	0.5392	0.0498	0.0005	171.33	2.79	173.63	2.52	139.65	23.18	173.14	2.49	-1.5
11	233.2	127.4	0.55	37.11	0.8577	0.0500	0.0008	168.49	4.95	171.12	3.90	131.76	51.27	170.86	3.88	-1.7
12	93.9	34.9	0.37	36.46	0.7069	0.0500	0.0009	172.44	4.22	174.26	3.34	147.61	42.63	174.07	3.32	-1.1
13	85.4	44.8	0.52	36.37	0.5415	0.0505	0.0011	166.17	4.84	174.88	2.57	43.73	66.68	174.50	2.56	-5.5
14	300.8	176.3	0.59	36.77	0.5834	0.0504	0.0006	175.43	3.27	173.00	2.71	208.37	29.46	173.25	2.71	1.5
15	734.9	747.7	1.02	38.98	0.8985	0.0719	0.0020	217.27	6.96	163.58	3.73	848.13	56.25	156.80	3.71	31.7
16	171.3	103.7	0.61	35.88	0.7585	0.0516	0.0009	177.91	4.57	177.39	3.69	184.78	43.13	177.45	3.68	0.3
17	544.6	199.0	0.37	36.94	0.8226	0.0503	0.0006	172.53	4.08	172.37	3.79	174.62	29.56	172.41	3.77	0.1
18	165.7	82.2	0.50	36.52	0.6752	0.0507	0.0008	174.07	3.92	174.26	3.18	171.50	37.17	174.24	3.17	-0.1
19	151.9	81.9	0.54	49.50	0.8776	0.0538	0.0009	140.23	3.21	128.92	2.26	336.24	38.53	128.53	2.27	9.0
20	111.4	37.3	0.33	36.44	0.6716	0.0494	0.0008	172.95	3.86	174.26	3.16	155.19	36.98	174.11	3.15	-0.8
21	48.4	24.7	0.51	35.57	0.6195	0.0497	0.0014	161.67	5.16	178.65	3.07	0.00	65.22	177.37	3.04	-10.8
22	64.3	37.1	0.58	36.47	0.7836	0.0521	0.0013	170.73	5.28	174.26	3.70	122.07	60.82	174.00	3.68	-2.2
23	615.9	528.1	0.86	38.07	0.8419	0.0846	0.0044	256.59	12.86	167.35	3.65	1179.20	103.20	163.68	3.63	47.5
24	236.6	91.1	0.39	36.59	0.8203	0.0494	0.0007	165.82	4.09	173.63	3.84	55.78	34.55	171.10	3.74	-5.1
25	157.0	74.1	0.47	36.11	0.7082	0.0507	0.0007	172.95	5.39	176.14	3.41	129.63	64.97	175.98	3.40	-2.0
26	93.5	56.7	0.61	35.78	0.7729	0.0501	0.0009	169.95	4.43	178.02	3.79	59.07	43.84	176.38	3.73	-5.1
27	87.4	50.2	0.57	35.82	0.6279	0.0499	0.0010	169.78	4.39	177.39	3.06	64.97	52.50	176.69	3.04	-4.8
28	85.3	29.8	0.35	36.21	0.6696	0.0497	0.0009	174.58	4.25	175.51	3.20	161.99	44.26	175.44	3.19	-0.6
29	499.0	479.5	0.96	37.42	0.8210	0.0496	0.0006	170.81	3.99	169.86	3.67	183.97	30.19	170.06	3.65	0.6
30	107.5	44.4	0.41	16.45	0.3324	0.0542	0.0008	377.70	7.89	380.49	7.46	360.63	33.08	379.48	7.25	-0.9
31	440.8	431.1	0.98	36.66	0.8055	0.0494	0.0007	173.72	4.23	173.63	3.77	175.03	34.48	173.64	3.75	0.1
32	260.0	145.3	0.56	37.24	0.5671	0.0497	0.0007	163.06	3.09	171.12	2.57	47.56	32.94	169.71	2.53	-5.2
33	298.8	209.2	0.70	36.26	0.7200	0.0498	0.0008	166.34	3.99	175.51	3.45	37.73	40.44	173.49	3.38	-5.9
34	150.8	69.9	0.46	35.01	0.8182	0.0502	0.0009	176.89	4.95	181.78	4.19	111.95	45.93	180.97	4.15	-3.0
35	255.4	118.8	0.47	35.59	0.5870	0.0529	0.0006	187.32	3.47	178.65	2.91	298.18	27.16	179.07	2.93	5.2
36	1430.4	1155.1	0.81	43.38	0.9083	0.0631	0.0009	178.42	4.16	147.22	3.04	614.84	31.40	139.64	3.04	21.8
37	135.1	51.3	0.38	35.90	0.6183	0.0501	0.0011	170.38	6.49	177.39	3.01	74.11	89.31	177.21	3.00	-4.4
38	595.6	195.3	0.33	37.92	0.8464	0.0505	0.0007	169.52	4.06	167.98	3.70	191.14	30.86	168.24	3.69	1.0
39	187.9	152.4	0.81	37.00	0.5965	0.0510	0.0010	171.07	4.17	171.75	2.73	161.71	49.11	171.71	2.72	-0.4
40	611.4	188.7	0.31	36.76	0.8621	0.0499	0.0006	174.67	4.30	173.00	4.01	197.26	29.58	173.35	4.00	1.1
41	50.4	24.0	0.48	37.04	0.6726	0.0836	0.0048	241.89	13.28	171.75	3.08	993.20	120.00	170.49	3.08	37.9
42	92.4	60.8	0.66	36.41	0.6101	0.0507	0.0009	169.87	3.74	174.88	2.90	100.55	40.37	174.29	2.87	-3.2
43	113.0	51.2	0.45	37.09	0.6029	0.0503	0.0007	152.80	3.18	171.75	2.76	0.00	33.68	166.45	2.66	-12.8
44	166.5	69.3	0.42	35.84	0.5480	0.0509	0.0007	156.64	2.98	177.39	2.68	0.00	32.03	170.76	2.57	-13.8
45	149.2	46.5	0.31	36.37	0.5186	0.0516	0.0010	163.84	3.81	174.88	2.47	7.02	50.26	173.91	2.45	-7.1
46	142.9	36.8	0.26	20.56	0.3132	0.0554	0.0006	313.33	5.47	305.92	4.54	368.86	30.25	306.95	4.53	2.8
47	193.7	67.9	0.35	35.59	0.6212	0.0499	0.0006	176.80	3.57	178.65	3.08	152.19	31.60	178.33	3.06	-1.1
48	338.3	221.3	0.65	36.92	0.5466	0.0504	0.0008	173.90	3.53	172.37	2.52	194.65	38.14	172.45	2.52	1.0
49	188.2	88.2	0.47	36.61	0.7435	0.0505	0.0008	173.47	4.19	173.63	3.48	171.28	39.17	173.61	3.46	-0.1
50	495.8	187.6	0.38	36.80	0.8090	0.0521	0.0008	179.95	4.49	173.00	3.76	272.25	36.56	173.37	3.78	4.3
London Geochronology Centre – SIB																
1	1259.0	539.5	0.43	34.28	0.3761	0.0535	0.0011	197.70	4.28	185.35	2.0	347.8	47.8	185.37	2.01	7.1
2	1909.9	987.1	0.52	36.52	0.4269	0.0533	0.0013	186.17	4.57	174.13	2.01	341.8	54.8	174.12	2.01	7.3
3	1484.6	618.2	0.42	30.30	0.3581	0.1002	0.0021	381.36	7.65	209.3	2.43	1627.5	39	195.23	2.38	70.0
4	1274.3	722.2	0.57	35.45	0.3895	0.0572	0.0012	203.99	4.46	179.34	1.94	499.4	47.3	178.93	1.95	14.0
5	703.2	332.3	0.47	36.30	0.4216	0.0513	0.0015	180.64	5.3	175.2	2.01	252.4	68.6	175.23	2.01	3.3
6	1426.3	348.1	0.24	12.42	0.1295	0.0678	0.0010	569.73	7.82	499.29	5.01	861.8	30.3	500.39	5.09	17.0
7	635.6	329.6	0.52	36.27	0.4210	0.0563	0.0017	196.8	5.82	175.32	2.01	462.8	67.3	175.16	2.01	13.0
8	1099.3	462.7	0.42	34.54	0.3937	0.0580	0.0014	211.46	5.09	183.97	2.07	529.9	52.9	183.54	2.07	15.0
9	1067.0	427.2	0.40	37.44	0.4205	0.0556	0.0013	189.04	4.47	169.92	1.88	435	52.1	169.73	1.89	12.0
10	826.0	419.6	0.51	35.84	0.4111	0.0512	0.0014	182.54	4.95	177.39	2.01	249.7	62.9	177.43	2.01	3.1
11	956.5	476.8	0.50	35.09	0.3940	0.0517	0.0013	187.72	4.63	181.15	2.01	271.1	56.3	181.2	2.01	3.9
12	3783.0	4304.6	1.14	32.50	0.3380	0.1275	0.0018	438.82	6.16	195.37	2	2062.7	24.3	162.68	1.85	97.0
13	761.5	290.3	0.38	35.93	0.4132	0.0494	0.0014	176.31	5.04	176.95	2.01	167.7	67.6	176.94	2.01	-0.4
14	864.4	523.9	0.61	36.26	0.4075	0.0488	0.0013	172.68	4.71	175.38	1.94	135.7	64.6	175.34	1.94	-1.7
15	1698.1	678.1	0.40	34.83	0.3761	0.0519	0.0010	189.65	3.79	182.47	1.94	280	43.7	182.55	1.94	4.2
16	810.6	532.4	0.66	38.26	0.4683	0.0496	0.0016	167.02	5.31	166.34	2.01	176.7	75.2	166.35	2.01	0.4
17	1145.3	660.7	0.58	34.07	0.3715	0.1816	0.0029	559.18	8.24	186.48	2	2666.6	26.1	149.7	1.82	130.0

18	707.8	403.0	0.57	36.44	0.4250	0.0476	0.0015	168.04	5.08	174.51	2.01	77.9	72.9	174.38	2	-4.1
19	819.9	557.8	0.68	35.87	0.4117	0.0528	0.0014	187.43	4.83	177.27	2.01	317.5	58.6	177.29	2.01	6.1
20	804.5	485.7	0.60	35.71	0.4082	0.0551	0.0015	195.88	5.23	178.02	2.01	416.9	60.4	177.92	2.01	10.0
London Geochronology Centre – SIC																
1	1002.6	550.2	0.55	36.10	0.4040	0.0494	0.0012	175.33	4.43	176.14	1.94	164.4	58.7	176.12	1.94	-0.5
2	3982.6	919.0	0.23	36.38	0.3838	0.0520	0.0008	182.59	3.14	174.82	1.82	284.4	35.6	174.91	1.82	4.7
3	803.0	280.3	0.35	36.08	0.4165	0.0512	0.0014	181.27	4.9	176.26	2.01	247	62.6	176.3	2.01	3.1
4	846.0	485.5	0.57	35.47	0.4027	0.0526	0.0014	188.94	4.93	179.21	2.01	312.3	59.7	179.24	2.01	5.8
5	664.8	350.3	0.53	37.16	0.4281	0.0485	0.0016	167.98	5.32	171.18	1.95	123.2	76.2	171.14	1.94	-2.0
6	801.4	427.3	0.53	27.08	0.3006	0.0587	0.0013	265.39	5.82	233.78	2.55	554.6	48.7	233.42	2.56	14.0
7	336.2	149.8	0.45	36.52	0.4802	0.0543	0.0026	189.17	8.7	174.13	2.26	381	109	174.11	2.26	9.0
8	784.5	454.1	0.58	36.01	0.4150	0.0503	0.0014	178.7	5.03	176.58	2.01	206.9	66	176.6	2.01	1.3
9	1636.6	1057.6	0.65	36.81	0.4199	0.0503	0.0012	175.25	4.17	172.81	1.95	208.3	53.9	172.85	1.95	1.5
10	1226.7	624.2	0.51	36.50	0.3996	0.0513	0.0011	179.73	4.05	174.26	1.88	252.4	50.7	174.31	1.88	3.4
11	858.2	445.2	0.52	36.50	0.4129	0.0529	0.0014	185.02	4.9	174.26	1.95	324.8	60.5	174.27	1.95	6.5
12	1317.3	749.7	0.57	36.64	0.4028	0.0492	0.0011	172.49	3.89	173.56	1.88	157.7	51.3	173.54	1.88	-0.7
13	1123.8	612.3	0.54	37.01	0.4109	0.0483	0.0012	168.04	4.1	171.87	1.88	114.4	56.6	171.78	1.88	-2.4
14	396.1	252.7	0.64	36.46	0.4652	0.0540	0.0023	188.72	7.78	174.44	2.2	371.3	97.5	174.43	2.2	8.6
15	687.8	451.7	0.66	36.83	0.4341	0.0528	0.0016	183.1	5.45	172.69	2.01	319.6	68.9	172.7	2.01	6.4
16	3125.9	1258.3	0.40	36.66	0.3897	0.0682	0.0011	231.77	4.05	173.5	1.82	873.7	34	169.22	1.81	32.0
17	555.8	282.3	0.51	37.05	0.4393	0.0492	0.0019	170.77	6.19	171.68	2.01	158.2	87.9	171.67	2.01	-0.6
18	4513.8	2138.3	0.47	37.58	0.3954	0.1518	0.0021	449.43	6.37	169.3	1.76	2365.8	23.9	135.56	1.59	120.0
19	488.2	270.0	0.55	36.79	0.4467	0.0518	0.0019	179.94	6.32	172.87	2.07	273.8	83.2	172.9	2.07	4.4
20	994.9	560.0	0.56	36.72	0.4046	0.0498	0.0012	173.81	4.29	173.19	1.88	182.3	57.1	173.2	1.88	0.4

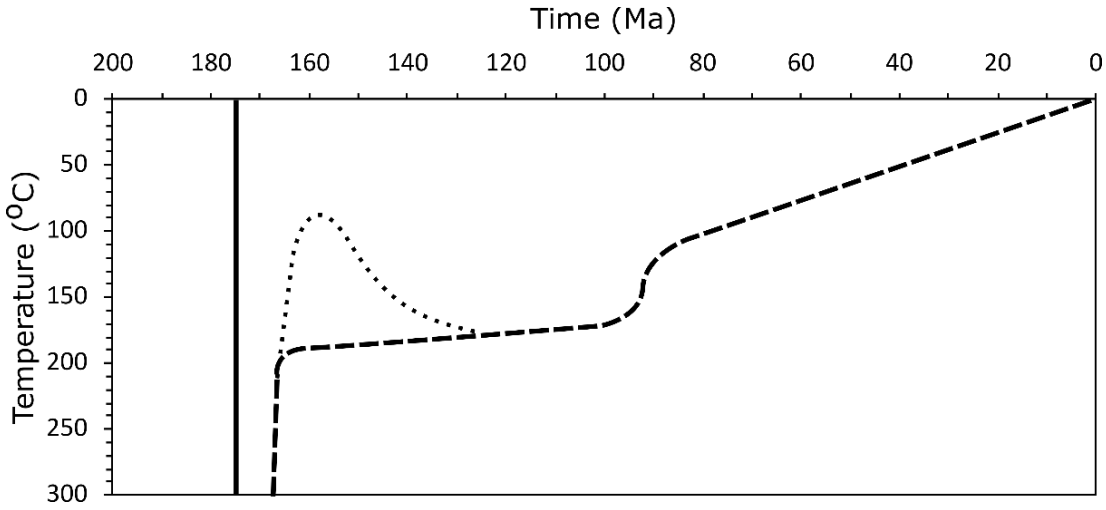


Figure 4.9. *Sketch cooling history of Sif Island. Following crystallisation (solid vertical line), there was rapid cooling, followed by another period of rapid cooling at ~92 Ma. The dotted line sketches potential cooling in the Jurassic as seen on Thurston Island (Zundel et al., 2019), implying the ZHe and AFT chronometers were later reset. Fission track lengths are yet to be counted and are required for quantitative thermal history modelling.*

Although based on a single grain, the single zircon (U-Th)/He age of 92.3 ± 1.3 Ma is likely to be accurate as there are very few processes that can lead to ages being biased younger. Furthermore, the closure temperature for this dating system lies between the ZFT and AFT cooling ranges, so an age slightly older than the AFT age (91.7 ± 5.7 Ma) is plausible. The close agreement between the AFT and ZHe ages therefore indicates quick cooling through the ZHe and AFT temperature range at ~92-91 Ma. Rapid cooling is supported by long apatite fission track lengths (mean 14.57 μm) suggesting quick cooling through the partial

annealing zone. The Sif Island granite must therefore have been uplifted and cooled to less than ~200 ºC within approximately 10 Myrs of formation (Fig. 4.9). It then remained at this temperature (or cooler; dotted line in Fig. 4.9) until ~92 Ma, at which point it rapidly cooled through the ZHe partial retention zone to temperatures below the AFT partial annealing zone (~80ºC). Since this time, the rocks forming Sif Island have remained close to the earth's surface.

4.5.3 Neodymium and Strontium Isotope Composition of the Sif Island Granite

Table 4.3. *Bulk rock neodymium and strontium isotope data for Sif Island including a full procedural replicate. Initial compositions (i) are calculated at 174 Ma.*

Sample	$^{143}Nd/^{144}Nd$	ε_{Nd}	± 2σ S.E.	± 2 S.D.	$^{87}Sr/^{86}Sr$	$^{87}Sr/^{86}Sr_{(i)}$	± 2σ S.E.	$^{143}Nd/^{144}Nd_{(i)}$	$\varepsilon_{Nd(i)}$
SIB	0.512432	-4.02	0.000008	0.29	0.725176	0.706092	0.000008	0.512291	-2.40
replicate	0.512446	-3.75	0.000010	0.29	0.725175	0.706092	0.000008	0.512305	-2.13

The $^{143}Nd/^{144}Nd$ ratio grants insight into the initial magma composition and the likely mantle separation age of a rock. The mean ε_{Nd} value of -3.88 for Sif Island suggests there was relatively little crustal contamination compared to the Triassic granites in the Jones Mountains (Pankhurst et al., 1993). Instead, the Nd isotope composition more closely resembles other Mesozoic granitoids (Fig. 4.6; see literature data compilation in Simões Pereira et al., 2018), as the mean initial Sif Island ε_{Nd} value was -2.27 (Table 4.3). The $^{87}Sr/^{86}Sr$ ratio of the Sif Island granite was initially 0.706092 but is now unusually high (0.725175) due to the high Rb/Sr ratio (Table 4.3; 4.5).

Table 4.4. *Zircon hafnium isotope data for sample SIA.*

Grain No.	$(^{176}Yb + ^{176}Lu) / ^{176}Hf$ (%)	Volts Hf	$^{176}Hf/^{177}Hf$	± (1s)	$^{176}Lu/^{177}Hf$	$^{176}Hf/^{177}Hf_{(t)}$	$\varepsilon Hf_{(0)}$	$\varepsilon Hf_{(0)}$ ± (1s)	$\varepsilon Hf_{(i)}$	Grain Age (Ma)	±1s
2	22.456	2.279	0.283	2.776E-05	0.001241	0.283	-2.949	0.982	0.697	170.4	4.0
6	25.977	2.366	0.283	2.309E-05	0.001496	0.283	-2.578	0.816	0.993	168.2	3.0
10	31.305	2.447	0.283	2.453E-05	0.001863	0.283	-9.600	0.868	-5.970	173.1	2.5
11	24.248	1.904	0.283	2.104E-05	0.001459	0.283	-5.707	0.744	-2.075	170.9	3.9
13	23.156	2.059	0.283	2.165E-05	0.001386	0.283	-7.763	0.766	-4.047	174.5	2.6
18	29.495	2.248	0.283	3.014E-05	0.001745	0.283	-5.293	1.066	-1.625	174.2	3.2
20	23.479	2.051	0.283	1.892E-05	0.001445	0.283	-4.891	0.669	-1.189	174.1	3.1
22	30.408	1.961	0.283	3.370E-05	0.001929	0.283	-5.253	1.192	-1.610	174.0	3.7
24	23.840	2.493	0.283	2.006E-05	0.001496	0.283	-6.011	0.709	-2.380	171.1	3.7
42	30.832	1.852	0.283	1.823E-05	0.001834	0.283	-0.011	0.645	3.652	174.3	2.9
49	22.670	2.342	0.283	3.294E-05	0.001570	0.283	-0.785	1.165	2.893	173.6	3.5
50	45.559	2.040	0.283	2.486E-05	0.002465	0.283	-7.946	0.879	-4.377	173.4	3.8

The zircons of the Sif Island granite have a mean εHf_i value of -1.25 ± 2.89 (SD), evenly distributed between extremes of -5.97 and +3.65 (Table 4.4). The rock also has a depleted mantle model age of 1197 Ma. These data suggest a contribution from an older crustal source.

4.5.4 Major and Trace Element Composition of the Sif Island Granite

Table 4.5. *Selected major and trace element concentrations for the Sif Island granite. Shown are the results from two procedural replicates and mean values.*

	Sample		
Element	**SIB**	**replicate**	**Mean**
Major Elements (%)			
Al	7.58	7.76	7.67
Ca	0.64	0.65	0.64
Ti	0.09	0.10	0.10
Mn	0.03	0.03	0.03
Fe	1.00	0.99	1.00
Trace elements (ppm)			
Sc	4.49	4.49	4.49
V	5.34	5.43	5.39
Rb	251.9	252.1	252.0
Sr	94.46	94.95	94.70
Mo	0.36	0.35	0.36
Ba	611.3	607.5	609.4
La	31.83	31.62	31.73
Ce	65.13	65.74	65.43
Pr	7.38	7.40	7.39
Nd	26.85	27.09	26.97
Sm	5.51	5.56	5.53
Eu	0.54	0.54	2.85
Gd	4.75	4.74	4.75
Tb	0.79	0.78	0.78
Dy	4.73	4.72	4.73
Ho	0.99	0.99	0.99
Er	2.94	2.93	2.94
Tm	0.48	0.48	0.48
Yb	3.13	3.14	3.14
Lu	0.46	0.47	0.46
Re	0.00	0.00	0.00
208Pb	33.24	32.94	33.09
232Th	19.87	19.86	19.87
238U	5.67	5.57	5.62

The Sif Island granite sample SIB is relatively fractionated, with a high proportion of incompatible elements. Compared to rocks from islands on the northern side of Pine Island Rift (Kipf et al., 2012), it is rich in Rb, Th, U, Pb, Sm, Gd, Tb, Dy, Ho, Er, Tm, and Yb and poor in Sr, Ti, Mn and Fe (Table 4.5). Trace element data show a positive Eu/Eu* anomaly of 2.62 and high Rb/Sr ratio of 2.66, consistent with a high plagioclase content.

4.6 New Geological Constraints

4.6.1 Sediment Provenance: Thwaites Glacier

Seafloor surface sediments offer information on often unknown geological composition of substrate beneath the ice sheet. Our new data show that the Thwaites Glacier endmember is approximately -2, slightly more radiogenic than the ε_{Nd} value of ~-4 suggested by Simões Pereira et al. (2020) which was based on the provenance of marine sediment samples collected from slightly further offshore. Sediments from upstream of the Thwaites Glacier grounding zone and from under the Eastern Ice Shelf have more radiogenic ε_{Nd} values than those further away from the coast (Fig. 4.5). These observations are consistent with detritus from Thwaites Glacier providing a radiogenic ε_{Nd} endmember, mixing with the signal from Pine Island Glacier (and other glaciers) further offshore. Examining samples upstream and downstream of the grounding zone shows a subtle, but measurable difference (ε_{Nd} of -2.12 vs. -2.69, respectively), suggesting this introduction of different detritus - likely sourced from east of the Easter Ice Shelf - begins very close to the grounding zone. Such an observation implies that ocean currents advect fine grained detritus under the Thwaites Eastern Ice Shelf.

The $^{87}Sr/^{86}Sr$ ratios near Thwaites Glacier are relatively low compared to other Amundsen Sea Embayment seafloor surface sediments. This is consistent with the hypothesis that this detritus comprises an endmember with low $^{87}Sr/^{86}Sr$ ratios which mixes further offshore with detritus with higher $^{87}Sr/^{86}Sr$ ratios delivered from other sources (Simões Pereira et al., 2020). The new data presented here may, however, suggest some heterogeneity beneath Thwaites Glacier, as the expected negative correlation between ε_{Nd} values and $^{87}Sr/^{86}Sr$ ratios is not present in the Eastern Ice Shelf and Thwaites Glacier Tongue samples analysed here (orange and purple circles with black outlines in Fig. 4.6). Specifically, the Eastern Ice Shelf samples appear to be characterised by higher $^{87}Sr/^{86}Sr$ ratios than the samples further west, despite higher ε_{Nd} values (Fig. 4.5; 4.6). A breakdown in the negative correlation between radiogenic Nd and Sr isotope ratios was noted in late Quaternary sediment core records from the Amundsen Sea continental slope and rise and attributed to changes in weathering based on

correlation with kaolinite content (Simões Pereira, 2018). This phenomenon may have arisen due to effects of pre-glacial weathering or grain size sorting on pre-glacial sediments (Eisenhauer et al., 1999; Blum and Erel, 1995), which when re-eroded could influence detrital $^{87}Sr/^{86}Sr$ ratios further offshore.

By demonstrating that the branches of Thwaites Glacier feeding into the (former) Glacier Tongue and Eastern Ice Shelf are clearly distinct (Fig. 4.5; 4.6), our data offer an alternative potential explanation; they suggest that the Thwaites Glacier catchment may contain spatially variable $^{87}Sr/^{86}Sr$ ratios linked to source rock composition. Relatively high $^{87}Sr/^{86}Sr$ ratios towards the Eastern Ice Shelf could be traced to rocks like the Sif Island granite which, due to its high Rb/Sr ratio, has a high $^{87}Sr/^{86}Sr$ ratio compared to that of many other Mesozoic granitoids with similar ε_{Nd} values (Fig. 4.6). Unusually high $^{87}Sr/^{86}Sr$ ratios are seen in isolated samples of similar Jurassic rocks (e.g. Scarrow et al., 1996; Ryan, 2005), but these are not considered representative of their mean composition (Simões Pereira et al., 2018). This makes the Sif Island data more difficult to interpret and highlights the necessity of considering many measurements of a rock group to obtain its average isotopic composition when studying sediment provenance. However, if the $^{87}Sr/^{86}Sr$ ratio of the Sif Island granite measured here is representative of the bulk of rocks underlying the drainage area with slow-flowing ice between Thwaites and Pine Island glaciers, it could represent an as-yet unaccounted for low ε_{Nd} and high $^{87}Sr/^{86}Sr$ endmember. Such a composition would raise detrital $^{87}Sr/^{86}Sr$ ratios without substantially lowering ε_{Nd} values.

Regardless of the cause, our data show changes to erosion patterns within the Thwaites catchment could yield detritus with different $^{87}Sr/^{86}Sr$ ratios without the expected change in ε_{Nd} values. A differing geology leading to a contrasting $^{87}Sr/^{86}Sr$ ratio under different branches of Thwaites Glacier is supported by distinct major and trace element compositions in marine sediments near to the Thwaites Glacier Tongue and Eastern Ice Shelf (Lepp et al., 2022). Precisely determining both whether the Sif Island granite is representative of the local area and the spatial pattern of rock $^{87}Sr/^{86}Sr$ variability would require both more detrital samples adjacent to Sif Island and more samples of as-yet unexposed rocks close to Sif Island.

4.6.2 Sediment Provenance: Eastern Pine Island Bay and Pine Island Glacier

The portion of the WAIS draining into Cranton Bay on the eastern coast of the Amundsen Sea Embayment is slow-flowing, suggesting little basal sliding and consequently a low

erosion rate. The low erosion rate in the hinterland of Cranton Bay is reflected in the lithology of the sediments deposited in the bay, which consist of biosiliceous muds.

Relatively shallow bathymetry on the western side of Cranton Bay (see Fig. 1 in Zheng et al., 2021) restricts input of detritus from non-local sediment sources suspended in the water column (Fig. 4.5). Fine-grained glacigenic detritus is believed to be suspended in high concentrations within subsurface meltwater plumes close to the fronts of Pine Island and Thwaites glaciers and to be advected far offshore (e.g., Lepp et al., 2022), but significant concentrations of glacial meltwater originating from major sub-ice shelf melting in Pine Island Bay extend seaward for a maximum of ca. 120 km and are restricted to the main bathymetric trough in the eastern Amundsen Sea Embayment (Biddle et al., 2017) (Fig. 4.5). Furthermore, iceberg concentration is low in Cranton Bay (Mazur et al., 2017), with icebergs calved from glacial outlets elsewhere in the Amundsen Sea Embayment usually bypassing the bay (Mazur et al., 2019), so that supply of "allochtonous" iceberg-rafted debris can be ruled out. Finally, a local sediment source is probable given the contrasting ε_{Nd} values and $^{87}Sr/^{86}Sr$ ratios compared to other surface sediment samples along the eastern coast of the Amundsen Sea Embayment (Fig. 4.5). At present, detritus originating from Thwaites and Pine Island glaciers overprints the detrital input from this coastline rather than the other way round (Simões Pereira et al., 2018, 2020), but this appears to not be the case in Cranton Bay.

The detrital Nd and Sr isotope composition of the sample from Cranton Bay is therefore likely to be governed by the ice-covered source rocks directly adjacent to the bay. The detrital ε_{Nd} value of -3.85 ± 0.25 and $^{87}Sr/^{86}Sr$ ratio of 0.709465 suggest these are most likely Mesozoic granitoids, similar to those cropping out on islands between Cranton Bay and Pine Island Bay (Fig 4.1, 4.6; Table 4.1).

The two new samples from the southern flank side of Pine Island Bay (Fig. 4.1) have radiogenic Nd and Sr isotope compositions that fall within the range of other samples collected from close to PIG (Fig. 4.5; 4.6). Consistent with other data from Pine Island Bay, the sample further away from PIG (NBP20-02 MC66) shows incorporation of detritus with a more radiogenic ε_{Nd} value/less radiogenic $^{87}Sr/^{86}Sr$ ratio than the sample just in front of PIG Ice Shelf (NBP20-02 MC19). Such material is either sourced from the Northern Ice Shelf (Simões Pereira et al. 2020) or, on this flank of Pine Island Bay more likely, Thwaites Glacier's Eastern Ice Shelf (Fig. 4.5).

Detritus shed from PIG has a provenance signature characterised by an ε_{Nd} value of ~-8.5, an $^{87}Sr/^{86}Sr$ ratio of 0.728, and $^{40}Ar/^{39}Ar$ ages of ~250-170 Ma (Simões Pereira et al., 2020). These characteristics are difficult to reconcile with exposed geology as, although present, outcrops of rock with a Triassic-Jurassic age are very limited in extent (Pankhurst et al., 1993; Mukhasa and Daziel, 2000) and only seem to form the majority in nunataks of the Whitmore Mountains, hundreds of kilometres to the southeast (Craddock et al., 2017). Furthermore, the ε_{Nd} value of ~-8.5 is substantially less radiogenic than most outcrops in the vicinity of Pine Island Bay, with the exception of a single outcrop of more evolved granite in the Jones Mountains (Pankhurst et al., 1993; Fig. 4.1; 4.6). This lack of exposure limits constraints on the extent of the rocks giving PIG these distinctive provenance characteristics and, thus, also knowledge of how sediment provenance might change during past ice sheet retreat.

Sif Island's zircon U-Pb age of ~178-173 Ma is similar to the youngest end of the broad Triassic-Jurassic age peak revealed by the vast majority of $^{40}Ar/^{39}Ar$ dated hornblende and biotite grains in surface sediments from eastern Pine Island Bay (Simões Pereira et al., 2020). Some of these ages may therefore be locally derived from the rocks of Sif Island and those nearby. However, a similar broad Triassic-Jurassic zircon U-Pb age population is also found in sediments shed from the West Antarctic interior into the Ross Sea, suggesting mineral grains of this age must be widespread beneath the WAIS (Licht et al., 2014; Perotti et al., 2017; Marschalek et al., 2021). The distribution of crystalline rocks or sedimentary strata with Triassic-Jurassic aged mineral grains may therefore extend well inland beneath PIG. This distribution could be explained if they are present in crystalline rocks and/or eroded sediments in the Bentley Subglacial Trench, which underlies mainly the drainage basins of PIG and the Siple Coast ice streams, but only to a small extent the drainage basin of Thwaites Glacier (Vaughan et al., 2006; Diehl et al., 2008; Morlighem et al., 2020). Regardless of the precise origin, a source of mineral ages of ~250-170 Ma far inland would imply that any hypothetical change in the abundance of grains of this age in offshore Amundsen Sea sediments is unlikely to be diagnostic of a retreat of PIG. The new Sif Island Nd isotope data do, however, help constrain the source of the unradiogenic isotope compositions observed in offshore data from Pine Island Bay (Simões Pereira et al., 2020). The mean ε_{Nd} value of -3.88 obtained for the Sif Island granite eliminates the southwestern flank of the glacier near its terminus as a potential source for unradiogenic ε_{Nd} values, implying this signature must derive from further inland.

4.6.3 Comparisons to Surrounding Crustal Blocks

As there is uncertainty regarding the position of the boundaries between West Antarctic crustal blocks in the Amundsen Sea Embayment region, we use the new data from the Sif Island granite to remove some of this uncertainty by concluding which crustal block Sif Island most likely belongs to. Evidence for Jurassic magmatism dating to ~190-170 Ma is notably lacking along the coast of Marie Byrd Land (Riley et al., 2017b), except for one inherited zircon $^{206}Pb/^{238}U$ age of 181±11 Ma (Korhonen et al., 2010). Furthermore, the ~178-173 Ma U-Pb zircon age of the Sif Island granite (Table 4.2) cannot be directly correlated to any rocks in the Pine Island Bay area. Jurassic magmatism is recorded in granitoids found on the Brownson Islands and Edwards Islands (Fig. 4.1); these have $^{206}Pb/^{238}U$ ages clustering around ~165 Ma and ~194 Ma (Mukasa and Daziel, 2000). Direct temporal correlatives can be found in the intra-plate granites in the Ellsworth-Whitmore Mountains block, more than 600 km to the south. This series of nunataks provided ages of 180-164 Ma, with the exception of one nunatak that gave an age of ~200 Ma (Craddock et al., 2017). They are, however, geochemically distinct, with higher $^{87}Sr/^{86}Sr$ ratios and a low initial ε_{Nd} value indicating greater incorporation of evolved crustal material in these intra-plate granites (Storey et al., 1988; Pankhurst et al., 1991; Craddock et al., 2017). The geographical distance and together with the geochemical contrast make the Jurassic granites of the Ellsworth-Whitmore Mountains unlikely correlatives.

Rocks of Early-Middle Jurassic age are, however, also present in the Antarctic Peninsula and the Thurston Island crustal blocks. The Antarctic Peninsula contains the most widespread outcrops of Jurassic igneous rocks, although they are predominantly extrusive. Ages corresponding to the ~178-173 Ma old Sif Island granite are sparse on the Antarctic Peninsula, with a lull in magmatism (Bastias et al., 2021). However, the earliest part of the V2 phase (~173-160 Ma; Bastias et al., 2021) nearly coincides with our youngest crystallisation age (173.3 Ma). Thus, magmatism associated with the V2 episode may extend considerably further southwest than previously documented (Pankhurst et al., 2000; Bastias et al., 2021). Our isotopic data support this correlation with the V2 province, which is hypothesised to have formed through partial melting of andesitic Grenville-aged lower crustal rocks (Pankhurst and Rapela, 1995; Riley et al., 2001; Bastias et al., 2021). The initial Sif Island $^{87}Sr/^{86}Sr$ ratio of 0.706092 and ε_{Nd} value of -2.27 (at 174 Ma) closely resemble those of the Mapple Formation, part of the V2 episode, and other Early-Middle Jurassic rocks on

the Antarctic Peninsula (Wever et al., 1994; Millar et al., 2001). The Sif Island granite may represent an intrusive and fractionated part of a shared parent magma.

The Sif Island granite thus appears to be part of the Thurston Island/Antarctic Peninsula crustal blocks and represents the western most extent of exposed rocks of Early-Middle Jurassic age, which likely extend beneath PIG (Simões Pereira et al., 2020). Zircon hafnium isotopes corroborate a match with Antarctic Peninsula and Thurston Island tectonic development, matching the range of values observed here through the Jurassic, which has been linked to an extensional tectonic setting (Nelson and Cottle, 2018). Given this closer correlation to rocks from the Thurston Island/Antarctic Peninsula crustal block and a similar cooling history, the new Sif Island granite data favour an interpretation that places the edges of the Thurston Island and Marie Byrd Land crustal blocks between PIG and Thwaites Glacier (e.g. Spiegel et al., 2016; Zundel et al., 2019; Fig. 4.1). In contrast, tectonic reconstructions placing the boundary along Pine Island Rift (e.g. Gohl et al., 2007; Jordan et al., 2020) would place Sif Island as part of the MBL crustal block. The similar initial isotopic composition to Antarctic Peninsula rocks also supports the proposed ~180º rotation of the Thurston Island Block (Riley et al., 2017a), which would place Sif Island adjacent to the southern Antarctic Peninsula at the time when its granite was emplaced.

4.6.4 Thermal History and Structural Control of Pine Island Rift

Thermochronological analysis of the Sif Island granite reveals that the crust forming the southern flank of Pine Island Bay has a different cooling history to the predominantly granitic islands further north. Whilst these rocks also record a rapid cooling at ~90 Ma, the Sif Island granite is unique in having a ZFT age of 165.5 Ma; this is significantly older than the ~100 Ma ZFT ages obtained for rocks on the northern side of the bay (Lindow et al., 2016).

This disagreement in ZFT ages is the first thermochronological confirmation of geophysical studies suggesting that Pine Island Glacier lies on a tectonic feature (Jordan et al., 2010; Gohl, 2012; Gohl et al., 2013b), as previous data have only constrained the cooling history of the northern side of PIG thus could not prove that rocks either side of the glacier have been subject to different thermal histories.

Sif Island's thermochronological data can be compared with the thermal history of Thurston Island, where, prior to ~175 Ma, pre-Jurassic rocks cooled rapidly (Zundel et al., 2019). Here, exhumation to crustal depths <1.2 km has been attributed to erosion resulting from tectonic

uplift and crustal thickening driven by subduction of proto-Pacific oceanic crust under the West Antarctic margin (Zundel et al., 2019). The Sif Island granite was intruded at the peak of this cooling on Thurston Island, where volcaniclastic rocks at Mt Dowling imply a palaeo land surface. The rapid cooling of the Sif Island granite soon after its emplacement (Fig. 4.9) must therefore have occurred slightly later than the cooling recorded on Thurston Island.

Although it is possible that the rocks forming Sif Island remained between temperatures associated with the ZFT and ZHe chronometers from ~165 to ~92 Ma, this is a relatively narrow temperature range. Reheating of Thurston Island rocks to ~100-115 ºC occurred from ~175-130 Ma and was attributed to burial in a volcanic basin (Zundel et al., 2019). It therefore seems more likely that the Sif Island granite cooled quickly during the Middle Jurassic, before warming occurred in the Late Jurassic/Early Cretaceous. This warming was sufficient to reset the ZHe and AFT ages, but not the ZFT ages (Fig. 4.9)

Rapid cooling through the closure temperature range of the ZHe system and partial annealing and partial retention zones of the AFT system at ~92-91 Ma is supported by the close agreement of these dating methods and generally long fission track lengths for the Sif Island granite. Rapid cooling at this time is a ubiquitous feature of rocks along the paleo-Pacific margin (Lindow et al., 2016; Spiegel et al., 2016; Zundel et al., 2019). It is assumed to be a consequence of a switch from convergence to extension, leading to tectonic denudation as previously high topography dropped to near sea level (Mukasa and Daziel, 2000; Lindow et al., 2016; Spiegel et al., 2016; Nelson and Cottle, 2018; Zundel et al., 2019).

The lack of AHe data makes it difficult to constrain the most recent, lowest temperature evolution of the Sif Island granite. However, a similar thermal history to rocks on the other side of Pine Island Bay is likely, given the close agreement of the Cretaceous cooling age for these rocks and the Sif Island granite (Lindow et al., 2016) and given tectonic reconstructions which show that the relative position of the crustal blocks of West Antarctica has not changed substantially since ~100 Ma (e.g. Zundel et al., 2019). The AFT age is also older than those typical for central MBL, which record Cenozoic cooling (Spiegel et al., 2016). It therefore seems likely that Sif Island has gradually cooled since ~90 Ma (Lindow et al., 2016).

4.7 Topographic Implications

Basal topography is a key control on ice sheet flow and the resolution of these data can influence the result of ice sheet modelling studies. Current estimates of bed topography from inversion of ice flow velocities (Morlighem et al., 2020) and gravity-derived bathymetric data (Millan et al., 2017) underestimate the local topography, showing the bed slightly below sea level at the location of Sif Island. This is consistent with observed smoothing of data when comparing these datasets to higher resolution multibeam swath bathymetry data from deglaciated former beds (Hogan et al., 2020). The existence of subaerial rock at the location of Sif Island, which is not predicted from existing elevation data, emphasises these issues with current datasets. These smaller-scale topographic and bathymetric features can impact basal sliding beneath grounded ice and provide pinning points for ice shelves which could potentially trigger a re-advance of the grounding zone following isostatic rebound. If present further offshore, they can also prevent/restrict delivery of warm deep water to the ice-sheet grounding zone and undersides of ice shelves (e.g., Hogan et al., 2020).

4.8 Conclusions and Outlook

The exposure of a new island due to ice-front retreat in an area of slow-flowing ice in Pine Island Bay has allowed characterisation of its geology. Sif Island contains the only bedrock outcrop between Thwaites and Pine Island glaciers, enabling new inferences to be made regarding the geological and tectonic development of the crust underlying the 'weak underbelly' of the WAIS. The geochemistry and age of the granite constituting Sif Island reveals a close link to the Jurassic rocks in the Antarctic Peninsula and Thurston Island crustal blocks, setting the western-most limit of intrusive Jurassic magmatic arc rocks in West Antarctica. This is consistent with offshore detrital mineral grains dated to this period sourced from beneath PIG. In addition, we reveal Sif Island has a different thermal history to islands on the northern side of Pine Island Bay, providing the first thermochronological evidence for a major tectonic feature beneath PIG.

Comparing the geochemistry of the Sif Island granite to detrital sediments nearby also helps refine the fingerprinting of the provenance signatures of glaciogenic detritus supplied by Thwaites and Pine Island glaciers. A subglacial sample collected upstream from the grounding zone of Thwaites Glacier's eastern trunk has isolated the endmember composition of detritus supplied by the glacier offshore, which has slightly more radiogenic ε_{Nd} values of -2 than previously suggested (Simões Pereira et al., 2020). The sample from Thwaites

Glacier's Eastern Ice Shelf has a slightly less radiogenic ε_{Nd} signature than the upstream sample, which may point to the advection of PIG derived unradiogenic detritus by a westward coastal current. In addition, $^{87}Sr/^{86}Sr$ ratios between Pine Island and Thwaites glaciers appear to be elevated relative to their ε_{Nd} values (Fig. 4.5; 4.6). Rocks similar to Sif Island may therefore be partially responsible for the changes to $^{87}Sr/^{86}Sr$ ratios without a corresponding shift in ε_{Nd} values sometimes observed in marine sediments (Simões Pereira et al., 2018). Finally, marine samples from beneath the former Thwaites Glacier Tongue are characterised by slightly higher $^{87}Sr/^{86}Sr$ ratios compared to their eastern counterparts, suggesting that the western branch of Thwaites Glacier delivers glaciogenic detritus with a provenance fingerprint distinct from that of its eastern branch. In the future, these data will help interpret downcore provenance changes in offshore sediment records analysed to reconstruct past changes to these vulnerable glaciers.

As ice extent and grounding zones around Antarctica are likely to continue to retreat over the coming decades and centuries, more islands previously covered by ice will be exposed. This effect will be compounded by isostatic rebound of the lithosphere due to ice sheet mass loss; the rate of uplift in the Amundsen Sea is currently estimated to be in the region of a few millimetres per year (Whitehouse et al., 2019). This uplift could lead to significant increases in the area of exposed rock over centennial and millennial timescales, compounded by local sea-level fall due to reduced gravitational pull of ocean water by the waning ice sheet. In Pine Island Bay, the bed underlying the slow-flowing sector between Thwaites and Pine Island glaciers is predicted to have other areas above sea level (Morlighem et al., 2020), which may be revealed as the ice front between these topographic highs retreats. While providing new opportunities to study the geological history of Antarctica, this will likely be accompanied by retreat of these glaciers from topographic pinning points, with major implications for global sea-level rise.

Chapter 5. Constraining the Sediment Provenance Signature of West Antarctic Ice Sheet Collapse

James Marschalek designed and led the project. Contributions from others include guidance from Tina van de Flierdt, Martin Siegert and Claus-Dieter Hillenbrand. Sampling and sieving of the Byrd ice core was performed by Pierre-Henri Blard and Jean-Louis Tison. Pierre-Henri Blard and Emilia Sarigulyan performed the SEM imaging and microprobe mineralogy analysis. Werner Ehrmann collected the clay mineralogy data. Sidney Hemming performed the $^{40}Ar/^{39}Ar$ dating. Although not yet complete, U-Pb dating of zircon grains is currently being undertaken by Kathy Licht and Claire Allen is searching the debris for presence of diatoms.



A rhyolite cobble in-situ in the Byrd Ice core prior to melting. Photo courtesy of Dr Pierre-Henri Blard.

Chapter Summary

The stability of the West Antarctic Ice Sheet (WAIS) in response to environmental change is recorded in glacimarine sediments offshore of the continent. Changes to the composition of these sediments can inform reconstructions of where the ice sheet was eroding sediment/bedrock and thus where ice was present (e.g. Chapter 2).

Tracing of sediment provenance relies on knowledge of the rocks beneath the ice sheet, particularly when seeking to reconstruct warmer-than-present times when the ice sheet margin had retreated landwards of its position today. In West Antarctica, where ice cover is nearly complete inland of coastal outcrops, this presents a significant challenge, which limits conclusions that can be made from studying sediment provenance, even when aided computationally (see Chapter 3). This chapter seeks to reduce uncertainties regarding the sediment provenance signature of the geology beneath the WAIS by assessing the provenance characteristics of detritus from the basal ice of the Byrd ice core in central West Antarctica.

The Byrd ice core was drilled to the ice sheet base in 1968. Entrained in the lower part of the ice column was detritus that underwent little geological characterisation at the time of recovery. This chapter documents how I located and obtained this debris, before describing the broad suite of analyses being conducted by myself and a team of collaborators that I assembled. Techniques include measurement of the radiogenic Nd and Sr isotope composition, clay mineralogy, SEM imaging for textural analyses, microprobe mineralogy, and dating of detrital minerals through hornblende $^{40}Ar/^{39}Ar$ and zircon U-Pb geochronology.

These analyses show that the composition of the basal debris in the Byrd ice core changes with height in the ice column, implying the accretion of the basal ice occurred gradually and not as a single episode. The debris is kaolinite rich and has an endmember with a high ε_{Nd} value and low $^{87}Sr/^{86}Sr$ ratio. This information will help diagnose WAIS collapse in future marine and subglacial sediment provenance records seeking to study key warmer-than-present periods such as the Last Interglacial.

Detrital mineral dating will further elucidate the signature of detritus eroded from this region if the WAIS margin was to retreat. The debris is also being searched for marine diatoms. These have the potential to reveal the age and environmental conditions of sedimentary strata contributing to the debris which predate the onset of major Cenozoic glaciation, as well as the time that the site most recently deglaciated and was in contact with the ocean.

A rhyolite clast recovered from the ice has an age of ~218 Ma, providing the first englacial sample of early Mesozoic rocks known from marine sediments to be common in the West Antarctic interior. The evidence for volcanic rocks contributing to the debris may also help explain the occurrence of smectite sourced from West Antarctica (Balshaw-Biddle, 1980; Ehrmann et al., 2011; Simões Pereira et al., 2018; Marschalek et al., 2021) despite the apparent lack of mafic minerals offshore (Licht et al., 2005; Andrews and LeMasurier, 2021).

5.1 Introduction

5.1.1 The Byrd Ice Core

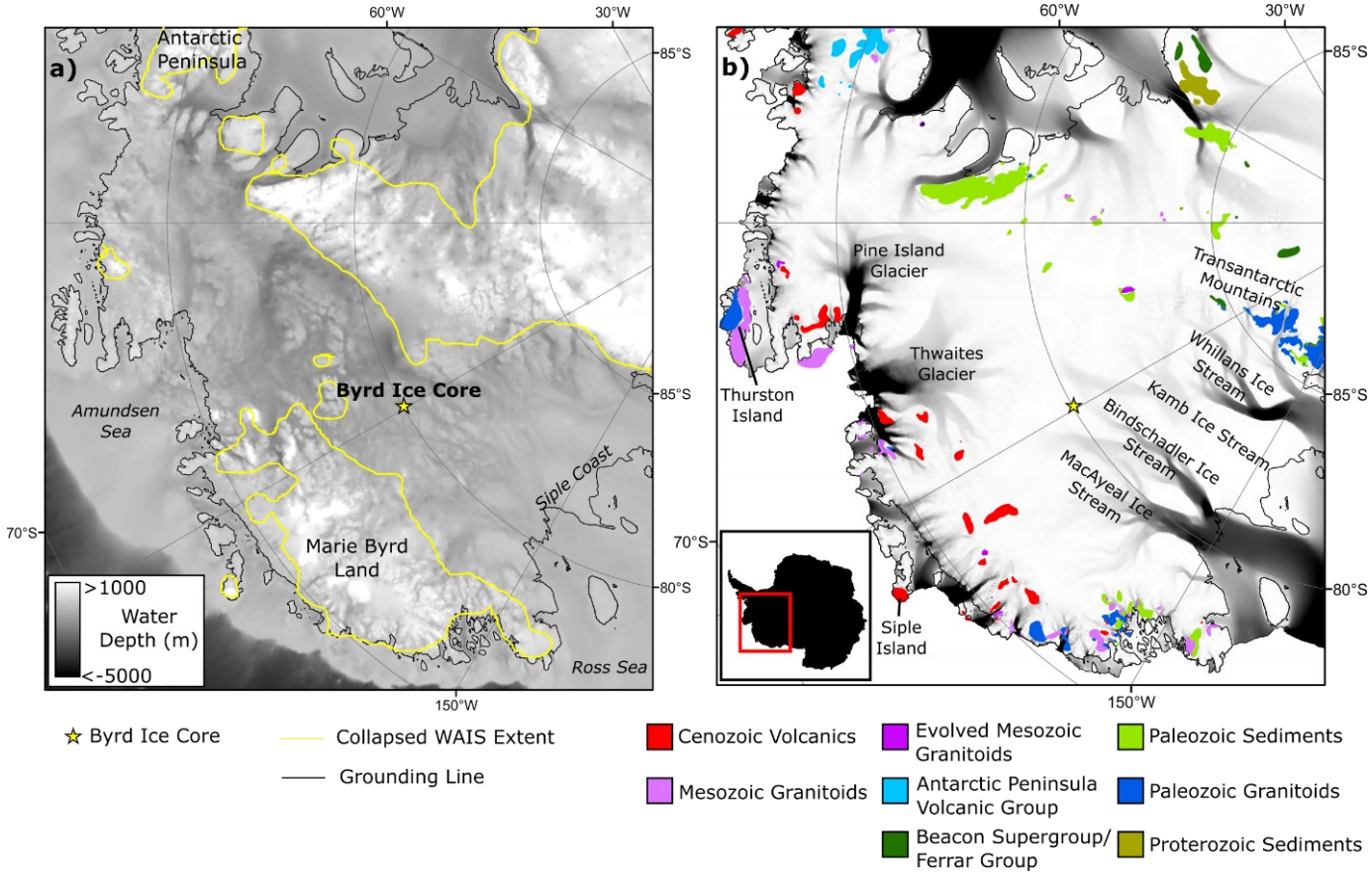


Figure 5.1. *a) Location of the Byrd ice core (yellow star) on BedMachine V1 Antarctica bed topography (Morlighem et al., 2020). The black line denotes the modern grounding line (Rignot et al., 2013; Mouginot et al., 2017) and the yellow line a modelled Last Interglacial ice sheet extent with the marine sectors of the WAIS having undergone collapse (DeConto and Pollard, 2016). b) Geological map of West Antarctica (excluding the Antarctic Peninsula) around the location of the Byrd ice core, based on GeoMAP Antarctica (Cox et al., 2019). Plotted on surface velocity data (Mouginot et al., 2019). The location of the main panels within Antarctica is shown in the inset.*

The Byrd ice core (80° 0.1'S, 119° 31'W) was drilled at Byrd Station in January 1968, penetrating 2164 m of ice to reach the bed, which currently lies at 634 m below sea level (Gow et al., 1968). Byrd Station lies at the centre of the WAIS, more than 340 km from the nearest rock outcrop and at a critical junction between the Amundsen Sea and Ross Sea sectors. As with most ice core drill sites, the location is currently close to the ice divide where basal ice velocities are very slow, although it falls slightly within the upper catchment of

Bindschadler Ice Stream (Fig. 5.1). Although attempts to retrieve subglacial sediments at the site failed, a small quantity of englacial debris was recovered entrained within the lowermost 4.83 m of the ice column (Gow et al., 1979).

Determining the provenance signature of the Byrd ice core debris can inform predictions of what changes to sediment deposited around the ice sheet margin would be expected following past collapses of the WAIS (e.g., ice extent in Fig. 5.1a). Such a collapse may have happened as recently as the Last Interglacial at ca. 130 ka (Dutton and Lambeck, 2012), when grounding zone retreat could have intensified erosion far inland of the modern ice sheet margin. The substantial distance of the Byrd ice core from any outcropping rocks means little is known about the subglacial geology, and thus sediment provenance signature, of this part of West Antarctica. The Byrd ice core debris therefore provide an invaluable data point for reconstructions of past ice stability under changing environmental conditions.

5.1.2 Glacial Setting and Existing Analyses on the Byrd Ice Core Debris

Reports on the Byrd ice core debris which were made soon after drilling focussed on glaciological aspects such as entrainment processes and revealed that the debris was likely frozen onto the base of the ice (Gow et al., 1979). However, there is likely to be some slow basal motion at the site, with observed surface velocities of approximately 4.0 m/yr (Mouginot et al., 2019), and modelled basal velocities of approximately 0.5 m/yr (DeConto et al., 2021). This modelled velocity is compatible with the substantial basal meltwater observed at the core site (Gow et al., 1979), which could allow sliding to occur. Although much of the West Antarctic interior may have been above sea level in the early Cenozoic (Paxman et al., 2019a), The site is likely to have remained below sea level for much of the Cenozoic; complete removal of the modern ice sheet would cause the site to rise ~520 m (Paxman et al., 2022), leaving it ~100 m below sea level.

Seismic data show the ice sheet bed at Byrd Station is unlikely to be underlain by significant thicknesses of low velocity, unconsolidated sediments (Chaput et al., 2013). However, at least some till cover seems to be present, as observations at the base of the hole suggested unconsolidated till or gravel rather than bedrock (Gow and Meese, 1996). Thus, although the englacial debris present in the ice could have been transported from an area with basal till upstream, an in-situ source for the ice core debris is also feasible.

Basic petrographic classification of pebble-sized rocks showed the basal debris contained granite, quartz-monzonite, basalt, tuff and arkosic arenite clasts (Gow et al., 1979). Minerals including quartz, plagioclase, muscovite, chlorite, and kaolinite were identified in x-ray diffraction analyses (Gow et al., 1979), but further characterisation of the debris was not conducted at the time. Vogel et al. (2006) and Vogel (2004) performed later analyses on the Byrd ice core detritus. Grain size analyses revealed high variability in the dominance of sand and silt, although clay was generally rarer and always <40% (Vogel, 2004). Sand fraction petrology of the sediment was limited to differentiation between quartz (30-65%), feldspar (20-40%) and lithic fragments (10-30%) (Vogel et al., 2006).

$^{40}Ar/^{39}Ar$ dating of two basaltic pebbles recovered from the Byrd ice core gave ages of 82.29 ± 0.15 Ma and 515 ± 4 Ma (Vogel et al., 2006). The ~82 Ma dated basalt was likely thermally reset during late-stage breakup of Gondwana (Vogel, 2004); although no basalts of this age are exposed in Antarctica, intraplate volcanism associated with the breakup is found in New Zealand with very similar mid-Cretaceous ages (Panter et al., 2006; Hoernle et al., 2020). The age of the ~515 Ma pebble implies it formed during the Ross Orogeny. The Ross Orogeny is primarily associated with intrusion of granitic plutons along the length of the Transantarctic Mountains. However, the Glasgow Volcanics in the Bowers Terrane of Northern Victoria Land (west of area shown in Fig. 5.1; Weaver et al., 1984; Rocchi et al., 2011) and the Liv Group in the southern Transantarctic Mountains (Wareham et al., 2001) contain volcanic rocks which are sometimes basaltic in composition and of a similar age.

5.1.3 Geology Beneath the WAIS

To place the debris from the Byrd ice core in a regional setting, we summarise the current state of knowledge of the geology of the interior of West Antarctica. Beyond direct samples from sites such as the Byrd ice core (Gow et al., 1979; Vogel et al., 2006) and till collected from drilling through the Siple Coast ice streams (e.g. Licht et al., 2005; 2014; Farmer et al., 2006), this endeavour is reliant on the study of constraints from sediments deposited offshore in the Ross and Amundsen seas (e.g. Hillenbrand et al., 2003; Farmer et al., 2006; Ehrmann et al., 2011; Licht et al., 2014; Simões Pereira et al., 2018; 2020; Marschalek et al., 2021; Andrews and LeMasurier, 2021). These sediment samples represent a mixture of the rock types present in the respective drainage basins. To compliment these data, geophysical methods such as radar, seismics, gravity, and magnetic field analyses data, are invaluable (e.g. Rooney et al., 1987; Behrendt, 1999; 2013; van Wyk de Vries et al., 2017). Together,

these approaches suggest the occurrence of different rock types beneath the ice sheet. The main outcropping rock types within and around the WAIS and key interpretations of how these may extend under the ice are summarised chronologically here (Fig. 5.1b).

Basalt and tuff clasts are found in the Byrd ice core debris (Gow et al., 1979) and mafic volcanic rocks make up nearly 50% of lithic fragments in the sand fraction (Vogel et al., 2006). These rocks could derive from subglacial Cenozoic volcanoes which are part of the Marie Byrd Land volcanic province (Behrendt, 1999; van Wyk de Vries et al., 2017). However, $^{40}Ar/^{39}Ar$ clast dating from the Byrd ice core suggests there are no volcanic clasts of Cenozoic age (Vogel et al., 2006). Given that Mt. Resnik, located only ~60 km from the Byrd ice core site (Fig. 5.7), is almost certainly a subglacially erupted volcano based on its magnetic anomaly and ~1.6 km conical peak (Behrendt, 2013), this lack of Cenozoic volcanic debris is unexpected. Detrital mineral populations in the Ross Sea region also appear to lack minerals common in alkali basalt (Andrews and LeMasurier, 2021), meaning these rocks could be rarer in the sedimentary record than might be expected based on their proposed extent in geophysical studies (e.g. Behrendt, 1999; 2013; van Wyk de Vries et al., 2017). Intrusive Cenozoic rocks present may also include gabbroic rocks underlying Thwaites Glacier, as suggested by marine geochemical provenance analyses (Simões Pereira et al., 2020) and high-density, magnetic bodies (Bingham et al, 2012; Jordan, pers. comm., 2021). Other Cenozoic age subglacial rocks present in the Thwaites Glacier catchment include pre-Oligocene kaolinite-bearing sedimentary strata (Ehrmann et al., 2011; Simões Pereira et al., 2020).

The granite and quartz-monzonite clasts described from the Byrd ice core could derive from many sources (Gow et al., 1979). They may be of Cretaceous age, as Cretaceous granitoids are common throughout West Antarctica (Weaver et al., 1992; Mukasa and Daziel, 2000; Korhonen et al., 2010; Craddock et al., 2017). These are thought to extend under much of the catchment of Thwaites Glacier, although not beneath Pine Island Glacier, as Cretaceous (~115 Ma) $^{40}Ar/^{39}Ar$ ages are common in western, but not eastern, marine sediments from Pine Island Bay (Simões Pereira et al., 2020). Cretaceous zircon U-Pb ages are found beneath Kamb and Bindschadler ice streams (Licht et al., 2014), suggesting these rocks continue under the catchment of these ice streams towards the Ross Sea.

Zircon and hornblende bearing Triassic to Early Jurassic rocks are also present beneath the WAIS; a broad age peak spanning ~250-180 Ma is seen both in Ross Sea sediments (Licht et

al., 2014; Perotti et al., 2017; Marschalek et al., 2021) and Amundsen Sea sediments (Simões Pereira et al., 2018; 2020). The abundance of these mineral ages does not match the very limited exposures of rocks of this age around the coast (Pankhurst et al., 1993; Korhonen et al., 2010; Riley et al., 2017). They must therefore be far more common under the ice. Rocks of Triassic-Early Jurassic age are best exposed in the Antarctic Peninsula, where they record intrusion and metamorphism in a long-lived convergent tectonic setting (Millar et al., 2002; Bastias et al., 2020; Riley et al., 2020).

Older Palaeozoic granitic rocks are also found exposed along the coast of West Antarctica (e.g. Weaver et al., 1992; Korhonen et al., 2010; Yakymchuk et al., 2015) and likely beneath Pine Island and Thwaites glaciers (Simões Pereira et al., 2020). The arkosic arenite clast found in the Byrd ice core (Gow et al., 1979) may derive from Palaeozoic sediments such as the Swanson Formation and equivalents in the Whitmore Mountains (Storey and MacDonald, 1987; Korhonen et al., 2010; Yakymchuk et al., 2015). Occurrence of such rocks is also inferred from the presence of clastic sedimentary rock fragments and metasedimentary rock fragments beneath the Siple Coast ice streams (Licht et al., 2005). Furthermore, the relatively unradiogenic ε_{Nd} of both these outcropping Palaeozoic metasediments (Adams, 1986; Yakymchuk et al., 2015) and till samples from beneath Bindschadler Ice Stream (Farmer et al., 2006) suggests they probably extend under the WAIS.

Transantarctic Mountain rocks almost certainly comprise a significant fraction of the sediment underlying parts of the WAIS adjacent to the mountain range. For instance, Whillans Ice Stream has detrital zircon U-Pb ages indistinguishable from Transantarctic Mountain samples (Licht et al., 2014). However, the site of the Byrd ice core is located close to Marie Byrd Land and distant from the Transantarctic Mountains; a dominant detritus supply from East Antarctica thus seems very unlikely. The site also lies well within the West Antarctic rift system, and, based on the crustal boundary mapped under the Ross Ice Shelf, likely on West Antarctic crust (Tinto et al., 2019). Transantarctic Mountain rock types can therefore likely be neglected when considering the Byrd ice core debris.

5.2 Methods

5.2.1 Core Sampling and Debris Recovered

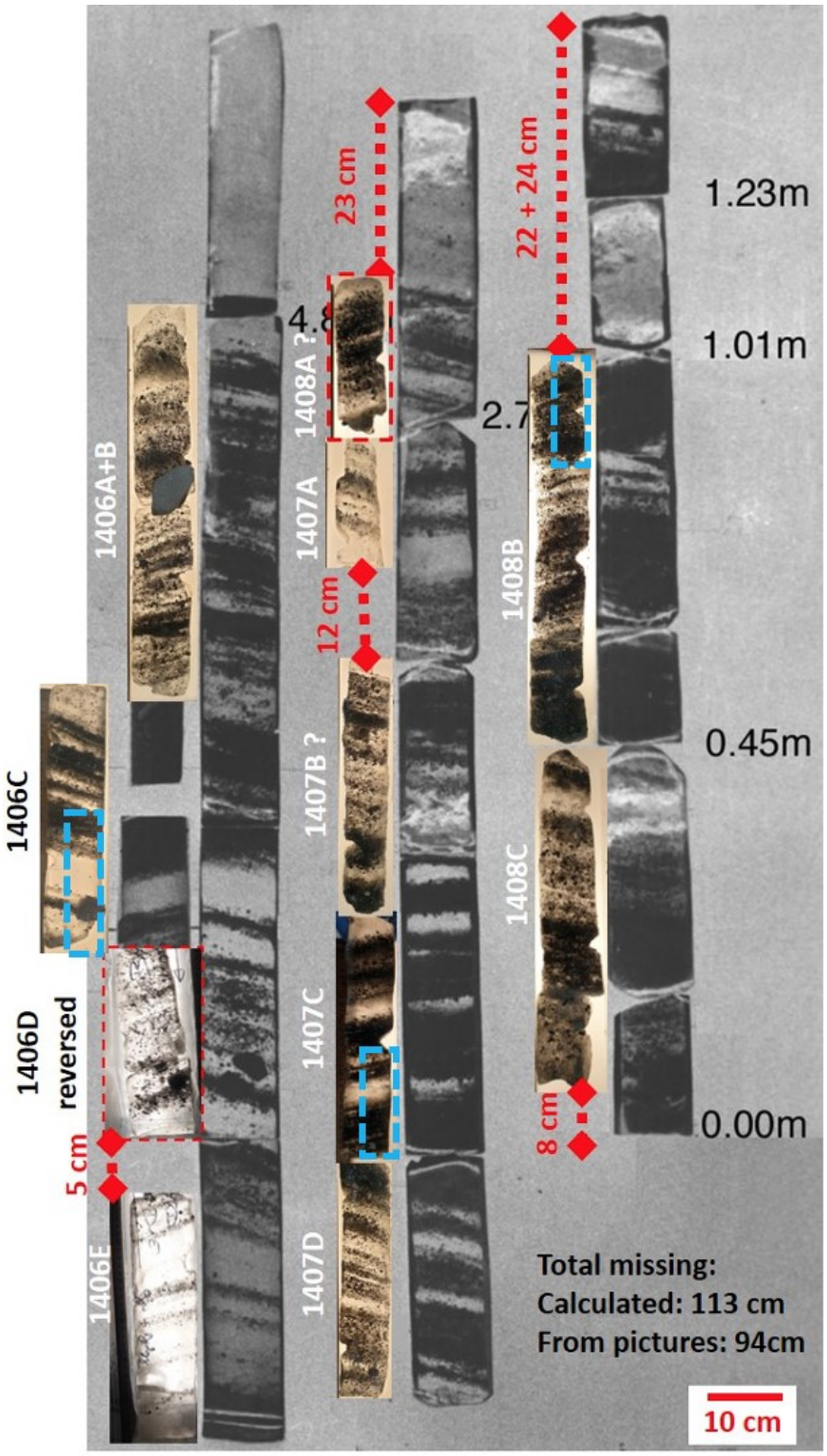


Figure 5.2. *Recent images of the Byrd ice core basal ice (beige colours) and correlation with the original 1960s images (grey shaded). Missing intervals are marked in red, and blue boxes denote samples taken. Image courtesy of Pierre-Henri Blard.*

Due to the decades elapsed since the drilling of the Byrd ice core, no record could be found of the clay- to sand-sized detritus collected or melted from the ice near the time of drilling, despite thorough searches of sediment repositories and the assistance of Debra Meese, an author of the original papers on the debris. However, the bottom 4.83 m of the ice core has been described as debris rich (Gow et al., 1979), so information on this was searched for specifically. The US National Science Foundation Ice Core Facility (Denver Federal Center in Lakewood, Colorado) advised this basal ice was transferred to the Centre for Ice and Climate at the Niels Bohr Institute (University of Copenhagen) in the 1970s. When contacted, the repository manager Jørgen Peder Steffensen confirmed the basal ice was there and suggested the englacial debris was already of interest to studies of cosmogenic nuclide exposure dating, which can reveal when an area may have last been ice-free (e.g. Schaefer et al., 2016). A plan was made for Pierre-Henri Blard (Centre de recherches pétrographiques et géochimiques, Nancy, France; and Université Libre de Bruxelles) and Jean-Louis Tison (Université Libre de Bruxelles) to cut sections of the ice core to obtain debris samples. As cosmogenic nuclide techniques use quartz grains in coarser size fractions, I suggested sharing the limited sample volume between this method and provenance proxies. Sections of the ice core had been lost and/or partially melted for earlier studies when compared to the original photographs, but sufficient volumes of debris-rich ice remained (Fig. 5.2).



Figure 5.3. *Rhyolite porphyry cobble ~4-5 cm in diameter recovered from section 1406-C2.*

Three intervals were cut from the parts of the ice core containing debris-rich ice in November 2021 in Copenhagen by Pierre-Henri Blard, Jean-Louis Tison and Jørgen Peder Steffensen.

Ascending from the base of the ice, sample depths were approximately 86-101 cm (1408-B1), ~183-197 cm (1407-C2) and ~403-419.5 cm (1406-C2) above bed, although melting since the original coring means stratigraphic position had to be derived from matching original and modern core photographs (Fig. 5.2). Consequently, there is some uncertainty on the exact height of samples 1407-C2 and 1406-C2. The age of the ice is uncertain, but must be younger than that of the meteoric ice it is frozen onto, which dates to ~90 ka (Blunier and Brook, 2001).

Samples were then transported frozen to the Laboratoire of Glaciologie, Brussels, where they were melted and sieved to collect the detritus by Pierre-Henri Blard. Debris comprised 29.5%, 6.5% and 13.2% of the mass of samples 1406-C2, 1407-C2 and 1408-B1, respectively (Table 5.1). The debris comprised mainly medium to coarse sand; silt and very fine sand (<75 μm) was relatively rare, and its proportion highly variable, comprising only 1%, 28% and 4% of the debris, respectively.

Table 5.1. *The length, position relative to the bed, ice mass, debris content and grain size fractions of the Byrd ice core samples. Note that the height of samples 1406-C2 and 1407-C2 above the bed is subject to some uncertainty due to sample loss compared to the core photographs from the 1960s used to assign section positions.*

Sample	Length (cm)	Top position above bed (cm)	Bottom position above bed (cm)	Initial mass (g)	Mass of pure ice (g)	Debris %	Total Debris (g)	<75 μm	75-210 μm	210-800 μm	>800 μm
1406-C2	16.5	~419.5	~403	225	159	29.5	66.43	0.89	0.939	1.611	62.99
1407-C2	14	~197	~183	143	134	6.5	9.348	2.644	1.636	3.105	1.963
1408-B1	15	101	86	107	93	13.2	14.165	0.594	1.705	7.12	4.746

As the sample material is very limited, efforts were made to maximise the number of useful analyses that could be performed on the three samples. These included the measurement of Nd and Sr isotope composition, performed in the MAGIC laboratories at Imperial College London, and clay mineralogy, measured by Werner Ehrmann at the University of Leipzig. These techniques used the <75 μm fraction and <2 μm fraction, respectively. The residual fraction 2-75 μm fraction left over from the clay mineral analyses is currently being searched for diatoms by Claire Allen at the British Antarctic Survey. Dating of detrital minerals in the 75-210 μm fraction is currently being undertaken by Sidney Hemming (Lamont Doherty Earth Observatory) and Kathy Licht (Indiana University–Purdue University Indianapolis). The 210-800 μm fraction is being utilised for cosmogenic nuclide surface exposure dating,

with unused mineral types supplementing the mineral dating, where appropriate. All grain sizes are therefore being utilised. This includes a rhyolite porphyry cobble weighing ~25 g recovered from section 1406-C2, which has been analysed for Nd and Sr isotopes (Fig. 5.3). The groundmass of this clast was also suitable for $^{40}Ar/^{39}Ar$ dating.

5.2.2 Neodymium and Strontium Isotopes

Neodymium and Sr isotope measurements were conducted on the <75 μm fractions of the bulk detritus and the rhyolite clast. This size fraction is assumed to be representative of the bulk composition and its use allowed for the coarser grain sizes to be processed for mineral dating. A leaching step was assumed to be unnecessary due to the debris being englacial, and therefore not in contact with marine waters where authigenic Fe-Mn oxyhydroxide phases can be deposited. One sample was, however, leached in a mixture of 0.05 M hydroxylamine hydrochloride, 15% acetic acid and 0.03 M EDTA (Gutjahr et al., 2007) to test this assumption. The sample material was then dried and homogenised. For the rhyolite clast, a ~0.3 g chip containing a representative sample of groundmass and phenocryst was thoroughly homogenised. 50 mg aliquots of each sample were then digested on a hotplate in concentrated HF, $HClO_4$, and HNO_3 for three to five days. Samples were processed alongside ~75 mg of USGS BCR-2 rock standard. The Nd was isolated from the sample matrix using a cation exchange resin (AG50W-X8, 200-400 μm mesh) and HCl in increasing molarity, followed by a low molarity HCl Ln-Spec resin procedure (50–100 μm mesh). The sample matrix from the cation exchange step was dried, taken up in HNO_3, then loaded onto Eichrom Sr Spec resin to wash down the matrix and elute the Sr (for more details on the methods, see Simões Pereira et al. 2018).

Neodymium isotopes were measured in the MAGIC laboratories at Imperial College London on a Nu high resolution multi-collector inductively coupled plasma mass spectrometer (HR MC-ICP-MS). To account for instrumental mass bias, isotope ratios were corrected using an exponential law and a $^{146}Nd/^{144}Nd$ ratio of 0.7219. Although negligible, interference of ^{144}Sm on ^{144}Nd was corrected for. Bracketing standards were used to correct measured $^{143}Nd/^{144}Nd$ ratios to the commonly used JNdi-1 value of 0.512115 (Tanaka et al., 2000). USGS BCR-2 rock standard measurements yielded $^{143}Nd/^{144}Nd$ ratios consistently within error of the published ratio of 0.512638 ± 0.000015 (Weis et al., 2006). A full procedural blank for Nd was 18 pg. $^{143}Nd/^{144}Nd$ ratios are expressed using epsilon notation (ε_{Nd}), which denotes the

deviation of a measured ratio from the modern Chondritic Uniform Reservoir (0.512638) in parts per 10,000 (Jacobsen and Wasserburg, 1980).

Strontium isotopes were measured in the MAGIC laboratories at Imperial College London on a Triton TIMS (Thermal Ionisation Mass Spectrometer). Samples were loaded in 1 µL of 6M HCl onto degassed tungsten filaments with 1 µL of $TaCl_5$ activator. The measured $^{87}Sr/^{86}Sr$ ratios were corrected for instrumental mass bias using an exponential law and an $^{88}Sr/^{86}Sr$ ratio of 8.375. Interference of ^{87}Rb was corrected for using an $^{87}Rb/^{85}Rb$ ratio of 0.386. Analyses of the NIST 987 standard reference material were completed every four unknowns, yielding a mean of 0.710303 ± 0.000049 (2SD, n = 14). Samples were corrected to the published value of 0.710252 ± 0.000013 (Weis et al., 2006). The relatively poor reproducibility for our NIST 987 runs was due to technical issues, but is still more than sufficient for interpreting sample results, which change in the 3rd to 4th digit. Accuracy of results was confirmed using rock standard USGS BCR-2, processed with every batch of samples, which yielded $^{87}Sr/^{86}Sr$ ratios of 0.705001 ± 0.00014 (2SD, n = 6). This is within error of the published ratio of 0.705013 ± 0.00010 (Weis et al., 2006).

5.2.3 Clay Mineralogy

Smectite, illite, chlorite and kaolinite percentages were measured by Werner Ehrmann at the Institute for Geophysics and Geology, University of Leipzig. The <2 µm fraction was separated from the <75 µm fraction in settling tubes. Sample preparation and analysis, then identification and analysis of clay minerals, followed standard x-ray diffraction procedures (Ehrmann et al., 2011).

5.2.4 $^{40}Ar/^{39}Ar$ Dating

The $^{40}Ar/^{39}Ar$ dating was performed by Sidney Hemming at the Lamont-Doherty Earth Observatory Argon Geochronology for the Earth Sciences (AGES) laboratory, Palisades, USA. A sample of the clast groundmass was co-irradiated with Fish Canyon sanidine (28.201 ± 0.046 Ma) (Kupier et al., 2008) for 8 hours in the CLICIT (Cadmium Lined In-Core Irradiation Tube) facility at Oregon State University reactor, Corvallis, USA. The sample was loaded into a planchette, evacuated in a chamber with a ZnSe window, then heated with a CO_2 laser to release the gas. The sample was exposed to hot Zr-Al getters to remove reactive gases, and the inert gases were let into a VG5400 noble gas mass spectrometer and measured with peak hopping on an analogue multiplier in static vacuum mode. Backgrounds were

corrected based on frequent measurements of blanks (~ every 4 unknowns) and mass discrimination was corrected based on measurements of air (~ every 12 unknowns). Corrections for nuclear interferences are based on reported measurements from the Berkeley Geochronology Lab (Renne, 1995). Analyses and data reduction were performed using MassSpec, a program written by Al Deino at the BGC. Error is reported at 1 sigma.

5.2.5 SEM Imaging and Electron Microprobe Mineralogy

SEM imaging and electron microprobe analysis of the 75-210 µm and 210-800 µm fractions was conducted by Pierre-Henri Blard and Emilia Sarigulyan at the Centre de Recherches Pétrographiques et Géochemiques, Nancy (France).

5.3 Results

5.3.1 Neodymium and Strontium Isotopes

Table 5.2. *Results of Nd and Sr isotope analyses on the fine grained (<75 µm) Byrd ice core debris.*

Approx. midpoint height above bed (m)	Sample Name	$^{143}Nd/^{144}Nd$	2SE	ε_{Nd}	2SD	$^{87}Sr/^{86}Sr$	2SE
0.935	1408-B1 <75 µm	0.512428	0.000012	-4.09	0.25	0.712506	0.000009
1.9	1407-C2 <75 µm	0.512470	0.000010	-3.27	0.27	0.710890	0.000008
1.9	1407-C2 <75 µm (leached)	0.512422	0.000010	-4.21	0.25	0.712998	0.000010
4.1125	1406-C2 <75 µm	0.512487	0.000010	-2.95	0.21	0.708653	0.000007
4.1125	1406-C2 clast	0.512500	0.000009	-2.70	0.21	0.705810	0.000007

Neodymium and strontium isotope analyses conducted on the debris show clear variation with depth. Descending the ice column, ε_{Nd} values are -2.95 ± 0.21, -3.27 ± 0.27 and -4.09 ± 0.25 (Fig. 5.4; Table 5.2). Although the change in ε_{Nd} values is only ~1.2 epsilon units between the uppermost and lowermost samples, the difference exceeds the measurement error. The rhyolite clast has an ε_{Nd} value of -2.70 ± 0.21, very close to the <75 µm fraction value of -2.95 for the same sample. $^{87}Sr/^{86}Sr$ ratios show the opposite trend with depth, with ratios of 0.712506 ± 0.000009, 0.710890 ± 0.000008 and 0.708653 ± 0.000007 (Table 5.2). The rhyolite clast has a slightly lower $^{87}Sr/^{86}Sr$ ratio than the fine fraction: 0.705810 ± 0.000007.

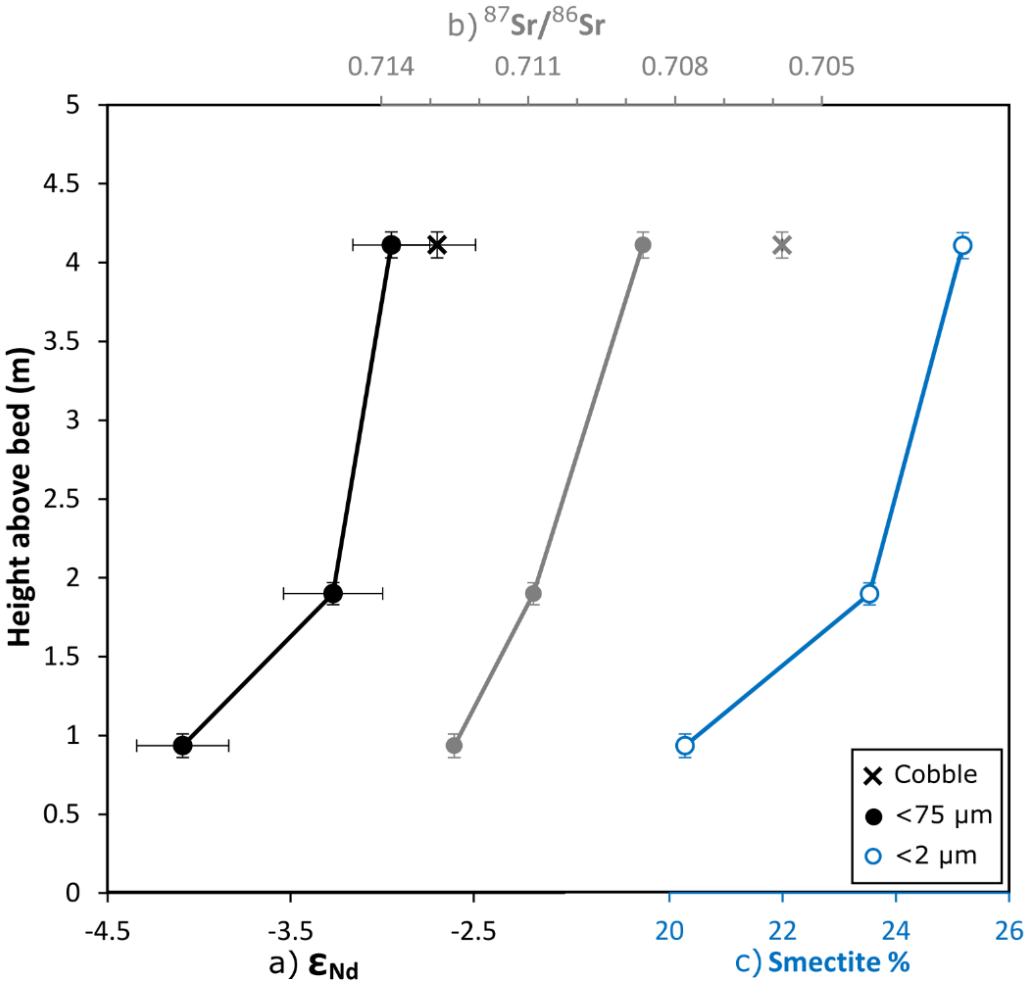


Figure 5.4. *Changes over depth in the ice column in a) Nd isotope ratios (black), b) Sr isotope ratios (grey) and smectite content (blue hollow circles). Black and grey crosses represent Nd and Sr isotope analyses of the ryholite porphyry clast from section 1406-C2.*

Given the englacial setting, grain coatings capable of impacting isotopic compositions were not expected and leaching was not expected to impact results. Analysis of one leached sample showed this is clearly not the case; it is probably removing the mineral coatings visible in the SEM images (Fig. 5.6). As water masses are unlikely to vary significantly in their isotopic composition over the tens of kilometres scale relevant here, it is assumed the ~-1 ε_{Nd} and ~+0.002 $^{87}Sr/^{86}Sr$ offset would likely remain approximately constant which depth in the ice core. Leaching would thus be unlikely to impact the trends seen in the unleached sample data, but further investigation is needed to verify this. The leached sample is not shown on plots for clarity.

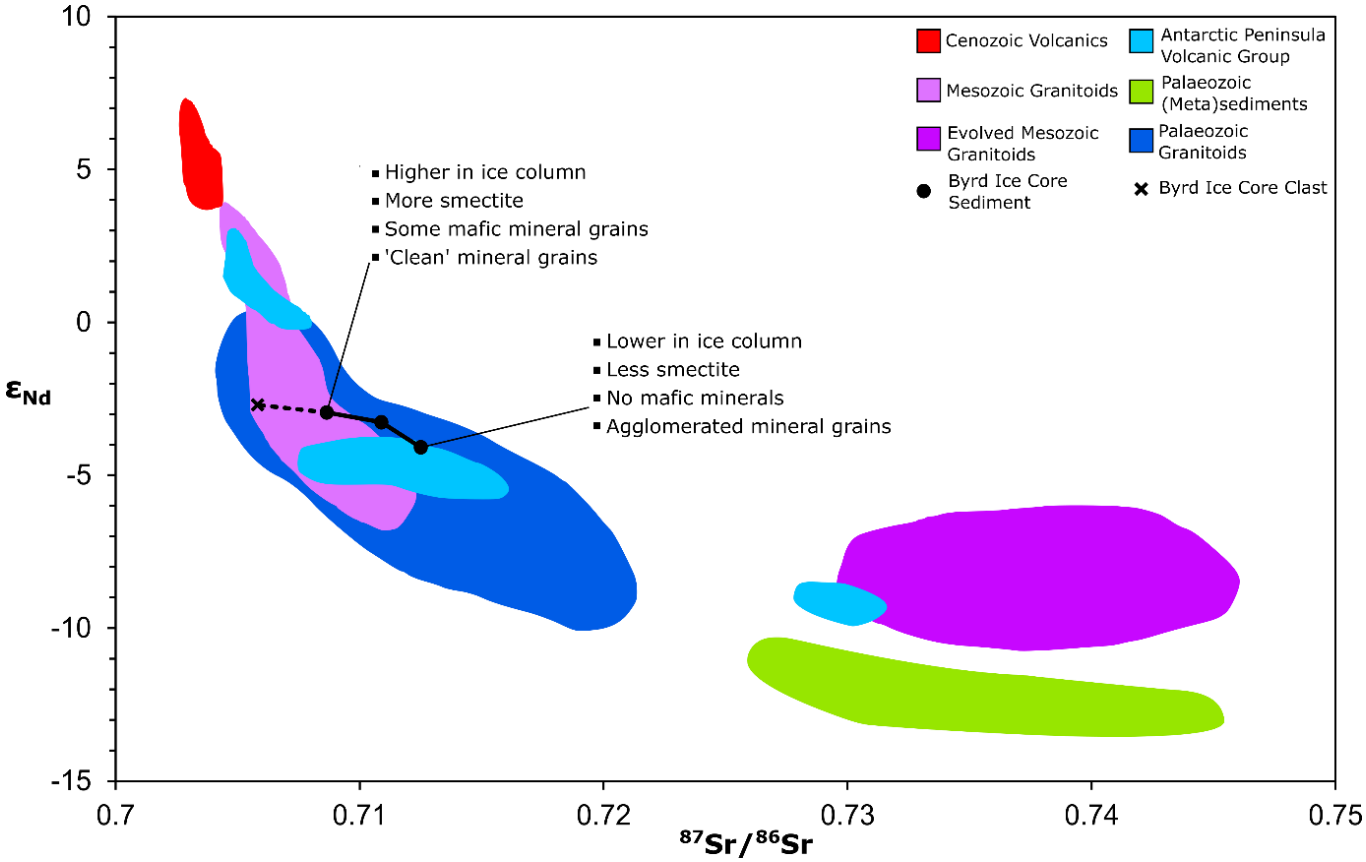


Figure 5.5. *Cross plot of Nd and Sr isotope compositions of the Byrd ice core debris (black points) compared to compiled literature data for West Antarctic rocks (Simões Pereira et al., 2018). Key features of each 'endmember' sample are listed as bullet points. Rock unit colours correspond to those in Figure 5.1.*

Typically, rocks with high ε_{Nd} values and low $^{87}Sr/^{86}Sr$ ratios (e.g. the Cenozoic volcanic rocks) have higher Sr concentrations relative to their Nd concentrations (i.e. a higher [Sr]/[Nd] ratio) compared to rocks with low ε_{Nd} values and high $^{87}Sr/^{86}Sr$ ratios (e.g. the Palaeozoic metasediments). This is a result of Nd being more incompatible than Sr during fractional crystallisation, giving the non-linear 'concave' relationship in rock data (Fig. 5.5). However, when plotted together, the Nd and Sr isotope compositions of the Byrd ice core samples show the opposite ('convex') trend. This suggests an unusual reversal in this relationship. The clast and the uppermost debris in the ice column, which plot towards the upper left, must have a lower [Sr]/[Nd] ratio than the the lowermost debris in the ice column, which plots towards the lower right. Element concentration data could test this hypothesis.

5.3.2 Clay Mineralogy

Clay mineral compositions are broadly similar at all depths in the ice core. Kaolinite is the most abundant clay mineral in all samples (~40%), with the other three clay mineral groups occurring in approximately equal proportions (Table 5.3). Kaolinite is unlikely to form beneath the modern ice sheet in large quantities; it is assumed to be detrital when found offshore of Antarctica (Ehrmann et al., 2011; Simões Pereira et al., 2020). This assumption is evidenced by large differences in the amount of kaolinite deposited offshore of different parts of West Antarctica, despite similar subglacial conditions and rock types (Hillenbrand et al., 2003; Ehrmann et al., 2011). Its formation must therefore predate the dominance of physical weathering caused by the onset of Antarctic glaciation, meaning it can be traced to pre-glacial sedimentary strata.

Table 5.3. *Results of clay mineral composition from x-ray diffraction of the three sample depths.*

Sample	% Smectite	% Illite	% Chlorite	% Kaolinite
1408-B1	20.3	24.0	18.6	37.2
1407-C2	23.5	19.2	15.5	41.8
1406-C2	25.2	22.5	15.5	36.8

In contrast, illite and chlorite are associated with physical weathering regimes, and would therefore be expected to be very common clay minerals in a subglacial setting. In the Byrd ice core, they are not the dominant clay minerals present; each one comprises 15-24% of the samples, far less than kaolinite contribution (Table 5.3).

Unlike the other clay minerals, which show no trend with depth, smectite abundance decreases towards the base of the ice (Fig. 5.4c). The correlation between smectite content and the isotopic data suggest that, although small, the smectite trend is a real feature. Due to a correlation between the occurrence of volcanism and smectite content in modern seafloor surface sediments, smectite is often considered to be a weathering product of mafic volcanic rocks (Ehrmann et al., 1992; see also Cook et al., 2013; Marschalek et al., 2021). In the Byrd ice core, these precursor rocks likely include the basalt and tuff clasts observed within the ice column (Gow et al., 1979).

5.3.3 SEM Imaging and Electron Microprobe Mineralogy

SEM imaging was conducted on the 75-210 and 210-800 µm grain size fractions to examine textural features that can indicate the history and depositional setting of the sand (e.g. Mahaney, 2002). All three samples lack rounded grains (Sarigulyan, 2022). Sub-rounded to angular grains are instead present, showing glacial microtextural features such as conchoidal fractures, linear steps, mechanically-upturned plates and glacial striations (Mahaney, 2002; Fig. 5.6). These are associated with transport beneath ice >~1000 m thick (Mahaney, 1995). Aeolian transport is unlikely, with common features such as mechanically upturned plates and linear steps that are characteristic of a subglacial environment.

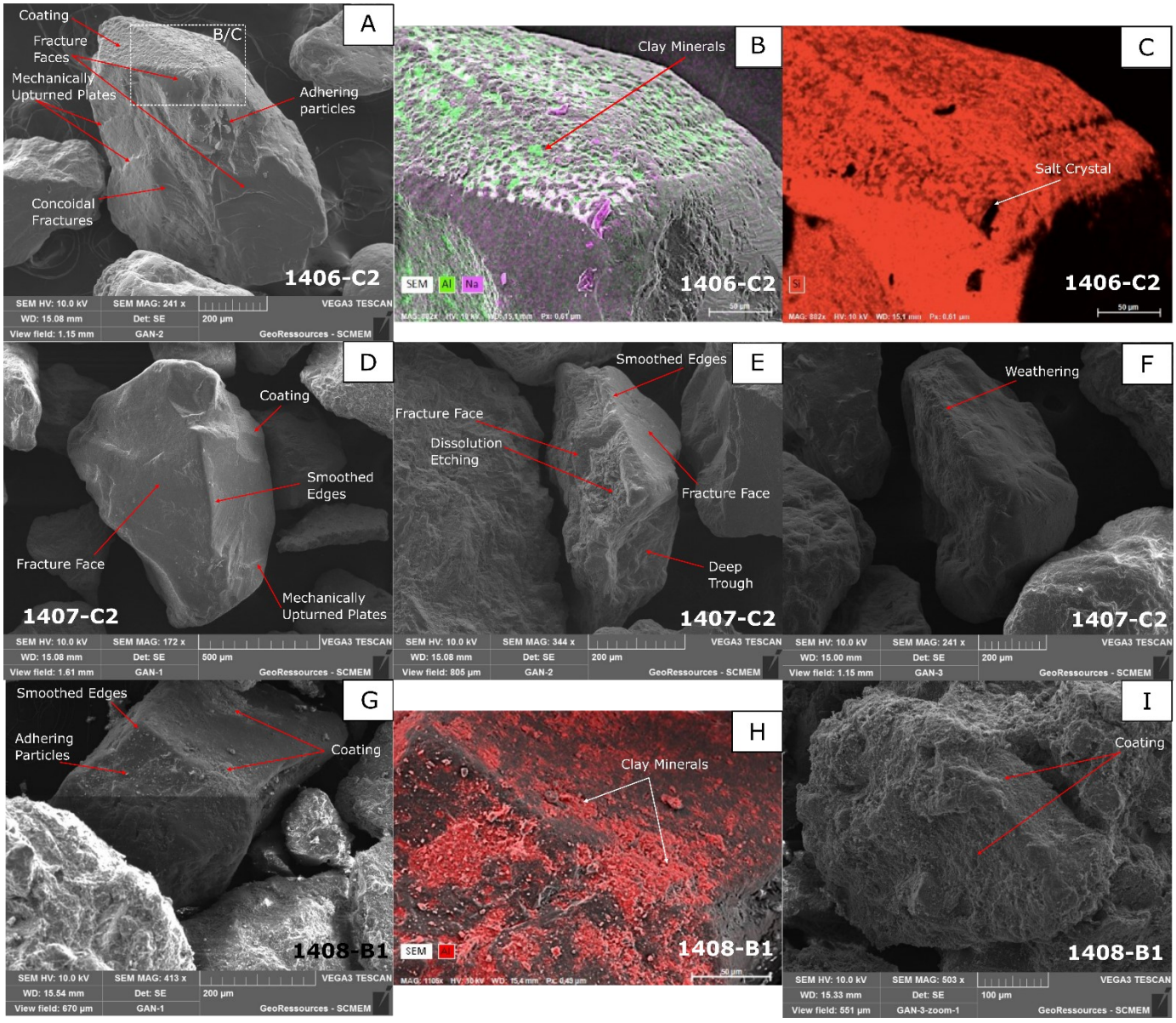


Figure 5.6*. SEM images of 200-810 µm mineral grain textures from sample 1406-C2 (a-c), 1407-C2 (d-f) and 1408-B1 (g-i). Key microtextural features and coatings are labelled.*

Grains in all three samples often have coatings with clay minerals filling depressions in these coatings (Fig. 5.6b) or adhered to grains (Fig. 5.6h). These coatings are cut by the glacial microtextures, suggesting they formed before the debris was entrained in the ice. These grains are therefore unlikely to be derived from primary erosion of crystalline bedrock, having instead been previously deposited in a setting with clay minerals present. Salt crystals are also visible (Fig. 5.6c), suggesting saline porewater has been present; the grain coatings may therefore have formed in a marine setting. Coatings are less common and grains more angular in sample 1407-C2.

Whilst the upper two samples contain mainly monocrystalline grains showing strong evidence of glacial abrasion (Fig. 5.6 a-f), the lowermost sample in the ice column (1408-B1) was dominated by aggregates and polycrystalline grains (e.g. Fig. 5.6i), with few monocrystalline grains. This debris therefore has a different provenance and derives from erosion of finer grained sediments. Clay mineral coatings are common, and there are generally fewer features likely to have formed recently during transport in ice.

Table 5.4. *Results of electron microprobe analysis of the 210-800 μm size fraction.*

Sample	Quartz	Feldspar	Oxides	Pyroxene
1408-B1	33	67	0	0
1407-C2	32	61	7	0
1406-C2	56	32	5	7

Microprobe analysis revealed all the samples were dominated by quartz and feldspar. The uppermost sample in the ice column (1406-C2) contained the most pyroxene, suggesting more mafic source material. In the lower samples, pyroxene was absent. Feldspar abundance broadly mirrors the trends seen in the radiogenic isotope and clay mineral data, with more feldspar in the sample with the least smectite, highest $^{87}Sr/^{86}Sr$ ratio and lowest ε_{Nd} value.

5.3.4 $^{40}Ar/^{39}Ar$ Dating and Pending Analyses

The groundmass of the rhyolite porphyry clast was dated with the $^{40}Ar/^{39}Ar$ method to ~218 Ma. No formal plateau was reached, meaning this datum is still subject to some uncertainty, but this age is likely indicative. Furthermore, the $^{40}Ar/^{39}Ar$ dating of detrital hornblende (Sidney Hemming at the Lamont-Doherty Earth Observatory) and U-Pb dating of detrital zircon (Kathy Licht at Indiana University–Purdue University Indianapolis) is currently

ongoing. These data should provide information regarding the ages of the rocks from which these minerals were eroded.

5.4 Discussion

5.4.1 Debris Provenance

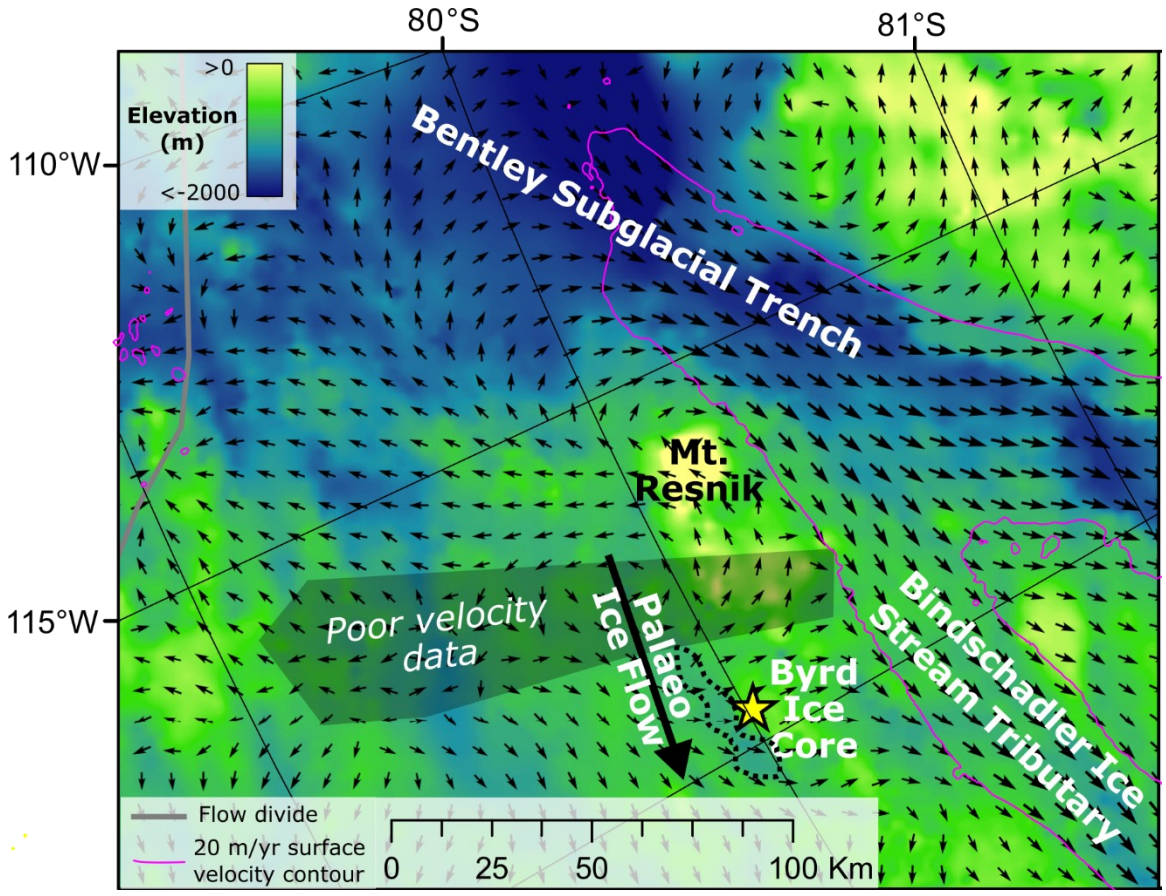


Figure 5.7. *MEaSUREs velocity vectors over the Byrd ice core location (yellow star) and upper portion of Bindschadler Ice Stream (Mouginot et al., 2019). Areas with surface ice velocities exceeding 20 m/yr are outlined by a magenta line. An area of low-quality velocity data is highlighted using dark shading. The base map is the BedMachine V1 bed topography (Morlighem et al., 2020). A palaeo ice-flow trajectory inferred from internal radar layers is shown using a black arrow (Siegert et al., 2006). The ice divide between the Amundsen Sea drainage sector to the north east and the Siple Coast drainage sector of the WAIS is indicated by the thick grey line. The black dotted line indicated a topographic low adjacent to the site.*

Gow et al. (1979) state that "We have no way of telling if the zone of basally accreted dirty ice was incorporated during a single phase of "freezing-in" or was episodic and interrupted by periods of bottom melting". Our data show there are clear changes to the composition of

the debris entrained in the ice frozen to the base of the Byrd ice core, which we interpret as the ice gradually entraining different underlying rocks and sediments as the ice moved over its bed. The trend in Nd isotope composition, which is not typically impacted by grain size sorting (Eisenhauer et al., 1999; Garçon et al., 2013), argues against sedimentary sorting processes creating the changes seen down the ice column. A weathering control on the down-core geochemical and mineralogical trend cannot be fully excluded, but is improbable given that the immobility of Sm and Nd mean that the decay system is unlikely to be perturbed by weathering (Goldstein and Hemming, 2003). Additionally, it is still uncertain whether chemical weathering in an englacial/subglacial environment is significant. Provenance change as the key control on down core trends should be confirmed by different detrital mineral age populations from the different samples down the ice column.

A change in provenance proves that accretion of the basal ice did not occur as a single phase and instead occurred episodically or gradually as the ice moved across the bed, incorporating detritus from substrate in different areas as it moved. Retention of debris which was presumably sourced from some distance away also excludes the possibility of recent complete melting of the basal debris-rich layer.

The distance the basal ice may have incorporated this debris over is uncertain. However, as the Byrd ice core site is close to the modern-day ice divide with slow surface velocities of ~4.0 m/yr (Mouginot et al., 2019) and therefore slow basal ice velocities, the Byrd ice core basal debris is unlikely to have been transported far. Assuming a subglacial origin of the englacial debris, a constant basal ice velocity of ~0.5 m/yr (DeConto et al., 2021) and a <90 ka age of the uppermost accreted basal ice (Blunier and Brook, 2001), this would imply a transport distance not exceeding 45 km for the uppermost debris (i.e., sample 1406-C2). The basal ice flow trajectory at Byrd Station is also of interest, but internal ice layers detected by radar suggest ice flow directions changed significantly at ~1.5 ka at the Byrd ice core site (Siegert et al., 2004). This makes it difficult to determine exactly where different debris may have been entrained but, despite this flow direction change, phase-based velocity mapping (Mouginot et al., 2019; Fig. 5.7) suggests that the sediment source is likely to have been broadly to the east, somewhere north of Mt. Resnik, both now and in the past.

5.4.2 Debris Endmember Contributions

The rhyolite porphyry clast may be representative of the isotopic composition of the volcanic rocks contributing to the uppermost debris in the ice column. As smectite is often derived

from mafic volcanic rocks (Ehrmann et al., 1992; Fagel, 2007) and there is a clear correlation between smectite content and Nd and Sr isotope ratios (Fig. 5.4), it may be that a change in the contribution of mafic volcanic rocks is responsible for both changes with depth. This is supported by the mineral assemblage of the sand fraction containing pyroxene (Table 5.4), suggesting mafic rocks contribute to the most smectite-rich sample 1406-C2. Specifically, higher in the basal ice column, mafic volcanic rocks together with regolith derived from the weathering of these rocks and characterised by higher ε_{Nd} values, lower $^{87}Sr/^{86}Sr$ ratios and higher smectite contents, could comprise more of the detritus than closer to the bed. Mafic equivalents to the rhyolite clast could represent this endmember, as the rhyolite also has an isotopic compositon in close agreement with the <75 μm fraction, consitent with the clast rock group comprising the majority of the debris higher in the ice column. Presence of felsic volcanic rocks in the upstream parts of Bindschadler and MacAyeal ice stream is consistent with the occurance of (rare) felsic volcanic clasts in the eastern Ross Sea (Perotti et al., 2017).

The other endmember composition, represented by sample 1408-B1, may be a mixture of granitic, felsic metamorphic and/or clastic sedimentary rocks. The mineralogical composition comprises entirely of feldspar and quartz, strongly implying felsic lithologies. It also seems the debris consists largely of reworked material derived from older sedimentary strata, as suggested by both the polycrystaline grains seen in the SEM imaging (Fig. 5.6i) and the high kaolinite content (Table 5.3). The observed downcore increase in the $^{87}Sr/^{86}Sr$ ratios of the englacial debris implies a contribution from Palaeozoic granitoids, evolved Mesozoic granitoids or Palaeozoic metasediments for the detritus closer to the bed (Fig. 5.5).

The down-core provenance changes could be interpreted as a result of the ice initially flowing over an area dominated by volcanic bedrock, with a relatively thin regolith layer or a thin sedimentary cover containing mafic rocks and pre-glacial sediments. The rhyolite clast may represent this bedrock given the close agreement of the isotope compositions (Fig. 5.4; 5.5). Some contribution from preglacial sedimentary strata is likely given the high kaolinite content of the clay mineral assemblage (Table 5.3), but the small amount of fine-grained material present suggests this contribution is very minor. The basal ice may then have gradually moved away from this region towards an area covered by thicker semi-lithified, presumably marine, sediments, as shown in the SEM images (Fig. 5.6). These are likely of pre-Oligocene age given the high kaolinite content in the clay fraction; diatom identification may help confirm this. The Nd and Sr isotopic composition of this debris is similar to the

various Mesozoic granitoids exposed along the coast of West Antarctica (Fig. 5.5), and a granitic source is also inferred from the dominance of quartz and feldspar in the sand fraction (Table 5.4).

5.4.3 Volcanic Material Beneath the WAIS

There has been discussion regarding the abundance of Cenozoic volcanic material present beneath the central area of the WAIS. Geologically young volcanoes will increase basal heat flux, influencing the flow of the overlying ice sheet, but also contribute detritus with highly radiogenic ε_{Nd} values and unradiogenic $^{87}Sr/^{86}Sr$ ratios when eroded. Evidence in favour of large volumes of volcanic material include interpretations of airborne and land-based magnetic and radar surveys, suggesting these rocks are widespread (e.g. Behrendt et al., 1994, 1996; Behrendt, 1999, 2013; van Wyk der Vries et al., 2017). Large amounts of smectite in the eastern Ross Sea also imply volcanic rocks beneath the ice sheet (Balshaw-Biddle, 1980; Marschalek et al., 2021). On the other hand, no basalt clasts of Cenozoic age have been found in the Byrd ice core or in subglacial till samples recovered from beneath the Siple Coast ice streams (Vogel et al., 2006). They are also very rare when found offshore from the eastern Ross Ice Shelf (Perotti et al., 2017). This could be due to long transport distances and/or the fact that such rocks are physically weathered, but they are nevertheless likely to be volumetrically minor. Mineral identification in sediments from the Ross Sea shelf using sand fraction petrography (Licht et al., 2005) and x-ray diffraction (Andrews and LeMasurier, 2021) also suggests there are few mafic minerals present.

The data presented here offer a potential reconciliation between these two lines of evidence. We suggest that most of the mafic volcanic rocks present beneath the WAIS are located in regions with slow ice flow, such as near the Byrd ice core, so are not eroded at present. However, in past warmer periods when the extent of the WAIS was reduced or absent, ice flow in these areas was faster, resulting in intensified subglacial erosion. This led to the deposition of smectite-rich sediments in palaeo topographic lows. When the WAIS had (re)grown and these basins in topographic lows were covered by ice, such as at the present, they were subglacially re-eroded and deposited offshore. This could explain the presence of high amounts of smectite (Balshaw-Biddle, 1980; Table A.2.5) but without the mafic volcanic protolith minerals (Licht et al., 2005; Andrews and LeMasurier, 2021) in modern and LGM Ross Sea sediments shed from the WAIS. This hypothesis does not exclude the

possibility for some Cenozoic volcanic rocks beneath the ice, but suggests the contribution of these may be relatively minor contributors to the sediment provenance signature.

5.4.4 Kaolinite as a Sediment Provenance Tracer

Offshore of Antarctica, kaolinite is only found in large quantities (>~20% of clay minerals) in the Amundsen Sea (Hillenbrand et al., 2003; Ehrmann et al., 2011; Simões Pereira et al., 2020). It has therefore been traced to sedimentary rocks in the West Antarctic interior which pre-date the beginning of glaciation in the Oligocene (Hillenbrand et al., 2003; Ehrmann et al., 2011). The source of such sedimentary strata has been traced specifically to the Thwaites catchment, and likely areas such as the Byrd Subglacial Basin and Bentley Subglacial Trench (Hillenbrand et al., 2003; Simões Pereira et al., 2020).

The high kaolinite concentration in the Byrd ice core detritus (Table 5.3) suggests that there is a consistent contribution to this detritus from pre-glacial sedimentary strata. As the debris is relatively locally sourced, this kaolinite-bearing strata must be located nearby; it could potentially be sourced from the slight topographic low immediately to the north of Byrd Station (black dotted line in Fig. 5.7). This helps to pinpoint the source of kaolinite found offshore. These kaolinite-rich clay mineral assemblages may help diagnose partial retreat of the WAIS as a greatly reduced ice extent, which has been suggested for the Last Interglacial or Pliocene by recent modelling studies (e.g. DeConto and Pollard, 2016; Golledge et al., 2017; Clark et al., 2020), may lead to fast ice flow and thus erosion further inland and close to the Byrd ice core location. Material eroded from the Byrd ice core site during partial WAIS collapse would either feed westwards towards the Ross Sea (Goelzer et al., 2016) or eastwards towards the Amundsen Sea (Clark et al., 2020), depending on which sector collapsed first. Deposition of kaolinite-rich clays further towards the modern coast might therefore provide useful constraints on the mechanisms and extent of past WAIS collapse.

5.4.5 Constraints on Offshore Nd and Sr Isotope Compositions

Neodymium and strontium isotope compositions from marine sediments and till samples obtained from drilling through ice streams offer insight into the integrated signature of West Antarctic detritus and can be used to reconstruct WAIS history (e.g. Farmer et al., 2006; Marschalek et al., 2021). Studies focussing on such analyses have show that some regions of West Antarctica have a rock endmember with a high ε_{Nd} value and low $^{87}Sr/^{86}Sr$ ratio compared to sediments from East Antarctica (Farmer et al., 2006; Marschalek et al., 2021).

However, isotopic sediment provenance techniques struggle to identify this endmember as they cannot differentiate mixtures of different rock endmembers that can give the same sediment isotope ratio. This poses a problem in diagnosing the isotopic signature of detritus from West Antarctica as, mixed in different proportions, either Cenozoic volcanic rocks or Mesozoic igneous rocks towards the high ε_{Nd} value/low $^{87}Sr/^{86}Sr$ ratio end of their range could provide the high ε_{Nd} value/low $^{87}Sr/^{86}Sr$ ratio endmember (Fig. 5.5). Volcanic endmembers are also unlikely to be zircon, hornblende or biotite bearing in size fractions coarse enough for dating, meaning they cannot be identified by detrital mineral dating (e.g. Cook et al., 2017).

By showing that an endmember with an ε_{Nd} value of ~-3, likely with a significant contribution from rocks of early Mesozoic age, is present beneath at least part of the WAIS, we help resolve this debate. The rhyolite porphyry cobble contained within the uppermost sample (1406-C2) suggest an endmember rock type contributing to the detritus of -2.7. These radiogenic ε_{Nd} values suggest mixing between this endmember and less radiogenic rocks can explain the integrated ε_{Nd} values of ~-6 to -7 characterising offshore sediments (Famer et al., 2006; Marschalek et al., 2021). Although a small amount of Cenozoic volcanic material may well be contributing to the provenance of marine sediments, there is no need for a substantial contribution from these rocks to explain the ε_{Nd} values of sediments beneath ice streams and offshore.

5.4.6 Rhyolite Clast

Although the possibility for transport in a 'palaeo iceberg' cannot be excluded, the ~218 Ma age of the rhyolite porphyry clast implies this rock type is present locally. Rocks of this age in central West Antarctica have not previously been observed directly, although they have been inferred from detrital mineral dating. U-Pb dated detrital zircons of this age are found in WAIS-derived sediments in the Ross Sea (Licht et al., 2014; Perotti et al., 2017; Marschalek et al., 2021) and $^{40}Ar/^{39}Ar$ dated hornblende and biotite in the Amundsen Sea (Simões Pereira et al., 2018; 2020). These detrital mineral populations typically show a broad peak spanning ~250-180 Ma. The lack of coastal outcrops of comparable age suggests that clasts of Triassic-Jurassic age derive from sources far inland (Perotti et al., 2017), and the Byrd ice core rhyolite supports this inference. We note, however, that this rhyolite is itself unlikely to yield zircon, hornblende or biotite grains of sufficient size to be measurable in detrital sediments. It

must therefore be associated with widespread intrusive magmatism, likely granitoids, of similar age.

The occurrence of a Triassic rhyolite is difficult to compare to outcropping rock types. Triassic activity in Antarctica is best recorded in the Antarctic Peninsula and Thurston Island block. The clast age falls within the Peninsula Orogeny (220-207 Ma; Riley et al., 2020). However, rocks of this age are typically metamorphic or plutonic (Riley et al., 2020). Rhyolites are nevertheless common on the Antarctic Peninsula, where the Jurassic silicic volcanic rocks of the voluminous Chon Aike Province outcrop (Pankhurst et al., 2000; Riley et al., 2001). However, these rhyolites are younger, typically spanning ~188-145 Ma (Pankhurst et al., 2000; Bastias et al., 2021). They are also isotopically dissimilar, with $^{87}Sr/^{86}Sr$ ratios that are too low and ε_{Nd} values that are too high (Riley et al., 2001) or, on Alexander Island, the opposite case, with $^{87}Sr/^{86}Sr$ ratios that are too high and ε_{Nd} values that are too low (McCarron and Smellie, 1998). Volcanic rocks with more similar isotopic ranges to the Byrd rhyolite are, however, found at Parker Peak on Thurston Island (Pankhurst et al., 1993). These rocks are loosely dated to the Jurassic and have $^{87}Sr/^{86}Sr$ ratios with a mean of 0.705788 (n = 4), in very close agreement with the measured clast. A single ε_{Nd} measurement gave a value of -4.8 (Pankhurst et al., 1993), slightly less radiogenic (lower) than the Byrd core clast, but not too dissimilar. The Thurston Island block may therefore provide the closest match outcropping analogue, although the poor dating of the Parker Peak rhyolite (approximately 190-150 Ma; Pankhurst et al., 1993) mean these rocks could be of a very different age, implying a different tectonic setting and magmatic history. The rhyolite porphyry from the Byrd ice core is therefore difficult to correlate to other known rock types and represents a previously uncharacterised lithology beneath the WAIS.

5.5 Conclusions and Future Work

The debris-rich basal ice of the Byrd ice core records a significant change in provenance with depth in the ice column, showing that the ice was accreted over different parts of the bed and not in a single episode. The upper debris is primarily comprised of the rock group represented by the rhyolite clast or rocks with a similar isotopic composition. There are also minor contributions from mafic rocks and pre-glacial sedimentary strata. The lower debris shows a transition to flow over a bed with semi-lithified sediments of pre-glacial age. These sediments derive from felsic protoliths.

The high fraction of kaolinite at the site has the potential to help trace past collapse of the WAIS. If there was retreat of the ice sheet margin in the Ross Sea towards a position near the modern ice divide, as ice sheet modelling suggests might have occurred in the geologically recent past (e.g. DeConto and Pollard, 2016; Golledge et al., 2017), then fast ice flow and erosion would be expected to shift towards the Byrd ice core site. This would lead to a greater input of kaolinite to the Ross Sea. Future sediment provenance studies will also benefit from the knowledge that rocks with a relatively high ε_{Nd} value and low $^{87}Sr/^{86}Sr$ ratio, but not linked to Cenozoic volcanism, are present beneath at least part of the WAIS. Such rocks may provide the high ε_{Nd} value and low $^{87}Sr/^{86}Sr$ ratio endmember observed in West Antarctic sediments deposited offshore (Farmer et al., 2006; Simões Pereira et al., 2018; 2020; Marschalek et al., 2021) if Cenozoic volcanic rocks are less prevalent than magnetic anomalies would suggest (Vogel et al., 2006; Andrews and LeMasurier, 2021).

The rhyolite porphyry clast has no comparable exposed rocks of a similar age and lithology and represents the first measured rock of Triassic age from the WAIS interior, corresponding to sediments around the continental margin.

Detrital mineral dating, both zircon U-Pb and hornblende $^{40}Ar/^{39}Ar$, are still in progress. Whilst the clast date of ~218 Ma provides useful information about this individual rock type, detrital mineral data will provide information regarding how representative this single date is of the broader local geology. Such data will also provide an endmember to compare to similar data offshore or under the ice seeking to constrain WAIS retreat or collapse.

Diatom results are also still to come. If present in sufficient quantity, these will help date the age of pre-Oligocene sediments and could potentially determine when the site was last exposed to the ocean. Combined with planned cosmogenic nuclide surface exposure dating, this may help determine the time of the most recent WAIS collapse.

Chapter 6. New Insight into Ross Sea Sediment Provenance from Subglacial Sediments

James Marschalek conducted the Nd and Sr isotopic analyses. James Marschalek and Pieter Vermeesch performed the zircon U-Pb dating of the HWD-2b sample. The KIS-GZ, HWD-2b and J9 cores were provided by Gavin Dunbar. Sampling of the Whillans grounding zone sediment core was performed by Mark Skidmore. Theo Calkin and Gavin Dunbar provided clast and sand petrographic data for the HWD-2b core.



Outside of the core barrel of the sediment core obtained from the Kamb Ice Stream Grounding Zone site during a New Zealand-led field campaign in 2019/2020 where hot water drilling and gravity coring was conducted. Photo courtesy of Gavin Dunbar.

Chapter Summary

Interpretation of sediment provenance records from the Ross Sea (e.g. Chapter 2) rely on knowledge of the composition of till and rocks beneath the West Antarctic Ice Sheet (WAIS) (e.g. Chapter 5). To build upon this knowledge, Nd and Sr isotope compositions were collected for short cores from close to the grounding zone of two West Antarctic ice streams (Kamb and Whillans) and two locations below the Ross Sea ice shelf (J9 and HWD-2b).

The seafloor surface samples near the grounding zones of Kamb Ice Stream and Whillans Ice Stream yielded ε_{Nd} values of -7.0 and -8.6, respectively, closely resembling published results from further upstream (Farmer et al., 2006; ε_{Nd} ~-7.0 and ~-8.4). This implies that either the sediments beneath these ice streams are relatively well mixed in their lower trunks, or that little erosion of new rock or sediment occurs in their lower trunks.

Seafloor surface sediment at the J9 site, to the west of the Kamb and Whillans ice streams and below the Ross Ice Shelf, yielded an ε_{Nd} value of -7.3, in between the values of ~-7.0 and ~-8.4 previously measured for the neighbouring Kamb and Whillans ice streams, respectively (Farmer et al., 2006). This suggests a mixed provenance from Kamb and Whillans ice streams at the J9 site, compatible with the centennial timescale cycles of stagnation and reactivation observed for these ice streams changing ice flow trajectories over the site (Hulbe and Fahnestock, 2007).

Seafloor surface sediment at the HWD-2b site, located in the central Ross Ice Shelf, can be clearly traced via its provenance signature (ε_{Nd} value of -10.9, $^{87}Sr/^{86}Sr$ ratio of 0.732341) and modern ice flow lines to the Liv/Scott Glacier region. However, downcore the values reach -7.7 and 0.726945, suggesting a very different sediment source. Modelled LGM ice flow lines would suggest ice flow from Nimrod Glacier, but this glacier is characterised by low ε_{Nd} values of <~-12 (Farmer and Licht, 2016) which do not match observations at HWD-2b. The downcore sediment source remains difficult to pinpoint, but likely lies south of Nimrod Glacier, between Beardmore and Shackleton glaciers. Consequently, there is a mismatch between the sediment provenance data and LGM ice sheet models. This suggests either that the HWD-2b core diamict records a late stage of deglaciation, or that ice flow into the central Ross Sea during deglaciation is not well represented in current ice sheet models.

6.1 Introduction

Sediment provenance records from the Ross Sea, such as those discussed in Chapter 2, benefit from widespread exposures in the Transantarctic Mountains to constrain sediment sources. However, most of the eastern Ross Sea catchment is covered by the WAIS. This hinders geological characterisation of the region, and limits direct petrographic, geochronological and geochemical sampling. Insights into the average subglacial geology can be obtained from offshore sediment provenance studies (e.g. Roy et al., 2007; Simões Pereira et al., 2018), and this knowledge can be refined and spot-checked with hot water drilling which can access the sediments beneath the ice sheet/shelf. Such subglacial material is key for more precise interpretation of offshore records in the Ross Sea and beyond. In particular, the upcoming 'Sensitivity of the West Antarctic Ice Sheet to +2 °C' (SWAIS-2C) project, which aims to collect Last Interglacial sediments from near the grounding zone of Kamb Ice Stream, will benefit from improved knowledge of subglacial geology around the Ross Sea (Patterson et al., 2022).

Until recently, the significant costs and technical challenges associated with recovering subglacial sediments have limited provenance data collected from subglacial samples in the Ross Sea sector of the WAIS to three sites from glaciological drilling through Whillans, Kamb and Bindschadler Ice Streams in the 1990s, plus a site beneath the Ross Ice Shelf drilled as part of the Ross Ice Shelf Project (J9) (Fig. 6.1; 6.3). These samples have been analysed for Nd and Sr isotopes (Farmer et al., 2006), sand fraction petrography (Licht et al., 2005) and detrital zircon U-Pb dates (Licht et al., 2014), providing invaluable information regarding the rocks and sediments present beneath the WAIS to compare to marine sediments. We here expand the spatial coverage of these measurements to new sites beneath the Ross Sea sector of the WAIS drilled in recent years. Newly available sample locations include ones near the grounding zone of Kamb and Whillans ice streams, plus two samples from beneath the Ross Ice Shelf (Fig. 6.1). Details of these sites are provided below. These new sediment samples can shed light onto the regional geology and, by comparison to samples further upstream, the processes of mixing down ice flow lines. Downhole trends were examined at some sites, elucidating Last Glacial Maximum (LGM) to recent changes to ice flow. Interpretations are reliant on an understanding of local Antarctic geology; a relevant summary for the Ross Sea sector can be found in Section 2.3.

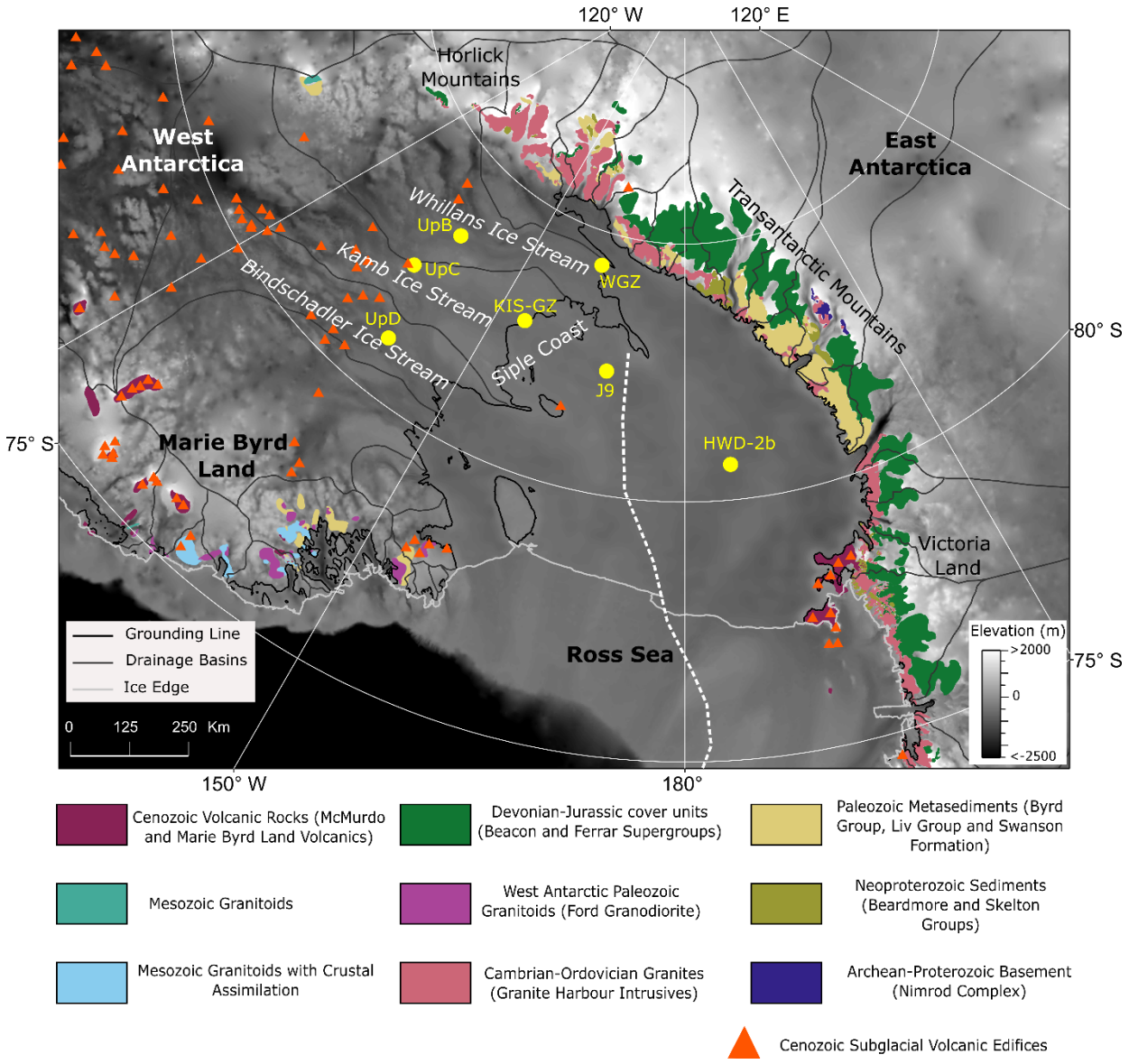


Figure 6.1. *Geological map of the Ross Sea region, based on Marschalek et al. (2021) Fig. 1. The outcropping regional geology (Cox et al., 2019) around the Ross Sea is overlain on the BedMachine Antarctica V1 modern bed topography (Morlighem et al., 2020). The MEaSUREs grounding line, ice sheet margin and basins are used (Rignot et al., 2013; Mouginot et al., 2017). The white dashed line indicates the boundary between East and West Antarctic lithosphere (Tinto et al., 2019). Orange triangles show potential Cenozoic subglacial volcanic edifices detected based on morphological characteristics, gravity anomalies and magnetic anomalies (van Wyk de Vries et al., 2017).*

6.2 Samples Sites

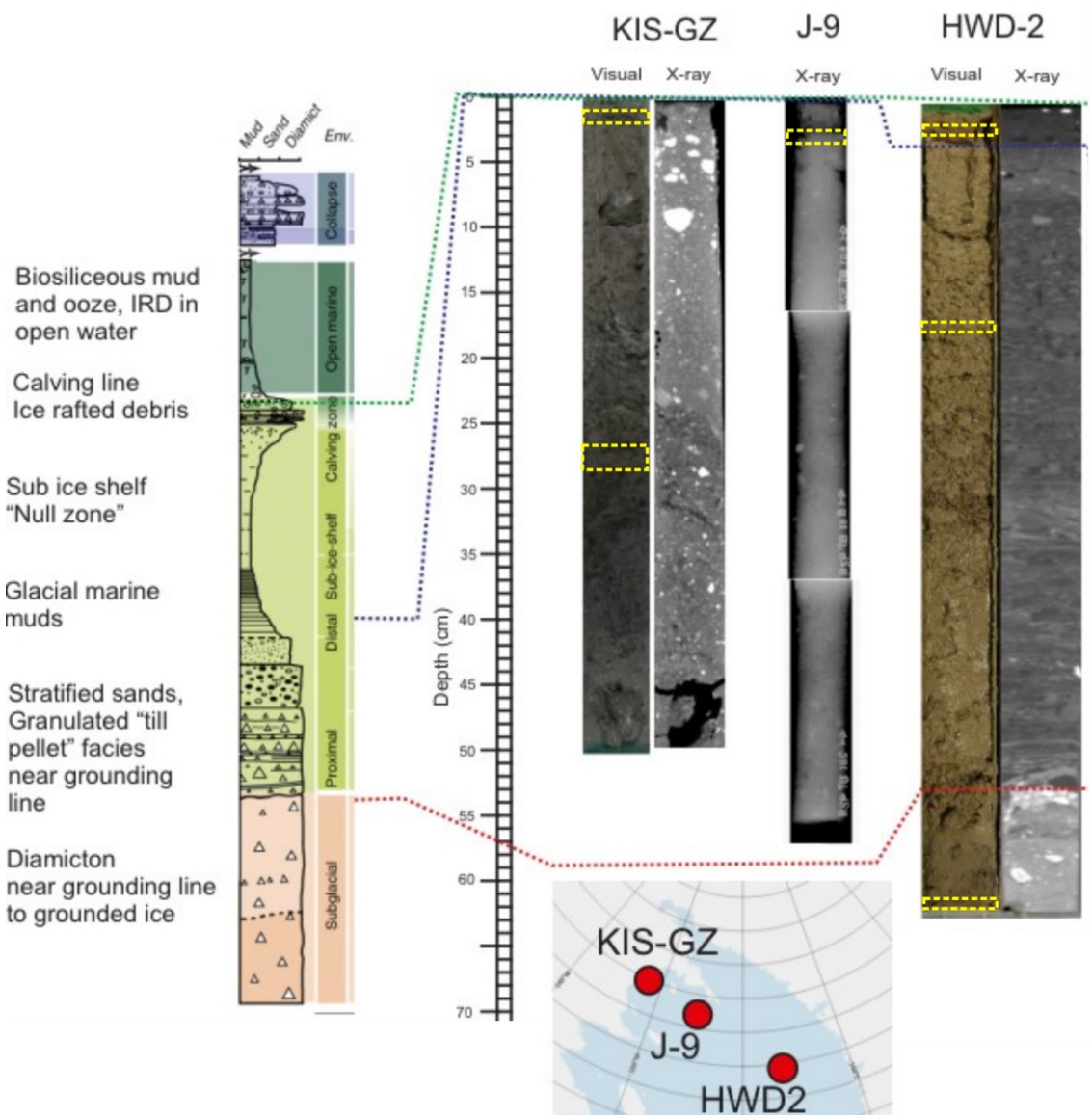


Figure 6.2. *Core photographs and x-ray scans of three of the sediment cores, with sample depths indicated using yellow dashed boxes. Lithologies are placed in the context of the glacial retreat facies synthesis of Smith et al. (2019). Figure adapted from Calkin et al. (in prep.). The WGZ sample is excluded as core photography was not available.*

6.2.1 J9

The J9 site (82º22.5'S, 168º37.5'W) was cored as part of the Ross Ice Shelf Project in the 1970s (Clough and Hansen, 1979). The site is located ~200 km from the grounding zone in the centre of the Ross Ice Shelf (Fig. 6.1). Eleven gravity cores up to 102 cm in length were collected (Webb et al., 1979). Lithologically, cores at the site comprise entirely of

diatomaceous sandy mud containing gravel-sized clastic material and sediment clasts (Fig. 6.2; Webb et al., 1979; Kellogg and Kellogg, 1986). Granite, gneiss, schist and sedimentary clasts were found, with Ferrar dolerite and Beacon Supergroup rocks notably absent. Farmer et al. (2006) analysed the Nd and Sr isotope composition of the sediments towards the base of the core, but did not examine the seafloor surface sediments. The core was therefore resampled in 2020 by Gavin Dunbar and a sample taken at a depth of ~3 cm below the sea floor (cm bsf). The new sample is thus assumed to represent late Holocene deposition.

6.2.2 Kamb Ice Stream Grounding Zone (KIS-GZ)

The Kamb Ice Stream Grounding Zone (KIS-GZ) site (82º47.52'S, 154º32.70'W), approximately 4 km seaward of the grounding zone, was accessed via hot water drilling in 2019 by a team from New Zealand (Calkin et al., in prep.). A 49 cm core comprising weakly stratified sandy diamict with dioritoid, granitoid, immature sandstone and conglomeritic clasts was recovered using a gravity corer (Fig. 6.2; Calkin et al., in prep.). These clast lithologies are consistent with known rock types in the nearby Transantarctic Mountains and beneath the WAIS (see geological summaries in other chapters). Excess ^{210}Pb suggests the entire core is <120 years old (Calkin et al., in prep.). Diatoms are Oligocene to Miocene in age (Calkin et al., in prep.) and the taxa are similar to the Miocene sediments with a West Antarctic provenance recovered from IODP Site U1521 (see Chapter 2). Two samples from KIS-GZ at depths of 1-2 and 26.5-28.5 cm bsf were provided by Gavin Dunbar to investigate Nd and Sr isotope composition of the surface sediments and identify any change with depth. A large amount of sediment was also stuck to the outside of the core barrel, providing a large sample for zircon U-Pb dating.

6.2.3. Hot Water Drill 2b (HWD-2b)

The Hot Water Drill 2b (HWD-2b) site is located in the central portion of the Ross Ice Shelf at 80°39.50'S, 174°27.68'E (Stevens et al., 2020). The access hole was drilled in December 2017 by a New Zealand team and cored using a gravity corer. An overconsolidated diamict, likely representing subglacial deposition, was recovered at the base, followed by a 47 cm till pellet facies (Calkin et al., in prep.) which probably formed in a subglacial to proximal glacimarine environment (Robinson et al., 2021). The till pellet facies is overlain by ~7 cm of fine muds, likely to reflect subsequent sub-ice shelf deposition (Fig. 6.2). This sedimentary succession is interpreted as recording the retreat of the ice sheet following the end of the last

glacial period (Calkin et al., in prep.). The core thus potentially spans several millennia, although precise dating of the core remains difficult. A sample from each facies was provided by Gavin Dunbar.

6.2.4 Whillans Grounding Zone (WGZ)

Gravity cores were taken from beneath Whillans Grounding Zone (WGZ) as part of the Whillans Ice Stream Subglacial Access Research Drilling (WISSARD) project in 2014/5 (Tulackzyk et al., 2014; Puttkammer, 2016). The WISSARD project was led by the US, and also recovered sediments from Subglacial Lake Whillans, which are not discussed here. The longest WGZ gravity core recovered sediment to ~85 cm below the seafloor. The core's base up to 47 cm bsf is a clast poor, muddy diamict with till pellets (Puttkammer, 2016). Above this is 13 cm of silty-sandy diamict, overlain by a further 30 cm of the muddy diamict with till pellets similar to the base of the core. The upper 4 cm of sediment consists of rainout debris with an absence of till pellets (Puttkammer, 2016). Three samples were taken to explore any changes in provenance over time. Samples spanned 63-61 cm bsf (the lowermost muddy diamict), 35-33 cm bsf (the top of the sandy diamict, containing the greatest concentration of pebbles) and 8-6 cm bsf (the top of the uppermost muddy diamict). The samples were sieved at 63 μm during processing, qualitatively revealing the samples were increasingly fine-grained up core.

6.3 Methods

The nine sediment samples were prepared for Nd and Sr isotope measurements by sieving to isolate the <63 μm fraction, which is assumed to be representative of the bulk sediment as samarium and neodymium are incorporated in equal proportions into most rock-forming minerals, meaning grain-size sorting is not likely to impact results (Goldstein and Hemming, 2003; Garçon et al., 2013). This fraction was leached in a mixture of 0.05 M hydroxylamine hydrochloride, 15% acetic acid, and 0.03 M EDTA at a pH of 4 (Gutjahr et al., 2007). A carbonate removal step was not included as a very low carbonate content was anticipated given the sub-ice sheet settings of the cores. Leached sediment was dried, homogenised, and 50 mg aliquots were digested on a hotplate in concentrated HF, $HClO_4$, and HNO_3 for three to five days. Samples were processed alongside ~75 mg of USGS BCR-2 rock standard. The Nd was isolated from the sample matrix using a cation exchange resin (AG50W-X8, 200-400 μm mesh) and HCl in increasing molarity, followed by a low molarity HCl Ln-Spec resin

procedure (50–100 μm mesh). The sample matrix from the cation exchange step was dried, taken up in HNO_3, then loaded onto Eichrom Sr Spec resin to wash down the matrix and elute the Sr (Simões Pereira et al., 2018).

Neodymium isotopes were measured in the MAGIC laboratories at Imperial College London on a Nu high resolution multi-collector inductively coupled plasma mass spectrometer (HR MC-ICP-MS). To account for instrumental mass bias, isotope ratios were corrected using an exponential law and a $^{146}Nd/^{144}Nd$ ratio of 0.7219. Although negligible, interference of ^{144}Sm on ^{144}Nd was corrected for. Bracketing standards were used to correct measured $^{143}Nd/^{144}Nd$ ratios to the commonly used JNdi-1 value of 0.512115 (Tanaka et al., 2000). USGS BCR-2 rock standard measurements yielded $^{143}Nd/^{144}Nd$ ratios of 0.512638 ± 0.000008 (n = 6), identical to the published ratio of 0.512638 ± 0.000015 (Weis et al., 2006). Full procedural blanks for Nd were 13-22 pg. $^{143}Nd/^{144}Nd$ ratios are expressed using epsilon notation (ε_{Nd}), which denotes the deviation of a measured ratio from the modern Chondritic Uniform Reservoir (0.512638) in parts per 10,000 (Jacobsen and Wasserburg, 1980).

Strontium isotopes were measured in the MAGIC laboratories at Imperial College London on a Triton TIMS (Thermal Ionisation Mass Spectrometer). Samples were loaded in 1 μL of 6M HCl onto degassed tungsten filaments with 1 μL of $TaCl_5$ activator. The measured $^{87}Sr/^{86}Sr$ ratios were corrected for instrumental mass bias using an exponential law and an $^{88}Sr/^{86}Sr$ ratio of 8.375. Interference of ^{87}Rb was corrected for using an $^{87}Rb/^{85}Rb$ ratio of 0.386. Analyses of the NIST 987 standard reference material were completed every four unknowns, yielding a mean of 0.710307 ± 0.000042 (2SD, n = 39). Samples were corrected to the published value of 0.710252 ± 0.000013 (Weis et al., 2006). The relatively poor reproducibility for our NIST 987 runs was due to technical issues, but is still insignificant given natural changes in the $^{87}Sr/^{86}Sr$ ratio of bedrock around West Antarctica in the 3rd to 4th digit. Accuracy of results was confirmed using rock standard USGS BCR-2, processed with every batch of samples, which yielded $^{87}Sr/^{86}Sr$ ratios of 0.705010 ± 0.00028 (2SD, n = 12). This is in close agreement with the published ratio of 0.705013 ± 0.00010 (Weis et al., 2006).

6.4 Results and Discussion

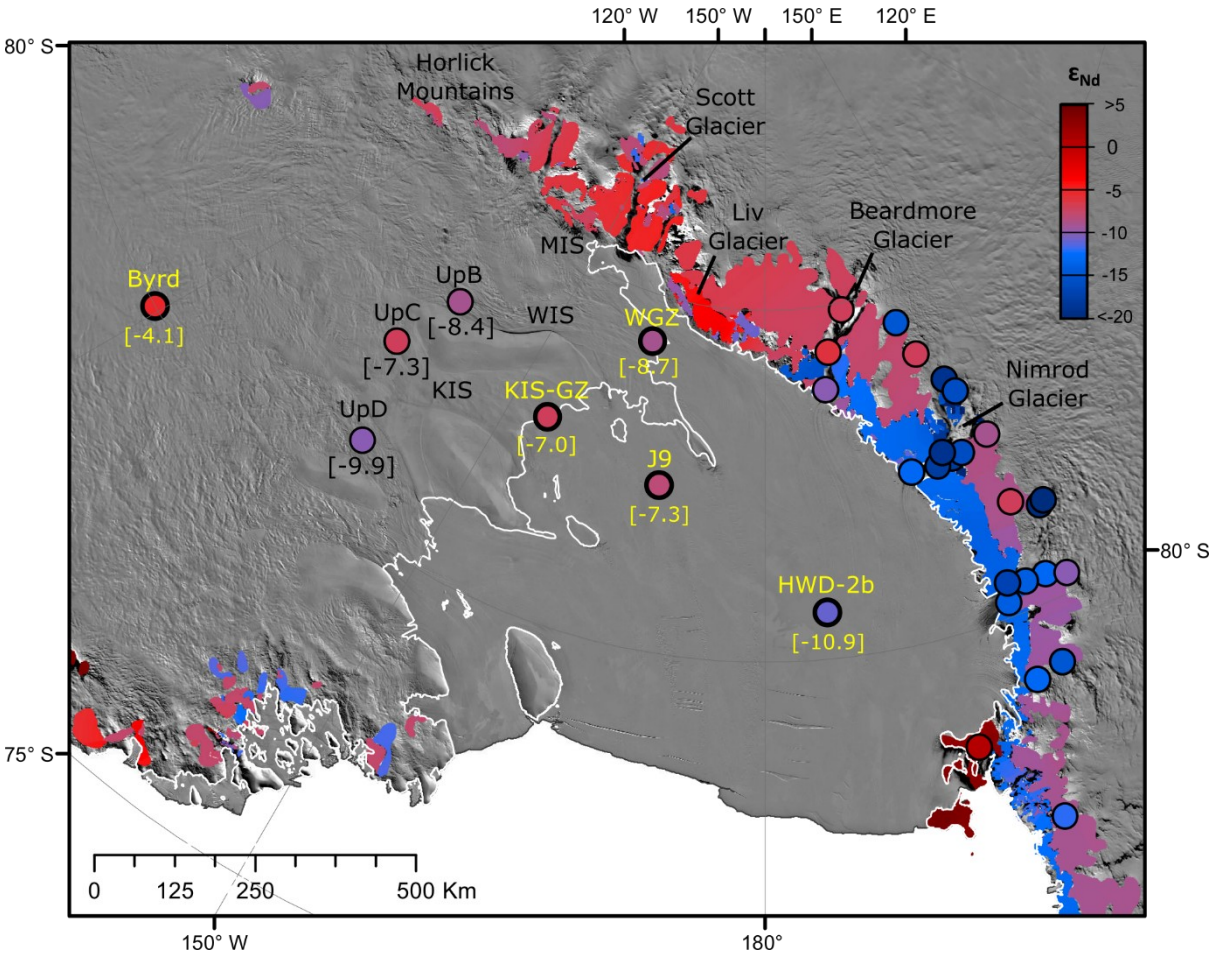


Figure 6.3. *Map of ε_{Nd} values around the Ross Sea as complied in Marschalek et al. (2021). New subglacial core top data have a bold outline and are labelled using yellow text with the site and ε_{Nd} values in square bracket. This includes the new data from the Byrd Ice Core (see Chapter 5). Other circles denote literature measurements of unconsolidated sediment (Farmer et al., 2006; Farmer and Licht et al., 2016). Also labelled are key Transantarctic Mountain glaciers, Whillans Ice Stream (WIS), Kamb Ice Stream (KIS) and Mercer Ice Stream (MIS). Data are plotted on MODIS imagery (Haran et al., 2014), with the grounding line position from MEaSUREs data (Rignot et al., 2013; Mouginot et al., 2017). Modified from Marschalek et al. (2021) Fig. S4.*

Table 6.1 *Neodymium and strontium isotope data collected at the new sub-ice sites. The 2 standard deviation errors reported for the ε_{Nd} values are based on the JNdi-1 measurements during each session.*

Site	Upper depth (cm bsf)	Lower depth (cm bsf)	Midpoint depth (cm bsf)	$^{143}Nd/^{144}Nd$	2SE	ε_{Nd}	2SD	$^{87}Sr/^{86}Sr$	2SE
J9	2.5	3.5	3	0.512265	0.000008	-7.27	0.19	0.725563	0.000008
KIS-GZ	1	2	1.5	0.512280	0.000009	-6.99	0.19	0.725471	0.000007
KIS-GZ	26.5	28.5	27.5	0.512274	0.000009	-7.10	0.19	0.724382	0.000007
HWD-2b	2	3	2.5	0.512079	0.000007	-10.91	0.19	0.732341	0.000008
HWD-2b	17	18	17.5	0.512156	0.000011	-9.40	0.19	0.734232	0.000008
HWD-2b	61	62	61.5	0.512243	0.000009	-7.71	0.19	0.726945	0.000008
WGZ	61	63	62	0.512206	0.000013	-8.42	0.31	0.731458	0.000008
WGZ	33	35	34	0.512199	0.000012	-8.56	0.31	0.731949	0.000008
WGZ	6	8	7	0.512190	0.000013	-8.74	0.31	0.730801	0.000009

6.4.1 J9

The seafloor surface sediments at the J9 site had an ε_{Nd} value of -7.27 ± 0.19 and $^{87}Sr/^{86}Sr$ ratio of 0.725562 ± 0.000008 (Fig. 6.3; Table 6.1). Ice flow over site J9 is complicated by the centennial stagnation/reactivation cycles of the Siple Coast ice streams, which cause ice provenance to change (Hulbe and Fahnestock, 2007). At the present day, the provenance of this ice at this site lies at the border between the Whillans Ice Stream (WIS) and Mercer Ice Stream (MIS) catchments (Hulbe and Fahnestock, 2007). However, compared to the new ε_{Nd} value of -7.3 for the J9 site, WIS has less radiogenic ε_{Nd} values of -8.0 and -8.8 (Farmer et al., 2006). This suggests the sediment reaching site J9 is unlikely to be sourced from this glacier.

MIS sediment has not been characterised, but rocks may be relatively radiogenic in the region and sediment produced beneath MIS could feasibly reach values of ~-7 (Fig. 6.3). This ice stream is part of the WAIS but, as most of its catchment drains or lies adjacent to the East Antarctic Transantarctic Mountains, its provenance signature is dominated by Transantarctic Mountain rocks (Licht et al., 2014). This is a region where Beacon Supergroup and Ferrar Group rocks are common. These rock types are absent from the clasts at the J9 site, suggesting this sediment source is unlikely (Webb et al., 1979).

The sediment beneath Kamb Ice Stream (KIS), with ε_{Nd} values of ~-7 (Farmer et al., 2006), is also a close match with the -7.27 measured at site J9 (see KIS-GZ section below). The current stagnation of KIS means that ice derived from this ice stream could well flow over site J9 when KIS is fast flowing. The J9 sample may therefore represent a KIS provenance,

potentially with a contribution from the WIS catchment as the value of -7.3 lies between those of KIS (~-7) and WIS (~-8.4) (Farmer et al., 2006; Table 6.1). Further evidence for a mixture of WIS and KIS sediment is the $^{87}Sr/^{86}Sr$ ratio of ~0.726 for the J9 sample (Table 6.1), which lies between the KIS (~0.720) and WIS (~0.731) ratios (Farmer et al., 2006). Diatom assemblages are distinct from the KIS-GZ site (Calkin et al., in prep.; see section 6.3.2), also suggesting a direct KIS provenance is unlikely.

No samples were taken from lower in the core, but Farmer et al. (2006) measured Nd and Sr isotope compositions at two additional J9 cores in sediments assumed to represent retreating facies at the end of the last glacial period. Their ε_{Nd} values of -8.2 and -8.3 are less radiogenic than the seafloor surface sediment measured here. We tentatively suggest that this sediment from lower in J9 may be sourced from a part of the WIS catchment, consistent with ice sheet models showing more East Antarctic ice flow forcing flow lines in the Ross Ice Shelf further east during the LGM (Golledge et al., 2013; Fig. 6.5c).

6.4.2 KIS-GZ

The Nd and Sr isotope measurements on the KIS-GZ samples revealed ε_{Nd} values at the two different stratigraphic heights were within error of each other: -6.99 ± 0.19 and -7.10 ± 0.19 for the upper and lower samples, respectively. $^{87}Sr/^{86}Sr$ ratios were 0.725471 and 0.724382 (± 0.000007) at the respective depths, also in very close agreement.

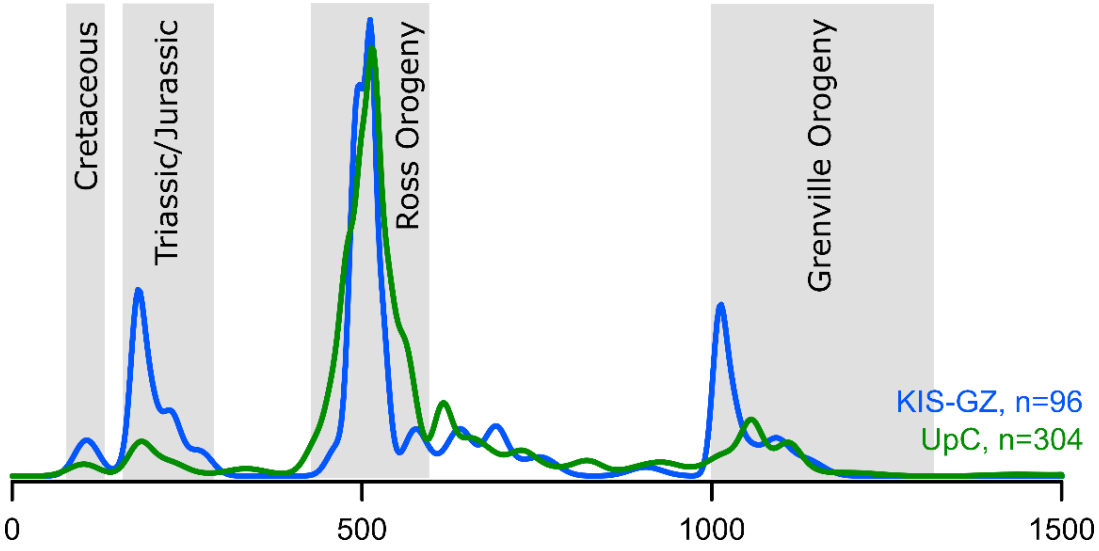


Figure 6.4. *Zircon U-Pb age kernel density estimate for the KIS-GZ site (this study) and the upstream Kamb Ice Stream ('UpC') site (Licht et al., 2014). The number of sampled zircon grains is indicated (n).*

A sample of the material covering the outside of the core barrel also provided an opportunity for statistical analysis of zircon U-Pb ages (Fig. 6.4; Table 6.2). As the radiogenic isotope data suggest little provenance change with depth in the core, this sample is likely to be representative of the entire core regardless of stratigraphic position. These data revealed few Paleoproterozoic grains (3 out of 96), a significant Grenville age peak (~1010 Ma), a dominant Pan-African/Ross Orogeny peak (~505 Ma) and more minor populations of late Triassic/Jurassic grains (~175-225 Ma; 14 out of 96) and Cretaceous grains (~115-100 Ma; 3 out of 96). These populations closely agree with the age spectra seen in the 'UpC' site from further upstream Kamb Ice Stream (Licht et al., 2014). Contrasts between the two sites include the relative size of the Ross Orogeny peak, which is more dominant at UpC. The peak associated with the Grenville Orogeny is also larger and younger at KIS-GZ.

The Nd isotope composition at KIS-GZ varies little with stratigraphic depth, implying consistent ice flow trajectories above the site during the sediment's deposition. Furthermore, the values at the KIS-GZ site (~-7) are in close agreement with the two measurements from a Kamb Ice Stream site further upstream (-7.6 and -7.0; 'UpC' site), implying a similar mixture of rock types (Farmer et al., 2006). A consistent sediment source between the UpC and KIS-GZ sites is also indicated by the close alignment of peaks in the zircon U-Pb data. For instance, the dominant Ross Orogeny peak is nearly exactly the same age (~505-510 Ma) in both samples (Fig. 6.4). Differences between the sites exist, but are small compared to contrasts between the different Siple Coast ice streams (Licht et al., 2014). The reduced dominance of the Ross Orogeny peak in the grounding zone site sample may be linked to different method choices used in the analyses. Perhaps most importantly, these new data were collected from a broader range of grain sizes (~30-300 μm) than the upstream data (63-150 μm; Licht et al., 2014). If zircons falling in the 63-150 μm size range are biased towards Ross Orogeny ages, this could explain the difference in the relative sizes of the peaks. The close agreement between the UpC and KIS-GZ sites suggests that either the debris entrained between these sites has a near identical composition, or that little generation of new till occurs between the sites.

Table 6.2. *New zircon U-Pb data for the KIS-GZ sample at the London Geochronology Centre.*

Grain No.	U (ppm)	Th (ppm)	Th/U	238U/ 206Pb	±s.e.	207Pb/ 206Pb	±s.e.	207/235 Age	±s.e.	206/238 Age	±s.e.	207/206 Age	±s.e.	Conc. Age	±s.e.	Disc. (%)
1	3127.4	166.2	0.05	5.42	0.0564	0.0759	0.0009	1091.6	10.4	1091.6	10.4	1091.5	23.2	1091.6	9.5	0.0
2	1071.6	385.1	0.36	5.75	0.0607	0.0765	0.0010	1058.4	10.8	1034.3	10.1	1108.3	25.1	1043.7	9.6	3.4
3	164.3	79.7	0.49	5.92	0.0777	0.0712	0.0022	992.8	21.1	1006.5	12.2	962.8	62.5	1004.7	12.0	-2.1
4	1145.3	267.0	0.23	11.85	0.1264	0.0584	0.0009	526.06	7.41	522.15	5.35	543.1	31.8	522.7	5.3	0.9
5	528.1	193.9	0.37	5.25	0.0563	0.0765	0.0011	1117.7	11.8	1123.2	11	1107	27.4	1120.9	10.2	-0.7
6	1332.6	110.6	0.08	9.39	0.0995	0.0619	0.0008	656.43	8.2	652.68	6.58	669.3	28.4	653.5	6.4	0.8
7	2069.6	1419.8	0.69	8.90	0.0942	0.0760	0.0010	790.24	9.27	686.56	6.9	1095.2	26.3	692.3	7.1	19.5
8	1493.9	1036.3	0.69	35.93	0.4261	0.0514	0.0014	182.8	5	176.95	2.07	259.1	63	177.0	2.1	3.5
9	1546.1	1309.5	0.85	33.42	0.3686	0.0500	0.0010	190.16	3.99	190.05	2.07	191.6	47	190.1	2.1	0.1
10	2619.2	768.5	0.29	38.31	0.4110	0.0493	0.0009	165.73	3.11	166.09	1.76	160.6	40.3	166.1	1.8	-0.2
11	1636.6	508.3	0.31	55.25	0.6105	0.0479	0.0013	114.63	3.22	115.64	1.27	93.8	65.2	115.6	1.3	-0.9
12	970.3	688.8	0.71	11.72	0.1249	0.0579	0.0009	527.35	7.7	527.98	5.4	524.6	33.7	527.9	5.3	-0.2
13	1572.2	785.3	0.50	8.81	0.0923	0.0625	0.0008	692.9	8.37	693.27	6.89	691.7	27.6	693.2	6.7	-0.1
14	1222.1	760.2	0.62	12.40	0.1323	0.0586	0.0009	508.98	7.21	499.94	5.13	549.8	31.7	501.0	5.1	2.2
15	503.6	185.7	0.37	11.76	0.1301	0.0558	0.0012	510.57	9.45	525.96	5.58	442.2	46.3	524.5	5.5	-3.7
16	853.6	232.7	0.27	11.72	0.1263	0.0582	0.0009	529.38	7.95	528.04	5.46	535.2	35	528.2	5.4	0.3
17	912.0	118.3	0.13	12.07	0.1341	0.0599	0.0011	529.39	8.67	513.05	5.48	600.4	38.6	514.4	5.5	4.0
18	898.2	562.7	0.63	12.62	0.1354	0.0568	0.0009	490.21	7.61	491.47	5.08	484.3	36.1	491.3	5.0	-0.3
19	2783.5	2261.0	0.81	30.33	0.3220	0.0674	0.0010	271.13	4.26	209.11	2.18	848	29.9	203.8	2.2	29.5
20	1214.4	611.6	0.50	11.93	0.1268	0.0589	0.0009	526.73	7.37	518.71	5.29	561.7	31.5	519.8	5.2	1.9
21	265.6	100.0	0.38	5.89	0.0703	0.0728	0.0016	1010.2	16.1	1011.5	11.2	1007.5	44.9	1011.2	10.8	-0.2
22	540.4	218.1	0.40	10.33	0.1131	0.0604	0.0011	599.76	9.5	595.69	6.23	615.2	38.6	596.2	6.2	0.9
23	931.9	831.9	0.89	35.30	0.3987	0.0516	0.0015	186.43	5.25	180.09	2.01	267.6	65.8	180.1	2.0	3.8
25	261.0	109.6	0.42	6.03	0.0680	0.0995	0.0017	1204.4	14.4	989.1	10.3	1614.3	31.6	995.5	10.9	31.9
26	4423.2	2082.1	0.47	31.87	0.3453	0.0873	0.0013	325.07	5.15	199.18	2.13	1365.2	28.9	183.6	2.1	56.7
27	899.7	437.7	0.49	12.57	0.1359	0.0697	0.0011	576.2	8.31	493.5	5.14	917.4	31.9	493.3	5.2	19.9
28	962.6	482.9	0.50	2.77	0.0290	0.1756	0.0020	2311.4	14.2	1987.7	17.9	2611.2	19.2	2196.9	18.5	27.0
29	3853.6	4044.9	1.05	35.45	0.3770	0.0501	0.0008	180.57	3.29	179.34	1.88	196.7	39	179.4	1.9	0.7
30	1348.0	810.1	0.60	11.66	0.1238	0.0595	0.0008	540.91	7.4	530.29	5.4	585.9	30.6	531.7	5.4	2.5
31	743.1	169.1	0.23	6.64	0.0706	0.0695	0.0010	906.7	10.4	903.82	8.96	913.9	28.4	904.7	8.6	0.5
32	535.8	453.9	0.85	12.91	0.1434	0.0576	0.0012	486.48	9.07	480.82	5.15	513.2	45.4	481.2	5.1	1.5
33	947.3	69.1	0.07	11.62	0.1243	0.0660	0.0010	586.91	8.21	532.07	5.46	805.1	31.4	534.8	5.5	12.6
34	1913.0	1540.0	0.81	12.26	0.1293	0.1340	0.0017	932.76	9.89	505.31	5.13	2150.3	21.5	416.4	4.9	91.1
35	577.3	275.7	0.48	5.83	0.0622	0.0766	0.0011	1049.5	11.4	1020.8	10.1	1109.6	27.6	1029.9	9.7	4.1
36	1622.8	310.6	0.19	12.19	0.1277	0.0586	0.0008	516.35	6.97	508.41	5.12	551.7	29.8	509.5	5.1	1.9
37	1891.5	1073.7	0.57	23.79	0.2547	0.0514	0.0008	264.54	4.51	265.4	2.78	256.9	37.1	265.4	2.8	-0.4
39	479.0	734.6	1.53	36.11	0.4434	0.0514	0.0023	181.77	7.85	176.07	2.13	256	105	176.1	2.1	3.5
40	695.5	194.6	0.28	10.92	0.1181	0.0571	0.0010	551.25	8.5	564.82	5.85	495.6	37	562.8	5.7	-3.1
41	452.9	304.0	0.67	5.44	0.0585	0.0778	0.0011	1106.3	12	1088.2	10.8	1141.9	28.4	1094.5	10.2	2.5
42	468.3	186.6	0.40	12.12	0.1351	0.0589	0.0012	520.95	9.64	511.21	5.48	563.9	45.5	511.9	5.5	2.4
43	334.7	296.8	0.89	12.01	0.1370	0.0631	0.0015	552.8	11.2	515.61	5.65	709	50.3	516.8	5.7	8.9
44	669.4	706.7	1.06	2.67	0.0280	0.1278	0.0015	2059.7	13.9	2052.6	18.4	2066.7	20.8	2058.8	13.9	0.6
45	698.6	290.0	0.42	7.97	0.0852	0.0653	0.0010	767.02	9.72	761.74	7.68	782.4	30.6	762.9	7.5	0.9
46	1306.5	153.2	0.12	12.26	0.1323	0.0593	0.0009	518.69	7.62	505.43	5.25	577.5	33.3	506.8	5.2	3.2
47	964.2	480.4	0.50	12.85	0.1369	0.0579	0.0009	490.41	7.28	483.28	4.96	523.9	33.7	484.0	4.9	1.8
48	565.0	387.2	0.69	11.67	0.1280	0.0595	0.0011	540.46	9.13	530	5.58	584.8	40.9	530.9	5.6	2.5
50	1756.4	1230.7	0.70	35.91	0.3868	0.0499	0.0010	177.9	3.66	177.08	1.88	188.8	45.7	177.1	1.9	0.5
52	560.4	247.3	0.44	11.93	0.1309	0.0674	0.0012	584.95	9.13	518.88	5.47	850.5	36.1	520.4	5.5	15.5
53	1073.2	694.9	0.65	26.93	0.2972	0.0514	0.0012	236.95	5.31	235.08	2.55	255.5	51.9	235.1	2.5	0.9
54	503.6	307.0	0.61	12.76	0.1416	0.0561	0.0012	480.74	9.05	486.51	5.2	453.4	46.3	486.1	5.2	-1.5
55	944.2	1054.2	1.12	13.46	0.1448	0.0560	0.0009	460.07	7.21	462.13	4.8	449.8	36.1	461.9	4.8	-0.5
56	867.5	223.8	0.26	5.82	0.0616	0.0744	0.0010	1032.1	11.1	1022.7	10	1052.2	27.1	1026.1	9.5	1.3
58	456.0	346.7	0.76	60.98	0.8551	0.0510	0.0035	110.69	7.41	104.86	1.46	238	160	104.9	1.5	5.7
59	555.8	425.7	0.77	23.39	0.2680	0.0522	0.0014	272.43	7.05	269.92	3.03	294	62.1	270.0	3.0	1.1
60	38.4	13.2	0.35	2.61	0.0381	0.1308	0.0032	2098.1	25.5	2088.4	26	2107.7	43.5	2093.4	22.4	0.9
63	807.6	288.5	0.36	12.11	0.1305	0.0583	0.0010	516.78	7.91	511.44	5.3	540.4	35.6	512.0	5.3	1.3
64	1160.7	949.7	0.82	33.80	0.3769	0.0496	0.0012	187.18	4.43	187.98	2.07	177.1	54.5	188.0	2.1	-0.5
65	896.6	317.1	0.35	9.76	0.1037	0.0600	0.0009	623.68	8.44	629.1	6.37	604	31.7	628.1	6.2	-1.1
66	245.6	153.6	0.63	12.83	0.1530	0.0567	0.0018	483.1	13.3	483.93	5.56	479.3	71.7	483.9	5.5	-0.2
67	776.9	610.1	0.79	12.48	0.1354	0.0581	0.0011	503.32	8.49	497.08	5.19	531.8	40.3	497.6	5.2	1.6
68	267.1	269.3	1.01	5.51	0.0607	0.0744	0.0013	1067.5	13.3	1075.4	10.9	1051.4	34.1	1073.1	10.3	-1.1
69	488.2	265.6	0.54	12.63	0.1403	0.0578	0.0012	496.47	9.43	491.29	5.26	520.4	46.7	491.6	5.2	1.3
70	4633.6	403.5	0.09	12.46	0.1289	0.0568	0.0007	495	6.25	497.56	4.95	483.2	26.8	497.1	4.9	-0.6
71	821.4	372.4	0.45	10.68	0.1141	0.0662	0.0010	626.99	8.83	576.91	5.89	812.1	32.5	580.3	5.9	10.9
72	1447.8	691.0	0.48	32.03	0.3488	0.0490	0.0010	194.07	4.09	198.18	2.13	144.4	47.9	198.0	2.1	-2.3
73	588.0	302.9	0.52	12.06	0.1310	0.0594	0.0011	525.7	8.63	513.35	5.36	579.7	39.2	514.3	5.3	3.0
75	122.8	56.2	0.46	6.40	0.0786	0.0751	0.0021	976.5	18.9	935.9	10.7	1068.9	55.4	939.5	10.6	6.4
76	431.4	217.0	0.50	12.54	0.1400	0.0597	0.0013	511.83	9.55	494.51	5.31	589.9	45.4	495.5	5.3	4.3
77	706.2	734.9	1.04	31.65	0.4006	0.0517	0.0018	206.08	6.85	200.55	2.5	269.8	79	200.6	2.5	3.0
78	1283.5	122.2	0.10	5.92	0.0617	0.0730	0.0009	1008.1	10.5	1005.83	9.71	1013	25.5	1006.7	9.1	0.3
79	456.0	300.0	0.66	28.34	0.3453	0.0522	0.0020	229.6	8.08	223.57	2.68	291.8	85.4	223.6	2.7	3.0

81	233.4	318.3	1.36	28.56	0.3995	0.0528	0.0036	230.5	14.3	221.89	3.05	319	154	221.9	3.1	4.2
82	3756.9	1237.4	0.33	29.13	0.3139	0.0601	0.0010	254.07	4.39	217.59	2.31	605.8	35.3	216.4	2.3	17.4
83	480.6	1266.8	2.64	12.87	0.1473	0.0604	0.0014	506.5	10.6	482.56	5.32	615.9	51.5	483.4	5.3	6.1
84	1817.8	690.4	0.38	59.59	0.7103	0.0542	0.0016	119.86	3.68	107.27	1.27	377.5	68.1	107.1	1.3	11.7
85	546.6	366.0	0.67	12.68	0.1398	0.0585	0.0012	500	8.9	489.43	5.2	548.7	42.9	490.1	5.2	2.7
86	1013.3	413.4	0.41	6.92	0.0729	0.0848	0.0011	1003.7	10.7	869.55	8.56	1309.4	25.4	882.9	8.9	21.4
87	2114.1	48.5	0.02	8.67	0.0902	0.0655	0.0008	724.73	8.49	703.57	6.94	790.8	26.6	708.2	6.8	4.0
88	273.3	167.0	0.61	11.54	0.1331	0.0575	0.0016	531.3	12.1	535.93	5.93	511.3	59.2	535.7	5.9	-1.1
90	382.3	69.5	0.18	9.43	0.1048	0.0673	0.0013	695.4	11.2	650.06	6.88	844.9	39.9	653.3	6.9	9.1
91	2289.1	43.8	0.02	9.69	0.1014	0.0622	0.0008	643.5	7.96	633.13	6.31	680	27.8	635.2	6.2	2.1
92	2180.1	449.7	0.21	6.23	0.0659	0.0765	0.0010	1005.8	11	960.11	9.44	1106.8	27.2	972.4	9.3	6.8
93	1271.2	164.0	0.13	12.39	0.1336	0.0609	0.0010	525.31	8.28	500.24	5.19	635.8	36.7	501.9	5.2	6.2
94	1741.0	1756.7	1.01	27.75	0.3003	0.0511	0.0009	229.75	4.21	228.24	2.43	245.2	40.1	228.3	2.4	0.7
96	1922.2	1676.5	0.87	10.68	0.1117	0.0623	0.0008	599.25	7.67	577.15	5.78	683.8	28.4	580.3	5.8	4.8
97	386.9	208.2	0.54	36.34	0.4753	0.0522	0.0026	183.42	8.61	175.01	2.26	293	113	175.0	2.3	5.1
98	810.6	89.0	0.11	12.12	0.1351	0.0604	0.0012	530.83	9.48	511.09	5.48	616.6	43.3	512.3	5.5	4.8
99	449.8	65.9	0.15	12.17	0.1349	0.0628	0.0012	545.56	9.49	508.88	5.42	701.9	41.7	510.5	5.4	8.9
100	5084.9	113.0	0.02	5.21	0.0538	0.0799	0.0010	1153.3	10.9	1131.5	10.7	1194.4	23.7	1141.4	10.0	2.8
101	448.3	250.6	0.56	12.27	0.1354	0.0573	0.0012	504.29	9.42	505.19	5.36	500.2	46.2	505.1	5.3	-0.2
102	833.7	527.5	0.63	14.04	0.1518	0.0634	0.0011	491.29	8.12	443.44	4.63	721.1	37.8	444.4	4.7	12.7
103	1575.2	1749.7	1.11	13.57	0.1437	0.0737	0.0011	567.52	7.71	458.29	4.68	1033.5	28.8	453.1	4.8	27.5
104	4377.2	674.9	0.15	8.20	0.0848	0.0895	0.0011	931.58	9.79	741.49	7.24	1413.2	23.5	734.0	7.7	33.8
105	561.9	183.0	0.33	5.93	0.0636	0.0755	0.0011	1029.5	11.8	1005.11	9.98	1081.7	29.5	1012.1	9.6	3.5
106	1332.6	168.8	0.13	11.95	0.1271	0.0669	0.0010	580.51	8.06	518.05	5.29	833.1	30.9	520.2	5.4	14.6
107	390.0	138.1	0.35	5.87	0.0654	0.0741	0.0014	1024	13.8	1014.8	10.5	1043.6	36.8	1016.9	10.1	1.3
108	1160.7	66.0	0.06	7.44	0.0781	0.0708	0.0010	850.54	9.94	812.75	8.01	950.4	28	820.6	7.9	6.4
109	1840.8	55.0	0.03	12.37	0.1301	0.0645	0.0009	549.48	7.42	501.02	5.07	755.8	29.5	503.6	5.1	11.7
110	1622.8	876.4	0.54	3.42	0.0355	0.2738	0.0033	2525.6	14.7	1652.8	15.1	3327.3	18.6	1354.6	16.6	117.1
112	2596.2	491.9	0.19	12.65	0.1329	0.0574	0.0008	493.37	6.87	490.33	4.96	507.5	31	490.7	4.9	0.8
113	2574.7	219.0	0.09	13.40	0.1400	0.0587	0.0008	479.66	6.67	464.05	4.68	555	30.5	465.6	4.7	4.1
114	2511.8	557.6	0.22	9.72	0.1020	0.0935	0.0012	857.43	9.74	631.44	6.31	1498	24.9	607.1	6.6	44.4
115	1615.1	915.2	0.57	12.40	0.1308	0.0593	0.0009	514.13	7.45	499.82	5.07	578.2	33	501.2	5.1	3.5
116	921.2	8.0	0.01	11.74	0.1255	0.0617	0.0010	553.39	8.34	526.85	5.41	664.2	35	528.9	5.4	6.3
117	2852.6	345.1	0.12	9.51	0.0985	0.0610	0.0008	643.39	7.84	644.75	6.36	638.6	27.5	644.4	6.2	-0.3
118	2537.9	1044.3	0.41	11.37	0.1253	0.0634	0.0011	579.06	9.13	543.52	5.75	721.1	37.1	545.8	5.8	8.2
119	1142.3	1007.0	0.88	6.03	0.0630	0.0906	0.0012	1138.7	11.4	988.65	9.57	1437.1	24.8	1009.2	10.0	21.9
120	1836.2	55.4	0.03	8.85	0.1864	0.0632	0.0047	695.5	38.6	690.2	13.8	713	156	690.4	13.7	1.0
121	69.1	45.7	0.66	67.02	2.6055	0.0546	0.0232	108.1	43.7	95.47	3.68	396	953	95.5	3.7	13.0
122	2101.8	1373.8	0.65	15.76	0.1665	0.0955	0.0013	616.46	7.92	396.51	4.06	1537.5	25.4	363.8	4.0	58.0
123	191.9	170.1	0.89	10.06	0.1223	0.0782	0.0021	739.8	15.7	611.19	7.09	1151.6	54.3	610.6	7.2	26.1
124	213.4	81.5	0.38	26.76	0.4440	0.1026	0.0056	430.6	20.1	236.51	3.85	1670	102	231.7	3.8	70.2
125	1192.9	118.2	0.10	9.63	0.1019	0.0836	0.0012	799.4	9.81	637.11	6.42	1283.3	27.7	630.7	6.7	31.9
126	528.1	212.9	0.40	10.45	0.1103	0.0637	0.0010	619.28	8.95	589.04	5.94	731.4	34.2	591.8	5.9	6.5
127	221.1	116.5	0.53	32.30	0.4382	0.0475	0.0030	187.5	11.1	196.55	2.63	75.4	150.5	196.5	2.6	-5.2
128	251.8	101.4	0.40	12.88	0.1460	0.0562	0.0015	478.1	10.7	481.96	5.26	459.7	57.2	481.8	5.2	-1.0
129	862.8	434.2	0.50	12.53	0.1304	0.0582	0.0009	502.25	7.33	494.81	4.96	536.3	33.5	495.6	4.9	1.9
130	1056.3	1002.2	0.95	12.72	0.1310	0.0564	0.0008	484.36	6.86	488	4.84	467.2	32.2	487.5	4.8	-0.9
131	1318.8	529.5	0.40	64.43	0.7058	0.0503	0.0014	103.78	2.9	99.28	1.08	208.3	63.1	99.3	1.1	4.7
132	2038.9	915.9	0.45	13.58	0.1421	0.0641	0.0010	508.39	7.36	457.93	4.62	742.3	32	459.3	4.7	13.1
133	683.2	224.0	0.33	12.10	0.1260	0.0585	0.0010	518.35	7.83	511.74	5.12	547.6	35.5	512.4	5.1	1.6
134	1096.2	406.1	0.37	5.64	0.0572	0.0745	0.0009	1053.5	10.6	1052.92	9.86	1054.7	25.4	1053.1	9.2	0.1
135	1137.7	103.8	0.09	10.60	0.1090	0.0693	0.0010	652.06	8.25	581.15	5.71	905.9	28.3	584.7	5.8	15.2
136	502.0	205.8	0.41	11.91	0.1262	0.0592	0.0010	529.92	8.41	519.78	5.29	573.8	37.8	520.7	5.3	2.4
138	611.1	223.0	0.36	31.22	0.3509	0.0485	0.0014	196.95	5.58	203.24	2.25	122.2	68.5	203.1	2.2	-3.5
139	816.8	511.0	0.63	20.09	0.2140	0.0776	0.0013	433.41	7	313.11	3.25	1136.3	33.3	303.9	3.3	39.3
140	760.0	226.7	0.30	5.93	0.0609	0.0735	0.0010	1010.7	10.8	1003.9	9.54	1025.5	27	1006.2	9.1	1.0
141	1323.4	123.9	0.09	10.83	0.1103	0.0591	0.0008	569.19	7.5	569.13	5.55	569.4	30.2	569.1	5.5	0.0
142	859.8	160.4	0.19	12.41	0.1294	0.0581	0.0009	505.26	7.44	499.58	5.01	531	34	500.2	5.0	1.4
143	806.0	554.2	0.69	10.77	0.1114	0.0603	0.0009	580.99	8.15	572.37	5.66	614.8	32.9	573.5	5.6	1.9
144	1622.8	267.5	0.16	9.90	0.1010	0.0699	0.0010	690.19	8.51	620.33	6.03	925.1	27.9	625.1	6.1	14.3
145	2564.0	845.6	0.33	5.93	0.0598	0.0733	0.0009	1009.6	10.2	1004.5	9.38	1020.8	25.1	1006.4	8.8	0.7
146	324.0	258.0	0.80	3.36	0.0350	0.1036	0.0014	1685.2	14.1	1681.7	15.4	1689.5	25.1	1683.8	13.2	0.3
147	1202.1	765.2	0.64	32.53	0.3492	0.0495	0.0010	193.13	4.06	195.18	2.06	168.2	47.7	195.1	2.1	-1.2
149	1371.0	690.7	0.50	23.28	0.2439	0.0500	0.0009	263.43	4.67	271.09	2.78	195.8	39.9	270.6	2.8	-3.2
150	680.1	302.1	0.44	12.22	0.1285	0.0586	0.0010	515.12	8.1	506.92	5.12	551.7	37.2	507.6	5.1	2.0
151	231.8	102.0	0.44	12.10	0.1390	0.0588	0.0015	520.5	11.4	512.04	5.66	558	55.6	512.4	5.6	2.1
152	152.0	110.5	0.73	2.59	0.0279	0.1326	0.0019	2118.3	16	2104.1	19.3	2132.2	25.2	2114.4	15.5	1.2
153	620.3	71.4	0.12	12.10	0.1288	0.0574	0.0010	510.74	8.2	511.98	5.24	505.2	38.3	511.9	5.2	-0.3
154	270.2	111.3	0.41	5.81	0.0624	0.0741	0.0012	1030.8	12.9	1024.4	10.2	1044.4	33.7	1026.1	9.8	0.9
155	634.1	264.4	0.42	65.79	0.8224	0.0536	0.0023	108.11	4.51	97.25	1.21	354.5	95.2	97.2	1.2	11.1
156	2184.7	968.2	0.44	8.98	0.0920	0.0635	0.0009	690.32	8.57	680.41	6.61	722.7	29.1	682.3	6.5	1.9
157	2576.3	1023.7	0.40	31.47	0.3267	0.0511	0.0008	205.22	3.58	201.68	2.06	246.1	37.4	201.8	2.1	1.9
158	938.1	339.7	0.36	5.94	0.0610	0.0752	0.0011	1025.2	11.2	1003.34	9.54	1072.1	28.1	1009.8	9.2	3.2
159	583.4	145.9	0.25	12.42	0.1326	0.0554	0.0010	486.41	8.29	499.29	5.13	426.2	41.5	497.9	5.1	-3.2
160	3264.1	552.9	0.17	8.14	0.0829	0.0642	0.0009	746.65	8.96	746.54	7.18	746.9	28.6	746.6	7.0	0.0

Between the sites, the $^{87}Sr/^{86}Sr$ ratios are, however, distinct; Farmer et al. (2006) measure values of 0.718687 ± 0.000010 and 0.722141 ± 0.000013, which are lower than the 0.725471 measured at KIS-GZ. As the Rb-Sr and Sm-Nd isotope systems typically negatively correlate due to the relative compatibility of the parent and daughter isotopes during partial melting of the mantle (Goldstein and Hemming, 2003), a change in one system without a change in the other is rare. Beneath Kamb Ice Stream, the difference may be linked to fractionation of the Sr isotope system due to grain size sorting or weathering during ice-free times as, in contrast to the Nd isotope system, Sr isotopes can be fractionated by these processes (Blum and Erel, 1995; Eisenhauer et al., 1999). These processes may be sufficient to result in the change in $^{87}Sr/^{86}Sr$ ratios observed downstream without indicating a significant change to sediment provenance as suggested by the Nd isotope and zircon U-Pb data.

6.4.3 HWD-2b

As discussed, the core is split into a diamict, till pellet and fine mud facies interpreted as a post-glacial retreat sequence (Calkin et al., in prep.; Fig. 6.2; 6.5). Sand and clast compositions (>300 μm) are consistent throughout these three facies. This includes contribution from Ferrar Dolerite and a quartziferous sandstone source, for example the Byrd Group or Beacon Supergroup (Dunbar, pers. comm., 2021). In contrast, ε_{Nd} values decline markedly up-core through the facies of the retreat sequence (Fig. 6.5). The base of the core, assumed to represent a depositional environment beneath grounded ice, has an ε_{Nd} value of -7.71 ± 0.19. Above this, a sample from the till pellet facies has an ε_{Nd} value of -9.40 ± 0.19. At the top of the core, containing fine-grained, sub-ice shelf muds, we find the most radiogenic ε_{Nd} value of -10.91 ± 0.19. Ascending the core, corresponding $^{87}Sr/^{86}Sr$ ratios are 0.726945, 0.734232 and 0.732341 (± 0.00008). These do not, therefore, reflect such a clear trend with depth, although the most radiogenic ε_{Nd} value (-7.71) and most unradiogenic $^{87}Sr/^{86}Sr$ ratio (0.726945) are found in the diamict. These are not plotted as in the Ross Sea, trends in $^{87}Sr/^{86}Sr$ ratios have proven to be less clear than changes in ε_{Nd} values (e.g. Chapter 2).

The clast/sand composition indicates a consistent source from the Transantarctic Mountains, which was anticipated given the close proximity to the mountain range. However, the radiogenic isotope data reveal clear changes to provenance downcore. These changes are difficult to date given the lack of chronological constraint in the sediments but, based on the

large changes to sedimentary facies, they may record deglaciation following the end of the last glacial period.

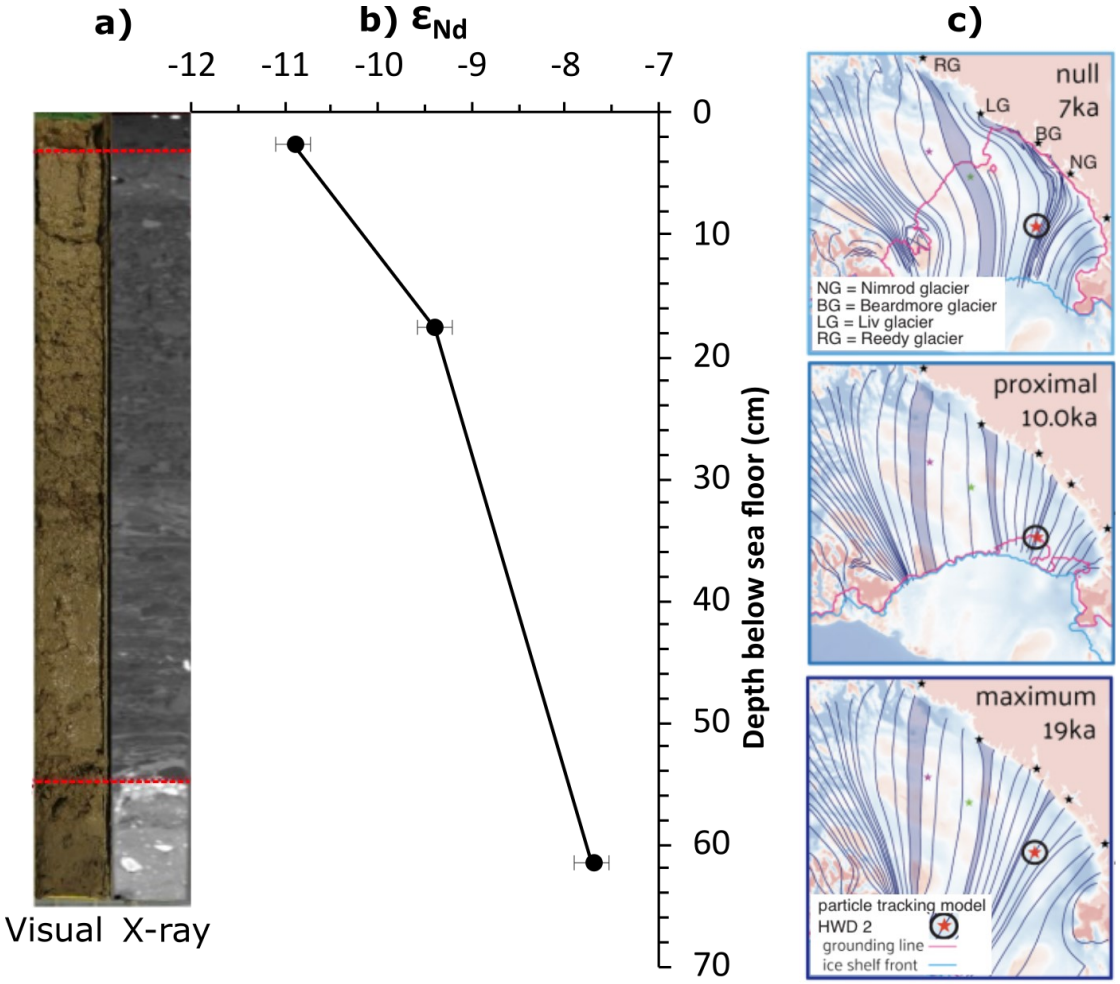


Figure 6.5. *a) Visual and x-ray images of the HWD-2b core, with red dashed lines indicating facies boundaries (Calkin et al., in prep.). b) Downcore variations in ε_{Nd} values. c) Ice sheet model particle tracking experiments at 19 ka, 10 ka and 7 ka from the lowermost to uppermost panel, respectively (adapted from Calkin et al., in prep). Although changes to ice flow have occurred since, the 7 ka panel broadly aligns with modern ice flow directions.*

Modern ice flow lines, which approximately align with the modelled flowlines shown at 7 ka in Figure 6.5c, can be used to trace the uppermost muds back to the Liv/Scott Glacier region (glaciers are labelled in Fig. 6.3), giving a high confidence that they are derived from that region. This portion of the Transantarctic Mountains contains Beacon Supergroup and Ferrar Group rocks in its upper reaches, before reaching Granite Harbour Intrusive granitic rocks and Liv Group metasediments (predominantly the Duncan and Party Formations) downstream. The relatively unradiogenic -10.9 ε_{Nd} value of these muds is similar to marine

sediments thought to be sourced from the central Transantarctic Mountains (Farmer et al., 2006), as well as an ε_{Nd} measurement of -9.7 for a local outcrop of the Duncan Formation of the Liv Group (Marschalek et al., 2021), which is a dominant lithology in this area.

However, the endmembers contributing to the older sediments is more difficult to constrain. Potential rocks with less negative ε_{Nd} values in the Transantarctic Mountains include: i) Cenozoic volcanic rocks, ii) certain Granite Harbour Intrusive rocks and some Liv Group volcaniclastic rocks, and iii) the Ferrar Group (see Fig. 2.5). No evidence was found for basaltic/volcanic rocks in the clast petrography. HWD-2b is also upstream and distant from the McMurdo Volcanic Group and too close to the Transantarctic Mountains for a strong Marie Byrd Land volcanic province source (Fig 6.1). A Cenozoic volcanic endmember (option i) can therefore be eliminated.

Differentiating between a Ferrar Group endmember (option iii) and other relatively radiogenic rocks in the southern TAM (option ii) is more challenging. If option (ii) was correct, source rocks could include the Liv Group, which comprises of Palaeozoic sedimentary rocks with variable volcanic input that outcrop widely in the southern TAM (Fig. 6.1). Epsilon Nd values in this group vary considerably, but formations are generally radiogenic with La Gorce and Leverett formation values of ~-7 and ~-5 (Marschalek et al., 2021). Volcanic beds are even more radiogenic, with values between -3.1 and +5.7 (Wareham et al., 2001). Other common rock groups in the southern TAM include the Granite Harbour Intrusive series; in this region this is more radiogenic than exposures further north, with values varying between -1.1 and -8.8 (Borg et al., 1990; Borg and DePaulo, 1994). Ice flow from areas where these rocks are more common (option ii) could therefore explain the radiogenic isotope ratios in the diamict.

Alternatively, to give an ε_{Nd} value of -7.7, the Ferrar Group, with a mean composition around -6 (e.g. Hergt et al., 1989; Molzahn et al., 1996; Elliot et al., 1999), could comprise a substantial fraction of the sediment deposited offshore. Furthermore, Ferrar Group rocks would be likely to be accompanied by Beacon Supergroup sediments, which the Ferrar Group intrudes. The Beacon Supergroup is poorly constrained and variable in its isotopic composition, but likely to relatively unradiogenic, potentially <-10, based on nearby rock samples (Marschalek et al., 2021). An ε_{Nd} value of -7.7 would therefore suggest a very high fraction of mixed Beacon and Ferrar Group rocks. Such a mixture is likely given the potential dominance of these rock types in the clast types.

Beacon Supergroup and Ferrar Group rocks often derive from the inland side of the Transantarctic Mountains, where they are common at higher elevations (Fig. 6.1). The more radiogenic ε_{Nd} values could therefore potentially reflect erosion focussed more on the inland side of the mountain range and/or at higher elevations by the larger glacial period ice sheet. However, glaciers passing through the TAM would be expected to pick up material along their length, integrating the signature perpendicular to the strike of the mountain range (Farmer and Licht, 2016). If a strong Beacon/Ferrar signature is responsible for the more radiogenic values (option iii), this requires that the LGM ice sheet incorporated relatively little material nearer the coast. Ferrar Group rocks are particularly common in the upper Beardmore Glacier catchment, as lateral moraines in its upper reaches have relatively radiogenic ε_{Nd} values of ~-6 (Farmer et al., 2006). However, $^{87}Sr/^{86}Sr$ ratios here are ~0.713, lower than the ~0.727 measured, meaning the diamict sample at the HWD-2b site does not lie on a mixing line between upper and lower Beardmore Glacier samples.

Modelling of the ice sheet during deglaciation helps explore potential source areas by suggesting changes to ice flow trajectories (Calkin et al., in prep.; Fig. 6.3 c). This modelling suggests a source from Nimrod Glacier, or slightly to the south, would be expected for the greatest modelled ice sheet extent. However, Farmer and Licht (2016) measured particularly unradiogenic values from Nimrod Glacier moraines, from -18.9 to -12.7. This is very different to the measured value of -7.7 (Table 6.1). As ice sheet model simulations do not produce ice flow from areas further to the north of the Transantarctic Mountains (e.g. Fig. 6.5c), we therefore suggest that the sediment provenance of the HWD-2b core diamict records flow from an area south of Nimrod Glacier.

Measurements from unconsolidated sediment samples from between Beardmore and Shackleton Glacier do not exist, but this region may provide a good fit with the more radiogenic measured ε_{Nd} values; the Ferrar Group (and Beacon Supergroup) have exposures relatively close to the coast (Fig. 6.1), and Granite Harbour Intrusive rocks have radiogenic ε_{Nd} values here compared to elsewhere (Borg et al., 1990). Byrd Group rocks also outcrop. This mixture of rock types fits with the sand and clast petrography. Above the diamict, the ε_{Nd} value of the till pellet facies (-9.4) matches well with a more coastal till sample from Beardmore Glacier (-9.6; Farmer et al., 2006), so may reflect erosion closer to the coast or small changes to the provenance source as ice flow over the site switched to areas further south. A source between Beardmore and Shackleton Glacier would also fit with the ice sheet

model showing the general trend of the sediment source continuing to move southwards during deglaciation to the present day (Fig. 6.5).

Detrital zircon U-Pb dating could help confirm this hypothesis derived from the radiogenic isotope data. If the isotopic shift represents a greater Ferrar and Beacon input, zircons from the Beacon Supergroup would be expected to have a relatively early Ross/Pan African Orogeny peak, more pre-Neoproterozoic grains, and potentially ages such as a ~250 Ma peak associated with certain Beacon Supergroup formations (as seen in Miocene Ross Sea sediments; Marschalek et al., 2021). On the other hand, an ε_{Nd} value shift cause by ice flow from more southerly portions of the Transantarctic Mountains would likely lead to a younger Ross/Pan African peak (~500 Ma), consistent with the age of the granites in this region (Goodge et al., 2012; Paulsen et al., 2013) and Liv Group detrital zircons (Paulsen et al., 2015; 2018).

Overall, the modelled LGM source from Nimrod Glacier is clearly incompatible with the radiogenic isotope data. A source further south, but difficult to precisely determine, seems more likely. This model/data mismatch is consistent with previous data demonstrating disagreement between LGM modelled flow configurations, which show EAIS dominance in the central Ross Sea, and provenance data, which show more WAIS input (Licht et al., 2014). Potentially, the diamict records a transient ice sheet configuration during the retreat of the ice sheet, and not the true glacial maximum deposition. Similarly, Holocene retreat of the WAIS grounding zone in the Ross Sea to a position landwards of its current location is another potential mechanism that sediment core records may be recording, but which is not accounted for in the flow line modelling (Kingslake et al., 2018).

As well as these considerations regarding what ice sheet state is being recorded in the HWD-2b core, subtle changes to ice sheet flow not accurately represented in current models of the LGM ice sheet could be responsible for the discrepancy between the ice sheet modelling and sediment provenance data. Ice is funnelled into the Ross Ice Shelf, meaning flow lines within a few tens of kilometres of the modern HWD-2b site span a far wider section along the strike of the Transantarctic Mountains. Consequently, relatively subtle changes to modelled ice flow could lead to substantial sediment provenance shifts.

6.4.4 Whillans Grounding Zone

The WGZ samples spanned three sample depths, but ε_{Nd} values were almost within error of each other, with a mean of -8.6 (Table 5.1). $^{87}Sr/^{86}Sr$ ratios were also extremely similar, with

a mean of 0.731403. Given the grounding zone setting, these data point to a high deposition rate. Additional data relevant to sediment provenance tracing include gravel-sized clasts counts; these are 56% metamorphic, 29% plutonic, 3% feldspar, 11% quartz, and 1% till aggregates (Puttkammer, 2016). Sand-sized grains are predominantly quartz (72%) (Puttkammer, 2016).

Modern flow lines trace the WGZ sediment source to the area around the Horlick Mountains. Outcrops here include Beacon Supergroup rocks, Ferrar Group dolerites and Granite Harbour Intrusive granitoids (Fig. 6.1). The Whitmore Mountains to the northeast contain granites dating to ~200-170 Ma and metasediments surrounding them of approximately early to middle Cambrian age (Craddock et al., 2017; Storey and MacDonald, 1987). The clast petrography data are consistent with this source in the southern TAM, where granitic plutons and metasediments are common. However, the data cannot exclude input from subglacial West Antarctic metasediments and Triassic-Jurassic granitoids. Plutonic clasts probably derive from either the Granite Harbour Instrusives or Mesozoic granitoids, and metamorphic rocks may derive from the La Gorce Formation or subglacial metasediments of similar (Cambrian) age, such as those exposed in the Whitmore Mountains. The lack of dolerite implies the Ferrar Group and associated Beacon Supergroup are not major contributors to the sediments.

The consistent ε_{Nd} values and $^{87}Sr/^{86}Sr$ ratios down the core suggest temporal consistency in the provenance of the sediments. Furthermore, both the gravel and sand petrographic composition remained similar down core (Puttkammer, 2016). There has therefore been little change to flow trajectories or erosion patterns during the deposition of the sediments. It is also interesting to note that the ε_{Nd} values (~-8.6) are between those measured for LGM tills at a more upstream site, which span -8.0 to -8.8 (Farmer et al., 2006). $^{87}Sr/^{86}Sr$ ratios of 0.731049 and 0.731077 from upstream (Farmer et al., 2006) are also extremely similar to those measured at the grounding zone (mean of 0.731403). This agreement between upstream and grounding zone proximal sediments is similar to observations from Kamb Ice Stream discussed above, and again suggests the sediments are already well mixed upstream and/or that there is little erosion of new sediment between the upstream and downstream sites.

6.5 Concluding Remarks

Sediment samples from beneath the Ross Ice Shelf have revealed new information regarding ice flow in the Ross Ice Shelf since the LGM and the sediment transport processes beneath

the Siple Coast ice streams. The HWD-2b site in the centre of the Ross Ice Shelf shows substantial temporal changes in sediment provenance. We tentatively suggest this is linked to erosion shifting from the Beardmore/Shackleton Glacier area at the base of the sequence towards its current position near Liv/Scott Glacier. These data highlight that either the sedimentary record represents a relatively late stage of deglaciation, or that ice sheet modelling of the LGM Antarctic ice sheet continues to show flow lines from the Transantarctic Mountains further eastward in the Ross Sea than sediment provenance would suggest.

Samples from the grounding zones of Whillans and Kamb ice streams show little change to ice flow during their deposition. The consistency of ice flow trajectories implies the direction of the flow of the Siple Coast ice streams is unlikely to have migrated significantly during the late Holocene. They also match closely with the provenance of sediments further upstream, suggesting that till beneath the Siple Coast ice streams may be well mixed down ice flow lines. Alternatively, or in addition, the consistency between upstream and grounding zone samples could indicate these ice streams erode only small amounts of sediment in their fast-flowing trunks, with till predominantly generated further upstream. This is likely linked to the low driving stress and consequently low basal shear stress beneath these glaciers, despite the high basal velocities. Indeed, till beneath fast ice streaming in the Siple Coast region has been suggested to lead to slow erosion rates and long-distance transport of debris (Alley et al., 1989; Cuffey and Alley, 1996). Entrainment of till here may be linked to the centennial cessation and resumption of fast flow of these glaciers, which may allow till to freeze on as the ice stream stagnates before being transported as basal slip resumes (Christofferson et al., 2010).

Relevant Appendix Section – Appendix A.7 provides a brief discussion of results from the debris collected from the BEAMISH drilling through Rutford Ice Stream, which was outside the geographical remit of this chapter.

7. Thesis Summary and Concluding Remarks

7.1 Thesis Summary

Sediment provenance records from the Antarctic continental margin offer unique potential to reconstruct past ice sheet erosion patterns, and thus ice extent and flow trajectories. This thesis offers a step forward in our understanding of Antarctica's ice sheet history by constructing a new Early Miocene sediment provenance record. Other chapters use numerical techniques to provide a new way of interpreting existing records and constraining the subglacial geology of West Antarctica.

The new Early Miocene sediment provenance record presented in Chapter 2 explores the early history of the WAIS. Previously, evidence for the existence of a continental-scale WAIS before the Middle Miocene was limited to sedimentary records near East Antarctica (e.g. ANDRILL; Levy et al., 2016) or seismic data which, although useful, cannot distinguish between local marine-terminating glaciers or a large scale ice sheet (e.g. Sorlien et al., 2007; Pérez et al., 2021). New sediment provenance data including radiogenic Nd and Sr isotope compositions, clay mineralogy, zircon U-Pb ages, hornblende $^{40}Ar/^{39}Ar$ ages and clast petrography all demonstrate sedimentary sequences at IODP Site U1521, in the central Ross Sea, derived from West Antarctica. Dinocycts and palynology showed significant reworked sediment contributions, consistent with this interpretation. West Antarctic sediment could only reach IODP Site U1521 if a WAIS existed that was large enough to expand across much of the Antarctic continental shelf. Critically, this sedimentary sequence was dated to ~17.72 to 17.40 Ma, in the Early Miocene and prior to the cooling of the Miocene Climatic Transition (~14 Ma) often interpreted as the first widespread glaciation of West Antarctica (e.g. Westerhold et al., 2020).

Sediment provenance proxies provide otherwise unobtainable information about past ice sheets; however, they can only record where erosion was taking place. It is typically assumed ice sheets erode most near their margins, but this is a simplification of what is often a very complex system. Furthermore, sediment provenance studies must make assumptions regarding how sediment is transported beneath the ice and beyond the ice sheet margin once it reaches the ocean. Chapter 3 presents a new method of predicting the Nd isotope composition of marine sediments using the output of an ice sheet model, reducing the need for qualitative statements regarding where sediment was likely derived from. In this way, the Nd isotope composition of sediments deposited offshore can be used to make a quantitative estimate of ice sheet extent. The method was applied to the existing records from IODP Site

U1361 (Cook et al., 2013; 2017; Bertram et al., 2018; Bertram, 2018; Wilson et al., 2018), where the most radiogenic ε_{Nd} values in the Pliocene were suggested to represent a sea-level equivalent total Antarctic ice volume ~9.3 m lower than today.

When reconstructing the history of the WAIS, a key limitation on the precision that sediment provenance techniques are capable of is the uncertain geology beneath the modern ice sheet. Chapter 4 discusses a new island discovered between Thwaites Glacier and Pine Island Glacier. This is a region which is changing rapidly and sensitive to warming ocean temperatures (Scambos et al., 2017), but where sediment provenance techniques are limited by near complete ice cover. The island ('Sif Island') is made of granite dated to the Jurassic (~178-174 Ma) and has an initial Nd and Sr isotopic composition resembling rocks in the Thurston Island and Antarctic Peninsula tectonic blocks to the north and east. The island therefore extends the known range of these rocks, suggesting the boundary of these crustal blocks does not lie beneath Pine Island Glacier, as some had previously suggested (e.g. Jordan et al., 2020). However, the thermochronological data from the Sif Island granite revealed that Pine Island Glacier does lie on a tectonic feature, as the zircon fission track age of 165.5 Ma is substantially older than the ~100 Ma ages recorded in island groups on the other side of Pine Island Bay (Lindow et al., 2016), implying a different cooling history. These new geological data ultimately help build knowledge of the geological history of West Antarctica, making future and existing sediment provenance records more precise.

Combined with marine sediments deposited beyond the ice sheet margin, exposed rocks such as Sif Island provide the framework for determining the geology beneath the WAIS. However, subglacial sediment samples offer otherwise unobtainable information about the rocks present in the ice sheet interior, constraining the known extent of indicative provenance characteristics expressed in glacimarine sediments. In particular, there is very little constraint on how retreat of ice into the WAIS interior would be represented in the sedimentary record, as ice cover is near complete. Chapter 5 examines the provenance signature of debris recovered from the Byrd ice core, drilled in the 1960s near the ice divide at the centre of the WAIS. Small amounts of debris entrained in the basal ice were sampled. The dominance of kaolinite, which is not produced under ice sheets, offers a way of detecting past WAIS collapse. The site also records an endmember with a relatively high ε_{Nd} value and low $^{87}Sr/^{86}Sr$ ratio, implying that widespread Cenozoic volcanic rocks are not required to reach the isotopic compositions of sediments deposited offshore. A Triassic rhyolite clast confirms

the presence of, and begins to explore, the previously uncharacterised Mesozoic bedrock known to exist beneath the WAIS based on marine samples.

Chapter 6 offers additional new insight into West Antarctic subglacial geology using sediment samples obtained from drilling through the ice sheet in the Ross Sea sector. New samples reveal remarkable conservation of the provenance signature of sediment down Siple Coast ice stream flowlines, implying either a consistent substrate or little erosion of new detritus. A downhole record from the centre of the Ross Ice Shelf suggests that ice sheet models may not correctly capture the exact position of ice flow lines during the LGM and subsequent deglaciation.

7.2 Future Study and Closing Remarks

Future work should include further study of the IODP Expedition 374 sediments (particularly Sites U1521, U1522 and U1524), as exciting sediment provenance trends are present which have the potential to significantly build understanding of late Cenozoic Antarctic ice sheet history (see Appendix Sections A.3, A.4). The various datasets being produced by other IODP participants are highly complementary when interpreted with sediment provenance proxies and offer a far deeper understanding of these sedimentary records (e.g. Chapter 2). Furthermore, other IODP legs to the Amundsen Sea (Exp. 379) and Iceberg Alley (Exp. 382) are already producing excellent datasets to offer a more complete Antarctic-wide picture of past environmental conditions and the Antarctic ice sheet response.

Interpreting sediment provenance records could benefit greatly from further development of the computational provenance tracing method outlined in Chapter 3. Such an approach has the potential to maximise the potential information gained from existing and future sediment provenance records. Additionally, the method could be adapted for different provenance indicators such as detrital mineral ages. Comparing the results for different provenance proxies would be highly beneficial, as different proxies are likely to provide different degrees of precision in different areas. Furthermore, such numerical provenance tracing is underpinned by knowledge of subglacial erosion processes, which are currently poorly parameterised in glacial erosion models. Continued efforts to better understand and model subglacial erosion would benefit this work as well as other glaciological research.

Further exploration of Antarctic geology is key, not only for provenance tracing, but also for mapping the mechanical properties of the ice sheet bed and geothermal heat flux for accurate

ice sheet modelling. As well as targeted sampling of rock outcrops, accessing the ice sheet bed in regions where there is little geological information will build a fuller picture of the ice-covered rocks present.

Overall, this thesis offers new insight into how Antarctica's ice sheets have changed in the past and provides the foundations to help better interpret future Antarctic sediment provenance records. It also highlights the importance of integrating ocean drilling records with the glaciological community, as the glacimarine sedimentary record is intrinsically linked to weathering, erosion and entrainment processes beneath ice sheets.

Future drilling projects, such as the upcoming SWAIS-2C drilling through the Ross Ice Shelf (Patterson et al., 2022), will target sedimentary records under the modern ice sheet. Such sediments are required to unambiguously determine the extent and flow of past smaller-than-present ice sheets. Provenance records from these sites will reveal where ice was lost from in different stages of deglaciation of marine-based parts of the WAIS, which can ultimately guide the inclusion and parameterisation of different physical processes used in numerical models to predict future sea level rise. The SWAIS-2C project and other future projects seeking to reconstruct Antarctic ice sheet history using sediment provenance will benefit from the tools and geological constraints developed in this thesis.

Bibliography

Adams, C. J. (1986). Geochronological studies of the Swanson Formation of Marie Byrd Land, West Antarctica, and correlation with northern Victoria Land, East Antarctica, and South Island, New Zealand. *New Zealand Journal of Geology and Geophysics*, *29*(3), 345-358.

Adams, C. J. (1987). Geochronology of granite terranes in the Ford Ranges, Marie Byrd Land, West Antarctica. *New Zealand journal of geology and geophysics*, *30*(1), 51-72.

Aitken, A. R. A., & Urosevic, L. (2021). A probabilistic and model-based approach to the assessment of glacial detritus from ice sheet change. *Palaeogeography, Palaeoclimatology, Palaeoecology*, *561*, 110053.

Alley, R. B., Blankenship, D. D., Rooney, S. T., & Bentley, C. R. (1989). Sedimentation beneath ice shelves—the view from ice stream B. *Marine Geology*, *85*(2-4), 101-120.

Alley, R. B., Cuffey, K. M., & Zoet, L. K. (2019). Glacial erosion: status and outlook. *Annals of Glaciology* 60, 1-13.

Amelin, Y., and Davis, W.J. (2005). Geochemical test for branching decay of 176Lu. *Geochimica et Cosmochimica Acta* 69, 465-473.

Anderson, J. B., & Bartek, L. R. (1992). Cenozoic glacial history of the Ross Sea revealed by intermediate resolution seismic reflection data combined with drill site information. *The Antarctic Paleoenvironment: A Perspective on Global Change: Part One* 56, 231-264.

Andersen, T. (2002). Correction of common lead in U–Pb analyses that do not report 204Pb. *Chemical geology*, *192*(1-2), 59-79.

Andrews, J. T., & LeMasurier, W. (2021). Resolving the argument about volcanic bedrock under the West Antarctic Ice Sheet and implications for ice sheet stability and sea level change. *Earth and Planetary Science Letters*, *568*, 117035.

Armienti, P., Ghezzo, C., Innocenti, F., Manetti, P., Rocchi, S., & Tonarini, S. (1990). Isotope geochemistry and petrology of granitoid suites from Granite Harbour intrusives of the Wilson Terrane, North Victoria Land, Antarctica. *European Journal of Mineralogy*, 103-124.

Askin, R.A. and Raine, J. I. (2000). Oligocene and Early Miocene terrestrial palynology of the Cape Roberts Drillhole CRP-2/2A, Victoria Land Basin, Antarctica. *Terra Antarctica* 7, 493-501.

Askin, R.A. (2000). *Spores and pollen from the McMurdo Sound erratics, Antarctica*. In: Palaeobiology and Palaeoenvironments of Eocene Rocks, McMurdo Sound, East Antarctica. Antarctic Research Series v76 (Eds. Stilwel, J.D. and Feldman, R.M.), American Geophysical Union 2000.

Aviado, K. B., Rilling-Hall, S., Bryce, J. G., & Mukasa, S. B. Submarine and subaerial lavas in the West Antarctic Rift System: Temporal record of shifting magma source components from the lithosphere and asthenosphere. *Geochemistry, Geophysics, Geosystems 16*, 4344-4361 (2015).

Azetsu-Scott, K., & Syvitski, J. P. (1999). Influence of melting icebergs on distribution, characteristics and transport of marine particles in an East Greenland fjord. *Journal of Geophysical Research: Oceans*, *104*(C3), 5321-5328.

Bader, N. A., Licht, K. J., Kaplan, M. R., Kassab, C., & Winckler, G. (2017). East Antarctic ice sheet stability recorded in a high-elevation ice-cored moraine. *Quaternary Science Reviews 159*, 88-102.

Bahlburg, H., Vervoort, J.D., and DuFrane, S.A. (2010). Plate tectonic significance of Middle Cambrian and Ordovician siliciclastic rocks of the Bavarian facies, Armorican terrane

assemblage, Germany -- U-Pb and Hf isotope evidence from detrital zircons. *Gondwana Research*, 17 (2-3), 223-235.

Bakker, A. M., Wong, T. E., Ruckert, K. L., & Keller, K. (2017). Sea-level projections representing the deeply uncertain contribution of the West Antarctic ice sheet. *Scientific reports*, *7*(1), 1-7.

Balshaw-Biddle, K. M. (1980). *Antarctic glacial chronology reflected in the Oligocene through Pliocene sedimentary section in the Ross Sea* [PhD Thesis]. Rice University.

Barrett, P. J (1975). Characteristics of pebbles from Cenozoic marine glacial sediments in the Ross Sea (DSDP Sites 270–274) and the South Indian Ocean (Site 268). In: *Initial Reports of the Deep-Sea Drilling Project* 28, 769-784.

Barrett, P. J. (1991). *The Devonian to Jurassic Beacon Supergroup of the Transantarctic Mountains and correlatives in other parts of Antarctica*. In: The geology of Antarctica, 120-152.

Bart, P. J. (2001). Did the Antarctic ice sheets expand during the early Pliocene? *Geology, 29*(1), 67-70.

Bart, P. J. (2003). Were West Antarctic ice sheet grounding events in the Ross Sea a consequence of East Antarctic ice sheet expansion during the middle Miocene? *Earth and Planetary Science Letters* 216, 93-107.

Bastias, J., Spikings, R., Riley, T., Ulianov, A., Grunow, A., Chiaradia, M., & Hervé, F. (2021). A revised interpretation of the Chon Aike magmatic province: active margin origin and implications for the opening of the Weddell Sea. *Lithos*, *386*, 106013.

Bastias, J., Spikings, R., Ulianov, A., Riley, T., Burton-Johnson, A., Chiaradia, M., ... & Bouvier, A. S. (2020). The Gondwanan margin in West Antarctica: insights from Late Triassic magmatism of the Antarctic Peninsula. *Gondwana Research*, *81*, 1-20.

Batchelor, C. L., & Dowdeswell, J. A. (2015). Ice-sheet grounding-zone wedges (GZWs) on high-latitude continental margins. *Marine Geology*, *363*, 65-92.

Behrendt, J. C. (1999). Crustal and lithospheric structure of the West Antarctic Rift System from geophysical investigations—a review. *Global and Planetary Change*, *23*(1-4), 25-44.

Behrendt, J. C. (2013). The aeromagnetic method as a tool to identify Cenozoic magmatism in the West Antarctic Rift System beneath the West Antarctic Ice Sheet—A review; Thiel subglacial volcano as possible source of the ash layer in the WAISCORE. *Tectonophysics*, *585*, 124-136.

Behrendt, J. C. et al. (1991). Geophysical studies of the West Antarctic rift system. *Tectonics* 10, 1257-1273.

Behrendt, J. C., Blankenship, D. D., Finn, C. A., Bell, R. E., Sweeney, R. E., Hodge, S. M., & Brozena, J. M. (1994). CASERTZ aeromagnetic data reveal late Cenozoic flood basalts (?) in the West Antarctic rift system. *Geology*, *22*(6), 527-530.

Behrendt, J. C., Saltus, R., Damaske, D., McCafferty, A., Finn, C. A., Blankenship, D., & Bell, R. E. (1996). Patterns of late Cenozoic volcanic and tectonic activity in the West Antarctic rift system revealed by aeromagnetic surveys. *Tectonics*, *15*(3), 660-676.

Benninghoff, W. S. Calculation of pollen and spores density in sediments by addition of exotic pollen in known quantities. *Pollen et Spores 6*, 332–333 (1962).

Ben Othman, D., Tilton, G. R., & Menzies, M. A. (1990). Pb, Nd and Sr isotopic investigations of kaersutite and clinopyroxene from ultramafic nodules, and their host basalts: The nature of the subcontinental mantle. *Geochimica et Cosmochimica Acta* 54, 3449-3460.

Beny, F. et al. (2020). Radiogenic isotopic and clay mineralogical signatures of terrigenous particles as water-masses tracers : New insights into South Atlantic deep circulation during the last termination. *Quaternary Science Reviews* 228, 106089. doi.org/10.1016/j.quascirev.2019.106089

Bertram, R.A. (2018). *Reconstructing the East Antarctic Ice Sheet during the Plio-Pleistocene using Geochemical Provenance Analysis.* [PhD Thesis] Imperial College London.

Bertram, R. A., Wilson, D. J., van de Flierdt, T., McKay, R. M., Patterson, M. O., Jimenez-Espejo, F. J., ... & Riesselman, C. R. (2018). Pliocene deglacial event timelines and the biogeochemical response offshore Wilkes Subglacial Basin, East Antarctica. *Earth and Planetary Science Letters*, *494*, 109-116.

Biddle, L. C., Heywood, K. J., Kaiser, J., & Jenkins, A. (2017). Glacial meltwater identification in the Amundsen Sea. *Journal of Physical Oceanography*, *47*(4), 933-954.

Bijl P., et al. (2018). Stratigraphic calibration of Oligocene–Miocene organic-walled dinoflagellate cysts from offshore Wilkes Land, East Antarctica, and a zonation proposal. *J. Micropalaeontology* 37, 105–138. https://doi.org/10.5194/jm-37-105-2018

Billups et al. (2004). Astronomic calibration of the late Oligocene through early Miocene geomagnetic polarity time scale, *Earth and Planetary Science Letters 224*, 33-44. doi:10.1016/j.epsl.2004.05.004

Bingham, R. G., Ferraccioli, F., King, E. C., Larter, R. D., Pritchard, H. D., Smith, A. M., & Vaughan, D. G. (2012). Inland thinning of West Antarctic Ice Sheet steered along subglacial rifts. *Nature*, *487*(7408), 468-471.

Blum, J. D., & Erel, Y. (1995). A silicate weathering mechanism linking increases in marine 87Sr/86Sr with global glaciation. *Nature*, *373*(6513), 415-418.

Blum, J. D., & Erel, Y. (1997). Rb/ Sr isotope systematics of a granitic soil chronosequence: The importance of biotite weathering. *Geochimica et Cosmochimica Acta 61*, 3193-3204.

Blunier, T., & Brook, E. J. (2001). Timing of millennial-scale climate change in Antarctica and Greenland during the last glacial period. *science*, *291*(5501), 109-112.

Boger, S. D. (2011). Antarctica—before and after Gondwana. *Gondwana Research*, *19*(2), 335-371.

Borg, S. G., & DePaolo, D. J. (1994). Laurentia, Australia, and Antarctica as a Late Proterozoic supercontinent: constraints from isotopic mapping. *Geology*, *22*(4), 307-310.

Borg, S. G., Depaolo, D. J., & Smith, B. M. (1990). Isotopic structure and tectonics of the central Transantarctic Mountains. *Journal of Geophysical Research: Solid Earth*, *95*(B5), 6647-6667.

Brodie, J. W. (1959). A shallow shelf around Franklin Island in the Ross Sea, Antarctica. *New Zealand Journal of Geology and Geophysics 2*, 108-119.

Brown, C. R., Yakymchuk, C., Brown, M., Fanning, C. M., Korhonen, F. J., Piccoli, P. M., & Siddoway, C. S. (2016). From source to sink: petrogenesis of Cretaceous anatectic granites from the Fosdick migmatite–granite complex, West Antarctica. *Journal of Petrology*, *57*(7), 1241-1278.

Brown, G. & Brindley, G.W. (1984). X-RAY DIFFRACTION PROCEDURES for CLAY MINERAL IDENTIFICATION. Crystal Structures of Clay Minerals and their X-ray Identification, Mineralogical Society, London.

Burgess, S. D., Bowring, S. A., Fleming, T. H., & Elliot, D. H. (2015). High-precision geochronology links the Ferrar large igneous province with early-Jurassic ocean anoxia and biotic crisis. *Earth and Planetary Science Letters 415*, 90-99.

Burke, K. D., Williams, J. W., Chandler, M. A., Haywood, A. M., Lunt, D. J., & Otto-Bliesner, B. L. (2018). Pliocene and Eocene provide best analogs for near-future climates. *Proceedings of the National Academy of Sciences*, *115*(52), 13288-13293.

Burton-Johnson, A., & Riley, T. R. (2015). Autochthonous v. accreted terrane development of continental margins: a revised in situ tectonic history of the Antarctic Peninsula. *Journal of the Geological Society*, *172*(6), 822-835.

Calkin, T., Dunbar, G., Atkins, C., Harwood, D., Marschalek, J., Hulbe, C., Horgan, H., Martin, A., Ginnane, C., Turnball, J., Vandergoes, M., Geibert, W., Vermeesch, P., Carter, A. (in prep.). Sedimentology of the grounding zone of the Kamb Ice Stream: Implications for post-LGM depositional processes, changes in sediment source, and Quaternary stability of the Ross Ice Shelf.

Camerlenghi, A., Crise, A., Pudsey, C. J., Accerboni, E., Laterza, R., & Rebesco, M. (1997). Ten-month observation of the bottom current regime across a sediment drift of the Pacific margin of the Antarctic Peninsula. *Antarctic Science*, *9*(4), 426-433.

Carter, A., Riley, T. R., Hillenbrand, C. D., & Rittner, M. (2017). Widespread Antarctic glaciation during the late Eocene. *Earth and Planetary Science Letters*, *458*, 49-57.

Cecil, M. R., Gehrels, G., Ducea, M. N., & Patchett, P. J. (2011). U-Pb-Hf characterization of the central Coast Mountains batholith: Implications for petrogenesis and crustal architecture. *Lithosphere*, *3*(4), 247-260.

Chaput, J., Aster, R. C., Huerta, A., Sun, X., Lloyd, A., Wiens, D., ... & Wilson, T. (2014). The crustal thickness of West Antarctica. *Journal of Geophysical Research: Solid Earth*, *119*(1), 378-395.

Cherniak, D. J., & Watson, E. B. (2001). Pb diffusion in zircon. *Chemical Geology 172*, 5-24.

Chow, J. M., & Bart, P. J. (2003). West Antarctic Ice Sheet grounding events on the Ross Sea outer continental shelf during the middle Miocene. *Palaeogeogr., Palaeoclimatol., Palaeoecolf. 198*, 169-186.

Christoffersen, P., Bougamont, M., Carter, S. P., Fricker, H. A., & Tulaczyk, S. (2014). Significant groundwater contribution to Antarctic ice streams hydrologic budget. *Geophysical Research Letters*, *41*(6), 2003-2010.

Christoffersen, P., Tulaczyk, S., & Behar, A. (2010). Basal ice sequences in Antarctic ice stream: exposure of past hydrologic conditions and a principal mode of sediment transfer. *Journal of Geophysical Research: Earth Surface*, *115*.

Clark, P. U., He, F., Golledge, N. R., Mitrovica, J. X., Dutton, A., Hoffman, J. S., & Dendy, S. (2020). Oceanic forcing of penultimate deglacial and last interglacial sea-level rise. *Nature*, *577*(7792), 660-664.

Clough, J. W., & Hansen, B. L. (1979). The Ross ice shelf project. *Science*, *203*(4379), 433-434.

Clowes, C. D., Hannah, M. J., Wilson, G. J. & Wrenn, J. H. (2016). Marine palynostratigraphy of the Cape Roberts Drill-holes, Victoria Land Basin, Antarctica, with descriptions of six new species of organic-walled dinoflagellate cyst. *Mar. Micropaleontol. 126*, 65–84.

Cody, R. D., Levy, R. H., Harwood, D. M., & Sadler, P. M. (2008). Thinking outside the zone: high-resolution quantitative diatom biochronology for the Antarctic Neogene. *Palaeogeog. Palaeoclimatol. Palaeoecol. 260*, 92-121.

Colleoni, F., De Santis, L., Montoli, E., Olivo, E., Sorlien, C. C., Bart, P. J., ... & Prato, S. (2018). Past continental shelf evolution increased Antarctic ice sheet sensitivity to climatic conditions. *Nature Scientific reports*, *8*(1), 1-12.

Compston, W., McDougall, I., & Heier, K. S. (1968). Geochemical comparison of the mesozoic basaltic rocks of Antarctica, South Africa, South America and Tasmania. *Geochimica et Cosmochimica Acta* 32, 129-149.

Cook, C. P., Hemming, S. R., van de Flierdt, T., Davis, E. L. P., Williams, T., Galindo, A. L., ... & Escutia, C. (2017). Glacial erosion of East Antarctica in the Pliocene: A comparative study of multiple marine sediment provenance tracers. *Chemical Geology*, *466*, 199-218.

Cook, C. P., van de Flierdt, T., Williams, T., Hemming, S. R., Iwai, M., Kobayashi, M., ... & McKay, R. M. (2013). Dynamic behaviour of the East Antarctic ice sheet during Pliocene warmth. *Nature Geoscience,* 6(9), 765.

Cooper, A. F., Maas, R., Scott, J. M., & Barber, A. J. (2011). Dating of volcanism and sedimentation in the Skelton Group, Transantarctic Mountains: implications for the Rodinia-Gondwana transition in southern Victoria Land, Antarctica. *GSA Bulletin 123*, 681-702.

Corr, H. F., & Vaughan, D. G. (2008). A recent volcanic eruption beneath the West Antarctic ice sheet. *Nature Geoscience*, *1*(2), 122-125.

Cox, S.C., Parkinson, D.L., Allibone, A.H. & Cooper, A.F. (2000). Isotopic character of Cambro-Ordovician plutonism, southern Victoria Land, Antarctica. *New Zealand Journal of Geology and Geophysics, 43*(4): 501-520, DOI: 10.1080/00288306.2000.9514906.

Cox S.C., Smith Lyttle B. and the GeoMAP team (2019). *SCAR GeoMAP dataset*. GNS Science, Lower Hutt, New Zealand. Release v.201907. https://doi.org/10.21420/7SH7-6K05

Cox, S.C., Turnbull, I.M., Isaac, M.J., Townsend, D.B. & Smith Lyttle, B. (2012). Geology of southern Victoria Land, Antarctica. Institute of Geological & Nuclear Sciences geological map 22, scale 1:250 000, 1 sheet.

Craddock, J. P., Schmitz, M. D., Crowley, J. L., Larocque, J., Pankhurst, R. J., Juda, N., ... & Storey, B. (2017). Precise U-Pb zircon ages and geochemistry of Jurassic granites, Ellsworth-Whitmore terrane, central Antarctica. *GSA Bulletin*, *129*(1-2), 118-136.

Crampton, J. S. et al. (2016). Southern Ocean phytoplankton turnover in response to stepwise Antarctic cooling over the past 15 million years. *Proc. Natl Acad. Sci. USA 113*, 6868–6873.

Cuffey, K., & Alley, R. B. (1996). Is erosion by deforming subglacial sediments significant? (Toward till continuity). *Annals of Glaciology*, *22*, 17-24.

Cuffey, K. M., Conway, H., Gades, A. M., Hallet, B., Lorrain, R., Severinghaus, J. P., ... & White, J. W. (2000). Entrainment at cold glacier beds. *Geology*, *28*(4), 351-354.

Curtis, M. L., Leat, P. T., Riley, T. R., Storey, B. C., Millar, I. L., & Randall, D. E. (1999). Middle Cambrian rift-related volcanism in the Ellsworth Mountains, Antarctica: tectonic implications for the palaeo-Pacific margin of Gondwana. *Tectonophysics*, *304*(4), 275-299.

Dallai, L., Ghezzo, C., & Sharp, Z. D. (2003). Oxygen isotope evidence for crustal assimilation and magma mixing in the Granite Harbour Intrusives, Northern Victoria Land, Antarctica. *Lithos*, *67*(1-2), 135-151.

DeConto, R. M., & Pollard, D. (2016). Contribution of Antarctica to past and future sea-level rise. *Nature*, *531*(7596), 591-597.

DeConto, R. M., Pollard, D., Alley, R. B., Velicogna, I., Gasson, E., Gomez, N., ... & Dutton, A. (2021). The Paris Climate Agreement and future sea-level rise from Antarctica. *Nature*, *593*(7857), 83-89.

Delmonte, B., Petit, J. R., Andersen, K. K., Basile-Doelsch, I., Maggi, V., & Ya Lipenkov, V. (2004). Dust size evidence for opposite regional atmospheric circulation changes over east Antarctica during the last climatic transition. *Climate Dynamics*, *23*(3), 427-438.

Depoorter, M. A., Bamber, J. L., Griggs, J. A., Lenaerts, J. T., Ligtenberg, S. R., van den Broeke, M. R., & Moholdt, G. (2013). Calving fluxes and basal melt rates of Antarctic ice shelves. *Nature*, *502*(7469), 89-92.

De Santis, L., Anderson, J. B., Brancolini, G., & Zayatz, I. (1995). Seismic record of late Oligocene through Miocene glaciation on the central and eastern continental shelf of the Ross Sea. *Geology and Seismic Stratigraphy of the Antarctic Margin 68*, 235-260.

De Santis, L., Prato, S., Brancolini, G., Lovo, M., & Torelli, L. (1999). The Eastern Ross Sea continental shelf during the Cenozoic: implications for the West Antarctic ice sheet development. *Global and Planetary Change 23*, 173-196.

Diehl, T. M., Holt, J. W., Blankenship, D. D., Young, D. A., Jordan, T. A., & Ferraccioli, F. (2008). First airborne gravity results over the Thwaites Glacier catchment, West Antarctica. *Geochemistry, Geophysics, Geosystems*, *9*(4).

Di Vincenzo, G., Bracciali, L., Del Carlo, P., Panter, K., & Rocchi, S. (2010). 40Ar–39Ar dating of volcanogenic products from the AND-2A core (ANDRILL Southern McMurdo Sound Project, Antarctica): correlations with the Erebus Volcanic Province and implications for the age model of the core. *Bulletin of Volcanology 72*, 487-505.

Donelick, R.A., O'Sullivan, P.B., and Ketcham, R.A. (2005). Apatite fission-track analysis. *Reviews in Mineralogy and Geochemistry* 58, 49–94.

Dowdeswell, J. A. (1987). Processes of glacimarine sedimentation. *Progress in Physical Geography*, *11*(1), 52-90.

Dowdeswell, J. A., Maslin, M. A., Andrews, J. T., & McCave, I. N. (1995). Iceberg production, debris rafting, and the extent and thickness of Heinrich layers (H-1, H-2) in North Atlantic sediments. *Geology*, *23*(4), 301-304.

Dowdeswell, J. A., & Murray, T. (1990). Modelling rates of sedimentation from icebergs. *Geological Society, London, Special Publications*, *53*(1), 121-137.

Drewry, D. J., & Cooper, A. P. R. (1981). Processes and models of Antarctic glaciomarine sedimentation. *Annals of Glaciology*, *2*, 117-122.

Dühnforth, M., Anderson, R. S., Ward, D., & Stock, G. M. (2010). Bedrock fracture control of glacial erosion processes and rates. *Geology*, *38*(5), 423-426.

Dunbar, N. W., Iverson, N. A., Smellie, J. L., McIntosh, W. C., Zimmerer, M. J., & Kyle, P. R. (2021). Active volcanoes in Marie Byrd Land. *Geological Society, London, Memoirs*, *55*(1), 759-783.

Dutton, A., & Lambeck, K. (2012). Ice volume and sea level during the last interglacial. S*cience*, *337*(6091), 216-219.

Dutton, A., Webster, J. M., Zwartz, D., Lambeck, K., & Wohlfarth, B. (2015). Tropical tales of polar ice: evidence of Last Interglacial polar ice sheet retreat recorded by fossil reefs of the granitic Seychelles islands. *Quaternary Science Reviews*, *107*, 182-196.

Edwards, T. L., Brandon, M. A., Durand, G., Edwards, N. R., Golledge, N. R., Holden, P. B., ... & Wernecke, A. (2019). Revisiting Antarctic ice loss due to marine ice-cliff instability. *Nature*, *566*(7742), 58-64.

Ehrmann, W., Hillenbrand, C. D., Smith, J. A., Graham, A. G., Kuhn, G., & Larter, R. D. (2011). Provenance changes between recent and glacial-time sediments in the Amundsen Sea embayment, West Antarctica: clay mineral assemblage evidence. *Antarctic Science*, *23*(5), 471-486.

Ehrmann, W. U., & Mackensen, A. (1992). Sedimentological evidence for the formation of an East Antarctic ice sheet in Eocene/Oligocene time. *Palaeogeography, Palaeoclimatology, Palaeoecology*, *93*(1-2), 85-112.

Ehrmann, W. U., Melles, M., Kuhn, G., & Grobe, H. (1992). Significance of clay mineral assemblages in the Antarctic Ocean. *Marine Geology*, *107*(4), 249-273.

Einstein, H. A., & Krone, R. B. (1962). Experiments to determine modes of cohesive sediment transport in salt water. *Journal of Geophysical Research*, *67*(4), 1451-1461.

Eisenhauer, A., Meyer, H., Rachold, V., Tütken, T., Wiegand, B., Hansen, B. T., ... & Kassens, H. (1999). Grain size separation and sediment mixing in Arctic Ocean sediments: evidence from the strontium isotope systematic. *Chemical geology*, *158*(3-4), 173-188.

Elliot, D. H. (1996). The Hanson Formation: a new stratigraphical unit in the Transantarctic Mountains, Antarctica. *Antarctic Science 8*, 389-394.

Elliot, D. H., & Fanning, C. M. (2008). Detrital zircons from upper Permian and lower Triassic Victoria Group sandstones, Shackleton Glacier region, Antarctica: evidence for multiple sources along the Gondwana plate margin. *Gondwana Research 13*, 259-274.

Elliot, D. H., Fanning, C. M., & Hulett, S. R. (2015). Age provinces in the Antarctic craton: Evidence from detrital zircons in Permian strata from the Beardmore Glacier region, Antarctica. *Gondwana Research 28*, 152-164.

Elliot, D.H., Fanning, C.M., Isbell, J.L., Hulett, S.R.W. (2017). The Permo-Triassic Gondwana sequence, central Transantarctic Mountains, Antarctica: Zircon geochronology, provenance, and basin evolution. *Geosphere 13*, 155–178. https://doi.org/10.1130/GES01345.1.

Elliot, D. H., & Fleming, T. H. (2004). Occurrence and dispersal of magmas in the Jurassic Ferrar large igneous province, Antarctica. *Gondwana Research 7*, 223-237.

Elliot, D. H., Fleming, T. H., Kyle, P. R., & Foland, K. A. (1999). Long-distance transport of magmas in the Jurassic Ferrar large igneous province, Antarctica. *Earth and Planetary Science Letters*, 167(1-2), 89-104.

Elliot, D. H., Larsen, D., Fanning, C. M., Fleming, T. H., & Vervoort, J. D. (2016). The Lower Jurassic Hanson Formation of the Transantarctic Mountains: implications for the Antarctic sector of the Gondwana plate margin. *Geological Magazine*, *154*(4), 777-803.

Elsner, M., Schöner, R., Gerdes, A., & Gaupp, R. (2013). Reconstruction of the early Mesozoic plate margin of Gondwana by U–Pb ages of detrital zircons from northern Victoria Land, Antarctica. *Geological Society, London, Special Publications, 383*(1), 211-232.

Encarnación, J., & Grunow, A. (1996). Changing magmatic and tectonic styles along the paleo-Pacific margin of Gondwana and the onset of early Paleozoic magmatism in Antarctica. *Tectonics 15*, 1325-1341.

Encarnación, J., Fleming, T. H., Elliot, D. H., & Eales, H. V. (1996). Synchronous emplacement of Ferrar and Karoo dolerites and the early breakup of Gondwana. *Geology 24*, 535-538.

Encarnación, J., Rowell, A.J., Grunow, A.M. (1999). A U-Pb age for the Cambrian Taylor Formation, Antarctica: Implications for the Cambrian time scale. *Journal of Geology 107*, 497–504.

Escutia, C., & Brinkhuis, H. (2014). From greenhouse to icehouse at the Wilkes Land Antarctic margin: IODP Expedition 318 synthesis of results. *Developments in marine geology*, 7, 295-328.

Esquevin, J. (1969). Influence de la composition chimique des illites sur leur cristallinité. *Bull. Centre Rech. Pau-SNPA* 3, 147–153.

Estrada, S., Läufer, A., Eckelmann, K., Hofmann, M., Gärtner, A., & Linnemann, U. (2016). Continuous Neoproterozoic to Ordovician sedimentation at the East Gondwana margin—Implications from detrital zircons of the Ross Orogen in northern Victoria Land, Antarctica. *Gondwana Research 37*, 426-448.

Fagel N. (2007). Clay minerals, deep circulation and climate. *Proxies Late Cenozoic Paleoceanography* 1, 139-184.

Farmer, G. L., & Licht, K. J. (2016). Generation and fate of glacial sediments in the central Transantarctic Mountains based on radiogenic isotopes and implications for reconstructing past ice dynamics. *Quaternary Science Reviews* 150, 98-109.

Farmer, G. L., Licht, K., Swope, R. J. & Andrews, J. (2006). Isotopic constraints on the provenance of fine-grained sediment in LGM tills from the Ross Embayment, Antarctica. *Earth Planet. Sci. Lett.* 249, 90–107.

Farmer, R.K. (2011). *The application of biostratigraphy and paleoecology at Southern Ocean drill sites to resolve early to middle Miocene paleoclimatic events* [M.S. thesis]. University of Nebraska-Lincoln.

Faure, G., Bowman, J. R., Elliot, D. H., & Jones, L. M. (1974). Strontium isotope composition and petrogenesis of the Kirkpatrick basalt, Queen Alexandra Range, Antarctica. *Contributions to Mineralogy and Petrology* 48, 153-169.

Faure, G., Eastin, R., Ray, P.T., McLelland, D., and Shultz, C.H. (1979). *Geochronology of igneous and metamorphic rocks, central Transantarctic Mountains.* In Laskar, B. and Raja Rao, C.S. (eds.), Fourth International Gondwana Symposium. Calcutta, India, Hindustan Publishing Corporation.

Feakins, S., Warny, S. & Lee, JE. (2012). Hydrologic cycling over Antarctica during the middle Miocene warming. *Nature Geosci*. 5, 557–560. https://doi.org/10.1038/ngeo1498

Fensome, R. A. & Williams, G. L. (2004). *The Lentin and Williams index of fossil dinoflagellates*. American Association of Stratigraphic Palynologists Foundation Contribution Series 42.

Ferraccioli, F., Armadillo, E., Jordan, T., Bozzo, E., & Corr, H. (2009). Aeromagnetic exploration over the East Antarctic Ice Sheet: a new view of the Wilkes Subglacial Basin. *Tectonophysics*, *478*(1-2), 62-77.

Ferris, J., Johnson, A., & Storey, B. (1998). Form and extent of the Dufek intrusion, Antarctica, from newly compiled aeromagnetic data. *Earth and Planetary Science Letters*, *154*(1-4), 185-202.

Fleming, T. H. *Isotopic and chemical evolution of the Ferrar Group. Beardmore Glacier region, Antarctica*. [PhD thesis], Columbus, Ohio State University (1995).

Florindo, F. et al. (2013). Paleomagnetism and biostratigraphy of sediments from Southern Ocean ODP Site 744 (southern Kerguelen Plateau): implications for early-to-middle Miocene climate in Antarctica. *Global and Planetary Change 110*, 434–454.

Florindo, F., Siegert, M., De Santis, L., & Naish, T. (Eds.). (2021). *Antarctic climate evolution*. Elsevier.

Flowerdew, M. J. et al. (2007). Combined U-Pb geochronology and Hf isotope geochemistry of detrital zircons from early Paleozoic sedimentary rocks, Ellsworth-Whitmore Mountains block, Antarctica. *Geological Society of America Bulletin 119*, 275-288.

Flowerdew, M. J., Millar, I. L., Vaughan, A. P. M., Horstwood, M. S. A., & Fanning, C. M. (2006). The source of granitic gneisses and migmatites in the Antarctic Peninsula: a combined U–Pb SHRIMP and laser ablation Hf isotope study of complex zircons. *Contributions to Mineralogy and Petrology*, *151*(6), 751-768.

Ford, A. B. (1976). Stratigraphy of the layered gabbroic Dufek intrusion, Antarctica. *U.S. Geol. Surv. Bull.,* vol. 1405-D.

Ford, A. B., & Barrett, P. J. (1975). Basement rocks of the south-central Ross Sea, Site 270, DSDP Leg 28. *Initial Reports of the Deep Sea Drilling Project 28*, 861-868.

Frederick, B. C., Young, D. A., Blankenship, D. D., Richter, T. G., Kempf, S. D., Ferraccioli, F., & Siegert, M. J. (2016). Distribution of subglacial sediments across the Wilkes Subglacial Basin, East Antarctica. *Journal of Geophysical Research: Earth Surface*, *121*(4), 790-813.

Fretwell, P., Pritchard, H. D., Vaughan, D. G., Bamber, J. L., Barrand, N. E., Bell, R., ... & Zirizzotti, A. (2013). Bedmap2: improved ice bed, surface and thickness datasets for Antarctica. *The Cryosphere*, *7*(1), 375-393.

Futa, K., and LeMasurier, W. E. Nd and Sr isotopic studies on Cenozoic mafic lavas from West Antarctica - another source for continental alkali basalts. *Contributions to Mineralogy and Petrology 83*, 38-44 (1983).

Galbraith, R.F. (2005). Statistics for Fission Track Analysis, Chapman & Hall/CRC, Boca Raton, 219.

Galbraith, R.F., and Laslett, G.M. (1993). Statistical models for mixed fission track ages. *Nuclear Tracks* 21, 459-470.

Galeotti, S., DeConto, R., Naish, T., Stocchi, P., Florindo, F., Pagani, M., ... & Zachos, J. C. (2016). Antarctic Ice Sheet variability across the Eocene-Oligocene boundary climate transition. *Science*, *352*(6281), 76-80.

Garcia, M., & Parker, G. (1993). Experiments on the entrainment of sediment into suspension by a dense bottom current. *Journal of Geophysical Research: Oceans*, *98*(C3), 4793-4807.

Garçon, M., Chauvel, C., France-Lanord, C., Huyghe, P., & Lavé, J. (2013). Continental sedimentary processes decouple Nd and Hf isotopes. *Geochimica et Cosmochimica Acta*, *121*, 177-195.

Gardner, W.D., A.V. Mishonov, M.J. Richardson (2020). Global Transmissometer Database V3. https://odv.awi.de/data/ocean/global-transmissometer-database/

Gasson, E., DeConto, R. M., Pollard, D., & Levy, R. H. (2016). Dynamic Antarctic ice sheet during the early to mid-Miocene. *Proceedings of the National Academy of Sciences*, *113*(13), 3459-3464.

Gasson, E. G., & Keisling, B. A. (2020). The Antarctic Ice Sheet: A Paleoclimate Modelling Perspective. *Oceanography 33*, 90-100.

Gehrels, G. E., Valencia, V. A., & Ruiz, J. (2008). Enhanced precision, accuracy, efficiency, and spatial resolution of U-Pb ages by laser ablation–multicollector–inductively coupled plasma–mass spectrometry. *Geochemistry, Geophysics, Geosystems*, *9*(3).

Gil, I. M., Keigwin, L. D., & Abrantes, F. G. (2009). Deglacial diatom productivity and surface ocean properties over the Bermuda Rise, northeast Sargasso Sea. *Paleoceanography*, *24*(4).

Gilbert, I. M., Pudsey, C. J., & Murray, J. W. (1998). A sediment record of cyclic bottom-current variability from the northwest Weddell Sea. *Sedimentary geology*, *115*(1-4), 185-214.

Giorgetti, A., Crise, A., Laterza, R., Perini, L., Rebesco, M., & Camerlenghi, A. (2003). Water masses and bottom boundary layer dynamics above a sediment drift of the Antarctic Peninsula Pacific Margin. *Antarctic Science*, *15*(4), 537-546.

Gleadow, A.J.W. (1981). Fission-track dating methods: what are the real alternatives? *Nuclear Tracks 5*, 3-14.

Gleadow, A.J.W., Hurford, A.J. and Quaife, R.D. (1976). Fission track dating of zircon: improved etching techniques. *Earth and Planetary Science Letters* 33, 273-276.

Goelzer, H., Huybrechts, P., Loutre, M. F., & Fichefet, T. (2016). Last Interglacial climate and sea-level evolution from a coupled ice sheet–climate model. *Climate of the Past*, *12*(12), 2195-2213.

Gohl, K. (2012). Basement control on past ice sheet dynamics in the Amundsen Sea Embayment, West Antarctica. *Palaeogeography, Palaeoclimatology, Palaeoecology*, *335*, 35-41.

Gohl, K., Denk, A., Eagles, G., & Wobbe, F. (2013b). Deciphering tectonic phases of the Amundsen Sea Embayment shelf, West Antarctica, from a magnetic anomaly grid. *Tectonophysics*, *585*, 113-123.

Gohl, K. et al. (2013a). Seismic stratigraphic record of the Amundsen Sea Embayment shelf from pre-glacial to recent times: Evidence for a dynamic West Antarctic Ice Sheet. *Marine Geology 344*, 115-131.

Gohl, K., Teterin, D., Eagles, G., Netzeband, G., Grobys, J., Parsiegla, N., ... & Udintsev, G. B. (2007). Geophysical survey reveals tectonic structures in the Amundsen Sea embayment, West Antarctica. *US Geological Survey Open-File Report, 2007-1047.* http://pubs. usgs. gov/of/2007/1047/srp/srp047/.

Goldich, S. S., Treves, S. B., Suhr, N. H., & Stuckless, J. S. (1975). Geochemistry of the Cenozoic volcanic rocks of Ross Island and vicinity, Antarctica. *The Journal of Geology 83*, 415-435.

Goldstein, S. L., & Hemming, S. R. (2003). Long-lived isotopic tracers in oceanography, paleoceanography, and ice-sheet dynamics. *Treatise on geochemistry*, *6*, 625.

Golledge, N. R., Clark, P. U., He, F., Dutton, A., Turney, C. S. M., Fogwill, C. J., ... & Carlson, A. E. (2021). Retreat of the Antarctic Ice Sheet during the Last Interglaciation and implications for future change. *Geophysical Research Letters*, *48*(17), e2021GL094513.

Golledge, N. R., Kowalewski, D. E., Naish, T. R., Levy, R. H., Fogwill, C. J., & Gasson, E. G. (2015). The multi-millennial Antarctic commitment to future sea-level rise. *Nature*, *526*(7573), 421-425.

Golledge, N. R., Levy, R. H., McKay, R. M., Fogwill, C. J., White, D. A., Graham, A. G., ... & Hall, B. L. (2013). Glaciology and geological signature of the Last Glacial Maximum Antarctic ice sheet. *Quaternary Science Reviews*, *78*, 225-247.

Golledge, N. R., Thomas, Z. A., Levy, R. H., Gasson, E. G., Naish, T. R., McKay, R. M., ... & Fogwill, C. J. (2017). Antarctic climate and ice-sheet configuration during the early Pliocene interglacial at 4.23 Ma. *Climate of the Past*, *13*(7), 959-975.

Golynsky, A. V., Ferraccioli, F., Hong, J. K., Golynsky, D. A., von Frese, R. R. B., Young, D. A., ... & Roberts, J. L. (2018). New magnetic anomaly map of the Antarctic. *Geophysical Research Letters*, *45*(13), 6437-6449.

Goodge, J. W. (2020). Geological and tectonic evolution of the Transantarctic Mountains, from ancient craton to recent enigma. *Gondwana Research*, *80*, 50-122.

Goodge, J. W., & Fanning, C. M. (1999). 2.5 by of punctuated Earth history as recorded in a single rock. *Geology 27*, 1007-1010.

Goodge, J. W., & Fanning, C. M. (2010). Composition and age of the East Antarctic Shield in eastern Wilkes Land determined by proxy from Oligocene-Pleistocene glaciomarine sediment and Beacon Supergroup sandstones, Antarctica. *GSA Bulletin 122*, 1135-1159.

Goodge, J. W., & Fanning, C. M. (2016). Mesoarchean and Paleoproterozoic history of the Nimrod Complex, central Transantarctic Mountains, Antarctica: stratigraphic revisions and relation to the Mawson Continent in East Gondwana. *Precambrian Research 285*, 242-271.

Goodge, J. W., Fanning, C. M., & Bennett, V. C. (2001). U–Pb evidence of ~1.7 Ga crustal tectonism during the Nimrod Orogeny in the Transantarctic Mountains, Antarctica: implications for Proterozoic plate reconstructions. *Precambrian Research 112*, 261-288.

Goodge, J. W., Fanning, C. M., Norman, M. D., & Bennett, V. C. (2012). Temporal, isotopic and spatial relations of early Paleozoic Gondwana-margin arc magmatism, central Transantarctic Mountains, Antarctica. *Journal of Petrology 53*, 2027-2065.

Goodge, J. W., & Finn, C. A. (2010). Glimpses of East Antarctica: Aeromagnetic and satellite magnetic view from the central Transantarctic Mountains of East Antarctica. *Journal of Geophysical Research: Solid Earth*, *115*(B9).

Goodge, J. W., Hansen, V. L., Peacock, S. M., Smith, B. K., & Walker, N. W. (1993). Kinematic evolution of the Miller Range shear zone, central Transantarctic Mountains, Antarctica, and implications for Neoproterozoic to early Paleozoic tectonics of the East Antarctic margin of Gondwana. *Tectonics 12*, 1460-1478.

Goodge, J. W., Myrow, P., Williams, I. S., & Bowring, S. A. (2002). Age and provenance of the Beardmore Group, Antarctica: constraints on Rodinia supercontinent breakup. *The Journal of geology 110*, 393-406.

Goodge, J. W., Vervoort, J. D., Fanning, C. M., Brecke, D. M., Farmer, G. L., Williams, I. S., ... & DePaolo, D. J. (2008). A positive test of East Antarctica–Laurentia juxtaposition within the Rodinia supercontinent. *Science*, *321*(5886), 235-240.

Goodge, J. W., Williams, I. S., & Myrow, P. (2004). Provenance of Neoproterozoic and lower Paleozoic siliciclastic rocks of the central Ross orogen, Antarctica: Detrital record of rift-, passive-, and active-margin sedimentation. *Geological Society of America Bulletin 116*, 1253-1279.

Gootee, B., & Stump, E. (2006). *Depositional environments of the Byrd Group, Byrd Glacier area: a Cambrian record of sedimentation, tectonism, and magmatism*. In: Fütterer D.K., Damaske D., Kleinschmidt G., Miller H. &Tessensohn F. (Eds.) Antarctica. Springer, Berlin, Heidelberg.

Gow, A. J., & Meese, D. A. (1996). Nature of basal debris in the GISP2 and Byrd ice cores and its relevance to bed processes. *Annals of Glaciology*, *22*, 134-140.

Gow, A. J., Ueda, H. T., & Garfield, D. E. (1968). Antarctic ice sheet: preliminary results of first core hole to bedrock. *Science*, *161*(3845), 1011-1013.

Gow, A. J., Epstein, S., & Sheehy, W. (1979). On the origin of stratified debris in ice cores from the bottom of the Antarctic ice sheet. *Journal of Glaciology*, *23*(89), 185-192.

Grant, G. R., Naish, T. R., Dunbar, G. B., Stocchi, P., Kominz, M. A., Kamp, P. J., ... & Patterson, M. O. (2019). The amplitude and origin of sea-level variability during the Pliocene epoch. *Nature*, *574*(7777), 237-241.

Greenop, R., Sosdian, S. M., Henehan, M. J., Wilson, P. A., Lear, C. H., & Foster, G. L. (2019). Orbital forcing, ice volume, and CO2 across the Oligocene-Miocene transition. *Paleoceanography and Paleoclimatology*, *34*(3), 316-328.

Griffin, W. L. (2008). GLITTER: data reduction software for laser ablation ICP-MS. Laser Ablation ICP-MS in the Earth Sciences: Current practices and outstanding issues, 308-311.

Grindley, G. W., McGregor, V. R., & Walcott, R. I. (1964). Outline of the geology of the Nimrod-Beardmore-Axel Heiberg glaciers region, Ross Dependency. *Antarctic Geology,* 206-219.

Gross, T. F., & Williams III, A. J. (1991). Characterization of deep-sea storms. *Marine Geology*, *99*(3-4), 281-301.

Guenthner, W.R., Reiners, P.W., and Chowdhury, U. (2016). Isotope dilution analysis of Ca and Zr in apatite and zircon (U-Th)/He chronometry. *Geochemistry Geophysics Geosystems* 17, 1623–1640. doi:10.1002/2016GC006311.

Gulick, S. P., Shevenell, A. E., Montelli, A., Fernandez, R., Smith, C., Warny, S., ... & Blankenship, D. D. (2017). Initiation and long-term instability of the East Antarctic Ice Sheet. *Nature*, *552*(7684), 225-229.

Gunn, B. M., & Warren, G. (1962). Geology of Victoria Land between the Mawson and Mulock Glaciers, Antarctica. *New Zea. Geol. Bull. 71*, 157.

Gunner, J. (1976). ISOTOPIC and GEOCHEMICAL STUDIES of the PRE-DEVONAIN BASEMENT COMPLEX, BEARDMORE GLACIER REGION, ANTARCTICA. Ohio State University, Columbus, Institute of Polar Studies Report No. 41.

Gutjahr, M., Frank, M., Stirling, C. H., Klemm, V., Van de Flierdt, T., & Halliday, A. N. (2007). Reliable extraction of a deepwater trace metal isotope signal from Fe–Mn oxyhydroxide coatings of marine sediments. *Chemical Geology*, *242*(3-4), 351-370.

Hagedorn, B., Gersonde, R., Gohl, K., & Hubberten, H. W. (2007). Petrology, geochemistry and K/Ar age constraints of the eastern De Gerlache Seamount alkaline basalts (Bellingshausen Sea, southeast Pacific). *Polarforschung*, *76*(3), 87-94.

Hagen, R. A., Gohl, K., Gersonde, R., Kuhn, G., Völker, D., & Kodagali, V. N. (1998). A geophysical survey of the De Gerlache Seamounts: preliminary results. *Geo-Marine Letters*, *18*(1), 19-25.

Hallet, B., Hunter, L., & Bogen, J. (1996). Rates of erosion and sediment evacuation by glaciers: A review of field data and their implications. *Global and Planetary Change*, *12*(1-4), 213-235.

Hannah, M. J. (2006). The palynology of ODP site 1165, Prydz Bay, East Antarctica: a record of Miocene glacial advance and retreat. *Palaeogeogr. Palaeoclimatol. Palaeoecol. 231*, 120–133.

Hannah, M. J., Wilson, G. J. & Wrenn, J. H. (2000). Oligocene and miocene marine palynomorphs from CRP-2/2A, Victoria Land Basin, Antarctica. *Terra Antarctica 7*, 503–511.

Hansen, K., Stevens, J. & Shuman, C. (2022, 27 April). Ice Lost, Island Found? *NASA Earth Observatory*. https://www.earthobservatory.nasa.gov/images/149755/ice-lost-island-found

Haran, T., Bohlander, J., Scambos, T., Painter, T., & Fahnestock, M. (2014 – updated 2019). MODIS Mosaic of Antarctica 2008–2009 (MOA2009) image map. *Boulder, Colorado USA, National Snow and Ice Data Center* (accessed 8th June 2020).

Harland, R., & Pudsey, C. J. (1999). Dinoflagellate cysts from sediment traps deployed in the Bellingshausen, Weddell and Scotia seas, Antarctica. *Marine Micropaleontology 37*, 77-99.

Hart, S. R., Blusztajn, J., LeMasurier, W. E. & Rex, D. C. (1997). Hobbs Coast Cenozoic volcanism: Implications for the West Antarctic rift system. *Chemical Geology 139*, 223-248.

Hartman, J. D., Bijl, P. K., & Sangiorgi, F. (2018). A review of the ecological affinities of marine organic microfossils from a Holocene record offshore of Adélie Land (East Antarctica). *Journal of Micropalaeontology 37*, 445-497.

Hauck, J., Gerdes, D., Hillenbrand, C. D., Hoppema, M., Kuhn, G., Nehrke, G., ... & Wolf-Gladrow, D. A. (2012). Distribution and mineralogy of carbonate sediments on Antarctic shelves. *Journal of Marine Systems*, *90*(1), 77-87.

Hauptvogel, D. W., & Passchier, S. (2012). Early–Middle Miocene (17–14 Ma) Antarctic ice dynamics reconstructed from the heavy mineral provenance in the AND-2A drill core, Ross Sea, Antarctica. *Global and Planetary Change 82*, 38-50.

Henjes-Kunst, F., & Schussler, U. (2003). Metasedimentary units of the Cambro-Ordovician Ross Orogen in northern Victoria Land and Oates Land: implications for their provenance and geotectonic setting from geochemical and Nd-Sr isotope data. *Terra Antartica*, *10*, 105-128.

Herbert, T. D., Lawrence, K. T., Tzanova, A., Peterson, L. C., Caballero-Gill, R., & Kelly, C. S. (2016). Late Miocene global cooling and the rise of modern ecosystems. *Nature Geoscience*, *9*(11), 843-847.

Hergt, J. M., Chappell, B. W., Faure, G., & Mensing, T. M. (1989). The geochemistry of Jurassic dolerites from Portal Peak, Antarctica. *Contributions to Mineralogy and Petrology*, 102(3), 298-305.

Hillenbrand, C. D., Baesler, A., & Grobe, H. (2005). The sedimentary record of the last glaciation in the western Bellingshausen Sea (West Antarctica): implications for the interpretation of diamictons in a polar-marine setting. *Marine Geology*, *216*(4), 191-204.

Hillenbrand, C. D., Crowhurst, S. J., Williams, M., Hodell, D. A., McCave, I. N., Ehrmann, W., ... & Larter, R. D. (2021). New insights from multi-proxy data from the West Antarctic continental rise: Implications for dating and interpreting Late Quaternary palaeoenvironmental records. *Quaternary Science Reviews*, *257*, 106842.

Hillenbrand, C. D., & Ehrmann, W. (2005). Late Neogene to Quaternary environmental changes in the Antarctic Peninsula region: evidence from drift sediments. *Global and Planetary Change*, *45*(1-3), 165-191.

Hillenbrand, C. D., Grobe, H., Diekmann, B., Kuhn, G., & Fütterer, D. K. (2003). Distribution of clay minerals and proxies for productivity in surface sediments of the Bellingshausen and Amundsen seas (West Antarctica)–Relation to modern environmental conditions. *Marine Geology*, *193*(3-4), 253-271.

Hinkel, J., Aerts, J. C., Brown, S., Jiménez, J. A., Lincke, D., Nicholls, R. J., ... & Addo, K. A. (2018). The ability of societies to adapt to twenty-first-century sea-level rise. *Nature Climate Change*, *8*(7), 570-578.

Hoernle, K., Timm, C., Hauff, F., Tappenden, V., Werner, R., Jolis, E. M., ... & Gohl, K. (2020). Late Cretaceous (99-69 Ma) basaltic intraplate volcanism on and around Zealandia: Tracing upper mantle geodynamics from Hikurangi Plateau collision to Gondwana breakup and beyond. *Earth and Planetary Science Letters*, *529*, 115864.

Hogan, K. A., Larter, R. D., Graham, A. G., Arthern, R., Kirkham, J. D., Totten Minzoni, R., ... & Wellner, J. (2020). Revealing the former bed of Thwaites Glacier using sea-floor bathymetry: implications for warm-water routing and bed controls on ice flow and buttressing. *The Cryosphere*, *14*(9), 2883-2908.

Hooke, R. L., Cummings, D. I., Lesemann, J. E., & Sharpe, D. R. (2013). Genesis of dispersal plumes in till. *Canadian Journal of Earth Sciences*, *50*(8), 847-855.

Hopwood, M. J., Carroll, D., Höfer, J., Achterberg, E. P., Meire, L., Le Moigne, F. A., ... & González, H. E. (2019). Highly variable iron content modulates iceberg-ocean fertilisation and potential carbon export. *Nature communications*, *10*(1), 1-10.

Hourigan, J.K., Reiners, P.W., and Brandon, M.T. (2005). U-Th zonation-dependent alpha-ejection in (U-Th)/He chronometry. *Geochimica et Cosmochimica Acta* 69, 3349–3365. doi:10.1016/j.gea.2005.01.024.

Hughes, T. J. (1981). The weak underbelly of the West Antarctic ice sheet. *Journal of Glaciology*, *27*(97), 518-525.

Hulbe, C., & Fahnestock, M. (2007). Century-scale discharge stagnation and reactivation of the Ross ice streams, West Antarctica. *Journal of Geophysical Research: Earth Surface*, *112*(F3).

Hurford, A. J., and Green, P. F. (1983). The Zeta-Age Calibration of Fission-Track Dating. *Isotope Geoscience* 1, 285-317.

Hurford, A.J. (1990). Standardization of fission track dating calibration: Recommended by the Fission Track Working Group of the I.U.G.S. Subcommission on Geochronology. *Chemical Geology* 80, 171-178.

Iverson, N. R. (2012). A theory of glacial quarrying for landscape evolution models. *Geology*, *40*(8), 679-682.

Jamieson, S. S., Hulton, N. R., & Hagdorn, M. (2008). Modelling landscape evolution under ice sheets. *Geomorphology*, *97*(1-2), 91-108.

Jamieson, S. S., Sugden, D. E., & Hulton, N. R. (2010). The evolution of the subglacial landscape of Antarctica. *Earth and Planetary Science Letters*, *293*(1-2), 1-27.

Jackson, S. E., Pearson, N. J., Griffin, W. L., & Belousova, E. A. (2004). The application of laser ablation-inductively coupled plasma-mass spectrometry to in situ U–Pb zircon geochronology. *Chemical Geology* 211, 47-69.

Jacobsen, S. B., & Wasserburg, G. J. (1980). Sm-Nd isotopic evolution of chondrites. *Earth and Planetary Science Letters*, *50*(1), 139-155.

Johnson, G. L., Kyle, P. R., Vanney, J. R., & Campsie, J. (1982). Geology of Scott and Balleny Islands, Ross Sea, Antarctica, and morphology of adjacent seafloor. *New Zealand Journal of Geology and Geophysics*, *25*(4), 427-436.

Johnson, J. S., O'Donnell, J. P., & Thomas, E. R. (2018). In situ measurements of snow accumulation in the Amundsen Sea Embayment during 2016. *Antarctic Science*, *30*(3), 197-203.

Jones, L. M., & Faure, G. (1967). Origin of the salts in Lake Vanda, Wright Valley, southern Victoria Land, Antarctica. *Earth and Planetary Science Letters* 3, 101-106.

Jordan, T. A. (Personal Communication, January 2021).

Jordan, T. A., Ferraccioli, F., Armadillo, E., & Bozzo, E. (2013a). Crustal architecture of the Wilkes Subglacial Basin in East Antarctica, as revealed from airborne gravity data. *Tectonophysics*, *585*, 196-206.

Jordan, T. A., Ferraccioli, F., Ross, N., Corr, H. F., Leat, P. T., Bingham, R. G., ... & Siegert, M. J. (2013b). Inland extent of the Weddell Sea Rift imaged by new aerogeophysical data. *Tectonophysics*, *585*, 137-160.

Jordan, T. A., Ferraccioli, F., Vaughan, D. G., Holt, J. W., Corr, H., Blankenship, D. D., & Diehl, T. M. (2010). Aerogravity evidence for major crustal thinning under the Pine Island Glacier region (West Antarctica). *GSA Bulletin*, *122*(5-6), 714-726.

Jordan, T. A., Riley, T. R., & Siddoway, C. S. (2020). The geological history and evolution of West Antarctica. *Nature Reviews Earth & Environment*, *1*(2), 117-133.

Joughin, I., Smith, B. E., & Medley, B. (2014). Marine ice sheet collapse potentially under way for the Thwaites Glacier Basin, West Antarctica. *Science*, *344*(6185), 735-738.

Kellogg, D. E., & Kellogg, T. B. (1986). Diatom biostratigraphy of sediment cores from beneath the Ross Ice Shelf. *Micropaleontology*, 74-94.

Kennett, J. P. (1977). Cenozoic evolution of Antarctic glaciation, the circum-Antarctic Ocean, and their impact on global paleoceanography. *Journal of Geophysical Research* 82, 3843-3860.

Kennett, J.P., & Barker, P.F. (1990). Latest Cretaceous to Cenozoic climate and oceanographic developments in the Weddell Sea, Antarctica: an ocean-drilling perspective. *Proc. Ocean Drill. Program Sci. Results 113*, 937–960. doi:10.2973/odp.proc.sr.113.195.1990

Kennicutt, M. C. et al. (2014). A roadmap for Antarctic and Southern Ocean science for the next two decades and beyond. *Antarctic Science 27*, 3-18.

Ketcham, R.A., Gautheron, C., and Tassan-Got, L. (2011). Accounting for long alpha-particle stopping distances in (U-Th-Sm)/He geochronology: Refinement of the baseline case. *Geochimica et Cosmochimica Acta* 75, 7779–7791. doi:10.1016/j.gca.2011.10.011.

Kingslake, J., Scherer, R. P., Albrecht, T., Coenen, J., Powell, R. D., Reese, R., ... & Whitehouse, P. L. (2018). Extensive retreat and re-advance of the West Antarctic Ice Sheet during the Holocene. *Nature*, *558*(7710), 430-434.

Kipf, A., Hauff, F., Werner, R., Gohl, K., van den Bogaard, P., Hoernle, K., ... & Klügel, A. (2014). Seamounts off the West Antarctic margin: A case for non-hotspot driven intraplate volcanism. *Gondwana Research*, *25*(4), 1660-1679.

Kipf, A., Mortimer, N., Werner, R., Gohl, K., Van Den Bogaard, P., Hauff, F., & Hoernle, K. (2012). Granitoids and dykes of the Pine Island Bay region, West Antarctica. *Antarctic Science*, *24*(5), 473-484.

Klages, J. P., Salzmann, U., Bickert, T., Hillenbrand, C. D., Gohl, K., Kuhn, G., ... & Dziadek, R. (2020). Temperate rainforests near the South Pole during peak Cretaceous warmth. *Nature*, *580*(7801), 81-86.

Kochhann, K.G. et al. (2016). Eccentricity pacing of eastern equatorial Pacific carbonate dissolution cycles during the Miocene Climatic Optimum. *Paleoceanography 31*, 1-17. doi: 10.1002/2016PA002988

Kominz, M. A. et al. (2016). Miocene relative sea level on the New Jersey shallow continental shelf and coastal plain derived from one-dimensional backstripping: A case for both eustasy and epeirogeny. *Geosphere 12*, 1437-1456.

Koppes, M., Hallet, B., Rignot, E., Mouginot, J., Wellner, J. S., & Boldt, K. (2015). Observed latitudinal variations in erosion as a function of glacier dynamics. *Nature*, *526*(7571), 100-103.

Korhonen, F. J., Saito, S., Brown, M., Siddoway, C. S., & Day, J. M. D. (2010). Multiple generations of granite in the Fosdick Mountains, Marie Byrd Land, West Antarctica: implications for polyphase intracrustal differentiation in a continental margin setting. *Journal of Petrology*, *51*(3), 627-670.

Kristoffersen, Y., Strand, K., Vorren, T., Harwood, D. and Webb, P. (2000). Pilot shallow drilling on the continental shelf, Dronning Maud Land, Antarctica. *J. Antarct. Sci.* 4, 463–470.

Kuiper, K. F., Deino, A., Hilgen, F. J., Krijgsman, W., Renne, P. R., & Wijbrans, A. J. (2008). Synchronizing rock clocks of Earth history. *Science*, *320*(5875), 500-504.

Kulhanek, D. K., Levy, R. H., Clowes, C. D., Prebble, J. G., Rodelli, D., Jovane, L., ... & Naish, T. R. (2019). Revised chronostratigraphy of DSDP Site 270 and late Oligocene to early Miocene paleoecology of the Ross Sea sector of Antarctica. *Global and Planetary Change*, *178*, 46-64.

Kurasawa, H. (1975). Strontium isotopic studies of the Ross Island volcanics, Antarctica. *Memoirs of National Institue of Polar Research, Special Issue 4*, 67-74.

Kyle, P. R., Moore, J. A., & Thirlwall, M. F. (1992). Petrologic evolution of anorthoclase phonolite lavas at Mount Erebus, Ross Island, Antarctica. *Journal of Petrology* 33, 849-875.

Kyle, R.A. & Schopf, J.M. (1982). *Permian and Triassic palynostratigraphy of the Victoria Group, Transantarctic Mountains*: in Craddock, C., ed., Antarctic geoscience: Madison, University of Wisconsin Press, International Union of Geological Sciences, Series B-4, 649–659.

Laird, M. G. (1991). *The late Proterozoic-middle Palaeozoic rocks of Antarctica.* In R. J. Tingey (Ed.) The Geology of Antarctica (pp. 74-119). Oxford University Press, Oxford.

Larter, R. D., Rebesco, M., Vanneste, L. E., Gamboa, L. A. P., & Barker, P. F. (1997). Cenozoic tectonic, sedimentary and glacial history of the continental shelf west of Graham Land, Antarctic Peninsula. *Geology and seismic stratigraphy of the Antarctic margin*, *2*, 1-27.

Laskar, J. et al. (2004). A long-term numerical solution for the insolation quantities of the Earth. *Astronomy & Astrophysics 428*, 261-285.

Lawver, L., Lee, J., Kim, Y., & Davey, F. (2012). Flat-topped mounds in western Ross Sea: Carbonate mounds or subglacial volcanic features? *Geosphere 8*, 645-653.

Leat, P. T., Scarrow, J. H., & Millar, I. L. (1995). On the Antarctic Peninsula batholith. *Geological Magazine*, *132*(4), 399-412.

LeMasurier, W. (2013). Shield volcanoes of Marie Byrd Land, West Antarctic rift: oceanic island similarities, continental signature, and tectonic controls. *Bulletin of Volcanology*, *75*(6), 1-18.

LeMasurier, W. E., & Landis, C. A. (1996). Mantle-plume activity recorded by low-relief erosion surfaces in West Antarctica and New Zealand. *Geological Society of America Bulletin*, *108*(11), 1450-1466.

LeMasurier, W. E., & Rocchi, S. (2005). Terrestrial record of post-Eocene climate history in Marie Byrd Land, West Antarctica. Geografiska Annaler: Series A, *Physical Geography 87*, 51-66.

LeMasurier, W. E., Thomson, J. W., Baker, P. E., Kyle, P. R., Rowley, P. D., Smellie, J. L., & Verwoerd, W. J. (1990). *Volcanoes of the Antarctic plate and Southern Ocean* (Vol. 48). American Geophysical Union.

Levy, R., Harwood, D., Florindo, F., Sangiorgi, F., Tripati, R., Von Eynatten, H., ... & SMS Science Team. (2016). Antarctic ice sheet sensitivity to atmospheric CO2 variations in the early to mid-Miocene. *Proceedings of the National Academy of Sciences*, *113*(13), 3453-3458.

Levy, R. H., Meyers, S. R., Naish, T. R., Golledge, N. R., McKay, R. M., Crampton, J. S., ... & Kulhanek, D. K. (2019). Antarctic ice-sheet sensitivity to obliquity forcing enhanced through ocean connections. *Nature Geoscience*, *12*(2), 132-137.

Lewis, A. R., Marchant, D. R., Ashworth, A. C., Hedenäs, L., Hemming, S. R., Johnson, J. V., ... & Wolfe, A. P. (2008). Mid-Miocene cooling and the extinction of tundra in continental Antarctica. *Proceedings of the National Academy of Sciences*, *105*(31), 10676-10680.

Licht, K. J. et al. (2018). Evidence for extending anomalous Miocene volcanism at the edge of the East Antarctic craton. *Geophysical Research Letters 45*, 3009-3016.

Licht, K. J., & Hemming, S. R. (2017). Analysis of Antarctic glacigenic sediment provenance through geochemical and petrologic applications. *Quaternary Science Reviews 164*, 1-24.

Licht, K. J., Hennessy, A. J. & Welke, B. M. (2014). The U-Pb detrital zircon signature of West Antarctic ice stream tills in the Ross embayment, with implications for Last Glacial Maximum ice flow reconstructions. *Antarctic Science* 26, 687–697.

Licht, K. J., Lederer, J. R., & Swope, R. J. (2005). Provenance of LGM glacial till (sand fraction) across the Ross embayment, Antarctica. *Quaternary Science Reviews*, *24*(12-13), 1499-1520.

Licht, K. J., & Palmer, E. F. (2013). Erosion and transport by Byrd Glacier, Antarctica during the last glacial maximum. *Quaternary Science Reviews 62*, 32-48.

Lindow, J., Kamp, P. J., Mukasa, S. B., Kleber, M., Lisker, F., Gohl, K., ... & Spiegel, C. (2016). Exhumation history along the eastern Amundsen Sea coast, West Antarctica, revealed by low-temperature thermochronology. *Tectonics*, *35*(10), 2239-2257.

Lipp, A. G., Roberts, G. G., Whittaker, A. C., Gowing, C. J., & Fernandes, V. M. (2020). River sediment geochemistry as a conservative mixture of source regions: Observations and predictions from the Cairngorms, UK. *Journal of Geophysical Research: Earth Surface 125*(12), e2020JF005700.

Locarnini, M. M., Mishonov, A. V., Baranova, O. K., Boyer, T. P., Zweng, M. M., Garcia, H. E., ... & Smolyar, I. (2018). World ocean atlas 2018, volume 1: Temperature.

Lough, A. C. et al. (2013). Seismic detection of an active subglacial magmatic complex in Marie Byrd Land, Antarctica. *Nature Geoscience 6*, 1031-1035.

Lumborg, U. (2005). Modelling the deposition, erosion, and flux of cohesive sediment through Øresund. *Journal of Marine Systems*, *56*(1-2), 179-193.

Luyendyk, B. P., Wilson, D. S., & Siddoway, C. S. (2003). Eastern margin of the Ross Sea Rift in western Marie Byrd Land, Antarctica: Crustal structure and tectonic development. *Geochemistry, Geophysics, Geosystems*, *4*(10).

Maasch, K. A. (1988). Statistical detection of the mid-Pleistocene transition. *Climate dynamics*, *2*(3), 133-143.

MacAyeal, D. R. (1992). The basal stress distribution of Ice Stream E, Antarctica, inferred by control methods. *Journal of Geophysical Research: Solid Earth*, *97*(B1), 595-603.

Mahaney, W. C. (1995). Pleistocene and Holocene glacier thicknesses, transport histories and dynamics inferred from SEM microtextures on quartz particles. *Boreas*, *24*(4), 293-304.

Mahaney, W. C. (2002). *Atlas of sand grain surface textures and applications*. Oxford University Press, USA.

Marschalek, J.W., Zurli, L., Talarico, F., van de Flierdt, T., Vermeesch, P., … & McKay, R.M. (2021). A large West Antarctic Ice Sheet explains early Neogene sea-level amplitude. *Nature 600*(7889), 450–455. https://doi.org/10.1038/s41586-021-04148-0

Marsland, S. J., Bindoff, N. L., Williams, G. D., & Budd, W. F. (2004). Modeling water mass formation in the Mertz Glacier Polynya and Adélie Depression, east Antarctica. *Journal of Geophysical Research: Oceans*, *109*(C11).

Martin, A. P., Cooper, A. F., & Price, R. C. Petrogenesis of Cenozoic, alkalic volcanic lineages at Mount Morning, West Antarctica and their entrained lithospheric mantle xenoliths: Lithospheric versus asthenospheric mantle sources. *Geochimica et Cosmochimica Acta 122*, 127-152 (2013).

Martin, A. P., Price, R. C., Cooper, A. F., & McCammon, C. A. (2015). Petrogenesis of the rifted southern Victoria Land lithospheric mantle, Antarctica, inferred from petrography, geochemistry, thermobarometry and oxybarometry of peridotite and pyroxenite xenoliths from the Mount Morning eruptive centre. *Journal of Petrology 56*, 193-226.

Massom, R. A., Hill, K. L., Lytle, V. I., Worby, A. P., Paget, M. J., & Allison, I. (2001). Effects of regional fast-ice and iceberg distributions on the behaviour of the Mertz Glacier polynya, East Antarctica. *Annals of Glaciology*, *33*, 391-398.

Masson-Delmotte, V. et al. (2013). Information from paleoclimate archives. *Climate change* 383–464.

Mazur, A. K., Wåhlin, A. K., & Krężel, A. (2017). An object-based SAR image iceberg detection algorithm applied to the Amundsen Sea. *Remote Sensing of Environment*, *189*, 67-83.

Mazur, A. K., Wahlin, A. K., & Kalén, O. (2019). The life cycle of small-to medium-sized icebergs in the Amundsen sea embayment. *Polar Research*, *38*.

McArthur, J. M. (1994). Recent trends in strontium isotope stratigraphy. *Terra nova* 6, 331-358.

McArthur, J. M., Howarth, R. J., Shields, G. A., & Zhou, Y. (2020). *Strontium isotope stratigraphy.* In Geologic Time Scale 2020 (eds. Gradstein, F. M. et al.) 211-238. (Elsevier).

McCarron, J. J., & Smellie, J. L. (1998). Tectonic implications of fore-arc magmatism and generation of high-magnesian andesites: Alexander Island, Antarctica. *Journal of the Geological Society*, *155*(2), 269-280.

McCave, I. N. (2005) *Deposition from suspension.* In: Encyclopedia of Geology. Elsevier Science Ltd., Amsterdam, pp. 8-17.

McCave, I. N. (2008). Size sorting during transport and deposition of fine sediments: sortable silt and flow speed. *Developments in Sedimentology*, *60*, 121-142.

McCave, I. N., & Hall, I. R. (2006). Size sorting in marine muds: Processes, pitfalls, and prospects for paleoflow-speed proxies. *Geochemistry, Geophysics, Geosystems*, *7*(10).

McDougall, I. & Harrison, T. M. (1999). GEOCHRONOLOGY and THERMOCHRONOLOGY by the 40Ar/39Ar METHOD. Oxford University Press, Oxford.

McIntosh, W. C. (2000). 40Ar/39Ar geochronology of tephra and volcanic clasts in CRP-2A, Victoria Land Basin, Antarctica. *Terra Antartica 7*, 621-630.

McKay, R., Browne, G., Carter, L., Cowan, E., Dunbar, G., Krissek, L., ... & Wilch, T. (2009). The stratigraphic signature of the late Cenozoic Antarctic Ice Sheets in the Ross Embayment. *Geological Society of America Bulletin*, *121*(11-12), 1537-1561.

McKay, R., De Santis, L., Kulhanek, D. K., and the Expedition 374 Science Party (2019). *Ross Sea West Antarctic Ice Sheet History*. College Station, Texas, International Ocean Discovery Program, Proceedings of the International Ocean Discovery Program.

McKay, R., Naish, T., Carter, L., Riesselman, C., Dunbar, R., Sjunneskog, C., ... & Powell, R. D. (2012). Antarctic and Southern Ocean influences on Late Pliocene global cooling. *Proceedings of the National Academy of Sciences*, *109*(17), 6423-6428.

Mercer, J. H. (1978). West Antarctic ice sheet and CO2 greenhouse effect: a threat of disaster. *Nature*, *271*(5643), 321-325.

Meyers, S.R. (2014). astrochron: An R Package for Astrochronology. http://cran.rproject.org/package=astrochron

Meyers, S. R. (2015). The evaluation of eccentricity-related amplitude modulation and bundling in paleoclimate data: An inverse approach for astrochronologic testing and time scale optimization. *Paleoceanography 30*, 1625-1640.

Meyers, S. R. (2019). Cyclostratigraphy and the problem of astrochronologic testing. *Earth-Science Reviews 190,* 190-223.

Millan, R., Rignot, E., Bernier, V., Morlighem, M., & Dutrieux, P. (2017). Bathymetry of the Amundsen Sea Embayment sector of West Antarctica from Operation IceBridge gravity and other data. *Geophysical Research Letters*, *44*(3), 1360-1368.

Millar, I. L., & Pankhurst, R. J. (1987). Rb-Sr geochronology of the region between the Antarctic Peninsula and the Transantarctic Mountains: Haag Nunataks and Mesozoic granitoids. *Gondwana six: structure, tectonics, and geophysics*, *40*, 151-160.

Millar, I. L., Pankhurst, R. J., & Fanning, C. M. (2002). Basement chronology of the Antarctic Peninsula: recurrent magmatism and anatexis in the Palaeozoic Gondwana Margin. *Journal of the Geological Society*, *159*(2), 145-157.

Millar, I. L., Willan, R. C. R., Wareham, C. D., & Boyce, A. J. (2001). The role of crustal and mantle sources in the genesis of granitoids of the Antarctic Peninsula and adjacent crustal blocks. *Journal of the Geological Society*, *158*(5), 855-867.

Miller, K. G., Browning, J. V., Schmelz, W. J., Kopp, R. E., Mountain, G. S., & Wright, J. D. (2020). Cenozoic sea-level and cryospheric evolution from deep-sea geochemical and continental margin records. *Science advances*, *6*(20), eaaz1346.

Miller, K. G., Wright, J. D., & Fairbanks, R. G. (1991). Unlocking the ice house: Oligocene-Miocene oxygen isotopes, eustasy, and margin erosion. *Journal of Geophysical Research: Solid Earth*, *96*(B4), 6829-6848.

Mofjeld, H. O. (1988). Depth dependence of bottom stress and quadratic drag coefficient for barotropic pressure-driven currents. *Journal of physical oceanography*, *18*(11), 1658-1669.

Molzahn, M., Reisberg, L., & Wörner, G. (1996). Os, Sr, Nd, Pb, O isotope and trace element data from the Ferrar flood basalts, Antarctica: evidence for an enriched subcontinental lithospheric source. *Earth and Planetary Science Letters*, 144(3-4), 529-545.

Morlighem, M., Rignot, E., Binder, T., Blankenship, D., Drews, R., Eagles, G., ... & Young, D. A. (2020). Deep glacial troughs and stabilizing ridges unveiled beneath the margins of the Antarctic ice sheet. *Nature Geoscience*, *13*(2), 132-137.

Morlighem, M., Seroussi, H., Larour, E., & Rignot, E. (2013). Inversion of basal friction in Antarctica using exact and incomplete adjoints of a higher-order model. *Journal of Geophysical Research: Earth Surface*, *118*(3), 1746-1753.

Morrison A.D. & Reay A. (1995). Geochemistry of Ferrar Dolerite sills and dikes at Terra Cotta Mountain, south Victoria Land, Antarctica. *Antarctic Science 7*, 73-85.

Mouginot, J., Rignot, E. and Scheuchl, B. (2019). Continent-wide, interferometric SAR phase-mapping of Antarctic ice velocity, *Geophysical Research Letters*. 46. 9710-9718. https://doi.org/10.1029/2019GL083826

Mouginot, J., Scheuchl, B. and Rignot. E. (2017). MEaSUREs Antarctic Boundaries for IPY 2007-2009 from Satellite Radar, Version 2. Boulder, Colorado USA. NASA National Snow and Ice Data Center Distributed Active Archive Center. https://doi.org/10.5067/AXE4121732AD.

Mukasa, S. B., & Dalziel, I. W. (2000). Marie Byrd Land, West Antarctica: Evolution of Gondwana's Pacific margin constrained by zircon U-Pb geochronology and feldspar common-Pb isotopic compositions. *Geological Society of America Bulletin*, *112*(4), 611-627.

Muto, A., Anandakrishnan, S., Alley, R. B., Horgan, H. J., Parizek, B. R., Koellner, S., ... & Holschuh, N. (2019). Relating bed character and subglacial morphology using seismic data from Thwaites Glacier, West Antarctica. *Earth and Planetary Science Letters*, *507*, 199-206.

Naish, T., Powell, R., Levy, R., Wilson, G., Scherer, R., Talarico, F., ... & Williams, T. (2009). Obliquity-paced Pliocene West Antarctic ice sheet oscillations. *Nature*, *458*(7236), 322-328.

National Snow and Ice Data Center (NSIDC) "Chartic Interactive Sea Ice Graph." Accessed 21/03/2022. https://nsidc.org/arcticseaicenews/charctic-interactive-sea-ice-graph/

Nelson, D. A., & Cottle, J. M. (2018). The secular development of accretionary orogens: linking the Gondwana magmatic arc record of West Antarctica, Australia and South America. *Gondwana Research*, *63*, 15-33.

Nicholls, K. W., Corr, H. F. J., Makinson, K., & Pudsey, C. J. (2012). Rock debris in an Antarctic ice shelf. *Annals of Glaciology*, *53*(60), 235-240.

Niessen, F., Gebhardt, A. C., Kuhn, G., Magens, D., & Monien, D. (2013). Porosity and density of the AND-1B sediment core, McMurdo Sound region, Antarctica: Field consolidation enhanced by grounded ice. *Geosphere 9*, 489-509.

Ogg, J. (2020) *Geomagnetic Polarity Time Scale.* In Geologic Time Scale 2020 (eds. Gradstein, F. M. et al.) 159–192 Elsevier.

Orejola, N., Passchier, S., & Expedition, I.O.D.P. (2014). Sedimentology of lower Pliocene to Upper Pleistocene diamictons from IODP Site U1358, Wilkes Land margin, and implications for East Antarctic ice sheet dynamics. *Antarctic Science*, *26*(2), 183-192.

Orheim, O., Giles, B., Moholdt, G., Jacka, J., & Bjørdal, A. (2021). The SCAR International Iceberg Database [Data set]. Norwegian Polar Institute. https://doi.org/10.21334/npolar.2021.e4b9a604

Orsi, A. H., Whitworth III, T., & Nowlin Jr, W. D. (1995). On the meridional extent and fronts of the Antarctic Circumpolar Current. *Deep Sea Research Part I: Oceanographic Research Papers*, *42*(5), 641-673.

Pandey, M., Pant, N. C., Biswas, P., Shrivastava, P. K., Joshi, S., & Nagi, N. (2018). Heavy mineral assemblage of marine sediments as an indicator of provenance and east antarctic ice sheet fluctuations. *Geological Society, London, Special Publications*, *461*(1), 95-111.

Pankhurst, R. J., Millar, I. L., Grunow, A. M., & Storey, B. C. (1993). The pre-Cenozoic magmatic history of the Thurston Island crustal block, West Antarctica. *Journal of Geophysical Research: Solid Earth*, *98*(B7), 11835-11849.

Pankhurst, R. J., & Rapela, C. R. (1995). Production of Jurassic rhyolite by anatexis of the lower crust of Patagonia. *Earth and Planetary Science Letters*, *134*(1-2), 23-36.

Pankhurst, R. J., Riley, T. R., Fanning, C. M., & Kelley, S. P. (2000). Episodic silicic volcanism in Patagonia and the Antarctic Peninsula: chronology of magmatism associated with the break-up of Gondwana. *Journal of Petrology*, *41*(5), 605-625.

Pankhurst, R. J., Storey, B. C., & Millar, U. (1991). Magmatism related to the break-up of Gondwana. In Crame, J. A. Thomson, J. W (eds.), *Geological evolution of Antarctica* (Vol. 1), Cambridge University Press, 573-579.

Pankhurst, R. J., Weaver, S. D., Bradshaw, J. D., Storey, B. C., Ireland, T. R. (1998). Geochronology and geochemistry of pre-Jurassic superterranes in Marie Byrd Land, Antarctica. *Journal of Geophysical Research: Solid Earth 103*, 2529-2547.

Panter, K. S. et al. (2018). Melt origin across a rifted continental margin: a case for subduction-related metasomatic agents in the lithospheric source of alkaline basalt, NW Ross Sea, Antarctica. *Journal of Petrology 59*, 517-558.

Panter, K. S., Blusztajn, J., Hart, S. R., Kyle, P. R., Esser, R., & McIntosh, W. C. (2006). The origin of HIMU in the SW Pacific: evidence from intraplate volcanism in southern New Zealand and subantarctic islands. *Journal of Petrology*, *47*(9), 1673-1704.

Panter, K. S. & Castillo, P. (2007), Petrogenesis and source of lavas from seamounts in the Adare Basin, Western Ross Sea: Implications for the origin of Cenozoic magmatism in Antarctica, in Antarctica: A Keystone in a Changing World – Online Proceedings of the 10th ISAES X, edited by A. K. Cooper and C. R. Raymond et al., USGS Open-File Report 2007-1047, Extended Abstract 069, 4 p.

Panter, K. S., Kyle, P. R., & Smellie, J. L. (1997). Petrogenesis of a phonolite–trachyte succession at Mount Sidley, Marie Byrd Land, Antarctica. *Journal of Petrology* 38, 1225-1253.

Passchier, S., & Krissek, L. A. (2008). Oligocene–Miocene Antarctic continental weathering record and paleoclimatic implications, Cape Roberts drilling project, Ross Sea, Antarctica. *Palaeogeogr., Palaeoclimatol., Palaeoecol. 260*, 30-40.

Patchett, P.J. (1983). Importance of the Lu-Hf isotopic system in studies of planetary chronology and chemical evolution. *Geochimica and Cosmochimica Acta* 47, 81-91.

Patchett, P.J., and Tatsumoto, M. (1980). A routine high-precision method for Lu-Hf isotope geochemistry and chronology. *Contributions to Mineralogy and Petrology* 75, 263-267.

Patrick, M. R., & Smellie, J. L. (2013). Synthesis A spaceborne inventory of volcanic activity in Antarctica and southern oceans, 2000–10. *Antarctic Science*, *25*(4), 475-500.

Patterson, M. O., Levy, R. H., Kulhanek, D. K., van de Flierdt, T., Horgan, H., Dunbar, G. B., ... & Koch, D. (2022). Sensitivity of the West Antarctic Ice Sheet to+ 2° C (SWAIS 2C). *Scientific Drilling*, *30*, 101-112.

Pattyn, F. (2018). The paradigm shift in Antarctic ice sheet modelling. *Nature communications*, *9*(1), 1-3.

Pattyn, F., & Morlighem, M. (2020). The uncertain future of the Antarctic Ice Sheet. *Science*, *367*(6484), 1331-1335.

Paulsen, T., Deering, C., Sliwinski, J., Bachmann, O., Guillong, M. (2017). New detrital zircon age and trace element evidence for 1450 Ma igneous zircon sources in East Antarctica. *Precambrian Res. 300*, 53–58. http://dx.doi.org/10.1016/j.precamres.2017.07.011

Paulsen, T. S., Encarnación, J., Grunow, A. M., Stump, E., Pecha, M., & Valencia, V. A. (2018). Correlation and late-stage deformation of Liv Group volcanics in the Ross-Delamerian orogen, Antarctica, from new U-Pb ages. *The Journal of Geology*, *126*(3), 307-323.

Paulsen, T. S., Encarnación, J., Grunow, A. M., Valencia, V. A., Layer, P. W., Pecha, M., ... & Rasoazanamparany, C. (2015). Detrital mineral ages from the Ross Supergroup, Antarctica: Implications for the Queen Maud terrane and outboard sediment provenance on the Gondwana margin. *Gondwana Research*, *27*(1), 377-391.

Paulsen, T. S., Encarnación, J., Grunow, A. M., Valencia, V. A., Pecha, M., Layer, P. W., & Rasoazanamparany, C. (2013). Age and significance of 'outboard' high-grade metamorphics and intrusives of the Ross orogen, Antarctica. *Gondwana Research*, *24*(1), 349-358.

Paxman, G. J., Austermann, J., & Hollyday, A. (2022). Total isostatic response to the complete unloading of the Greenland and Antarctic Ice Sheets. *Scientific Reports*, *12*(1), 1-10.

Paxman, G. J., Gasson, E. G., Jamieson, S. S., Bentley, M. J., & Ferraccioli, F. (2020). Long-Term Increase in Antarctic Ice Sheet Vulnerability Driven by Bed Topography Evolution. *Geophysical Research Letters 47*, e2020GL090003.

Paxman, G. J., Jamieson, S. S., Ferraccioli, F., Jordan, T. A., Bentley, M. J., Ross, N., ... & Casal, T. G. (2019b). Subglacial Geology and Geomorphology of the Pensacola-Pole Basin, East Antarctica. *Geochemistry, Geophysics, Geosystems*, *20*(6), 2786-2807.

Paxman, G. J., Jamieson, S. S., Hochmuth, K., Gohl, K., Bentley, M. J., Leitchenkov, G., & Ferraccioli, F. (2019a). Reconstructions of Antarctic topography since the Eocene–Oligocene boundary. *Palaeogeography, palaeoclimatology, palaeoecology*, *535*, 109346.

Pearce, N. J. et al. A compilation of new and published major and trace element data for NIST SRM 610 and NIST SRM 612 glass reference materials. *Geostandards newsletter* **21**, 115-144 (1997).

Pekar, S. F., & DeConto, R. M. (2006). High-resolution ice-volume estimates for the early Miocene: Evidence for a dynamic ice sheet in Antarctica. *Palaeogeogr., Palaeoclimatol., Palaeoecol. 231*, 101-109.

Pérez, L. F., De Santis, L., McKay, R. M., Larter, R. D., Ash, J., Bart, P. J., ... & van De Flierdt, T. (2021). Early and middle Miocene ice sheet dynamics in the Ross Sea: Results from integrated core-log-seismic interpretation. *GSA Bulletin*, *134*(1-2), 348-370.

Perotti, M., Andreucci, B., Talarico, F., Zattin, M., & Langone, A. (2017). Multianalytical provenance analysis of E astern Ross Sea LGM till sediments (Antarctica): Petrography, geochronology, and thermochronology detrital data. *Geochemistry, Geophysics, Geosystems*, *18*(6), 2275-2304.

Petschick, R. MacDiff 4.2.5 [WWW Document]. Inst. Geol. Univ. Erlangen Ger. (2004) http://www.geol-pal.uni- frankfurt.de/Staff/Homepages/Petschick/classicsoftware.html#MacDiff

Pettit, E. C., Whorton, E. N., Waddington, E. D., & Sletten, R. S. (2014). Influence of debris-rich basal ice on flow of a polar glacier. *Journal of Glaciology*, *60*(223), 989-1006.

Peucat, J. J., Ménot, R. P., Monnier, O., & Fanning, C. M. (1999). The Terre Adélie basement in the East-Antarctica Shield: geological and isotopic evidence for a major 1.7 Ga thermal event; comparison with the Gawler Craton in South Australia. *Precambrian Research*, *94*(3-4), 205-224.

Phillips, E. H. et al. (2018). The nature and evolution of mantle upwelling at Ross Island, Antarctica, with implications for the source of HIMU lavas. *Earth and Planetary Science Letters 498*, 38-53.

Pierce, E. L., van de Flierdt, T., Williams, T., Hemming, S. R., Cook, C. P., & Passchier, S. (2017). Evidence for a dynamic East Antarctic ice sheet during the mid-Miocene climate transition. *Earth and Planetary Science Letters*, *478*, 1-13.

Pollard, D., & DeConto, R. M. (2003). Antarctic ice and sediment flux in the Oligocene simulated by a climate–ice sheet–sediment model. *Palaeogeography, Palaeoclimatology, Palaeoecology*, *198*(1-2), 53-67.

Pollard, D., & DeConto, R. M. (2020). Continuous simulations over the last 40 million years with a coupled Antarctic ice sheet-sediment model. *Palaeogeography, Palaeoclimatology, Palaeoecology*, *537*, 109374.

Pollard, D., DeConto, R. M., & Alley, R. B. (2015). Potential Antarctic Ice Sheet retreat driven by hydrofracturing and ice cliff failure. *Earth and Planetary Science Letters*, *412*, 112-121.

Pörtner, H. O., Roberts, D. C., Masson-Delmotte, V., Zhai, P., Tignor, M., Poloczanska, E., & Weyer, N. M. (2019). The ocean and cryosphere in a changing climate. *IPCC Special Report on the Ocean and Cryosphere in a Changing Climate*.

Prestvik, T., & Duncan, R. A. (1991). The geology and age of Peter I Øy, Antarctica. *Polar research*, *9*(1), 89-98.

Prebble, J. G. (2016). Descriptions and occurrences of pollen and spores from New Zealand Cenozoic sediments, *GNS Science Internal Report 2016/09*, 137.

Prebble, J. G. et al. (2013). An expanded modern dinoflagellate cyst dataset for the Southwest Pacific and Southern Hemisphere with environmental associations. *Marine Micropaleontology 101*, 33–48

Prebble, J. G., Hannah, M. J., & Barrett, P. J. (2006). Changing Oligocene climate recorded by palynomorphs from two glacio-eustatic sedimentary cycles, Cape Roberts Project, Victoria Land Basin, Antarctica. *Palaeogeogr., Palaeoclimatol., Palaeoecol. 231*, 58-70.

Pross, J., Contreras, L., Bijl, P. K., Greenwood, D. R., Bohaty, S. M., Schouten, S., ... & Brinkhuis, H. (2012). Persistent near-tropical warmth on the Antarctic continent during the early Eocene epoch. *Nature*, *488*(7409), 73-77.

Prothro, L. O., Simkins, L. M., Majewski, W., & Anderson, J. B. (2018). Glacial retreat patterns and processes determined from integrated sedimentology and geomorphology records. *Marine Geology*, *395*, 104-119.

Puttkammer, R. A. (2016). *Subglacial sediment transport, ice stream dynamics, and chemical weathering of the Whillans Ice Stream inferred from particle surface texture, form, and composition.* [Master's Thesis], Northern Illinois University.

Rackow, T., Wesche, C., Timmermann, R., Hellmer, H. H., Juricke, S., & Jung, T. (2017). A simulation of small to giant Antarctic iceberg evolution: Differential impact on climatology estimates. *Journal of Geophysical Research: Oceans*, *122*(4), 3170-3190.

Rae, J. W., Zhang, Y. G., Liu, X., Foster, G. L., Stoll, H. M., & Whiteford, R. D. (2021). Atmospheric CO2 over the past 66 million years from marine archives. *Annual Review of Earth and Planetary Sciences*, *49*, 599-631.

Raine, J.I., Mildenhall, D.C., Kennedy, E.M. (2011). New Zealand fossil spores and pollen: an illustrated catalogue. In: GNS Science Miscellaneous Series No. 4, 4th edition. http://data.gns.cri.nz/sporepollen/index.htm.

Renne, P. R. (1995). Excess 40Ar in biotite and hornblende from the Noril'sk 1 intrusion, Siberia: implications for the age of the Siberian Traps. *Earth and Planetary Science Letters*, *131*(3-4), 165-176.

Riesselman, C. R., & Dunbar, R. B. (2013). Diatom evidence for the onset of Pliocene cooling from AND-1B, McMurdo Sound, Antarctica. *Palaeogeography, Palaeoclimatology, Palaeoecology*, *369*, 136-153.

Rignot, E., Jacobs, S., Mouginot, J., & Scheuchl, B. (2013). Ice-shelf melting around Antarctica. *Science*, *341*(6143), 266-270.

Rignot, E., Mouginot, J., Scheuchl, B., Van Den Broeke, M., Van Wessem, M. J., & Morlighem, M. (2019). Four decades of Antarctic Ice Sheet mass balance from 1979–2017. *Proceedings of the National Academy of Sciences*, *116*(4), 1095-1103.

Riley, T. R., Flowerdew, M. J., Millar, I. L., & Whitehouse, M. J. (2020). Triassic magmatism and metamorphism in the Antarctic Peninsula: identifying the extent and timing of the Peninsula orogeny. *Journal of South American Earth Sciences*, *103*, 102732.

Riley, T. R., Flowerdew, M. J., Pankhurst, R. J., Curtis, M. L., Millar, I. L., Fanning, C. M., & Whitehouse, M. J. (2017b). Early Jurassic magmatism on the Antarctic Peninsula and potential correlation with the Subcordilleran plutonic belt of Patagonia. *Journal of the Geological Society*, *174*(2), 365-376.

Riley, T. R., Flowerdew, M. J., Pankhurst, R. J., Leat, P. T., Millar, I. L., Fanning, C. M., & Whitehouse, M. J. (2017a). A revised geochronology of Thurston Island, West Antarctica, and correlations along the proto-Pacific margin of Gondwana. *Antarctic Science*, *29*(1), 47-60.

Riley, T. R., Flowerdew, M. J., & Whitehouse, M. J. (2012). U–Pb ion-microprobe zircon geochronology from the basement inliers of eastern Graham Land, Antarctic Peninsula. *Journal of the Geological Society*, *169*(4), 381-393.

Riley, T. R., Leat, P. T., Pankhurst, R. J., & Harris, C. (2001). Origins of large volume rhyolitic volcanism in the Antarctic Peninsula and Patagonia by crustal melting. *Journal of petrology*, *42*(6), 1043-1065.

Rilling, S., Mukasa, S., Wilson, T., Lawver, L., & Hall, C. (2009). New determinations of 40Ar/39Ar isotopic ages and flow volumes for Cenozoic volcanism in the Terror Rift, Ross Sea, Antarctica. *Journal of Geophysical Research: Solid Earth*, *114*(B12).

Roberts, A.P. & Winklhofer, M. (2004). Why are geomagnetic excursions not always recorded in sediments? Constraints from post-depositional remanent magnetization lock-in modelling. *Earth and Planetary Science Letters 227*, 345-359. doi: 10.1016/j.epsl.2004.07.040

Robinson, D. E., Menzies, J., Wellner, J. S., & Clark, R. W. (2021). Subglacial sediment deformation in the Ross Sea, Antarctica. *Quaternary Science Advances*, *4*, 100029.

Rocchi, S., Bracciali, L., Di Vincenzo, G., Gemelli, M., & Ghezzo, C. (2011). Arc accretion to the early Paleozoic Antarctic margin of Gondwana in Victoria Land. *Gondwana Research*, *19*(3), 594-607.

Rocchi, S., Di Vincenzo, G., Ghezzo, C., & Nardini, I. (2009). Granite-lamprophyre connection in the latest stages of the early Paleozoic Ross Orogeny (Victoria Land, Antarctica). *Geological Society of America Bulletin*, *121*(5-6), 801-819.

Rocchi, S., LeMasurier, W. E., & Di Vincenzo, G. (2006). Oligocene to Holocene erosion and glacial history in Marie Byrd Land, West Antarctica, inferred from exhumation of the Dorrel Rock intrusive complex and from volcano morphologies. *GSA Bulletin. 118*, 991-1005.

Rocchi, S., Tonarini, S., Armienti, P., Innocenti, F., & Manetti, P. (1998). Geochemical and isotopic structure of the early Palaeozoic active margin of Gondwana in northern Victoria Land, Antarctica. *Tectonophysics*, *284*(3-4), 261-281.

Rose, K. C., Ferraccioli, F., Jamieson, S. S., Bell, R. E., Corr, H., Creyts, T. T., ... & Damaske, D. (2013). Early east Antarctic Ice Sheet growth recorded in the landscape of the Gamburtsev Subglacial Mountains. *Earth and Planetary Science Letters*, *375*, 1-12.

Rosenblume, J. A., & Powell, R. D. (2019). Glacial sequence stratigraphy of ANDRILL-1B core reveals a dynamic subpolar Antarctic Ice Sheet in Ross Sea during the late Miocene. *Sedimentology*, *66*(6), 2072-2097.

Rosenqvist, I. T. (1975). Origin and mineralogy glacial and interglacial clays of southern Norway. *Clays and Clay Minerals 23*, 153-159.

Rooney, S. T., Blankenship, D. D., & Bentley, C. R. (1987). Seismic refraction measurements of crustal structure in West Antarctica. *Gondwana Six: Structure, Tectonics, and Geophysics*, *40*, 1-7.

Rosier, S. H., Reese, R., Donges, J. F., De Rydt, J., Gudmundsson, G. H., & Winkelmann, R. (2021). The tipping points and early warning indicators for Pine Island Glacier, West Antarctica. *The Cryosphere*, *15*(3), 1501-1516.

Rowell, A. J. et al. (1993). An active Neoproterozoic margin: evidence from the Skelton Glacier area, Transantarctic Mountains. *Journal of the Geological Society 150*, 677-682.

Roy, M., van de Flierdt, T., Hemming, S. R., & Goldstein, S. L. (2007). 40Ar/39Ar ages of hornblende grains and bulk Sm/Nd isotopes of circum-Antarctic glacio-marine sediments: Implications for sediment provenance in the southern ocean. *Chemical Geology*, *244*(3-4), 507-519.

Russell-Head, D. S. (1980). The melting of free-drifting icebergs. *Annals of glaciology*, *1*, 119-122.

Ryan, C. J. (2005). *Mesozoic to Cenozoic igneous rocks from Northwestern Graham Land: constraints on the tectonomagmatic evolution of the Antarctic Peninsula.* [PhD thesis], University of Brighton.

Sandroni, S., and Talarico, F. M. (2001). Petrography and provenance of basement clasts and clast variability in CRP-3 drillcore (Victoria Land Basin, Antarctica), *Terra Antarctica 8*, 449-467.

Sangiorgi, F., Bijl, P. K., Passchier, S., Salzmann, U., Schouten, S., McKay, R., ... & Brinkhuis, H. (2018). Southern Ocean warming and Wilkes Land ice sheet retreat during the mid-Miocene. *Nature communications*, *9*(1), 1-11.

Sarigulyan, A. (2022). *Études Des Carottes Byrd et Camp Century: Reconstruction Des Conditions Pré et Post Glaciation à L'Aide du Meb* [Masters Thesis]. Université de Lorraine, France.

Scambos, T. A., Bell, R. E., Alley, R. B., Anandakrishnan, S., Bromwich, D. H., Brunt, K., ... & Yager, P. L. (2017). How much, how fast?: A science review and outlook for research on the instability of Antarctica's Thwaites Glacier in the 21st century. *Global and Planetary Change*, *153*, 16-34.

Scarrow, J. H., Pankhurst, R. J., Leat, P. T., & Vaughan, A. P. (1996). Antarctic Peninsula granitoid petrogenesis: a case study from Mount Charity, north-eastern Palmer Land. *Antarctic Science*, *8*(2), 193-206.

Schaefer, J. M., Finkel, R. C., Balco, G., Alley, R. B., Caffee, M. W., Briner, J. P., ... & Schwartz, R. (2016). Greenland was nearly ice-free for extended periods during the Pleistocene. *Nature*, *540*(7632), 252-255.

Scherer, E., Münker, C., and Mezger, K. (2001). Calibration of the Lutetium-Hafnium Clock. *Science*, 683–687.

Scherer, R., Bohaty, S. M., & Harwood, D. M. (2000). Oligocene and lower Miocene siliceous microfossil biostratigraphy of Cape Roberts Project Core CRP-2/2A, Victoria Land Basin, Antarctica. *Terra Antartica 7,* 417-442.

Schroeder, D. M., Blankenship, D. D., Young, D. A., & Quartini, E. (2014). Evidence for elevated and spatially variable geothermal flux beneath the West Antarctic Ice Sheet. *Proceedings of the National Academy of Sciences 111*, 9070-9072.

Shaw, T. J., Raiswell, R., Hexel, C. R., Vu, H. P., Moore, W. S., Dudgeon, R., & Smith Jr, K. L. (2011). Input, composition, and potential impact of terrigenous material from free-drifting icebergs in the Weddell Sea. *Deep Sea Research Part II: Topical Studies in Oceanography*, *58*(11-12), 1376-1383.

Shevenell, A. E., Kennett, J. P., & Lea, D. W. (2008). Middle Miocene ice sheet dynamics, deep-sea temperatures, and carbon cycling: A Southern Ocean perspective. *Geochemistry, Geophysics, Geosystems*, *9*(2).

Shi, B., Wang, Y. P., Yang, Y., Li, M., Li, P., Ni, W., & Gao, J. (2015). Determination of critical shear stresses for erosion and deposition based on in situ measurements of currents and waves over an intertidal mudflat. *Journal of Coastal Research*, *31*(6), 1344-1356.

Siddoway, C. S. (2008). Tectonics of the West Antarctic Rift System: new light on the history and dynamics of distributed intracontinental extension. *Antarctica: A keystone in a changing world*, 91-114.

Siegert, M., Hein, A. S., White, D., & Gore, D. (2021). Antarctica at the Last Glacial Maximum and its retreat to the Holocene. In *Antarctic climate evolution (eds. Florindo, F., Siegert, M., De Santis, L., & Naish, T.)*. Elsevier.

Siegert, M. J., Welch, B., Morse, D., Vieli, A., Blankenship, D. D., Joughin, I., ... & Jacobel, R. (2004). Ice flow direction change in interior West Antarctica. *Science*, *305*(5692), 1948-1951.

Simões Pereira, P. (2018). *Insights into West Antarctica`s Geology and Late Pleistocene Ice Sheet Behaviour from Isotopic Sedimentary Provenance Studies* [PhD Thesis]. Imperial College London, UK. Retrieved from: https://spiral.imperial.ac.uk/handle/10044/1/88145

Simões Pereira, P., van de Flierdt, T., Hemming, S. R., Frederichs, T., Hammond, S. J., Brachfeld, S., ... & Hillenbrand, C. D. (2020). The geochemical and mineralogical fingerprint of West Antarctica's weak underbelly: Pine Island and Thwaites glaciers. *Chemical Geology*, *550*, 119649.

Simões Pereira, P., van de Flierdt, T., Hemming, S. R., Hammond, S. J., Kuhn, G., Brachfeld, S., ... & Hillenbrand, C. D. (2018). Geochemical fingerprints of glacially eroded bedrock from West Antarctica: Detrital thermochronology, radiogenic isotope systematics and trace element geochemistry in Late Holocene glacial-marine sediments. *Earth-Science Reviews*, *182*, 204-232.

Sims, K. W., Blichert-Toft, J., Kyle, P. R., Pichat, S., Gauthier, P. J., Blusztajn, J., ... & Layne, G. (2008). A Sr, Nd, Hf, and Pb isotope perspective on the genesis and long-term evolution of alkaline magmas from Erebus volcano, Antarctica. *Journal of Volcanology and Geothermal Research, 177*(3), 606-618.

Sims, K. W., & Hart, S. R. (2006). Comparison of Th, Sr, Nd and Pb isotopes in oceanic basalts: implications for mantle heterogeneity and magma genesis. *Earth and Planetary Science Letters* 245, 743-761.

Sláma, J., Košler, J., Condon, D. J., Crowley, J. L., Gerdes, A., Hanchar, J. M., ... & Whitehouse, M. J. (2008). Plešovice zircon—a new natural reference material for U–Pb and Hf isotopic microanalysis. *Chemical Geology*, *249*(1-2), 1-35.

Smith, J. A., Andersen, T. J., Shortt, M., Gaffney, A. M., Truffer, M., Stanton, T. P., ... & Vaughan, D. G. (2017). Sub-ice-shelf sediments record history of twentieth-century retreat of Pine Island Glacier. *Nature*, *541*(7635), 77-80.

Smith, J. A., Graham, A. G., Post, A. L., Hillenbrand, C. D., Bart, P. J., & Powell, R. D. (2019). The marine geological imprint of Antarctic ice shelves. *Nature Communications*, *10*(1), 1-16.

Smith, J. A., Hillenbrand, C. D., Larter, R. D., Graham, A. G., & Kuhn, G. (2009). The sediment infill of subglacial meltwater channels on the West Antarctic continental shelf. *Quaternary Research*, *71*(2), 190-200.

Söderlund, U., Patchett, P.J., Vervoort, J.D., and Isachsen, C.E. (2004). The 176Lu decay constant determined by Lu-Hf and U-Pb isotope systematics of Precambrian mafic intrusions. *Earth and Planetary Science Letters* 219, 311-324.

Sorlien, C. C., Luyendyk, B. P., Wilson, D. S., Decesari, R. C., Bartek, L. R., & Diebold, J. B. (2007). Oligocene development of the West Antarctic Ice Sheet recorded in eastern Ross Sea strata. *Geology*, *35*(5), 467-470.

Spiegel, C., Lindow, J., Kamp, P. J., Meisel, O., Mukasa, S., Lisker, F., ... & Gohl, K. (2016). Tectonomorphic evolution of Marie Byrd Land–Implications for Cenozoic rifting activity and onset of West Antarctic glaciation. *Global and Planetary Change*, *145*, 98-115.

Stevens, C., Hulbe, C., Brewer, M., Stewart, C., Robinson, N., Ohneiser, C., & Jendersie, S. (2020). Ocean mixing and heat transport processes observed under the Ross Ice Shelf control its basal melting. *Proceedings of the National Academy of Sciences*, *117*(29), 16799-16804.

Storey, B. C., Hole, M. J., Pankhurst, R. J., Millar, I. L., & Vennum, W. (1988). Middle Jurassic within-plate granites in West Antarctica and their bearing on the break-up of Gondwanaland. *Journal of the Geological Society*, *145*(6), 999-1007.

Storey, B.C., & MacDonald, D.I.M. (1987). Sedimentary rocks of the Ellsworth-Thiel Mountains ridge and their regional equivalents: *Bulletin of the British Antarctic Survey 76*, 21-49.

Storey, B. C., Pankhurst, R. J., & Johnson, A. C. (1994). The Grenville Province within Antarctica: a test of the SWEAT hypothesis. *Journal of the Geological Society*, *151*(1), 1-4.

Stow, D.A.V. (1994). Deep sea processes of sediment transport and deposition K. Pye (Ed.), *Sediment Transport and Depositional Processes*, Blackwell Scientific Publications, Oxford, pp. 257-291

Struve, T., Van De Flierdt, T., Burke, A., Robinson, L. F., Hammond, S. J., Crocket, K. C., ... & White, N. J. (2017). Neodymium isotopes and concentrations in aragonitic scleractinian cold-water coral skeletons-Modern calibration and evaluation of palaeo-applications. *Chemical Geology*, *453*, 146-168.

Stuart, K. M., & Long, D. G. (2011). Tracking large tabular icebergs using the SeaWinds Ku-band microwave scatterometer. *Deep Sea Research Part II: Topical Studies in Oceanography*, *58*(11-12), 1285-1300.

Stuckless, J. S., & Ericksen, R. L. (1976). Strontium isotopic geochemistry of the volcanic rocks and associated megacrysts and inclusions from Ross Island and vicinity, Antarctica. *Contributions to Mineralogy and Petrology* 58, 111-126.

Studinger, M., Bell, R. E., Fitzgerald, P. G., & Buck, W. R. (2006). Crustal architecture of the Transantarctic Mountains between the Scott and Reedy Glacier region and South Pole from aerogeophysical data. *Earth and Planetary Science Letters*, *250*(1-2), 182-199.

Stump, E. (1995). *The Ross Orogen of the transantarctic mountains.* Cambridge University Press.

Stump, E., Gehrels, G., Talarico, F. M., & Carosi, R. (2007). *Constraints from detrital zircon geochronology on the early deformation of the Ross orogen, Transantarctic Mountains, Antarctica.* In Antarctica: A Keystone in a Changing World – Online Proceedings of the 10th ISAES, edited by A.K. Cooper and C.R. Raymond et al., USGS Open-File Report 2007-1047, Extended Abstract 166.

Suganuma, Y. et al. (2010). 10Be evidence for delayed acquisition of remanent magnetization in marine sediments: Implication for a new age for the Matuyama–Brunhes boundary. *Earth and Planetary Science Letters 296*, 443-450. doi:10.1016/j.epsl.2010.05.031

Suganuma, Y. et al. (2011). Post-depositional remanent magnetization lock-in for marine sediments deduced from 10Be and paleomagnetic records through the Matuyama–Brunhes boundary. *Earth and Planetary Science Letters 311*, 39-52. doi: 10.1016/j.epsl.2011.08.038

Talarico, F., Borsi, L., & Lombardo, B. (1995). Relict granulites in the Ross Orogen of northern Victoria Land (Antarctica), II. Geochemistry and palaeo-tectonic implications. *Precambrian Research*, *75*(3-4), 157-174.

Talarico F. & Sandroni S. (1998). Petrography, Mineral Chemistry and Provenance of Basement Clasts in the CRP-1 Drillcore (Victoria Land Basin, Antarctica). *Terra Antartica 5*, 601-610.

Talarico F., Sandroni S., Fielding C.R. & Atkins C. (2000). Variability, Petrography and Provenance of Basement Clasts from CRP-2/2A Drillcore (Victoria Land Basin, Ross Sea, Antarctica). *Terra Antarctica 7*, 529-544.

Talarico, F. et al. (2009). Provenance signature of the Antarctic Ice Sheets in the Ross Embayment during the Late Miocene to Early Pliocene: the ANDRILL AND-1B core record. *Global and Planetary Change 69*, 103–123.

Tanaka, T., Togashi, S., Kamioka, H., Amakawa, H., Kagami, H., Hamamoto, T., ... & Dragusanu, C. (2000). JNdi-1: a neodymium isotopic reference in consistency with LaJolla neodymium. *Chemical Geology*, *168*(3-4), 279-281.

Taner, M. T. (1992). Attributes Revisited. Technical Report. Rock Solid Images, Inc.

Taviani, M. et al. (2008). Palaeontological characterisation and analysis of the AND-2A core, ANDRILL Southern McMurdo Sound Project, Antarctica. Terra Antartica 15, 113-146.

The IMBIE team (2018). Mass balance of the Antarctic Ice Sheet from 1992 to 2017. *Nature 558*, 219–222. https://doi.org/10.1038/s41586-018-0179-y

The RAISED Consortium (2014). A community-based geological reconstruction of Antarctic Ice Sheet deglaciation since the Last Glacial Maximum. *Quaternary Science Reviews*, *100*, 1-9.

Thomas, R. H., & Bentley, C. R. (1978). A model for Holocene retreat of the West Antarctic ice sheet. *Quaternary Research*, *10*(2), 150-170.

Tinto, K. J., Padman, L., Siddoway, C. S., Springer, S. R., Fricker, H. A., Das, I., ... & Bell, R. E. (2019). Ross Ice Shelf response to climate driven by the tectonic imprint on seafloor bathymetry. *Nature Geoscience*, *12*(6), 441-449.

Tonarini, S., and Rocchi, S., 1994, Geochronology of Cambro-Ordovician intrusives in Victoria Land: A review: *Terra Antarctica 1*, 46-50.

Tournadre, J., Bouhier, N., Girard-Ardhuin, F., & Rémy, F. (2016). Antarctic icebergs distributions 1992–2014. *Journal of Geophysical Research: Oceans*, *121*(1), 327-349.

Toyos, M. H., Lamy, F., Lange, C. B., Lembke-Jene, L., Saavedra-Pellitero, M., Esper, O., & Arz, H. W. (2020). Antarctic Circumpolar Current dynamics at the Pacific entrance to the Drake Passage over the past 1.3 million years. *Paleoceanography and Paleoclimatology*, *35*(7), e2019PA003773.

Truffer, M., & Echelmeyer, K. A. (2003). Of isbrae and ice streams. *Annals of Glaciology*, *36*, 66-72.

Truswell, E.M. (1983). Recycled Cretaceous and Tertiary pollen and spores in Antarctic marine sediments: a catalogue. *Palaeontographica Abteilung B 186*, 121-174.

Tucholke, B. E. (1977). Sedimentation processes and acoustic stratigraphy in the Bellingshausen Basin. *Marine Geology*, *25*(1-3), 209-230.

Tulaczyk, S., Kamb, B., Scherer, R. P., & Engelhardt, H. F. (1998). Sedimentary processes at the base of a West Antarctic ice stream; constraints from textural and compositional properties of subglacial debris. *Journal of Sedimentary Research 68*, 487-496.

Tulaczyk, S., Mikucki, J. A., Siegfried, M. R., Priscu, J. C., Barcheck, C. G., Beem, L. H., ... & Schwartz, S. Y. (2014). WISSARD at Subglacial Lake Whillans, West Antarctica: scientific operations and initial observations. *Annals of Glaciology*, *55*(65), 51-58.

Umlauf, L., & Arneborg, L. (2009). Dynamics of rotating shallow gravity currents passing through a channel. Part I: Observation of transverse structure. *Journal of Physical Oceanography*, *39*(10), 2385-2401.

Van Schmus, W. R., McKenna, L. W., Gonzales, D. A., Fetter, A. H., & Rowell, A. J. (1997). U-Pb geochronology of parts of the Pensacola, Thiel, and Queen Maud mountains, Antarctica. The Antarctic Region: Geological Evolution and Processes. *Terra Antartica*, Siena 187, 200.

van Wyk de Vries, M., Bingham, R. G. & Hein, A. S. (2017). A new volcanic province: an inventory of subglacial volcanoes in West Antarctica. *Geological Society, London, Special Publications*, *461*(1), 231-248.

Vaughan, D. G., Corr, H. F., Ferraccioli, F., Frearson, N., O'Hare, A., Mach, D., ... & Young, D. A. (2006). New boundary conditions for the West Antarctic ice sheet: Subglacial topography beneath Pine Island Glacier. *Geophysical Research Letters*, *33*(9).

Veevers, J. J., & Saeed, A. (2011). Age and composition of Antarctic bedrock reflected by detrital zircons, erratics, and recycled microfossils in the Prydz Bay–Wilkes Land–Ross Sea–Marie Byrd Land sector (70–240 E). *Gondwana Research 20*, 710-738.

Vermeesch, P. (2021). On the treatment of discordant detrital zircon U-Pb data. *Geochronology* 3, 247-257.

Vermeesch, P. (2018a). IsoplotR: A free and open toolbox for geochronology. *Geoscience Frontiers* 9, 1479-1493.

Vermeesch, P. (2018b). Statistical models for point-counting data. *Earth and Planetary Science Letters* 501, 112-118.

Vermeesch, P. (2013). Multi-sample comparison of detrital age distributions. *Chemical Geology* 341, 140-146.

Vermeesch, P. (2004). How many grains are needed for a provenance study*? Earth and Planetary Science Letters* 224, 441-451.

Vervoort, J.D. (2010). Hf analysis in zircon by LA-MC-ICPMS: Promise and pitfalls. *Geological Society of America Abstracts with Programs* 42 (5), 667.

Vervoort, J.D., Patchett, P.J., Söderlund, U. & Baker, M. (2004). The isotopic composition of Yb and the precise and accurate determination of Lu concentrations and Lu/Hf ratios by isotope dilution using MC-ICPMS. *Geochem. Geophys. Geosyst*. 5, 1-15, 10.1029/2004GC000721

Vogel, M. B., Ireland, T. R., & Weaver, S. D. (2002). The multistage history of the Queen Maud Batholith, La Gorce Mountains, central Transantarctic Mountains. In Antarctica at the close of a millennium: proceedings of the 8th International Symposium on Antarctic Earth Sciences, Wellington 1999.

Vogel, S. W. (2004). *The basal regime of the West-Antarctic ice sheet interaction of subglacial geology with ice dynamics [PhD Thesis]*. University of California, Santa Cruz.

Vogel, S. W., Tulaczyk, S., Carter, S., Renne, P., Turrin, B., & Grunow, A. (2006). Geologic constraints on the existence and distribution of West Antarctic subglacial volcanism. *Geophysical research letters*, *33*(23).

Wagner, T. J., Dell, R. W., & Eisenman, I. (2017). An analytical model of iceberg drift. *Journal of Physical Oceanography*, *47*(7), 1605-1616.

Walter, H. J., Hegner, E., Diekmann, B., & Kuhn, G. (2000). Provenance and transport of terrigenous sediment in the South Atlantic Ocean and their relations to glacial and interglacial cycles: Nd and Sr isotopic evidence. *Geochimica et Cosmochimica Acta*, *64*(22), 3813-3827.

Wareham, C. D., Stump, E., Storey, B. C., Millar, I. L., & Riley, T. R. (2001). Petrogenesis of the Cambrian Liv Group, a bimodal volcanic rock suite from the Ross orogen, Transantarctic Mountains. *Geological Society of America Bulletin* 113, 360-372.

Warny, S., Askin, R. A., Hannah, M. J., Mohr, B. A., Raine, J. I., Harwood, D. M., ... & SMS Science Team. (2009). Palynomorphs from a sediment core reveal a sudden remarkably warm Antarctica during the middle Miocene. *Geology*, *37*(10), 955-958.

Weaver, S. D., Adams, C. J., Pankhurst, R. J. & Gibson, I. L. (1992). Granites of Edward VII Peninsula, Marie Byrd Land: anorogenic magmatism related to Antarctic-New Zealand rifting. *Transactions of the Royal Society of Edinburgh: Earth Sciences* 83 (1-2), 281-290.

Weaver, S. D., Bradshaw, J. D., & Laird, M. G. (1984). Geochemistry of Cambrian volcanics of the Bowers Supergroup and implications for the Early Palaeozoic tectonic evolution of northern Victoria Land, Antarctica. *Earth and Planetary Science Letters*, *68*(1), 128-140.

Webb, P. N., Ronan Jr, T. E., Lipps, J. H., & DeLaca, T. E. (1979). Miocene glaciomarine sediments from beneath the southern Ross Ice Shelf, Antarctica. *Science*, *203*(4379), 435-437.

Weber, M. E., Golledge, N. R., Fogwill, C. J., Turney, C. S., & Thomas, Z. A. (2021). Decadal-scale onset and termination of Antarctic ice-mass loss during the last deglaciation. *Nature communications*, *12*(1), 1-13.

Weertman, J. (1974). Stability of the junction of an ice sheet and an ice shelf. *Journal of Glaciology*, *13*(67), 3-11.

Weis, D., Kieffer, B., Maerschalk, C., Barling, J., De Jong, J., Williams, G. A., ... & Mahoney, J. B. (2006). High-precision isotopic characterization of USGS reference materials by TIMS and MC-ICP-MS. *Geochemistry, Geophysics, Geosystems*, *7*(8).

Welke, B. et al. (2016). Applications of detrital geochronology and thermochronology from glacial deposits to the Paleozoic and Mesozoic thermal history of the Ross Embayment, Antarctica. *Geochemistry, Geophysics, Geosystems 17,* 2762-2780.

Westerhold, T., Marwan, N., Drury, A. J., Liebrand, D., Agnini, C., Anagnostou, E., ... & Zachos, J. C. (2020). An astronomically dated record of Earth's climate and its predictability over the last 66 million years. *Science*, *369*(6509), 1383-1387.

Wever, H. E., Millar, I. L., & Pankhurst, R. J. (1994). Geochronology and radiogenic isotope geology of Mesozoic rocks from eastern Palmer Land, Antarctic Peninsula: crustal anatexis in arc-related granitoid genesis. *Journal of South American Earth Sciences*, *7*(1), 69-83.

Whitehouse, P. L., Gomez, N., King, M. A., & Wiens, D. A. (2019). Solid Earth change and the evolution of the Antarctic Ice Sheet. *Nature communications*, *10*(1), 1-14.

Wieser, M.E. (2006). Atomic weights of the elements 2005 (IUPAC Technical Report). *Pure and Applied Chemistry*, 78 (11), 2051–2066. doi:10.1351/pac200678112051

Williams, T. (Personal Communication, July 2019).

Wilson, D. J., Bertram, R. A., Needham, E. F., van de Flierdt, T., Welsh, K. J., McKay, R. M., ... & Escutia, C. (2018). Ice loss from the East Antarctic Ice Sheet during late Pleistocene interglacials. *Nature*, *561*(7723), 383-386.

Wilson, D. S., Pollard, D., DeConto, R. M., Jamieson, S. S., & Luyendyk, B. P. (2013). Initiation of the West Antarctic Ice Sheet and estimates of total Antarctic ice volume in the earliest Oligocene. *Geophysical Research Letters*, *40*(16), 4305-4309.

Wilson, D. S. et al. (2012). Antarctic topography at the Eocene-Oligocene boundary, *Palaeogeogr. Palaeoclimatol. Palaeoecol.* 335-336, 24–34. doi:10.1016/j.palaeo.2011.05.028.

Wingham, D. J., Siegert, M. J., Shepherd, A., & Muir, A. S. (2006). Rapid discharge connects Antarctic subglacial lakes. *Nature*, *440*(7087), 1033-1036.

Winter, K., Woodward, J., Ross, N., Dunning, S. A., Hein, A. S., Westoby, M. J., ... & Siegert, M. J. (2019). Radar-detected englacial debris in the West Antarctic Ice Sheet. *Geophysical Research Letters*, *46*(17-18), 10454-10462.

Wood, G. D., Gabriel, A. M. & Lawson, J. C. 1(996). In: Palynology: Principles and Applications (Eds Jansonius, J. & McGregor, D. C.) 29–50. American Association of Stratigraphic Palynologists Foundation, Dallas, TX.

Woodhead, J., Hergt, J., Shelley, M., Eggins, S., and Kemp, R. (2004). Zircon Hf-isotope analysis with an excimer laser, depth profiling, ablation of complex geometries, and concomitant age estimation. *Chemical Geology*, 209, 121-135.

Yakymchuk, C. et al. (2013). Anatectic reworking and differentiation of continental crust along the active margin of Gondwana: a zircon Hf–O perspective from West Antarctica. *Geological Society, London, Special Publication 383.* https://doi.org/10 .1144/SP383.7

Yakymchuk, C., Brown, C. R., Brown, M., Siddoway, C. S., Fanning, C. M., & Korhonen, F. J. (2015). Paleozoic evolution of western marie byrd land, Antarctica. *Bulletin*, *127*(9-10), 1464-1484.

Yamane, M., Yokoyama, Y., Abe-Ouchi, A., Obrochta, S., Saito, F., Moriwaki, K., & Matsuzaki, H. (2015). Exposure age and ice-sheet model constraints on Pliocene East Antarctic ice sheet dynamics. *Nature Communications*, *6*(1), 1-8.

Zachos, J. C., Dickens, G. R., & Zeebe, R. E. (2008). An early Cenozoic perspective on greenhouse warming and carbon-cycle dynamics. *Nature*, *451*(7176), 279-283.

Zachos, J., Pagani, M., Sloan, L., Thomas, E., & Billups, K. (2001). Trends, rhythms, and aberrations in global climate 65 Ma to present. *science*, *292*(5517), 686-693.

Ziaja, W., & Ostafin, K. (2019). Origin and location of new Arctic islands and straits due to glacial recession. *Ambio*, *48*(1), 25-34.

Zheng, Y., Heywood, K. J., Webber, B. G., Stevens, D. P., Biddle, L. C., Boehme, L., & Loose, B. (2021). Winter seal-based observations reveal glacial meltwater surfacing in the southeastern Amundsen Sea. *Communications Earth & Environment*, *2*(1), 1-9.

Zonneveld, K. A. et al. (2013). Atlas of modern dinoflagellate cyst distribution based on 2405 data points. *Review of Palaeobotany and Palynology* 191, 1-197.

Zonneveld, K.A.F., Bockelmann, F. & Holzwarth, U. (2007). Selective preservation of organic-walled dinoflagellate cysts as a tool to quantify past net primary production and bottom water oxygen concentrations. *Marine Geology* 237, 109–126.

Zundel, M., Spiegel, C., Mehling, A., Lisker, F., Hillenbrand, C. D., Monien, P., & Klügel, A. (2019). Thurston Island (West Antarctica) between Gondwana subduction and continental separation: A multistage evolution revealed by apatite thermochronology. *Tectonics*, *38*(3), 878-897.

Zuo, H., Balmaseda, M. A., Tietsche, S., Mogensen, K., & Mayer, M. (2019). The ECMWF operational ensemble reanalysis–analysis system for ocean and sea ice: a description of the system and assessment. *Ocean science*, *15*(3), 779-808.

Zurli, L., Cornamusini, G., Woo, J., Liberato, G. P., Han, S., Kim, Y., & Talarico, F. M. (2021). Detrital zircons from Late Paleozoic Ice Age sequences in Victoria Land (Antarctica): New constraints on the glaciation of southern Gondwana. *GSA Bulletin*, *134*(1-2), 160-178.

Appendices

A.2 Chapter 2 Supplementary Data Tables

Table A.2.1. *Clast data for IODP Expedition 374 Site U1521.*

Core Number	Core Bottom Depth (mbsf)	Core Length (m)	Core Midpoint Depth (mbsf)	Granitoid	Quartz	Dolerite	Basalt	Metamorphic	Sedimentary	Intraclast	Total Clasts	Clasts/core length (m)
22	204.75	5.35	207.425	0	0	0	0	0	0	0	0	0
23	214.6	5.6	217.4	18	13	3	12	60	0	2	108	19
24	221.56	3.13	223.125	11	3	5	5	12	0	1	37	12
25	232.91	4.81	235.315	16	13	3	18	59	3	8	120	25
26	244.53	7.05	248.055	63	29	8	27	147	2	8	284	40
27	253.03	6.04	256.05	30	9	15	21	49	4	8	136	23
28	262.82	6.22	265.93	19	13	14	12	71	0	6	135	22
29	272.83	6.73	276.195	26	15	33	12	40	1	10	137	20
30	282.22	6.52	285.48	7	1	0	1	23	0	6	38	6
31	287.04	1.74	287.91	0	0	0	0	0	0	0	0	0
32	295.61	0.71	295.965	0	0	0	0	0	0	0	0	0
33	305.24	0.74	305.61	0	0	0	0	0	0	0	0	0
34	314.95	0.85	315.375	0	0	0	0	0	0	0	0	0
35	326.63	3.17	328.215	39	11	21	4	62	2	9	148	47
36	336.99	3.69	338.835	126	0	16	11	145	0	5	303	82
37	347.07	4.35	349.245	83	11	25	7	94	1	9	230	53
38	356.34	3.84	358.26	79	2	23	1	94	1	3	203	53
39	359.42	2.32	360.58	71	5	14	2	83	1	3	179	77
40	365.4	3.53	367.165	144	9	30	2	135	0	0	320	91
41	371.55	4.86	373.98	191	51	39	37	183	0	2	503	103
42	375.73	4.03	377.745	105	7	21	16	127	0	0	276	68
43	380.29	3.99	382.285	132	19	45	25	277	0	4	502	126
44	390.34	9.04	394.86	213	2	12	27	201	1	3	459	51
45	397.94	7.04	401.46	164	27	22	38	245	0	10	506	72
46	404.92	4.42	407.13	46	0	5	2	78	0	0	131	30
47	419.09	8.99	423.585	223	50	11	32	285	7	11	619	69
48	428.88	9.18	433.47	122	4	8	12	192	0	3	341	37
49	438.85	9.59	443.645	152	14	2	21	156	0	2	347	36
50	448.33	9.84	453.25	193	39	24	23	222	1	12	514	52
51	450.34	2.07	451.375	17	8	1	4	19	2	4	55	27
52	467.13	9.03	471.645	124	6	0	11	136	0	12	289	32
53	477.07	10.06	482.1	160	27	11	19	229	1	15	462	46
54	486.63	10.1	491.68	135	1	2	15	207	0	8	368	36
55	492.91	5.08	495.45	142	19	8	18	236	2	7	432	85
56	504.22	7.59	508.015	69	2	0	4	77	0	5	157	21
57	514.34	9.98	519.33	101	15	4	1	121	1	12	255	26
58	522.74	8.2	526.84	86	30	9	0	104	0	0	229	28
59	531.78	7.35	535.455	106	11	5	1	163	0	5	291	40
60	542.74	9.04	547.26	263	28	16	2	377	0	13	699	77
61	553.78	9.82	558.69	175	14	4	3	215	0	6	417	42
62	561.95	9.38	566.64	182	13	8	3	332	2	10	550	59
63	568.81	6.43	572.025	178	11	42	1	269	2	11	514	80
64	579.75	7.91	583.705	270	3	38	2	277	0	2	592	75
65	588.45	6.84	591.87	221	24	87	2	391	0	5	730	107
66	600.07	9.07	604.605	257	20	32	0	312	0	1	622	69
67	610.47	9.81	615.375	232	24	52	0	425	1	6	740	75
68	619.54	9.22	624.15	175	14	34	0	209	0	0	432	47
69	628.25	8.17	632.335	180	14	121	3	292	0	5	615	75
70	638.86	8.49	643.105	231	27	69	1	159	0	4	491	58
71	647.24	7.51	650.995	109	3	15	0	94	1	2	224	30

Table A.2.2. *Nd and Sr isotope data for IODP Expedition 374 Site U1521.*

Core	Section	Top Offset (cm)	Bottom Offset (cm)	Sample Depth (m.b.s.f)	$^{143}Nd/^{144}Nd$	2SE	ε_{Nd}	2SD	$^{86}Sr/^{87}Sr$	2SE
1	1	4	6	0.05	0.512243	0.000009	-7.7	0.26	0.7194	0.000009
1	3	62	91	3.265	0.512169	0.000008	-9.15	0.27	0.728106	0.000007
2	1	85	88	8.265	0.512189	0.000007	-8.76	0.22	0.720287	0.000007
3	1	77	115	17.96	0.512218	0.000009	-8.19	0.24	0.720305	0.000008
4	1	75	78	27.365	0.512205	0.00001	-8.45	0.26	0.722911	0.000008
5	2	66	69	38.375	0.512234	0.000007	-7.87	0.27	0.717806	0.000008
8	1	13	53	65.33	0.51219	0.000009	-8.73	0.24	0.720382	0.000007
9	2	70	73	76.755	0.512303	0.000009	-6.54	0.27	0.716224	0.000008
10	1	81	84	85.025	0.512295	0.000008	-6.69	0.24	0.716965	0.000008
11	1	95	97	94.76	0.512209	0.000007	-8.36	0.26	0.719045	0.000009
12	3	50	53	106.305	0.512141	0.000009	-9.69	0.22	0.722344	0.000007
12	4	145	147	108.76	0.51214	0.000009	-9.72	0.22	0.723105	0.000008
12	5	113	116	109.955	0.512306	0.000007	-6.47	0.26	0.720533	0.000008
Procedural Replicate					0.512313	0.000011	-6.33	0.26	0.721226	0.000008
12	6	70	72	111.02	0.512285	0.000008	-6.89	0.22	0.718458	0.000009
13	1	99	102	114.005	0.512268	0.000006	-7.21	0.26	0.72049	0.00001
Procedural Replicate					0.512307	0.000007	-6.45	0.22	0.718573	0.000008
13	3	67	69	116.28	0.512272	0.000008	-7.14	0.22	0.719216	0.000009
Procedural Replicate					0.512264	0.000007	-7.3	0.22	0.719179	0.000007
15	1	10	13	132.315	0.512338	0.00001	-5.85	0.16	0.719924	0.000009
16	2	60	62	143.53	0.512388	0.00001	-4.89	0.26	0.713446	0.000008
17	3	65	68	154.245	0.512409	0.000008	-4.47	0.16	0.713205	0.000008
18	4	30	33	164.445	0.512343	0.000008	-5.75	0.22	0.717288	0.000007
19	5	63	65	176.4	0.512303	0.00001	-6.54	0.22	0.716062	0.000008
20	4	78	81	184.605	0.512402	0.000009	-4.61	0.22	0.714394	0.000007
20	7	5	7	187.99	0.512179	0.000008	-8.95	0.26	0.721163	0.000009
21	1	84	87	190.655	0.512297	0.000008	-6.64	0.26	0.714803	0.000009
21	2	93	96	192.255	0.512354	0.000007	-5.55	0.26	0.71439	0.000007
21	3	46	49	193.035	0.51237	0.000008	-5.22	0.22	0.715816	0.000009
21	4	7	9	194.15	0.512463	0.000007	-3.42	0.22	0.712278	0.000007
21	5	62	64	196.21	0.512302	0.000006	-6.56	0.26	0.717378	0.000009
21	6	12	14	197.22	0.51228	0.000008	-6.99	0.22	0.71827	0.000007
22	1	32	35	199.735	0.512228	0.000008	-7.99	0.27	0.719153	0.000008
22	2	17	19	200.79	0.512159	0.000007	-9.35	0.22	0.722039	0.000007
22	4	60	62	204.1	0.51215	0.000007	-9.52	0.22	0.722286	0.000007
23	1	60	62	209.61	0.51215	0.00001	-9.52	0.22	0.721559	0.000008
24	2	5	45	220.23	0.512152	0.000011	-9.49	0.24	0.720283	0.000008
25	3	40	43	230.885	0.512165	0.000009	-9.23	0.27	0.720755	0.000008
26	2	110	112	240.06	0.512151	0.000007	-9.5	0.22	0.720556	0.000007
26	4	60	63	242.405	0.512169	0.000009	-9.15	0.27	0.719565	0.000008
27	4	72	75	251.715	0.51216	0.000012	-9.33	0.23	0.720625	0.000008

28	4	36	39	260.935	0.512155	0.000008	-9.42	0.27	0.72116	0.000008
29	4	5	45	270.03	0.512137	0.000008	-9.77	0.24	0.722339	0.000008
30	3	15	18	278.655	0.512179	0.000009	-8.95	0.22	0.721159	0.000008
31	1	30	33	285.615	0.512231	0.000008	-7.93	0.09	0.720046	0.000007
32	1	44	47	295.355	0.512323	0.000008	-6.15	0.22	0.717504	0.000008
34	1	57	60	314.685	0.512321	0.000006	-6.18	0.27	0.719279	0.000009
35	2	42	45	324.905	0.512175	0.000011	-9.04	0.23	0.719013	0.000007
36	2	87	127	335.72	0.512158	0.000008	-9.36	0.24	0.721069	0.000007
37	3	77	80	346.475	0.512163	0.000008	-9.26	0.27	0.721182	0.000008
38	2	100	103	355.015	0.512159	0.00001	-9.34	0.22	0.720842	0.000008
39	1	57	60	357.885	0.512152	0.000009	-9.49	0.23	0.720674	0.000008
40	2	69	72	364.265	0.512145	0.000009	-9.63	0.16	0.720599	0.000008
41	3	45	48	370.075	0.512166	0.00001	-9.21	0.23	0.720056	0.000008
42	2	50	90	373.58	0.512114	0.00001	-10.22	0.24	0.722226	0.000008
44	3	81	84	384.985	0.512269	0.000007	-7.19	0.27	0.718348	0.000009
47	1	52	92	410.82	0.512269	0.00001	-7.2	0.24	0.721194	0.000009
49	4	79	82	433.865	0.512273	0.00001	-7.13	0.16	0.720854	0.000007
51	1	50	53	449.015	0.512278	0.000008	-7.02	0.24	0.717936	0.000008
53	3	33	36	470.495	0.512278	0.000008	-7.03	0.22	0.718345	0.000006
Procedural Replicate					0.512292	0.000008	-6.75	0.22	0.718445	0.000008
55	1	30	70	487.4	0.512283	0.000008	-6.92	0.24	0.722095	0.000008
57	2	50	53	507.795	0.512283	0.000008	-6.92	0.22	0.717587	0.000008
59	5	73	76	531.475	0.512313	0.00001	-6.35	0.23	0.720898	0.000007
61	2	53	56	546.495	0.512333	0.000008	-5.95	0.27	0.717613	0.000008
63	1	96	99	564.675	0.512324	0.000009	-6.13	0.22	0.718857	0.000006
63	5	20	23	569.025	0.512199	0.000009	-8.56	0.22	0.7241	0.000008
65	4	63	103	588	0.512171	0.000008	-9.1	0.24	0.725335	0.000007
67	4	43	46	606.515	0.512161	0.00001	-9.31	0.22	0.72596	0.000008
69	3	56	59	624.665	0.512128	0.000007	-9.95	0.22	0.723791	0.000008
71	2	24	64	642.21	0.512169	0.00001	-9.15	0.24	0.723136	0.000009

Table A.2.3. *U-Pb zircon data for IODP Expedition 374 Site U1521. A .csv version can be found here: https://doi.org/10.5285/cfadf931-0804-484c-a9d0-96254239c421*

Core	Section	Top Offset (cm)	Bottom Offset (cm)	Sample Depth (m.b.s.f)	U (ppm)	Th (ppm)	Th/U	$^{207}Pb/^{235}U$	±s.e.	$^{206}Pb/^{238}U$	±s.e.	$^{207}Pb/^{206}Pb$	±s.e.	207/ 235 Age	±s.e.	207/ 206 Age	±s.e.	206/ 238 Age	±s.e.	% Disc 7/6	% Disc 5/8	Best Age	±s.e.	Pb corrected age	±s.e.
3	1	77	115	17.96	1069	315	0.30	2.0212	0.0361	0.1940	0.0024	0.0758	0.0013	1122.7	12.2	1087.6	34.0	1142.8	13.1	-5.1	1.8	1087.6	13.1	1145.6	32.6
3	1	77	115	17.96	476	391	0.80	1.9178	0.0422	0.1877	0.0025	0.0743	0.0016	1087.3	14.7	1047.9	43.2	1108.8	13.3	-5.8	1.9	1047.9	13.3	1111.7	41.4
3	1	77	115	17.96	864	319	0.40	0.7586	0.0167	0.0935	0.0012	0.0590	0.0013	573.2	9.7	564.6	47.0	576.3	7.1	-2.1	0.5	576.3	7.1	576.5	7.1
3	1	77	115	17.96	736	457	0.60	0.2218	0.0109	0.0279	0.0005	0.0577	0.0029	203.4	9.0	518.9	109.1	177.5	2.9	65.8	-14.6	177.5	2.9	175.7	2.9
3	1	77	115	17.96	774	334	0.40	0.7398	0.0223	0.0951	0.0013	0.0565	0.0017	562.3	13.0	472.6	66.6	585.7	7.7	-23.9	4.0	585.7	7.7	587.8	7.7
3	1	77	115	17.96	745	800	1.10	0.6430	0.0158	0.0817	0.0011	0.0572	0.0014	504.2	9.8	497.5	53.2	506.5	6.3	-1.8	0.5	506.5	6.3	506.6	6.3
3	1	77	115	17.96	672	88	0.10	0.6753	0.0208	0.0853	0.0012	0.0575	0.0018	523.9	12.6	510.5	67.7	527.9	7.0	-3.4	0.8	527.9	7.0	528.2	7.0
3	1	77	115	17.96	985	456	0.50	13.4817	0.2029	0.5322	0.0065	0.1841	0.0025	2714.0	14.3	2689.8	23.0	2750.6	27.6	-2.3	1.3	2689.8	27.6	2775.2	21.5
3	1	77	115	17.96	726	210	0.30	0.7696	0.0185	0.0914	0.0012	0.0612	0.0014	579.5	10.6	645.3	50.6	563.8	7.0	12.6	-2.8	563.8	7.0	562.2	7.0
3	1	77	115	17.96	1319	96	0.10	0.6975	0.0159	0.0879	0.0011	0.0577	0.0013	537.3	9.5	517.0	49.2	543.0	6.7	-5.0	1.1	543.0	6.7	543.4	6.7
3	1	77	115	17.96	857	330	0.40	1.7792	0.0378	0.1778	0.0023	0.0728	0.0015	1037.9	13.8	1006.1	41.9	1054.7	12.5	-4.8	1.6	1054.7	12.5	1056.9	12.6
3	1	77	115	17.96	422	276	0.70	0.1998	0.0115	0.0282	0.0005	0.0515	0.0030	184.9	9.7	261.8	133.8	179.3	2.9	31.5	-3.2	179.3	2.9	178.9	2.9
3	1	77	115	17.96	1667	207	0.10	0.6691	0.0163	0.0814	0.0011	0.0598	0.0014	520.2	9.9	593.9	51.9	504.3	6.3	15.1	-3.1	504.3	6.3	502.8	6.3
3	1	77	115	17.96	689	511	0.70	0.2788	0.0109	0.0392	0.0006	0.0517	0.0020	249.7	8.7	271.1	90.0	247.9	3.5	8.6	-0.7	247.9	3.5	247.7	3.5
3	1	77	115	17.96	3071	621	0.20	0.6113	0.0108	0.0778	0.0010	0.0571	0.0010	484.4	6.8	495.6	36.7	482.8	5.7	2.6	-0.3	482.8	5.7	482.6	5.7
3	1	77	115	17.96	1662	310	0.20	0.8242	0.0157	0.0969	0.0012	0.0618	0.0011	610.4	8.8	666.6	39.2	596.3	7.1	10.5	-2.4	596.3	7.1	594.9	7.1
3	1	77	115	17.96	324	812	2.50	0.7889	0.0254	0.0955	0.0013	0.0600	0.0019	590.5	14.4	603.3	69.6	588.2	7.8	2.5	-0.4	588.2	7.8	587.9	7.8
3	1	77	115	17.96	598	260	0.40	0.6886	0.0190	0.0856	0.0011	0.0585	0.0016	531.9	11.4	545.7	59.9	529.6	6.8	3.0	-0.4	529.6	6.8	529.3	6.8
3	1	77	115	17.96	2607	736	0.30	0.1873	0.0048	0.0264	0.0003	0.0517	0.0013	174.3	4.1	269.8	57.7	167.7	2.1	37.9	-4.0	167.7	2.1	167.2	2.1
3	1	77	115	17.96	740	79	0.10	0.7446	0.0243	0.0930	0.0013	0.0582	0.0019	565.1	14.2	535.2	71.9	573.5	7.7	-7.2	1.5	573.5	7.7	574.2	7.7
3	1	77	115	17.96	750	454	0.60	4.3752	0.0806	0.3167	0.0040	0.1004	0.0018	1707.7	15.3	1630.7	32.9	1773.8	19.7	-8.8	3.7	1630.7	19.7	1789.9	29.3
3	1	77	115	17.96	951	494	0.50	1.9785	0.0357	0.1863	0.0023	0.0772	0.0013	1108.2	12.2	1124.9	34.4	1101.4	12.6	2.1	-0.6	1124.9	12.6	1100.3	35.0
3	1	77	115	17.96	2520	283	0.10	0.7705	0.0140	0.0947	0.0012	0.0592	0.0010	580.1	8.0	572.0	37.6	583.0	6.9	-1.9	0.5	583.0	6.9	583.2	6.9
3	1	77	115	17.96	878	177	0.20	0.8888	0.0196	0.1034	0.0013	0.0625	0.0013	645.7	10.5	689.3	45.8	634.4	7.7	8.0	-1.8	634.4	7.7	633.2	7.7
3	1	77	115	17.96	1088	425	0.40	1.0542	0.0218	0.1111	0.0014	0.0690	0.0014	731.0	10.8	897.5	41.3	679.0	8.2	24.4	-7.7	679.0	8.2	673.5	8.1
3	1	77	115	17.96	1912	1614	0.80	0.1865	0.0055	0.0273	0.0004	0.0497	0.0015	173.7	4.7	179.9	68.0	173.5	2.3	3.6	-0.1	173.5	2.3	173.5	2.3
3	1	77	115	17.96	1004	2156	2.10	1.0585	0.0227	0.1200	0.0015	0.0641	0.0013	733.1	11.2	745.3	44.2	730.3	8.8	2.0	-0.4	730.3	8.8	729.9	8.8
3	1	77	115	17.96	1324	475	0.40	0.8296	0.0177	0.0999	0.0013	0.0604	0.0013	613.4	9.9	615.9	45.1	613.8	7.5	0.3	0.1	613.8	7.5	613.7	7.5
3	1	77	115	17.96	447	266	0.60	0.6993	0.0214	0.0858	0.0012	0.0593	0.0018	538.3	12.8	575.7	66.8	530.4	7.0	7.9	-1.5	530.4	7.0	529.6	7.0
3	1	77	115	17.96	2315	22	0.00	0.7467	0.0138	0.0925	0.0011	0.0587	0.0010	566.3	8.0	554.6	38.4	570.2	6.7	-2.8	0.7	570.2	6.7	570.5	6.7
3	1	77	115	17.96	656	348	0.50	0.7834	0.0204	0.0942	0.0012	0.0604	0.0016	587.4	11.6	618.4	55.8	580.4	7.3	6.1	-1.2	580.4	7.3	579.7	7.3
3	1	77	115	17.96	638	297	0.50	0.6733	0.0189	0.0817	0.0011	0.0599	0.0017	522.7	11.5	600.1	60.4	506.0	6.6	15.7	-3.3	506.0	6.6	504.4	6.5
3	1	77	115	17.96	402	257	0.60	0.6615	0.0226	0.0812	0.0012	0.0592	0.0020	515.6	13.8	574.2	74.9	503.3	6.9	12.4	-2.4	503.3	6.9	502.1	6.8
3	1	77	115	17.96	435	386	0.90	0.2457	0.0165	0.0324	0.0006	0.0552	0.0038	223.1	13.4	417.3	152.7	205.4	3.9	50.8	-8.6	205.4	3.9	204.2	3.8
3	1	77	115	17.96	385	254	0.70	0.3901	0.0192	0.0503	0.0008	0.0564	0.0028	334.4	14.0	466.4	110.8	316.3	5.0	32.2	-5.7	316.3	5.0	314.9	5.0
3	1	77	115	17.96	674	1480	2.20	0.1986	0.0097	0.0265	0.0004	0.0544	0.0027	183.9	8.2	385.8	111.1	168.9	2.6	56.2	-8.9	168.9	2.6	167.8	2.6
3	1	77	115	17.96	1237	135	0.10	0.8269	0.0200	0.0977	0.0013	0.0616	0.0015	611.9	11.1	657.5	51.3	600.7	7.5	8.6	-1.9	600.7	7.5	599.5	7.5
3	1	77	115	17.96	2323	113	0.00	0.6935	0.0134	0.0855	0.0011	0.0589	0.0011	534.9	8.0	563.9	40.7	529.0	6.3	6.2	-1.1	529.0	6.3	528.4	6.3
3	1	77	115	17.96	542	540	1.00	10.0259	0.1705	0.4566	0.0057	0.1596	0.0026	2437.2	15.8	2450.6	27.4	2424.6	25.4	1.1	-0.5	2450.6	25.4	2417.6	28.2
3	1	77	115	17.96	1392	455	0.30	0.7576	0.0183	0.0939	0.0012	0.0587	0.0014	572.6	10.6	553.9	52.1	578.4	7.1	-4.4	1.0	578.4	7.1	578.8	7.1
3	1	77	115	17.96	694	405	0.60	1.7925	0.0392	0.1744	0.0023	0.0747	0.0016	1042.7	14.3	1059.3	43.2	1036.5	12.4	2.2	-0.6	1036.5	12.4	1035.5	12.4
3	1	77	115	17.96	1063	571	0.50	0.7551	0.0188	0.0883	0.0012	0.0622	0.0015	571.2	10.9	678.3	52.7	545.5	6.8	19.6	-4.7	545.5	6.8	543.1	6.8
3	1	77	115	17.96	357	240	0.70	13.5038	0.2712	0.5263	0.0072	0.1865	0.0037	2715.6	19.1	2710.9	32.5	2725.7	30.5	-0.5	0.4	2710.9	30.5	2731.5	32.0
3	1	77	115	17.96	1715	273	0.20	1.3606	0.0259	0.1367	0.0017	0.0723	0.0013	872.1	11.2	994.6	37.5	826.0	9.7	16.9	-5.6	826.0	9.7	820.5	9.6
3	1	77	115	17.96	438	205	0.50	0.7479	0.0254	0.0900	0.0013	0.0604	0.0021	567.0	14.7	617.7	73.6	555.4	7.6	10.1	-2.1	555.4	7.6	554.2	7.6
3	1	77	115	17.96	476	624	1.30	0.2282	0.0134	0.0333	0.0006	0.0498	0.0030	208.7	11.0	182.8	138.1	211.3	3.5	-15.6	1.2	211.3	3.5	211.5	3.5
3	1	77	115	17.96	203	169	0.80	2.2518	0.0645	0.2074	0.0029	0.0789	0.0023	1197.3	20.1	1169.5	56.8	1214.8	15.5	-3.9	1.4	1169.5	15.5	1217.3	54.9
3	1	77	115	17.96	2216	4096	1.80	0.8544	0.0168	0.1005	0.0013	0.0618	0.0012	627.1	9.2	666.2	40.6	617.3	7.3	7.3	-1.6	617.3	7.3	616.3	7.3
3	1	77	115	17.96	608	568	0.90	1.2982	0.0329	0.1361	0.0018	0.0694	0.0018	844.9	14.6	908.2	52.0	822.3	10.2	9.5	-2.7	822.3	10.2	819.6	10.2
3	1	77	115	17.96	292	661	2.30	0.7054	0.0279	0.0867	0.0013	0.0591	0.0024	542.0	16.6	571.3	86.8	535.9	7.7	6.2	-1.1	535.9	7.7	535.3	7.6
3	1	77	115	17.96	340	312	0.90	3.2075	0.0722	0.2532	0.0033	0.0921	0.0020	1459.0	17.4	1468.2	42.2	1454.9	17.1	0.9	-0.3	1468.2	17.1	1453.9	42.6
3	1	77	115	17.96	743	269	0.40	0.7977	0.0271	0.1009	0.0014	0.0575	0.0020	595.5	15.3	507.9	75.1	619.8	8.4	-22.0	3.9	619.8	8.4	622.0	8.4
3	1	77	115	17.96	4800	227	0.00	0.5884	0.0126	0.0677	0.0009	0.0631	0.0013	469.8	8.1	711.7	44.5	422.5	5.1	40.6	-11.2	422.5	5.1	418.5	5.1
3	1	77	115	17.96	836	597	0.70	2.8571	0.0538	0.2335	0.0029	0.0889	0.0016	1370.7	14.2	1401.6	34.8	1353.0	15.3	3.5	-1.3	1401.6	15.3	1349.6	36.1
3	1	77	115	17.96	132	94	0.70	0.6705	0.0414	0.0856	0.0015	0.0569	0.0036	521.0	25.2	487.1	138.5	529.7	9.1	-8.8	1.6	529.7	9.1	530.4	9.1
3	1	77	115	17.96	300	237	0.80	3.2953	0.0762	0.2661	0.0035	0.0900	0.0021	1479.9	18.0	1424.7	43.8	1521.2	17.9	-6.8	2.7	1424.7	17.9	1529.2	40.6
3	1	77	115	17.96	2835	213	0.10	0.8523	0.0178	0.0981	0.0012	0.0632	0.0013	625.9	9.8	712.3	43.1	603.2	7.2	15.3	-3.8	603.2	7.2	601.0	7.2
3	1	77	115	17.96	922	1251	1.40	2.1893	0.0442	0.2029	0.0026	0.0784	0.0015	1177.6	14.1	1156.9	39.0	1190.8	13.7	-2.9	1.1	1156.9	13.7	1192.7	38.1
3	1	77	115	17.96	858	415	0.50	0.8691	0.0213	0.1025	0.0013	0.0617	0.0015	635.1	11.6	661.0	52.2	628.8	7.7	4.9	-1.0	628.8	7.7	628.1	7.7
3	1	77	115	17.96	625	1061	1.70	0.9468	0.0260	0.1124	0.0015	0.0612	0.0017	676.4	13.6	646.7	59.0	686.6	8.6	-6.2	1.5	686.6	8.6	687.5	8.7
3	1	77	115	17.96	2809	73	0.00	1.1138	0.0213	0.1199	0.0015	0.0675	0.0013	760.0	10.2	852.3	38.6	730.2	8.5	14.3	-4.1	730.2	8.5	726.9	8.5
3	1	77	115	17.96	646	168	0.30	1.5083	0.0386	0.1560	0.0021	0.0703	0.0018	933.8	15.7	935.6	52.3	934.5	11.5	0.1	0.1	934.5	11.5	934.5	11.5
3	1	77	115	17.96	801	796	1.00	0.2363	0.0106	0.0318	0.0005	0.0540	0.0025	215.4	8.7	371.7	102.1	201.7	3.1	45.7	-6.8	201.7	3.1	200.7	3.0
3	1	77	115	17.96	1159	646	0.60	0.6959	0.0180	0.0864	0.0011	0.0585	0.0015	536.3	10.8	548.7	56.0	534.3	6.7	2.6	-0.4	534.3	6.7	534.0	6.6
3	1	77	115	17.96	1060	168	0.20	1.6401	0.0343	0.1602	0.0020	0.0744	0.0015	985.7	13.2	1052.2	41.2	957.7	11.2	9.0	-2.9	957.7	11.2	953.9	11.2
3	1	77	115	17.96	1297	2177	1.70	0.2258	0.0084	0.0318	0.0005	0.0516	0.0019	206.7	6.9	266.2	85.4	201.9	2.8	24.2	-2.4	201.9	2.8	201.5	2.8
3	1	77	115	17.96	1203	64	0.10	1.0125	0.0234	0.1123	0.0014	0.0655	0.0015	710.1	11.8	790.1	48.1	686.3	8.3	13.1	-3.5	686.3	8.3	683.7	8.3
3	1	77	115	17.96	338	267	0.80	0.8132	0.0320	0.0997	0.0015	0.0593	0.0024	604.3	17.9	576.8	86.5	612.6	8.7	-6.2	1.4	612.6	8.7	613.3	8.7
3	1	77	115	17.96	695	227	0.30	1.6328	0.0384	0.1620	0.0021	0.0733	0.0017	982.9	14.8	1021.1	47.3	967.6	11.6	5.2	-1.6	967.6	11.6	965.5	11.6
3	1	77	115	17.96	993	323	0.30	0.6789	0.0187	0.0846	0.0011	0.0584	0.0016	526.1	11.3	542.7	60.3	523.2	6.6	3.6	-0.6	523.2	6.6	522.9	6.6
3	1	77	115	17.96	782	5	0.00	0.7856	0.0228	0.0939	0.0013	0.0608	0.0018	588.7	13.0	632.3	62.7	578.4	7.4	8.5	-1.8	578.4	7.4	577.4	7.4
3	1	77	115	17.96	1588	1326	0.80	0.7111	0.0170	0.0869	0.0011	0.0595	0.0014	545.4	10.1	583.7	51.5	537.2	6.6	8.0	-1.5	537.2	6.6	536.4	6.6
3	1	77	115	17.96	944	398	0.40	0.6832	0.0187	0.0858	0.0011	0.0579	0.0016	528.7	11.3	523.5	59.9	530.8	6.7	-1.4	0.4	530.8	6.7	531.0	6.7
3	1	77	115	17.96	1434	928	0.60	0.6369	0.0186	0.0776	0.0010	0.0597	0.0017	500.4	11.5	591.0	63.3	481.6	6.2	18.5	-3.9	481.6	6.2	479.9	6.2
3	1	77	115	17.96	843	239	0.30	1.2260	0.0286	0.1309	0.0017	0.0681	0.0016	812.5	13.1	870.7	47.8	792.8	9.5	8.9	-2.5	792.8	9.5	790.5	9.5
3	1	77	115	17.96	1594	339	0.20	0.9015	0.0198	0.1011	0.0013	0.0648	0.0014	652.5	10.6	766.9	45.6	621.1	7.4	19.0	-5.1	621.1	7.4	617.9	7.4
3	1	77	115	17.96	8057	888	0.10	0.4294	0.0085	0.0518	0.0006	0.0603	0.0012	362.7	6.1	613.4	41.6	325.3	3.9	47.0	-11.5	325.3	3.9	322.4	3.9

3	1	77	115	17.96	1321	330	0.20	0.9365	0.0213	0.1065	0.0013	0.0639	0.0014	671.1	11.2	737.4	47.8	652.6	7.8	11.5	-2.8	652.6	7.8	650.7	7.8
3	1	77	115	17.96	1463	419	0.30	0.8494	0.0254	0.0962	0.0013	0.0642	0.0019	624.3	13.9	747.6	63.6	591.9	7.7	20.8	-5.5	591.9	7.7	588.7	7.7
3	1	77	115	17.96	1370	141	0.10	0.7560	0.0179	0.0908	0.0012	0.0605	0.0014	571.7	10.4	620.9	50.7	560.4	6.8	9.7	-2.0	560.4	6.8	559.3	6.8
3	1	77	115	17.96	1352	734	0.50	0.7423	0.0178	0.0915	0.0012	0.0590	0.0014	563.8	10.4	565.4	51.7	564.3	6.9	0.2	0.1	564.3	6.9	564.3	6.9
3	1	77	115	17.96	559	57	0.10	0.6978	0.0271	0.0844	0.0013	0.0601	0.0024	537.5	16.2	606.9	84.9	522.2	7.4	14.0	-2.9	522.2	7.4	520.8	7.4
3	1	77	115	17.96	826	615	0.70	3.1010	0.0660	0.2462	0.0031	0.0916	0.0019	1432.9	16.4	1457.8	40.0	1418.6	16.0	2.7	-1.0	1457.8	16.0	1415.7	41.2
3	1	77	115	17.96	269	246	0.90	0.7325	0.0303	0.0868	0.0013	0.0613	0.0026	558.0	17.7	649.9	90.0	536.8	7.8	17.4	-4.0	536.8	7.8	534.8	7.8
3	1	77	115	17.96	843	164	0.20	0.6554	0.0189	0.0811	0.0011	0.0588	0.0017	511.8	11.6	557.2	63.1	502.6	6.4	9.8	-1.8	502.6	6.4	501.7	6.4
3	1	77	115	17.96	1772	1493	0.80	0.3512	0.0098	0.0470	0.0006	0.0543	0.0015	305.6	7.4	383.7	62.9	296.0	3.8	22.9	-3.2	296.0	3.8	295.3	3.7
3	1	77	115	17.96	467	390	0.80	0.7246	0.0244	0.0847	0.0012	0.0622	0.0021	553.4	14.3	680.4	72.5	523.9	7.0	23.0	-5.6	523.9	7.0	521.2	7.0
3	1	77	115	17.96	1252	584	0.50	1.8612	0.0413	0.1772	0.0022	0.0764	0.0017	1067.4	14.7	1103.4	44.1	1051.7	12.2	4.7	-1.5	1051.7	12.2	1049.4	12.2
3	1	77	115	17.96	1732	1317	0.80	0.7592	0.0187	0.0907	0.0012	0.0609	0.0015	573.5	10.8	633.3	52.8	559.6	6.9	11.6	-2.5	559.6	6.9	558.2	6.8
3	1	77	115	17.96	633	241	0.40	0.6743	0.0238	0.0833	0.0012	0.0589	0.0021	523.3	14.4	560.9	77.8	515.7	7.0	8.1	-1.5	515.7	7.0	515.0	7.0
3	1	77	115	17.96	1052	185	0.20	8.2874	0.1719	0.4100	0.0051	0.1469	0.0030	2262.9	18.9	2309.8	35.3	2215.1	23.3	4.1	-2.2	2309.8	23.3	2195.0	38.6
3	1	77	115	17.96	670	510	0.80	1.9502	0.0487	0.1843	0.0024	0.0770	0.0019	1098.5	16.8	1119.0	49.8	1090.2	13.0	2.6	-0.8	1090.2	13.0	1088.8	13.0
3	1	77	115	17.96	2545	704	0.30	0.9710	0.0248	0.1072	0.0014	0.0659	0.0017	689.0	12.8	800.7	53.5	656.5	8.0	18.0	-4.9	656.5	8.0	653.2	8.0
3	1	77	115	17.96	717	292	0.40	0.7118	0.0227	0.0872	0.0012	0.0593	0.0019	545.8	13.5	578.6	70.0	539.0	7.1	6.8	-1.3	539.0	7.1	538.3	7.1
3	1	77	115	17.96	920	1019	1.10	0.8378	0.0240	0.0986	0.0013	0.0618	0.0018	617.9	13.3	666.6	61.7	605.9	7.7	9.1	-2.0	605.9	7.7	604.7	7.7
3	1	77	115	17.96	428	135	0.30	0.7126	0.0272	0.0895	0.0013	0.0579	0.0022	546.3	16.1	524.6	84.9	552.5	7.6	-5.3	1.1	552.5	7.6	553.0	7.6
3	1	77	115	17.96	506	250	0.50	1.1362	0.0346	0.1198	0.0016	0.0689	0.0021	770.7	16.4	896.0	63.5	729.5	9.4	18.6	-5.6	729.5	9.4	725.0	9.3
3	1	77	115	17.96	75	15	0.20	0.7061	0.0501	0.0933	0.0018	0.0550	0.0040	542.4	29.8	410.8	161.1	575.2	10.4	-40.0	5.7	575.2	10.4	578.1	10.5
3	1	77	115	17.96	823	485	0.60	2.3838	0.0467	0.2004	0.0026	0.0865	0.0016	1237.8	14.1	1348.1	36.7	1177.2	13.8	12.7	-5.1	1348.1	13.8	1167.5	41.7
3	1	77	115	17.96	4460	6594	1.50	0.2560	0.0066	0.0295	0.0004	0.0630	0.0016	231.4	5.3	707.3	54.7	187.6	2.4	73.5	-23.4	187.6	2.4	184.5	2.4
3	1	77	115	17.96	402	182	0.50	6.7703	0.1298	0.3265	0.0042	0.1507	0.0028	2081.9	17.0	2353.6	32.0	1821.2	20.4	22.6	-14.3	2353.6	20.4	1740.1	51.0
3	1	77	115	17.96	1446	559	0.40	0.1742	0.0162	0.0506	0.0007	0.0250	0.0023	163.1	14.0	0.0	118.3	318.2	4.3	-2E8	48.8	318.2	4.3	329.0	4.4
3	1	77	115	17.96	1089	301	0.30	4.7101	0.0923	0.3025	0.0038	0.1132	0.0022	1769.0	16.5	1850.4	34.6	1703.6	18.9	7.9	-3.8	1850.4	18.9	1686.8	39.0
3	1	77	115	17.96	1816	787	0.40	4.6240	0.0834	0.3037	0.0037	0.1107	0.0019	1753.6	15.1	1810.0	31.7	1709.4	18.5	5.6	-2.6	1810.0	18.5	1698.1	34.4
3	1	77	115	17.96	1037	670	0.60	2.8850	0.0577	0.2222	0.0028	0.0944	0.0018	1378.0	15.1	1515.1	36.9	1293.3	14.7	14.6	-6.5	1515.1	14.7	1278.2	43.6
3	1	77	115	17.96	2056	1211	0.60	1.8878	0.0429	0.1152	0.0015	0.1192	0.0027	1076.8	15.1	1943.0	40.6	702.6	8.7	63.8	-53.3	702.6	8.7	655.6	8.2
3	1	77	115	17.96	593	294	0.50	3.0427	0.0668	0.2389	0.0030	0.0926	0.0020	1418.4	16.8	1478.5	41.3	1381.0	15.8	6.6	-2.7	1478.5	15.8	1373.8	44.4
3	1	77	115	17.96	618	563	0.90	2.2252	0.0525	0.1958	0.0025	0.0826	0.0019	1189.0	16.6	1258.9	46.0	1152.9	13.5	8.4	-3.1	1258.9	13.5	1147.2	49.7
3	1	77	115	17.96	2374	941	0.40	4.9864	0.1024	0.2649	0.0033	0.1368	0.0028	1817.0	17.4	2186.8	35.3	1515.0	16.7	30.7	-19.9	2186.8	16.7	1442.0	61.5
3	1	77	115	17.96	478	235	0.50	1.6735	0.0510	0.0988	0.0015	0.1232	0.0038	998.5	19.4	2001.8	55.5	607.3	8.5	69.7	-64.4	607.3	8.5	561.4	7.9
8	1	13	53	65.33	241	72	0.30	8.9805	0.1421	0.3772	0.0058	0.1731	0.0019	2336.0	14.5	2586.6	18.7	2063.1	27.3	20.2	-13.2	2586.6	27.3	1955.5	30.4
8	1	13	53	65.33	540	287	0.50	1.6608	0.0282	0.1397	0.0022	0.0864	0.0011	993.7	10.8	1346.9	24.7	842.8	12.4	37.4	-17.9	842.8	12.4	823.8	12.1
8	1	13	53	65.33	7298	2003	0.30	0.4502	0.0066	0.0488	0.0007	0.0671	0.0008	377.4	4.6	840.9	23.4	306.8	4.2	63.5	-23.0	306.8	4.2	301.3	4.2
8	1	13	53	65.33	305	170	0.60	2.5459	0.0420	0.1973	0.0031	0.0938	0.0011	1285.3	12.1	1502.6	22.7	1161.0	16.5	22.7	-10.7	1502.6	16.5	1140.9	29.3
8	1	13	53	65.33	755	306	0.40	1.2609	0.0226	0.1126	0.0018	0.0814	0.0011	828.3	10.2	1230.7	27.6	687.6	10.4	44.1	-20.5	687.6	10.4	672.1	10.2
8	1	13	53	65.33	3212	1341	0.40	11.6362	0.1653	0.4600	0.0065	0.1839	0.0019	2575.6	13.4	2687.3	17.5	2439.4	28.5	9.2	-5.6	2687.3	28.5	2365.8	22.5
8	1	13	53	65.33	2339	960	0.40	1.0785	0.0163	0.0981	0.0014	0.0799	0.0009	742.9	8.0	1193.6	23.4	603.3	8.2	49.5	-23.1	603.3	8.2	589.0	8.0
8	1	13	53	65.33	2363	1209	0.50	2.1596	0.0318	0.1875	0.0027	0.0837	0.0009	1168.1	10.3	1284.9	21.8	1107.8	14.4	13.8	-5.4	1284.9	14.4	1098.6	14.3
8	1	13	53	65.33	2049	792	0.40	0.7975	0.0120	0.0683	0.0010	0.0849	0.0010	595.4	6.8	1311.9	23.0	425.8	5.9	67.5	-39.8	425.8	5.9	410.5	5.7
8	1	13	53	65.33	278	221	0.80	5.6023	0.0919	0.3367	0.0052	0.1209	0.0014	1916.5	14.2	1969.3	21.3	1870.5	25.2	5.0	-2.5	1969.3	25.2	1856.9	23.1
8	1	13	53	65.33	3784	1478	0.40	0.7824	0.0117	0.0808	0.0011	0.0704	0.0008	586.8	6.7	938.2	23.7	501.0	6.8	46.6	-17.1	501.0	6.8	493.1	6.7
8	1	13	53	65.33	426	149	0.30	12.8438	0.2061	0.4900	0.0075	0.1905	0.0022	2668.3	15.2	2745.7	18.9	2570.6	32.7	6.4	-3.8	2745.7	32.7	2510.6	22.7
8	1	13	53	65.33	618	660	1.10	12.2772	0.1966	0.4809	0.0074	0.1855	0.0021	2625.8	15.1	2702.2	18.9	2531.3	32.2	6.3	-3.7	2702.2	32.2	2475.7	22.6
8	1	13	53	65.33	527	509	1.00	2.3810	0.0381	0.2149	0.0033	0.0806	0.0009	1236.9	11.5	1209.6	22.4	1254.6	17.5	-3.7	1.4	1209.6	17.5	1257.3	21.7
8	1	13	53	65.33	2323	840	0.40	0.6763	0.0099	0.0842	0.0012	0.0584	0.0007	524.5	6.0	543.4	24.4	521.1	7.1	4.1	-0.7	521.1	7.1	520.7	7.1
8	1	13	53	65.33	5789	5042	0.90	0.6488	0.0093	0.0819	0.0012	0.0576	0.0006	507.7	5.7	512.4	23.4	507.5	6.9	1.0	0.0	507.5	6.9	507.4	6.9
8	1	13	53	65.33	1402	1328	0.90	0.2505	0.0044	0.0361	0.0006	0.0504	0.0007	227.0	3.6	212.0	30.9	228.8	3.5	-7.9	0.8	228.8	3.5	228.9	3.5
8	1	13	53	65.33	294	160	0.50	4.6787	0.0752	0.3171	0.0049	0.1072	0.0012	1763.4	13.5	1752.2	21.0	1775.6	24.0	-1.3	0.7	1752.2	24.0	1778.4	20.6
8	1	13	53	65.33	948	622	0.70	0.6453	0.0107	0.0809	0.0012	0.0580	0.0007	505.6	6.6	529.2	26.5	501.2	7.4	5.3	-0.9	501.2	7.4	500.8	7.4
8	1	13	53	65.33	916	387	0.40	0.8270	0.0135	0.1000	0.0015	0.0601	0.0007	611.9	7.5	606.2	25.7	614.5	9.0	-1.4	0.4	614.5	9.0	614.7	9.0
8	1	13	53	65.33	257	155	0.60	20.7546	0.3242	0.6118	0.0094	0.2466	0.0026	3127.2	15.3	3162.2	17.4	3077.3	37.8	2.7	-1.6	3162.2	37.8	3018.2	19.6
8	1	13	53	65.33	643	235	0.40	0.8431	0.0143	0.1008	0.0016	0.0608	0.0008	620.9	7.9	631.6	27.4	619.0	9.1	2.0	-0.3	619.0	9.1	618.7	9.1
8	1	13	53	65.33	907	552	0.60	0.6353	0.0106	0.0813	0.0013	0.0568	0.0007	499.4	6.6	481.6	26.9	504.1	7.5	-4.7	0.9	504.1	7.5	504.5	7.5
8	1	13	53	65.33	2778	359	0.10	0.7829	0.0114	0.0954	0.0013	0.0597	0.0007	587.1	6.5	589.9	23.7	587.3	7.9	0.4	0.0	587.3	7.9	587.3	7.9
8	1	13	53	65.33	763	1081	1.40	0.8248	0.0137	0.1010	0.0016	0.0593	0.0007	610.7	7.6	578.2	26.5	620.5	9.1	-7.3	1.6	620.5	9.1	621.4	9.1
8	1	13	53	65.33	388	219	0.60	0.8480	0.0150	0.1009	0.0016	0.0611	0.0008	623.6	8.3	641.4	29.3	619.6	9.3	3.4	-0.6	619.6	9.3	619.2	9.3
8	1	13	53	65.33	576	166	0.30	0.7222	0.0124	0.0911	0.0014	0.0576	0.0008	551.9	7.3	514.0	28.7	562.1	8.3	-9.4	1.8	562.1	8.3	563.0	8.3
8	1	13	53	65.33	198	66	0.30	0.6829	0.0174	0.0857	0.0015	0.0579	0.0013	528.5	10.5	525.0	49.7	530.3	9.0	-1.0	0.3	530.3	9.0	530.3	9.0
8	1	13	53	65.33	807	274	0.30	0.8195	0.0151	0.1026	0.0016	0.0581	0.0008	607.8	8.4	531.8	31.8	629.4	9.5	-18.3	3.4	629.4	9.5	631.3	9.5
8	1	13	53	65.33	777	330	0.40	1.3844	0.0232	0.1382	0.0021	0.0728	0.0009	882.3	9.9	1008.0	25.2	834.3	12.1	17.2	-5.8	834.3	12.1	828.6	12.1
8	1	13	53	65.33	547	207	0.40	0.7272	0.0126	0.0916	0.0014	0.0577	0.0008	554.9	7.4	518.9	29.0	564.7	8.4	-8.8	1.7	564.7	8.4	565.6	8.4
8	1	13	53	65.33	593	477	0.80	0.6622	0.0115	0.0831	0.0013	0.0579	0.0008	515.9	7.0	525.4	28.5	514.6	7.7	2.0	-0.3	514.6	7.7	514.5	7.7
8	1	13	53	65.33	141	177	1.30	3.8863	0.0664	0.2837	0.0045	0.0996	0.0013	1610.8	13.8	1615.0	23.9	1610.0	22.6	0.3	-0.1	1615.0	22.6	1609.5	24.0
8	1	13	53	65.33	470	387	0.80	12.2800	0.1903	0.5035	0.0077	0.1773	0.0019	2626.0	14.7	2626.7	17.9	2628.9	33.0	-0.1	0.1	2626.7	33.0	2629.6	17.8
8	1	13	53	65.33	1511	169	0.10	1.7608	0.0278	0.1780	0.0027	0.0719	0.0008	1031.1	10.2	982.2	22.5	1056.0	14.8	-7.5	2.4	1056.0	14.8	1059.2	14.9
8	1	13	53	65.33	36	41	1.10	1.4621	0.0410	0.1547	0.0029	0.0687	0.0017	914.9	16.9	888.5	52.4	927.3	16.4	-4.4	1.3	927.3	16.4	928.7	16.4
8	1	13	53	65.33	1073	593	0.60	0.7703	0.0128	0.0845	0.0013	0.0663	0.0008	580.0	7.4	813.7	25.7	522.9	7.7	35.7	-10.9	522.9	7.7	517.7	7.7
8	1	13	53	65.33	542	341	0.60	0.6456	0.0113	0.0815	0.0013	0.0576	0.0008	505.8	7.0	512.4	29.5	505.1	7.6	1.4	-0.1	505.1	7.6	505.0	7.6
8	1	13	53	65.33	1329	504	0.40	1.9305	0.0304	0.1880	0.0029	0.0746	0.0008	1091.7	10.5	1057.4	22.0	1110.7	15.5	-5.0	1.7	1057.4	15.5	1113.3	21.2
8	1	13	53	65.33	451	471	1.00	0.8213	0.0145	0.0992	0.0016	0.0602	0.0008	608.8	8.1	609.8	29.2	609.5	9.1	0.0	0.1	609.5	9.1	609.5	9.1
8	1	13	53	65.33	743	464	0.60	0.7105	0.0121	0.0897	0.0014	0.0576	0.0007	545.0	7.2	513.2	27.9	553.6	8.2	-7.9	1.5	553.6	8.2	554.3	8.2
8	1	13	53	65.33	796	310	0.40	9.9029	0.1529	0.4522	0.0069	0.1592	0.0017	2425.8	14.3	2446.1	18.1	2405.0	30.6	1.7	-0.9	2446.1	30.6	2394.2	18.8
8	1	13	53	65.33	600	337	0.60	14.0573	0.2171	0.5459	0.0083	0.1872	0.0020	2753.6	14.8	2716.8	17.6	2808.0	34.7	-3.4	1.9	2716.8	34.7	2847.6	15.9
8	1	13	53	65.33	3558	1974	0.60	1.4789	0.0213	0.1449	0.0020	0.0742	0.0008	921.8	8.7	1045.7	21.6	872.3	11.5	16.6	-5.7	872.3	11.5	866.2	11.4

8	1	13	53	65.33	390	384	1.00	0.8120	0.0145	0.0977	0.0015	0.0604	0.0008	603.6	8.2	618.4	29.7	600.6	9.0	2.9	-0.5	600.6	9.0	600.3	9.0
8	1	13	53	65.33	495	245	0.50	4.8838	0.0768	0.3246	0.0050	0.1094	0.0012	1799.5	13.3	1788.0	20.0	1812.1	24.2	-1.3	0.7	1788.0	24.2	1815.0	19.6
8	1	13	53	65.33	1253	127	0.10	1.0595	0.0169	0.1155	0.0018	0.0667	0.0008	733.6	8.4	827.5	23.6	704.4	10.2	14.9	-4.1	704.4	10.2	701.2	10.1
8	1	13	53	65.33	1898	375	0.20	1.9288	0.0278	0.1852	0.0026	0.0757	0.0008	1091.1	9.7	1086.5	21.6	1095.2	14.2	-0.8	0.4	1095.2	14.2	1095.6	14.2
8	1	13	53	65.33	1427	437	0.30	0.6240	0.0102	0.0797	0.0012	0.0569	0.0007	492.3	6.4	486.3	26.1	494.4	7.3	-1.7	0.4	494.4	7.3	494.6	7.3
8	1	13	53	65.33	335	124	0.40	0.7543	0.0140	0.0932	0.0015	0.0588	0.0009	570.7	8.1	559.1	32.0	574.6	8.7	-2.8	0.7	574.6	8.7	574.9	8.7
8	1	13	53	65.33	2947	1641	0.60	0.6675	0.0097	0.0841	0.0012	0.0577	0.0006	519.2	5.9	517.8	24.1	520.4	7.0	-0.5	0.2	520.4	7.0	520.4	7.0
8	1	13	53	65.33	1160	333	0.30	1.5430	0.0244	0.1576	0.0024	0.0712	0.0008	947.7	9.7	960.8	22.5	943.6	13.4	1.8	-0.4	943.6	13.4	943.0	13.4
8	1	13	53	65.33	1848	201	0.10	0.8118	0.0120	0.0995	0.0014	0.0593	0.0007	603.4	6.7	576.4	24.3	611.7	8.2	-6.1	1.3	611.7	8.2	612.4	8.2
8	1	13	53	65.33	428	193	0.50	0.6866	0.0124	0.0861	0.0014	0.0580	0.0008	530.8	7.5	528.0	30.7	532.2	8.0	-0.8	0.3	532.2	8.0	532.3	8.0
8	1	13	53	65.33	552	616	1.10	0.7292	0.0126	0.0914	0.0014	0.0580	0.0008	556.1	7.4	528.4	28.8	563.8	8.4	-6.7	1.4	563.8	8.4	564.4	8.4
8	1	13	53	65.33	1792	117	0.10	0.8684	0.0129	0.1042	0.0015	0.0606	0.0007	634.7	7.0	622.7	24.7	639.1	8.6	-2.6	0.7	639.1	8.6	639.4	8.6
8	1	13	53	65.33	950	1148	1.20	0.9724	0.0158	0.1123	0.0017	0.0630	0.0007	689.7	8.1	705.6	24.8	685.9	10.0	2.8	-0.6	685.9	10.0	685.5	10.0
8	1	13	53	65.33	253	1138	4.50	0.7624	0.0145	0.0927	0.0015	0.0598	0.0009	575.4	8.4	595.0	33.1	571.4	8.7	4.0	-0.7	571.4	8.7	571.0	8.7
8	1	13	53	65.33	759	505	0.70	0.6392	0.0108	0.0804	0.0012	0.0578	0.0007	501.8	6.7	521.2	27.8	498.4	7.4	4.4	-0.7	498.4	7.4	498.0	7.4
8	1	13	53	65.33	1201	682	0.60	0.7217	0.0117	0.0905	0.0014	0.0580	0.0007	551.7	6.9	528.0	25.4	558.3	8.2	-5.7	1.2	558.3	8.2	558.9	8.2
8	1	13	53	65.33	307	315	1.00	6.2648	0.0994	0.3668	0.0057	0.1241	0.0014	2013.5	14.0	2015.8	19.8	2014.4	26.7	0.1	0.0	2015.8	26.7	2014.1	19.8
8	1	13	53	65.33	3651	883	0.20	0.5830	0.0086	0.0696	0.0010	0.0609	0.0007	466.4	5.5	635.4	24.5	433.5	5.9	31.8	-7.6	433.5	5.9	430.7	5.9
8	1	13	53	65.33	1080	363	0.30	0.8720	0.0155	0.1043	0.0016	0.0608	0.0008	636.6	8.4	630.1	29.5	639.5	9.5	-1.5	0.4	639.5	9.5	639.7	9.5
8	1	13	53	65.33	987	55	0.10	1.3629	0.0217	0.1416	0.0022	0.0699	0.0008	873.1	9.4	925.7	23.0	853.8	12.2	7.8	-2.3	853.8	12.2	851.5	12.2
8	1	13	53	65.33	520	278	0.50	1.3420	0.0237	0.1389	0.0022	0.0702	0.0010	864.1	10.3	934.5	27.9	838.3	12.4	10.3	-3.1	838.3	12.4	835.2	12.4
8	1	13	53	65.33	793	234	0.30	0.6991	0.0117	0.0886	0.0014	0.0573	0.0007	538.2	7.0	502.9	27.4	547.4	8.1	-8.9	1.7	547.4	8.1	548.2	8.1
8	1	13	53	65.33	4242	129	0.00	0.8366	0.0121	0.1010	0.0014	0.0602	0.0007	617.3	6.7	610.9	23.4	620.0	8.3	-1.5	0.4	620.0	8.3	620.2	8.3
8	1	13	53	65.33	882	460	0.50	0.4413	0.0077	0.0598	0.0009	0.0537	0.0007	371.1	5.4	355.4	29.5	374.3	5.7	-5.3	0.8	374.3	5.7	374.5	5.7
8	1	13	53	65.33	180	73	0.40	1.6238	0.0358	0.1642	0.0028	0.0719	0.0014	979.5	13.9	981.9	38.3	979.9	15.6	0.2	0.0	979.9	15.6	979.9	15.6
8	1	13	53	65.33	392	123	0.30	0.8450	0.0151	0.1018	0.0016	0.0603	0.0008	621.9	8.3	614.1	29.8	625.0	9.4	-1.8	0.5	625.0	9.4	625.3	9.4
8	1	13	53	65.33	1951	791	0.40	0.8247	0.0125	0.0980	0.0014	0.0612	0.0007	610.7	7.0	643.5	25.4	602.8	8.2	6.3	-1.3	602.8	8.2	602.0	8.2
8	1	13	53	65.33	292	298	1.00	1.3684	0.0237	0.1404	0.0022	0.0708	0.0009	875.5	10.2	951.6	27.0	847.0	12.4	11.0	-3.4	847.0	12.4	843.5	12.4
8	1	13	53	65.33	1814	409	0.20	1.2087	0.0182	0.1236	0.0018	0.0711	0.0008	804.6	8.4	959.4	24.0	751.1	10.1	21.7	-7.1	751.1	10.1	745.1	10.0
8	1	13	53	65.33	483	167	0.30	0.8233	0.0143	0.0919	0.0014	0.0651	0.0009	609.9	8.0	776.9	27.6	566.8	8.4	27.0	-7.6	566.8	8.4	562.7	8.4
8	1	13	53	65.33	445	182	0.40	0.6988	0.0124	0.0882	0.0014	0.0576	0.0008	538.1	7.4	514.0	29.8	544.6	8.2	-6.0	1.2	544.6	8.2	545.2	8.2
8	1	13	53	65.33	1816	666	0.40	0.7099	0.0105	0.0895	0.0013	0.0577	0.0007	544.7	6.2	516.3	24.9	552.4	7.5	-7.0	1.4	552.4	7.5	553.0	7.5
8	1	13	53	65.33	502	272	0.50	0.8471	0.0146	0.1011	0.0016	0.0609	0.0008	623.1	8.0	634.7	27.7	620.9	9.2	2.2	-0.3	620.9	9.2	620.6	9.2
8	1	13	53	65.33	355	182	0.50	3.1329	0.0504	0.2516	0.0039	0.0905	0.0010	1440.8	12.4	1435.2	21.9	1446.7	19.9	-0.8	0.4	1435.2	19.9	1447.6	21.7
8	1	13	53	65.33	287	180	0.60	0.6850	0.0136	0.0864	0.0014	0.0576	0.0009	529.8	8.2	514.0	35.5	534.3	8.3	-4.0	0.8	534.3	8.3	534.7	8.3
8	1	13	53	65.33	1064	983	0.90	1.3533	0.0221	0.1415	0.0022	0.0695	0.0008	869.0	9.5	912.4	24.1	853.3	12.3	6.5	-1.8	853.3	12.3	851.4	12.2
8	1	13	53	65.33	843	490	0.60	0.7088	0.0121	0.0868	0.0013	0.0594	0.0008	544.1	7.2	579.7	27.9	536.4	8.0	7.5	-1.4	536.4	8.0	535.7	7.9
8	1	13	53	65.33	2012	528	0.30	0.3005	0.0048	0.0425	0.0006	0.0514	0.0007	266.8	3.7	257.8	29.6	268.2	3.8	-4.1	0.5	268.2	3.8	268.3	3.8
8	1	13	53	65.33	1370	378	0.30	1.4639	0.0242	0.1435	0.0022	0.0741	0.0009	915.6	10.0	1044.1	24.3	864.5	12.5	17.2	-5.9	864.5	12.5	858.2	12.4
8	1	13	53	65.33	640	249	0.40	4.0095	0.0645	0.2911	0.0045	0.1001	0.0011	1636.1	13.1	1624.9	21.4	1647.2	22.3	-1.4	0.7	1624.9	22.3	1649.4	21.0
8	1	13	53	65.33	558	562	1.00	0.7357	0.0160	0.0871	0.0015	0.0614	0.0011	559.9	9.4	651.6	39.6	538.4	8.6	17.4	-4.0	538.4	8.6	536.4	8.6
8	1	13	53	65.33	203	247	1.20	5.5767	0.0928	0.3387	0.0053	0.1197	0.0015	1912.5	14.4	1950.2	21.9	1880.6	25.5	3.6	-1.7	1950.2	25.5	1871.0	23.2
8	1	13	53	65.33	180	109	0.60	0.6726	0.0145	0.0846	0.0014	0.0578	0.0011	522.3	8.8	520.1	40.0	523.7	8.3	-0.7	0.3	523.7	8.3	523.7	8.3
8	1	13	53	65.33	1898	315	0.20	0.8324	0.0126	0.1006	0.0014	0.0602	0.0007	614.9	7.0	608.4	25.3	617.6	8.4	-1.5	0.4	617.6	8.4	617.8	8.4
8	1	13	53	65.33	814	323	0.40	0.8154	0.0138	0.0997	0.0015	0.0595	0.0007	605.5	7.7	583.0	27.1	612.4	9.0	-5.1	1.1	612.4	9.0	613.0	9.0
8	1	13	53	65.33	1532	1173	0.80	1.5235	0.0228	0.1573	0.0022	0.0704	0.0008	939.9	9.2	938.5	23.7	941.9	12.4	-0.4	0.2	941.9	12.4	942.0	12.4
8	1	13	53	65.33	1842	1349	0.70	0.8127	0.0129	0.0972	0.0014	0.0607	0.0008	604.0	7.2	629.1	27.8	598.2	8.2	4.9	-1.0	598.2	8.2	597.6	8.2
8	1	13	53	65.33	70	23	0.30	0.8799	0.0234	0.1030	0.0019	0.0621	0.0015	640.9	12.6	676.2	50.7	632.0	10.9	6.6	-1.4	632.0	10.9	631.0	10.9
8	1	13	53	65.33	754	261	0.30	1.7127	0.0286	0.1712	0.0027	0.0727	0.0009	1013.3	10.7	1004.7	25.0	1018.8	14.6	-1.4	0.5	1018.8	14.6	1019.4	14.6
8	1	13	53	65.33	388	159	0.40	4.1171	0.0675	0.2886	0.0045	0.1037	0.0012	1657.7	13.4	1690.0	21.9	1634.7	22.4	3.3	-1.4	1690.0	22.4	1629.1	22.9
8	1	13	53	65.33	271	185	0.70	2.2780	0.0392	0.2107	0.0033	0.0786	0.0010	1205.5	12.2	1160.9	25.6	1232.3	17.6	-6.1	2.2	1160.9	17.6	1236.3	24.3
8	1	13	53	65.33	168	193	1.20	3.1169	0.0566	0.2496	0.0040	0.0908	0.0013	1436.9	14.0	1440.9	27.0	1436.1	20.8	0.3	-0.1	1440.9	20.8	1435.8	27.1
8	1	13	53	65.33	4882	5248	1.10	0.6451	0.0096	0.0805	0.0011	0.0582	0.0007	505.4	5.9	537.4	24.9	499.2	6.8	7.1	-1.2	499.2	6.8	498.6	6.8
8	1	13	53	65.33	894	459	0.50	0.7706	0.0130	0.0944	0.0015	0.0593	0.0007	580.1	7.5	577.5	27.2	581.7	8.6	-0.7	0.3	581.7	8.6	581.7	8.6
8	1	13	53	65.33	549	214	0.40	0.7962	0.0140	0.0976	0.0015	0.0593	0.0008	594.7	7.9	577.2	29.0	600.2	8.9	-4.0	0.9	600.2	8.9	600.7	8.9
8	1	13	53	65.33	1493	666	0.40	0.7722	0.0119	0.0956	0.0014	0.0587	0.0007	581.0	6.8	555.0	26.5	588.6	8.0	-6.1	1.3	588.6	8.0	589.3	8.0
8	1	13	53	65.33	617	526	0.90	0.6553	0.0117	0.0832	0.0013	0.0572	0.0008	511.7	7.2	499.4	30.1	515.3	7.7	-3.2	0.7	515.3	7.7	515.6	7.7
8	1	13	53	65.33	148	42	0.30	0.7698	0.0194	0.0927	0.0016	0.0604	0.0013	579.6	11.1	615.9	48.0	571.2	9.6	7.3	-1.5	571.2	9.6	570.4	9.6
8	1	13	53	65.33	560	274	0.50	1.5029	0.0252	0.1542	0.0024	0.0708	0.0009	931.6	10.2	951.3	25.3	924.6	13.4	2.8	-0.7	924.6	13.4	923.7	13.3
8	1	13	53	65.33	3139	1070	0.30	0.6249	0.0095	0.0778	0.0011	0.0584	0.0007	492.9	5.9	542.3	26.0	483.1	6.6	10.9	-2.0	483.1	6.6	482.2	6.6
8	1	13	53	65.33	1238	359	0.30	0.6864	0.0115	0.0863	0.0013	0.0578	0.0007	530.7	6.9	522.0	27.0	533.5	7.9	-2.2	0.5	533.5	7.9	533.7	7.9
8	1	13	53	65.33	704	286	0.40	1.8066	0.0302	0.1774	0.0027	0.0740	0.0009	1047.8	10.9	1041.4	24.7	1052.5	15.0	-1.1	0.4	1052.5	15.0	1053.0	15.0
8	1	13	53	65.33	937	331	0.40	11.4734	0.1834	0.4800	0.0074	0.1737	0.0020	2562.4	15.0	2592.9	19.0	2527.4	32.0	2.5	-1.4	2592.9	32.0	2507.0	20.3
8	1	13	53	65.33	364	257	0.70	0.8307	0.0153	0.1010	0.0016	0.0598	0.0009	614.0	8.5	594.6	31.3	620.1	9.3	-4.3	1.0	620.1	9.3	620.7	9.3
8	1	13	53	65.33	1684	800	0.50	0.7332	0.0114	0.0918	0.0013	0.0580	0.0007	558.4	6.7	530.3	26.9	566.2	7.7	-6.8	1.4	566.2	7.7	566.9	7.7
8	1	13	53	65.33	456	213	0.50	0.7638	0.0139	0.0906	0.0014	0.0612	0.0009	576.2	8.0	646.7	30.6	559.3	8.5	13.5	-3.0	559.3	8.5	557.7	8.4
8	1	13	53	65.33	966	658	0.70	0.6274	0.0109	0.0792	0.0012	0.0576	0.0008	494.5	6.8	512.8	28.7	491.3	7.4	4.2	-0.6	491.3	7.4	491.0	7.3
8	1	13	53	65.33	305	150	0.50	0.7516	0.0145	0.0927	0.0015	0.0589	0.0009	569.1	8.4	563.2	33.7	571.6	8.7	-1.5	0.4	571.6	8.7	571.7	8.7
8	1	13	53	65.33	900	205	0.20	0.8500	0.0144	0.1021	0.0016	0.0605	0.0008	624.6	7.9	620.2	27.2	626.8	9.2	-1.1	0.3	626.8	9.2	626.9	9.2
8	1	13	53	65.33	805	341	0.40	0.7402	0.0127	0.0904	0.0014	0.0595	0.0008	562.5	7.4	585.6	28.2	557.7	8.3	4.8	-0.9	557.7	8.3	557.2	8.3
8	1	13	53	65.33	695	431	0.60	0.6736	0.0117	0.0850	0.0013	0.0576	0.0008	522.9	7.1	512.4	28.7	526.1	7.8	-2.7	0.6	526.1	7.8	526.3	7.9
24	2	5	45	220.23	1303	205	0.20	2.0362	0.0298	0.1764	0.0025	0.0839	0.0010	1127.7	10.0	1290.1	22.2	1047.0	13.5	18.8	-7.7	1047.0	13.5	1035.4	13.4
24	2	5	45	220.23	1387	406	0.30	0.8849	0.0139	0.1012	0.0014	0.0636	0.0008	643.6	7.5	725.7	27.1	621.6	8.4	14.3	-3.5	621.6	8.4	619.4	8.3
24	2	5	45	220.23	4462	3644	0.80	0.6212	0.0091	0.0732	0.0010	0.0617	0.0007	490.6	5.7	662.1	25.8	455.4	6.0	31.2	-7.7	455.4	6.0	452.3	5.9
24	2	5	45	220.23	500	258	0.50	0.7271	0.0124	0.0924	0.0013	0.0572	0.0008	554.8	7.3	498.3	31.7	569.7	7.9	-14.3	2.6	569.7	7.9	571.0	7.9
24	2	5	45	220.23	572	662	1.20	0.7667	0.0129	0.0941	0.0014	0.0592	0.0008	577.8	7.4	573.1	31.0	580.0	8.0	-1.2	0.4	580.0	8.0	580.1	8.0
24	2	5	45	220.23	1341	2060	1.50	0.7801	0.0118	0.0944	0.0013	0.0601	0.0007	585.6	6.8	605.5	26.0	581.5	7.8	4.0	-0.7	581.5	7.8	581.0	7.8

24	2	5	45	220.23	658	565	0.90	0.3125	0.0063	0.0428	0.0006	0.0531	0.0010	276.2	4.8	333.8	41.0	269.9	4.0	19.1	-2.3	269.9	4.0	269.4	4.0
24	2	5	45	220.23	593	13	0.00	0.7972	0.0139	0.0967	0.0014	0.0599	0.0009	595.2	7.9	599.4	32.6	595.2	8.3	0.7	0.0	595.2	8.3	595.1	8.3
24	2	5	45	220.23	264	216	0.80	0.9942	0.0192	0.1126	0.0017	0.0642	0.0011	700.8	9.8	745.6	36.3	688.1	9.9	7.7	-1.9	688.1	9.9	686.7	9.8
24	2	5	45	220.23	654	410	0.60	1.0375	0.0169	0.1169	0.0017	0.0645	0.0009	722.7	8.5	757.4	28.6	712.8	9.6	5.9	-1.4	712.8	9.6	711.6	9.6
24	2	5	45	220.23	329	562	1.70	2.1591	0.0352	0.1979	0.0029	0.0793	0.0011	1168.0	11.3	1178.7	26.8	1164.1	15.5	1.2	-0.3	1178.7	15.5	1163.3	27.1
24	2	5	45	220.23	764	140	0.20	0.8466	0.0145	0.1014	0.0015	0.0607	0.0009	622.8	8.0	628.4	31.7	622.4	8.6	1.0	-0.1	622.4	8.6	622.3	8.6
24	2	5	45	220.23	1314	432	0.30	16.0947	0.2281	0.5669	0.0079	0.2064	0.0022	2882.4	13.7	2876.6	17.6	2895.0	32.4	-0.6	0.4	2876.6	32.4	2904.3	17.2
24	2	5	45	220.23	356	413	1.20	13.2957	0.1944	0.5165	0.0073	0.1871	0.0021	2700.9	13.9	2716.4	18.7	2684.3	31.2	1.2	-0.6	2716.4	31.2	2672.1	19.4
24	2	5	45	220.23	156	94	0.60	0.7887	0.0205	0.0929	0.0016	0.0617	0.0015	590.4	11.7	663.5	53.2	572.5	9.3	13.7	-3.1	572.5	9.3	570.8	9.2
24	2	5	45	220.23	497	736	1.50	7.4698	0.1094	0.3998	0.0056	0.1358	0.0015	2169.4	13.2	2173.5	19.9	2168.3	26.0	0.2	-0.1	2173.5	26.0	2167.3	20.0
24	2	5	45	220.23	722	318	0.40	0.7551	0.0135	0.0941	0.0014	0.0584	0.0009	571.2	7.8	541.9	33.8	579.6	8.1	-6.9	1.5	579.6	8.1	580.3	8.1
24	2	5	45	220.23	779	922	1.20	0.6917	0.0116	0.0867	0.0012	0.0580	0.0008	533.8	7.0	529.5	31.1	535.8	7.4	-1.2	0.4	535.8	7.4	535.9	7.4
24	2	5	45	220.23	393	191	0.50	1.0014	0.0184	0.1169	0.0017	0.0623	0.0010	704.5	9.3	682.1	34.4	712.8	10.0	-4.5	1.2	712.8	10.0	713.6	10.0
24	2	5	45	220.23	1335	578	0.40	3.8235	0.0552	0.2875	0.0040	0.0967	0.0011	1597.7	11.7	1560.0	20.8	1629.2	20.0	-4.4	1.9	1560.0	20.0	1635.9	19.7
24	2	5	45	220.23	2021	443	0.20	1.0056	0.0151	0.1047	0.0015	0.0698	0.0008	706.6	7.7	922.4	24.3	641.8	8.6	30.4	-10.1	641.8	8.6	635.1	8.5
24	2	5	45	220.23	1486	280	0.20	1.7056	0.0253	0.1694	0.0024	0.0732	0.0009	1010.6	9.5	1018.6	23.6	1008.6	13.1	1.0	-0.2	1008.6	13.1	1008.2	13.1
24	2	5	45	220.23	437	352	0.80	0.7883	0.0144	0.0941	0.0014	0.0609	0.0010	590.2	8.2	633.7	34.4	580.0	8.2	8.5	-1.8	580.0	8.2	579.0	8.2
24	2	5	45	220.23	381	459	1.20	0.2909	0.0078	0.0420	0.0007	0.0503	0.0013	259.3	6.2	208.3	60.0	265.4	4.3	-27.4	2.3	265.4	4.3	265.8	4.3
24	2	5	45	220.23	649	1013	1.60	0.8073	0.0143	0.0967	0.0014	0.0607	0.0009	600.9	8.1	627.7	33.1	594.9	8.3	5.2	-1.0	594.9	8.3	594.3	8.3
24	2	5	45	220.23	3300	12	0.00	0.8005	0.0115	0.0957	0.0013	0.0608	0.0007	597.1	6.5	630.8	24.9	589.3	7.6	6.6	-1.3	589.3	7.6	588.5	7.6
24	2	5	45	220.23	872	529	0.60	1.9221	0.0294	0.1865	0.0026	0.0749	0.0009	1088.8	10.2	1065.7	24.5	1102.3	14.4	-3.4	1.2	1065.7	14.4	1104.0	23.9
24	2	5	45	220.23	2534	1324	0.50	0.2257	0.0039	0.0322	0.0005	0.0509	0.0007	206.7	3.2	234.8	33.6	204.6	2.9	12.9	-1.0	204.6	2.9	204.4	2.9
24	2	5	45	220.23	2032	333	0.20	0.6557	0.0102	0.0838	0.0012	0.0569	0.0007	512.0	6.3	487.1	28.0	518.5	7.0	-6.4	1.3	518.5	7.0	519.0	7.0
24	2	5	45	220.23	289	518	1.80	0.8718	0.0189	0.1052	0.0016	0.0603	0.0012	636.6	10.3	612.3	43.1	644.5	9.6	-5.3	1.2	644.5	9.6	645.2	9.6
24	2	5	45	220.23	162	140	0.90	0.7712	0.0286	0.0918	0.0019	0.0610	0.0023	580.5	16.4	639.7	79.3	566.4	11.2	11.4	-2.5	566.4	11.2	565.1	11.2
24	2	5	45	220.23	1368	443	0.30	1.1746	0.0214	0.1241	0.0019	0.0688	0.0011	788.8	10.0	892.1	33.1	754.1	10.6	15.5	-4.6	754.1	10.6	750.2	10.6
24	2	5	45	220.23	3616	921	0.30	12.8098	0.1823	0.5293	0.0073	0.1760	0.0019	2665.8	13.5	2614.3	18.1	2738.3	30.9	-4.7	2.6	2614.3	30.9	2786.5	15.8
24	2	5	45	220.23	144	154	1.10	12.3479	0.1986	0.4873	0.0074	0.1842	0.0024	2631.2	15.2	2690.4	21.6	2558.9	32.1	4.9	-2.8	2690.4	32.1	2515.2	24.8
24	2	5	45	220.23	1124	190	0.20	0.7580	0.0122	0.0885	0.0013	0.0623	0.0008	572.9	7.1	683.1	28.6	546.4	7.5	20.0	-4.8	546.4	7.5	543.9	7.4
24	2	5	45	220.23	137	158	1.20	1.4370	0.0334	0.1462	0.0024	0.0714	0.0016	904.5	13.9	969.1	44.6	879.7	13.6	9.2	-2.8	879.7	13.6	876.6	13.6
24	2	5	45	220.23	235	146	0.60	0.8605	0.0196	0.1065	0.0017	0.0588	0.0012	630.4	10.7	556.9	46.1	652.3	9.9	-17.1	3.4	652.3	9.9	654.3	9.9
24	2	5	45	220.23	743	494	0.70	0.8092	0.0140	0.0964	0.0014	0.0610	0.0009	602.0	7.9	638.6	31.8	593.4	8.2	7.1	-1.5	593.4	8.2	592.5	8.2
24	2	5	45	220.23	943	514	0.50	0.7210	0.0125	0.0835	0.0012	0.0628	0.0009	551.3	7.4	700.2	31.6	516.9	7.2	26.2	-6.7	516.9	7.2	513.7	7.2
24	2	5	45	220.23	741	1207	1.60	0.7583	0.0139	0.0924	0.0014	0.0596	0.0010	573.0	8.0	589.6	34.6	569.9	8.0	3.3	-0.5	569.9	8.0	569.6	8.0
24	2	5	45	220.23	400	190	0.50	0.7580	0.0161	0.0932	0.0014	0.0592	0.0012	572.8	9.3	571.6	42.4	574.2	8.5	-0.4	0.2	574.2	8.5	574.2	8.5
24	2	5	45	220.23	262	214	0.80	2.3496	0.0407	0.2074	0.0031	0.0823	0.0012	1227.4	12.4	1252.7	28.9	1215.2	16.5	3.0	-1.0	1252.7	16.5	1213.0	29.7
24	2	5	45	220.23	878	580	0.70	0.8154	0.0135	0.0992	0.0014	0.0597	0.0008	605.5	7.6	593.2	29.8	609.8	8.3	-2.8	0.7	609.8	8.3	610.2	8.3
24	2	5	45	220.23	1116	425	0.40	0.8062	0.0132	0.0979	0.0014	0.0599	0.0008	600.3	7.4	598.3	29.4	602.0	8.2	-0.6	0.3	602.0	8.2	602.1	8.2
24	2	5	45	220.23	904	712	0.80	2.3747	0.0365	0.2107	0.0030	0.0820	0.0010	1235.0	11.0	1243.4	24.0	1232.4	15.9	0.9	-0.2	1243.4	15.9	1231.7	24.2
24	2	5	45	220.23	616	463	0.80	3.9658	0.0609	0.2854	0.0041	0.1010	0.0012	1627.2	12.5	1642.3	22.8	1618.3	20.4	1.5	-0.6	1642.3	20.4	1616.0	23.2
24	2	5	45	220.23	774	1078	1.40	0.6375	0.0114	0.0792	0.0012	0.0585	0.0009	500.7	7.1	549.0	34.0	491.2	6.9	10.5	-2.0	491.2	6.9	490.2	6.9
24	2	5	45	220.23	79	143	1.80	0.8722	0.0403	0.0901	0.0021	0.0704	0.0033	636.8	21.9	938.5	95.3	556.0	12.6	40.8	-14.5	556.0	12.6	548.3	12.4
24	2	5	45	220.23	595	132	0.20	1.3414	0.0226	0.1415	0.0021	0.0689	0.0010	863.8	9.8	895.1	29.2	853.2	11.6	4.7	-1.2	853.2	11.6	851.8	11.6
24	2	5	45	220.23	404	832	2.10	0.8024	0.0160	0.0953	0.0015	0.0612	0.0011	598.2	9.0	645.0	38.7	586.9	8.5	9.0	-1.9	586.9	8.5	585.8	8.5
24	2	5	45	220.23	10393	4850	0.50	0.5138	0.0075	0.0591	0.0008	0.0632	0.0008	421.0	5.0	714.3	25.3	370.1	4.9	48.2	-13.7	370.1	4.9	366.0	4.8
24	2	5	45	220.23	1564	1102	0.70	14.1480	0.2036	0.5338	0.0074	0.1927	0.0021	2759.7	13.8	2764.4	18.2	2757.4	31.2	0.3	-0.1	2764.4	31.2	2754.5	18.4
24	2	5	45	220.23	943	339	0.40	4.5122	0.0661	0.3017	0.0042	0.1087	0.0012	1733.2	12.2	1777.4	20.7	1699.6	20.9	4.4	-2.0	1777.4	20.9	1691.0	22.0
24	2	5	45	220.23	772	432	0.60	1.7791	0.0270	0.1658	0.0023	0.0780	0.0009	1037.9	9.9	1146.7	24.1	988.6	12.9	13.8	-5.0	988.6	12.9	981.9	12.8
24	2	5	45	220.23	1049	812	0.80	13.1104	0.1896	0.5135	0.0072	0.1856	0.0020	2687.6	13.8	2702.8	18.5	2671.7	30.5	1.2	-0.6	2702.8	30.5	2660.1	19.1
24	2	5	45	220.23	662	422	0.60	0.8558	0.0234	0.0976	0.0017	0.0638	0.0017	627.8	12.8	732.4	55.9	600.2	10.0	18.0	-4.6	600.2	10.0	597.5	10.0
24	2	5	45	220.23	341	431	1.30	2.3006	0.0363	0.2090	0.0030	0.0800	0.0010	1212.5	11.2	1196.8	25.3	1223.4	16.0	-2.2	0.9	1196.8	16.0	1224.9	24.8
24	2	5	45	220.23	362	151	0.40	0.8137	0.0132	0.0995	0.0014	0.0595	0.0008	604.5	7.4	582.6	28.9	611.5	8.3	-5.0	1.1	611.5	8.3	612.1	8.3
24	2	5	45	220.23	916	278	0.30	1.4951	0.0230	0.1525	0.0022	0.0713	0.0009	928.4	9.4	964.2	25.0	915.0	12.0	5.1	-1.5	915.0	12.0	913.2	12.0
24	2	5	45	220.23	1337	1511	1.10	1.3757	0.0207	0.1474	0.0021	0.0679	0.0008	878.6	8.9	863.0	24.6	886.4	11.6	-2.7	0.9	886.4	11.6	887.1	11.6
24	2	5	45	220.23	620	257	0.40	0.8013	0.0139	0.0973	0.0014	0.0599	0.0009	597.6	7.8	598.3	31.9	598.4	8.3	0.0	0.1	598.4	8.3	598.4	8.3
24	2	5	45	220.23	4043	1597	0.40	0.6449	0.0094	0.0733	0.0010	0.0639	0.0008	505.3	5.8	738.7	24.9	456.1	6.0	38.3	-10.8	456.1	6.0	451.8	5.9
24	2	5	45	220.23	1112	388	0.30	0.9067	0.0142	0.1058	0.0015	0.0623	0.0008	655.3	7.6	684.5	27.2	648.1	8.7	5.3	-1.1	648.1	8.7	647.3	8.7
24	2	5	45	220.23	1867	1563	0.80	0.5616	0.0089	0.0699	0.0010	0.0584	0.0008	452.5	5.8	543.8	28.2	435.6	6.0	19.9	-3.9	435.6	6.0	434.1	5.9
24	2	5	45	220.23	150	75	0.50	0.7829	0.0185	0.0968	0.0016	0.0588	0.0013	587.1	10.6	559.1	48.2	595.5	9.2	-6.5	1.4	595.5	9.2	596.2	9.2
24	2	5	45	220.23	575	352	0.60	0.7278	0.0129	0.0900	0.0013	0.0588	0.0009	555.2	7.6	559.5	33.4	555.3	7.8	0.7	0.0	555.3	7.8	555.2	7.8
24	2	5	45	220.23	539	136	0.30	13.6610	0.2026	0.5390	0.0076	0.1843	0.0021	2726.5	14.2	2690.9	19.2	2779.1	31.9	-3.3	1.9	2690.9	31.9	2815.8	17.4
24	2	5	45	220.23	1251	1090	0.90	0.8822	0.0139	0.0974	0.0014	0.0658	0.0008	642.2	7.5	800.0	26.8	599.3	8.1	25.1	-7.2	599.3	8.1	595.0	8.1
24	2	5	45	220.23	985	188	0.20	0.7316	0.0121	0.0913	0.0013	0.0582	0.0008	557.5	7.1	537.4	30.1	563.4	7.7	-4.8	1.1	563.4	7.7	563.9	7.8
24	2	5	45	220.23	804	366	0.50	1.5167	0.0239	0.1536	0.0022	0.0718	0.0009	937.2	9.7	979.6	25.9	920.8	12.2	6.0	-1.8	920.8	12.2	918.7	12.2
24	2	5	45	220.23	1066	759	0.70	0.8950	0.0145	0.1065	0.0015	0.0611	0.0008	649.0	7.8	641.1	28.6	652.6	8.9	-1.8	0.5	652.6	8.9	652.8	8.9
24	2	5	45	220.23	1006	896	0.90	2.0804	0.0320	0.1925	0.0027	0.0786	0.0010	1142.4	10.6	1160.2	24.4	1135.0	14.7	2.2	-0.7	1160.2	14.7	1133.7	24.8
24	2	5	45	220.23	491	1190	2.40	0.8623	0.0156	0.0968	0.0014	0.0648	0.0010	631.4	8.5	766.6	33.3	595.4	8.4	22.3	-6.0	595.4	8.4	591.8	8.4
24	2	5	45	220.23	1353	383	0.30	1.5519	0.0241	0.1545	0.0022	0.0730	0.0009	951.2	9.6	1013.6	25.4	926.2	12.2	8.6	-2.7	926.2	12.2	922.9	12.2
24	2	5	45	220.23	989	374	0.40	0.8379	0.0151	0.0997	0.0014	0.0611	0.0010	618.0	8.3	641.4	34.2	612.8	8.0	4.5	-0.8	612.8	8.0	612.2	8.0
24	2	5	45	220.23	234	278	1.20	1.4342	0.0338	0.1484	0.0021	0.0703	0.0016	903.3	14.1	935.9	45.6	891.8	12.0	4.7	-1.3	891.8	12.0	890.2	12.0
24	2	5	45	220.23	997	441	0.40	0.8668	0.0158	0.1053	0.0015	0.0598	0.0010	633.8	8.6	596.5	34.8	645.6	8.5	-8.2	1.8	645.6	8.5	646.6	8.5
24	2	5	45	220.23	576	198	0.30	1.8576	0.0318	0.1785	0.0025	0.0757	0.0011	1066.1	11.3	1084.9	29.8	1058.9	13.5	2.4	-0.7	1058.9	13.5	1057.8	13.5
24	2	5	45	220.23	675	347	0.50	0.4678	0.0115	0.0604	0.0009	0.0563	0.0013	389.6	8.0	462.0	52.0	378.3	5.2	18.1	-3.0	378.3	5.2	377.3	5.2
24	2	5	45	220.23	532	439	0.80	4.0287	0.0641	0.2925	0.0040	0.1002	0.0013	1640.0	13.0	1626.0	25.0	1653.9	20.0	-1.7	0.8	1626.0	20.0	1656.7	24.5
24	2	5	45	220.23	416	415	1.00	2.3395	0.0418	0.2138	0.0030	0.0796	0.0013	1224.4	12.7	1185.2	31.1	1249.0	15.8	-5.4	2.0	1185.2	15.8	1252.7	29.7
24	2	5	45	220.23	358	142	0.40	13.1441	0.1992	0.5066	0.0070	0.1886	0.0023	2690.0	14.4	2729.6	20.6	2642.1	29.9	3.2	-1.8	2729.6	29.9	2610.0	22.7
24	2	5	45	220.23	1234	925	0.70	0.8236	0.0149	0.0990	0.0014	0.0605	0.0010	610.1	8.3	620.9	34.3	608.3	8.0	2.0	-0.3	608.3	8.0	608.1	8.0

24	2	5	45	220.23	265	321	1.20	0.7843	0.0227	0.0944	0.0014	0.0604	0.0017	587.9	12.9	618.0	60.8	581.2	8.3	6.0	-1.2	581.2	8.3	580.5	8.2
24	2	5	45	220.23	345	816	2.40	2.3775	0.0446	0.2107	0.0030	0.0820	0.0014	1235.9	13.4	1245.6	33.0	1232.5	15.7	1.1	-0.3	1245.6	15.7	1231.7	33.4
24	2	5	45	220.23	372	217	0.60	1.9502	0.0375	0.1922	0.0027	0.0738	0.0013	1098.5	12.9	1034.8	35.1	1133.0	14.6	-9.5	3.0	1034.8	14.6	1137.8	32.7
24	2	5	45	220.23	354	305	0.90	12.7841	0.1962	0.5129	0.0071	0.1812	0.0023	2663.9	14.6	2663.4	21.1	2668.9	30.2	-0.2	0.2	2663.4	30.2	2670.9	21.0
24	2	5	45	220.23	733	647	0.90	0.8265	0.0167	0.0994	0.0014	0.0604	0.0011	611.7	9.3	618.4	39.7	611.0	8.2	1.2	-0.1	611.0	8.2	610.9	8.2
24	2	5	45	220.23	563	185	0.30	25.1481	0.3705	0.6761	0.0093	0.2705	0.0032	3314.0	14.6	3307.9	18.8	3329.3	35.7	-0.6	0.5	3307.9	35.7	3353.0	18.1
24	2	5	45	220.23	1409	832	0.60	3.1062	0.0471	0.2483	0.0034	0.0910	0.0011	1434.2	11.7	1444.9	23.6	1429.6	17.5	1.1	-0.3	1444.9	17.5	1428.4	23.9
24	2	5	45	220.23	294	596	2.00	0.8094	0.0228	0.0987	0.0015	0.0596	0.0016	602.1	12.8	589.2	59.0	606.7	8.6	-3.0	0.8	606.7	8.6	607.1	8.6
24	2	5	45	220.23	808	442	0.50	13.5534	0.2072	0.5229	0.0072	0.1884	0.0024	2719.0	14.6	2727.9	20.8	2711.6	30.6	0.6	-0.3	2727.9	30.6	2705.2	21.2
24	2	5	45	220.23	2233	511	0.20	1.9674	0.0342	0.1848	0.0026	0.0774	0.0012	1104.4	11.7	1130.9	30.2	1093.0	14.0	3.3	-1.0	1093.0	14.0	1091.2	14.0
24	2	5	45	220.23	910	640	0.70	0.8152	0.0163	0.0999	0.0014	0.0593	0.0011	605.4	9.1	578.6	39.6	613.7	8.2	-6.1	1.4	613.7	8.2	614.4	8.2
24	2	5	45	220.23	615	210	0.30	0.7640	0.0174	0.0953	0.0014	0.0583	0.0012	576.3	10.0	539.7	46.6	586.7	8.0	-8.7	1.8	586.7	8.0	587.6	8.0
24	2	5	45	220.23	1431	801	0.60	4.8986	0.0731	0.3260	0.0045	0.1093	0.0013	1802.0	12.6	1786.5	21.9	1818.7	21.7	-1.8	0.9	1786.5	21.7	1822.7	21.3
24	2	5	45	220.23	309	84	0.30	16.9556	0.2663	0.5718	0.0080	0.2156	0.0028	2932.3	15.2	2947.3	21.3	2915.3	32.9	1.1	-0.6	2947.3	32.9	2898.4	22.1
24	2	5	45	220.23	260	259	1.00	6.7424	0.1165	0.3715	0.0053	0.1320	0.0020	2078.2	15.3	2123.3	26.5	2036.6	24.7	4.1	-2.0	2123.3	24.7	2021.9	28.6
24	2	5	45	220.23	352	338	1.00	5.4975	0.0912	0.3410	0.0048	0.1172	0.0017	1900.2	14.3	1913.3	25.4	1891.5	22.9	1.1	-0.5	1913.3	22.9	1888.5	25.9
24	2	5	45	220.23	744	445	0.60	18.2397	0.2747	0.5933	0.0082	0.2235	0.0027	3002.5	14.6	3005.5	19.7	3002.7	33.2	0.1	0.0	3005.5	33.2	3001.1	19.8
24	2	5	45	220.23	543	316	0.60	0.8037	0.0187	0.0983	0.0014	0.0595	0.0013	598.9	10.5	582.6	47.5	604.4	8.3	-3.7	0.9	604.4	8.3	604.8	8.3
24	2	5	45	220.23	222	171	0.80	1.4581	0.0347	0.1499	0.0022	0.0707	0.0016	913.2	14.4	947.8	46.1	900.6	12.3	5.0	-1.4	900.6	12.3	898.9	12.3
24	2	5	45	220.23	648	177	0.30	1.1804	0.0224	0.1293	0.0018	0.0664	0.0011	791.5	10.4	817.4	35.3	783.8	10.3	4.1	-1.0	783.8	10.3	782.8	10.3
24	2	5	45	220.23	269	155	0.60	0.7038	0.0211	0.0895	0.0013	0.0572	0.0017	541.0	12.6	498.6	64.0	552.3	7.9	-10.8	2.0	552.3	7.9	553.2	7.9
24	2	5	45	220.23	574	406	0.70	0.8587	0.0184	0.1030	0.0015	0.0606	0.0012	629.4	10.0	623.7	42.4	632.2	8.5	-1.4	0.4	632.2	8.5	632.4	8.5
24	2	5	45	220.23	2443	458	0.20	0.8374	0.0138	0.0988	0.0014	0.0616	0.0009	617.7	7.6	660.7	29.6	607.2	8.0	8.1	-1.7	607.2	8.0	606.1	8.0
24	2	5	45	220.23	585	399	0.70	0.7715	0.0185	0.0897	0.0013	0.0626	0.0014	580.6	10.6	692.3	48.1	553.6	7.7	20.0	-4.9	553.6	7.7	551.0	7.7
24	2	5	45	220.23	842	499	0.60	2.8311	0.0460	0.2428	0.0034	0.0848	0.0012	1363.8	12.2	1309.9	26.5	1401.0	17.4	-7.0	2.7	1309.9	17.4	1407.5	24.7
24	2	5	45	220.23	940	1022	1.10	16.3807	0.2461	0.5624	0.0078	0.2118	0.0025	2899.3	14.5	2918.3	19.7	2876.7	32.1	1.4	-0.8	2918.3	32.1	2855.8	20.8
24	2	5	45	220.23	1209	452	0.40	0.7652	0.0147	0.0956	0.0013	0.0582	0.0010	577.0	8.5	537.4	37.6	588.3	7.9	-9.5	1.9	588.3	7.9	589.2	7.9
24	2	5	45	220.23	755	339	0.40	1.5037	0.0270	0.1573	0.0022	0.0695	0.0011	931.9	11.0	912.7	32.4	941.9	12.3	-3.2	1.1	941.9	12.3	943.0	12.3
24	2	5	45	220.23	358	148	0.40	0.7098	0.0207	0.0871	0.0013	0.0593	0.0017	544.6	12.3	575.3	61.3	538.3	7.8	6.4	-1.2	538.3	7.8	537.7	7.8
24	2	5	45	220.23	666	161	0.20	9.9977	0.1565	0.4549	0.0063	0.1598	0.0021	2434.6	14.5	2452.9	21.9	2416.8	28.1	1.5	-0.7	2452.9	28.1	2407.2	22.7
24	2	5	45	220.23	2416	372	0.20	1.1780	0.0190	0.1257	0.0017	0.0681	0.0009	790.4	8.9	871.6	27.8	763.3	10.0	12.4	-3.5	763.3	10.0	760.3	9.9
24	2	5	45	220.23	959	815	0.90	0.8337	0.0161	0.1033	0.0015	0.0587	0.0010	615.7	8.9	555.4	37.6	633.4	8.5	-14.1	2.8	633.4	8.5	635.0	8.5
24	2	5	45	220.23	358	166	0.50	12.9101	0.2058	0.4979	0.0070	0.1885	0.0025	2673.1	15.1	2728.6	22.0	2604.6	30.2	4.5	-2.6	2728.6	30.2	2561.0	25.2
24	2	5	45	220.23	874	316	0.40	7.8881	0.1122	0.3680	0.0051	0.1558	0.0017	2218.3	12.9	2410.0	18.5	2019.9	24.1	16.2	-9.8	2410.0	24.1	1947.7	26.2
24	2	5	45	220.23	427	332	0.80	5.7271	0.0876	0.3051	0.0044	0.1364	0.0017	1935.5	13.3	2181.7	21.4	1716.7	21.8	21.3	-12.7	2181.7	21.8	1656.1	31.6
24	2	5	45	220.23	187	427	2.30	5.1185	0.0833	0.2793	0.0042	0.1332	0.0018	1839.2	13.9	2140.1	23.7	1587.8	21.0	25.8	-15.8	2140.1	21.0	1524.8	37.3
24	2	5	45	220.23	3396	1429	0.40	2.4626	0.0354	0.2032	0.0028	0.0881	0.0010	1261.1	10.4	1383.4	21.1	1192.6	15.1	13.8	-5.7	1383.4	15.1	1181.5	24.3
24	2	5	45	220.23	1022	479	0.50	3.8140	0.0564	0.2634	0.0037	0.1053	0.0012	1595.7	11.9	1718.0	21.1	1507.2	18.9	12.3	-5.9	1718.0	18.9	1488.1	24.9
24	2	5	45	220.23	1137	186	0.20	4.5100	0.0664	0.2879	0.0041	0.1139	0.0013	1732.8	12.3	1861.1	20.8	1631.2	20.3	12.4	-6.2	1861.1	20.3	1606.6	25.0
24	2	5	45	220.23	137	170	1.20	0.7280	0.0233	0.0956	0.0018	0.0554	0.0017	555.4	13.7	426.6	69.7	588.3	10.3	-37.9	5.6	588.3	10.3	591.2	10.4
24	2	5	45	220.23	564	496	0.90	2.9777	0.0472	0.2214	0.0032	0.0978	0.0013	1401.9	12.1	1581.6	24.3	1289.0	16.9	18.5	-8.8	1581.6	16.9	1268.6	30.3
24	2	5	45	220.23	1295	1033	0.80	2.1243	0.0319	0.1899	0.0027	0.0813	0.0010	1156.7	10.4	1227.8	23.3	1121.1	14.5	8.7	-3.2	1227.8	14.5	1115.6	25.2
24	2	5	45	220.23	593	441	0.70	1.3461	0.0233	0.1163	0.0017	0.0842	0.0013	865.9	10.1	1295.6	29.0	709.1	9.9	45.3	-22.1	709.1	9.9	691.4	9.7
24	2	5	45	220.23	379	512	1.40	11.9723	0.1939	0.6108	0.0089	0.1425	0.0018	2602.2	15.3	2257.0	22.5	3073.0	35.7	-36.2	15.3	2257.0	35.7	3573.3	8.3
24	2	5	45	220.23	1232	687	0.60	2.5192	0.0375	0.1989	0.0028	0.0921	0.0011	1277.6	10.9	1468.4	22.2	1169.2	15.0	20.4	-9.3	1468.4	15.0	1151.6	27.7
24	2	5	45	220.23	2696	1275	0.50	12.6081	0.1754	0.4747	0.0064	0.1931	0.0021	2650.8	13.2	2768.0	18.3	2504.0	27.8	9.5	-5.9	2768.0	27.8	2418.3	24.1
24	2	5	45	220.23	219	90	0.40	1.2246	0.0253	0.0687	0.0015	0.1296	0.0031	811.9	11.6	2091.9	42.3	428.3	9.1	79.5	-89.6	428.3	9.1	389.6	8.3
24	2	5	45	220.23	23	24	1.00	4.6737	0.1160	0.0902	0.0023	0.3769	0.0106	1762.5	20.8	3818.6	42.7	556.4	13.4	85.4	-216.7	556.4	13.4	338.5	8.3
24	2	5	45	220.23	562	697	1.20	3.8281	0.0592	0.2449	0.0035	0.1137	0.0014	1598.7	12.5	1857.9	22.4	1411.8	18.1	24.0	-13.2	1857.9	18.1	1373.0	31.8
24	2	5	45	220.23	1220	551	0.50	0.7814	0.0143	0.1322	0.0019	0.0430	0.0007	586.3	8.2	0.0	34.7	800.1	10.6	-4E8	26.7	800.1	10.6	821.5	10.9
24	2	5	45	220.23	1345	1048	0.80	0.8275	0.0133	0.0859	0.0012	0.0700	0.0009	612.2	7.4	928.0	27.1	531.4	7.2	42.7	-15.2	531.4	7.2	523.7	7.1
24	2	5	45	220.23	764	208	0.30	0.8153	0.0139	0.0822	0.0012	0.0721	0.0011	605.4	7.8	987.6	30.3	509.4	7.3	48.4	-18.9	509.4	7.3	500.4	7.2
24	2	5	45	220.23	1165	449	0.40	1.6671	0.0289	0.1364	0.0019	0.0889	0.0013	996.1	11.0	1400.1	28.8	824.4	10.7	41.1	-20.8	824.4	10.7	802.9	10.4
24	2	5	45	220.23	1331	118	0.10	16.6621	0.2422	0.5434	0.0074	0.2229	0.0026	2915.6	14.1	3001.3	18.7	2797.7	31.0	6.8	-4.2	3001.3	31.0	2701.7	23.9
24	2	5	45	220.23	2685	1686	0.60	2.1380	0.0335	0.1892	0.0026	0.0822	0.0011	1161.2	10.9	1248.5	25.2	1117.0	14.2	10.5	-4.0	1248.5	14.2	1110.2	27.7
29	4	5	45	270.03	1186	334	0.30	0.6871	0.0163	0.0847	0.0011	0.0590	0.0014	531.1	9.8	564.6	50.7	524.3	6.6	7.1	-1.3	524.3	6.6	523.6	6.6
29	4	5	45	270.03	597	384	0.60	1.4321	0.0316	0.1490	0.0019	0.0699	0.0015	902.4	13.2	923.3	44.2	895.5	10.9	3.0	-0.8	895.5	10.9	894.5	10.9
29	4	5	45	270.03	1452	1142	0.80	0.8046	0.0167	0.0973	0.0012	0.0601	0.0012	599.4	9.4	606.6	43.6	598.6	7.3	1.3	-0.1	598.6	7.3	598.4	7.3
29	4	5	45	270.03	338	167	0.50	1.3482	0.0386	0.1391	0.0019	0.0705	0.0020	866.8	16.7	941.7	58.5	839.3	11.0	10.9	-3.3	839.3	11.0	835.9	10.9
29	4	5	45	270.03	451	580	1.30	0.8166	0.0247	0.0976	0.0014	0.0609	0.0018	606.1	13.8	633.0	65.2	600.2	8.0	5.2	-1.0	600.2	8.0	599.5	8.0
29	4	5	45	270.03	2122	973	0.50	0.6938	0.0140	0.0840	0.0011	0.0601	0.0012	535.1	8.4	604.8	42.2	519.8	6.4	14.0	-2.9	519.8	6.4	518.4	6.4
29	4	5	45	270.03	368	329	0.90	1.8918	0.0480	0.1716	0.0024	0.0802	0.0020	1078.2	16.9	1200.0	49.7	1020.9	12.9	14.9	-5.6	1020.9	12.9	1012.8	12.8
29	4	5	45	270.03	529	197	0.40	1.6835	0.0413	0.1653	0.0022	0.0741	0.0018	1002.3	15.6	1042.2	48.8	985.9	12.3	5.4	-1.7	985.9	12.3	983.6	12.3
29	4	5	45	270.03	60	94	1.60	0.8985	0.0756	0.0954	0.0023	0.0685	0.0059	650.9	40.4	881.9	178.2	587.5	13.8	33.4	-10.8	587.5	13.8	581.2	13.6
29	4	5	45	270.03	347	99	0.30	2.2234	0.0585	0.2000	0.0028	0.0808	0.0021	1188.4	18.4	1215.9	51.4	1175.4	14.9	3.3	-1.1	1215.9	14.9	1173.2	53.0
29	4	5	45	270.03	607	353	0.60	0.7826	0.0246	0.0953	0.0013	0.0597	0.0019	586.9	14.0	591.4	68.3	586.9	7.9	0.8	0.0	586.9	7.9	586.8	7.9
29	4	5	45	270.03	3374	678	0.20	0.7496	0.0136	0.0915	0.0011	0.0596	0.0010	568.0	7.9	587.0	37.2	564.3	6.7	3.9	-0.7	564.3	6.7	563.9	6.7
29	4	5	45	270.03	209	104	0.50	1.4480	0.0459	0.1392	0.0020	0.0757	0.0024	909.0	19.0	1084.9	63.9	839.9	11.5	22.6	-8.2	839.9	11.5	831.5	11.4
29	4	5	45	270.03	572	208	0.40	0.7122	0.0228	0.0884	0.0012	0.0586	0.0019	546.0	13.5	549.4	70.2	546.2	7.3	0.6	0.0	546.2	7.3	546.2	7.3
29	4	5	45	270.03	231	165	0.70	0.6683	0.0303	0.0868	0.0014	0.0560	0.0026	519.7	18.4	449.4	102.1	536.8	8.1	-19.4	3.2	536.8	8.1	538.2	8.2
29	4	5	45	270.03	1085	1356	1.20	1.8364	0.0351	0.1775	0.0023	0.0752	0.0014	1058.6	12.6	1073.7	36.9	1053.1	12.3	1.9	-0.5	1053.1	12.3	1052.2	12.3
29	4	5	45	270.03	455	633	1.40	0.8163	0.0255	0.0950	0.0013	0.0624	0.0020	606.0	14.3	688.3	66.7	585.3	7.9	15.0	-3.5	585.3	7.9	583.2	7.9
29	4	5	45	270.03	592	527	0.90	0.7990	0.0211	0.0945	0.0013	0.0614	0.0016	596.3	11.9	653.7	55.9	582.3	7.5	10.9	-2.4	582.3	7.5	580.9	7.5
29	4	5	45	270.03	1226	236	0.20	0.7816	0.0188	0.0868	0.0011	0.0654	0.0016	586.4	10.7	787.6	49.8	536.8	6.8	31.8	-9.2	536.8	6.8	532.1	6.7
29	4	5	45	270.03	839	6	0.00	0.6486	0.0163	0.0817	0.0011	0.0577	0.0014	507.6	10.0	518.9	54.4	506.0	6.4	2.5	-0.3	506.0	6.4	505.8	6.4
29	4	5	45	270.03	1715	531	0.30	0.6083	0.0129	0.0683	0.0009	0.0647	0.0013	482.5	8.1	764.6	43.4	426.0	5.3	44.3	-13.3	426.0	5.3	421.2	5.2
29	4	5	45	270.03	1037	1189	1.10	2.3945	0.0430	0.2089	0.0026	0.0833	0.0014	1241.0	12.9	1276.1	33.3	1223.1	14.0	4.2	-1.5	1276.1	14.0	1220.0	34.7

29	4	5	45	270.03	290	199	0.70	0.9329	0.0312	0.1044	0.0015	0.0650	0.0022	669.1	16.4	772.1	70.7	640.1	8.8	17.1	-4.5	640.1	8.8	637.2	8.8
29	4	5	45	270.03	587	153	0.30	0.6398	0.0188	0.0813	0.0011	0.0572	0.0017	502.2	11.7	498.3	64.7	503.9	6.6	-1.1	0.4	503.9	6.6	504.0	6.6
29	4	5	45	270.03	373	252	0.70	0.6369	0.0231	0.0802	0.0012	0.0577	0.0021	500.4	14.3	517.8	80.3	497.5	7.0	3.9	-0.6	497.5	7.0	497.2	7.0
29	4	5	45	270.03	380	326	0.90	8.6182	0.1523	0.4227	0.0054	0.1482	0.0025	2298.5	16.1	2324.8	28.8	2272.6	24.7	2.2	-1.1	2324.8	24.7	2260.9	30.3
29	4	5	45	270.03	-257	-40	0.20	0.6883	0.0168	0.0849	0.0011	0.0589	0.0014	531.8	10.1	563.5	52.2	525.4	6.6	6.8	-1.2	525.4	6.6	524.7	6.6
29	4	5	45	270.03	1745	154	0.10	0.7443	0.0158	0.0902	0.0012	0.0600	0.0012	564.9	9.2	601.9	44.8	556.8	6.8	7.5	-1.5	556.8	6.8	556.0	6.8
29	4	5	45	270.03	335	129	0.40	1.0845	0.0373	0.1200	0.0018	0.0657	0.0023	745.8	18.2	795.6	72.5	730.7	10.1	8.1	-2.1	730.7	10.1	729.0	10.1
29	4	5	45	270.03	254	13	0.10	0.8470	0.0331	0.0891	0.0014	0.0691	0.0027	623.0	18.2	900.8	81.5	550.3	8.2	38.9	-13.2	550.3	8.2	543.3	8.1
29	4	5	45	270.03	1239	367	0.30	1.8876	0.0350	0.1728	0.0022	0.0794	0.0014	1076.7	12.3	1182.0	34.9	1027.3	11.9	13.1	-4.8	1027.3	11.9	1020.3	11.9
29	4	5	45	270.03	257	409	1.60	13.6241	0.2485	0.5079	0.0067	0.1950	0.0034	2723.9	17.3	2784.1	28.8	2647.7	28.8	4.9	-2.9	2784.1	28.8	2596.7	33.5
29	4	5	45	270.03	1148	1335	1.20	1.5480	0.0345	0.1458	0.0019	0.0772	0.0017	949.7	13.7	1124.7	43.5	877.5	10.8	22.0	-8.2	877.5	10.8	868.4	10.7
29	4	5	45	270.03	868	327	0.40	4.3160	0.0766	0.2965	0.0037	0.1058	0.0018	1696.4	14.7	1728.0	31.0	1673.8	18.6	3.1	-1.3	1728.0	18.6	1668.1	32.4
29	4	5	45	270.03	902	585	0.60	1.7399	0.0381	0.1667	0.0022	0.0759	0.0016	1023.4	14.1	1091.3	42.8	993.7	12.0	8.9	-3.0	993.7	12.0	989.6	12.0
29	4	5	45	270.03	1040	838	0.80	0.8160	0.0186	0.0956	0.0012	0.0621	0.0014	605.8	10.4	674.9	47.6	588.6	7.2	12.8	-2.9	588.6	7.2	586.9	7.2
29	4	5	45	270.03	2253	405	0.20	0.8042	0.0160	0.0965	0.0012	0.0606	0.0012	599.2	9.0	623.0	41.4	594.0	7.2	4.7	-0.9	594.0	7.2	593.4	7.2
29	4	5	45	270.03	1672	147	0.10	0.6781	0.0207	0.0791	0.0011	0.0623	0.0019	525.6	12.5	683.5	65.2	490.9	6.6	28.2	-7.1	490.9	6.6	487.8	6.5
29	4	5	45	270.03	1584	170	0.10	0.7081	0.0153	0.0871	0.0011	0.0591	0.0012	543.6	9.1	569.8	45.7	538.4	6.6	5.5	-1.0	538.4	6.6	537.9	6.6
29	4	5	45	270.03	529	532	1.00	5.1493	0.0942	0.3247	0.0041	0.1153	0.0020	1844.3	15.6	1883.6	31.5	1812.6	20.1	3.8	-1.7	1883.6	20.1	1803.6	33.5
29	4	5	45	270.03	431	290	0.70	0.7551	0.0245	0.0905	0.0013	0.0607	0.0020	571.2	14.2	625.9	70.1	558.6	7.6	10.8	-2.3	558.6	7.6	557.3	7.6
29	4	5	45	270.03	705	867	1.20	0.6981	0.0214	0.0828	0.0012	0.0613	0.0019	537.7	12.8	648.5	65.9	512.9	6.9	20.9	-4.8	512.9	6.9	510.6	6.8
29	4	5	45	270.03	912	1518	1.70	0.6743	0.0190	0.0828	0.0011	0.0592	0.0017	523.3	11.5	572.7	61.1	513.0	6.7	10.4	-2.0	513.0	6.7	512.0	6.7
29	4	5	45	270.03	1946	88	0.00	1.5423	0.0300	0.1509	0.0019	0.0743	0.0014	947.4	12.0	1049.3	37.8	905.8	10.7	13.7	-4.6	905.8	10.7	900.5	10.6
29	4	5	45	270.03	202	281	1.40	1.1063	0.0504	0.1167	0.0020	0.0689	0.0032	756.4	24.3	894.8	95.6	711.7	11.3	20.5	-6.3	711.7	11.3	706.8	11.2
29	4	5	45	270.03	1161	172	0.10	0.8112	0.0236	0.0895	0.0012	0.0659	0.0019	603.1	13.2	801.3	60.8	552.8	7.3	31.0	-9.1	552.8	7.3	548.0	7.2
29	4	5	45	270.03	897	309	0.30	1.4355	0.0302	0.1456	0.0019	0.0717	0.0015	903.8	12.6	975.4	41.6	876.4	10.5	10.1	-3.1	876.4	10.5	873.0	10.4
29	4	5	45	270.03	529	409	0.80	1.3997	0.0383	0.1431	0.0020	0.0711	0.0019	888.8	16.2	959.1	55.5	862.4	11.1	10.1	-3.1	862.4	11.1	859.1	11.0
29	4	5	45	270.03	924	216	0.20	0.7731	0.0201	0.0940	0.0012	0.0598	0.0015	581.6	11.5	595.4	55.8	579.1	7.3	2.7	-0.4	579.1	7.3	578.8	7.3
29	4	5	45	270.03	687	382	0.60	0.6717	0.0211	0.0832	0.0012	0.0587	0.0018	521.8	12.8	554.6	68.4	515.2	6.9	7.1	-1.3	515.2	6.9	514.5	6.9
29	4	5	45	270.03	848	440	0.50	1.6433	0.0351	0.1585	0.0020	0.0754	0.0016	987.0	13.5	1077.2	41.9	948.6	11.3	11.9	-4.0	948.6	11.3	943.5	11.3
29	4	5	45	270.03	524	860	1.60	0.7281	0.0244	0.0893	0.0013	0.0593	0.0020	555.4	14.3	577.2	73.0	551.2	7.5	4.5	-0.8	551.2	7.5	550.7	7.5
29	4	5	45	270.03	1873	107	0.10	0.7881	0.0175	0.0944	0.0012	0.0607	0.0013	590.1	9.9	626.9	46.6	581.6	7.1	7.2	-1.5	581.6	7.1	580.8	7.1
29	4	5	45	270.03	576	225	0.40	0.7193	0.0229	0.0881	0.0012	0.0594	0.0019	550.2	13.5	579.0	69.2	544.3	7.3	6.0	-1.1	544.3	7.3	543.7	7.3
29	4	5	45	270.03	2080	414	0.20	0.7690	0.0173	0.0918	0.0012	0.0609	0.0013	579.2	9.9	635.8	47.4	565.9	6.9	11.0	-2.4	565.9	6.9	564.6	6.9
29	4	5	45	270.03	679	128	0.20	0.7353	0.0221	0.0877	0.0012	0.0610	0.0018	559.6	13.0	637.6	64.6	541.7	7.2	15.0	-3.3	541.7	7.2	540.0	7.2
29	4	5	45	270.03	1740	691	0.40	1.1452	0.0251	0.1179	0.0015	0.0706	0.0015	775.0	11.9	945.8	43.8	718.3	8.7	24.0	-7.9	718.3	8.7	712.2	8.6
29	4	5	45	270.03	1941	1181	0.60	1.3215	0.0284	0.1359	0.0017	0.0707	0.0015	855.2	12.4	948.4	42.9	821.2	9.9	13.4	-4.1	821.2	9.9	817.2	9.8
29	4	5	45	270.03	387	40	0.10	0.8694	0.0287	0.0989	0.0014	0.0639	0.0021	635.3	15.6	737.4	70.3	608.0	8.3	17.5	-4.5	608.0	8.3	605.3	8.2
29	4	5	45	270.03	1534	833	0.50	0.2921	0.0087	0.0411	0.0006	0.0517	0.0015	260.2	6.8	272.0	67.8	259.4	3.4	4.6	-0.3	259.4	3.4	259.3	3.4
29	4	5	45	270.03	775	184	0.20	0.7676	0.0208	0.0915	0.0012	0.0610	0.0016	578.4	12.0	636.9	57.9	564.6	7.2	11.3	-2.4	564.6	7.2	563.3	7.2
29	4	5	45	270.03	231	187	0.80	2.0149	0.0647	0.1843	0.0027	0.0795	0.0026	1120.6	21.8	1183.0	64.0	1090.6	14.7	7.8	-2.7	1090.6	14.7	1086.1	14.7
29	4	5	45	270.03	1047	407	0.40	1.9726	0.0414	0.1853	0.0024	0.0774	0.0016	1106.2	14.2	1130.6	40.7	1095.7	12.8	3.1	-1.0	1095.7	12.8	1094.0	12.8
29	4	5	45	270.03	1485	681	0.50	0.6369	0.0155	0.0783	0.0010	0.0591	0.0014	500.4	9.6	571.3	52.3	485.9	6.1	14.9	-3.0	485.9	6.1	484.6	6.1
29	4	5	45	270.03	888	338	0.40	12.1785	0.2245	0.4891	0.0061	0.1810	0.0032	2618.3	17.4	2661.5	29.3	2566.7	26.5	3.6	-2.0	2661.5	26.5	2535.3	32.4
29	4	5	45	270.03	3407	400	0.10	0.7376	0.0166	0.0885	0.0011	0.0606	0.0013	561.0	9.7	624.1	47.7	546.5	6.7	12.4	-2.6	546.5	6.7	545.1	6.7
29	4	5	45	270.03	1166	239	0.20	0.7316	0.0185	0.0895	0.0012	0.0594	0.0015	557.5	10.8	581.9	54.1	552.5	6.9	5.1	-0.9	552.5	6.9	552.0	6.9
29	4	5	45	270.03	650	373	0.60	0.7162	0.0210	0.0839	0.0011	0.0621	0.0018	548.4	12.4	675.9	62.7	519.2	6.8	23.2	-5.6	519.2	6.8	516.5	6.8
29	4	5	45	270.03	625	632	1.00	0.7183	0.0205	0.0855	0.0012	0.0611	0.0017	549.7	12.1	640.4	61.3	528.9	6.9	17.4	-3.9	528.9	6.9	527.0	6.9
29	4	5	45	270.03	712	234	0.30	0.6024	0.0180	0.0769	0.0011	0.0570	0.0017	478.8	11.4	488.6	65.9	477.6	6.3	2.3	-0.2	477.6	6.3	477.4	6.3
29	4	5	45	270.03	615	377	0.60	0.8578	0.0246	0.1008	0.0014	0.0619	0.0018	628.9	13.5	669.0	61.3	618.9	8.0	7.5	-1.6	618.9	8.0	617.9	8.0
29	4	5	45	270.03	839	112	0.10	0.7645	0.0208	0.0909	0.0012	0.0611	0.0017	576.6	12.0	642.5	58.1	561.0	7.2	12.7	-2.8	561.0	7.2	559.5	7.1
29	4	5	45	270.03	964	327	0.30	0.6157	0.0174	0.0771	0.0010	0.0580	0.0016	487.2	10.9	530.3	61.6	478.9	6.2	9.7	-1.7	478.9	6.2	478.1	6.2
29	4	5	45	270.03	174	211	1.20	0.7242	0.0390	0.0886	0.0015	0.0595	0.0033	553.2	22.9	583.0	118.7	547.0	9.1	6.2	-1.1	547.0	9.1	546.4	9.1
29	4	5	45	270.03	217	362	1.70	0.7320	0.0391	0.0891	0.0016	0.0597	0.0032	557.7	22.9	591.7	117.7	550.4	9.2	7.0	-1.3	550.4	9.2	549.7	9.2
29	4	5	45	270.03	340	313	0.90	1.3821	0.0503	0.1452	0.0022	0.0692	0.0025	881.4	21.4	904.1	75.7	873.9	12.3	3.3	-0.8	873.9	12.3	872.9	12.3
29	4	5	45	270.03	705	280	0.40	0.7009	0.0208	0.0854	0.0012	0.0597	0.0018	539.3	12.4	590.3	64.4	528.3	6.9	10.5	-2.1	528.3	6.9	527.3	6.9
29	4	5	45	270.03	287	29	0.10	0.7974	0.0333	0.0879	0.0014	0.0660	0.0028	595.3	18.8	805.1	88.5	542.8	8.2	32.6	-9.7	542.8	8.2	537.9	8.1
29	4	5	45	270.03	1846	848	0.50	0.6588	0.0165	0.0788	0.0010	0.0608	0.0015	513.9	10.1	629.8	53.6	489.1	6.2	22.3	-5.1	489.1	6.2	486.8	6.1
29	4	5	45	270.03	700	358	0.50	0.7331	0.0221	0.0862	0.0012	0.0618	0.0019	558.4	12.9	666.6	64.5	533.2	7.0	20.0	-4.7	533.2	7.0	530.8	7.0
29	4	5	45	270.03	718	566	0.80	0.8124	0.0231	0.0971	0.0013	0.0608	0.0017	603.8	12.9	632.3	60.9	597.3	7.7	5.5	-1.1	597.3	7.7	596.6	7.7
29	4	5	45	270.03	264	129	0.50	0.7860	0.0302	0.0899	0.0013	0.0635	0.0025	588.9	17.2	725.1	82.5	555.2	7.9	23.4	-6.1	555.2	7.9	552.0	7.9
29	4	5	45	270.03	725	458	0.60	0.7783	0.0228	0.0941	0.0013	0.0601	0.0018	584.5	13.0	606.9	63.0	579.8	7.5	4.5	-0.8	579.8	7.5	579.3	7.5
29	4	5	45	270.03	2289	1044	0.50	0.7656	0.0178	0.0913	0.0012	0.0610	0.0014	577.3	10.2	636.5	49.1	563.4	6.9	11.5	-2.5	563.4	6.9	562.0	6.9
29	4	5	45	270.03	219	64	0.30	0.8706	0.0405	0.0947	0.0016	0.0668	0.0032	635.9	22.0	831.9	98.9	583.2	9.3	29.9	-9.0	583.2	9.3	578.0	9.2
29	4	5	45	270.03	737	450	0.60	0.7648	0.0250	0.0934	0.0013	0.0596	0.0020	576.8	14.4	586.3	71.1	575.5	7.7	1.8	-0.2	575.5	7.7	575.3	7.7
29	4	5	45	270.03	2316	1390	0.60	1.6355	0.0348	0.1656	0.0021	0.0718	0.0015	984.0	13.4	979.9	42.3	987.6	11.6	-0.8	0.4	987.6	11.6	987.9	11.6
29	4	5	45	270.03	1372	664	0.50	0.7398	0.0189	0.0845	0.0011	0.0637	0.0016	562.3	11.0	729.7	53.6	522.7	6.6	28.4	-7.6	522.7	6.6	519.1	6.6
29	4	5	45	270.03	395	325	0.80	0.5991	0.0232	0.0766	0.0011	0.0569	0.0022	476.7	14.7	485.5	86.6	475.7	6.8	2.0	-0.2	475.7	6.8	475.5	6.8
29	4	5	45	270.03	1055	535	0.50	1.7491	0.0405	0.1666	0.0022	0.0763	0.0017	1026.8	15.0	1102.3	45.7	993.6	11.9	9.9	-3.3	993.6	11.9	989.0	11.8
29	4	5	45	270.03	1994	263	0.10	0.6930	0.0175	0.0827	0.0011	0.0609	0.0015	534.6	10.5	636.1	53.7	512.1	6.4	19.5	-4.4	512.1	6.4	510.0	6.4
29	4	5	45	270.03	1374	531	0.40	4.8584	0.1037	0.3176	0.0040	0.1112	0.0023	1795.1	18.0	1818.6	38.0	1777.9	19.8	2.2	-1.0	1818.6	19.8	1773.0	39.3
29	4	5	45	270.03	1045	128	0.10	2.7610	0.0473	0.2028	0.0026	0.0990	0.0016	1345.1	12.8	1604.2	30.1	1190.4	13.7	25.8	-13.0	1604.2	13.7	1164.3	41.1
29	4	5	45	270.03	635	347	0.50	12.7779	0.2112	0.4289	0.0055	0.2166	0.0034	2663.4	15.7	2954.9	25.3	2300.6	25.0	22.1	-15.8	2954.9	25.0	2110.1	49.9
29	4	5	45	270.03	126	136	1.10	2.5770	0.0819	0.2096	0.0032	0.0894	0.0029	1294.1	23.3	1411.7	61.3	1226.6	17.0	13.1	-5.5	1411.7	17.0	1215.2	70.4
29	4	5	45	270.03	362	309	0.90	3.5841	0.0863	0.2612	0.0036	0.0998	0.0024	1546.0	19.1	1619.0	44.5	1495.8	18.5	7.6	-3.4	1619.0	18.5	1485.1	49.0
29	4	5	45	270.03	838	800	1.00	2.9872	0.0528	0.2376	0.0030	0.0914	0.0015	1404.4	13.5	1453.9	32.0	1374.3	15.6	5.5	-2.2	1453.9	15.6	1368.5	34.0
29	4	5	45	270.03	292	144	0.50	3.7485	0.0779	0.2520	0.0033	0.1081	0.0022	1581.8	16.7	1767.3	37.1	1448.9	17.2	18.0	-9.2	1767.3	17.2	1421.1	47.7
29	4	5	45	270.03	360	196	0.50	0.8176	0.0290	0.0815	0.0012	0.0729	0.0026	606.7	16.2	1010.0	72.7	505.3	7.3	50.0	-20.1	505.3	7.3	495.9	7.1

29	4	5	45	270.03	523	193	0.40	10.0553	0.1800	0.3929	0.0052	0.1861	0.0032	2439.9	16.6	2707.1	28.4	2136.0	23.9	21.1	-14.2	2707.1	23.9	2005.1	49.4
29	4	5	45	270.03	667	247	0.40	4.7100	0.0903	0.2849	0.0037	0.1202	0.0022	1769.0	16.1	1958.2	33.1	1616.0	18.6	17.5	-9.5	1958.2	18.6	1578.5	43.8
29	4	5	45	270.03	1075	363	0.30	2.8001	0.0500	0.2243	0.0028	0.0908	0.0015	1355.6	13.4	1440.9	32.2	1304.3	14.9	9.5	-3.9	1440.9	14.9	1295.1	35.7
29	4	5	45	270.03	2618	145	0.10	3.3445	0.0548	0.2501	0.0031	0.0972	0.0015	1491.5	12.9	1571.0	28.6	1438.7	16.0	8.4	-3.7	1571.0	16.0	1428.1	31.7
29	4	5	45	270.03	60	78	1.30	4.1678	0.2272	0.2496	0.0057	0.1214	0.0068	1667.7	44.6	1975.7	100.4	1436.6	29.5	27.3	-16.1	1975.7	29.5	1386.4	154.9
29	4	5	45	270.03	778	287	0.40	3.8585	0.0729	0.2758	0.0035	0.1017	0.0018	1605.1	15.3	1654.9	33.6	1570.0	17.8	5.1	-2.2	1654.9	17.8	1562.0	36.0
29	4	5	45	270.03	249	134	0.50	2.7130	0.0791	0.2221	0.0032	0.0888	0.0026	1332.0	21.7	1399.2	56.2	1292.9	17.0	7.6	-3.0	1399.2	17.0	1285.9	60.9
29	4	5	45	270.03	1478	54	0.00	1.5933	0.0409	0.1235	0.0017	0.0938	0.0024	967.6	16.0	1503.6	48.4	750.4	9.8	50.1	-28.9	750.4	9.8	724.3	9.4
29	4	5	45	270.03	406	162	0.40	0.6609	0.0378	0.0507	0.0011	0.0948	0.0056	515.2	23.1	1523.3	111.8	318.7	6.5	79.1	-61.7	318.7	6.5	302.3	6.2
29	4	5	45	270.03	493	175	0.40	9.4826	0.2219	0.3861	0.0056	0.1785	0.0042	2385.9	21.6	2638.6	38.8	2104.8	26.1	20.2	-13.4	2638.6	26.1	1988.8	64.7
29	4	5	45	270.03	105	305	2.90	10.0900	0.2423	0.4364	0.0064	0.1681	0.0040	2443.1	22.2	2538.1	40.2	2334.4	28.6	8.0	-4.7	2538.1	28.6	2282.3	49.3
29	4	5	45	270.03	1486	276	0.20	3.0947	0.0588	0.2363	0.0030	0.0952	0.0017	1431.4	14.6	1531.4	34.3	1367.5	15.5	10.7	-4.7	1531.4	15.5	1355.3	38.9
29	4	5	45	270.03	551	145	0.30	3.1307	0.0675	0.2383	0.0031	0.0955	0.0020	1440.3	16.6	1537.3	39.7	1377.8	16.1	10.4	-4.5	1537.3	16.1	1365.8	44.9
29	4	5	45	270.03	1161	473	0.40	18.7455	0.3606	0.5425	0.0069	0.2512	0.0047	3028.8	18.7	3191.6	29.5	2794.1	28.9	12.5	-8.4	3191.6	28.9	2594.5	49.0
29	4	5	45	270.03	206	7	0.00	1.5567	0.0827	0.1001	0.0021	0.1131	0.0062	953.2	32.9	1848.5	99.9	614.9	12.4	66.7	-55.0	614.9	12.4	576.2	11.7
29	4	5	45	270.03	373	144	0.40	11.9219	0.2672	0.4520	0.0062	0.1918	0.0042	2598.3	21.1	2756.6	36.5	2404.1	27.7	12.8	-8.1	2756.6	27.7	2300.1	52.7
29	4	5	45	270.03	470	290	0.60	7.4630	0.1841	0.3122	0.0044	0.1738	0.0043	2168.6	22.1	2593.8	41.3	1751.4	21.8	32.5	-23.8	2593.8	21.8	1618.7	87.6
29	4	5	45	270.03	798	309	0.40	6.4436	0.1348	0.2950	0.0038	0.1588	0.0032	2038.2	18.4	2442.1	34.7	1666.6	18.8	31.8	-22.3	2442.1	18.8	1559.8	67.8
29	4	5	45	270.03	2178	216	0.10	3.3025	0.0712	0.2462	0.0031	0.0975	0.0021	1481.7	16.8	1576.8	39.4	1418.6	16.2	10.0	-4.4	1576.8	16.2	1406.1	44.6
36	2	87	127	335.72	271	262	1.00	20.6008	0.2867	0.5652	0.0078	0.2650	0.0028	3120.0	13.6	3276.2	17.0	2888.0	32.2	11.9	-8.0	3276.2	32.2	2666.4	28.4
36	2	87	127	335.72	850	484	0.60	16.0409	0.2206	0.4938	0.0067	0.2362	0.0024	2879.2	13.3	3093.8	16.9	2587.1	29.1	16.4	-11.3	3093.8	29.1	2386.2	30.0
36	2	87	127	335.72	995	537	0.50	1.2974	0.0187	0.0876	0.0012	0.1077	0.0012	844.6	8.3	1759.4	21.1	541.4	7.2	69.2	-56.0	541.4	7.2	509.3	6.8
36	2	87	127	335.72	4426	1832	0.40	2.9187	0.0391	0.2237	0.0030	0.0949	0.0010	1386.8	10.2	1524.8	19.7	1301.2	15.6	14.7	-6.6	1524.8	15.6	1285.7	23.2
36	2	87	127	335.72	1298	31	0.00	5.2174	0.0722	0.2370	0.0032	0.1601	0.0017	1855.5	11.9	2455.4	18.0	1371.2	16.9	44.2	-35.3	2455.4	16.9	1257.3	43.9
36	2	87	127	335.72	3745	1147	0.30	4.2226	0.0566	0.2068	0.0027	0.1485	0.0015	1678.4	11.1	2327.5	18.1	1211.8	14.7	47.9	-38.5	2327.5	14.7	1117.2	43.8
36	2	87	127	335.72	385	323	0.80	3.5800	0.0520	0.2563	0.0036	0.1016	0.0012	1545.1	11.6	1652.0	21.4	1470.8	18.3	11.0	-5.0	1652.0	18.3	1455.3	24.6
36	2	87	127	335.72	3923	5285	1.30	0.3624	0.0058	0.0421	0.0006	0.0627	0.0009	314.0	4.3	695.4	30.0	265.6	3.6	61.8	-18.2	265.6	3.6	262.0	3.5
36	2	87	127	335.72	165	71	0.40	-1.6229	0.0464	0.1380	0.0021	-0.0855	0.0023	NA	-70.7	NA	0.0	NA	11.6	-4E8	100.0	NA	11.6	NA	NA
36	2	87	127	335.72	242	169	0.70	4.0419	0.0614	0.2676	0.0038	0.1098	0.0013	1642.7	12.4	1795.4	22.4	1528.7	19.4	14.9	-7.5	1795.4	19.4	1503.4	27.6
36	2	87	127	335.72	2416	2072	0.90	0.5433	0.0083	0.0593	0.0008	0.0666	0.0009	440.6	5.5	825.6	27.0	371.2	4.9	55.0	-18.7	371.2	4.9	365.5	4.9
36	2	87	127	335.72	743	293	0.40	6.4558	0.0924	0.3325	0.0046	0.1412	0.0016	2039.9	12.7	2240.7	19.2	1850.5	22.4	17.4	-10.2	2240.7	22.4	1792.0	26.9
36	2	87	127	335.72	949	243	0.30	2.8913	0.0411	0.2276	0.0031	0.0924	0.0010	1379.6	10.8	1474.2	20.9	1321.8	16.5	10.3	-4.4	1474.2	16.5	1311.2	23.5
36	2	87	127	335.72	424	177	0.40	23.1217	0.3250	0.6040	0.0084	0.2783	0.0029	3232.1	13.9	3352.9	16.9	3045.8	33.6	9.2	-6.1	3352.9	33.6	2830.4	26.4
36	2	87	127	335.72	2939	224	0.10	15.0216	0.2032	0.4997	0.0067	0.2186	0.0023	2816.6	13.0	2969.5	17.1	2612.4	28.7	12.0	-7.8	2969.5	28.7	2474.2	25.5
36	2	87	127	335.72	504	157	0.30	1.1598	0.0174	0.1272	0.0018	0.0663	0.0008	781.9	8.2	814.6	25.3	771.9	10.1	5.2	-1.3	771.9	10.1	770.7	10.1
36	2	87	127	335.72	1155	213	0.20	1.4746	0.0209	0.1448	0.0020	0.0740	0.0008	920.0	8.6	1041.7	22.5	871.8	11.2	16.3	-5.5	871.8	11.2	865.9	11.1
36	2	87	127	335.72	1689	328	0.20	0.8853	0.0123	0.1050	0.0014	0.0613	0.0007	643.8	6.6	648.8	23.9	643.6	8.2	0.8	0.0	643.6	8.2	643.5	8.2
36	2	87	127	335.72	526	351	0.70	0.6752	0.0106	0.0849	0.0012	0.0578	0.0008	523.8	6.4	521.2	28.9	525.5	7.1	-0.8	0.3	525.5	7.1	525.6	7.1
36	2	87	127	335.72	325	117	0.40	0.7123	0.0121	0.0845	0.0012	0.0613	0.0009	546.1	7.2	647.8	31.6	523.1	7.2	19.2	-4.4	523.1	7.2	521.0	7.2
36	2	87	127	335.72	1194	663	0.60	0.6885	0.0101	0.0812	0.0011	0.0617	0.0007	531.9	6.1	661.0	25.1	503.3	6.7	23.9	-5.7	503.3	6.7	500.7	6.6
36	2	87	127	335.72	727	414	0.60	0.6924	0.0106	0.0832	0.0012	0.0605	0.0008	534.2	6.3	620.2	26.9	515.4	6.9	16.9	-3.7	515.4	6.9	513.6	6.9
36	2	87	127	335.72	833	876	1.10	0.6296	0.0096	0.0788	0.0011	0.0581	0.0007	495.8	6.0	532.2	27.6	489.0	6.5	8.1	-1.4	489.0	6.5	488.3	6.5
36	2	87	127	335.72	758	182	0.20	0.6559	0.0100	0.0820	0.0011	0.0582	0.0007	512.1	6.1	535.6	27.2	507.9	6.8	5.2	-0.8	507.9	6.8	507.4	6.8
36	2	87	127	335.72	1041	244	0.20	0.7183	0.0105	0.0872	0.0012	0.0599	0.0007	549.6	6.2	598.3	25.4	539.1	7.1	9.9	-2.0	539.1	7.1	538.0	7.1
36	2	87	127	335.72	843	1579	1.90	0.7137	0.0107	0.0885	0.0012	0.0586	0.0007	546.9	6.4	552.8	26.5	546.6	7.2	1.1	-0.1	546.6	7.2	546.5	7.2
36	2	87	127	335.72	1253	707	0.60	0.7050	0.0104	0.0786	0.0011	0.0653	0.0008	541.8	6.2	781.5	24.9	487.5	6.5	37.6	-11.1	487.5	6.5	482.6	6.4
36	2	87	127	335.72	11431	507	0.00	0.6640	0.0089	0.0841	0.0011	0.0574	0.0006	517.0	5.4	505.9	22.7	520.6	6.6	-2.9	0.7	520.6	6.6	520.8	6.6
36	2	87	127	335.72	431	448	1.00	8.0397	0.1124	0.4087	0.0056	0.1430	0.0015	2235.5	12.7	2263.6	18.7	2208.9	25.7	2.4	-1.2	2263.6	25.7	2197.6	19.7
36	2	87	127	335.72	756	300	0.40	0.6491	0.0107	0.0813	0.0012	0.0581	0.0008	507.9	6.6	530.7	31.0	503.9	6.9	5.0	-0.8	503.9	6.9	503.5	6.9
36	2	87	127	335.72	450	424	0.90	0.7753	0.0126	0.0947	0.0013	0.0595	0.0008	582.8	7.2	584.5	29.6	583.5	7.9	0.2	0.1	583.5	7.9	583.5	7.9
36	2	87	127	335.72	668	688	1.00	0.7573	0.0118	0.0936	0.0013	0.0589	0.0008	572.5	6.8	560.6	28.2	576.6	7.7	-2.9	0.7	576.6	7.7	576.9	7.7
36	2	87	127	335.72	843	204	0.20	0.7940	0.0122	0.0959	0.0013	0.0602	0.0008	593.5	6.9	611.2	27.4	590.0	7.9	3.5	-0.6	590.0	7.9	589.6	7.9
36	2	87	127	335.72	725	473	0.70	0.8520	0.0129	0.1010	0.0014	0.0614	0.0008	625.7	7.1	650.6	26.4	620.1	8.2	4.7	-0.9	620.1	8.2	619.5	8.2
36	2	87	127	335.72	782	2267	2.90	1.3358	0.0197	0.1422	0.0020	0.0683	0.0008	861.4	8.6	877.6	24.4	856.8	11.1	2.4	-0.5	856.8	11.1	856.1	11.1
36	2	87	127	335.72	397	542	1.40	0.7718	0.0126	0.0939	0.0013	0.0598	0.0008	580.8	7.2	593.6	29.8	578.7	7.8	2.5	-0.4	578.7	7.8	578.4	7.8
36	2	87	127	335.72	419	244	0.60	0.6398	0.0108	0.0803	0.0011	0.0580	0.0008	502.2	6.7	527.6	31.8	497.7	6.8	5.7	-0.9	497.7	6.8	497.2	6.8
36	2	87	127	335.72	603	822	1.40	0.7818	0.0122	0.0958	0.0013	0.0594	0.0008	586.5	6.9	579.3	27.9	589.6	7.9	-1.8	0.5	589.6	7.9	589.8	7.9
36	2	87	127	335.72	1848	693	0.40	0.8203	0.0114	0.0969	0.0013	0.0615	0.0007	608.2	6.4	657.2	23.8	596.4	7.6	9.3	-2.0	596.4	7.6	595.2	7.6
36	2	87	127	335.72	1255	170	0.10	0.7899	0.0116	0.0955	0.0013	0.0601	0.0007	591.1	6.6	607.3	25.3	588.1	7.8	3.2	-0.5	588.1	7.8	587.8	7.8
36	2	87	127	335.72	838	680	0.80	0.8093	0.0122	0.0970	0.0014	0.0606	0.0007	602.0	6.9	625.5	26.4	597.0	7.9	4.6	-0.9	597.0	7.9	596.4	7.9
36	2	87	127	335.72	2420	856	0.40	1.3929	0.0190	0.1429	0.0019	0.0709	0.0008	885.9	8.1	952.7	22.1	861.0	10.7	9.6	-2.9	861.0	10.7	857.9	10.7
36	2	87	127	335.72	221	670	3.00	0.7921	0.0151	0.0949	0.0014	0.0607	0.0010	592.3	8.6	626.9	37.0	584.5	8.3	6.8	-1.3	584.5	8.3	583.7	8.3
36	2	87	127	335.72	598	171	0.30	0.8456	0.0132	0.1019	0.0014	0.0604	0.0008	622.2	7.3	615.2	28.0	625.4	8.4	-1.7	0.5	625.4	8.4	625.7	8.4
36	2	87	127	335.72	509	266	0.50	0.6415	0.0107	0.0799	0.0011	0.0584	0.0008	503.2	6.6	543.1	31.5	495.5	6.8	8.8	-1.6	495.5	6.8	494.8	6.8
36	2	87	127	335.72	1854	1359	0.70	0.7942	0.0111	0.0955	0.0013	0.0605	0.0007	593.5	6.3	619.8	24.4	587.9	7.5	5.1	-1.0	587.9	7.5	587.3	7.5
36	2	87	127	335.72	484	242	0.50	0.6599	0.0110	0.0841	0.0012	0.0571	0.0008	514.5	6.8	493.6	31.8	520.2	7.1	-5.4	1.1	520.2	7.1	520.7	7.1
36	2	87	127	335.72	1206	642	0.50	0.5948	0.0090	0.0773	0.0011	0.0560	0.0007	473.9	5.7	450.6	27.1	479.7	6.4	-6.5	1.2	479.7	6.4	480.1	6.4
36	2	87	127	335.72	1490	863	0.60	0.7180	0.0105	0.0789	0.0011	0.0662	0.0008	549.5	6.2	810.8	24.5	489.5	6.5	39.6	-12.3	489.5	6.5	484.0	6.4
36	2	87	127	335.72	569	676	1.20	0.6295	0.0103	0.0788	0.0011	0.0581	0.0008	495.8	6.4	531.8	30.3	489.0	6.6	8.0	-1.4	489.0	6.6	488.3	6.6
36	2	87	127	335.72	363	201	0.60	1.7743	0.0286	0.1654	0.0024	0.0780	0.0011	1036.1	10.5	1145.7	27.1	986.7	13.1	13.9	-5.0	986.7	13.1	980.0	13.0
36	2	87	127	335.72	1948	664	0.30	0.7076	0.0100	0.0878	0.0012	0.0586	0.0007	543.3	6.0	550.5	25.1	542.7	7.0	1.4	-0.1	542.7	7.0	542.6	7.0
36	2	87	127	335.72	4099	1351	0.30	0.7185	0.0098	0.0881	0.0012	0.0593	0.0006	549.8	5.8	577.9	23.2	544.1	6.9	5.8	-1.0	544.1	6.9	543.5	6.9
36	2	87	127	335.72	336	190	0.60	0.8163	0.0139	0.0958	0.0014	0.0619	0.0009	606.0	7.8	671.1	31.5	589.9	8.1	12.1	-2.7	589.9	8.1	588.2	8.1
36	2	87	127	335.72	82	50	0.60	0.6828	0.0193	0.0797	0.0014	0.0623	0.0017	528.5	11.7	684.5	59.3	494.1	8.3	27.8	-7.0	494.1	8.3	490.9	8.3
36	2	87	127	335.72	989	1085	1.10	0.8032	0.0123	0.0844	0.0012	0.0692	0.0009	598.6	6.9	902.9	25.7	522.5	7.0	42.1	-14.6	522.5	7.0	515.4	6.9
36	2	87	127	335.72	1747	205	0.10	0.9551	0.0133	0.1120	0.0015	0.0620	0.0007	680.8	6.9	673.5	23.9	684.3	8.7	-1.6	0.5	684.3	8.7	684.5	8.7
36	2	87	127	335.72	439	234	0.50	1.5539	0.0244	0.1539	0.0022	0.0734	0.0010	952.0	9.7	1024.9	26.3	922.5	12.2	10.0	-3.2	922.5	12.2	918.7	12.1

36	2	87	127	335.72	349	189	0.50	5.0974	0.0737	0.3341	0.0047	0.1109	0.0013	1835.7	12.3	1813.7	20.7	1858.3	22.5	-2.5	1.2	1813.7	22.5	1864.1	19.9
36	2	87	127	335.72	458	424	0.90	0.7584	0.0125	0.0916	0.0013	0.0602	0.0008	573.1	7.2	610.9	30.2	564.7	7.7	7.6	-1.5	564.7	7.7	563.9	7.7
36	2	87	127	335.72	594	165	0.30	1.9192	0.0280	0.1863	0.0026	0.0749	0.0009	1087.8	9.8	1065.5	23.2	1101.1	14.0	-3.3	1.2	1065.5	14.0	1102.8	22.6
36	2	87	127	335.72	582	124	0.20	0.6823	0.0111	0.0848	0.0012	0.0585	0.0008	528.2	6.7	546.4	30.0	525.0	7.1	3.9	-0.6	525.0	7.1	524.6	7.1
36	2	87	127	335.72	657	149	0.20	0.6564	0.0106	0.0829	0.0012	0.0576	0.0008	512.4	6.5	513.2	29.5	513.3	7.0	0.0	0.2	513.3	7.0	513.3	7.0
36	2	87	127	335.72	593	741	1.30	1.7653	0.0273	0.1568	0.0022	0.0819	0.0010	1032.8	10.0	1241.5	25.0	938.9	12.4	24.4	-10.0	938.9	12.4	926.4	12.2
36	2	87	127	335.72	1264	971	0.80	1.9317	0.0275	0.1824	0.0025	0.0770	0.0008	1092.1	9.5	1120.8	21.9	1079.9	13.7	3.7	-1.1	1079.9	13.7	1078.0	13.7
36	2	87	127	335.72	780	439	0.60	1.4360	0.0214	0.1490	0.0021	0.0701	0.0008	904.1	8.9	930.1	24.4	895.2	11.6	3.8	-1.0	895.2	11.6	893.9	11.6
36	2	87	127	335.72	1640	866	0.50	0.7331	0.0108	0.0866	0.0012	0.0616	0.0007	558.4	6.3	658.6	24.8	535.1	7.1	18.7	-4.3	535.1	7.1	533.0	7.0
36	2	87	127	335.72	918	474	0.50	4.9045	0.0687	0.3172	0.0044	0.1124	0.0012	1803.0	11.9	1838.1	19.5	1776.1	21.4	3.4	-1.5	1838.1	21.4	1768.6	20.6
36	2	87	127	335.72	2243	856	0.40	0.7253	0.0107	0.0867	0.0012	0.0608	0.0007	553.8	6.3	631.6	25.3	536.1	7.1	15.1	-3.3	536.1	7.1	534.4	7.1
36	2	87	127	335.72	1424	76	0.10	1.3724	0.0198	0.1416	0.0020	0.0705	0.0008	877.2	8.5	941.7	23.1	853.5	11.0	9.4	-2.8	853.5	11.0	850.6	11.0
36	2	87	127	335.72	1509	756	0.50	0.6735	0.0100	0.0847	0.0012	0.0578	0.0007	522.8	6.1	522.7	25.9	523.9	7.0	-0.2	0.2	523.9	7.0	523.9	7.0
36	2	87	127	335.72	298	361	1.20	0.7482	0.0136	0.0893	0.0013	0.0609	0.0010	567.2	7.9	636.1	34.7	551.2	7.8	13.4	-2.9	551.2	7.8	549.6	7.7
36	2	87	127	335.72	1328	778	0.60	0.6182	0.0093	0.0786	0.0011	0.0572	0.0007	488.7	5.8	497.5	26.3	487.8	6.5	2.0	-0.2	487.8	6.5	487.6	6.5
36	2	87	127	335.72	436	247	0.60	0.7902	0.0131	0.0956	0.0014	0.0601	0.0009	591.3	7.5	605.5	30.7	588.8	8.0	2.8	-0.4	588.8	8.0	588.4	8.0
36	2	87	127	335.72	2595	1354	0.50	0.5632	0.0081	0.0657	0.0009	0.0623	0.0007	453.6	5.2	684.8	24.8	410.1	5.3	40.1	-10.6	410.1	5.3	406.5	5.3
36	2	87	127	335.72	594	712	1.20	0.6348	0.0103	0.0801	0.0011	0.0577	0.0008	499.1	6.4	515.5	29.8	496.5	6.7	3.7	-0.5	496.5	6.7	496.2	6.7
36	2	87	127	335.72	1168	810	0.70	0.6585	0.0099	0.0826	0.0012	0.0580	0.0007	513.7	6.1	527.6	26.6	511.5	6.9	3.1	-0.4	511.5	6.9	511.3	6.8
36	2	87	127	335.72	795	473	0.60	1.8983	0.0282	0.1819	0.0025	0.0759	0.0009	1080.5	9.9	1091.0	23.9	1077.2	13.9	1.3	-0.3	1077.2	13.9	1076.6	13.9
36	2	87	127	335.72	255	149	0.60	2.1228	0.0332	0.1933	0.0028	0.0798	0.0010	1156.2	10.8	1192.2	25.6	1139.3	14.9	4.4	-1.5	1192.2	14.9	1136.6	26.6
36	2	87	127	335.72	562	172	0.30	0.7219	0.0118	0.0834	0.0012	0.0630	0.0009	551.8	7.0	705.6	29.5	516.2	7.0	26.8	-6.9	516.2	7.0	513.0	7.0
36	2	87	127	335.72	879	520	0.60	0.8383	0.0126	0.1003	0.0014	0.0608	0.0007	618.2	7.0	630.1	26.0	616.1	8.2	2.2	-0.3	616.1	8.2	615.9	8.1
36	2	87	127	335.72	5437	2930	0.50	0.4772	0.0067	0.0580	0.0008	0.0599	0.0007	396.1	4.6	597.2	24.4	363.3	4.8	39.2	-9.0	363.3	4.8	360.6	4.7
36	2	87	127	335.72	296	143	0.50	0.7556	0.0136	0.0929	0.0014	0.0592	0.0009	571.5	7.9	571.6	34.3	572.5	8.0	-0.2	0.2	572.5	8.0	572.5	8.0
36	2	87	127	335.72	591	211	0.40	0.7356	0.0118	0.0905	0.0013	0.0591	0.0008	559.8	6.9	569.8	29.2	558.5	7.6	2.0	-0.2	558.5	7.6	558.3	7.6
36	2	87	127	335.72	567	266	0.50	0.6505	0.0109	0.0833	0.0012	0.0568	0.0008	508.8	6.7	483.2	31.6	515.5	7.0	-6.7	1.3	515.5	7.0	516.1	7.0
36	2	87	127	335.72	2611	600	0.20	1.4932	0.0206	0.1500	0.0020	0.0724	0.0008	927.6	8.4	996.0	22.0	900.7	11.3	9.6	-3.0	900.7	11.3	897.3	11.2
36	2	87	127	335.72	136	178	1.30	12.6357	0.1871	0.4991	0.0072	0.1841	0.0021	2652.9	14.0	2689.1	19.4	2609.9	30.9	2.9	-1.6	2689.1	30.9	2582.2	21.1
36	2	87	127	335.72	325	214	0.70	1.9045	0.0296	0.1880	0.0027	0.0737	0.0009	1082.7	10.4	1031.3	25.6	1110.5	14.4	-7.7	2.5	1031.3	14.4	1114.3	24.2
36	2	87	127	335.72	771	155	0.20	0.5834	0.0094	0.0766	0.0011	0.0554	0.0008	466.7	6.1	427.8	30.3	475.5	6.5	-11.2	1.9	475.5	6.5	476.2	6.5
36	2	87	127	335.72	763	217	0.30	1.2404	0.0186	0.1306	0.0018	0.0690	0.0008	819.0	8.4	898.7	24.6	791.5	10.4	11.9	-3.5	791.5	10.4	788.3	10.3
36	2	87	127	335.72	540	77	0.10	0.6875	0.0116	0.0841	0.0012	0.0595	0.0009	531.3	7.0	582.6	31.1	520.5	7.1	10.7	-2.1	520.5	7.1	519.4	7.1
36	2	87	127	335.72	521	308	0.60	2.2757	0.0334	0.2060	0.0029	0.0803	0.0009	1204.8	10.4	1204.2	23.0	1207.3	15.4	-0.3	0.2	1204.2	15.4	1207.5	22.9
36	2	87	127	335.72	1321	226	0.20	0.6860	0.0103	0.0848	0.0012	0.0588	0.0007	530.4	6.2	559.8	26.0	524.6	7.0	6.3	-1.1	524.6	7.0	524.0	7.0
36	2	87	127	335.72	346	1283	3.70	0.7564	0.0132	0.0917	0.0013	0.0600	0.0009	571.9	7.7	601.2	32.9	565.6	7.9	5.9	-1.1	565.6	7.9	565.0	7.9
36	2	87	127	335.72	683	317	0.50	1.0891	0.0168	0.1143	0.0016	0.0693	0.0009	748.0	8.2	905.9	25.7	697.7	9.3	23.0	-7.2	697.7	9.3	692.3	9.2
36	2	87	127	335.72	288	145	0.50	0.7256	0.0135	0.0914	0.0013	0.0577	0.0010	553.9	8.0	518.2	36.6	563.7	7.9	-8.8	1.7	563.7	7.9	564.6	7.9
36	2	87	127	335.72	1689	1890	1.10	1.9397	0.0277	0.1838	0.0025	0.0768	0.0008	1094.9	9.6	1113.8	22.0	1087.4	13.8	2.4	-0.7	1087.4	13.8	1086.2	13.8
36	2	87	127	335.72	1032	435	0.40	0.8897	0.0133	0.1068	0.0015	0.0606	0.0007	646.2	7.2	623.4	25.7	654.0	8.6	-4.9	1.2	654.0	8.6	654.6	8.6
36	2	87	127	335.72	1177	512	0.40	1.9168	0.0275	0.1778	0.0025	0.0784	0.0009	1087.0	9.6	1155.6	22.2	1055.0	13.5	8.7	-3.0	1055.0	13.5	1050.4	13.4
36	2	87	127	335.72	2835	1952	0.70	0.6211	0.0088	0.0753	0.0010	0.0600	0.0007	490.5	5.5	601.2	24.7	468.0	6.1	22.1	-4.8	468.0	6.1	466.0	6.0
36	2	87	127	335.72	1073	6	0.00	1.2386	0.0181	0.1334	0.0019	0.0675	0.0008	818.3	8.2	852.6	23.8	807.3	10.5	5.3	-1.4	807.3	10.5	805.9	10.5
36	2	87	127	335.72	589	342	0.60	1.3183	0.0200	0.1398	0.0020	0.0686	0.0008	853.8	8.8	884.3	25.5	843.6	11.1	4.6	-1.2	843.6	11.1	842.3	11.1
36	2	87	127	335.72	906	706	0.80	0.6704	0.0104	0.0842	0.0012	0.0579	0.0007	520.9	6.4	525.8	28.1	520.9	7.0	0.9	0.0	520.9	7.0	520.8	7.0
36	2	87	127	335.72	1003	453	0.50	1.9159	0.0276	0.1771	0.0025	0.0787	0.0009	1086.6	9.6	1162.7	22.1	1051.0	13.4	9.6	-3.4	1051.0	13.4	1045.8	13.4
36	2	87	127	335.72	589	481	0.80	18.2394	0.2560	0.5763	0.0080	0.2301	0.0024	3002.4	13.7	3052.1	17.3	2933.6	32.6	3.9	-2.3	3052.1	32.6	2867.3	20.1
36	2	87	127	335.72	1160	159	0.10	8.4879	0.1189	0.4233	0.0058	0.1458	0.0015	2284.6	12.8	2296.5	18.4	2275.2	26.4	0.9	-0.4	2296.5	26.4	2270.5	18.8
36	2	87	127	335.72	511	372	0.70	3.1060	0.0458	0.2439	0.0034	0.0926	0.0011	1434.2	11.4	1478.3	22.1	1407.1	17.7	4.8	-1.9	1478.3	17.7	1401.7	23.3
36	2	87	127	335.72	133	103	0.80	1.8808	0.0334	0.1711	0.0026	0.0799	0.0012	1074.4	11.8	1194.4	30.7	1018.0	14.0	14.8	-5.5	1018.0	14.0	1010.1	13.9
36	2	87	127	335.72	846	1101	1.30	0.7205	0.0117	0.0830	0.0012	0.0631	0.0009	550.9	6.9	710.0	29.1	514.3	7.0	27.6	-7.1	514.3	7.0	510.9	7.0
36	2	87	127	335.72	1882	162	0.10	1.7495	0.0242	0.1735	0.0023	0.0733	0.0008	1027.0	9.0	1022.2	21.9	1031.1	12.8	-0.9	0.4	1031.1	12.8	1031.5	12.8
36	2	87	127	335.72	914	302	0.30	1.0882	0.0164	0.1196	0.0017	0.0661	0.0008	747.6	8.0	809.9	25.1	728.3	9.6	10.1	-2.7	728.3	9.6	726.1	9.6
42	2	50	90	373.58	1378	557	0.40	2.4859	0.0355	0.2082	0.0029	0.0868	0.0010	1267.9	10.4	1355.6	21.3	1219.1	15.3	10.1	-4.0	1355.6	15.3	1210.9	23.5
42	2	50	90	373.58	845	223	0.30	14.1318	0.1989	0.4583	0.0063	0.2242	0.0024	2758.6	13.5	3010.4	17.4	2431.9	28.0	19.2	-13.4	3010.4	28.0	2238.9	32.4
42	2	50	90	373.58	1190	517	0.40	6.1543	0.0870	0.3229	0.0045	0.1386	0.0015	1998.0	12.4	2208.5	18.8	1804.0	21.8	18.3	-10.8	2208.5	21.8	1746.4	26.5
42	2	50	90	373.58	1129	995	0.90	4.9253	0.0734	0.3120	0.0044	0.1148	0.0014	1806.6	12.6	1875.6	21.4	1750.4	21.7	6.7	-3.2	1875.6	21.7	1735.4	23.7
42	2	50	90	373.58	1962	272	0.10	1.2412	0.0180	0.1118	0.0016	0.0807	0.0009	819.4	8.2	1212.8	22.1	683.4	9.0	43.6	-19.9	683.4	9.0	668.5	8.8
42	2	50	90	373.58	1141	54	0.00	6.3724	0.0906	0.3587	0.0050	0.1292	0.0014	2028.5	12.6	2085.9	19.2	1975.8	23.6	5.3	-2.7	2085.9	23.6	1958.4	21.1
42	2	50	90	373.58	1364	937	0.70	4.5541	0.0659	0.3002	0.0042	0.1103	0.0012	1740.9	12.1	1803.4	20.3	1692.2	20.7	6.2	-2.9	1803.4	20.7	1679.8	22.2
42	2	50	90	373.58	1117	94	0.10	2.9694	0.0436	0.2207	0.0031	0.0978	0.0011	1399.8	11.2	1582.1	21.4	1285.4	16.3	18.8	-8.9	1582.1	16.3	1264.8	26.8
42	2	50	90	373.58	869	521	0.60	5.6466	0.0822	0.3326	0.0046	0.1234	0.0014	1923.2	12.6	2005.6	19.9	1850.8	22.5	7.7	-3.9	2005.6	22.5	1829.5	22.7
42	2	50	90	373.58	250	238	1.00	11.9274	0.1803	0.4713	0.0068	0.1840	0.0022	2598.7	14.3	2688.2	19.8	2489.2	29.9	7.4	-4.4	2688.2	29.9	2427.3	24.3
42	2	50	90	373.58	3166	494	0.20	13.7849	0.1973	0.2113	0.0029	0.4742	0.0051	2735.0	13.7	4162.3	16.6	1235.8	15.7	70.3	-121.3	4162.3	15.7	642.2	8.5
42	2	50	90	373.58	574	161	0.30	9.6588	0.1432	0.3992	0.0057	0.1759	0.0020	2402.8	13.7	2613.6	19.4	2165.4	26.1	17.1	-11.0	2613.6	26.1	2063.8	29.7
42	2	50	90	373.58	708	252	0.40	3.1504	0.0481	0.1963	0.0028	0.1167	0.0014	1445.1	11.8	1904.9	22.1	1155.4	15.1	39.3	-25.1	1904.9	15.1	1104.5	39.1
42	2	50	90	373.58	695	244	0.40	4.3653	0.0656	0.2931	0.0041	0.1083	0.0013	1705.8	12.5	1769.4	21.6	1657.2	20.7	6.3	-2.9	1769.4	20.7	1645.2	23.6
42	2	50	90	373.58	441	178	0.40	0.9910	0.0232	0.0889	0.0015	0.0811	0.0018	699.2	11.8	1222.0	44.0	548.8	8.8	55.1	-27.4	548.8	8.8	534.0	8.6
42	2	50	90	373.58	661	606	0.90	4.9933	0.0753	0.3089	0.0044	0.1175	0.0014	1818.2	12.8	1917.9	21.3	1735.1	21.6	9.5	-4.8	1917.9	21.6	1713.1	24.7
42	2	50	90	373.58	1430	349	0.20	15.5662	0.2263	0.5028	0.0070	0.2250	0.0025	2850.6	14.0	3016.4	18.1	2625.7	30.1	13.0	-8.6	3016.4	30.1	2469.8	28.1
42	2	50	90	373.58	1708	1223	0.70	2.2433	0.0319	0.2021	0.0028	0.0807	0.0009	1194.7	10.0	1213.8	21.4	1186.3	14.9	2.3	-0.7	1213.8	14.9	1184.8	21.8
42	2	50	90	373.58	353	459	1.30	0.7194	0.0131	0.0879	0.0013	0.0595	0.0010	550.3	7.7	584.8	34.7	543.0	7.6	7.2	-1.3	543.0	7.6	542.3	7.6
42	2	50	90	373.58	482	311	0.60	0.6315	0.0110	0.0794	0.0012	0.0578	0.0009	497.0	6.9	521.2	33.1	492.8	6.9	5.5	-0.9	492.8	6.9	492.3	6.9
42	2	50	90	373.58	322	84	0.30	0.7352	0.0136	0.0894	0.0013	0.0598	0.0010	559.6	8.0	594.6	35.6	552.0	7.8	7.2	-1.4	552.0	7.8	551.3	7.8
42	2	50	90	373.58	962	263	0.30	1.3489	0.0199	0.1419	0.0020	0.0691	0.0008	867.1	8.6	900.8	24.0	855.5	11.1	5.0	-1.4	855.5	11.1	854.0	11.1
42	2	50	90	373.58	1052	210	0.20	1.0584	0.0159	0.1170	0.0016	0.0658	0.0008	733.0	7.8	798.4	25.0	713.1	9.4	10.7	-2.8	713.1	9.4	710.9	9.4
42	2	50	90	373.58	3447	2657	0.80	0.6238	0.0088	0.0781	0.0011	0.0581	0.0007	492.3	5.5	532.9	24.6	484.5	6.3	9.1	-1.6	484.5	6.3	483.7	6.3

42	2	50	90	373.58	998	159	0.20	0.6711	0.0109	0.0841	0.0012	0.0580	0.0008	521.4	6.6	529.5	29.9	520.5	7.1	1.7	-0.2	520.5	7.1	520.4	7.1
42	2	50	90	373.58	640	195	0.30	1.8031	0.0270	0.1710	0.0024	0.0767	0.0009	1046.6	9.8	1111.7	23.8	1017.6	13.2	8.5	-2.9	1017.6	13.2	1013.5	13.1
42	2	50	90	373.58	1121	301	0.30	0.9272	0.0142	0.1046	0.0015	0.0644	0.0008	666.2	7.5	754.8	26.3	641.4	8.6	15.0	-3.9	641.4	8.6	638.9	8.6
42	2	50	90	373.58	431	276	0.60	0.6373	0.0115	0.0807	0.0012	0.0575	0.0009	500.7	7.1	507.9	34.9	500.0	7.0	1.5	-0.1	500.0	7.0	499.9	7.0
42	2	50	90	373.58	433	237	0.50	1.4952	0.0240	0.1496	0.0021	0.0726	0.0010	928.4	9.8	1003.0	26.9	898.9	12.0	10.4	-3.3	898.9	12.0	895.2	12.0
42	2	50	90	373.58	1172	1264	1.10	0.3107	0.0053	0.0418	0.0006	0.0541	0.0008	274.7	4.1	373.8	33.0	263.8	3.7	29.4	-4.1	263.8	3.7	262.9	3.7
42	2	50	90	373.58	615	295	0.50	0.8257	0.0134	0.0992	0.0014	0.0605	0.0008	611.2	7.5	620.5	29.3	609.8	8.3	1.7	-0.2	609.8	8.3	609.6	8.3
42	2	50	90	373.58	972	628	0.60	0.7487	0.0117	0.0920	0.0013	0.0592	0.0008	567.5	6.8	573.5	27.6	567.1	7.6	1.1	-0.1	567.1	7.6	567.0	7.6
42	2	50	90	373.58	296	202	0.70	0.8002	0.0148	0.0966	0.0014	0.0602	0.0010	597.0	8.4	610.2	35.3	594.6	8.4	2.5	-0.4	594.6	8.4	594.3	8.3
42	2	50	90	373.58	1429	699	0.50	0.8073	0.0120	0.0988	0.0014	0.0594	0.0007	600.9	6.8	580.4	25.7	607.5	8.0	-4.7	1.1	607.5	8.0	608.0	8.1
42	2	50	90	373.58	1160	1030	0.90	0.8560	0.0130	0.1016	0.0014	0.0613	0.0008	627.9	7.1	647.1	26.4	623.7	8.3	3.6	-0.7	623.7	8.3	623.2	8.3
42	2	50	90	373.58	109	144	1.30	0.7664	0.0182	0.0936	0.0015	0.0595	0.0013	577.7	10.5	585.2	48.9	576.8	8.9	1.4	-0.1	576.8	8.9	576.7	8.9
42	2	50	90	373.58	436	145	0.30	1.4870	0.0232	0.1521	0.0022	0.0711	0.0009	925.1	9.5	958.8	26.0	912.6	12.0	4.8	-1.4	912.6	12.0	910.9	12.0
42	2	50	90	373.58	751	84	0.10	0.7095	0.0115	0.0889	0.0013	0.0580	0.0008	544.4	6.9	528.8	29.6	549.2	7.5	-3.9	0.9	549.2	7.5	549.6	7.5
42	2	50	90	373.58	702	1048	1.50	12.6550	0.1799	0.4942	0.0069	0.1862	0.0020	2654.3	13.5	2707.9	18.0	2588.8	29.6	4.4	-2.5	2707.9	29.6	2547.8	20.5
42	2	50	90	373.58	20	9	0.40	0.7700	0.0475	0.0942	0.0025	0.0594	0.0037	579.8	27.2	581.2	135.3	580.5	14.8	0.1	0.1	580.5	14.8	580.4	14.8
42	2	50	90	373.58	1042	306	0.30	6.0365	0.0859	0.3506	0.0049	0.1252	0.0014	1981.1	12.5	2030.5	19.3	1937.4	23.2	4.6	-2.3	2030.5	23.2	1923.5	20.9
42	2	50	90	373.58	800	376	0.50	0.7681	0.0123	0.0931	0.0013	0.0600	0.0008	578.7	7.1	601.9	28.6	573.9	7.8	4.6	-0.8	573.9	7.8	573.4	7.8
42	2	50	90	373.58	49	2	0.00	1.5344	0.0456	0.1598	0.0030	0.0698	0.0020	944.3	18.3	921.6	59.8	955.7	16.7	-3.7	1.2	955.7	16.7	957.0	16.8
42	2	50	90	373.58	211	467	2.20	0.8426	0.0175	0.0999	0.0015	0.0613	0.0012	620.6	9.7	649.9	41.0	613.8	9.0	5.6	-1.1	613.8	9.0	613.0	9.0
42	2	50	90	373.58	318	61	0.20	0.8425	0.0158	0.1000	0.0015	0.0613	0.0010	620.5	8.7	647.1	35.9	614.4	8.7	5.0	-1.0	614.4	8.7	613.8	8.7
42	2	50	90	373.58	676	359	0.50	0.8485	0.0138	0.1022	0.0015	0.0603	0.0008	623.8	7.6	614.8	29.4	627.4	8.5	-2.1	0.6	627.4	8.5	627.7	8.5
42	2	50	90	373.58	1900	525	0.30	14.6098	0.2062	0.5236	0.0072	0.2029	0.0022	2790.2	13.5	2848.6	17.6	2714.3	30.6	4.7	-2.8	2848.6	30.6	2659.2	20.5
42	2	50	90	373.58	305	112	0.40	1.9933	0.0382	0.1707	0.0027	0.0849	0.0015	1113.2	13.0	1312.4	33.5	1015.9	14.6	22.6	-9.6	1015.9	14.6	1002.0	14.4
42	2	50	90	373.58	1058	433	0.40	2.8455	0.0418	0.2380	0.0033	0.0869	0.0010	1367.6	11.1	1357.9	22.1	1376.3	17.3	-1.4	0.6	1357.9	17.3	1377.6	21.8
42	2	50	90	373.58	736	326	0.40	1.7556	0.0278	0.1669	0.0024	0.0765	0.0010	1029.2	10.2	1106.5	26.0	995.0	13.2	10.1	-3.4	995.0	13.2	990.2	13.1
42	2	50	90	373.58	388	182	0.50	0.6519	0.0144	0.0866	0.0014	0.0547	0.0011	509.6	8.9	399.8	46.3	535.4	8.0	-33.9	4.8	535.4	8.0	537.6	8.0
42	2	50	90	373.58	1139	481	0.40	0.7223	0.0122	0.0927	0.0013	0.0567	0.0008	552.0	7.2	476.9	31.7	571.4	7.9	-19.8	3.4	571.4	7.9	573.1	7.9
42	2	50	90	373.58	286	287	1.00	0.7028	0.0163	0.0828	0.0013	0.0617	0.0014	540.5	9.8	662.4	46.9	512.9	7.9	22.6	-5.4	512.9	7.9	510.4	7.8
42	2	50	90	373.58	172	142	0.80	0.8206	0.0215	0.0939	0.0016	0.0635	0.0016	608.4	12.0	725.1	53.8	578.6	9.4	20.2	-5.2	578.6	9.4	575.7	9.4
42	2	50	90	373.58	1083	272	0.30	1.3203	0.0210	0.1437	0.0020	0.0668	0.0009	854.6	9.2	830.0	27.3	865.6	11.5	-4.3	1.3	865.6	11.5	866.8	11.5
42	2	50	90	373.58	1912	699	0.40	0.8575	0.0131	0.1034	0.0015	0.0603	0.0007	628.8	7.2	613.0	26.6	634.3	8.5	-3.5	0.9	634.3	8.5	634.7	8.5
42	2	50	90	373.58	943	564	0.60	14.1542	0.2026	0.5386	0.0075	0.1911	0.0021	2760.1	13.7	2750.5	18.1	2777.5	31.5	-1.0	0.6	2750.5	31.5	2789.0	17.6
42	2	50	90	373.58	894	123	0.10	1.5003	0.0233	0.1567	0.0022	0.0696	0.0009	930.5	9.5	915.9	25.8	938.3	12.3	-2.4	0.8	938.3	12.3	939.1	12.3
42	2	50	90	373.58	979	389	0.40	0.8479	0.0136	0.1030	0.0015	0.0598	0.0008	623.5	7.5	596.5	28.7	632.2	8.5	-6.0	1.4	632.2	8.5	632.9	8.5
42	2	50	90	373.58	337	475	1.40	0.8282	0.0160	0.1012	0.0015	0.0595	0.0010	612.6	8.9	584.8	37.6	621.2	8.8	-6.2	1.4	621.2	8.8	622.0	8.9
42	2	50	90	373.58	26	18	0.70	0.8400	0.0489	0.0954	0.0026	0.0640	0.0038	619.1	27.0	741.7	124.9	587.3	15.0	20.8	-5.4	587.3	15.0	584.2	14.9
42	2	50	90	373.58	525	282	0.50	0.8500	0.0148	0.1028	0.0015	0.0601	0.0009	624.6	8.1	605.8	32.5	631.0	8.7	-4.2	1.0	631.0	8.7	631.6	8.7
42	2	50	90	373.58	526	294	0.60	1.9240	0.0312	0.1841	0.0027	0.0760	0.0010	1089.5	10.9	1093.9	27.0	1089.2	14.4	0.4	0.0	1089.2	14.4	1088.9	14.4
42	2	50	90	373.58	516	439	0.90	2.0139	0.0336	0.1843	0.0027	0.0795	0.0011	1120.2	11.3	1182.7	28.0	1090.2	14.7	7.8	-2.8	1090.2	14.7	1085.7	14.6
42	2	50	90	373.58	213	104	0.50	1.8069	0.0323	0.1772	0.0026	0.0741	0.0012	1048.0	11.7	1044.1	31.4	1051.6	14.5	-0.7	0.3	1051.6	14.5	1052.0	14.5
42	2	50	90	373.58	242	165	0.70	2.3629	0.0397	0.2142	0.0031	0.0802	0.0011	1231.5	12.0	1201.3	27.9	1250.9	16.6	-4.1	1.6	1201.3	16.6	1253.9	26.9
42	2	50	90	373.58	2239	769	0.30	1.9960	0.0280	0.1910	0.0026	0.0760	0.0008	1114.1	9.5	1093.9	22.0	1126.5	13.9	-3.0	1.1	1093.9	13.9	1128.1	21.5
42	2	50	90	373.58	1086	555	0.50	0.6700	0.0109	0.0839	0.0012	0.0581	0.0008	520.7	6.6	531.0	29.9	519.2	7.1	2.2	-0.3	519.2	7.1	519.0	7.1
42	2	50	90	373.58	531	549	1.00	0.6421	0.0111	0.0835	0.0012	0.0559	0.0008	503.6	6.9	448.6	33.0	516.7	7.1	-15.2	2.5	516.7	7.1	517.8	7.2
42	2	50	90	373.58	106	95	0.90	4.4941	0.0782	0.3049	0.0047	0.1072	0.0016	1729.9	14.5	1750.8	27.3	1715.5	23.0	2.0	-0.8	1750.8	23.0	1711.5	28.1
42	2	50	90	373.58	1168	623	0.50	0.7475	0.0117	0.0925	0.0013	0.0588	0.0008	566.8	6.8	557.6	27.9	570.1	7.7	-2.2	0.6	570.1	7.7	570.3	7.7
42	2	50	90	373.58	405	824	2.00	0.9255	0.0166	0.1088	0.0016	0.0618	0.0010	665.3	8.8	667.3	33.7	665.9	9.3	0.2	0.1	665.9	9.3	665.8	9.3
42	2	50	90	373.58	681	162	0.20	1.6302	0.0255	0.1617	0.0023	0.0733	0.0009	981.9	9.8	1021.1	25.8	966.1	12.7	5.4	-1.6	966.1	12.7	963.9	12.7
42	2	50	90	373.58	553	187	0.30	0.8188	0.0142	0.1012	0.0015	0.0588	0.0009	607.4	7.9	559.8	32.3	621.3	8.6	-11.0	2.2	621.3	8.6	622.5	8.6
42	2	50	90	373.58	690	433	0.60	1.7051	0.0262	0.1728	0.0024	0.0717	0.0009	1010.4	9.8	977.1	25.1	1027.6	13.4	-5.2	1.7	1027.6	13.4	1029.8	13.4
42	2	50	90	373.58	1371	505	0.40	0.8352	0.0129	0.1008	0.0014	0.0603	0.0007	616.5	7.1	611.6	26.6	618.9	8.3	-1.2	0.4	618.9	8.3	619.0	8.3
42	2	50	90	373.58	530	195	0.40	4.5922	0.0686	0.3076	0.0043	0.1085	0.0013	1747.9	12.5	1774.1	21.5	1728.8	21.4	2.5	-1.1	1774.1	21.4	1723.7	22.3
42	2	50	90	373.58	983	194	0.20	2.2707	0.0336	0.2035	0.0029	0.0811	0.0009	1203.2	10.5	1223.0	22.7	1194.3	15.3	2.3	-0.7	1223.0	15.3	1192.7	23.2
42	2	50	90	373.58	404	289	0.70	23.2426	0.3357	0.6585	0.0092	0.2566	0.0028	3237.2	14.2	3225.2	17.6	3261.2	36.0	-1.1	0.7	3225.2	36.0	3295.6	16.6
42	2	50	90	373.58	145	74	0.50	2.4870	0.0460	0.2205	0.0034	0.0820	0.0013	1268.3	13.4	1244.6	31.9	1284.3	17.8	-3.2	1.2	1244.6	17.8	1286.7	31.0
42	2	50	90	373.58	422	825	2.00	0.7924	0.0145	0.0957	0.0014	0.0602	0.0010	592.6	8.2	610.5	34.9	588.9	8.3	3.5	-0.6	588.9	8.3	588.5	8.3
42	2	50	90	373.58	2577	1510	0.60	0.8503	0.0126	0.1019	0.0014	0.0607	0.0007	624.8	6.9	626.2	25.0	625.4	8.3	0.1	0.1	625.4	8.3	625.4	8.3
42	2	50	90	373.58	2345	626	0.30	1.9716	0.0286	0.1899	0.0026	0.0755	0.0008	1105.9	9.8	1080.7	22.2	1120.7	14.3	-3.7	1.3	1080.7	14.3	1122.6	21.6
42	2	50	90	373.58	1318	921	0.70	0.2712	0.0049	0.0385	0.0006	0.0513	0.0008	243.6	3.9	251.5	36.0	243.3	3.5	3.3	-0.1	243.3	3.5	243.2	3.5
42	2	50	90	373.58	1705	1330	0.80	0.7095	0.0111	0.0826	0.0012	0.0624	0.0008	544.4	6.6	687.2	27.1	511.8	7.0	25.5	-6.4	511.8	7.0	508.8	6.9
42	2	50	90	373.58	460	383	0.80	0.7331	0.0130	0.0894	0.0013	0.0596	0.0009	558.4	7.6	588.8	33.2	551.9	7.7	6.3	-1.2	551.9	7.7	551.3	7.7
42	2	50	90	373.58	909	1153	1.30	0.6910	0.0111	0.0860	0.0012	0.0584	0.0008	533.4	6.6	544.2	28.9	531.9	7.2	2.3	-0.3	531.9	7.2	531.6	7.2
42	2	50	90	373.58	543	342	0.60	20.0384	0.2884	0.6213	0.0087	0.2344	0.0026	3093.2	14.1	3081.9	17.7	3115.2	34.5	-1.1	0.7	3081.9	34.5	3139.2	16.9
42	2	50	90	373.58	1543	522	0.30	0.7441	0.0115	0.0910	0.0013	0.0594	0.0007	564.8	6.7	581.5	27.1	561.6	7.6	3.4	-0.6	561.6	7.6	561.2	7.6
42	2	50	90	373.58	150	127	0.80	0.8384	0.0200	0.0996	0.0016	0.0612	0.0014	618.3	11.0	645.3	48.5	612.0	9.4	5.2	-1.0	612.0	9.4	611.4	9.4
42	2	50	90	373.58	526	210	0.40	1.0793	0.0178	0.1193	0.0017	0.0657	0.0009	743.3	8.7	797.2	28.8	726.7	9.9	8.8	-2.3	726.7	9.9	724.9	9.8
42	2	50	90	373.58	2405	2367	1.00	0.8384	0.0126	0.1033	0.0014	0.0590	0.0007	618.2	7.0	565.7	25.6	633.8	8.4	-12.0	2.5	633.8	8.4	635.2	8.4
42	2	50	90	373.58	104	33	0.30	1.9604	0.0515	0.1901	0.0034	0.0750	0.0019	1102.0	17.7	1066.3	50.8	1122.1	18.6	-5.2	1.8	1066.3	18.6	1124.8	48.8
42	2	50	90	373.58	496	290	0.60	1.9379	0.0306	0.1859	0.0027	0.0758	0.0010	1094.3	10.6	1088.1	25.8	1099.2	14.4	-1.0	0.4	1099.2	14.4	1099.7	14.4
42	2	50	90	373.58	237	373	1.60	1.4685	0.0269	0.1552	0.0023	0.0688	0.0011	917.5	11.1	891.5	33.1	929.9	12.9	-4.3	1.3	929.9	12.9	931.3	12.9
42	2	50	90	373.58	434	223	0.50	2.3498	0.0371	0.2112	0.0030	0.0809	0.0010	1227.5	11.3	1217.9	25.2	1235.0	16.1	-1.4	0.6	1217.9	16.1	1236.0	24.9
42	2	50	90	373.58	639	438	0.70	0.8299	0.0140	0.0987	0.0014	0.0611	0.0009	613.5	7.8	642.1	30.7	606.8	8.3	5.5	-1.1	606.8	8.3	606.1	8.3
42	2	50	90	373.58	276	291	1.10	0.7669	0.0162	0.0957	0.0015	0.0583	0.0011	578.0	9.3	538.6	42.1	589.2	8.7	-9.4	1.9	589.2	8.7	590.1	8.7
42	2	50	90	373.58	1379	326	0.20	1.7154	0.0258	0.1702	0.0024	0.0733	0.0009	1014.3	9.7	1020.5	23.9	1013.2	13.2	0.7	-0.1	1013.2	13.2	1012.9	13.2
42	2	50	90	373.58	1553	679	0.40	0.6767	0.0109	0.0838	0.0012	0.0587	0.0008	524.8	6.6	556.5	28.7	518.5	7.1	6.8	-1.2	518.5	7.1	517.9	7.1
42	2	50	90	373.58	332	210	0.60	1.0133	0.0193	0.1144	0.0017	0.0644	0.0011	710.5	9.8	753.5	35.8	698.2	10.0	7.3	-1.8	698.2	10.0	696.9	9.9

42	2	50	90	373.58	1374	1326	1.00	2.3607	0.0350	0.2139	0.0030	0.0802	0.0009	1230.8	10.6	1201.3	22.8	1249.8	15.9	-4.0	1.5	1201.3	15.9	1252.6	22.0
42	2	50	90	373.58	426	290	0.70	5.4294	0.0823	0.3467	0.0049	0.1138	0.0014	1889.5	13.1	1860.6	21.6	1918.9	23.7	-3.1	1.5	1860.6	23.7	1927.0	20.6
42	2	50	90	373.58	1158	167	0.10	8.6719	0.1260	0.4365	0.0061	0.1444	0.0016	2304.1	13.3	2280.2	19.2	2334.8	27.4	-2.4	1.3	2280.2	27.4	2347.5	18.3
42	2	50	90	373.58	966	644	0.70	1.9515	0.0298	0.1726	0.0024	0.0822	0.0010	1098.9	10.3	1249.4	24.0	1026.3	13.4	17.9	-7.1	1026.3	13.4	1015.9	13.3
42	2	50	90	373.58	1160	859	0.70	0.6984	0.0116	0.0847	0.0012	0.0600	0.0008	537.8	7.0	600.8	30.4	524.0	7.2	12.8	-2.6	524.0	7.2	522.7	7.2
42	2	50	90	373.58	1407	547	0.40	0.8534	0.0134	0.1035	0.0015	0.0600	0.0008	626.5	7.4	601.2	27.5	634.6	8.5	-5.6	1.3	634.6	8.5	635.3	8.5
42	2	50	90	373.58	82	80	1.00	0.7018	0.0243	0.0867	0.0017	0.0588	0.0020	539.8	14.5	559.1	74.9	536.2	10.0	4.1	-0.7	536.2	10.0	535.8	10.0
42	2	50	90	373.58	186	628	3.40	0.7861	0.0190	0.0978	0.0016	0.0584	0.0013	588.9	10.8	544.9	49.8	601.5	9.3	-10.4	2.1	601.5	9.3	602.6	9.3
42	2	50	90	373.58	472	40	0.10	0.7082	0.0135	0.0880	0.0013	0.0585	0.0010	543.7	8.0	546.4	37.1	543.9	7.8	0.5	0.0	543.9	7.8	543.9	7.8
42	2	50	90	373.58	569	265	0.50	0.8556	0.0151	0.1043	0.0015	0.0596	0.0009	627.7	8.3	588.8	33.2	639.6	8.9	-8.6	1.9	639.6	8.9	640.7	8.9
42	2	50	90	373.58	499	160	0.30	2.1901	0.0351	0.2069	0.0030	0.0769	0.0010	1177.9	11.2	1118.7	26.3	1212.3	15.9	-8.4	2.8	1118.7	15.9	1217.4	24.6
42	2	50	90	373.58	356	101	0.30	1.4256	0.0255	0.1434	0.0021	0.0723	0.0011	899.7	10.7	992.9	31.6	863.7	12.0	13.0	-4.2	863.7	12.0	859.3	12.0
42	2	50	90	373.58	458	226	0.50	8.1230	0.1214	0.4085	0.0058	0.1445	0.0017	2244.8	13.6	2281.4	20.1	2208.2	26.6	3.2	-1.7	2281.4	26.6	2193.0	21.5
42	2	50	90	373.58	1018	647	0.60	0.7736	0.0128	0.0945	0.0014	0.0595	0.0008	581.8	7.3	584.1	30.0	582.2	8.0	0.3	0.1	582.2	8.0	582.2	8.0
42	2	50	90	373.58	530	240	0.50	0.7082	0.0130	0.0884	0.0013	0.0583	0.0009	543.7	7.7	538.2	35.4	546.0	7.7	-1.4	0.4	546.0	7.7	546.1	7.7
42	2	50	90	373.58	695	342	0.50	0.7571	0.0134	0.0943	0.0014	0.0584	0.0009	572.3	7.7	541.9	33.4	581.0	8.1	-7.2	1.5	581.0	8.1	581.7	8.1
42	2	50	90	373.58	269	108	0.40	0.6737	0.0150	0.0820	0.0013	0.0597	0.0012	523.0	9.1	592.1	44.7	508.1	7.7	14.2	-2.9	508.1	7.7	506.7	7.7
42	2	50	90	373.58	620	262	0.40	0.7976	0.0143	0.0859	0.0013	0.0675	0.0011	595.5	8.1	852.3	32.4	531.2	7.5	37.7	-12.1	531.2	7.5	525.2	7.4
42	2	50	90	373.58	378	253	0.70	0.2830	0.0078	0.0389	0.0007	0.0529	0.0014	253.0	6.2	321.8	60.6	246.1	4.0	23.5	-2.8	246.1	4.0	245.6	4.0
42	2	50	90	373.58	1999	258	0.10	0.8757	0.0134	0.1060	0.0015	0.0600	0.0007	638.6	7.3	603.7	26.4	649.7	8.7	-7.6	1.7	649.7	8.7	650.7	8.7
42	2	50	90	373.58	2062	530	0.30	1.3370	0.0200	0.1395	0.0020	0.0697	0.0008	861.9	8.7	917.4	24.0	841.8	11.0	8.2	-2.4	841.8	11.0	839.4	11.0
42	2	50	90	373.58	882	243	0.30	3.8155	0.0571	0.2802	0.0040	0.0990	0.0012	1596.0	12.1	1604.3	21.8	1592.2	19.9	0.8	-0.2	1604.3	19.9	1591.0	22.1
42	2	50	90	373.58	472	239	0.50	1.5585	0.0261	0.1546	0.0022	0.0733	0.0010	953.9	10.4	1021.1	28.6	926.5	12.5	9.3	-3.0	926.5	12.5	922.9	12.5
42	2	50	90	373.58	361	777	2.20	0.8085	0.0165	0.0987	0.0015	0.0596	0.0011	601.6	9.3	587.0	40.1	606.6	8.9	-3.3	0.8	606.6	8.9	606.9	8.9
42	2	50	90	373.58	969	519	0.50	1.1913	0.0191	0.1341	0.0019	0.0646	0.0008	796.6	8.8	760.1	27.5	811.1	10.9	-6.7	1.8	811.1	10.9	812.6	10.9
42	2	50	90	373.58	315	180	0.60	0.7488	0.0159	0.0893	0.0014	0.0609	0.0012	567.5	9.2	636.1	42.1	551.4	8.2	13.3	-2.9	551.4	8.2	549.9	8.2
42	2	50	90	373.58	283	482	1.70	2.3255	0.0393	0.2069	0.0030	0.0817	0.0012	1220.1	12.0	1237.7	28.0	1212.1	16.3	2.1	-0.7	1237.7	16.3	1210.7	28.5
42	2	50	90	373.58	1608	1826	1.10	0.7486	0.0122	0.0849	0.0012	0.0641	0.0009	567.4	7.1	743.7	28.5	525.3	7.2	29.4	-8.0	525.3	7.2	521.4	7.1
42	2	50	90	373.58	2694	1132	0.40	0.7243	0.0110	0.0900	0.0013	0.0585	0.0007	553.2	6.5	547.2	26.2	555.6	7.5	-1.5	0.4	555.6	7.5	555.8	7.5
42	2	50	90	373.58	960	298	0.30	0.6654	0.0115	0.0858	0.0012	0.0564	0.0008	517.9	7.0	466.4	32.7	530.5	7.4	-13.8	2.4	530.5	7.4	531.6	7.4
42	2	50	90	373.58	2018	894	0.40	0.8301	0.0128	0.0956	0.0014	0.0631	0.0008	613.6	7.1	710.6	26.4	588.6	7.9	17.2	-4.2	588.6	7.9	586.2	7.9
42	2	50	90	373.58	1650	362	0.20	0.6928	0.0111	0.0875	0.0012	0.0576	0.0008	534.5	6.7	512.8	28.7	540.5	7.4	-5.4	1.1	540.5	7.4	540.9	7.4
47	1	52	92	410.82	1848	407	0.20	2.5781	0.0381	0.1716	0.0024	0.1092	0.0013	1294.4	10.9	1785.0	21.1	1021.1	13.3	42.8	-26.8	1021.1	13.3	978.7	12.8
47	1	52	92	410.82	3582	690	0.20	0.7794	0.0117	0.0779	0.0011	0.0727	0.0009	585.1	6.7	1004.4	23.9	483.8	6.6	51.8	-20.9	483.8	6.6	474.6	6.5
47	1	52	92	410.82	798	288	0.40	11.5500	0.1848	0.4702	0.0072	0.1785	0.0020	2568.6	15.1	2638.6	19.0	2484.6	31.6	5.8	-3.4	2638.6	31.6	2437.7	22.2
47	1	52	92	410.82	477	191	0.40	4.6274	0.0761	0.3011	0.0047	0.1117	0.0013	1754.2	13.8	1826.6	21.6	1696.7	23.1	7.1	-3.4	1826.6	23.1	1682.0	24.0
47	1	52	92	410.82	2844	349	0.10	0.8633	0.0147	0.0672	0.0010	0.0934	0.0012	631.9	8.0	1494.1	24.1	419.4	6.3	71.9	-50.7	419.4	6.3	400.0	6.0
47	1	52	92	410.82	8231	3754	0.50	0.6520	0.0107	0.0623	0.0010	0.0760	0.0009	509.7	6.6	1095.2	23.8	389.7	5.8	64.4	-30.8	389.7	5.8	379.5	5.7
47	1	52	92	410.82	1759	502	0.30	0.6633	0.0117	0.0672	0.0011	0.0718	0.0010	516.7	7.1	978.2	27.4	419.1	6.3	57.2	-23.3	419.1	6.3	410.7	6.2
47	1	52	92	410.82	6771	7575	1.10	0.3469	0.0060	0.0356	0.0006	0.0709	0.0009	302.4	4.5	952.5	26.4	225.3	3.4	76.3	-34.2	225.3	3.4	219.7	3.3
47	1	52	92	410.82	768	576	0.80	3.9109	0.0647	0.2738	0.0042	0.1038	0.0012	1615.9	13.4	1692.3	22.2	1560.2	21.4	7.8	-3.6	1692.3	21.4	1547.7	24.6
47	1	52	92	410.82	1451	809	0.60	14.4536	0.2167	0.4047	0.0057	0.2595	0.0030	2780.0	14.4	3243.2	18.7	2190.8	26.3	32.5	-26.9	3243.2	26.3	1875.9	56.7
47	1	52	92	410.82	2404	963	0.40	7.4656	0.1221	0.3764	0.0058	0.1442	0.0017	2168.9	14.7	2277.0	20.3	2059.3	27.0	9.6	-5.3	2277.0	27.0	2019.6	24.7
47	1	52	92	410.82	720	410	0.60	1.0186	0.0184	0.0880	0.0014	0.0842	0.0012	713.2	9.3	1295.1	27.2	543.5	8.2	58.0	-31.2	543.5	8.2	526.7	8.0
47	1	52	92	410.82	1257	311	0.20	6.2923	0.1042	0.2167	0.0034	0.2110	0.0025	2017.4	14.6	2912.7	19.7	1264.4	17.8	56.6	-59.6	2912.7	17.8	1076.2	15.4
47	1	52	92	410.82	6174	5990	1.00	0.7475	0.0128	0.0736	0.0011	0.0738	0.0009	566.8	7.4	1035.4	25.6	457.7	6.8	55.8	-23.8	457.7	6.8	448.0	6.7
47	1	52	92	410.82	1550	150	0.10	0.7236	0.0125	0.0843	0.0013	0.0624	0.0008	552.8	7.4	686.9	28.1	521.7	7.8	24.1	-6.0	521.7	7.8	518.8	7.8
47	1	52	92	410.82	341	95	0.30	1.8271	0.0339	0.1754	0.0028	0.0757	0.0011	1055.2	12.2	1087.3	29.2	1041.5	15.4	4.2	-1.3	1041.5	15.4	1039.5	15.4
47	1	52	92	410.82	1126	181	0.20	0.8519	0.0147	0.0992	0.0015	0.0624	0.0008	625.7	8.1	688.3	27.8	609.5	9.0	11.4	-2.7	609.5	9.0	607.9	9.0
47	1	52	92	410.82	759	158	0.20	0.6496	0.0115	0.0806	0.0013	0.0586	0.0008	508.2	7.1	551.3	29.5	499.6	7.5	9.4	-1.7	499.6	7.5	498.8	7.5
47	1	52	92	410.82	867	729	0.80	0.6761	0.0118	0.0836	0.0013	0.0588	0.0008	524.4	7.2	557.6	29.0	517.7	7.7	7.2	-1.3	517.7	7.7	517.0	7.7
47	1	52	92	410.82	520	324	0.60	0.6660	0.0130	0.0769	0.0012	0.0629	0.0010	518.3	7.9	705.2	33.6	477.7	7.4	32.3	-8.5	477.7	7.4	474.1	7.3
47	1	52	92	410.82	643	622	1.00	0.2330	0.0054	0.0309	0.0005	0.0548	0.0011	212.7	4.4	404.7	44.6	196.1	3.2	51.5	-8.5	196.1	3.2	194.9	3.2
47	1	52	92	410.82	1285	126	0.10	1.1140	0.0184	0.1224	0.0019	0.0662	0.0008	760.1	8.8	810.2	25.1	744.4	10.8	8.1	-2.1	744.4	10.8	742.7	10.8
47	1	52	92	410.82	792	112	0.10	0.8673	0.0139	0.1021	0.0015	0.0618	0.0008	634.1	7.6	664.5	28.2	626.6	8.5	5.7	-1.2	626.6	8.5	625.8	8.5
47	1	52	92	410.82	481	301	0.60	1.6433	0.0286	0.1616	0.0025	0.0739	0.0010	987.0	11.0	1037.8	26.6	965.9	14.0	6.9	-2.2	965.9	14.0	963.0	14.0
47	1	52	92	410.82	662	500	0.80	0.8207	0.0152	0.0981	0.0016	0.0608	0.0009	608.4	8.5	631.2	31.3	603.4	9.1	4.4	-0.8	603.4	9.1	602.8	9.1
47	1	52	92	410.82	1579	274	0.20	1.3392	0.0219	0.1375	0.0021	0.0708	0.0008	862.9	9.5	950.4	24.1	830.5	11.9	12.6	-3.9	830.5	11.9	826.6	11.9
47	1	52	92	410.82	1258	651	0.50	0.9095	0.0161	0.0886	0.0013	0.0746	0.0012	656.8	8.6	1057.6	31.1	547.0	7.8	48.3	-20.1	547.0	7.8	536.4	7.6
47	1	52	92	410.82	2894	661	0.20	0.6279	0.0096	0.0790	0.0011	0.0578	0.0007	494.8	6.0	519.7	26.7	490.3	6.6	5.7	-0.9	490.3	6.6	489.8	6.6
47	1	52	92	410.82	556	264	0.50	1.9091	0.0327	0.1825	0.0028	0.0760	0.0010	1084.3	11.4	1095.2	25.7	1080.5	15.5	1.3	-0.3	1080.5	15.5	1079.9	15.5
47	1	52	92	410.82	343	268	0.80	0.7150	0.0145	0.0873	0.0014	0.0595	0.0010	547.7	8.6	585.9	36.2	539.5	8.4	7.9	-1.5	539.5	8.4	538.7	8.4
47	1	52	92	410.82	522	397	0.80	0.3798	0.0082	0.0528	0.0009	0.0523	0.0009	326.9	6.0	296.2	41.1	331.8	5.3	-12.0	1.5	331.8	5.3	332.1	5.3
47	1	52	92	410.82	346	233	0.70	1.6437	0.0308	0.1595	0.0026	0.0749	0.0011	987.1	11.9	1064.4	29.9	954.2	14.2	10.3	-3.4	954.2	14.2	949.8	14.2
47	1	52	92	410.82	1523	674	0.40	0.5888	0.0103	0.0723	0.0011	0.0592	0.0008	470.1	6.6	574.2	29.1	449.9	6.7	21.7	-4.5	449.9	6.7	448.1	6.7
47	1	52	92	410.82	2042	1502	0.70	0.6524	0.0109	0.0804	0.0012	0.0590	0.0007	510.0	6.7	565.7	26.7	498.4	7.4	11.9	-2.3	498.4	7.4	497.3	7.4
47	1	52	92	410.82	994	422	0.40	0.7829	0.0124	0.0947	0.0014	0.0601	0.0008	587.1	7.1	604.8	28.2	583.5	8.0	3.5	-0.6	583.5	8.0	583.1	8.0
47	1	52	92	410.82	702	729	1.00	4.1317	0.0673	0.2957	0.0045	0.1016	0.0012	1660.6	13.4	1652.0	21.7	1669.9	22.6	-1.1	0.6	1652.0	22.6	1671.7	21.4
47	1	52	92	410.82	595	195	0.30	0.7037	0.0118	0.0895	0.0013	0.0571	0.0008	541.0	7.0	495.9	31.3	552.7	7.6	-11.4	2.1	552.7	7.6	553.7	7.7
47	1	52	92	410.82	1652	348	0.20	0.8559	0.0131	0.1026	0.0015	0.0606	0.0007	627.9	7.2	624.5	26.4	629.9	8.5	-0.9	0.3	629.9	8.5	630.0	8.5
47	1	52	92	410.82	3082	184	0.10	0.8186	0.0133	0.0949	0.0015	0.0627	0.0007	607.2	7.4	696.1	24.9	584.7	8.5	16.0	-3.9	584.7	8.5	582.5	8.5
47	1	52	92	410.82	1033	602	0.60	7.8521	0.1214	0.3743	0.0053	0.1524	0.0019	2214.2	14.0	2372.6	20.9	2049.7	25.0	13.6	-8.0	2372.6	25.0	1989.3	28.0
47	1	52	92	410.82	1260	632	0.50	13.7112	0.2197	0.5354	0.0082	0.1862	0.0021	2730.0	15.3	2707.7	18.9	2763.9	34.3	-2.1	1.2	2707.7	34.3	2787.1	17.8
47	1	52	92	410.82	253	174	0.70	0.6495	0.0138	0.0815	0.0013	0.0579	0.0010	508.2	8.5	525.8	38.7	505.0	7.9	3.9	-0.6	505.0	7.9	504.7	7.9
47	1	52	92	410.82	776	388	0.50	0.6757	0.0120	0.0816	0.0013	0.0602	0.0008	524.2	7.2	609.1	29.2	505.7	7.6	17.0	-3.7	505.7	7.6	504.0	7.5
47	1	52	92	410.82	550	119	0.20	0.8926	0.0150	0.0991	0.0014	0.0655	0.0009	647.8	8.1	789.5	30.2	608.8	8.5	22.9	-6.4	608.8	8.5	605.0	8.4
47	1	52	92	410.82	577	292	0.50	0.6320	0.0118	0.0804	0.0013	0.0571	0.0008	497.3	7.3	494.8	32.1	498.7	7.6	-0.8	0.3	498.7	7.6	498.7	7.6

47	1	52	92	410.82	689	167	0.20	1.6192	0.0275	0.1627	0.0025	0.0723	0.0009	977.7	10.7	994.0	25.7	971.9	14.0	2.2	-0.6	971.9	14.0	971.0	14.0
47	1	52	92	410.82	239	134	0.60	0.6455	0.0142	0.0817	0.0014	0.0574	0.0011	505.7	8.8	506.7	41.1	506.3	8.0	0.1	0.1	506.3	8.0	506.3	8.0
47	1	52	92	410.82	1197	151	0.10	1.5703	0.0240	0.1615	0.0023	0.0707	0.0009	958.5	9.5	947.5	25.0	964.8	12.7	-1.8	0.7	964.8	12.7	965.5	12.7
47	1	52	92	410.82	935	411	0.40	0.6822	0.0129	0.0834	0.0013	0.0595	0.0009	528.1	7.8	582.6	32.6	516.4	7.9	11.4	-2.3	516.4	7.9	515.3	7.8
47	1	52	92	410.82	958	703	0.70	0.6960	0.0123	0.0852	0.0013	0.0594	0.0008	536.4	7.4	579.0	29.4	527.3	7.9	8.9	-1.7	527.3	7.9	526.4	7.9
47	1	52	92	410.82	404	194	0.50	0.6633	0.0136	0.0839	0.0014	0.0574	0.0010	516.6	8.3	507.1	37.2	519.6	8.1	-2.5	0.6	519.6	8.1	519.8	8.1
47	1	52	92	410.82	368	143	0.40	0.6702	0.0140	0.0827	0.0014	0.0589	0.0010	520.8	8.5	562.8	37.8	512.1	8.0	9.0	-1.7	512.1	8.0	511.3	8.0
47	1	52	92	410.82	681	380	0.60	1.0035	0.0182	0.1172	0.0018	0.0622	0.0009	705.6	9.2	681.4	30.0	714.3	10.6	-4.8	1.2	714.3	10.6	715.2	10.6
47	1	52	92	410.82	3309	2134	0.60	0.7694	0.0119	0.0903	0.0013	0.0619	0.0008	579.4	6.8	670.7	26.4	557.3	7.6	16.9	-4.0	557.3	7.6	555.1	7.5
47	1	52	92	410.82	795	288	0.40	0.6760	0.0122	0.0836	0.0013	0.0588	0.0008	524.4	7.4	558.7	30.5	517.3	7.8	7.4	-1.4	517.3	7.8	516.7	7.8
47	1	52	92	410.82	1140	676	0.60	22.1991	0.3599	0.6287	0.0097	0.2566	0.0029	3192.5	15.9	3225.4	18.5	3144.5	38.2	2.5	-1.5	3225.4	38.2	3081.5	20.9
47	1	52	92	410.82	2384	589	0.20	3.6560	0.0572	0.2571	0.0037	0.1033	0.0013	1561.8	12.5	1684.1	23.0	1474.8	18.8	12.4	-5.9	1684.1	18.8	1456.6	27.1
47	1	52	92	410.82	3973	1250	0.30	1.6014	0.0252	0.1334	0.0019	0.0873	0.0011	970.8	9.8	1365.2	24.2	807.1	10.8	40.9	-20.3	807.1	10.8	787.0	10.6
47	1	52	92	410.82	928	917	1.00	0.1230	0.0030	0.0167	0.0003	0.0536	0.0011	117.8	2.7	354.1	48.1	106.6	1.8	69.9	-10.5	106.6	1.8	105.8	1.8
47	1	52	92	410.82	2689	1034	0.40	0.2710	0.0049	0.0379	0.0006	0.0520	0.0007	243.5	3.9	284.8	31.3	239.6	3.7	15.9	-1.6	239.6	3.7	239.3	3.7
47	1	52	92	410.82	428	142	0.30	0.7629	0.0149	0.0847	0.0014	0.0655	0.0010	575.7	8.6	788.5	33.1	524.1	8.1	33.5	-9.8	524.1	8.1	519.3	8.0
47	1	52	92	410.82	627	136	0.20	0.7330	0.0137	0.0897	0.0014	0.0594	0.0009	558.3	8.0	579.3	31.9	554.0	8.4	4.4	-0.8	554.0	8.4	553.5	8.4
47	1	52	92	410.82	633	11	0.00	0.7328	0.0138	0.0895	0.0014	0.0595	0.0009	558.2	8.1	584.1	32.2	552.8	8.4	5.4	-1.0	552.8	8.4	552.2	8.4
47	1	52	92	410.82	534	302	0.60	3.1524	0.0496	0.2486	0.0036	0.0922	0.0012	1445.6	12.2	1469.8	24.3	1431.3	18.4	2.6	-1.0	1469.8	18.4	1428.3	25.0
47	1	52	92	410.82	1475	366	0.20	1.3977	0.0216	0.1443	0.0021	0.0704	0.0009	888.0	9.2	938.5	25.5	869.2	11.6	7.4	-2.2	869.2	11.6	866.8	11.5
47	1	52	92	410.82	2870	2252	0.80	0.6234	0.0108	0.0719	0.0011	0.0630	0.0008	492.0	6.8	707.9	27.8	447.5	6.7	36.8	-9.9	447.5	6.7	443.6	6.7
47	1	52	92	410.82	3255	962	0.30	0.5888	0.0099	0.0720	0.0011	0.0594	0.0007	470.1	6.3	581.2	26.8	448.4	6.7	22.9	-4.9	448.4	6.7	446.5	6.7
47	1	52	92	410.82	480	256	0.50	0.7799	0.0147	0.0947	0.0015	0.0599	0.0009	585.4	8.4	597.9	32.3	583.0	8.8	2.5	-0.4	583.0	8.8	582.8	8.8
47	1	52	92	410.82	245	128	0.50	0.8156	0.0173	0.1009	0.0017	0.0588	0.0010	605.6	9.7	557.6	38.7	619.4	9.7	-11.1	2.2	619.4	9.7	620.7	9.7
47	1	52	92	410.82	693	469	0.70	0.9183	0.0152	0.1078	0.0016	0.0619	0.0009	661.5	8.1	669.3	29.8	660.1	9.1	1.4	-0.2	660.1	9.1	659.9	9.1
47	1	52	92	410.82	976	45	0.00	0.6823	0.0135	0.0843	0.0014	0.0588	0.0009	528.1	8.1	560.2	34.5	521.6	8.0	6.9	-1.3	521.6	8.0	520.9	8.0
47	1	52	92	410.82	1972	373	0.20	1.7573	0.0292	0.1750	0.0027	0.0730	0.0009	1029.9	10.8	1013.0	24.6	1039.3	14.8	-2.6	0.9	1039.3	14.8	1040.5	14.8
47	1	52	92	410.82	686	279	0.40	0.8558	0.0155	0.1007	0.0016	0.0618	0.0009	627.8	8.5	665.5	29.9	618.4	9.3	7.1	-1.5	618.4	9.3	617.4	9.2
47	1	52	92	410.82	985	439	0.40	0.6444	0.0130	0.0806	0.0013	0.0581	0.0010	505.0	8.0	532.9	35.9	499.7	7.8	6.2	-1.1	499.7	7.8	499.1	7.8
47	1	52	92	410.82	690	113	0.20	0.6489	0.0121	0.0815	0.0013	0.0579	0.0008	507.8	7.5	523.5	31.9	505.1	7.7	3.5	-0.5	505.1	7.7	504.8	7.7
47	1	52	92	410.82	1246	650	0.50	0.1877	0.0036	0.0280	0.0004	0.0486	0.0008	174.6	3.0	129.5	39.7	178.3	2.6	-37.7	2.0	178.3	2.6	178.5	2.6
47	1	52	92	410.82	3432	495	0.10	0.8348	0.0141	0.0904	0.0014	0.0671	0.0008	616.3	7.8	840.6	25.9	557.8	8.3	33.6	-10.5	557.8	8.3	552.3	8.2
47	1	52	92	410.82	215	128	0.60	0.9891	0.0215	0.1162	0.0019	0.0619	0.0011	698.2	11.0	668.3	39.2	708.6	11.2	-6.0	1.5	708.6	11.2	709.6	11.2
47	1	52	92	410.82	958	315	0.30	1.3172	0.0251	0.1399	0.0023	0.0684	0.0010	853.3	11.0	881.0	31.2	844.0	12.7	4.2	-1.1	844.0	12.7	842.8	12.7
47	1	52	92	410.82	1087	294	0.30	1.9076	0.0324	0.1866	0.0029	0.0743	0.0009	1083.7	11.3	1049.0	25.4	1102.7	15.7	-5.1	1.7	1049.0	15.7	1105.3	24.4
47	1	52	92	410.82	501	226	0.50	0.8177	0.0148	0.1007	0.0015	0.0590	0.0009	606.8	8.3	567.6	34.4	618.2	8.7	-8.9	1.9	618.2	8.7	619.2	8.7
47	1	52	92	410.82	1119	256	0.20	0.8657	0.0155	0.1033	0.0016	0.0609	0.0008	633.2	8.5	634.4	29.4	633.8	9.5	0.1	0.1	633.8	9.5	633.8	9.5
47	1	52	92	410.82	1149	360	0.30	0.6609	0.0120	0.0833	0.0013	0.0577	0.0008	515.2	7.3	517.0	30.5	515.5	7.8	0.3	0.1	515.5	7.8	515.5	7.8
47	1	52	92	410.82	922	944	1.00	0.2087	0.0048	0.0296	0.0005	0.0512	0.0010	192.5	4.1	248.8	45.9	188.2	3.1	24.4	-2.3	188.2	3.1	187.8	3.1
47	1	52	92	410.82	831	475	0.60	0.6641	0.0124	0.0829	0.0013	0.0582	0.0009	517.1	7.6	535.9	32.1	513.6	7.8	4.2	-0.7	513.6	7.8	513.3	7.8
47	1	52	92	410.82	934	522	0.60	2.1629	0.0370	0.1988	0.0031	0.0791	0.0010	1169.2	11.9	1172.5	25.2	1169.0	16.6	0.3	0.0	1172.5	16.6	1168.8	25.2
47	1	52	92	410.82	771	380	0.50	0.7250	0.0131	0.0906	0.0013	0.0582	0.0009	553.6	7.7	534.8	34.7	559.0	7.9	-4.5	1.0	559.0	7.9	559.4	7.9
47	1	52	92	410.82	1607	1037	0.60	0.9810	0.0170	0.1092	0.0017	0.0653	0.0008	694.1	8.7	781.8	27.2	668.3	9.9	14.5	-3.9	668.3	9.9	665.6	9.8
47	1	52	92	410.82	2670	697	0.30	1.5349	0.0238	0.1535	0.0022	0.0727	0.0009	944.5	9.6	1003.3	25.0	920.7	12.2	8.2	-2.6	920.7	12.2	917.6	12.2
47	1	52	92	410.82	1237	999	0.80	0.7416	0.0123	0.0914	0.0013	0.0590	0.0008	563.3	7.2	565.4	30.0	563.6	7.8	0.3	0.0	563.6	7.8	563.5	7.8
47	1	52	92	410.82	447	199	0.40	0.7604	0.0152	0.0922	0.0015	0.0599	0.0010	574.2	8.8	599.7	35.1	568.6	8.8	5.2	-1.0	568.6	8.8	568.1	8.8
47	1	52	92	410.82	621	218	0.40	0.6656	0.0131	0.0827	0.0013	0.0585	0.0009	518.0	8.0	547.9	34.4	512.0	7.9	6.6	-1.2	512.0	7.9	511.5	7.9
47	1	52	92	410.82	1236	621	0.50	0.5709	0.0104	0.0703	0.0011	0.0590	0.0008	458.6	6.7	567.6	30.7	437.8	6.7	22.9	-4.7	437.8	6.7	436.0	6.7
47	1	52	92	410.82	834	89	0.10	1.8788	0.0326	0.1813	0.0028	0.0753	0.0010	1073.6	11.5	1076.2	26.0	1073.9	15.5	0.2	0.0	1073.9	15.5	1073.8	15.5
47	1	52	92	410.82	2538	150	0.10	1.6260	0.0274	0.1608	0.0025	0.0735	0.0009	980.3	10.6	1026.9	24.9	961.0	13.8	6.4	-2.0	961.0	13.8	958.4	13.7
47	1	52	92	410.82	517	280	0.50	0.6822	0.0134	0.0843	0.0014	0.0588	0.0009	528.1	8.1	558.3	34.2	521.9	8.0	6.5	-1.2	521.9	8.0	521.3	8.0
47	1	52	92	410.82	1472	527	0.40	1.6171	0.0277	0.1626	0.0025	0.0723	0.0009	976.9	10.8	992.9	25.7	971.1	14.0	2.2	-0.6	971.1	14.0	970.2	14.0
47	1	52	92	410.82	870	114	0.10	0.6904	0.0128	0.0843	0.0013	0.0595	0.0009	533.1	7.7	585.2	31.4	521.7	7.9	10.9	-2.2	521.7	7.9	520.6	7.9
47	1	52	92	410.82	2644	1220	0.50	0.5787	0.0100	0.0702	0.0011	0.0599	0.0008	463.6	6.4	600.4	27.9	437.1	6.6	27.2	-6.1	437.1	6.6	434.9	6.5
47	1	52	92	410.82	971	1204	1.20	0.6917	0.0127	0.0866	0.0014	0.0580	0.0008	533.8	7.6	529.9	31.0	535.5	8.1	-1.0	0.3	535.5	8.1	535.6	8.1
47	1	52	92	410.82	758	377	0.50	0.6616	0.0125	0.0805	0.0013	0.0597	0.0009	515.6	7.6	591.7	32.0	499.3	7.6	15.6	-3.3	499.3	7.6	497.8	7.6
47	1	52	92	410.82	2294	297	0.10	1.4059	0.0246	0.1427	0.0022	0.0716	0.0009	891.4	10.4	974.0	26.9	859.7	12.6	11.7	-3.7	859.7	12.6	855.8	12.5
47	1	52	92	410.82	657	526	0.80	0.6415	0.0125	0.0803	0.0013	0.0580	0.0009	503.2	7.7	529.5	34.1	498.1	7.7	5.9	-1.0	498.1	7.7	497.6	7.7
47	1	52	92	410.82	1100	1034	0.90	1.5706	0.0276	0.1513	0.0024	0.0754	0.0010	958.7	10.9	1079.3	26.5	908.1	13.3	15.9	-5.6	908.1	13.3	901.7	13.2
47	1	52	92	410.82	1168	310	0.30	1.9968	0.0341	0.1888	0.0029	0.0769	0.0010	1114.4	11.6	1116.4	25.1	1115.0	15.9	0.1	0.0	1116.4	15.9	1114.9	25.1
47	1	52	92	410.82	580	514	0.90	0.7714	0.0135	0.0922	0.0014	0.0608	0.0009	580.6	7.8	630.5	32.7	568.7	8.0	9.8	-2.1	568.7	8.0	567.5	8.0
47	1	52	92	410.82	1962	1251	0.60	0.2066	0.0039	0.0299	0.0005	0.0502	0.0008	190.7	3.3	204.6	34.7	189.8	2.9	7.2	-0.4	189.8	2.9	189.8	2.9
47	1	52	92	410.82	287	200	0.70	0.6499	0.0141	0.0798	0.0013	0.0592	0.0011	508.4	8.7	573.5	39.7	494.7	7.9	13.7	-2.8	494.7	7.9	493.5	7.9
47	1	52	92	410.82	1048	879	0.80	0.7073	0.0128	0.0869	0.0014	0.0592	0.0008	543.1	7.6	571.6	30.2	537.0	8.1	6.1	-1.1	537.0	8.1	536.4	8.1
47	1	52	92	410.82	1116	364	0.30	0.6949	0.0125	0.0874	0.0014	0.0578	0.0008	535.7	7.5	521.6	30.1	539.8	8.1	-3.5	0.8	539.8	8.1	540.1	8.1
47	1	52	92	410.82	759	95	0.10	1.8960	0.0354	0.1870	0.0030	0.0737	0.0011	1079.7	12.4	1031.3	29.5	1105.3	16.3	-7.2	2.3	1031.3	16.3	1108.8	27.9
47	1	52	92	410.82	3201	4133	1.30	0.5922	0.0102	0.0745	0.0012	0.0577	0.0007	472.3	6.5	518.5	27.9	463.4	7.0	10.6	-1.9	463.4	7.0	462.6	7.0
47	1	52	92	410.82	376	138	0.40	0.7705	0.0141	0.0961	0.0014	0.0583	0.0009	580.1	8.1	538.9	35.0	591.5	8.4	-9.7	1.9	591.5	8.4	592.5	8.4
47	1	52	92	410.82	531	176	0.30	0.7597	0.0146	0.0930	0.0015	0.0594	0.0009	573.8	8.4	580.1	33.0	573.0	8.8	1.2	-0.1	573.0	8.8	572.8	8.8
47	1	52	92	410.82	183	98	0.50	0.8106	0.0190	0.0959	0.0016	0.0614	0.0012	602.8	10.7	653.0	43.0	590.4	9.7	9.6	-2.1	590.4	9.7	589.1	9.6
47	1	52	92	410.82	1140	111	0.10	1.0666	0.0187	0.1130	0.0018	0.0686	0.0009	737.1	9.2	884.9	26.9	690.3	10.3	22.0	-6.8	690.3	10.3	685.4	10.2
47	1	52	92	410.82	1028	774	0.80	0.7229	0.0131	0.0825	0.0013	0.0637	0.0009	552.4	7.8	731.4	29.7	510.7	7.7	30.2	-8.2	510.7	7.7	506.9	7.7
47	1	52	92	410.82	535	119	0.20	0.6955	0.0140	0.0850	0.0014	0.0595	0.0010	536.1	8.4	583.4	35.5	525.8	8.2	9.9	-2.0	525.8	8.2	524.8	8.2
47	1	52	92	410.82	2365	2130	0.90	0.2911	0.0053	0.0402	0.0006	0.0527	0.0007	259.4	4.1	313.6	31.2	253.8	3.9	19.1	-2.2	253.8	3.9	253.4	3.9
47	1	52	92	410.82	579	532	0.90	0.6493	0.0127	0.0803	0.0013	0.0588	0.0009	508.0	7.8	558.3	33.8	497.6	7.7	10.9	-2.1	497.6	7.7	496.7	7.7
47	1	52	92	410.82	350	127	0.40	0.7142	0.0145	0.0841	0.0014	0.0617	0.0010	547.2	8.6	662.8	35.5	520.6	8.2	21.5	-5.1	520.6	8.2	518.1	8.1
47	1	52	92	410.82	1084	151	0.10	1.4157	0.0227	0.1437	0.0021	0.0716	0.0009	895.5	9.6	972.8	26.6	865.7	11.6	11.0	-3.5	865.7	11.6	862.0	11.6

47	1	52	92	410.82	1171	412	0.40	2.4013	0.0381	0.2117	0.0030	0.0824	0.0011	1243.0	11.4	1254.6	25.1	1237.9	16.1	1.3	-0.4	1254.6	16.1	1236.9	25.4
47	1	52	92	410.82	640	305	0.50	10.5370	0.1803	0.4670	0.0073	0.1639	0.0020	2483.2	16.0	2495.8	21.2	2470.5	32.1	1.0	-0.5	2495.8	32.1	2463.3	21.8
47	1	52	92	410.82	883	879	1.00	0.6858	0.0128	0.0844	0.0013	0.0591	0.0009	530.3	7.7	568.7	31.4	522.0	8.0	8.2	-1.6	522.0	8.0	521.3	8.0
47	1	52	92	410.82	777	489	0.60	0.6248	0.0116	0.0792	0.0013	0.0574	0.0008	492.9	7.3	504.0	31.5	491.1	7.5	2.6	-0.4	491.1	7.5	490.9	7.5
47	1	52	92	410.82	2082	337	0.20	1.3042	0.0210	0.1340	0.0019	0.0707	0.0009	847.6	9.3	947.8	26.8	810.9	11.0	14.4	-4.5	810.9	11.0	806.6	10.9
47	1	52	92	410.82	489	391	0.80	0.8961	0.0156	0.1048	0.0015	0.0621	0.0009	649.6	8.4	676.6	31.8	642.7	9.0	5.0	-1.1	642.7	9.0	642.0	9.0
47	1	52	92	410.82	952	664	0.70	0.2279	0.0049	0.0320	0.0005	0.0518	0.0009	208.5	4.1	276.0	41.2	202.9	3.3	26.5	-2.8	202.9	3.3	202.5	3.2
47	1	52	92	410.82	964	872	0.90	0.3028	0.0062	0.0421	0.0007	0.0523	0.0009	268.6	4.9	296.2	38.5	265.8	4.2	10.3	-1.0	265.8	4.2	265.6	4.2
47	1	52	92	410.82	726	386	0.50	0.6971	0.0133	0.0871	0.0014	0.0582	0.0009	537.1	8.0	535.6	32.8	538.1	8.2	-0.5	0.2	538.1	8.2	538.2	8.2
47	1	52	92	410.82	1699	96	0.10	0.6403	0.0114	0.0791	0.0012	0.0589	0.0008	502.5	7.1	560.6	29.3	490.4	7.4	12.5	-2.5	490.4	7.4	489.3	7.4
47	1	52	92	410.82	562	616	1.10	0.6395	0.0126	0.0801	0.0013	0.0580	0.0009	502.0	7.8	528.8	34.5	496.8	7.7	6.0	-1.0	496.8	7.7	496.3	7.7
47	1	52	92	410.82	1171	222	0.20	0.8328	0.0150	0.1000	0.0016	0.0605	0.0008	615.1	8.3	620.5	29.7	614.5	9.2	1.0	-0.1	614.5	9.2	614.3	9.2
47	1	52	92	410.82	956	41	0.00	1.2180	0.0217	0.1306	0.0021	0.0678	0.0009	808.9	9.9	860.9	28.0	791.1	11.7	8.1	-2.2	791.1	11.7	789.0	11.7
47	1	52	92	410.82	607	240	0.40	1.8979	0.0340	0.1841	0.0029	0.0749	0.0010	1080.4	11.9	1064.9	27.2	1089.4	15.8	-2.3	0.8	1089.4	15.8	1090.5	15.8
47	1	52	92	410.82	1391	1209	0.90	0.1190	0.0027	0.0179	0.0003	0.0484	0.0009	114.2	2.4	118.8	44.4	114.1	1.8	3.9	0.0	114.1	1.8	114.1	1.8
47	1	52	92	410.82	4797	340	0.10	0.7660	0.0122	0.0937	0.0013	0.0594	0.0008	577.5	7.0	579.7	27.9	577.6	7.9	0.4	0.0	577.6	7.9	577.6	7.9
47	1	52	92	410.82	997	118	0.10	4.1364	0.0713	0.2867	0.0045	0.1048	0.0013	1661.5	14.1	1710.2	23.3	1625.2	22.4	5.0	-2.2	1710.2	22.4	1616.6	25.0
47	1	52	92	410.82	3796	682	0.20	0.5254	0.0094	0.0680	0.0011	0.0561	0.0008	428.8	6.3	456.5	30.1	424.1	6.5	7.1	-1.1	424.1	6.5	423.7	6.5
47	1	52	92	410.82	326	426	1.30	5.9068	0.1040	0.3497	0.0055	0.1227	0.0016	1962.2	15.3	1995.6	23.4	1933.0	26.4	3.1	-1.5	1995.6	26.4	1923.8	24.6
47	1	52	92	410.82	834	326	0.40	1.4831	0.0267	0.1507	0.0024	0.0715	0.0010	923.5	10.9	970.5	27.8	905.0	13.3	6.8	-2.0	905.0	13.3	902.6	13.3
47	1	52	92	410.82	777	163	0.20	0.7556	0.0134	0.0935	0.0014	0.0587	0.0009	571.5	7.7	554.6	33.2	576.4	8.1	-3.9	0.9	576.4	8.1	576.8	8.1
47	1	52	92	410.82	370	206	0.60	1.8741	0.0351	0.1824	0.0029	0.0747	0.0011	1072.0	12.4	1058.2	29.2	1080.1	15.9	-2.1	0.8	1080.1	15.9	1081.1	15.9
47	1	52	92	410.82	2181	820	0.40	0.6407	0.0104	0.0817	0.0012	0.0570	0.0008	502.7	6.5	489.0	29.5	506.4	7.0	-3.6	0.7	506.4	7.0	506.7	7.0
47	1	52	92	410.82	864	80	0.10	1.1040	0.0199	0.1191	0.0019	0.0674	0.0009	755.3	9.6	847.7	28.5	725.3	10.8	14.4	-4.1	725.3	10.8	722.1	10.8
47	1	52	92	410.82	422	329	0.80	0.6716	0.0134	0.0849	0.0014	0.0575	0.0009	521.7	8.2	508.6	35.3	525.4	8.1	-3.3	0.7	525.4	8.1	525.7	8.1
47	1	52	92	410.82	652	168	0.30	1.1570	0.0226	0.1250	0.0020	0.0672	0.0010	780.5	10.6	844.3	32.3	759.4	11.6	10.1	-2.8	759.4	11.6	757.0	11.5
47	1	52	92	410.82	1309	1064	0.80	0.2389	0.0048	0.0325	0.0005	0.0534	0.0009	217.5	4.0	344.8	36.9	206.1	3.2	40.2	-5.5	206.1	3.2	205.3	3.2
47	1	52	92	410.82	556	245	0.40	1.6137	0.0296	0.1610	0.0026	0.0728	0.0010	975.6	11.5	1007.8	28.5	962.4	14.2	4.5	-1.4	962.4	14.2	960.7	14.2
47	1	52	92	410.82	233	53	0.20	1.5530	0.0314	0.1610	0.0027	0.0701	0.0011	951.7	12.5	929.8	33.5	962.3	14.7	-3.5	1.1	962.3	14.7	963.6	14.7
55	1	30	70	487.40	531	259	0.50	2.4565	0.0546	0.2068	0.0027	0.0863	0.0019	1259.3	16.1	1344.9	42.1	1211.9	14.7	9.9	-3.9	1344.9	14.7	1204.0	46.5
55	1	30	70	487.40	1417	536	0.40	0.1755	0.0100	0.0380	0.0005	0.0336	0.0019	164.2	8.6	0.0	94.8	240.3	3.2	-1E8	31.7	240.3	3.2	245.5	3.2
55	1	30	70	487.40	1040	390	0.40	2.1506	0.0388	0.1907	0.0024	0.0820	0.0014	1165.2	12.5	1243.7	33.6	1125.4	13.0	9.5	-3.5	1243.7	13.0	1119.2	36.6
55	1	30	70	487.40	620	355	0.60	11.2486	0.1821	0.4451	0.0056	0.1837	0.0028	2543.9	15.2	2686.0	25.2	2373.3	24.9	11.6	-7.2	2686.0	24.9	2285.8	34.5
55	1	30	70	487.40	1964	319	0.20	5.8661	0.0956	0.3353	0.0041	0.1272	0.0019	1956.2	14.2	2058.4	26.9	1864.1	20.0	9.4	-4.9	2058.4	20.0	1836.5	31.8
55	1	30	70	487.40	985	1063	1.10	0.7822	0.0194	0.0789	0.0010	0.0721	0.0018	586.7	11.1	987.6	50.0	489.3	6.2	50.5	-19.9	489.3	6.2	480.4	6.1
55	1	30	70	487.40	348	199	0.60	0.3847	0.0253	0.0304	0.0007	0.0920	0.0063	330.5	18.5	1466.3	129.1	193.1	4.3	86.8	-71.2	193.1	4.3	183.0	4.0
55	1	30	70	487.40	624	409	0.70	9.2759	0.1799	0.4217	0.0054	0.1599	0.0030	2365.6	17.9	2453.9	31.9	2268.0	24.4	7.6	-4.3	2453.9	24.4	2224.5	38.1
55	1	30	70	487.40	187	26	0.10	0.9407	0.0499	0.0895	0.0016	0.0764	0.0041	673.2	26.1	1104.9	108.3	552.5	9.6	50.0	-21.8	552.5	9.6	540.7	9.5
55	1	30	70	487.40	1113	703	0.60	1.7368	0.0420	0.1732	0.0023	0.0729	0.0017	1022.3	15.6	1010.5	48.2	1029.4	12.7	-1.9	0.7	1029.4	12.7	1030.3	12.7
55	1	30	70	487.40	597	408	0.70	0.6801	0.0197	0.0839	0.0011	0.0589	0.0017	526.8	11.9	562.4	62.9	519.5	6.8	7.6	-1.4	519.5	6.8	518.8	6.8
55	1	30	70	487.40	1050	107	0.10	0.6785	0.0150	0.0852	0.0011	0.0579	0.0013	525.9	9.1	525.8	47.4	526.8	6.5	-0.2	0.2	526.8	6.5	526.8	6.5
55	1	30	70	487.40	486	154	0.30	0.6615	0.0187	0.0832	0.0011	0.0578	0.0016	515.5	11.4	521.6	61.5	515.1	6.7	1.2	-0.1	515.1	6.7	515.0	6.7
55	1	30	70	487.40	211	82	0.40	0.7084	0.0282	0.0877	0.0013	0.0587	0.0024	543.8	16.8	555.7	87.7	541.9	7.8	2.5	-0.4	541.9	7.8	541.6	7.8
55	1	30	70	487.40	566	126	0.20	0.8305	0.0199	0.0953	0.0013	0.0633	0.0015	613.9	11.0	718.7	50.0	586.8	7.4	18.4	-4.6	586.8	7.4	584.2	7.3
55	1	30	70	487.40	669	426	0.60	0.6179	0.0182	0.0776	0.0011	0.0579	0.0017	488.5	11.4	523.9	64.5	481.8	6.3	8.0	-1.4	481.8	6.3	481.2	6.3
55	1	30	70	487.40	1435	540	0.40	0.6250	0.0134	0.0782	0.0010	0.0581	0.0012	493.0	8.4	533.7	45.6	485.1	6.0	9.1	-1.6	485.1	6.0	484.4	6.0
55	1	30	70	487.40	2576	995	0.40	0.1293	0.0038	0.0184	0.0003	0.0511	0.0015	123.5	3.4	242.5	67.7	117.6	1.6	51.5	-5.0	117.6	1.6	117.2	1.6
55	1	30	70	487.40	2193	324	0.10	1.4622	0.0233	0.1488	0.0018	0.0714	0.0011	914.9	9.6	969.1	30.1	894.1	10.3	7.7	-2.3	894.1	10.3	891.4	10.3
55	1	30	70	487.40	743	236	0.30	0.6674	0.0157	0.0822	0.0011	0.0590	0.0014	519.1	9.6	565.7	50.3	509.5	6.4	9.9	-1.9	509.5	6.4	508.6	6.4
55	1	30	70	487.40	295	211	0.70	0.8518	0.0268	0.0977	0.0014	0.0634	0.0020	625.6	14.7	719.0	67.1	601.1	8.1	16.4	-4.1	601.1	8.1	598.7	8.0
55	1	30	70	487.40	2364	800	0.30	1.7663	0.0280	0.1707	0.0021	0.0752	0.0011	1033.2	10.3	1073.5	29.5	1016.0	11.6	5.4	-1.7	1016.0	11.6	1013.5	11.6
55	1	30	70	487.40	761	1174	1.50	14.0230	0.2251	0.5603	0.0071	0.1819	0.0027	2751.3	15.3	2669.7	24.9	2867.9	29.4	-7.4	4.1	2669.7	29.4	2959.2	19.7
55	1	30	70	487.40	539	316	0.60	0.1833	0.0112	0.0264	0.0005	0.0504	0.0031	170.9	9.6	212.0	143.0	168.2	2.9	20.6	-1.6	168.2	2.9	168.0	2.9
55	1	30	70	487.40	544	171	0.30	0.8921	0.0279	0.1018	0.0014	0.0637	0.0020	647.5	15.0	730.1	66.6	625.1	8.4	14.4	-3.6	625.1	8.4	622.9	8.4
55	1	30	70	487.40	742	199	0.30	0.6880	0.0177	0.0861	0.0011	0.0581	0.0015	531.6	10.6	531.0	55.5	532.6	6.8	-0.3	0.2	532.6	6.8	532.6	6.8
55	1	30	70	487.40	723	674	0.90	0.6413	0.0177	0.0798	0.0011	0.0584	0.0016	503.1	10.9	543.8	59.9	495.0	6.4	9.0	-1.6	495.0	6.4	494.3	6.4
55	1	30	70	487.40	1267	666	0.50	0.6679	0.0151	0.0845	0.0011	0.0575	0.0013	519.4	9.2	507.9	48.7	523.0	6.5	-3.0	0.7	523.0	6.5	523.2	6.5
55	1	30	70	487.40	2452	178	0.10	0.8435	0.0153	0.1006	0.0013	0.0610	0.0011	621.1	8.4	636.5	37.1	618.0	7.3	2.9	-0.5	618.0	7.3	617.6	7.3
55	1	30	70	487.40	914	597	0.70	0.7427	0.0180	0.0923	0.0012	0.0585	0.0014	564.0	10.5	546.4	52.0	569.3	7.1	-4.2	0.9	569.3	7.1	569.7	7.1
55	1	30	70	487.40	299	452	1.50	0.7969	0.0304	0.0954	0.0014	0.0607	0.0023	595.1	17.2	628.0	82.7	587.5	8.4	6.5	-1.3	587.5	8.4	586.7	8.4
55	1	30	70	487.40	1267	394	0.30	0.7533	0.0201	0.0897	0.0012	0.0611	0.0016	570.1	11.6	641.1	56.7	553.5	7.1	13.7	-3.0	553.5	7.1	551.9	7.1
55	1	30	70	487.40	1238	1122	0.90	0.2813	0.0104	0.0392	0.0006	0.0521	0.0019	251.7	8.3	289.2	85.1	248.1	3.5	14.2	-1.4	248.1	3.5	247.8	3.5
55	1	30	70	487.40	1231	297	0.20	0.7888	0.0169	0.0935	0.0012	0.0613	0.0013	590.5	9.6	649.5	44.5	576.2	7.0	11.3	-2.5	576.2	7.0	574.8	7.0
55	1	30	70	487.40	1352	240	0.20	2.2604	0.0441	0.2010	0.0026	0.0817	0.0015	1200.0	13.7	1238.4	36.8	1180.8	13.8	4.7	-1.6	1238.4	13.8	1177.6	38.4
55	1	30	70	487.40	1306	187	0.10	0.8861	0.0182	0.1021	0.0013	0.0631	0.0013	644.3	9.8	710.3	42.2	626.8	7.6	11.8	-2.8	626.8	7.6	625.0	7.6
55	1	30	70	487.40	544	150	0.30	1.6567	0.0368	0.1625	0.0021	0.0741	0.0016	992.1	14.1	1043.6	43.9	970.7	11.8	7.0	-2.2	970.7	11.8	967.7	11.7
55	1	30	70	487.40	358	137	0.40	1.8721	0.0460	0.1785	0.0024	0.0762	0.0019	1071.3	16.3	1100.5	48.6	1058.8	13.1	3.8	-1.2	1058.8	13.1	1056.9	13.1
55	1	30	70	487.40	2583	455	0.20	0.2640	0.0065	0.0374	0.0005	0.0514	0.0012	237.9	5.2	256.4	55.5	236.4	3.0	7.8	-0.6	236.4	3.0	236.3	3.0
55	1	30	70	487.40	295	373	1.30	0.2534	0.0187	0.0346	0.0007	0.0533	0.0040	229.4	15.1	340.6	169.5	219.0	4.1	35.7	-4.7	219.0	4.1	218.3	4.1
55	1	30	70	487.40	1996	1146	0.60	0.3872	0.0095	0.0516	0.0007	0.0545	0.0013	332.3	7.0	390.8	54.0	324.6	4.1	16.9	-2.4	324.6	4.1	324.0	4.1
55	1	30	70	487.40	697	97	0.10	0.7726	0.0214	0.0925	0.0013	0.0607	0.0017	581.2	12.3	628.4	59.3	570.2	7.4	9.3	-1.9	570.2	7.4	569.1	7.4
55	1	30	70	487.40	1053	304	0.30	0.7495	0.0180	0.0920	0.0012	0.0592	0.0014	567.9	10.4	573.5	51.5	567.5	7.1	1.0	-0.1	567.5	7.1	567.4	7.1
55	1	30	70	487.40	718	259	0.40	0.1709	0.0090	0.0251	0.0004	0.0495	0.0026	160.2	7.8	169.6	124.6	159.8	2.5	5.8	-0.2	159.8	2.5	159.8	2.5
55	1	30	70	487.40	771	233	0.30	0.8534	0.0214	0.1017	0.0013	0.0610	0.0015	626.5	11.7	639.0	53.3	624.1	7.8	2.3	-0.4	624.1	7.8	623.8	7.8
55	1	30	70	487.40	599	209	0.30	0.6039	0.0188	0.0770	0.0011	0.0571	0.0018	479.7	11.9	492.5	68.8	477.9	6.4	3.0	-0.4	477.9	6.4	477.7	6.3
55	1	30	70	487.40	977	160	0.20	1.6019	0.0339	0.1624	0.0021	0.0717	0.0015	970.9	13.3	977.1	42.1	969.8	11.6	0.7	-0.1	969.8	11.6	969.5	11.6
55	1	30	70	487.40	715	463	0.60	1.7949	0.0423	0.1802	0.0024	0.0724	0.0017	1043.6	15.4	997.1	47.2	1067.8	13.0	-7.1	2.3	1067.8	13.0	1071.0	13.0

55	1	30	70	487.40	536	762	1.40	1.7182	0.0364	0.1683	0.0022	0.0742	0.0015	1015.3	13.6	1046.5	41.6	1002.6	12.0	4.2	-1.3	1002.6	12.0	1000.8	12.0
55	1	30	70	487.40	1007	339	0.30	0.4185	0.0112	0.0558	0.0007	0.0545	0.0015	355.0	8.0	389.5	59.8	350.3	4.5	10.1	-1.3	350.3	4.5	349.9	4.5
55	1	30	70	487.40	566	164	0.30	0.3046	0.0121	0.0410	0.0006	0.0540	0.0022	270.0	9.4	368.4	90.2	259.3	3.7	29.6	-4.1	259.3	3.7	258.5	3.7
55	1	30	70	487.40	1224	655	0.50	1.7159	0.0309	0.1694	0.0021	0.0736	0.0013	1014.5	11.6	1030.7	34.7	1008.7	11.6	2.1	-0.6	1008.7	11.6	1007.8	11.6
55	1	30	70	487.40	1000	547	0.50	0.6433	0.0150	0.0817	0.0011	0.0572	0.0013	504.3	9.3	499.0	50.1	506.4	6.3	-1.5	0.4	506.4	6.3	506.5	6.3
55	1	30	70	487.40	1234	360	0.30	0.8035	0.0167	0.0978	0.0012	0.0597	0.0012	598.8	9.4	591.7	43.6	601.7	7.3	-1.7	0.5	601.7	7.3	601.9	7.3
55	1	30	70	487.40	294	162	0.60	2.2702	0.0527	0.2035	0.0027	0.0811	0.0019	1203.1	16.4	1223.0	44.9	1194.0	14.5	2.4	-0.8	1223.0	14.5	1192.4	45.9
55	1	30	70	487.40	1029	563	0.50	0.6704	0.0163	0.0840	0.0011	0.0580	0.0014	521.0	9.9	529.9	52.5	519.8	6.5	1.9	-0.2	519.8	6.5	519.7	6.5
55	1	30	70	487.40	360	492	1.40	0.7792	0.0260	0.0948	0.0014	0.0598	0.0020	585.0	14.9	593.6	72.6	583.9	8.0	1.6	-0.2	583.9	8.0	583.7	8.0
55	1	30	70	487.40	2669	684	0.30	1.5326	0.0269	0.1372	0.0017	0.0812	0.0014	943.5	10.8	1224.9	32.8	829.0	9.6	32.3	-13.8	829.0	9.6	815.0	9.5
55	1	30	70	487.40	597	194	0.30	0.8283	0.0239	0.0990	0.0014	0.0608	0.0018	612.7	13.3	631.9	62.0	608.5	7.9	3.7	-0.7	608.5	7.9	608.1	7.9
55	1	30	70	487.40	2976	970	0.30	1.8332	0.0309	0.1762	0.0022	0.0756	0.0012	1057.4	11.1	1083.9	31.7	1046.4	11.9	3.5	-1.1	1046.4	11.9	1044.7	11.9
55	1	30	70	487.40	1702	511	0.30	1.9852	0.0346	0.1895	0.0024	0.0762	0.0013	1110.5	11.8	1098.4	32.9	1118.6	12.7	-1.8	0.7	1098.4	12.7	1119.5	32.5
55	1	30	70	487.40	262	207	0.80	1.7309	0.0461	0.1714	0.0023	0.0734	0.0019	1020.1	17.2	1024.7	53.5	1019.7	12.8	0.5	0.0	1019.7	12.8	1019.4	12.8
55	1	30	70	487.40	1954	1244	0.60	0.2320	0.0063	0.0341	0.0005	0.0494	0.0013	211.8	5.2	166.8	63.4	216.3	2.8	-29.7	2.1	216.3	2.8	216.6	2.8
55	1	30	70	487.40	607	394	0.60	0.2265	0.0097	0.0319	0.0005	0.0516	0.0022	207.3	8.0	266.7	99.2	202.4	3.0	24.1	-2.4	202.4	3.0	202.1	3.0
55	1	30	70	487.40	128	167	1.30	2.1150	0.0817	0.2029	0.0032	0.0758	0.0030	1153.7	26.6	1087.8	78.3	1191.1	17.4	-9.5	3.1	1087.8	17.4	1196.6	72.6
55	1	30	70	487.40	1078	832	0.80	0.3000	0.0105	0.0386	0.0006	0.0564	0.0020	266.4	8.2	468.7	78.1	244.3	3.4	47.9	-9.0	244.3	3.4	242.7	3.4
55	1	30	70	487.40	1047	1544	1.50	0.1013	0.0054	0.0153	0.0002	0.0482	0.0026	97.9	5.0	110.0	127.3	97.6	1.5	11.2	-0.3	97.6	1.5	97.6	1.5
55	1	30	70	487.40	614	109	0.20	0.6964	0.0238	0.0861	0.0012	0.0588	0.0020	536.6	14.2	558.3	75.0	532.5	7.3	4.6	-0.8	532.5	7.3	532.0	7.3
55	1	30	70	487.40	526	329	0.60	3.4373	0.0702	0.2691	0.0035	0.0928	0.0018	1513.0	16.1	1483.8	37.7	1536.4	17.7	-3.5	1.5	1483.8	17.7	1541.0	36.1
55	1	30	70	487.40	544	279	0.50	5.4805	0.1032	0.3397	0.0043	0.1173	0.0021	1897.5	16.2	1914.4	32.6	1885.1	20.9	1.5	-0.7	1914.4	20.9	1881.1	33.4
55	1	30	70	487.40	786	357	0.50	0.8692	0.0229	0.1019	0.0014	0.0620	0.0016	635.1	12.4	673.8	55.9	625.4	7.9	7.2	-1.6	625.4	7.9	624.3	7.9
55	1	30	70	487.40	1130	252	0.20	1.1303	0.0251	0.1205	0.0016	0.0682	0.0015	767.9	12.0	874.0	45.0	733.2	8.9	16.1	-4.7	733.2	8.9	729.4	8.9
55	1	30	70	487.40	1831	218	0.10	0.7849	0.0172	0.0953	0.0012	0.0599	0.0013	588.3	9.8	598.3	46.0	586.7	7.2	1.9	-0.3	586.7	7.2	586.5	7.2
55	1	30	70	487.40	86	36	0.40	1.6159	0.0875	0.1553	0.0029	0.0756	0.0042	976.4	34.0	1084.4	110.6	930.7	16.1	14.2	-4.9	930.7	16.1	924.8	16.0
55	1	30	70	487.40	471	418	0.90	0.1124	0.0103	0.0160	0.0003	0.0509	0.0048	108.2	9.4	236.6	215.2	102.6	2.1	56.6	-5.4	102.6	2.1	102.2	2.1
55	1	30	70	487.40	494	264	0.50	0.6695	0.0233	0.0819	0.0012	0.0594	0.0021	520.4	14.2	581.5	76.1	507.5	7.0	12.7	-2.6	507.5	7.0	506.2	7.0
55	1	30	70	487.40	1772	593	0.30	1.4549	0.0274	0.1464	0.0018	0.0723	0.0013	911.9	11.3	992.1	36.7	880.6	10.3	11.2	-3.5	880.6	10.3	876.7	10.3
55	1	30	70	487.40	153	179	1.20	0.2978	0.0298	0.0393	0.0009	0.0551	0.0056	264.7	23.3	414.1	227.3	248.6	5.7	40.0	-6.5	248.6	5.7	247.4	5.7
55	1	30	70	487.40	552	211	0.40	1.9273	0.0428	0.1845	0.0024	0.0759	0.0017	1090.6	14.9	1092.1	43.6	1091.6	13.0	0.0	0.1	1091.6	13.0	1091.6	13.0
55	1	30	70	487.40	786	674	0.90	0.3016	0.0109	0.0427	0.0006	0.0514	0.0019	267.6	8.5	256.0	83.3	269.5	3.8	-5.3	0.7	269.5	3.8	269.6	3.8
55	1	30	70	487.40	1004	522	0.50	0.1379	0.0083	0.0190	0.0003	0.0529	0.0032	131.1	7.4	321.3	139.3	121.1	2.2	62.3	-8.3	121.1	2.2	120.4	2.1
55	1	30	70	487.40	965	690	0.70	0.6098	0.0176	0.0744	0.0010	0.0596	0.0017	483.4	11.1	586.3	62.7	462.7	6.1	21.1	-4.5	462.7	6.1	460.9	6.0
55	1	30	70	487.40	1390	73	0.10	0.6818	0.0152	0.0833	0.0011	0.0595	0.0013	527.9	9.2	584.1	47.5	515.8	6.3	11.7	-2.3	515.8	6.3	514.7	6.3
55	1	30	70	487.40	743	249	0.30	0.6857	0.0178	0.0845	0.0011	0.0590	0.0015	530.2	10.7	564.6	56.2	523.2	6.7	7.3	-1.3	523.2	6.7	522.5	6.7
55	1	30	70	487.40	868	517	0.60	0.6312	0.0175	0.0794	0.0011	0.0578	0.0016	496.8	10.9	520.4	60.4	492.6	6.3	5.3	-0.9	492.6	6.3	492.2	6.3
55	1	30	70	487.40	388	196	0.50	0.7040	0.0228	0.0903	0.0013	0.0567	0.0018	541.2	13.6	476.9	71.8	557.5	7.5	-16.9	2.9	557.5	7.5	559.0	7.5
55	1	30	70	487.40	702	559	0.80	0.7434	0.0190	0.0920	0.0012	0.0588	0.0015	564.4	11.1	557.6	55.0	567.1	7.1	-1.7	0.5	567.1	7.1	567.2	7.2
55	1	30	70	487.40	232	106	0.50	0.6951	0.0294	0.0863	0.0013	0.0586	0.0025	535.9	17.6	549.4	93.3	533.6	7.9	2.9	-0.4	533.6	7.9	533.3	7.9
55	1	30	70	487.40	2505	1492	0.60	0.3101	0.0074	0.0424	0.0005	0.0532	0.0012	274.2	5.7	334.2	52.9	267.7	3.3	19.9	-2.4	267.7	3.3	267.2	3.3
55	1	30	70	487.40	536	288	0.50	0.6834	0.0220	0.0860	0.0012	0.0578	0.0019	528.8	13.3	520.8	71.0	531.6	7.1	-2.1	0.5	531.6	7.1	531.8	7.1
55	1	30	70	487.40	509	160	0.30	0.7007	0.0215	0.0874	0.0012	0.0583	0.0018	539.2	12.8	538.6	67.3	540.3	7.1	-0.3	0.2	540.3	7.1	540.4	7.1
55	1	30	70	487.40	591	658	1.10	0.6310	0.0193	0.0810	0.0011	0.0566	0.0017	496.7	12.0	475.0	67.6	502.3	6.6	-5.7	1.1	502.3	6.6	502.7	6.6
55	1	30	70	487.40	1223	173	0.10	0.6822	0.0166	0.0859	0.0011	0.0578	0.0014	528.1	10.1	519.7	52.9	530.9	6.6	-2.2	0.5	530.9	6.6	531.1	6.6
55	1	30	70	487.40	398	198	0.50	1.6325	0.0418	0.1610	0.0022	0.0737	0.0019	982.8	16.1	1032.4	51.3	962.3	12.0	6.8	-2.1	962.3	12.0	959.6	12.0
55	1	30	70	487.40	1578	1830	1.20	0.2703	0.0086	0.0352	0.0005	0.0558	0.0018	242.9	6.9	441.8	71.4	223.3	3.1	49.5	-8.8	223.3	3.1	221.8	3.0
55	1	30	70	487.40	3044	604	0.20	0.8995	0.0174	0.1076	0.0013	0.0608	0.0011	651.4	9.3	630.8	40.1	658.6	7.8	-4.4	1.1	658.6	7.8	659.2	7.8
55	1	30	70	487.40	587	401	0.70	1.8744	0.0416	0.1821	0.0024	0.0748	0.0016	1072.1	14.7	1063.3	43.9	1078.2	12.8	-1.4	0.6	1078.2	12.8	1078.9	12.8
55	1	30	70	487.40	569	304	0.50	0.6404	0.0193	0.0813	0.0011	0.0573	0.0017	502.6	11.9	501.3	66.1	503.7	6.6	-0.5	0.2	503.7	6.6	503.7	6.6
55	1	30	70	487.40	566	217	0.40	0.7009	0.0211	0.0888	0.0012	0.0574	0.0017	539.3	12.6	504.8	66.0	548.5	7.2	-8.7	1.7	548.5	7.2	549.3	7.2
55	1	30	70	487.40	295	159	0.50	0.6657	0.0261	0.0838	0.0012	0.0577	0.0023	518.1	15.9	518.5	86.7	518.9	7.4	-0.1	0.2	518.9	7.4	518.9	7.4
55	1	30	70	487.40	1209	202	0.20	1.5023	0.0314	0.1529	0.0019	0.0714	0.0015	931.3	12.7	968.0	41.5	917.4	10.9	5.2	-1.5	917.4	10.9	915.5	10.8
55	1	30	70	487.40	630	315	0.50	0.6472	0.0204	0.0821	0.0011	0.0573	0.0018	506.8	12.5	503.6	69.1	508.3	6.7	-0.9	0.3	508.3	6.7	508.4	6.7
55	1	30	70	487.40	56	20	0.40	0.6781	0.0721	0.0851	0.0021	0.0579	0.0063	525.6	43.6	526.5	236.9	526.3	12.7	0.0	0.1	526.3	12.7	526.3	12.7
55	1	30	70	487.40	1209	533	0.40	0.8166	0.0202	0.0975	0.0013	0.0609	0.0015	606.1	11.3	634.0	52.7	599.7	7.5	5.4	-1.1	599.7	7.5	599.0	7.5
55	1	30	70	487.40	234	142	0.60	0.6972	0.0335	0.0893	0.0014	0.0568	0.0028	537.1	20.1	481.6	107.8	551.3	8.5	-14.5	2.6	551.3	8.5	552.5	8.5
55	1	30	70	487.40	435	194	0.40	0.7872	0.0267	0.0950	0.0014	0.0603	0.0021	589.6	15.2	611.6	73.9	584.9	8.0	4.4	-0.8	584.9	8.0	584.3	7.9
55	1	30	70	487.40	611	737	1.20	0.2778	0.0128	0.0372	0.0006	0.0543	0.0025	248.9	10.1	380.8	104.8	235.6	3.6	38.1	-5.7	235.6	3.6	234.6	3.6
55	1	30	70	487.40	742	611	0.80	0.2054	0.0100	0.0289	0.0005	0.0516	0.0025	189.7	8.4	268.0	112.4	183.8	2.8	31.4	-3.2	183.8	2.8	183.4	2.8
55	1	30	70	487.40	619	291	0.50	0.6748	0.0225	0.0838	0.0012	0.0585	0.0020	523.6	13.6	548.3	73.2	518.8	7.0	5.4	-0.9	518.8	7.0	518.3	7.0
55	1	30	70	487.40	403	499	1.20	0.1884	0.0146	0.0277	0.0005	0.0495	0.0039	175.3	12.4	171.5	182.9	175.9	3.3	-2.6	0.3	175.9	3.3	175.9	3.3
55	1	30	70	487.40	116	31	0.30	0.7762	0.0495	0.0959	0.0018	0.0588	0.0038	583.3	28.3	560.2	141.2	590.3	10.4	-5.4	1.2	590.3	10.4	590.9	10.4
55	1	30	70	487.40	1004	154	0.20	1.0532	0.0268	0.1201	0.0016	0.0637	0.0016	730.5	13.3	731.4	53.6	731.4	9.1	0.0	0.1	731.4	9.1	731.4	9.1
55	1	30	70	487.40	2021	1331	0.70	0.2148	0.0084	0.0310	0.0005	0.0504	0.0020	197.5	7.0	212.9	91.5	196.6	2.8	7.6	-0.5	196.6	2.8	196.5	2.8
55	1	30	70	487.40	730	376	0.50	0.6315	0.0201	0.0817	0.0011	0.0562	0.0018	497.0	12.5	458.1	70.7	506.3	6.7	-10.5	1.8	506.3	6.7	507.1	6.7
55	1	30	70	487.40	856	694	0.80	0.6722	0.0193	0.0834	0.0011	0.0586	0.0017	522.0	11.7	549.8	62.7	516.6	6.7	6.0	-1.1	516.6	6.7	516.0	6.7
55	1	30	70	487.40	357	138	0.40	0.7905	0.0279	0.0924	0.0013	0.0622	0.0022	591.5	15.8	679.0	76.0	569.9	7.9	16.1	-3.8	569.9	7.9	567.8	7.9
55	1	30	70	487.40	1405	711	0.50	0.2588	0.0080	0.0375	0.0005	0.0502	0.0015	233.7	6.4	202.8	71.3	237.2	3.2	-17.0	1.5	237.2	3.2	237.4	3.2
55	1	30	70	487.40	2092	852	0.40	0.1753	0.0053	0.0254	0.0003	0.0501	0.0015	164.0	4.5	200.0	69.5	161.8	2.1	19.1	-1.4	161.8	2.1	161.7	2.1
55	1	30	70	487.40	639	483	0.80	0.6929	0.0200	0.0852	0.0012	0.0591	0.0017	534.5	12.0	570.2	63.0	527.0	6.8	7.6	-1.4	527.0	6.8	526.3	6.8
55	1	30	70	487.40	1063	491	0.50	0.2734	0.0109	0.0389	0.0006	0.0511	0.0021	245.4	8.7	242.1	92.6	246.2	3.5	-1.7	0.3	246.2	3.5	246.2	3.5
55	1	30	70	487.40	2162	1250	0.60	0.2365	0.0068	0.0343	0.0005	0.0502	0.0014	215.5	5.6	200.9	66.2	217.3	2.8	-8.1	0.8	217.3	2.8	217.4	2.8
55	1	30	70	487.40	1984	1266	0.60	0.2219	0.0067	0.0328	0.0004	0.0492	0.0015	203.5	5.6	155.4	70.5	208.0	2.7	-33.9	2.2	208.0	2.7	208.3	2.8
55	1	30	70	487.40	924	564	0.60	0.9274	0.0231	0.1077	0.0014	0.0626	0.0015	666.2	12.2	693.7	52.5	659.3	8.2	5.0	-1.1	659.3	8.2	658.5	8.2
55	1	30	70	487.40	1440	639	0.40	0.6853	0.0168	0.0853	0.0011	0.0584	0.0014	530.0	10.1	544.2	53.2	527.5	6.6	3.1	-0.5	527.5	6.6	527.2	6.6
55	1	30	70	487.40	778	351	0.50	0.7680	0.0209	0.0853	0.0011	0.0655	0.0018	578.6	12.0	788.2	57.1	527.5	6.8	33.1	-9.7	527.5	6.8	522.8	6.7

55	1	30	70	487.40	1571	895	0.60	0.2865	0.0083	0.0402	0.0005	0.0519	0.0015	255.8	6.5	278.7	66.2	253.8	3.3	8.9	-0.8	253.8	3.3	253.6	3.3
55	1	30	70	487.40	574	125	0.20	0.7303	0.0223	0.0908	0.0012	0.0585	0.0018	556.7	13.1	546.8	66.9	560.1	7.3	-2.4	0.6	560.1	7.3	560.4	7.3
55	1	30	70	487.40	617	420	0.70	0.1977	0.0101	0.0271	0.0004	0.0531	0.0028	183.2	8.6	331.2	117.5	172.2	2.8	48.0	-6.4	172.2	2.8	171.4	2.8
55	1	30	70	487.40	3125	1139	0.40	0.1863	0.0051	0.0275	0.0004	0.0492	0.0013	173.4	4.3	155.4	63.4	175.1	2.3	-12.7	0.9	175.1	2.3	175.2	2.3
55	1	30	70	487.40	9600	3412	0.40	0.2366	0.0052	0.0337	0.0004	0.0510	0.0011	215.6	4.2	240.7	49.3	213.7	2.6	11.2	-0.9	213.7	2.6	213.6	2.6
55	1	30	70	487.40	329	296	0.90	0.1007	0.0108	0.0148	0.0003	0.0494	0.0054	97.4	10.0	166.8	254.4	94.8	2.2	43.2	-2.8	94.8	2.2	94.6	2.2
55	1	30	70	487.40	2361	1356	0.60	2.0265	0.0416	0.1860	0.0023	0.0792	0.0016	1124.4	14.0	1176.0	39.6	1099.7	12.7	6.5	-2.3	1099.7	12.7	1095.9	12.7
55	1	30	70	487.40	873	1012	1.20	0.8777	0.0234	0.1047	0.0014	0.0609	0.0016	639.7	12.7	636.1	57.3	641.8	8.1	-0.9	0.3	641.8	8.1	642.0	8.1
61	2	40	80	546.55	991	198	0.20	0.9277	0.0103	0.1100	0.0011	0.0613	0.0007	666.4	5.4	648.1	25.3	672.9	6.2	-3.8	1.0	672.9	6.2	673.4	6.2
61	2	40	80	546.55	265	58	0.20	1.9147	0.0226	0.1833	0.0018	0.0759	0.0010	1086.2	7.9	1091.5	25.2	1085.1	9.9	0.6	-0.1	1085.1	9.9	1084.8	9.9
61	2	40	80	546.55	1732	652	0.40	0.4029	0.0045	0.0535	0.0005	0.0547	0.0007	343.7	3.3	400.6	26.7	335.9	3.2	16.1	-2.3	335.9	3.2	335.3	3.2
61	2	40	80	546.55	1203	350	0.30	1.8759	0.0195	0.1754	0.0017	0.0777	0.0009	1072.6	6.9	1139.1	22.2	1041.6	9.2	8.6	-3.0	1041.6	9.2	1037.2	9.2
61	2	40	80	546.55	713	375	0.50	2.6506	0.0284	0.2317	0.0023	0.0831	0.0010	1314.8	7.9	1271.4	22.5	1343.5	11.8	-5.7	2.1	1271.4	11.8	1348.3	21.3
61	2	40	80	546.55	691	240	0.30	0.8589	0.0100	0.0922	0.0009	0.0677	0.0009	629.5	5.5	858.8	26.2	568.4	5.4	33.8	-10.7	568.4	5.4	562.5	5.3
61	2	40	80	546.55	589	131	0.20	1.8135	0.0197	0.1762	0.0017	0.0748	0.0009	1050.4	7.1	1062.2	23.5	1046.1	9.4	1.5	-0.4	1046.1	9.4	1045.4	9.4
61	2	40	80	546.55	1948	1108	0.60	0.1774	0.0024	0.0252	0.0003	0.0511	0.0007	165.8	2.0	244.8	33.0	160.6	1.6	34.4	-3.3	160.6	1.6	160.3	1.6
61	2	40	80	546.55	1063	455	0.40	0.9268	0.0105	0.1099	0.0011	0.0613	0.0007	665.9	5.6	648.8	26.0	671.9	6.2	-3.6	0.9	671.9	6.2	672.5	6.2
61	2	40	80	546.55	1620	1083	0.70	0.1566	0.0025	0.0224	0.0002	0.0508	0.0009	147.7	2.2	231.2	38.7	142.7	1.5	38.3	-3.5	142.7	1.5	142.4	1.4
61	2	40	80	546.55	2284	1678	0.70	1.6289	0.0169	0.1548	0.0015	0.0765	0.0009	981.4	6.6	1107.0	22.4	927.5	8.3	16.2	-5.8	927.5	8.3	920.6	8.2
61	2	40	80	546.55	691	180	0.30	0.8313	0.0098	0.1030	0.0010	0.0586	0.0007	614.3	5.5	552.8	27.6	632.0	5.9	-14.3	2.8	632.0	5.9	633.7	5.9
61	2	40	80	546.55	1427	848	0.60	1.7159	0.0179	0.1577	0.0015	0.0791	0.0009	1014.5	6.7	1173.2	22.2	943.9	8.4	19.6	-7.5	943.9	8.4	934.6	8.3
61	2	40	80	546.55	1010	616	0.60	0.2329	0.0032	0.0320	0.0003	0.0529	0.0008	212.5	2.7	321.8	33.6	203.1	2.0	36.9	-4.6	203.1	2.0	202.4	2.0
61	2	40	80	546.55	1344	206	0.20	1.7814	0.0189	0.1755	0.0017	0.0738	0.0008	1038.7	6.9	1034.5	22.9	1042.2	9.3	-0.7	0.3	1042.2	9.3	1042.5	9.3
61	2	40	80	546.55	1225	116	0.10	0.7275	0.0081	0.0910	0.0009	0.0581	0.0007	555.1	4.8	533.3	26.1	561.2	5.2	-5.2	1.1	561.2	5.2	561.7	5.2
61	2	40	80	546.55	367	253	0.70	1.8263	0.0208	0.1746	0.0017	0.0760	0.0009	1054.9	7.5	1094.2	24.4	1037.6	9.5	5.2	-1.7	1037.6	9.5	1035.1	9.4
61	2	40	80	546.55	1432	2425	1.70	0.1934	0.0026	0.0273	0.0003	0.0515	0.0007	179.6	2.2	263.6	33.0	173.5	1.7	34.2	-3.5	173.5	1.7	173.1	1.7
61	2	40	80	546.55	1681	2454	1.50	0.2845	0.0034	0.0363	0.0004	0.0569	0.0007	254.2	2.7	486.3	28.4	230.1	2.2	52.7	-10.5	230.1	2.2	228.4	2.2
61	2	40	80	546.55	1439	756	0.50	1.8342	0.0192	0.1727	0.0017	0.0772	0.0009	1057.8	6.9	1124.9	22.4	1027.0	9.1	8.7	-3.0	1027.0	9.1	1022.6	9.1
61	2	40	80	546.55	2745	1521	0.60	0.5228	0.0060	0.0634	0.0006	0.0599	0.0007	427.0	4.0	599.7	26.8	396.3	3.8	33.9	-7.8	396.3	3.8	393.7	3.7
61	2	40	80	546.55	2159	1432	0.70	0.0781	0.0018	0.0122	0.0001	0.0467	0.0011	76.3	1.7	32.3	56.5	77.9	0.8	-140.9	1.9	77.9	0.8	77.9	0.8
61	2	40	80	546.55	951	347	0.40	0.7316	0.0091	0.0878	0.0009	0.0606	0.0008	557.5	5.4	623.4	28.9	542.3	5.2	13.0	-2.8	542.3	5.2	540.8	5.2
61	2	40	80	546.55	1276	96	0.10	0.1816	0.0042	0.0270	0.0003	0.0489	0.0012	169.4	3.6	142.9	57.6	171.6	2.1	-20.0	1.3	171.6	2.1	171.7	2.1
61	2	40	80	546.55	1223	262	0.20	1.0074	0.0120	0.1170	0.0012	0.0626	0.0008	707.5	6.1	692.7	27.0	713.3	6.7	-3.0	0.8	713.3	6.7	713.8	6.7
61	2	40	80	546.55	764	280	0.40	0.6666	0.0098	0.0836	0.0009	0.0580	0.0009	518.6	6.0	527.6	34.1	517.3	5.2	2.0	-0.3	517.3	5.2	517.2	5.2
61	2	40	80	546.55	1538	634	0.40	1.5928	0.0176	0.1600	0.0016	0.0724	0.0009	967.4	6.9	995.2	24.0	956.7	8.7	3.9	-1.1	956.7	8.7	955.2	8.7
61	2	40	80	546.55	1385	389	0.30	1.0241	0.0112	0.1110	0.0011	0.0671	0.0008	716.0	5.6	838.7	24.3	678.4	6.3	19.1	-5.5	678.4	6.3	674.5	6.2
61	2	40	80	546.55	2277	951	0.40	0.6465	0.0076	0.0786	0.0008	0.0598	0.0008	506.3	4.7	593.9	27.3	487.8	4.6	17.9	-3.8	487.8	4.6	486.2	4.6
61	2	40	80	546.55	571	522	0.90	0.6221	0.0089	0.0757	0.0008	0.0597	0.0009	491.1	5.6	592.5	32.8	470.4	4.7	20.6	-4.4	470.4	4.7	468.6	4.7
61	2	40	80	546.55	2942	451	0.20	0.9164	0.0107	0.1044	0.0010	0.0638	0.0008	660.4	5.7	734.7	26.6	639.9	6.0	12.9	-3.2	639.9	6.0	637.8	6.0
61	2	40	80	546.55	433	165	0.40	0.6668	0.0113	0.0841	0.0009	0.0576	0.0010	518.8	6.9	514.7	39.3	520.5	5.4	-1.1	0.3	520.5	5.4	520.6	5.4
61	2	40	80	546.55	2204	121	0.10	1.6395	0.0187	0.1652	0.0016	0.0721	0.0009	985.5	7.2	988.7	24.7	985.6	9.0	0.3	0.0	985.6	9.0	985.4	9.0
61	2	40	80	546.55	735	234	0.30	1.5814	0.0182	0.1594	0.0016	0.0721	0.0009	962.9	7.2	987.6	25.0	953.6	8.8	3.4	-1.0	953.6	8.8	952.3	8.8
61	2	40	80	546.55	628	593	0.90	0.6894	0.0087	0.0850	0.0009	0.0589	0.0008	532.4	5.3	563.9	29.3	525.9	5.1	6.7	-1.2	525.9	5.1	525.3	5.1
61	2	40	80	546.55	346	22	0.10	0.7168	0.0125	0.0880	0.0010	0.0592	0.0011	548.8	7.4	572.7	40.1	543.9	5.7	5.0	-0.9	543.9	5.7	543.4	5.7
61	2	40	80	546.55	548	266	0.50	1.6701	0.0214	0.1651	0.0017	0.0735	0.0010	997.2	8.2	1027.1	27.6	985.1	9.4	4.1	-1.2	985.1	9.4	983.4	9.4
61	2	40	80	546.55	711	407	0.60	0.6504	0.0084	0.0826	0.0008	0.0572	0.0008	508.7	5.2	498.6	30.1	511.7	4.9	-2.6	0.6	511.7	4.9	512.0	5.0
61	2	40	80	546.55	436	347	0.80	0.6586	0.0092	0.0829	0.0009	0.0578	0.0009	513.8	5.7	520.1	32.7	513.1	5.1	1.3	-0.1	513.1	5.1	513.0	5.1
61	2	40	80	546.55	888	339	0.40	1.6759	0.0182	0.1666	0.0016	0.0731	0.0008	999.4	6.9	1016.1	23.4	993.2	9.0	2.2	-0.6	993.2	9.0	992.3	9.0
61	2	40	80	546.55	10500	2557	0.20	0.1084	0.0013	0.0163	0.0002	0.0485	0.0006	104.5	1.2	120.2	29.3	104.0	1.0	13.5	-0.5	104.0	1.0	103.9	1.0
61	2	40	80	546.55	932	280	0.30	0.8489	0.0101	0.1027	0.0010	0.0601	0.0008	624.1	5.5	605.1	27.5	630.3	6.0	-4.2	1.0	630.3	6.0	630.8	6.0
61	2	40	80	546.55	3713	56	0.00	0.5859	0.0062	0.0750	0.0007	0.0568	0.0006	468.2	4.0	482.0	25.0	466.1	4.3	3.3	-0.4	466.1	4.3	465.9	4.3
61	2	40	80	546.55	1029	369	0.40	2.0460	0.0219	0.1947	0.0019	0.0764	0.0009	1131.0	7.3	1103.9	22.9	1146.7	10.2	-3.9	1.4	1103.9	10.2	1148.9	22.2
61	2	40	80	546.55	1404	781	0.60	0.2536	0.0034	0.0352	0.0004	0.0523	0.0008	229.5	2.8	298.0	32.8	223.2	2.2	25.1	-2.8	223.2	2.2	222.7	2.2
61	2	40	80	546.55	639	634	1.00	0.7715	0.0094	0.0941	0.0009	0.0596	0.0008	580.6	5.4	588.8	28.1	579.4	5.5	1.6	-0.2	579.4	5.5	579.3	5.5
61	2	40	80	546.55	557	743	1.30	0.5964	0.0085	0.0760	0.0008	0.0570	0.0009	475.0	5.4	492.1	33.3	472.1	4.7	4.1	-0.6	472.1	4.7	471.9	4.7
61	2	40	80	546.55	714	974	1.40	0.2448	0.0041	0.0348	0.0004	0.0512	0.0009	222.4	3.3	248.8	40.5	220.2	2.3	11.5	-1.0	220.2	2.3	220.0	2.3
61	2	40	80	546.55	918	622	0.70	0.9801	0.0112	0.1140	0.0011	0.0625	0.0008	693.6	5.7	689.3	25.7	696.0	6.5	-1.0	0.3	696.0	6.5	696.2	6.5
61	2	40	80	546.55	942	3104	3.30	0.7377	0.0089	0.0907	0.0009	0.0591	0.0008	561.1	5.2	570.5	28.1	559.6	5.3	1.9	-0.3	559.6	5.3	559.4	5.3
61	2	40	80	546.55	907	351	0.40	0.6285	0.0080	0.0798	0.0008	0.0573	0.0008	495.1	5.0	500.2	29.7	494.7	4.8	1.1	-0.1	494.7	4.8	494.7	4.8
61	2	40	80	546.55	1650	293	0.20	1.4052	0.0151	0.1410	0.0014	0.0724	0.0008	891.2	6.4	996.9	23.1	850.4	7.8	14.7	-4.8	850.4	7.8	845.5	7.7
61	2	40	80	546.55	1663	300	0.20	0.9406	0.0103	0.1101	0.0011	0.0621	0.0007	673.2	5.4	676.6	24.9	673.2	6.2	0.5	0.0	673.2	6.2	673.1	6.2
61	2	40	80	546.55	5561	1289	0.20	0.7692	0.0081	0.0913	0.0009	0.0613	0.0007	579.3	4.7	647.4	24.0	563.0	5.2	13.0	-2.9	563.0	5.2	561.4	5.2
61	2	40	80	546.55	830	252	0.30	0.1988	0.0033	0.0283	0.0003	0.0510	0.0009	184.1	2.8	241.6	40.7	180.0	1.9	25.5	-2.3	180.0	1.9	179.7	1.9
61	2	40	80	546.55	1051	483	0.50	0.6446	0.0076	0.0817	0.0008	0.0574	0.0007	505.2	4.7	504.8	27.3	506.0	4.8	-0.2	0.2	506.0	4.8	506.0	4.8
61	2	40	80	546.55	1885	919	0.50	0.1056	0.0017	0.0157	0.0002	0.0490	0.0009	101.9	1.6	147.7	40.7	100.1	1.1	32.2	-1.8	100.1	1.1	100.0	1.1
61	2	40	80	546.55	808	549	0.70	0.6213	0.0077	0.0792	0.0008	0.0570	0.0008	490.7	4.8	492.1	29.1	491.2	4.7	0.2	0.1	491.2	4.7	491.2	4.7
61	2	40	80	546.55	265	343	1.30	0.2418	0.0063	0.0347	0.0004	0.0507	0.0014	219.9	5.1	225.3	62.5	219.7	2.6	2.5	-0.1	219.7	2.6	219.7	2.6
61	2	40	80	546.55	1111	607	0.50	0.6586	0.0077	0.0830	0.0008	0.0577	0.0007	513.8	4.7	516.3	27.1	514.1	4.9	0.4	0.1	514.1	4.9	514.0	4.9
61	2	40	80	546.55	7381	425	0.10	0.7105	0.0075	0.0864	0.0008	0.0597	0.0007	545.0	4.5	592.8	24.4	534.4	4.9	9.8	-2.0	534.4	4.9	533.4	4.9
61	2	40	80	546.55	493	191	0.40	0.2720	0.0048	0.0378	0.0004	0.0523	0.0010	244.3	3.8	296.2	42.0	239.2	2.5	19.2	-2.1	239.2	2.5	238.9	2.5
61	2	40	80	546.55	1230	229	0.20	0.6732	0.0083	0.0842	0.0008	0.0581	0.0008	522.6	5.0	532.2	28.7	521.3	5.0	2.1	-0.3	521.3	5.0	521.1	5.0
61	2	40	80	546.55	2155	366	0.20	2.0229	0.0225	0.1690	0.0017	0.0870	0.0010	1123.2	7.6	1359.4	23.0	1006.7	9.2	25.9	-11.6	1006.7	9.2	990.1	9.1
61	2	40	80	546.55	767	307	0.40	1.3286	0.0156	0.1394	0.0014	0.0693	0.0009	858.3	6.8	906.2	25.7	841.2	7.9	7.2	-2.0	841.2	7.9	839.1	7.9
61	2	40	80	546.55	752	564	0.70	0.1089	0.0027	0.0168	0.0002	0.0472	0.0012	105.0	2.5	59.3	62.1	107.2	1.3	-80.8	2.1	107.2	1.3	107.3	1.3
61	2	40	80	546.55	1551	1101	0.70	0.2383	0.0036	0.0329	0.0003	0.0527	0.0008	217.0	2.9	314.9	36.3	208.4	2.1	33.8	-4.1	208.4	2.1	207.8	2.1
61	2	40	80	546.55	1512	786	0.50	0.1174	0.0020	0.0175	0.0002	0.0489	0.0009	112.7	1.8	140.1	41.9	111.6	1.2	20.3	-1.0	111.6	1.2	111.6	1.2
61	2	40	80	546.55	1674	908	0.50	0.2187	0.0029	0.0318	0.0003	0.0500	0.0007	200.8	2.5	195.8	33.0	201.6	2.0	-2.9	0.4	201.6	2.0	201.6	2.0

61	2	40	80	546.55	1325	587	0.40	0.6313	0.0076	0.0804	0.0008	0.0571	0.0007	496.9	4.8	494.0	28.3	498.3	4.8	-0.9	0.3	498.3	4.8	498.4	4.8
61	2	40	80	546.55	544	326	0.60	0.1034	0.0032	0.0151	0.0002	0.0498	0.0016	99.9	2.9	183.2	74.0	96.6	1.2	47.3	-3.4	96.6	1.2	96.4	1.2
61	2	40	80	546.55	729	202	0.30	1.8833	0.0212	0.1779	0.0018	0.0770	0.0009	1075.2	7.5	1119.0	24.0	1055.4	9.6	5.7	-1.9	1055.4	9.6	1052.5	9.6
61	2	40	80	546.55	528	311	0.60	1.3350	0.0163	0.1445	0.0015	0.0672	0.0009	861.1	7.1	842.1	26.8	869.8	8.2	-3.3	1.0	869.8	8.2	870.7	8.2
61	2	40	80	546.55	95	22	0.20	0.8179	0.0206	0.0968	0.0012	0.0614	0.0016	606.9	11.5	652.0	56.7	595.8	7.2	8.6	-1.9	595.8	7.2	594.7	7.2
61	2	40	80	546.55	867	521	0.60	1.9848	0.0226	0.1903	0.0019	0.0758	0.0009	1110.3	7.7	1088.6	24.2	1123.2	10.2	-3.2	1.1	1088.6	10.2	1124.9	23.6
61	2	40	80	546.55	211	142	0.70	1.0994	0.0207	0.1254	0.0015	0.0637	0.0013	753.1	10.0	731.7	42.3	761.4	8.5	-4.1	1.1	761.4	8.5	762.2	8.5
61	2	40	80	546.55	3755	3069	0.80	0.2410	0.0030	0.0337	0.0003	0.0520	0.0007	219.2	2.4	282.6	30.0	213.7	2.1	24.4	-2.6	213.7	2.1	213.3	2.1
61	2	40	80	546.55	430	125	0.30	0.7458	0.0125	0.0909	0.0010	0.0597	0.0011	565.8	7.3	590.3	38.6	560.6	5.9	5.0	-0.9	560.6	5.9	560.0	5.9
61	2	40	80	546.55	1410	1034	0.70	0.7450	0.0095	0.0915	0.0009	0.0592	0.0008	565.3	5.6	573.1	29.5	564.3	5.5	1.5	-0.2	564.3	5.5	564.1	5.5
61	2	40	80	546.55	1236	524	0.40	0.6650	0.0093	0.0825	0.0009	0.0586	0.0009	517.7	5.7	551.7	32.1	510.8	5.1	7.4	-1.3	510.8	5.1	510.2	5.1
61	2	40	80	546.55	1873	1191	0.60	0.1172	0.0025	0.0174	0.0002	0.0489	0.0011	112.5	2.2	141.0	51.9	111.4	1.3	21.0	-1.0	111.4	1.3	111.3	1.3
61	2	40	80	546.55	2204	1500	0.70	0.6408	0.0096	0.0801	0.0009	0.0582	0.0009	502.8	5.9	534.8	34.7	496.7	5.1	7.1	-1.2	496.7	5.1	496.1	5.1
61	2	40	80	546.55	5742	2804	0.50	0.2001	0.0026	0.0253	0.0003	0.0574	0.0008	185.2	2.2	505.9	30.7	161.3	1.6	68.1	-14.8	161.3	1.6	159.7	1.6
61	2	40	80	546.55	1160	132	0.10	0.7478	0.0107	0.0936	0.0010	0.0581	0.0009	566.9	6.2	530.7	33.3	577.0	5.8	-8.7	1.7	577.0	5.8	577.8	5.8
61	2	40	80	546.55	3311	1997	0.60	0.0223	0.0010	0.0032	0.0001	0.0499	0.0023	22.3	1.0	187.0	107.9	20.9	0.3	88.8	-7.2	20.9	0.3	20.8	0.3
61	2	40	80	546.55	2160	571	0.30	1.6726	0.0194	0.1656	0.0017	0.0734	0.0009	998.2	7.4	1024.1	24.9	987.9	9.1	3.5	-1.0	987.9	9.1	986.5	9.1
61	2	40	80	546.55	2630	1726	0.70	1.9821	0.0224	0.1863	0.0018	0.0773	0.0009	1109.4	7.7	1128.6	23.8	1101.4	10.0	2.4	-0.7	1128.6	10.0	1100.1	24.3
61	2	40	80	546.55	260	66	0.30	0.8059	0.0198	0.0992	0.0013	0.0590	0.0015	600.1	11.2	566.9	56.1	610.0	7.3	-7.6	1.6	610.0	7.3	610.8	7.3
61	2	40	80	546.55	606	240	0.40	1.8641	0.0274	0.1829	0.0020	0.0741	0.0012	1068.4	9.7	1042.5	31.4	1082.9	10.9	-3.9	1.3	1082.9	10.9	1084.8	10.9
61	2	40	80	546.55	1287	520	0.40	0.6479	0.0090	0.0819	0.0009	0.0575	0.0008	507.2	5.6	510.5	32.2	507.2	5.1	0.7	0.0	507.2	5.1	507.2	5.1
61	2	40	80	546.55	156	100	0.60	0.6522	0.0285	0.0848	0.0013	0.0559	0.0025	509.8	17.5	448.2	100.2	524.5	7.8	-17.0	2.8	524.5	7.8	525.8	7.8
61	2	40	80	546.55	1544	709	0.50	0.2682	0.0041	0.0362	0.0004	0.0538	0.0009	241.3	3.3	362.9	36.1	229.3	2.4	36.8	-5.2	229.3	2.4	228.4	2.4
61	2	40	80	546.55	3939	1573	0.40	0.3665	0.0046	0.0510	0.0005	0.0523	0.0007	317.1	3.4	295.8	30.2	320.5	3.1	-8.4	1.1	320.5	3.1	320.7	3.1
61	2	40	80	546.55	184	98	0.50	0.8668	0.0151	0.1026	0.0012	0.0614	0.0011	633.8	8.2	653.0	39.6	629.5	6.7	3.6	-0.7	629.5	6.7	629.0	6.7
61	2	40	80	546.55	1009	215	0.20	1.1903	0.0175	0.1275	0.0014	0.0679	0.0011	796.1	8.1	863.3	32.5	773.5	7.9	10.4	-2.9	773.5	7.9	770.9	7.9
61	2	40	80	546.55	822	363	0.40	1.7362	0.0211	0.1681	0.0017	0.0751	0.0010	1022.1	7.9	1069.7	25.8	1001.5	9.4	6.4	-2.1	1001.5	9.4	998.6	9.4
61	2	40	80	546.55	1334	584	0.40	1.1727	0.0143	0.1200	0.0012	0.0710	0.0009	787.9	6.7	957.1	26.6	730.7	7.0	23.7	-7.8	730.7	7.0	724.4	6.9
61	2	40	80	546.55	713	161	0.20	0.7229	0.0100	0.0894	0.0009	0.0588	0.0009	552.4	5.9	558.7	32.0	551.8	5.5	1.2	-0.1	551.8	5.5	551.6	5.5
61	2	40	80	546.55	370	94	0.30	0.5236	0.0086	0.0654	0.0007	0.0582	0.0010	427.5	5.7	536.3	38.0	408.3	4.3	23.9	-4.7	408.3	4.3	406.7	4.3
61	2	40	80	546.55	879	445	0.50	1.7922	0.0209	0.1650	0.0017	0.0790	0.0010	1042.6	7.6	1170.5	24.5	984.3	9.1	15.9	-5.9	984.3	9.1	976.3	9.1
61	2	40	80	546.55	1051	564	0.50	0.2308	0.0035	0.0332	0.0004	0.0506	0.0008	210.9	2.9	221.6	37.1	210.3	2.2	5.1	-0.3	210.3	2.2	210.2	2.2
61	2	40	80	546.55	771	614	0.80	0.7615	0.0100	0.0930	0.0010	0.0595	0.0008	574.9	5.8	585.9	30.0	573.1	5.6	2.2	-0.3	573.1	5.6	572.8	5.6
61	2	40	80	546.55	1627	819	0.50	0.1008	0.0018	0.0153	0.0002	0.0479	0.0009	97.5	1.7	94.8	44.5	97.8	1.0	-3.2	0.3	97.8	1.0	97.8	1.0
61	2	40	80	546.55	639	792	1.20	0.2425	0.0045	0.0342	0.0004	0.0515	0.0010	220.4	3.7	261.8	45.1	217.0	2.4	17.1	-1.6	217.0	2.4	216.7	2.4
61	2	40	80	546.55	1975	508	0.30	1.3906	0.0158	0.1363	0.0014	0.0742	0.0009	884.9	6.7	1044.9	24.3	823.7	7.7	21.2	-7.4	823.7	7.7	816.4	7.6
61	2	40	80	546.55	1028	323	0.30	1.5967	0.0193	0.1583	0.0016	0.0733	0.0009	968.9	7.6	1021.3	25.8	947.5	8.9	7.2	-2.3	947.5	8.9	944.6	8.9
61	2	40	80	546.55	1655	427	0.30	1.9216	0.0217	0.1824	0.0018	0.0766	0.0009	1088.6	7.6	1109.6	23.9	1079.9	9.8	2.7	-0.8	1079.9	9.8	1078.5	9.8
61	2	40	80	546.55	1086	699	0.60	0.7335	0.0113	0.0855	0.0009	0.0624	0.0010	558.6	6.6	685.2	35.0	529.0	5.5	22.8	-5.6	529.0	5.5	526.2	5.5
61	2	40	80	546.55	1902	3688	1.90	0.6704	0.0080	0.0835	0.0008	0.0584	0.0007	521.0	4.9	543.1	27.4	516.8	4.9	4.8	-0.8	516.8	4.9	516.4	4.9
61	2	40	80	546.55	1159	579	0.50	0.6068	0.0079	0.0772	0.0008	0.0571	0.0008	481.5	5.0	495.2	30.6	479.5	4.7	3.2	-0.4	479.5	4.7	479.3	4.7
61	2	40	80	546.55	2222	1053	0.50	1.3198	0.0153	0.1417	0.0014	0.0677	0.0008	854.4	6.7	858.4	25.3	854.3	8.0	0.5	0.0	854.3	8.0	854.1	8.0
61	2	40	80	546.55	445	642	1.40	0.1916	0.0047	0.0276	0.0003	0.0504	0.0013	178.0	4.0	214.3	59.3	175.6	2.1	18.1	-1.4	175.6	2.1	175.4	2.1
61	2	40	80	546.55	764	557	0.70	0.6234	0.0088	0.0798	0.0008	0.0568	0.0009	492.0	5.5	481.6	33.2	495.1	5.0	-2.8	0.6	495.1	5.0	495.3	5.0
61	2	40	80	546.55	5503	2886	0.50	0.1022	0.0014	0.0147	0.0002	0.0505	0.0007	98.8	1.3	216.6	33.1	94.1	1.0	56.5	-4.9	94.1	1.0	93.8	1.0
61	2	40	80	546.55	749	352	0.50	1.6468	0.0198	0.1638	0.0017	0.0731	0.0009	988.3	7.6	1015.0	25.6	978.0	9.2	3.6	-1.1	978.0	9.2	976.5	9.1
61	2	40	80	546.55	641	596	0.90	4.7396	0.0555	0.3096	0.0031	0.1113	0.0014	1774.3	9.9	1819.6	22.5	1738.8	15.4	4.4	-2.0	1819.6	15.4	1729.4	24.1
61	2	40	80	546.55	3939	7841	2.00	0.1196	0.0016	0.0163	0.0002	0.0532	0.0008	114.7	1.5	338.0	32.8	104.4	1.1	69.1	-9.8	104.4	1.1	103.8	1.1
61	2	40	80	546.55	1019	539	0.50	0.2658	0.0040	0.0377	0.0004	0.0513	0.0008	239.3	3.2	252.4	36.4	238.4	2.4	5.5	-0.4	238.4	2.4	238.3	2.4
61	2	40	80	546.55	544	260	0.50	0.3455	0.0059	0.0460	0.0005	0.0546	0.0010	301.3	4.5	394.5	40.7	289.9	3.1	26.5	-3.9	289.9	3.1	289.0	3.1
61	2	40	80	546.55	5789	2420	0.40	0.1616	0.0020	0.0231	0.0002	0.0508	0.0007	152.1	1.8	232.1	30.1	147.3	1.5	36.5	-3.3	147.3	1.5	146.9	1.4
61	2	40	80	546.55	1079	272	0.30	1.7550	0.0207	0.1728	0.0017	0.0738	0.0009	1029.0	7.7	1036.2	25.3	1027.4	9.5	0.9	-0.2	1027.4	9.5	1027.0	9.5
61	2	40	80	546.55	697	201	0.30	1.8833	0.0227	0.1811	0.0018	0.0756	0.0010	1075.2	8.0	1083.1	25.3	1073.1	10.0	0.9	-0.2	1073.1	10.0	1072.6	10.0
61	2	40	80	546.55	134	69	0.50	0.7906	0.0165	0.0942	0.0011	0.0610	0.0013	591.5	9.4	639.3	47.3	580.2	6.7	9.3	-2.0	580.2	6.7	579.0	6.7
61	2	40	80	546.55	818	92	0.10	0.6575	0.0086	0.0827	0.0009	0.0578	0.0008	513.1	5.3	521.2	30.5	512.2	5.1	1.7	-0.2	512.2	5.1	512.1	5.1
61	2	40	80	546.55	2513	1430	0.60	0.2613	0.0034	0.0375	0.0004	0.0506	0.0007	235.7	2.7	222.5	31.6	237.4	2.4	-6.7	0.7	237.4	2.4	237.5	2.4
61	2	40	80	546.55	1589	964	0.60	0.2601	0.0038	0.0371	0.0004	0.0510	0.0008	234.8	3.1	241.1	35.3	234.5	2.4	2.7	-0.1	234.5	2.4	234.5	2.4
65	4	63	103	588.00	362	352	1.00	8.1426	0.1287	0.3488	0.0054	0.1697	0.0019	2247.0	14.4	2553.8	18.7	1928.7	25.7	24.5	-16.5	2553.8	25.7	1815.7	32.9
65	4	63	103	588.00	504	213	0.40	8.8155	0.1384	0.3964	0.0061	0.1617	0.0018	2319.1	14.4	2472.2	18.6	2152.2	28.1	12.9	-7.8	2472.2	28.1	2084.2	25.0
65	4	63	103	588.00	367	233	0.60	2.7579	0.0501	0.1750	0.0029	0.1146	0.0016	1344.2	13.6	1872.0	26.0	1039.5	15.7	44.5	-29.3	1039.5	15.7	990.7	15.0
65	4	63	103	588.00	1450	563	0.40	7.7438	0.1208	0.3432	0.0052	0.1640	0.0018	2201.7	14.1	2496.4	18.4	1902.2	25.2	23.8	-15.7	2496.4	25.2	1799.5	31.1
65	4	63	103	588.00	465	419	0.90	3.6004	0.0613	0.2944	0.0046	0.0889	0.0011	1549.6	13.6	1400.5	24.3	1663.7	23.1	-18.8	6.9	1400.5	23.1	1688.5	19.8
65	4	63	103	588.00	2373	747	0.30	0.6812	0.0110	0.0714	0.0010	0.0693	0.0009	527.5	6.7	907.6	27.7	444.6	6.2	51.0	-18.6	444.6	6.2	437.4	6.1
65	4	63	103	588.00	353	59	0.20	24.6255	0.3856	0.6173	0.0095	0.2900	0.0031	3293.5	15.4	3416.7	17.2	3099.0	37.8	9.3	-6.3	3416.7	37.8	2856.5	27.8
65	4	63	103	588.00	2719	726	0.30	1.2663	0.0191	0.1174	0.0017	0.0784	0.0009	830.7	8.6	1156.4	23.4	715.5	9.6	38.1	-16.1	715.5	9.6	702.6	9.5
65	4	63	103	588.00	4128	5771	1.40	0.6117	0.0093	0.0520	0.0007	0.0855	0.0010	484.6	5.9	1326.3	23.2	326.7	4.5	75.4	-48.3	326.7	4.5	313.7	4.4
65	4	63	103	588.00	1302	309	0.20	1.4237	0.0234	0.1177	0.0018	0.0879	0.0011	898.9	9.8	1379.4	23.1	717.4	10.5	48.0	-25.3	717.4	10.5	696.5	10.2
65	4	63	103	588.00	2138	1371	0.60	3.0354	0.0481	0.2033	0.0031	0.1085	0.0012	1416.6	12.1	1773.9	20.4	1192.9	16.7	32.8	-18.7	1773.9	16.7	1153.8	31.6
65	4	63	103	588.00	1769	249	0.10	13.3954	0.1930	0.4524	0.0064	0.2152	0.0023	2707.9	13.7	2944.5	17.6	2405.7	28.3	18.3	-12.6	2944.5	28.3	2234.5	31.1
65	4	63	103	588.00	866	339	0.40	1.1481	0.0194	0.1100	0.0017	0.0759	0.0010	776.3	9.2	1091.3	25.2	672.5	9.9	38.4	-15.5	672.5	9.9	661.4	9.8
65	4	63	103	588.00	390	112	0.30	2.8759	0.0483	0.1929	0.0030	0.1083	0.0014	1375.6	12.7	1770.9	22.9	1137.2	16.4	35.8	-21.0	1770.9	16.4	1097.1	15.9
65	4	63	103	588.00	1137	456	0.40	4.5724	0.0725	0.3023	0.0046	0.1099	0.0012	1744.2	13.3	1797.3	20.4	1702.8	22.9	5.3	-2.4	1797.3	22.9	1692.2	22.0
65	4	63	103	588.00	169	139	0.80	1.2196	0.0324	0.0972	0.0019	0.0912	0.0022	809.6	14.9	1450.8	46.6	597.7	11.0	58.8	-35.4	597.7	11.0	575.3	10.6
65	4	63	103	588.00	1908	1209	0.60	11.2757	0.1644	0.4492	0.0063	0.1824	0.0020	2546.2	13.7	2674.3	18.4	2391.7	28.2	10.6	-6.5	2674.3	28.2	2311.7	24.4
65	4	63	103	588.00	1817	678	0.40	1.8211	0.0264	0.1760	0.0025	0.0752	0.0008	1053.1	9.5	1072.7	22.1	1045.2	13.6	2.6	-0.7	1045.2	13.6	1044.0	13.6
65	4	63	103	588.00	713	450	0.60	0.6596	0.0113	0.0835	0.0013	0.0574	0.0007	514.4	6.9	505.6	28.1	517.2	7.7	-2.3	0.5	517.2	7.7	517.4	7.7
65	4	63	103	588.00	283	159	0.60	19.5780	0.3062	0.6098	0.0094	0.2334	0.0025	3070.7	15.3	3074.5	17.5	3069.0	37.6	0.2	-0.1	3074.5	37.6	3065.3	17.6

65	4	63	103	588.00	146	248	1.70	1.3587	0.0269	0.1447	0.0024	0.0683	0.0011	871.3	11.6	875.8	33.4	870.9	13.3	0.6	0.0	870.9	13.3	870.8	13.3
65	4	63	103	588.00	73	45	0.60	0.7159	0.0210	0.0873	0.0016	0.0596	0.0016	548.3	12.4	588.8	57.9	539.4	9.7	8.4	-1.6	539.4	9.7	538.6	9.7
65	4	63	103	588.00	75	28	0.40	0.6919	0.0285	0.0830	0.0019	0.0606	0.0024	533.9	17.1	624.1	84.7	513.9	11.2	17.7	-3.9	513.9	11.2	512.0	11.2
65	4	63	103	588.00	472	179	0.40	0.7723	0.0140	0.0939	0.0015	0.0598	0.0008	581.1	8.0	595.0	30.5	578.4	8.7	2.8	-0.5	578.4	8.7	578.1	8.7
65	4	63	103	588.00	1573	544	0.30	0.6600	0.0109	0.0784	0.0012	0.0612	0.0007	514.6	6.7	646.0	25.7	486.3	7.2	24.7	-5.8	486.3	7.2	483.8	7.1
65	4	63	103	588.00	704	221	0.30	0.2063	0.0051	0.0307	0.0005	0.0488	0.0011	190.4	4.3	137.2	51.1	195.1	3.3	-42.2	2.4	195.1	3.3	195.4	3.3
65	4	63	103	588.00	2067	1769	0.90	1.8442	0.0267	0.1813	0.0026	0.0740	0.0008	1061.4	9.6	1039.2	22.0	1073.9	13.9	-3.3	1.2	1073.9	13.9	1075.4	13.9
65	4	63	103	588.00	3050	1059	0.30	0.2178	0.0034	0.0321	0.0005	0.0494	0.0006	200.1	2.8	163.9	29.4	203.5	2.9	-24.1	1.7	203.5	2.9	203.7	2.9
65	4	63	103	588.00	271	98	0.40	1.8735	0.0360	0.1824	0.0030	0.0747	0.0012	1071.8	12.7	1058.2	31.1	1080.1	16.2	-2.1	0.8	1080.1	16.2	1081.1	16.2
65	4	63	103	588.00	1010	417	0.40	0.7281	0.0123	0.0903	0.0014	0.0586	0.0007	555.4	7.2	552.4	27.3	557.1	8.2	-0.9	0.3	557.1	8.2	557.2	8.2
65	4	63	103	588.00	4501	1590	0.40	0.7540	0.0110	0.0914	0.0013	0.0600	0.0007	570.5	6.4	600.8	23.6	563.9	7.6	6.1	-1.2	563.9	7.6	563.2	7.6
65	4	63	103	588.00	456	151	0.30	0.6997	0.0128	0.0874	0.0014	0.0582	0.0008	538.6	7.6	535.2	31.3	540.3	8.2	-1.0	0.3	540.3	8.2	540.4	8.2
65	4	63	103	588.00	1106	158	0.10	0.7667	0.0127	0.0932	0.0014	0.0598	0.0007	577.9	7.3	594.3	26.2	574.6	8.4	3.3	-0.6	574.6	8.4	574.3	8.4
65	4	63	103	588.00	308	194	0.60	3.4804	0.0574	0.2666	0.0042	0.0949	0.0011	1522.8	13.1	1524.8	22.6	1523.6	21.1	0.1	0.1	1524.8	21.1	1523.5	22.6
65	4	63	103	588.00	755	274	0.40	0.7717	0.0132	0.0960	0.0015	0.0584	0.0008	580.7	7.6	544.9	28.1	590.9	8.8	-8.4	1.7	590.9	8.8	591.7	8.8
65	4	63	103	588.00	973	883	0.90	0.8200	0.0136	0.1004	0.0016	0.0594	0.0007	608.0	7.6	579.0	26.5	616.8	9.1	-6.5	1.4	616.8	9.1	617.6	9.1
65	4	63	103	588.00	723	267	0.40	14.7808	0.2294	0.5570	0.0085	0.1929	0.0020	2801.2	14.9	2766.2	17.7	2854.0	35.2	-3.2	1.8	2766.2	35.2	2894.9	16.0
65	4	63	103	588.00	497	314	0.60	0.6926	0.0123	0.0864	0.0014	0.0583	0.0008	534.3	7.4	538.6	30.1	534.2	8.0	0.8	0.0	534.2	8.0	534.1	8.0
65	4	63	103	588.00	462	168	0.40	0.7678	0.0145	0.0897	0.0014	0.0622	0.0009	578.5	8.3	680.0	32.4	553.9	8.5	18.5	-4.4	553.9	8.5	551.6	8.4
65	4	63	103	588.00	674	395	0.60	2.2041	0.0352	0.2034	0.0031	0.0788	0.0009	1182.3	11.2	1165.0	22.5	1193.7	16.7	-2.5	1.0	1165.0	16.7	1195.3	22.1
65	4	63	103	588.00	405	474	1.20	0.8238	0.0156	0.0991	0.0016	0.0604	0.0009	610.2	8.7	617.0	32.6	609.4	9.3	1.2	-0.1	609.4	9.3	609.2	9.3
65	4	63	103	588.00	957	425	0.40	0.6754	0.0114	0.0850	0.0013	0.0577	0.0007	524.0	6.9	518.5	27.5	526.1	7.8	-1.5	0.4	526.1	7.8	526.3	7.8
65	4	63	103	588.00	1106	203	0.20	5.7167	0.0912	0.3520	0.0054	0.1181	0.0013	1933.9	13.8	1926.1	20.3	1944.0	25.9	-0.9	0.5	1926.1	25.9	1946.6	20.0
65	4	63	103	588.00	668	370	0.60	2.5355	0.0405	0.2218	0.0034	0.0831	0.0009	1282.3	11.7	1270.7	22.2	1291.2	18.0	-1.6	0.7	1270.7	18.0	1292.4	21.9
65	4	63	103	588.00	615	545	0.90	0.7768	0.0134	0.0966	0.0015	0.0585	0.0008	583.7	7.7	545.7	28.5	594.5	8.8	-8.9	1.8	594.5	8.8	595.4	8.8
65	4	63	103	588.00	576	622	1.10	1.7949	0.0293	0.1713	0.0026	0.0762	0.0009	1043.6	10.7	1098.4	23.5	1019.2	14.5	7.2	-2.4	1019.2	14.5	1015.8	14.5
65	4	63	103	588.00	617	258	0.40	0.7310	0.0128	0.0917	0.0014	0.0580	0.0008	557.1	7.5	527.3	29.2	565.4	8.4	-7.2	1.5	565.4	8.4	566.1	8.5
65	4	63	103	588.00	529	206	0.40	0.6666	0.0120	0.0841	0.0013	0.0576	0.0008	518.6	7.3	514.0	30.6	520.6	7.9	-1.3	0.4	520.6	7.9	520.7	7.9
65	4	63	103	588.00	2543	1120	0.40	0.6489	0.0097	0.0826	0.0012	0.0571	0.0007	507.8	6.0	494.4	25.2	511.6	7.0	-3.5	0.8	511.6	7.0	511.9	7.0
65	4	63	103	588.00	387	644	1.70	2.3002	0.0381	0.2035	0.0032	0.0822	0.0010	1212.4	11.8	1248.7	23.7	1193.8	16.9	4.4	-1.6	1248.7	16.9	1190.7	24.7
65	4	63	103	588.00	625	197	0.30	1.0603	0.0180	0.1216	0.0019	0.0634	0.0008	734.0	8.9	720.4	26.9	739.6	10.8	-2.7	0.8	739.6	10.8	740.1	10.8
65	4	63	103	588.00	1463	273	0.20	1.4864	0.0237	0.1519	0.0023	0.0711	0.0008	924.8	9.7	959.7	23.1	911.8	13.0	5.0	-1.4	911.8	13.0	910.0	13.0
65	4	63	103	588.00	399	210	0.50	4.0721	0.0658	0.2951	0.0046	0.1003	0.0012	1648.7	13.2	1628.6	21.5	1667.1	22.7	-2.4	1.1	1628.6	22.7	1671.0	20.9
65	4	63	103	588.00	1709	525	0.30	0.8099	0.0131	0.0966	0.0015	0.0609	0.0007	602.4	7.4	636.1	24.8	594.4	8.7	6.6	-1.3	594.4	8.7	593.6	8.7
65	4	63	103	588.00	846	188	0.20	0.7708	0.0131	0.0951	0.0015	0.0589	0.0007	580.2	7.5	562.8	27.5	585.6	8.7	-4.0	0.9	585.6	8.7	586.0	8.7
65	4	63	103	588.00	185	109	0.60	1.9335	0.0357	0.1868	0.0030	0.0752	0.0011	1092.8	12.4	1073.7	29.2	1104.0	16.3	-2.8	1.0	1073.7	16.3	1105.4	28.6
65	4	63	103	588.00	1377	4775	3.50	8.1466	0.1266	0.4135	0.0063	0.1432	0.0015	2247.4	14.1	2265.2	18.6	2231.1	28.7	1.5	-0.7	2265.2	28.7	2223.9	19.2
65	4	63	103	588.00	713	1262	1.80	0.1889	0.0041	0.0278	0.0005	0.0494	0.0009	175.7	3.5	166.3	43.1	176.6	2.8	-6.2	0.5	176.6	2.8	176.7	2.8
65	4	63	103	588.00	205	112	0.50	0.6866	0.0152	0.0834	0.0014	0.0599	0.0011	530.7	9.2	597.5	41.0	516.1	8.3	13.6	-2.8	516.1	8.3	514.8	8.3
65	4	63	103	588.00	3122	1396	0.40	0.6827	0.0120	0.0854	0.0013	0.0581	0.0008	528.4	7.2	532.2	29.1	528.3	7.9	0.7	0.0	528.3	7.9	528.3	7.9
65	4	63	103	588.00	2119	1110	0.50	1.0986	0.0185	0.1157	0.0018	0.0690	0.0009	752.7	9.0	898.7	25.8	705.5	10.3	21.5	-6.7	705.5	10.3	700.5	10.3
65	4	63	103	588.00	670	328	0.50	0.6718	0.0120	0.0813	0.0013	0.0601	0.0008	521.8	7.3	605.8	29.6	503.6	7.6	16.9	-3.6	503.6	7.6	501.9	7.6
65	4	63	103	588.00	246	220	0.90	0.7029	0.0151	0.0897	0.0015	0.0570	0.0010	540.5	9.0	489.8	39.9	553.5	8.8	-13.0	2.3	553.5	8.8	554.6	8.8
65	4	63	103	588.00	556	384	0.70	0.7174	0.0131	0.0894	0.0014	0.0583	0.0008	549.1	7.7	541.2	31.2	551.9	8.3	-2.0	0.5	551.9	8.3	552.1	8.4
65	4	63	103	588.00	884	467	0.50	1.8692	0.0302	0.1831	0.0028	0.0742	0.0009	1070.3	10.7	1046.0	23.2	1083.8	15.3	-3.6	1.3	1083.8	15.3	1085.6	15.3
65	4	63	103	588.00	303	86	0.30	0.7407	0.0151	0.0912	0.0015	0.0591	0.0010	562.8	8.8	568.7	36.9	562.3	8.7	1.1	-0.1	562.3	8.7	562.2	8.7
65	4	63	103	588.00	1805	295	0.20	1.8455	0.0293	0.1820	0.0028	0.0737	0.0008	1061.8	10.5	1032.9	22.6	1077.6	15.2	-4.3	1.5	1077.6	15.2	1079.6	15.2
65	4	63	103	588.00	590	312	0.50	0.1827	0.0043	0.0270	0.0005	0.0492	0.0010	170.4	3.7	157.3	47.6	171.6	2.8	-9.1	0.7	171.6	2.8	171.6	2.8
65	4	63	103	588.00	722	225	0.30	0.6479	0.0115	0.0820	0.0013	0.0574	0.0008	507.2	7.1	506.3	30.0	508.2	7.6	-0.4	0.2	508.2	7.6	508.2	7.6
65	4	63	103	588.00	992	262	0.30	0.7639	0.0129	0.0949	0.0015	0.0585	0.0007	576.3	7.4	547.6	27.4	584.5	8.7	-6.7	1.4	584.5	8.7	585.2	8.7
65	4	63	103	588.00	1686	656	0.40	2.0674	0.0332	0.1815	0.0028	0.0828	0.0009	1138.1	11.0	1263.2	22.3	1075.2	15.2	14.9	-5.8	1075.2	15.2	1066.0	15.1
65	4	63	103	588.00	1737	401	0.20	1.7396	0.0275	0.1719	0.0026	0.0736	0.0008	1023.3	10.2	1028.5	22.4	1022.5	14.4	0.6	-0.1	1022.5	14.4	1022.2	14.4
65	4	63	103	588.00	668	228	0.30	1.1827	0.0201	0.1286	0.0020	0.0669	0.0008	792.6	9.3	832.8	26.3	779.6	11.4	6.4	-1.7	779.6	11.4	778.0	11.4
65	4	63	103	588.00	565	228	0.40	1.7977	0.0298	0.1796	0.0028	0.0728	0.0009	1044.6	10.8	1006.4	24.7	1064.6	15.2	-5.8	1.9	1064.6	15.2	1067.2	15.2
65	4	63	103	588.00	543	313	0.60	0.7425	0.0134	0.0919	0.0014	0.0587	0.0008	563.8	7.8	555.4	30.6	566.9	8.5	-2.1	0.5	566.9	8.5	567.1	8.5
65	4	63	103	588.00	3106	1086	0.30	1.4033	0.0223	0.1338	0.0020	0.0763	0.0009	890.3	9.5	1101.0	22.4	809.3	11.6	26.5	-10.0	809.3	11.6	799.7	11.5
65	4	63	103	588.00	203	142	0.70	0.7381	0.0161	0.0920	0.0015	0.0583	0.0011	561.3	9.4	540.8	40.6	567.2	9.0	-4.9	1.1	567.2	9.0	567.7	9.0
65	4	63	103	588.00	132	58	0.40	2.3866	0.0457	0.2116	0.0035	0.0820	0.0013	1238.6	13.7	1243.7	30.2	1237.5	18.5	0.5	-0.1	1243.7	18.5	1237.1	30.4
65	4	63	103	588.00	308	277	0.90	0.6407	0.0127	0.0811	0.0013	0.0575	0.0009	502.8	7.9	508.2	35.7	502.4	7.8	1.2	-0.1	502.4	7.8	502.3	7.8
65	4	63	103	588.00	3011	2233	0.70	0.2148	0.0038	0.0310	0.0005	0.0504	0.0008	197.6	3.1	210.1	34.6	196.9	2.8	6.3	-0.4	196.9	2.8	196.8	2.8
65	4	63	103	588.00	1760	903	0.50	0.6248	0.0103	0.0790	0.0012	0.0575	0.0007	492.9	6.4	509.0	26.5	490.1	7.2	3.7	-0.6	490.1	7.2	489.8	7.2
65	4	63	103	588.00	643	369	0.60	1.2813	0.0214	0.1365	0.0021	0.0682	0.0008	837.4	9.6	874.3	25.6	824.8	12.0	5.7	-1.5	824.8	12.0	823.3	12.0
65	4	63	103	588.00	951	367	0.40	0.8617	0.0144	0.1031	0.0016	0.0608	0.0007	631.1	7.8	630.5	26.3	632.3	9.3	-0.3	0.2	632.3	9.3	632.3	9.3
65	4	63	103	588.00	1910	1271	0.70	0.2390	0.0039	0.0349	0.0005	0.0497	0.0007	217.6	3.2	180.9	31.5	221.4	3.1	-22.4	1.7	221.4	3.1	221.6	3.1
65	4	63	103	588.00	1224	540	0.40	1.9005	0.0302	0.1850	0.0028	0.0747	0.0008	1081.3	10.6	1058.5	22.5	1094.3	15.4	-3.4	1.2	1094.3	15.4	1096.0	15.4
65	4	63	103	588.00	171	123	0.70	2.2717	0.0411	0.2046	0.0033	0.0807	0.0011	1203.6	12.8	1213.5	27.7	1199.8	17.6	1.1	-0.3	1213.5	17.6	1199.0	27.9
65	4	63	103	588.00	331	37	0.10	21.1504	0.3338	0.6107	0.0094	0.2517	0.0028	3145.5	15.4	3194.9	17.7	3072.7	37.7	3.8	-2.4	3194.9	37.7	2987.6	21.0
65	4	63	103	588.00	397	127	0.30	1.4138	0.0323	0.1514	0.0026	0.0679	0.0013	894.7	13.6	864.0	40.7	908.7	14.7	-5.2	1.5	908.7	14.7	910.3	14.7
65	4	63	103	588.00	278	47	0.20	1.0749	0.0202	0.1218	0.0019	0.0642	0.0010	741.1	9.9	746.3	31.7	740.6	11.2	0.8	-0.1	740.6	11.2	740.5	11.2
65	4	63	103	588.00	260	146	0.60	1.7838	0.0314	0.1749	0.0028	0.0741	0.0010	1039.5	11.5	1043.6	27.1	1039.2	15.2	0.4	0.0	1039.2	15.2	1039.0	15.2
65	4	63	103	588.00	941	288	0.30	1.9929	0.0332	0.1874	0.0029	0.0773	0.0009	1113.1	11.3	1127.8	24.4	1107.3	15.8	1.8	-0.5	1127.8	15.8	1106.3	24.7
65	4	63	103	588.00	237	381	1.60	1.9391	0.0348	0.1865	0.0030	0.0756	0.0011	1094.7	12.1	1082.5	28.0	1102.5	16.1	-1.8	0.7	1082.5	16.1	1103.4	27.6
65	4	63	103	588.00	900	460	0.50	0.6582	0.0112	0.0841	0.0013	0.0569	0.0007	513.5	6.9	485.5	28.0	520.6	7.7	-7.2	1.4	520.6	7.7	521.2	7.7
65	4	63	103	588.00	437	231	0.50	0.6944	0.0130	0.0878	0.0014	0.0575	0.0009	535.4	7.8	509.8	32.6	542.3	8.2	-6.4	1.3	542.3	8.2	542.9	8.3
65	4	63	103	588.00	3622	213	0.10	0.8203	0.0121	0.0999	0.0014	0.0597	0.0007	608.2	6.8	590.3	24.5	614.0	8.3	-4.0	0.9	614.0	8.3	614.5	8.3
65	4	63	103	588.00	921	975	1.10	0.2562	0.0051	0.0364	0.0006	0.0511	0.0008	231.6	4.2	245.2	37.9	230.6	3.6	6.0	-0.4	230.6	3.6	230.5	3.6
65	4	63	103	588.00	12914	604	0.00	0.6328	0.0092	0.0756	0.0011	0.0609	0.0007	497.8	5.7	633.3	23.5	469.6	6.4	25.9	-6.0	469.6	6.4	467.1	6.3

65	4	63	103	588.00	535	214	0.40	2.9200	0.0480	0.2377	0.0037	0.0893	0.0011	1387.1	12.5	1409.5	22.9	1374.6	19.2	2.5	-0.9	1409.5	19.2	1372.1	23.5
65	4	63	103	588.00	549	358	0.70	25.7856	0.4052	0.6861	0.0105	0.2731	0.0030	3338.4	15.5	3323.4	17.4	3367.8	40.2	-1.3	0.9	3323.4	40.2	3422.1	16.0
65	4	63	103	588.00	608	151	0.20	1.6823	0.0281	0.1698	0.0026	0.0720	0.0009	1001.8	10.7	985.3	25.0	1011.0	14.5	-2.6	0.9	1011.0	14.5	1012.0	14.5
65	4	63	103	588.00	1532	306	0.20	0.7678	0.0127	0.0926	0.0014	0.0603	0.0007	578.5	7.3	612.3	26.3	570.9	8.4	6.8	-1.3	570.9	8.4	570.1	8.4
65	4	63	103	588.00	1507	766	0.50	0.7179	0.0119	0.0889	0.0014	0.0587	0.0007	549.4	7.0	553.9	26.5	549.2	8.1	0.8	0.0	549.2	8.1	549.1	8.1
65	4	63	103	588.00	344	171	0.50	1.7910	0.0314	0.1769	0.0028	0.0736	0.0010	1042.2	11.4	1029.1	27.0	1050.1	15.2	-2.0	0.8	1050.1	15.2	1051.0	15.2
65	4	63	103	588.00	1192	226	0.20	0.8166	0.0137	0.0947	0.0015	0.0627	0.0008	606.1	7.7	695.4	26.3	583.5	8.6	16.1	-3.9	583.5	8.6	581.2	8.6
65	4	63	103	588.00	221	226	1.00	0.7801	0.0166	0.0948	0.0016	0.0598	0.0011	585.5	9.5	594.6	38.9	584.1	9.2	1.8	-0.3	584.1	9.2	583.9	9.2
65	4	63	103	588.00	200	95	0.50	0.8564	0.0179	0.1004	0.0017	0.0620	0.0011	628.1	9.8	673.1	37.3	616.7	9.7	8.4	-1.9	616.7	9.7	615.5	9.7
65	4	63	103	588.00	346	234	0.70	13.2541	0.2111	0.5109	0.0079	0.1885	0.0021	2697.9	15.2	2728.7	18.7	2660.6	33.7	2.5	-1.4	2728.7	33.7	2635.2	20.1
65	4	63	103	588.00	144	72	0.50	1.4498	0.0299	0.1322	0.0022	0.0797	0.0014	909.8	12.4	1188.9	34.0	800.4	12.6	32.7	-13.7	800.4	12.6	787.3	12.4
65	4	63	103	588.00	1058	108	0.10	0.7115	0.0123	0.0893	0.0014	0.0579	0.0008	545.6	7.3	524.6	28.5	551.5	8.2	-5.1	1.1	551.5	8.2	552.0	8.2
65	4	63	103	588.00	1039	317	0.30	1.2643	0.0210	0.1348	0.0021	0.0682	0.0008	829.8	9.4	872.8	25.3	815.2	11.8	6.6	-1.8	815.2	11.8	813.4	11.8
65	4	63	103	588.00	641	1294	2.00	0.2100	0.0049	0.0296	0.0005	0.0516	0.0010	193.6	4.1	268.0	46.3	187.8	3.1	29.9	-3.1	187.8	3.1	187.4	3.1
65	4	63	103	588.00	1531	1261	0.80	1.9965	0.0332	0.1923	0.0030	0.0755	0.0009	1114.3	11.3	1079.9	24.3	1133.7	16.1	-5.0	1.7	1079.9	16.1	1136.4	23.4
65	4	63	103	588.00	205	175	0.90	0.9286	0.0204	0.1086	0.0018	0.0622	0.0012	666.9	10.8	678.3	40.0	664.5	10.6	2.0	-0.4	664.5	10.6	664.2	10.6
65	4	63	103	588.00	1490	595	0.40	0.7036	0.0117	0.0871	0.0013	0.0587	0.0007	540.9	7.0	555.7	26.8	538.3	8.0	3.1	-0.5	538.3	8.0	538.0	7.9
65	4	63	103	588.00	666	1903	2.90	0.7813	0.0141	0.0944	0.0015	0.0601	0.0008	586.2	8.0	607.6	30.3	581.7	8.7	4.3	-0.8	581.7	8.7	581.2	8.7
65	4	63	103	588.00	786	363	0.50	1.5494	0.0269	0.1533	0.0024	0.0734	0.0010	950.3	10.7	1025.2	26.6	919.6	13.4	10.3	-3.3	919.6	13.4	915.7	13.4
65	4	63	103	588.00	798	371	0.50	0.6434	0.0116	0.0809	0.0013	0.0578	0.0008	504.4	7.2	521.6	30.8	501.4	7.6	3.9	-0.6	501.4	7.6	501.1	7.6
65	4	63	103	588.00	522	194	0.40	1.9861	0.0337	0.1905	0.0030	0.0758	0.0010	1110.8	11.5	1088.1	25.3	1124.0	16.1	-3.3	1.2	1088.1	16.1	1125.8	24.6
65	4	63	103	588.00	540	384	0.70	0.2632	0.0060	0.0349	0.0006	0.0549	0.0011	237.3	4.9	406.3	44.5	220.9	3.6	45.6	-7.4	220.9	3.6	219.7	3.6
65	4	63	103	588.00	1026	516	0.50	5.0924	0.0816	0.3449	0.0053	0.1073	0.0012	1834.8	13.7	1753.6	20.8	1910.0	25.4	-8.9	3.9	1753.6	25.4	1930.8	18.3
65	4	63	103	588.00	535	249	0.50	1.7305	0.0298	0.1705	0.0027	0.0738	0.0010	1020.0	11.1	1034.8	26.1	1014.6	14.7	2.0	-0.5	1014.6	14.7	1013.7	14.7
65	4	63	103	588.00	1165	858	0.70	1.9671	0.0318	0.1908	0.0029	0.0749	0.0009	1104.3	10.9	1065.5	23.2	1125.9	15.9	-5.7	1.9	1065.5	15.9	1128.8	22.2
65	4	63	103	588.00	1326	678	0.50	1.8596	0.0302	0.1843	0.0028	0.0733	0.0009	1066.9	10.7	1022.2	23.6	1090.5	15.4	-6.7	2.2	1090.5	15.4	1093.6	15.5
65	4	63	103	588.00	656	652	1.00	1.3895	0.0242	0.1282	0.0020	0.0788	0.0010	884.5	10.3	1165.7	26.3	777.6	11.5	33.3	-13.8	777.6	11.5	765.1	11.3
65	4	63	103	588.00	2225	1952	0.90	0.6703	0.0121	0.0785	0.0012	0.0621	0.0009	520.9	7.4	674.9	30.1	487.2	7.4	27.8	-6.9	487.2	7.4	484.2	7.4
65	4	63	103	588.00	862	640	0.70	0.2451	0.0053	0.0352	0.0006	0.0506	0.0009	222.6	4.3	219.8	41.7	223.2	3.6	-1.6	0.3	223.2	3.6	223.2	3.6
65	4	63	103	588.00	1500	983	0.70	1.6098	0.0261	0.1593	0.0024	0.0734	0.0009	974.0	10.2	1024.9	23.6	953.1	13.6	7.0	-2.2	953.1	13.6	950.3	13.5
65	4	63	103	588.00	397	149	0.40	1.4157	0.0254	0.1474	0.0023	0.0698	0.0010	895.5	10.7	921.6	28.4	886.3	13.1	3.8	-1.0	886.3	13.1	885.1	13.1
65	4	63	103	588.00	1420	361	0.30	0.6881	0.0118	0.0875	0.0014	0.0572	0.0007	531.7	7.1	497.1	28.2	540.6	8.1	-8.8	1.7	540.6	8.1	541.4	8.1
65	4	63	103	588.00	492	258	0.50	0.6780	0.0132	0.0861	0.0014	0.0573	0.0009	525.6	8.0	500.6	34.7	532.1	8.2	-6.3	1.2	532.1	8.2	532.7	8.2
65	4	63	103	588.00	387	224	0.60	1.7647	0.0310	0.1735	0.0027	0.0739	0.0010	1032.6	11.4	1038.9	27.1	1031.1	15.0	0.7	-0.1	1031.1	15.0	1030.8	15.0
65	4	63	103	588.00	403	294	0.70	0.8532	0.0167	0.1022	0.0017	0.0607	0.0010	626.4	9.1	626.6	34.2	627.3	9.7	-0.1	0.1	627.3	9.7	627.3	9.7
65	4	63	103	588.00	2015	539	0.30	0.6572	0.0100	0.0830	0.0012	0.0575	0.0007	512.9	6.2	510.5	26.5	514.2	7.0	-0.7	0.3	514.2	7.0	514.3	7.0
65	4	63	103	588.00	415	271	0.70	0.7494	0.0141	0.0908	0.0014	0.0600	0.0009	567.9	8.2	603.0	32.5	560.0	8.5	7.1	-1.4	560.0	8.5	559.2	8.5
65	4	63	103	588.00	1694	504	0.30	0.8835	0.0147	0.1041	0.0016	0.0617	0.0008	642.9	7.9	662.1	26.2	638.4	9.3	3.6	-0.7	638.4	9.3	637.9	9.3
65	4	63	103	588.00	456	1069	2.30	0.8348	0.0151	0.1000	0.0016	0.0607	0.0009	616.2	8.4	626.6	30.3	614.3	9.2	2.0	-0.3	614.3	9.2	614.1	9.2
65	4	63	103	588.00	3107	1706	0.50	1.5506	0.0229	0.1504	0.0021	0.0749	0.0008	950.7	9.1	1066.0	22.7	903.0	11.9	15.3	-5.3	903.0	11.9	897.0	11.9
65	4	63	103	588.00	383	243	0.60	3.0767	0.0511	0.2498	0.0039	0.0895	0.0011	1426.9	12.8	1414.0	23.2	1437.7	20.0	-1.7	0.7	1414.0	20.0	1439.5	22.8
65	4	63	103	588.00	1670	1149	0.70	0.8097	0.0142	0.0968	0.0015	0.0608	0.0008	602.3	8.0	631.6	28.8	595.5	8.9	5.7	-1.1	595.5	8.9	594.8	8.9
65	4	63	103	588.00	349	211	0.60	0.8407	0.0158	0.1009	0.0016	0.0606	0.0009	619.5	8.7	623.0	32.1	619.5	9.4	0.6	0.0	619.5	9.4	619.4	9.4
71	2	24	64	642.21	269	182	0.70	2.1384	0.0518	0.1930	0.0026	0.0806	0.0019	1161.3	16.8	1209.6	47.0	1137.3	14.1	6.0	-2.1	1209.6	14.1	1133.6	49.5
71	2	24	64	642.21	1600	1010	0.60	0.7771	0.0188	0.0913	0.0012	0.0619	0.0015	583.8	10.7	668.3	50.9	563.3	7.1	15.7	-3.6	563.3	7.1	561.3	7.1
71	2	24	64	642.21	45	34	0.80	0.7663	0.0680	0.0911	0.0021	0.0611	0.0055	577.7	39.1	642.1	194.2	562.3	12.5	12.4	-2.7	562.3	12.5	560.8	12.4
71	2	24	64	642.21	146	53	0.40	1.9059	0.0727	0.1732	0.0028	0.0800	0.0031	1083.1	25.4	1195.6	76.3	1029.7	15.3	13.9	-5.2	1029.7	15.3	1022.2	15.2
71	2	24	64	642.21	958	635	0.70	13.2994	0.2089	0.5233	0.0065	0.1847	0.0027	2701.1	14.9	2694.9	24.1	2713.2	27.5	-0.7	0.4	2694.9	27.5	2720.4	23.6
71	2	24	64	642.21	2225	491	0.20	6.9146	0.1115	0.3354	0.0042	0.1499	0.0023	2100.5	14.4	2343.6	25.9	1864.3	20.1	20.5	-12.7	2343.6	20.1	1788.7	39.4
71	2	24	64	642.21	124	59	0.50	0.7324	0.0392	0.0927	0.0016	0.0574	0.0031	557.9	22.9	506.3	119.2	571.7	9.4	-12.9	2.4	571.7	9.4	572.9	9.4
71	2	24	64	642.21	621	780	1.30	9.2143	0.1732	0.4185	0.0055	0.1600	0.0029	2359.5	17.3	2455.1	30.8	2253.7	25.0	8.2	-4.7	2455.1	25.0	2207.2	37.4
71	2	24	64	642.21	260	277	1.10	1.8029	0.0475	0.1768	0.0024	0.0741	0.0019	1046.5	17.2	1043.3	52.9	1049.7	13.3	-0.6	0.3	1049.7	13.3	1050.0	13.3
71	2	24	64	642.21	203	0	0.00	0.8092	0.0333	0.0929	0.0014	0.0633	0.0026	602.0	18.7	717.4	88.3	572.7	8.5	20.2	-5.1	572.7	8.5	569.9	8.5
71	2	24	64	642.21	768	162	0.20	21.8814	0.3773	0.5622	0.0073	0.2829	0.0046	3178.5	16.9	3378.3	25.8	2875.7	30.1	14.9	-10.5	3378.3	30.1	2582.2	51.2
71	2	24	64	642.21	91	33	0.40	1.0831	0.0582	0.1206	0.0021	0.0653	0.0036	745.2	28.3	782.4	114.6	734.0	12.3	6.2	-1.5	734.0	12.3	732.7	12.3
71	2	24	64	642.21	538	196	0.40	1.7680	0.0378	0.1770	0.0023	0.0726	0.0015	1033.8	13.9	1001.9	42.3	1050.5	12.6	-4.9	1.6	1050.5	12.6	1052.6	12.6
71	2	24	64	642.21	2223	956	0.40	0.8141	0.0152	0.0967	0.0012	0.0612	0.0011	604.8	8.5	645.0	38.4	595.1	7.1	7.7	-1.6	595.1	7.1	594.1	7.1
71	2	24	64	642.21	696	48	0.10	1.0239	0.0283	0.1178	0.0016	0.0632	0.0017	715.9	14.2	712.3	58.6	718.1	9.3	-0.8	0.3	718.1	9.3	718.3	9.3
71	2	24	64	642.21	738	93	0.10	15.3822	0.2560	0.5193	0.0065	0.2153	0.0034	2839.2	16.0	2944.9	25.5	2696.3	27.6	8.4	-5.3	2944.9	27.6	2592.8	34.0
71	2	24	64	642.21	824	261	0.30	1.8098	0.0353	0.1785	0.0023	0.0737	0.0014	1049.0	12.8	1032.1	37.9	1058.8	12.4	-2.6	0.9	1058.8	12.4	1060.0	12.4
71	2	24	64	642.21	772	243	0.30	0.8394	0.0201	0.1002	0.0013	0.0609	0.0014	618.8	11.1	633.3	50.6	615.8	7.7	2.8	-0.5	615.8	7.7	615.5	7.7
71	2	24	64	642.21	393	87	0.20	0.7498	0.0255	0.0917	0.0013	0.0594	0.0020	568.1	14.8	582.3	74.2	565.5	7.8	2.9	-0.5	565.5	7.8	565.2	7.8
71	2	24	64	642.21	1033	314	0.30	0.6768	0.0163	0.0856	0.0011	0.0575	0.0014	524.9	9.9	508.6	52.1	529.5	6.7	-4.1	0.9	529.5	6.7	529.8	6.7
71	2	24	64	642.21	1561	202	0.10	1.3767	0.0262	0.1433	0.0018	0.0698	0.0013	879.0	11.2	922.7	37.5	863.2	10.2	6.5	-1.8	863.2	10.2	861.2	10.2
71	2	24	64	642.21	165	93	0.60	0.7551	0.0373	0.0912	0.0015	0.0602	0.0030	571.2	21.6	609.4	108.5	562.6	9.0	7.7	-1.5	562.6	9.0	561.7	9.0
71	2	24	64	642.21	268	189	0.70	0.8314	0.0325	0.0999	0.0015	0.0605	0.0024	614.4	18.0	619.8	85.3	613.9	8.9	1.0	-0.1	613.9	8.9	613.8	8.9
71	2	24	64	642.21	767	610	0.80	2.1608	0.0582	0.1750	0.0025	0.0897	0.0024	1168.5	18.7	1418.7	51.6	1039.8	13.6	26.7	-12.4	1039.8	13.6	1020.9	13.3
71	2	24	64	642.21	1377	405	0.30	1.2566	0.0249	0.1335	0.0017	0.0684	0.0013	826.4	11.2	881.0	39.4	807.5	9.6	8.3	-2.3	807.5	9.6	805.3	9.6
71	2	24	64	642.21	65	44	0.70	0.7761	0.0687	0.0975	0.0022	0.0579	0.0052	583.3	39.3	523.5	197.5	599.7	13.2	-14.6	2.7	599.7	13.2	601.2	13.2
71	2	24	64	642.21	796	205	0.30	1.9520	0.0565	0.1888	0.0027	0.0752	0.0022	1099.1	19.5	1071.6	58.3	1114.8	14.5	-4.0	1.4	1071.6	14.5	1116.9	56.5
71	2	24	64	642.21	455	267	0.60	0.6490	0.0229	0.0838	0.0012	0.0563	0.0020	507.9	14.1	463.2	78.8	518.7	7.2	-12.0	2.1	518.7	7.2	519.6	7.2
71	2	24	64	642.21	1006	415	0.40	0.8395	0.0200	0.1016	0.0013	0.0601	0.0014	618.8	11.0	605.5	50.8	623.5	7.8	-3.0	0.8	623.5	7.8	623.9	7.8
71	2	24	64	642.21	364	364	1.00	0.1861	0.0146	0.0280	0.0006	0.0484	0.0038	173.3	12.5	115.9	187.3	177.8	3.5	-53.4	2.5	177.8	3.5	178.1	3.5
71	2	24	64	642.21	497	149	0.30	0.6990	0.0227	0.0877	0.0012	0.0580	0.0019	538.2	13.6	527.3	71.5	541.6	7.4	-2.7	0.6	541.6	7.4	541.9	7.4
71	2	24	64	642.21	414	219	0.50	0.7292	0.0295	0.0902	0.0014	0.0588	0.0024	556.1	17.3	556.9	89.1	556.7	8.2	0.0	0.1	556.7	8.2	556.7	8.2
71	2	24	64	642.21	741	575	0.80	13.2721	0.2177	0.5208	0.0065	0.1852	0.0028	2699.2	15.6	2699.5	25.5	2702.4	27.6	-0.1	0.1	2699.5	27.6	2703.6	25.5
71	2	24	64	642.21	1307	336	0.30	1.4325	0.0278	0.1467	0.0019	0.0710	0.0013	902.6	11.6	955.9	38.1	882.3	10.5	7.7	-2.3	882.3	10.5	879.8	10.4

71	2	24	64	642.21	1157	351	0.30	1.2025	0.0355	0.1225	0.0017	0.0714	0.0021	801.7	16.4	966.8	60.4	744.8	9.9	23.0	-7.6	744.8	9.9	738.4	9.8
71	2	24	64	642.21	2868	2872	1.00	0.6171	0.0163	0.0790	0.0011	0.0568	0.0015	488.0	10.2	482.4	58.0	490.0	6.3	-1.6	0.4	490.0	6.3	490.1	6.3
71	2	24	64	642.21	733	436	0.60	0.6950	0.0207	0.0849	0.0012	0.0595	0.0018	535.8	12.4	584.8	64.6	525.2	7.0	10.2	-2.0	525.2	7.0	524.2	6.9
71	2	24	64	642.21	244	250	1.00	0.2009	0.0173	0.0289	0.0006	0.0505	0.0044	185.9	14.6	216.1	202.8	183.8	3.8	15.0	-1.1	183.8	3.8	183.6	3.8
71	2	24	64	642.21	198	54	0.30	1.1383	0.0435	0.1290	0.0020	0.0641	0.0025	771.7	20.7	744.3	81.8	782.4	11.2	-5.1	1.4	782.4	11.2	783.5	11.2
71	2	24	64	642.21	327	193	0.60	0.8357	0.0296	0.1010	0.0015	0.0601	0.0021	616.8	16.4	607.6	77.0	620.3	8.6	-2.1	0.6	620.3	8.6	620.5	8.6
71	2	24	64	642.21	121	112	0.90	3.4743	0.1287	0.2495	0.0042	0.1012	0.0038	1521.4	29.2	1645.6	70.1	1435.9	21.5	12.7	-6.0	1645.6	21.5	1418.6	82.5
71	2	24	64	642.21	1365	650	0.50	1.7342	0.0327	0.1721	0.0022	0.0732	0.0013	1021.3	12.2	1019.4	36.6	1023.8	11.9	-0.4	0.2	1023.8	11.9	1024.0	11.9
71	2	24	64	642.21	853	710	0.80	0.6425	0.0175	0.0814	0.0011	0.0574	0.0016	503.9	10.8	505.2	59.5	504.4	6.5	0.2	0.1	504.4	6.5	504.3	6.5
71	2	24	64	642.21	571	540	0.90	0.3037	0.0134	0.0428	0.0007	0.0516	0.0023	269.3	10.5	267.6	102.7	269.9	4.0	-0.9	0.2	269.9	4.0	269.9	4.0
71	2	24	64	642.21	538	259	0.50	1.8120	0.0569	0.1693	0.0025	0.0778	0.0025	1049.8	20.6	1140.4	62.9	1008.4	13.6	11.6	-4.1	1008.4	13.6	1002.6	13.6
71	2	24	64	642.21	1184	904	0.80	0.1792	0.0073	0.0263	0.0004	0.0496	0.0020	167.4	6.3	175.2	96.0	167.1	2.5	4.6	-0.2	167.1	2.5	167.1	2.5
71	2	24	64	642.21	643	380	0.60	12.6872	0.2322	0.4802	0.0061	0.1920	0.0034	2656.7	17.3	2758.9	29.0	2528.1	26.5	8.4	-5.1	2758.9	26.5	2451.7	37.2
71	2	24	64	642.21	522	193	0.40	0.6750	0.0222	0.0850	0.0012	0.0578	0.0019	523.8	13.4	519.3	72.2	525.7	7.1	-1.2	0.4	525.7	7.1	525.8	7.1
71	2	24	64	642.21	186	60	0.30	1.4974	0.0523	0.1519	0.0023	0.0717	0.0025	929.3	21.3	975.4	72.0	911.4	12.7	6.6	-2.0	911.4	12.7	909.1	12.7
71	2	24	64	642.21	380	259	0.70	0.6759	0.0300	0.0875	0.0014	0.0562	0.0025	524.3	18.2	458.1	99.9	540.5	8.2	-18.0	3.0	540.5	8.2	541.9	8.2
71	2	24	64	642.21	1078	206	0.20	0.7163	0.0177	0.0900	0.0012	0.0579	0.0014	548.5	10.5	523.1	53.5	555.5	7.0	-6.2	1.3	555.5	7.0	556.1	7.0
71	2	24	64	642.21	726	287	0.40	1.6780	0.0369	0.1650	0.0021	0.0739	0.0016	1000.2	14.0	1037.8	43.5	984.7	11.9	5.1	-1.6	984.7	11.9	982.5	11.8
71	2	24	64	642.21	572	414	0.70	0.8036	0.0287	0.0824	0.0012	0.0709	0.0026	598.9	16.1	952.7	73.9	510.6	7.3	46.4	-17.3	510.6	7.3	502.4	7.2
71	2	24	64	642.21	1008	665	0.70	0.4554	0.0134	0.0594	0.0008	0.0557	0.0016	381.0	9.3	439.8	65.1	372.1	4.9	15.4	-2.4	372.1	4.9	371.3	4.9
71	2	24	64	642.21	352	383	1.10	0.3022	0.0186	0.0381	0.0007	0.0576	0.0036	268.1	14.5	513.6	138.1	241.2	4.4	53.0	-11.1	241.2	4.4	239.3	4.4
71	2	24	64	642.21	2571	228	0.10	0.9289	0.0189	0.1142	0.0014	0.0591	0.0012	667.0	10.0	571.3	42.7	696.8	8.3	-22.0	4.3	696.8	8.3	699.7	8.4
71	2	24	64	642.21	662	128	0.20	0.8180	0.0245	0.0956	0.0013	0.0622	0.0019	606.9	13.7	678.7	64.0	588.8	7.8	13.2	-3.1	588.8	7.8	587.0	7.8
71	2	24	64	642.21	1372	478	0.30	0.8132	0.0187	0.1001	0.0013	0.0590	0.0013	604.3	10.5	567.6	49.1	615.1	7.6	-8.4	1.8	615.1	7.6	616.1	7.6
71	2	24	64	642.21	1313	734	0.60	0.3192	0.0101	0.0443	0.0006	0.0524	0.0017	281.3	7.7	300.6	71.9	279.5	3.8	7.0	-0.7	279.5	3.8	279.3	3.8
71	2	24	64	642.21	645	194	0.30	1.5434	0.0375	0.1581	0.0021	0.0710	0.0017	947.8	15.0	955.6	49.0	946.0	11.6	1.0	-0.2	946.0	11.6	945.7	11.6
71	2	24	64	642.21	5310	3660	0.70	0.4881	0.0133	0.0591	0.0008	0.0600	0.0016	403.6	9.1	601.9	58.5	370.4	4.8	38.5	-9.0	370.4	4.8	367.7	4.8
71	2	24	64	642.21	314	676	2.20	0.6979	0.0306	0.0861	0.0014	0.0589	0.0026	537.5	18.3	563.9	96.5	532.3	8.0	5.6	-1.0	532.3	8.0	531.7	8.0
71	2	24	64	642.21	2003	1097	0.50	0.2165	0.0082	0.0160	0.0003	0.0981	0.0038	199.0	6.9	1586.7	73.1	102.6	1.7	93.5	-93.9	102.6	1.7	96.2	1.5
71	2	24	64	642.21	276	116	0.40	1.8919	0.0546	0.1837	0.0026	0.0748	0.0022	1078.2	19.2	1063.3	58.1	1087.3	14.0	-2.3	0.8	1087.3	14.0	1088.4	14.0
71	2	24	64	642.21	1426	1060	0.70	2.5228	0.0472	0.2248	0.0028	0.0816	0.0015	1278.6	13.6	1234.1	35.5	1307.2	14.9	-5.9	2.2	1234.1	14.9	1311.9	33.6
71	2	24	64	642.21	1021	223	0.20	1.0759	0.0274	0.1082	0.0015	0.0723	0.0018	741.6	13.4	993.2	51.5	662.1	8.4	33.3	-12.0	662.1	8.4	653.8	8.3
71	2	24	64	642.21	960	208	0.20	1.2063	0.0284	0.1323	0.0017	0.0663	0.0015	803.5	13.1	813.3	48.7	801.2	9.8	1.5	-0.3	801.2	9.8	800.8	9.8
71	2	24	64	642.21	963	648	0.70	0.7623	0.0245	0.0927	0.0013	0.0598	0.0019	575.3	14.1	593.6	70.0	571.7	7.7	3.7	-0.6	571.7	7.7	571.3	7.7
71	2	24	64	642.21	747	398	0.50	0.6666	0.0185	0.0845	0.0011	0.0573	0.0016	518.7	11.3	502.9	61.1	523.1	6.7	-4.0	0.9	523.1	6.7	523.4	6.7
71	2	24	64	642.21	1637	290	0.20	0.8939	0.0190	0.1069	0.0014	0.0608	0.0013	648.5	10.2	630.8	44.7	654.6	7.9	-3.8	0.9	654.6	7.9	655.1	7.9
71	2	24	64	642.21	622	285	0.50	0.2518	0.0154	0.0348	0.0006	0.0526	0.0033	228.1	12.5	311.4	141.5	220.4	3.9	29.2	-3.5	220.4	3.9	219.8	3.9
71	2	24	64	642.21	1115	776	0.70	19.4987	0.3420	0.6056	0.0075	0.2340	0.0039	3066.8	17.1	3079.0	26.9	3052.4	30.3	0.9	-0.5	3079.0	30.3	3035.0	27.9
71	2	24	64	642.21	606	327	0.50	0.7937	0.0223	0.0977	0.0013	0.0591	0.0017	593.3	12.6	568.0	60.9	600.9	7.7	-5.8	1.3	600.9	7.7	601.5	7.7
71	2	24	64	642.21	758	726	1.00	0.6406	0.0178	0.0828	0.0011	0.0562	0.0016	502.7	11.0	460.9	61.5	512.8	6.6	-11.3	2.0	512.8	6.6	513.6	6.6
71	2	24	64	642.21	187	271	1.40	1.2141	0.0460	0.1365	0.0021	0.0647	0.0025	807.1	21.1	762.3	80.9	824.7	11.7	-8.2	2.1	824.7	11.7	826.5	11.7
71	2	24	64	642.21	514	241	0.50	2.3357	0.0518	0.2110	0.0027	0.0805	0.0018	1223.2	15.8	1207.2	42.9	1234.3	14.6	-2.2	0.9	1207.2	14.6	1235.9	42.1
71	2	24	64	642.21	1716	351	0.20	0.6644	0.0166	0.0808	0.0011	0.0598	0.0015	517.3	10.1	593.6	53.7	501.0	6.3	15.6	-3.3	501.0	6.3	499.5	6.3
71	2	24	64	642.21	799	545	0.70	0.7008	0.0180	0.0890	0.0012	0.0572	0.0015	539.2	10.8	499.0	56.2	549.7	6.9	-10.2	1.9	549.7	6.9	550.6	6.9
71	2	24	64	642.21	1003	333	0.30	0.6876	0.0172	0.0866	0.0011	0.0577	0.0014	531.3	10.3	517.8	54.4	535.3	6.7	-3.4	0.7	535.3	6.7	535.6	6.7
71	2	24	64	642.21	331	206	0.60	0.8413	0.0312	0.1013	0.0015	0.0604	0.0023	619.9	17.2	615.2	80.9	622.1	8.8	-1.1	0.4	622.1	8.8	622.3	8.8
71	2	24	64	642.21	915	92	0.10	1.4725	0.0322	0.1512	0.0019	0.0708	0.0015	919.2	13.2	950.4	44.0	907.6	10.9	4.5	-1.3	907.6	10.9	906.0	10.9
71	2	24	64	642.21	869	93	0.10	0.7121	0.0191	0.0907	0.0012	0.0571	0.0015	546.0	11.3	492.9	58.8	559.7	7.1	-13.6	2.4	559.7	7.1	560.9	7.1
71	2	24	64	642.21	299	160	0.50	0.2481	0.0155	0.0341	0.0006	0.0529	0.0034	225.0	12.6	323.9	143.8	216.0	3.8	33.3	-4.2	216.0	3.8	215.4	3.8
71	2	24	64	642.21	717	614	0.90	5.2298	0.1017	0.3342	0.0042	0.1138	0.0021	1857.5	16.6	1859.4	34.1	1858.6	20.4	0.0	0.1	1859.4	20.4	1858.5	34.1
71	2	24	64	642.21	713	124	0.20	0.6898	0.0195	0.0867	0.0012	0.0578	0.0016	532.7	11.7	522.3	61.9	536.0	6.9	-2.6	0.6	536.0	6.9	536.2	6.9
71	2	24	64	642.21	90	42	0.50	0.6963	0.0479	0.0876	0.0017	0.0578	0.0040	536.6	28.7	520.1	153.5	541.4	10.0	-4.1	0.9	541.4	10.0	541.8	10.0
71	2	24	64	642.21	2810	1353	0.50	1.5778	0.0325	0.1532	0.0019	0.0749	0.0015	961.5	12.8	1064.1	40.4	918.7	10.8	13.7	-4.7	918.7	10.8	913.1	10.7
71	2	24	64	642.21	1322	867	0.70	1.7848	0.0402	0.1676	0.0022	0.0774	0.0017	1039.9	14.7	1130.4	44.3	999.0	12.0	11.6	-4.1	999.0	12.0	993.4	11.9
71	2	24	64	642.21	758	177	0.20	1.0922	0.0314	0.1202	0.0016	0.0661	0.0019	749.5	15.3	807.3	60.2	731.5	9.4	9.4	-2.5	731.5	9.4	729.5	9.4
71	2	24	64	642.21	782	501	0.60	2.1425	0.0464	0.1962	0.0025	0.0794	0.0017	1162.6	15.0	1180.5	42.2	1154.9	13.5	2.2	-0.7	1180.5	13.5	1153.5	43.0
71	2	24	64	642.21	2782	635	0.20	0.6498	0.0140	0.0821	0.0010	0.0576	0.0012	508.3	8.6	511.7	46.6	508.5	6.2	0.6	0.0	508.5	6.2	508.4	6.2
71	2	24	64	642.21	131	1	0.00	2.3883	0.1188	0.2251	0.0041	0.0771	0.0039	1239.1	35.6	1123.7	101.3	1308.6	21.7	-16.5	5.3	1123.7	21.7	1319.9	88.3
71	2	24	64	642.21	729	389	0.50	0.6536	0.0193	0.0815	0.0011	0.0583	0.0017	510.7	11.8	538.9	64.6	505.2	6.6	6.3	-1.1	505.2	6.6	504.6	6.6
71	2	24	64	642.21	830	293	0.40	0.6640	0.0190	0.0833	0.0011	0.0580	0.0017	517.1	11.6	527.6	62.8	515.6	6.7	2.3	-0.3	515.6	6.7	515.4	6.7
71	2	24	64	642.21	842	651	0.80	0.3014	0.0103	0.0424	0.0006	0.0517	0.0018	267.5	8.1	271.1	79.0	267.5	3.7	1.3	0.0	267.5	3.7	267.5	3.7
71	2	24	64	642.21	717	170	0.20	7.4414	0.1477	0.3923	0.0050	0.1379	0.0027	2166.0	17.8	2200.1	33.6	2133.3	23.0	3.0	-1.5	2200.1	23.0	2120.6	35.8
71	2	24	64	642.21	198	148	0.80	0.6213	0.0320	0.0773	0.0013	0.0585	0.0031	490.6	20.0	545.7	114.4	479.7	7.8	12.1	-2.3	479.7	7.8	478.7	7.8
71	2	24	64	642.21	552	168	0.30	0.7291	0.0227	0.0877	0.0012	0.0605	0.0019	556.0	13.3	618.7	67.5	541.7	7.2	12.5	-2.6	541.7	7.2	540.3	7.2
71	2	24	64	642.21	697	138	0.20	0.7969	0.0285	0.0994	0.0014	0.0583	0.0021	595.1	16.1	538.6	79.3	611.0	8.4	-13.5	2.6	611.0	8.4	612.4	8.5
71	2	24	64	642.21	291	277	1.00	0.8372	0.0331	0.1010	0.0015	0.0603	0.0024	617.6	18.3	611.6	86.5	620.3	8.9	-1.4	0.4	620.3	8.9	620.4	8.9
71	2	24	64	642.21	95	53	0.60	0.4181	0.0437	0.0530	0.0013	0.0574	0.0061	354.7	31.3	504.0	233.7	332.9	7.9	34.0	-6.6	332.9	7.9	331.1	7.9
71	2	24	64	642.21	380	299	0.80	2.1905	0.0651	0.2055	0.0029	0.0775	0.0023	1178.0	20.7	1132.4	59.7	1204.9	15.5	-6.4	2.2	1132.4	15.5	1208.9	56.6
71	2	24	64	642.21	587	708	1.20	0.3093	0.0150	0.0400	0.0006	0.0562	0.0028	273.6	11.6	458.5	109.4	252.9	4.0	44.8	-8.2	252.9	4.0	251.4	3.9
71	2	24	64	642.21	747	295	0.40	0.6892	0.0214	0.0866	0.0012	0.0579	0.0018	532.3	12.9	523.9	68.3	535.2	7.1	-2.2	0.5	535.2	7.1	535.4	7.1
71	2	24	64	642.21	138	152	1.10	0.7461	0.0472	0.0917	0.0017	0.0591	0.0038	566.0	27.5	570.9	140.2	565.7	10.2	0.9	0.0	565.7	10.2	565.6	10.2
71	2	24	64	642.21	343	159	0.50	0.7308	0.0301	0.0918	0.0014	0.0579	0.0024	557.0	17.7	523.5	91.8	566.2	8.2	-8.2	1.6	566.2	8.2	566.9	8.2
71	2	24	64	642.21	129	40	0.30	0.8030	0.0500	0.0933	0.0018	0.0625	0.0040	598.5	28.2	691.3	135.4	575.2	10.5	16.8	-4.0	575.2	10.5	572.9	10.5
71	2	24	64	642.21	170	42	0.20	1.8094	0.0700	0.1800	0.0028	0.0731	0.0029	1048.8	25.3	1014.7	79.6	1067.0	15.4	-5.2	1.7	1067.0	15.4	1069.4	15.4
71	2	24	64	642.21	306	229	0.70	0.8325	0.0294	0.0974	0.0014	0.0621	0.0022	615.0	16.3	677.6	76.4	599.2	8.3	11.6	-2.6	599.2	8.3	597.6	8.3
71	2	24	64	642.21	182	137	0.80	1.2434	0.0473	0.1312	0.0020	0.0689	0.0027	820.4	21.4	893.9	79.8	794.8	11.3	11.1	-3.2	794.8	11.3	791.8	11.3
71	2	24	64	642.21	623	326	0.50	0.7345	0.0238	0.0856	0.0012	0.0624	0.0020	559.2	13.9	685.9	69.9	529.5	7.1	22.8	-5.6	529.5	7.1	526.7	7.1

71	2	24	64	642.21	970	405	0.40	0.8238	0.0227	0.1000	0.0013	0.0599	0.0017	610.2	12.6	597.5	59.7	614.6	7.8	-2.9	0.7	614.6	7.8	615.0	7.8
71	2	24	64	642.21	206	42	0.20	1.0074	0.0461	0.1142	0.0019	0.0641	0.0030	707.6	23.3	745.3	98.2	696.9	10.7	6.5	-1.5	696.9	10.7	695.7	10.7
71	2	24	64	642.21	297	204	0.70	13.3174	0.2918	0.5169	0.0068	0.1873	0.0041	2702.4	20.8	2717.5	35.9	2686.1	29.1	1.2	-0.6	2717.5	29.1	2674.2	37.2
71	2	24	64	642.21	2944	26	0.00	2.0343	0.0429	0.1916	0.0024	0.0772	0.0016	1127.1	14.4	1124.4	41.4	1130.3	13.1	-0.5	0.3	1124.4	13.1	1130.5	41.2
71	2	24	64	642.21	1626	921	0.60	1.5176	0.0376	0.1416	0.0019	0.0779	0.0019	937.5	15.2	1143.9	49.0	853.5	10.5	25.4	-9.8	853.5	10.5	843.2	10.4
71	2	24	64	642.21	564	239	0.40	0.7749	0.0314	0.0912	0.0014	0.0617	0.0025	582.6	17.9	664.2	88.2	562.8	8.3	15.3	-3.5	562.8	8.3	560.9	8.2
71	2	24	64	642.21	895	196	0.20	0.7023	0.0202	0.0843	0.0011	0.0606	0.0018	540.2	12.1	622.3	62.4	521.8	6.7	16.2	-3.5	521.8	6.7	520.1	6.7
71	2	24	64	642.21	1363	740	0.50	0.6428	0.0172	0.0811	0.0011	0.0576	0.0015	504.1	10.6	513.2	58.8	502.9	6.4	2.0	-0.2	502.9	6.4	502.8	6.4
71	2	24	64	642.21	402	246	0.60	21.0033	0.4497	0.6071	0.0079	0.2515	0.0053	3138.7	20.9	3193.2	33.7	3058.5	31.7	4.2	-2.6	3193.2	31.7	2966.6	41.0
71	2	24	64	642.21	1101	396	0.40	1.8717	0.0444	0.1825	0.0024	0.0745	0.0018	1071.1	15.7	1054.9	47.6	1080.8	12.9	-2.5	0.9	1080.8	12.9	1082.0	12.9
71	2	24	64	642.21	957	1293	1.40	0.7871	0.0265	0.0949	0.0013	0.0603	0.0021	589.5	15.0	612.7	73.5	584.5	7.9	4.6	-0.9	584.5	7.9	584.0	7.9
71	2	24	64	642.21	600	102	0.20	0.9260	0.0331	0.1002	0.0015	0.0672	0.0024	665.5	17.5	842.4	75.3	615.5	8.6	26.9	-8.1	615.5	8.6	610.5	8.6
71	2	24	64	642.21	663	51	0.10	0.9194	0.0290	0.1079	0.0015	0.0619	0.0020	662.0	15.4	670.4	68.1	660.7	8.7	1.5	-0.2	660.7	8.7	660.4	8.7
71	2	24	64	642.21	357	89	0.20	0.6991	0.0283	0.0845	0.0013	0.0601	0.0025	538.2	16.9	607.6	88.8	522.9	7.6	14.0	-2.9	522.9	7.6	521.4	7.6
71	2	24	64	642.21	734	166	0.20	0.6494	0.0204	0.0831	0.0011	0.0568	0.0018	508.1	12.6	482.8	70.0	514.7	6.8	-6.6	1.3	514.7	6.8	515.2	6.8
71	2	24	64	642.21	368	330	0.90	0.6632	0.0267	0.0804	0.0012	0.0600	0.0025	516.6	16.3	602.6	88.4	498.3	7.2	17.3	-3.7	498.3	7.2	496.6	7.2
71	2	24	64	642.21	306	245	0.80	0.2819	0.0187	0.0395	0.0007	0.0519	0.0035	252.1	14.8	280.9	154.7	249.5	4.4	11.2	-1.1	249.5	4.4	249.3	4.4
71	2	24	64	642.21	247	136	0.60	0.6472	0.0310	0.0815	0.0013	0.0577	0.0028	506.7	19.1	518.9	106.8	504.9	7.8	2.7	-0.4	504.9	7.8	504.7	7.8
71	2	24	64	642.21	2005	851	0.40	0.1955	0.0069	0.0287	0.0004	0.0496	0.0018	181.3	5.8	173.8	82.4	182.2	2.5	-4.8	0.5	182.2	2.5	182.2	2.5
71	2	24	64	642.21	816	655	0.80	0.6008	0.0183	0.0774	0.0011	0.0564	0.0017	477.8	11.6	467.2	68.0	480.8	6.3	-2.9	0.6	480.8	6.3	481.0	6.3
71	2	24	64	642.21	202	112	0.60	0.6262	0.0365	0.0800	0.0014	0.0569	0.0034	493.7	22.8	485.5	131.2	496.4	8.4	-2.2	0.5	496.4	8.4	496.5	8.4
71	2	24	64	642.21	409	849	2.10	0.7814	0.0290	0.0957	0.0014	0.0593	0.0022	586.3	16.6	578.6	81.7	589.3	8.2	-1.9	0.5	589.3	8.2	589.5	8.2
71	2	24	64	642.21	741	167	0.20	4.1789	0.0971	0.2950	0.0038	0.1030	0.0024	1669.9	19.1	1677.3	42.8	1666.6	19.0	0.6	-0.2	1677.3	19.0	1665.5	43.2
71	2	24	64	642.21	1176	496	0.40	0.7215	0.0200	0.0912	0.0012	0.0575	0.0016	551.5	11.8	510.2	61.2	562.6	7.2	-10.3	2.0	562.6	7.2	563.6	7.2
71	2	24	64	642.21	909	373	0.40	0.8318	0.0234	0.0986	0.0013	0.0613	0.0017	614.6	12.9	649.2	60.6	606.3	7.7	6.6	-1.4	606.3	7.7	605.4	7.7
71	2	24	64	642.21	1397	395	0.30	1.4486	0.0387	0.1488	0.0020	0.0708	0.0019	909.3	16.1	949.3	55.0	894.5	11.1	5.8	-1.7	894.5	11.1	892.5	11.1

Table A.2.4 *Data from Ar-Ar dating of hornblende grains from IODP Expedition 374 Site U1521. A csv version can be found here: https://doi.org/10.5285/926cad28-669f-4703-8a5b-5e7e843a4ee1*

Core	Section	Top Offset (cm)	Bottom Offset (cm)	Sample Depth (mbsf)	Ca/K	Cl/K	Mol ^{39}Ar	%^{40}Ar*	Age (Ma)	± Age	Notes
24	2	5	45	220.23	11.63291	0.00703	0.017	57.8	16.74	0.9	
24	2	5	45	220.23	3.54777	0.07191	0.001	43.4	163.22	22.94	Low signal
24	2	5	45	220.23	1.13248	-0.08024	0.002	47.3	165.8	6.81	
24	2	5	45	220.23	0.71151	0.00792	0.001	41.1	166.08	11.29	Low signal
24	2	5	45	220.23	237.69	0.13251	0.001	5.8	231.4	36.65	Low signal
24	2	5	45	220.23	8.07684	0.00699	0.008	88.3	287.62	2.37	
24	2	5	45	220.23	11.93558	-0.06144	0.002	66.2	346.56	17.4	
24	2	5	45	220.23	0.51106	-0.0257	0.002	85.7	371.97	7.94	
24	2	5	45	220.23	7.24708	0.02096	0.01	97.6	476.89	2.78	
24	2	5	45	220.23	15.28697	0.01985	0.009	95.1	477.1	2.81	
24	2	5	45	220.23	13.6711	0.00977	0.027	91.4	477.33	1.78	
24	2	5	45	220.23	9.53664	0.02718	0.005	86.1	477.72	4.32	
24	2	5	45	220.23	21.48445	0.04428	0.003	81.6	479.77	6.3	
24	2	5	45	220.23	7.23233	0.01464	0.01	93.2	480.12	2.63	
24	2	5	45	220.23	6.48904	0.02164	0.028	95.3	481	1.6	
24	2	5	45	220.23	15.05276	0.06212	0.005	93.3	485.61	4.45	
24	2	5	45	220.23	12.95411	0.01171	0.003	91.8	490.04	6.26	
24	2	5	45	220.23	25.36517	0.01436	0.007	90.6	495.01	3.9	
24	2	5	45	220.23	18.18786	-0.02194	0.003	94.7	496.76	6.7	
24	2	5	45	220.23	9.01979	0.01225	0.005	97.7	497.42	4.3	
24	2	5	45	220.23	7.67829	0.03753	0.007	98.6	499.61	3.65	
24	2	5	45	220.23	6.13241	0.00773	0.015	98.1	500.06	2.36	
24	2	5	45	220.23	8.1823	0.02132	0.007	96.1	501.87	3.84	
24	2	5	45	220.23	6.46608	0.02469	0.014	98.2	503.33	2.28	
24	2	5	45	220.23	8.29053	0.01064	0.012	96.8	509.48	2.66	
24	2	5	45	220.23	11.539	0.0328	0.002	95.5	511.39	7.48	
24	2	5	45	220.23	7.48653	0.0057	0.011	98.5	512.79	2.53	
24	2	5	45	220.23	5.94942	0.024	0.01	92.2	513.39	3.08	
24	2	5	45	220.23	8.67949	0.01753	0.014	93	513.73	2.57	
24	2	5	45	220.23	8.42192	0.05375	0.005	95.4	514.36	4.38	
24	2	5	45	220.23	8.9701	0.02248	0.045	96.1	515.18	1.35	
24	2	5	45	220.23	6.1458	0.01405	0.019	98.1	515.61	1.98	
24	2	5	45	220.23	6.29337	0.00893	0.014	98.4	516.71	2.43	
24	2	5	45	220.23	20.09026	0.05612	0.006	89.2	516.84	4.08	
24	2	5	45	220.23	9.36973	0.01928	0.008	93.6	518.51	3.3	
24	2	5	45	220.23	7.8793	-0.01019	0.007	94.3	518.71	4.06	
24	2	5	45	220.23	10.18124	0.01151	0.006	97.2	519.63	3.99	
24	2	5	45	220.23	8.3307	0.03114	0.011	96.9	520.49	2.58	
24	2	5	45	220.23	8.71158	0.01811	0.014	99.2	521.62	2.44	
24	2	5	45	220.23	5.47698	0.02409	0.007	95.8	524.73	3.44	
24	2	5	45	220.23	7.73641	0.01979	0.004	86.3	525.94	4.37	
24	2	5	45	220.23	10.86991	0.04657	0.008	93.9	526.3	3.43	
24	2	5	45	220.23	6.88792	0.02062	0.004	95.2	527.32	5.01	
24	2	5	45	220.23	9.86348	0.02188	0.005	94.1	529.1	4.71	
24	2	5	45	220.23	11.22433	0.00545	0.004	93.3	532.59	5.44	
24	2	5	45	220.23	10.00328	0.00711	0.006	90.9	534.49	4.01	
24	2	5	45	220.23	9.42497	0.00572	0.011	97.6	538.23	2.55	
24	2	5	45	220.23	8.24294	0.04487	0.009	96.4	539.07	2.97	
24	2	5	45	220.23	10.32688	0.04158	0.012	91	540.06	2.68	
24	2	5	45	220.23	8.98084	0.01773	0.009	96.2	541.45	3.01	
24	2	5	45	220.23	12.35006	0.02242	0.005	96.5	566.15	4.58	
24	2	5	45	220.23	6.40876	-0.0267	0.007	97.2	632.53	4.53	

24	2	5	45	220.23	18.60267	-0.05262	0.003	94.8	1109.14	12.22	
24	2	5	45	220.23	7.78141	0.00823	0.025	99.4	1140.42	3.34	
24	2	5	45	220.23	7.21302	0.02145	0.005	98.9	1181.73	7.73	
24	2	5	45	220.23	6.76952	0.00549	0.028	99.5	1201.97	3.04	
24	2	5	45	220.23	10.833	0.01199	0.003	97.5	1309.45	11.99	
29	4	5	45	270.03	7.13335	0.00665	0.013	37.6	17.08	1.2	
29	4	5	45	270.03	7.26786	0.14499	0.001	2.6	126.79	38.45	Low signal
29	4	5	45	270.03	3.24333	0.23501	0.001	3.5	130.49	44.16	Low signal
29	4	5	45	270.03	2.42904	0.00705	0.001	12.2	131.74	29.96	Low signal
29	4	5	45	270.03	5.60169	0.02184	0.002	20.7	152.52	17.56	
29	4	5	45	270.03	1.22152	0.08813	0.001	4.7	158.99	29.96	Low signal
29	4	5	45	270.03	2.87981	-0.00168	0.036	64.7	170.23	1.05	
29	4	5	45	270.03	39.16756	0.02497	0.004	28.8	175.82	7.09	
29	4	5	45	270.03	1.76352	0.02903	0.001	16.2	177.23	21.09	Low signal
29	4	5	45	270.03	9.90557	0.09449	0.011	89.3	178.57	1.63	
29	4	5	45	270.03	7.00661	0.12814	0.011	95.5	180.08	1.36	
29	4	5	45	270.03	9.29327	0.10705	0.008	86.4	181.32	2.02	
29	4	5	45	270.03	0.77145	-0.0064	0.016	40.9	183.6	2.21	
29	4	5	45	270.03	10.75175	0.12304	0.004	73.6	184.57	3.88	
29	4	5	45	270.03	9.12926	0.00858	0.014	75.5	190.94	1.56	
29	4	5	45	270.03	8.44169	0.12459	0.012	75.1	193.59	1.62	
29	4	5	45	270.03	9.62623	-0.0008	0.014	33.5	197.34	3.17	
29	4	5	45	270.03	3.53971	0.01116	0.006	45	232.87	3.87	
29	4	5	45	270.03	94.63753	-0.00023	0.001	7.5	244.87	24.86	Low signal
29	4	5	45	270.03	6.74889	0.00193	0.023	90.1	280.87	1.23	
29	4	5	45	270.03	197.9075	0.13439	0.001	28.8	339.83	20.63	Low signal
29	4	5	45	270.03	23.71074	0.03089	0.002	70.6	442.43	9.01	
29	4	5	45	270.03	0.05708	-0.00446	0.049	99	461.34	1.37	
29	4	5	45	270.03	9.38006	-0.00941	0.001	74.5	475.81	11.88	Low signal
29	4	5	45	270.03	6.29576	0.00761	0.011	98	479.89	3.39	
29	4	5	45	270.03	6.90941	0.04129	0.009	73	481.35	3.68	
29	4	5	45	270.03	24.52121	-0.00917	0.003	94.1	488.78	6.49	
29	4	5	45	270.03	13.04769	-0.00079	0.004	94.7	491.09	4.42	
29	4	5	45	270.03	9.7919	0.01214	0.008	97.1	491.5	3.11	
29	4	5	45	270.03	12.01342	0.02528	0.007	96	497.24	3.12	
29	4	5	45	270.03	39.87435	0.03394	0.004	91	499.75	6.02	
29	4	5	45	270.03	8.35644	0.03117	0.013	95.6	500.76	2.51	
29	4	5	45	270.03	6.06694	0.01252	0.011	97.1	505.11	2.73	
29	4	5	45	270.03	11.33493	0.00261	0.007	91.5	506.07	3.55	
29	4	5	45	270.03	6.52511	-0.01096	0.008	98.3	507.19	3.01	
29	4	5	45	270.03	5.76392	0.0047	0.016	76.9	508.23	2.58	
29	4	5	45	270.03	11.75795	0.00272	0.008	95.6	508.69	3.37	
29	4	5	45	270.03	7.98286	0.04146	0.007	89.6	513.09	3.42	
29	4	5	45	270.03	15.52274	-0.00427	0.005	75.4	514.6	4.81	
29	4	5	45	270.03	9.56602	0.03834	0.017	95.8	515.95	2.21	
29	4	5	45	270.03	7.44551	0.02704	0.011	90.7	516.34	2.65	
29	4	5	45	270.03	9.19612	0.01021	0.009	97.6	517.68	3.01	
29	4	5	45	270.03	11.80517	-0.00336	0.008	96.8	520.95	3.35	
29	4	5	45	270.03	7.71695	0.02925	0.014	96.8	533.34	2.18	
29	4	5	45	270.03	5.96345	0.02278	0.009	98.7	538.34	3.41	
29	4	5	45	270.03	13.11403	0.03414	0.007	94.7	547.59	3.6	
29	4	5	45	270.03	10.98759	0.04377	0.008	88	558.13	3.83	
29	4	5	45	270.03	13.62948	0.02346	0.003	96.8	577.1	6.67	
29	4	5	45	270.03	13.71605	-0.00603	0.003	92.5	592.93	7.03	
29	4	5	45	270.03	63.87472	0.00213	0.004	93.1	614.41	5.69	
29	4	5	45	270.03	13.63297	0.02025	0.006	98.4	935.38	6.11	
29	4	5	45	270.03	9.24227	0.00853	0.008	98	1103.08	6.12	
29	4	5	45	270.03	6.08065	0.00269	0.008	98.7	1107.76	5.56	

29	4	5	45	270.03	8.14709	0.00088	0.011	98.8	1166.64	5.18	
42	2	50	90	373.58	5.83811	0.00034	0.045	84.9	19.17	0.35	
42	2	50	90	373.58	0.08814	0.0019	0.035	87.8	177.29	0.83	
42	2	50	90	373.58	6.20737	0.00299	0.009	96.8	436.5	2.74	
42	2	50	90	373.58	11.89723	0.03803	0.007	89	440.88	3.5	
42	2	50	90	373.58	24.75291	0.05922	0.003	83.5	451.41	6.68	
42	2	50	90	373.58	10.02828	0.01298	0.006	88.3	465.42	3.77	
42	2	50	90	373.58	11.50261	0.04949	0.004	90.2	468.7	4.92	
42	2	50	90	373.58	10.05797	0.02332	0.007	94.6	470.53	3.39	
42	2	50	90	373.58	7.40086	0.01742	0.009	93.2	471.48	2.8	
42	2	50	90	373.58	12.40768	0.0261	0.034	96.6	478.74	1.64	
42	2	50	90	373.58	12.15809	0.0207	0.005	95.9	480.67	3.85	
42	2	50	90	373.58	13.43417	0.0219	0.007	95.8	481.28	3.37	
42	2	50	90	373.58	28.02797	-0.04442	0.002	77.4	482.1	10.33	
42	2	50	90	373.58	53.63224	0.01673	0.003	57.6	482.9	9	
42	2	50	90	373.58	11.54616	-0.00943	0.005	92.3	483.05	4.31	
42	2	50	90	373.58	15.88937	0.02613	0.007	80.7	483.3	3.77	
42	2	50	90	373.58	35.47539	0.01431	0.005	91.3	485.02	5.02	
42	2	50	90	373.58	7.09742	0.03944	0.011	97.6	485.18	2.45	
42	2	50	90	373.58	14.53582	0.04113	0.003	51.3	488.47	7.18	
42	2	50	90	373.58	9.25476	0.03771	0.017	97.9	488.63	2.04	
42	2	50	90	373.58	10.95498	0.03513	0.015	97	489.6	2.32	
42	2	50	90	373.58	21.68492	0.06996	0.002	66.5	490.32	8.52	
42	2	50	90	373.58	11.95259	0.0298	0.004	31	492.59	9.88	
42	2	50	90	373.58	21.2414	0.06668	0.005	84	494.75	4.77	
42	2	50	90	373.58	9.48703	0.00981	0.014	94.4	497.46	2.42	
42	2	50	90	373.58	6.34092	0.00298	0.01	96.3	504.6	2.95	
42	2	50	90	373.58	0.01907	0.00096	0.113	99.4	505.43	1.04	
42	2	50	90	373.58	5.67582	0.0599	0.013	91.5	506.09	2.48	
42	2	50	90	373.58	14.00976	0.02184	0.011	94.7	507.43	2.92	
42	2	50	90	373.58	5.67191	0.01485	0.045	99.1	509.99	1.49	
42	2	50	90	373.58	9.16257	0.02312	0.007	96.3	511.78	3.88	
42	2	50	90	373.58	8.10195	0.01346	0.04	97.4	513.26	1.59	
42	2	50	90	373.58	7.72285	0.03012	0.029	98.6	514.36	1.66	
42	2	50	90	373.58	6.90668	0.00258	0.006	95.5	536	4.32	
42	2	50	90	373.58	2.24862	0.00817	0.09	98.7	546.87	1.2	
42	2	50	90	373.58	9.07174	-0.00541	0.031	85.3	548.24	2.12	
42	2	50	90	373.58	16.41096	0.01942	0.004	81.5	1002.98	8.04	
42	2	50	90	373.58	6.66109	0.00338	0.012	95.9	1086.9	4.45	
42	2	50	90	373.58	7.11063	0.00245	0.04	98.2	1099.05	2.82	
42	2	50	90	373.58	8.79472	0.01356	0.006	96.7	1101.89	6.7	
42	2	50	90	373.58	5.78142	0.02098	0.01	90.6	1110.81	5.81	
42	2	50	90	373.58	7.3871	0.01907	0.021	98.3	1161.8	3.61	
42	2	50	90	373.58	10.50963	0.01274	0.008	96.7	1164.13	5.95	
42	2	50	90	373.58	6.84434	0.00679	0.018	99.3	1167.84	3.83	
42	2	50	90	373.58	10.69801	0.02241	0.003	98.1	1172.79	9.45	
42	2	50	90	373.58	7.13652	0.00582	0.006	98.6	1182.89	6.09	
55	1	30	70	487.4	0.3079	0.02374	0.006	36	122.87	4.12	
55	1	30	70	487.4	4.01632	-0.02182	0.001	35.6	211.14	19.61	Low signal
55	1	30	70	487.4	6.53231	0.01731	0.004	80.1	234.95	4.05	
55	1	30	70	487.4	6.93513	-0.00849	0.013	94.3	288.5	1.77	
55	1	30	70	487.4	23.58063	0.00736	0.002	3.2	350.57	67.39	Low signal
55	1	30	70	487.4	26.33213	0.05019	0.002	85.5	421.55	8.11	
55	1	30	70	487.4	20.39494	0.06942	0.004	64.6	421.71	7.28	
55	1	30	70	487.4	48.13717	0.17685	0.003	53.3	430.5	9.07	
55	1	30	70	487.4	6.03483	-0.01098	0.003	80.1	435.29	8.89	
55	1	30	70	487.4	22.63686	0.02955	0.003	86.5	439.1	5.26	
55	1	30	70	487.4	13.57995	0.09655	0.001	18.3	453.73	21.51	Low signal

55	1	30	70	487.4	33.44225	0.13114	0.002	84.4	456.93	9.76	
55	1	30	70	487.4	21.71303	0.01528	0.009	96.4	457.6	2.77	
55	1	30	70	487.4	42.80949	0.05964	0.005	85.7	458.8	5.17	
55	1	30	70	487.4	0.04242	-0.003	0.146	99.6	459.27	0.9	
55	1	30	70	487.4	11.22036	0.03182	0.004	78.9	462.28	4.62	
55	1	30	70	487.4	11.39983	0.06547	0.003	80.8	465.14	6.85	
55	1	30	70	487.4	13.42628	0.03496	0.005	81.8	467.14	5.04	
55	1	30	70	487.4	0.00556	-0.00259	0.029	99.2	470.21	1.25	
55	1	30	70	487.4	31.77802	-0.00225	0.004	90.2	471.12	5.04	
55	1	30	70	487.4	11.22923	0.04109	0.007	36	473.82	6.2	
55	1	30	70	487.4	19.78911	0.0224	0.019	84.1	475.26	2.53	
55	1	30	70	487.4	8.77179	0.04627	0.01	96.1	475.43	2.78	
55	1	30	70	487.4	12.32718	0.00631	0.02	98.7	477.52	1.84	
55	1	30	70	487.4	8.5096	0.00694	0.009	86.8	478.53	3.16	
55	1	30	70	487.4	26.61872	0.00404	0.014	96.3	478.58	2.3	
55	1	30	70	487.4	12.31767	0.01859	0.007	96.9	481.25	3.57	
55	1	30	70	487.4	6.7871	-0.00115	0.014	98.9	481.6	2.12	
55	1	30	70	487.4	18.70944	0.02317	0.005	91.1	482.01	4.4	
55	1	30	70	487.4	14.94662	0.03819	0.003	95.6	483.55	5.52	
55	1	30	70	487.4	11.42995	0.04422	0.009	98	484.22	2.81	
55	1	30	70	487.4	7.84375	0.04407	0.008	91.8	484.33	3.24	
55	1	30	70	487.4	0.19406	-0.0027	0.15	99.7	484.47	0.83	
55	1	30	70	487.4	14.03528	0.01573	0.013	98.7	485.05	2.19	
55	1	30	70	487.4	10.70663	0.04403	0.011	98.2	485.26	2.71	
55	1	30	70	487.4	10.51909	0.03773	0.005	94.7	485.31	4.36	
55	1	30	70	487.4	11.64249	0.01938	0.013	98.6	485.57	2.12	
55	1	30	70	487.4	11.21321	-0.011	0.005	98.8	485.89	3.76	
55	1	30	70	487.4	11.36742	0.00966	0.01	99.2	486.58	2.63	
55	1	30	70	487.4	21.53839	0.02726	0.005	94.4	486.86	4.25	
55	1	30	70	487.4	10.54712	0.00965	0.009	92.7	486.94	2.71	
55	1	30	70	487.4	12.60894	0.00741	0.009	99.4	487.82	2.4	
55	1	30	70	487.4	12.73501	0.02277	0.012	98.5	487.92	2.3	
55	1	30	70	487.4	10.40474	0.01899	0.012	99.2	488.71	2.4	
55	1	30	70	487.4	12.62738	0.03794	0.005	94.1	488.8	4.12	
55	1	30	70	487.4	10.47701	0.03376	0.008	97.5	488.94	2.92	
55	1	30	70	487.4	7.4378	0.01756	0.022	99.1	491.16	1.74	
55	1	30	70	487.4	12.06689	0.04928	0.006	97.7	492.95	3.52	
55	1	30	70	487.4	32.49359	0.01534	0.001	88.2	493.67	10.53	Low signal
55	1	30	70	487.4	11.29549	0.01164	0.005	97.3	494.11	4.36	
55	1	30	70	487.4	19.44763	-0.00149	0.002	92.5	498.63	9.67	
55	1	30	70	487.4	22.04587	0.06207	0.003	97.4	500.62	5.94	
55	1	30	70	487.4	26.26357	0.08837	0.001	94.6	501.64	10.9	Low signal
55	1	30	70	487.4	36.38151	0.05931	0.005	91.6	503.08	4.73	
55	1	30	70	487.4	6.92399	-0.00773	0.012	98.6	504.89	2.74	
55	1	30	70	487.4	12.53727	0.0536	0.007	97.1	509.9	3.5	
55	1	30	70	487.4	16.25771	0.01329	0.005	91.3	513.82	4.5	
55	1	30	70	487.4	15.39782	0.00151	0.007	63.3	537.72	5.16	
65	4	63	103	588	7.95635	0.04236	0.007	65	179.03	2.37	
65	4	63	103	588	6.44593	0.13173	0.016	96.1	180.44	1.12	
65	4	63	103	588	2.21087	-0.0144	0.009	66.9	185.22	2.1	
65	4	63	103	588	0.05636	0.00064	0.061	98.9	232.78	0.57	
65	4	63	103	588	0.09939	-0.00378	0.038	96	236.59	0.73	
65	4	63	103	588	10.6248	0.01134	0.025	95.2	249.47	1.47	
65	4	63	103	588	11.2597	0.06971	0.01	83.6	274.81	3.3	
65	4	63	103	588	9.09746	-0.00258	0.01	60.2	336.58	13.53	
65	4	63	103	588	11.0966	-0.01427	0.003	63.1	342.82	14.47	
65	4	63	103	588	0.30969	-0.00166	0.08	97.4	345.69	0.75	
65	4	63	103	588	0.92905	-0.00077	0.008	84.9	353.47	3.23	

65	4	63	103	588	4.26676	0.00955	0.021	94.1	355.93	1.45	
65	4	63	103	588	4.12654	0.01083	0.029	98.9	373.58	1.09	
65	4	63	103	588	8.07088	0.01534	0.001	84.1	385.76	16.36	Low signal
65	4	63	103	588	10.87852	0.01795	0.011	98	386.88	2.09	
65	4	63	103	588	20.6833	0.00896	0.002	74.2	409.64	17.89	
65	4	63	103	588	23.19409	0.02597	0.004	88.1	412.88	4.29	
65	4	63	103	588	0.04805	-0.00526	0.052	97.1	417.02	1.07	
65	4	63	103	588	35.57359	0.02422	0.004	77.5	422.13	9.34	
65	4	63	103	588	21.18443	0.01463	0.01	25.4	434.52	8.35	
65	4	63	103	588	20.81069	0.02028	0.005	75.4	435.37	6.41	
65	4	63	103	588	16.65701	0.03506	0.003	86.7	441	9.8	
65	4	63	103	588	15.53613	0.01009	0.006	78.4	443.33	8.66	
65	4	63	103	588	48.21663	0.01609	0.004	69	451.72	6.13	
65	4	63	103	588	0.05786	-0.00412	0.257	99.5	457.21	0.61	
65	4	63	103	588	8.46713	0.00914	0.012	96.3	457.75	2.21	
65	4	63	103	588	0.0175	-0.00601	0.047	96.3	458.65	1.08	
65	4	63	103	588	20.88251	-0.01886	0.006	93.4	459.1	4.1	
65	4	63	103	588	2.33602	0.00424	0.029	97.6	459.18	1.49	
65	4	63	103	588	14.10377	0.01035	0.011	93	462.49	3.92	
65	4	63	103	588	23.33227	0.04834	0.007	94.3	462.5	4.98	
65	4	63	103	588	0.17351	0.00128	0.068	96.9	462.81	0.87	
65	4	63	103	588	15.73958	0.00541	0.012	95.4	462.86	2.26	
65	4	63	103	588	15.5738	0.02552	0.018	89.4	463.54	2.02	
65	4	63	103	588	33.18095	0.00595	0.003	89.6	464.43	10.33	
65	4	63	103	588	10.46533	-0.0031	0.011	94.3	464.94	3.61	
65	4	63	103	588	0.1635	-0.00198	0.101	98.9	466.26	0.96	
65	4	63	103	588	0.03082	-0.00515	0.105	99.8	466.43	0.8	
65	4	63	103	588	0.05264	-0.00101	0.037	99.5	466.83	1.18	
65	4	63	103	588	12.67942	0.01816	0.02	95.9	467.34	1.95	
65	4	63	103	588	0.17299	-0.00083	0.106	99.4	467.48	0.83	
65	4	63	103	588	16.49375	0.02724	0.006	89.7	468.01	3.55	
65	4	63	103	588	9.74968	0.01647	0.014	97.8	468.55	2.71	
65	4	63	103	588	18.65906	0.03623	0.007	96.1	470.14	3.63	
65	4	63	103	588	8.13837	0.00577	0.025	98.7	470.25	1.6	
65	4	63	103	588	17.86337	0.01159	0.014	97.1	470.27	2.16	
65	4	63	103	588	22.04953	0.03018	0.011	95.1	470.6	2.54	
65	4	63	103	588	10.40431	0.00901	0.029	92.5	471.33	1.73	
65	4	63	103	588	10.55171	0.00986	0.008	95.5	473.45	4.52	
65	4	63	103	588	9.00449	0.02272	0.026	96.2	473.62	1.94	
65	4	63	103	588	8.00251	0.01327	0.02	95.9	474.03	1.74	
65	4	63	103	588	12.15122	0.01814	0.008	95.9	474.22	3.98	
65	4	63	103	588	22.40878	0.01045	0.004	97.2	474.5	4.74	
65	4	63	103	588	6.604	0.00561	0.025	94.9	475.53	1.89	
65	4	63	103	588	19.83464	0.00715	0.005	91.6	475.7	5.98	
65	4	63	103	588	0.13966	-0.00268	0.079	99.4	475.75	1.02	
65	4	63	103	588	9.19955	0.00905	0.012	98.9	477.12	2.4	
65	4	63	103	588	8.72609	0.04104	0.012	97.5	477.69	2.23	
65	4	63	103	588	10.45091	0.01427	0.018	99.3	478.04	1.79	
65	4	63	103	588	9.83033	0.03644	0.01	97	478.23	3.62	
65	4	63	103	588	33.28379	0.04866	0.005	96.7	478.97	4.42	
65	4	63	103	588	15.96425	0.05283	0.004	92.2	479.45	7.32	
65	4	63	103	588	10.47026	0.0261	0.006	97.2	479.5	3.92	
65	4	63	103	588	7.59275	0.01545	0.02	96.9	479.65	1.63	
65	4	63	103	588	0.02566	-0.00009	0.025	98.7	480.29	1.74	
65	4	63	103	588	9.38903	0.02832	0.012	95.3	480.33	3.01	
65	4	63	103	588	22.01871	0.06267	0.013	94.5	480.56	3.35	
65	4	63	103	588	10.96064	0.01772	0.02	98.5	480.74	1.98	
65	4	63	103	588	7.74758	0.00443	0.022	98.8	480.81	1.66	

65	4	63	103	588	8.45404	0.00138	0.005	95.8	480.92	6.94	
65	4	63	103	588	9.49706	0.01523	0.007	89.8	481.04	5.14	
65	4	63	103	588	10.27662	0.00613	0.008	87.1	481.68	3.53	
65	4	63	103	588	8.26988	0.00468	0.009	96.2	481.7	2.74	
65	4	63	103	588	0.00704	-0.00356	0.112	99.8	481.93	0.85	
65	4	63	103	588	7.71198	0.01875	0.013	99.4	482.1	2.24	
65	4	63	103	588	10.24115	0.02013	0.016	98.2	482.18	2.25	
65	4	63	103	588	9.4674	0.02403	0.018	97.9	482.22	2.12	
65	4	63	103	588	11.03264	0.00668	0.014	97.6	482.38	2.12	
65	4	63	103	588	13.5696	-0.003	0.021	93.4	482.52	2.88	
65	4	63	103	588	0.01822	-0.00111	0.028	99.7	482.54	1.49	
65	4	63	103	588	15.56377	0.02827	0.007	97.5	483.06	3.34	
65	4	63	103	588	8.69989	0.02081	0.021	99	483.23	1.6	
65	4	63	103	588	10.82791	0.01104	0.024	96	483.29	1.8	
65	4	63	103	588	8.85241	0.03133	0.028	99.1	483.38	1.7	
65	4	63	103	588	8.39975	0.01021	0.006	97	483.41	4.22	
65	4	63	103	588	12.49051	0.01007	0.005	98.5	483.64	4.14	
65	4	63	103	588	7.93094	0.03198	0.016	96.4	483.78	2.65	
65	4	63	103	588	9.2667	0.00715	0.011	97.4	484.01	3.19	
65	4	63	103	588	10.64646	0.02546	0.014	96.9	484.03	2.29	
65	4	63	103	588	10.51332	0.01984	0.012	95.7	484.3	2.51	
65	4	63	103	588	12.90057	0.0021	0.02	91.9	484.72	2.54	
65	4	63	103	588	15.82038	0.04001	0.017	95.3	484.93	2.05	
65	4	63	103	588	9.14289	-0.00318	0.021	96.4	485.2	1.71	
65	4	63	103	588	20.70962	0.01839	0.005	81.8	485.54	4.92	
65	4	63	103	588	8.82563	0.04795	0.02	95.4	485.94	2.5	
65	4	63	103	588	10.64906	0.01711	0.015	95.7	486.53	2.63	
65	4	63	103	588	11.59028	-0.00168	0.005	93.1	487.04	7.47	
65	4	63	103	588	15.50196	0.00653	0.008	95.9	487.5	4.08	
65	4	63	103	588	7.71847	0.02491	0.021	99.1	488.34	1.84	
65	4	63	103	588	8.74947	0.05207	0.005	96.5	488.42	4.08	
65	4	63	103	588	11.4064	0.04477	0.016	96.6	488.58	1.97	
65	4	63	103	588	9.04926	0.04157	0.011	97.8	489.7	2.54	
65	4	63	103	588	69.31066	0.0073	0.008	96.4	489.83	3.26	
65	4	63	103	588	7.0055	0.01552	0.008	98.9	490.27	3.07	
65	4	63	103	588	10.86759	0.03	0.005	96.9	490.58	4.26	
65	4	63	103	588	15.83581	0.02211	0.006	97.4	491	4.04	
65	4	63	103	588	11.44769	0.00879	0.011	94	491.45	3.45	
65	4	63	103	588	17.69147	0.02751	0.007	93.1	492.17	3.53	
65	4	63	103	588	15.98103	0.02206	0.015	97.6	492.32	2.27	
65	4	63	103	588	8.23404	0.01699	0.033	98.4	492.35	1.37	
65	4	63	103	588	12.51526	0.02145	0.008	93.3	492.58	3.04	
65	4	63	103	588	15.66658	0.06887	0.007	95.1	493.63	4.99	
65	4	63	103	588	0.07467	-0.00392	0.059	98.4	493.98	1.21	
65	4	63	103	588	8.26783	0.0156	0.007	97.8	497.37	3.63	
65	4	63	103	588	10.747	0.06785	0.007	96.9	497.99	3.04	
65	4	63	103	588	11.4721	0.02633	0.009	44	498.71	5.24	
65	4	63	103	588	0.11876	-0.0073	0.018	92.1	498.86	2.34	
65	4	63	103	588	25.8914	0.08758	0.003	96.9	499.33	6.39	
65	4	63	103	588	16.39953	0.01913	0.007	94	499.91	3.37	
65	4	63	103	588	8.87166	0.00228	0.024	97	500.29	2.18	
65	4	63	103	588	15.48753	0.03784	0.01	91.4	502.01	4.03	
65	4	63	103	588	20.82163	0.02657	0.004	96.4	502.38	5.48	
65	4	63	103	588	8.22931	0.00485	0.008	96.7	503.86	4.4	
65	4	63	103	588	9.94168	0.01476	0.009	91.8	504.8	4.12	
65	4	63	103	588	8.56967	0.01293	0.016	98.4	505.89	1.96	
65	4	63	103	588	7.18062	-0.00602	0.007	96	506.31	4.82	
65	4	63	103	588	7.1371	0.0035	0.026	99.2	506.43	1.51	

65	4	63	103	588	13.53884	0.01873	0.013	86.9	506.67	2.68	
65	4	63	103	588	10.84181	0.05211	0.009	96.2	506.83	3.86	
65	4	63	103	588	11.09503	0.01066	0.002	92.4	507.03	16.21	
65	4	63	103	588	11.08483	0.02376	0.007	98.6	507.11	3.36	
65	4	63	103	588	8.69298	0.01714	0.012	98.3	507.52	2.44	
65	4	63	103	588	9.0654	0.0114	0.028	97.9	507.89	2.14	
65	4	63	103	588	14.72175	0.00234	0.009	97.3	508.8	3.26	
65	4	63	103	588	6.57821	0.01069	0.024	98.8	512.03	1.82	
65	4	63	103	588	18.32427	0.01698	0.003	83.6	512.08	9.62	
65	4	63	103	588	27.10494	0.00423	0.004	93.2	522.67	4.5	
65	4	63	103	588	15.11879	0.01848	0.004	89.3	532.98	5.1	
65	4	63	103	588	20.9287	0.00544	0.003	94.1	543.62	6.86	
65	4	63	103	588	10.5265	0.05083	0.011	90.6	558.62	3.5	
65	4	63	103	588	11.99201	0.01511	0.004	75.4	561.43	9.52	
65	4	63	103	588	17.4826	0.00137	0.012	95.5	605.7	2.7	
65	4	63	103	588	5.91422	0.00091	0.011	95.5	626.26	2.82	
65	4	63	103	588	12.37703	0.01439	0.001	72.6	920.18	41.8	Low signal
65	4	63	103	588	5.21882	0.00142	0.014	99.6	939.27	4.08	
65	4	63	103	588	14.06882	-0.03376	0.004	97.4	1101.03	11.89	
65	4	63	103	588	7.98132	-0.00771	0.013	97.9	1105.99	3.77	
65	4	63	103	588	7.87343	0.00331	0.018	99.5	1110.19	3.64	
65	4	63	103	588	7.90811	0.01578	0.042	99.3	1151.34	2.37	
65	4	63	103	588	6.10671	0.03085	0.02	97	1156.88	3.81	
65	4	63	103	588	6.35236	0.0131	0.017	99.6	1157.37	3.9	
65	4	63	103	588	7.2096	0.02439	0.027	99.5	1164.17	2.79	
65	4	63	103	588	7.4258	0.00561	0.018	98.2	1165.14	3.67	
65	4	63	103	588	7.15433	0.01582	0.033	99.8	1182.53	2.71	
65	4	63	103	588	6.25779	-0.00619	0.005	99.3	1190.81	7.49	
65	4	63	103	588	35.2913	-0.01342	0.002	91.6	1297.94	23.88	

Table A.2.5. *Clay mineralogy data for IODP Expedition 374 Site U1521.*

Core	Section	Top Offset (cm)	Bottom Offset (cm)	Sample Depth (m.b.s.f)	Smectite %	Illite %	10-14 Mixed Layer %	Chlorite %	Kaolinite %	Esquevin Index	Kübler Index	1 :smectite 17Å (cts/s)	2 :IS 11-11.5 Å (cts/s)	3 :illite 10Å (cts/s)	4 :kaolinite+chlorite 7.2Å (cts/s)	6 :quartz 4.25Å (cts/s)	7 :kaolinite 3.58Å (cts/s)	8 :chlorite 3.54Å (cts/s)
1	1	4	6	0.05	21	44	7	21	7	0.197	0.314	13071	4440	27300	17813	763	509	1433
1	3	62	91	3.265	45	33	8	10	4	0.151	0.346	98252	17260	71223	29859	797	879	2217
3	1	77	115	17.96	2	43	18	29	8	0.195	0.259	858	7063	17199	15022	796	267	965
5	2	66	69	38.375	1	51	18	25	5	0.212	0.297	701	9907	27792	16289	1033	325	1542
8	1	13	53	65.33	1	46	22	24	7	0.16	0.305	481	11790	24996	16916	535	389	1315
9	2	70	73	76.755	2	47	18	25	8	0.129	0.172	795	7494	19808	13852	938	389	1295
10	1	81	84	85.03	1	39	22	31	7	0.199	0.281	509	10054	17760	17139	609	324	1477
12	4	145	147	108.76	6	35	26	25	8	0.168	0.291	1716	7572	10306	9933	655	244	760
15	1	10	13	132.32	0	41	32	26	2	0.237	0.323	0	9761	12435	8439	747	49	784
17	3	65	68	154.25	0	44	15	37	4	0.177	0.27	0	3700	10626	9926	672	81	860
21	4	7	9	194.15	26	30	14	26	3	0.202	0.215	8930	4885	10284	9820	1075	115	988
22	1	32	35	199.74	1	41	26	31	1	0.205	0.304	484	8399	13403	10648	1207	58	1287
22	2	17	19	200.79	1	40	23	30	5	0.193	0.282	326	5069	8971	7799	786	85	489
22	4	60	62	204.1	3	44	23	28	2	0.224	0.277	837	6881	12824	8783	865	63	833
24	2	5	45	220.23	3	38	19	34	7	0.176	0.246	1356	9176	18170	19705	1841	330	1734
25	3	40	43	230.89	3	44	17	31	4	0.204	0.259	1852	9607	24479	19184	1402	257	1924
26	2	110	112	240.06	4	42	16	34	4	0.222	0.239	2171	8644	22621	20393	1533	243	2070
26	4	60	63	242.41	5	42	19	31	3	0.194	0.252	2355	9860	22044	18046	1368	195	1863
26	4	74	76	242.54	3	46	16	31	4	0.197	0.269	1292	8415	23591	17873	1684	238	1695
28	4	36	39	260.94	2	48	19	28	4	0.201	0.248	646	5764	14756	9723	791	113	897
29	4	5	45	270.03	4	45	16	32	4	0.196	0.257	1901	8636	24232	19280	1475	195	1720
30	3	15	18	278.66	1	38	24	35	1	0.214	0.234	427	7226	11464	10864	1088	39	981
36	2	87	127	335.72	3	43	18	32	3	0.162	0.266	1120	6735	15932	13067	1161	85	908
37	3	77	80	346.48	2	49	16	30	3	0.16	0.261	644	5357	16139	10729	1658	87	883
40	2	69	72	364.27	2	49	17	28	3	0.164	0.252	913	7622	21864	13794	1831	166	1424
42	2	50	90	373.58	3	52	10	29	5	0.2	0.246	1210	3628	18752	12399	1509	182	1062
44	3	81	84	384.99	5	43	11	38	2	0.228	0.295	2661	5938	22779	21370	1949	127	2378
47	1	52	92	410.82	4	51	8	33	4	0.163	0.272	2227	4285	27917	20147	1247	231	1763
49	4	79	82	433.87	4	51	14	26	5	0.22	0.271	3274	9996	37865	22667	1306	463	2573
51	1	50	53	449.02	17	38	8	35	1	0.242	0.303	11144	5275	24511	22852	1808	89	2486
55	1	30	70	487.4	24	37	7	29	2	0.234	0.299	22727	6960	34921	29452	1721	285	3346
61	2	53	56	546.5	58	22	3	16	1	0.263	0.301	97485	4211	35924	29077	1575	279	3366
65	4	63	103	588	12	48	10	26	4	0.184	0.236	11210	9618	44103	27856	2342	459	2977
69	3	56	59	624.67	6	55	8	29	3	0.171	0.205	2597	3697	25625	14985	2250	163	1445
71	2	24	64	642.21	4	49	11	33	3	0.194	0.187	2365	6798	31098	23002	3829	269	2909

Table A.2.6. *Dinocyct counts for IODP Expedition 374 Site U1521 (continued on next page).*

Core	Section	Top offset (cm)	Bottom offset (cm)	Midpoint depth	weight sample	Lycopodium counted	Lycopodium total	weight counted (g)	Brigantedinium simplex	Brigantedinium pynei	Batiacasphaera "smooth"	Batiacasphaera "mini" (transparent)	Batiacasphaera cooperi	Arcticacysta	Spiniferites spp	P-cyst 1/long complex spines	P-cyst 2/short	P-cyst 3/long spines	P-cyst 4	P-cyst 5	P-cyst white, tranparent	p-cyst short/knots	Lejeunecysta spp	L. cowiei	L. acuminata	L. cinctoria (kepion) / Trinovantedinium	L. fallax
23	1	6	11	209.085	13.0139	36	9666	0.048469	23	7	32	0	3	2	2	34	0	65	60	63	0	0	3	0	4	0	7
24	1	122	127	219.845	15.6319	179	9666	0.28948	2	0	36	26	0	8	1	2	1	2	0	0	0	0	1	0	0	0	0
25	2	10	12	229.46	12.4132	165	19855	0.103157	5	1	143	45	1	16	6	0	5	5	0	0	2	0	0	0	0	0	0
25	3	80	82	231.28	15.3738	178	19855	0.137826	2	3	88	4	0	11	3	5	4	3	0	0	1	1	0	0	0	0	0
26	2	80	82	239.76	12.1198	221	19855	0.134902	5	2	163	14	0	20	3	0	5	3	0	0	5	0	2	0	0	0	0
27	3	60	62	250.33	7.9483	263	19855	0.105283	8	0	130	19	2	11	0	1	10	3	0	0	5	1	0	0	0	0	0
29	3	60	62	269.09	15.3207	153	19855	0.118059	5	1	144	21	2	16	8	3	8	2	0	0	11	1	2	0	0	0	0
31	2	27	32	286.605	15.0315	37	9666	0.057538	27	3	123	7	10	5	1	6	4	4	0	0	5	4	26	3	0	0	1
33	1	30	32	304.81	14.8802	74	19855	0.055459	79	20	71	2	12	1	0	0	1	1	0	0	0	0	56	8	4	3	10
34	1	31	33	314.42	15.2171	311	19855	0.238354	32	2	159	5	3	1	2	4	8	2	0	0	24	2	0	0	0	0	0
38	2	54	56	354.55	15.4545	618	19855	0.481032	7	1	73	0	4	0	1	0	0	0	0	0	3	1	0	0	0	0	0
39	1	53	55	357.84	15.0027	960	19855	0.725389	1	2	163	14	2	0	0	0	0	0	0	0	0	0	2	0	0	0	0
40	2	55	57	364.12	14.8609	645	19855	0.482764	14	0	57	11	4	0	1	0	0	0	0	0	0	0	3	0	0	0	1
42	3	54	56	374.9	15.0868	334	19855	0.25379	0	2	6	0	2	0	0	0	0	0	0	0	0	0	0	0	0	0	0
43	1	72	75	377.235	15.0381	645	19855	0.48852	3	1	88	7	5	0	0	0	1	0	0	0	0	0	1	0	0	0	0
45	2	54	56	392.61	15.2452	408	19855	0.313273	11	4	87	1	0	0	0	0	1	0	0	0	5	3	1	0	1	0	0
49	2	57	59	431	14.9791	421	19855	0.317613	5	4	83	7	5	0	1	0	1	0	0	0	1	3	1	0	0	0	0
52	3	23	26	461.205	14.9698	366	19855	0.275948	3	5	46	3	1	3	0	2	3	0	0	0	1	0	2	0	0	0	0
54	2	53	55	479.23	15.1137	400	19855	0.304481	4	2	89	2	2	0	2	1	0	0	0	0	1	0	2	0	0	0	0
58	3	80	83	519.235	15.3159	445	19855	0.343267	15	2	43	1	6	0	0	3	9	0	0	0	0	0	9	0	0	0	0
58	6	80	83	523.555	15.0778	159	19855	0.120744	6	1	100	1	1	0	0	0	3	1	0	0	0	0	0	0	0	0	0
63	3	110	113	567.75	15.0188	413	19855	0.312403	2	0	41	0	4	0	2	2	0	0	0	0	0	0	2	0	0	0	0
66	2	54	56	594.48	14.9776	927	19855	0.699282	0	0	37	0	1	0	0	0	0	0	0	0	0	0	1	0	0	0	0

Lejeunecysta attenuata	Lejeunecysta katanos	Lejeunecysta adeliensis?	Operculodinium centrocarpum	O. janduchenei	O. piasecki	O. centroc ss big	Pyxidinopsis/Batiacasphaera indet	Impagidinium pallidum	Selenopemphix spp.	Selenopemphix sp1	S. botrion	S. sp transparent	S. undulata	S. antarctica	Operculodinium sp yellow	Opercul sp. dark (REW?)	Vozzhennikovia (REW)	Enneadocysta (REW)	Spinidinium (REW)	Cymatiosphaera 1	Cymatiosphaera 2	Cymatiosphaera 3	Cymatiosphaera 4	Cymatiosphaera star	Cymatiosphaera more processes	Cymatiosphaera transparant sp. 1	Leiosphaeridea	Pediastrum	Pollen spp no bisaccate (incl rew)	Bisaccate pollen (incl. rew)	Spores (incl. rew)	Foram lining
0	0	0	5	0	0	0	3	2	1	3	0	0	0	0	0	0	0	0	0	60	78	2	93	0	0	0	280	0	15	3	5	0
0	0	0	12	0	0	0	1	0	0	0	0	0	0	0	0	0	0	0	0	37	0	0	0	0	0	0	377	2	19	3	1	1
0	0	0	32	0	0	0	0	7	0	0	0	0	0	0	0	0	0	0	0	3	3	1	0	0	20	13	101	0	8	4	5	8
0	0	0	39	0	0	1	0	0	0	0	0	0	0	0	0	0	0	0	0	4	0	0	0	0	15	24	158	0	1	3	4	9
0	0	0	39	0	0	0	0	8	0	0	0	0	0	0	2	0	0	0	0	0	0	0	0	0	35	28	98	0	3	4	1	9
0	0	0	32	0	0	0	0	0	0	0	0	0	0	1	3	0	0	0	0	0	0	0	0	0	18	55	108	0	3	9	1	5
1	0	0	27	0	0	0	0	6	0	0	0	0	0	0	4	0	0	0	0	0	0	0	0	0	28	29	78	0	4	5	3	7
1	1	0	17	0	0	1	0	7	1	0	0	0	0	1	0	0	1	0	0	0	0	0	0	0	3	0	8	0	5	7	10	22
9	1	1	1	0	0	0	0	7	14	0	0	0	0	1	0	0	0	0	0	0	0	0	0	0	0	1	4	0	1	1	2	7
0	0	0	7	0	0	0	0	3	1	0	0	0	0	0	0	4	0	1	0	0	0	0	0	0	0	2	0	0	16	6	44	14
0	0	0	7	0	0	0	0	3	0	0	0	0	0	0	1	1	0	0	0	0	0	0	0	0	0	2	4	0	12	11	10	18
0	0	0	10	0	0	0	0	3	1	0	0	0	0	0	2	0	0	0	0	0	0	0	0	0	0	3	11	0	8	8	18	15
0	0	0	14	0	0	0	0	2	0	0	0	0	0	0	1	1	0	0	0	0	0	0	0	0	0	4	69	1	13	13	11	9
0	0	0	2	0	0	0	0	0	0	0	0	0	0	0	0	0	0	0	0	0	0	0	0	0	1	2	0	0	4	2	3	5
0	0	0	4	0	0	0	0	1	0	0	0	0	0	0	0	1	1	0	0	0	0	0	0	0	0	1	3	0	5	4	8	13
0	0	0	2	0	0	0	0	0	0	0	0	0	0	0	0	6	0	2	0	0	0	0	0	0	0	3	18	0	57	15	20	7
0	0	0	3	0	0	0	0	11	2	0	0	0	0	0	1	9	38	5	0	0	0	0	0	0	3	7	37	0	83	16	16	21
0	0	0	4	0	0	0	0	4	1	0	0	0	0	0	0	1	47	4	1	0	0	0	0	0	0	1	96	0	101	11	23	25
0	0	0	13	0	0	0	0	7	2	0	0	0	0	0	1	3	71	7	1	0	0	0	0	2	2	2	93	0	120	22	41	40
0	0	0	2	0	0	0	0	19	2	0	0	0	0	0	2	2	27	3	1	0	0	0	0	1	0	0	59	0	35	12	14	18
0	0	0	0	0	0	0	0	2	0	0	0	0	0	0	0	1	55	2	1	0	0	0	0	0	1	0	172	0	80	9	14	10
0	0	0	1	0	0	0	0	2	0	0	0	0	0	2	0	2	74	2	0	1	0	0	0	1	0	1	66	1	117	20	24	8
0	0	0	3	0	0	0	0	3	0	0	0	0	0	0	0	2	57	4	0	0	0	0	0	0	0	0	166	0	63	9	10	4

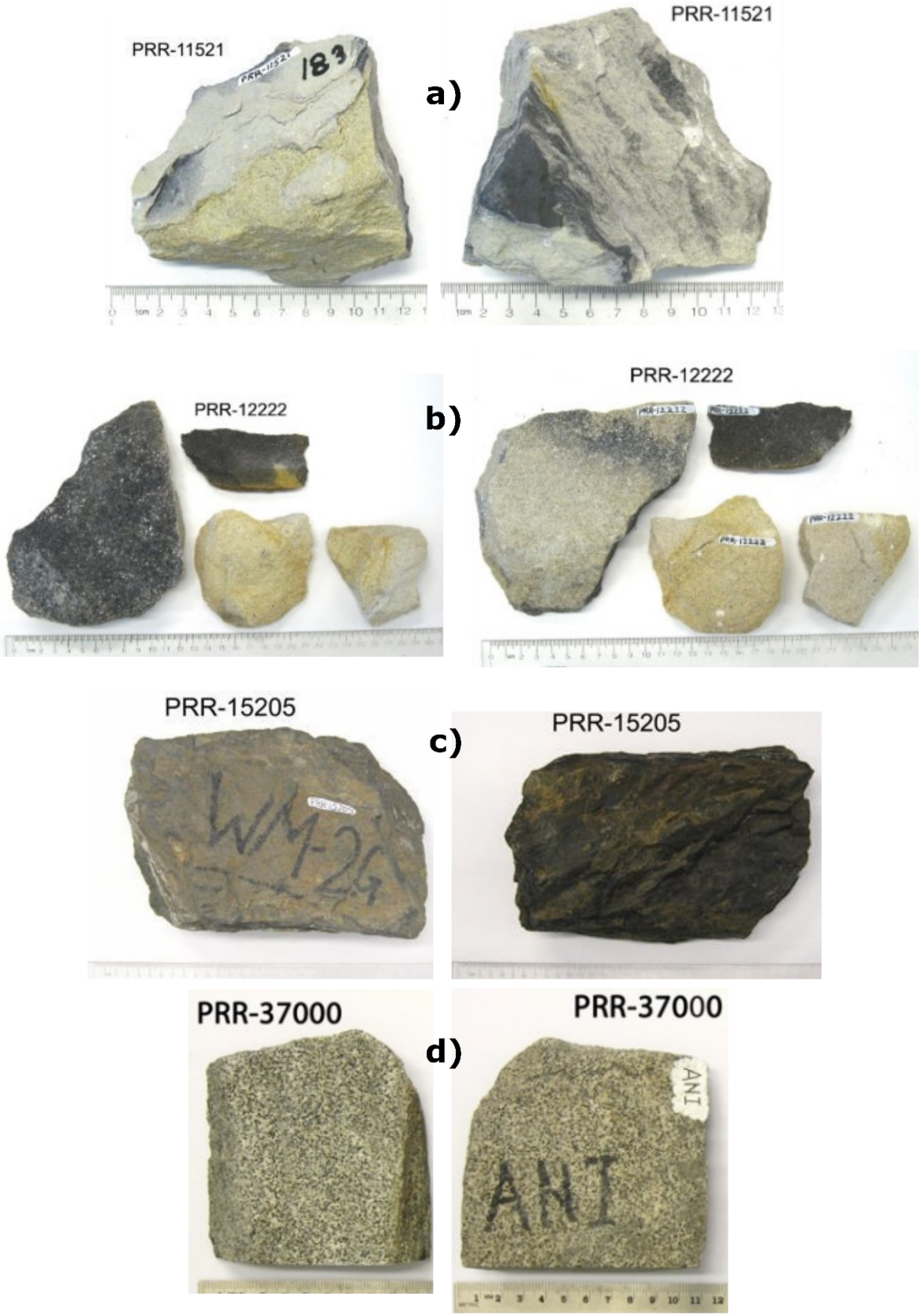
Table A.2.7. *Pollen and spore counts for IODP Expedition 374 Site U1521.*

Core	Section	Top offset (cm)	Bottom offset (cm)	Midpoint depth (mbsf)	Lycopodium counted	Lycopodium total	Sample Weight (g)	weight counted (g)	Total Pollen and Spore Counted	Total Mesozoic Pollen and Spore	Total Probable Paleogene Pollen and Spore	Pollen and Spore (grains/g)	Mesozoic Pollen and Spore (grains per gram)	Probable Paleogene Pollen and Spore (grains per	Mesozoic Pollen and Spore (%)	Probable Paleogene Pollen and Spore (%)
30	2	22	27	277.34	192	9666	15.17	0.301	105	1	2	348	3	7	1	1.9
30	3	65	70	279.17	160	9666	14.59	0.242	105	4	4	435	17	17	3.8	3.8
31	2	27	32	286.61	208	9666	14.2	0.306	101	6	5	331	20	16	5.9	5
38	2	54	56	354.55	786	19855	15.45	0.612	69	9	6	113	15	10	13	8.7
43	1	72	75	377.24	785	19855	15.04	0.595	42	13	0	71	22	0	31	0
54	2	53	55	479.23	255	19855	15.11	0.194	132	0	11	680	0	57	0	8.3
63	3	110	113	567.75	295	19855	15.01	0.223	121	0	10	543	0	45	0	8.3

Table A.2.8. *Neodymium and Sr isotope data from new Transantarctic Mountain rock samples.*

Location	Lat.	Long.	Sample Name	Rock Formation/ Type	Rock Group	$^{143}Nd/^{144}Nd$	2SE	ε_{Nd}	2SD	$^{87}Sr/^{86}Sr$	2SE
Whitmore Mnts.	-82.61	-105.76	WM-2G	Metasediment	Whitmore Mountain Metasediments	0.512150	0.000010	-9.53	0.19	0.742683	0.000008
Mt. Bjaaland	-86.55	-164.23	PRR-12222	Triassic Sandstone	Beacon Supergroup	0.512275	0.000008	-7.08	0.19	0.747423	0.000010
Mt. Schopf	-84.80	-113.25	H3-183	Permian Sandstone	Beacon Supergroup	0.512091	0.000008	-10.66	0.19	0.720159	0.000008
Ackerman Ridge	-86.61	-147.14	EAZ	La Gorce Fm.	Liv Group	0.512270	0.000012	-7.18	0.19	0.722112	0.000007
Cressey Peak	-85.48	-143.17	CIA	Leverett Fm.	Liv Group	0.512362	0.000008	-5.38	0.19	0.716022	0.000008
-	-85.01	-166.51	ANI	Duncan Fm.	Liv Group	0.512149	0.000008	-9.53	0.19	0.794694	0.000010
Procedural Replicate						0.512130	0.000008	-9.91	0.19	0.792204	0.000008
Mt. Ellis	-79.87	156.23	EL-01	Permain white siltsone-mudstone	Beacon Supergroup	0.511761	0.000007	-17.12	0.19	0.759285	0.000008

Figure A.2.1. *Pictures of Transantarctic Mountain rock samples analysed for Nd and Sr isotope compositions. a) H3-183, b) PRR-12222, c) WM-2G, d) ANI, e) CIA and f) EL-01. No photo was available for sample EAZ.*




PRR-37685
e)
PRR-37685
C1A
C1A


f)
PRR-22351

Table A.2.9. *Literature compilation of terrestrial rock and sediment Nd and Sr isotope data. Published as a csv file in the supplement of Marschalek et al. (2021). For the reference numbering, see Marschalek et al. (2021) (Appendix Section A.1).*

Region	Location	Lat.	Long.	Sample Name	Rock Type/ Formation	Group	Rb	Sr	$^{87}Rb/^{86}Sr$	87Sr/ 86Sr	Sm	Nd	$^{147}Sm/^{144}Nd$	$^{143}Nd/^{144}Nd$	eNd	Ref. #
Ross Ice Shelf	RISP	-82.38	-168.63		Sediment	Unconsolidated sediments				0.724298				0.512381	-8.23	28
WAIS	Whillans	-83.45	-137.76		Sediment	Unconsolidated sediments				0.731049				0.512226	-8.04	28
WAIS	Whillans	-83.45	-137.76		Sediment	Unconsolidated sediments				0.731077				0.512186	-8.82	28
WAIS	Kamb	-82.43	-135.95		Sediment	Unconsolidated sediments				0.718687				0.512247	-7.63	28
WAIS	Kamb	-82.43	-135.95		Sediment	Unconsolidated sediments				0.722141				0.512280	-6.98	28
WAIS	Binschadler	-81.07	-140.01		Sediment	Unconsolidated sediments				0.731654				0.512129	-9.93	28
Central Transantarctic Mnts.	Britannia Ridge (BR)	-80.39	155.33		Moraine sediment	Unconsolidated sediments				0.721234				0.511999	-12.5	30
Central Transantarctic Mnts.	Bates Nunatak (BN)	-80.26	153.65		Moraine sediment	Unconsolidated sediments				0.713919				0.512168	-9.2	30
Central Transantarctic Mnts.	Horney Bluff (HB)	-80.21	159.14		Moraine sediment	Unconsolidated sediments				0.731504				0.511956	-13.3	30
Central Transantarctic Mnts.	Crazy Jim (CJ)	-80.40	157.13		Moraine sediment	Unconsolidated sediments				0.736235				0.511941	-13.6	30
Central Transantarctic Mnts.	Lonewolf (LW)	-81.30	153.17		Moraine sediment	Unconsolidated sediments				0.733334				0.511614	-20.0	30
Central Transantarctic Mnts.	Lonewolf 2 (LW 2)	-81.34	152.68		Moraine sediment	Unconsolidated sediments				0.73402				0.511650	-19.3	30
Central Transantarctic Mnts.	All Blacks (AB)	-81.52	155.53		Moraine sediment	Unconsolidated sediments				0.71817				0.512307	-6.5	30
Central Transantarctic Mnts.	Mt. Tuatara (MT)	-80.48	158.67		Moraine sediment	Unconsolidated sediments				0.745465				0.511799	-16.4	30
Central Transantarctic Mnts.	Sanford Cliffs (SC)	-83.98	158.90		Moraine sediment	Unconsolidated sediments				0.71304				0.512310	-6.4	30
Central Transantarctic Mnts.	Gargoyle Ridge (GR)	-82.42	159.29		Moraine sediment	Unconsolidated sediments				0.728104				0.511721	-17.9	30
Central Transantarctic Mnts.	Cambrian Bluff (CB)	-82.38	161.03		Moraine sediment	Unconsolidated sediments				0.741674				0.511743	-17.5	30
Central Transantarctic Mnts.	Campbell Hills (CH)	-82.40	163.97		Moraine sediment	Unconsolidated sediments				0.725421				0.511990	-12.7	30
Central Transantarctic Mnts.	Turret Nunatak(TN)	-82.43	158.12		Moraine sediment	Unconsolidated sediments				0.72283				0.511869	-15.0	30
Central Transantarctic Mnts.	Argo Glacier (AG)	-83.50	156.74		Moraine sediment	Unconsolidated sediments				0.733107				0.511689	-18.5	30
Central Transantarctic Mnts.	Quest Cliffs (QC)	-82.54	154.83		Moraine sediment	Unconsolidated sediments				0.713201				0.512214	-8.3	30
Central Transantarctic Mnts.	Milan Ridge (MR)	-83.28	156.04		Moraine sediment	Unconsolidated sediments				0.727253				0.511841	-15.5	30
Central Transantarctic Mnts.	Kon Tiki Nuntak (*KT*)	-82.53	160.09		Moraine sediment	Unconsolidated sediments				0.735999				0.511670	-18.9	30
Edward VII Peninsula	Gould Peak	-78.12	-155.25	E7W87	Granite	Evolved Granitoids	372	45	24.1				0.1432	0.512233	-7.9	106
Edward VII Peninsula	Mt Schlossbach	-78.05	-154.80	E7W67	Granite	Evolved Granitoids				0.784722			0.1896	0.512325	-6.1	106
Edward VII Peninsula	Washington Ridge	-78.10	-154.80	E7W74	Granite	Evolved Granitoids							0.1805	0.512348	-5.7	106
Edward VII Peninsula	Mt Paterson	-78.03	-154.60	E7W90	Granite	Evolved Granitoids	279	112	7.22	0.74691			0.1226	0.512196	-8.6	106
Edward VII Peninsula	Bowman Peak	-77.48	-153.22	E7W10	Granite	Evolved Granitoids	391	25	45.1	0.7411			0.1352	0.512314	-6.3	106
Ford Ranges		-76.88	-145.70	D1/3	Granodiorite	Palaeozoic Granitoids (W.A.)					6.1	30.5	0.121	0.512336	-5.9	106
Ford Ranges		-76.66	-145.46	MB.227.4P	Granodiorite	Palaeozoic Granitoids (W.A.)	194	224	2.5089	0.720272	10.9	60.4	0.1092	0.512261	-7.4	106
Ford Ranges		-77.17	-145.00	R7460	Granodiorite	Palaeozoic Granitoids (W.A.)					5.5	31.8	0.1045	0.512282	-6.9	106
Ford Ranges		-76.23	-143.86	MB.219.2P	Granodiorite	Palaeozoic Granitoids (W.A.)	89	337	0.7654	0.708903	4.0	20.1	0.1204	0.512428	-4.1	106

Ford Ranges		-76.97	-143.75	R7205	Granodiorite	Palaeozoic Granitoids (W.A.)					7.1	36.8	0.1164	0.512275	-7.1	106
Ford Ranges	unnamed nunatak SW of Mt Iphigene	-76.54	-146.10	K6-NU01	Granite	Evolved Granitoids			23.3		2.8	7.3	0.2329	0.512400	-4.6	107
Ford Ranges	Sarnoff Mountains	-77.17	-145.00	9D12-2	Granite	Evolved Granitoids			21.53	0.7413	9.8	34.6	0.1713	0.512400	-4.6	107
Ford Ranges	Fosdick Mountains	-76.05	-146.05	K6-T35b	Granite	Palaeozoic Granitoids (W.A.)			1.78	0.7151	4.3	24.3	0.1067	0.512300	-6.6	107
Ford Ranges	Fosdick Mountains	-76.52	-146.01	K6-I60	Granite	Palaeozoic Granitoids (W.A.)			1.37	0.7127	5.6	29.7	0.113	0.512300	-6.6	107
Ford Ranges	Fosdick Mountains	-76.54	-145.82	C5-Is51A	Granite	Palaeozoic Granitoids (W.A.)			7.6	0.753	7.9	38.8	0.1228	0.512100	-10.5	107
Ford Ranges	Fosdick Mountains	-76.46	-145.49	K6-A21b	Granite	Palaeozoic Granitoids (W.A.)			1.36	0.7151	6.8	38.9	0.1053	0.512200	-8.5	107
Ford Ranges	Fosdick Mountains	-77.16	-144.94	912-2A	Granodiorite	Palaeozoic Granitoids (W.A.)			7.1	0.7411	9.4	50.1	0.1137	0.512300	-6.6	107
Ford Ranges	Fosdick Mountains	-76.97	-144.55	9N27-4	Granodiorite	Palaeozoic Granitoids (W.A.)			0.88	0.7106	4.0	20.2	0.1198	0.512300	-6.6	107
Ford Ranges	Swanson Range	-77.01	-144.88	K6-SR29	Metasediment	Swanson Fm	216	95	6.56	0.7585	7.6	42.8	0.107	0.512000	-12.4	107
Ford Ranges	Swanson Range	-77.01	-144.88	K6-SR30	Metasediment	Swanson Fm	171	112	4.41	0.7449	7.9	38.2	0.1246	0.512000	-12.4	107
Ford Ranges	Swanson Range	-77.01	-144.88	K6-SR31	Metasediment	Swanson Fm	118	136	2.5	0.732	7.2	37.9	0.1156	0.512000	-12.4	107
Ford Ranges	Swanson Range	-77.01	-144.88	K6-SR32	Metasediment	Swanson Fm	135	199	1.96	0.7264	6.0	27.9	0.1304	0.512100	-10.5	107
Ruppert-Hobbs Coast	Milan Rock	-76.02	-140.68	MB.221.1W	Metasediment	Swanson Fm	147	49	8.7495	0.7618	7.8	40.1	0.1175	0.511953	-13.4	107
Ellsworth-Whitmore Mnts.	Linck Nunataks	-82.68	-104.20	65-W-80	Linck Nunatak Granite	Mesozoic Granites			0.6727	0.71846	6.3	27.3	0.14	0.512310	-6.40	108
Ellsworth-Whitmore Mnts.	Whitmore Mountains	-82.58	-104.50	65-W-44	Mount Seelig Granite	Mesozoic Granites			0.0414	0.70948	13.9	53.3	0.1575	0.512463	-3.41	108
Ruppert-Hobbs Coast	Brunner Hill	-75.57	-141.90	MB.206.2P	Microgranite	Evolved Granitoids	178	53	9.693	0.758429	2.2	9.6	0.1411	0.512345	-5.7	109
Ruppert-Hobbs Coast	Mt McCoy	-75.87	-141.17	MB.201.5P	Granodiorite	Palaeozoic Granitoids (W.A.)					4.0	23.9	0.1009	0.512594	-0.9	109
Ruppert-Hobbs Coast	Patton Bluff	-75.22	-133.67	MB.208.7P	Paragneiss enclave	Palaeozoic Granitoids (W.A.)	164	341	1.393	0.71154	6.2	33.4	0.113	0.512380	-5.0	109
Central Transantarctic Mnts.	Dolphin Spur	-84.20	172.80	98-268D	Felsite	GHI	133	79	4.87	0.749939	2.2	5.1	0.2568	0.512600	-0.7	116
Central Transantarctic Mnts.	Southern Miller Range	-83.47	157.81	90-WMR1	Granodiorite	GHI	107	464	0.67	0.747202	1.0	4.3	0.1435	0.511694	-18.4	116
Central Transantarctic Mnts.	Argo Glacier	-83.28	157.63	90-104B	Granite	GHI	177	91	5.63	0.752023	6.193	29.367	0.1275	0.512249	-7.6	116
Central Transantarctic Mnts.	Argo Glacier	-83.28	157.63	99-305	Leucogranite	GHI	193	63	8.87	0.77677	6.1	24.7	0.1502	0.512258	-7.4	116
Central Transantarctic Mnts.	Argo Glacier	-83.28	157.63	99-306	Diorite	GHI	15	265	0.16	0.708376	1.4	5.5	0.1545	0.512369	-5.2	116
Central Transantarctic Mnts.	Milan Ridge	-83.25	156.13	90-GMR117	Granite	GHI	158	98	4.67	0.744638	18.6	116.2	0.0966	0.512203	-8.5	116
Central Transantarctic Mnts.	Milan Ridge	-83.25	156.13	03-408B	Gabbro	GHI	46	166	0.8	0.711544	5.0	22.3	0.1357	0.512371	-5.2	116
Central Transantarctic Mnts.	Ascent Glacier	-83.22	156.37	99-307	Granite	GHI	383	108	10.26	0.825385	4.5	21.8	0.1252	0.511849	-15.4	116
Central Transantarctic Mnts.	Kreiling Mesa	-83.22	157.90	03-407	Granite	GHI	159	160	2.88	0.747658	10.9	56.8	0.1164	0.511825	-15.9	116
Central Transantarctic Mnts.	Miller Range	-83.17	157.00	86-BMR3	Granite	GHI	213	138	4.47	0.751621	8.468	51.557	0.0993	0.511746	-17.4	116
Central Transantarctic Mnts.	Moody Nunatak	-83.12	159.50	03-400a	Granite	GHI	138	253	1.58	0.730171	7.7	38.9	0.1196	0.512152	-9.5	116
Central Transantarctic Mnts.	Moody Nunatak	-83.12	159.50	03-401	Granite	GHI	184	210	2.54	0.733555	5.2	23.5	0.1328	0.512137	-9.8	116
Central Transantarctic Mnts.	Mt Macbain	-83.10	162.30	98-226B	Felsite	GHI	48	115	1.21	0.723152	1.8	6.9	0.1605	0.512229	-8.0	116
Central Transantarctic Mnts.	Lookout Dome	-83.05	156.45	99-308	Granite	GHI	121	154	2.27	0.761328	3.9	19.7	0.1202	0.511836	-15.6	116
Central Transantarctic Mnts.	Snowshoe pass	-83.03	157.67	85-BCT93	Granite	GHI	220	147	4.33	0.771976	8.113	48.234	0.1017	0.511825	-15.9	116

Central Transantarctic Mnts.	Mt Tedrow	-82.88	163.00	03-405	Granite	GHI	308	116	7.68	0.762789	9.3	49.3	0.1136	0.512122	-10.1	116
Central Transantarctic Mnts.	Cambrian Bluff	-82.87	160.55	98-241B	Felsite	GHI	132	212	1.8	0.722467	6.2	29.7	0.127	0.512152	-9.5	116
Central Transantarctic Mnts.	Mt Summerson	-82.72	155.08	03-402	Granite	GHI	307	171	5.2	0.776484	4.1	17.7	0.1406	0.511875	-14.9	116
Central Transantarctic Mnts.	Lowery Glacier	-82.58	162.25	98-207A	Diorite	GHI	37	121	0.88	0.718173	3.1	11.8	0.1603	0.512188	-8.8	116
Central Transantarctic Mnts.	Algie Glacier	-82.13	162.08	98-244B	Felsite	GHI	129	161	2.32	0.731907	0.9	6.2	0.1071	0.512059	-11.3	116
Southern Transantarctic Mnts.	La Gorce Mountians	-86.75	-146.00	EGO	Wyatt	Liv Group (volcanic bed)	190			0.745027				0.512274	-3.1	137
Southern Transantarctic Mnts.	La Gorce Mountians	-86.75	-146.00	ES-228	Wyatt	Liv Group (volcanic bed)				0.743262				0.512383	-1.8	137
Southern Transantarctic Mnts.	La Gorce Mountians	-86.75	-146.00	ECE	Ackermann	Liv Group (volcanic bed)				0.738809				0.512238	-2.7	137
Southern Transantarctic Mnts.	?	-	-	ASB	Fairweather Fm.	Liv Group (volcanic bed)	5			0.707299	3.1	11.3		0.512589	1.2	137
Southern Transantarctic Mnts.	?	-	-	AUD	Fairweather Fm.	Liv Group (volcanic bed)					4.5	15.5		0.512854	5.7	137
Southern Transantarctic Mnts.	Shackleton Glacier/Duncan Moutains/Harold Byrd Mountains	-	-	AUQ	Fairweather Fm.	Liv Group (volcanic bed)	124			0.727476				0.512501	-1.1	137
Southern Transantarctic Mnts.	Shackleton Glacier/Duncan Moutains/Harold Byrd Mountains	-	-	AQV	Fairweather Fm.	Liv Group (volcanic bed)	169			0.7054				0.512251	-2.8	137
Southern Transantarctic Mnts.	Shackleton Glacier/Duncan Moutains/Harold Byrd Mountains	-	-	ES-93	Taylor Fm.	Liv Group (volcanic bed)				0.705461				0.512856	5.5	137
Southern Transantarctic Mnts.	Shackleton Glacier/Duncan Moutains/Harold Byrd Mountains	-	-	ES-78	Taylor Fm.	Liv Group (volcanic bed)				0.707425				0.512691	3.4	137
Southern Transantarctic Mnts.	Shackleton Glacier/Duncan Moutains/Harold Byrd Mountains	-	-	ES-94	Taylor Fm.	Liv Group (volcanic bed)				0.714349				0.512634	3.2	137
Southern Transantarctic Mnts.	Shackleton Glacier/Duncan Moutains/Harold Byrd Mountains	-	-	ES-42	Taylor Fm.	Liv Group (volcanic bed)				0.777557				0.512352	-1.1	137
Southern Transantarctic Mnts.	Shackleton Glacier/Duncan Moutains/Harold Byrd Mountains	-	-	COI	Leverett Fm.	Liv Group (volcanic bed)				0.707607				0.512732	3.3	137
Southern Transantarctic Mnts.	Shackleton Glacier/Duncan Moutains/Harold Byrd Mountains	-	-	CKD	Leverett Fm.	Liv Group (volcanic bed)				0.714704				0.512549	1.5	137
Southern Transantarctic Mnts.	Shackleton Glacier/Duncan Moutains/Harold Byrd Mountains	-	-	CPY	Leverett Fm.	Liv Group (volcanic bed)				0.708826				0.512598	2.1	137
Ford Ranges	Chester Mountains	-76.67	-145.58	51225-1	Granodiorite	Palaeozoic Granitoids (W.A.)	194	223	2.29	0.720773	9.2	45.9	0.0904	0.512378	-5.1	156
Ford Ranges	Chester Mountains	-76.67	-145.58	51225-2	Granodiorite	Palaeozoic Granitoids (W.A.)	221	220	2.9	0.72163	11.2	59.6	0.1134	0.512292	-6.7	156
Ford Ranges	Greer Peak	-76.78	-144.43	Y2-GP091	Granodiorite	Palaeozoic Granitoids (W.A.)	143	376	1.1	0.71077	4.3	21.5	0.1211	0.512432	-4	156
Ford Ranges	Herman Nunatak	-76.22	-143.88	Y2-HN097	Granodiorite	Palaeozoic Granitoids (W.A.)	85	357	0.69	0.708715	3.8	18.2	0.1109	0.512276	-7.1	156
Ford Ranges	Mount June	-76.25	-145.28	Y2-JU096	Granodiorite	Palaeozoic Granitoids (W.A.)	122	423	0.84	0.71085	8.6	46.6	0.1269	0.512438	-3.9	156

Ford Ranges	Saunders Mountains	-76.85	-145.69	Y2-SM095	Granodiorite	Palaeozoic Granitoids (W.A.)	100	346	0.84	0.710204	4.8	23.0	0.127	0.512368	-5.3	156
Ford Ranges	Mount Avers	-76.47	-145.27	Y1-AE035	Devonian-Carboniferous granite	Palaeozoic Granitoids (W.A.)	129	271	1.37	0.715979	6.1	31.4	0.1168	0.512254	-7.5	156
Ford Ranges	Mount Getz	-76.55	-145.22	M5-G175	Devonian-Carboniferous granite	Palaeozoic Granitoids (W.A.)	214	249	2.49	0.720081	10.2	53.6	0.1145	0.512225	-8.1	156
Ford Ranges	Mount Iphigene	-76.51	-145.81	Y1-IG071	Diatexites	Palaeozoic Granitoids (W.A.)	171	190	2.6	0.717636	8.5	41.3	0.1239	0.512175	-9	156
Ford Ranges	Mount Iphigene	-76.51	-145.81	Y2-IG073	Diatexites	Palaeozoic Granitoids (W.A.)	147	280	1.64	0.717636	11.5	61.6	0.1125	0.512217	-8.2	156
Ford Ranges	Clark Mountains	-77.28	-142.16	10CY-001	Metasediment	Swanson Fm	131	201	2.09	0.726291	6.6	35.3	0.1133	0.512117	-10.2	156
Ford Ranges	Clark Mountains	-77.28	-142.16	10CY-002	Metasediment	Swanson Fm	206	148	4.04	0.732242	6.7	32.8	0.1227	0.512084	-10.8	156
Ford Ranges	Bailey Ridge	-77.16	-145.28	Y2-BR086	Metasediment	Swanson Fm	155	129	3.5	0.738139	8.0	38.8	0.1243	0.512079	-10.9	156
Ford Ranges	Mount Dolber	-77.07	-145.75	Y2-MD092	Metasediment	Swanson Fm	100	195	1.49	0.727782	6.0	30.3	0.12	0.511979	-12.8	156
Ford Ranges	Mount Passel	-76.90	-144.87	Y2-MP098	Metasediment	Swanson Fm	96	151	1.84	0.72801	6.9	34.3	0.1208	0.512061	-11.3	156
Central Transantarctic Mnts.	Hampton Ridge	-83.87	167.03	A-2	Starshot Fm	Byrd Group	236	89	7.691	0.77249	7.1	36.3	0.118	0.512051	-11.5	175
Central Transantarctic Mnts.	Hampton Ridge	-83.87	167.03	A-3	Starshot Fm	Byrd Group	125	158	2.3	0.73626	6.0	29.9	0.1209	0.512124	-10.0	175
Central Transantarctic Mnts.	O'Leary Peak	-84.45	-179.23	85BCT 171	Granitoid	GHI				0.733162				0.512382	-6.1	175
Central Transantarctic Mnts.	Woodall Peak	-84.28	178.63	85BCT 167	Granitoid	GHI				0.741231				0.512381	-7.9	175
Central Transantarctic Mnts.	Beetle Spur	-84.17	172.00	672 MH	Granitoid	GHI				0.722735				0.512379	-10.4	175
Central Transantarctic Mnts.	Mt Harcourt	-83.82	172.00	647 MH	Granitoid	GHI				0.742207				0.512380	-7.3	175
Central Transantarctic Mnts.	Granite Pillars	-83.60	170.75	85BCT-44	Granitoid	GHI	207	214	2.788	0.727868	11.6	65.0	0.1075	0.512189	-8.8	175
Central Transantarctic Mnts.	Mt Hope	-83.52	171.27	593 MH	Granitoid	GHI				0.723389				0.512382	-8.4	175
Central Transantarctic Mnts.	Martin Dome	-83.30	157.20	85BCT-80	Granitoid	GHI	309	216	4.151	0.762329	5.1	27.7	0.1114	0.511823	-15.9	175
Central Transantarctic Mnts.	Hockey Cirque	-83.28	156.50	72MR	Granitoid	GHI	357	164	6.291	0.778957	4.6	23.3	0.1184	0.511797	-16.4	175
Central Transantarctic Mnts.	Macdonald Bluffs	-83.25	157.83	297MR	Granitoid	GHI	159	392	1.17	0.741393	9.3	57.2	0.0981	0.511776	-16.8	175
Central Transantarctic Mnts.	Dike Cirque	-83.23	157.95	315MR	Granitoid	GHI	184	204	2.621	0.751101	6.2	33.5	0.112	0.511756	-17.2	175
Central Transantarctic Mnts.	Moody Nunatak	-83.12	159.50	85BCT-8	Granitoid	GHI	195	208	2.718	0.735055	9.2	48.4	0.1148	0.512105	-10.4	175
Central Transantarctic Mnts.	Mt Macbain	-83.10	162.30	85BCT-116	Granitoid	GHI	150	392	1.11	0.715664	3.4	18.9	0.1085	0.512216	-8.2	175
Central Transantarctic Mnts.	Bartrum Plateau	-83.10	160.10	85BCT-3	Granitoid	GHI	101	262	1.121	0.717344	4.5	21.8	0.1245	0.512153	-9.5	175
Central Transantarctic Mnts.	Snowshoe pass	-83.05	157.60	85BCT-93	Granitoid	GHI	233	148	4.6	0.774517	6.5	33.0	0.1187	0.511846	-15.4	175
Central Transantarctic Mnts.	Panarama Point	-82.82	159.17	85BCT-1	Granitoid	GHI	147	188	2.267	0.73521	8.5	42.6	0.1207	0.511970	-13.0	175
Central Transantarctic Mnts.	Mt Heiser	-82.67	162.93	85BCT-21	Granitoid	GHI	399	86	13.566	0.811917	12.8	75.0	0.103	0.511985	-12.7	175
Central Transantarctic Mnts.	Cape Goldie	-82.63	165.90	85BCT-39	Granitoid	GHI	312	71	12.886	0.798658	2.2	8.8	0.1494	0.512173	-9.1	175
Central Transantarctic Mnts.	Campbell Hills	-82.43	163.78	85DCT-6	Granitoid	GHI	94	438	0.621	0.714765	7.3	38.2	0.1163	0.512079	-10.9	175
Central Transantarctic Mnts.	Campbell Hills	-82.43	163.78	85BCT-31	Granitoid	GHI	432	79	15.895	0.822098	11.2	62.3	0.1084	0.512002	-12.4	175
Miller Range	Orr Peak	-83.50	157.80	86BMR M37	Banded Gneiss	Nimrod Group	168	950	0.511	0.720034	12.0	70.2	0.169	0.511059	-30.8	175
Miller Range	Camp Ridge	-83.17	157.00	519 MR	Gneiss	Nimrod Group	60	72	2.4259	0.77806	1.5	8.8	0.1018	0.511094	-30.1	175
Miller Range	Camp Ridge	-83.17	157.00	517 MR	Gneiss	Nimrod Group	134	476	0.8187	0.72712	6.9	38.0	0.110	0.511163	-28.8	175
Miller Range	Camp Ridge	-83.17	157.00	86BMR M28	Orthogniess	Nimrod Group	169	315	1.557	0.740465	7.5	38.7	0.1182	0.511304	-26.0	175

Miller Range	Aurora Heights	-83.12	157.08	86BMR M24	Schist (Argosy)	Nimrod Group	120	435	0.798	0.730206	5.5	31.7	0.106	0.511195	-28.1	175
Southern Transantarctic Mnts.	Amphibole Peak	-84.73	-173.43	86 BGH 20		GHI	6	329	0.0510 8	0.704823	3.5	14.0	0.1522	0.512580	-1.1	175
Southern Transantarctic Mnts.	Olds Peak	-84.67	-174.68	86 BGH 25		GHI	84	181	1.3404	0.714931	5.9	25.7	0.1391	0.512480	-3.1	175
Southern Transantarctic Mnts.	Longhorn Spurs	-84.60	-174.75	86 BGH 31		GHI	90	149	1.761	0.717437	8.1	36.8	0.1326	0.512513	-2.4	175
Southern Transantarctic Mnts.	Sage Nunataks	-84.55	-173.00	86 BGH 9		GHI	73	224	0.9384	0.712577	6.3	25.3	0.1507	0.512510	-2.5	175
Southern Victoria Land	Mt Dromedary	-78.32	163.12	62207	Sub-alkaline gabbro	GHI	80	249	0.93	0.708562	4.6	2.1	0.123	0.512086	-10.8	176
Southern Victoria Land	Mt Dromedary	-78.32	163.08	62210	Alkaline gabbro	GHI	228	487	1.35	0.711108	11.7	25.0	0.126	0.511979	-12.9	176
Southern Victoria Land	Dry Valleys	-77.86	162.37	60766	enclave Bonney Pluton	GHI	152	454	0.97	0.714591	5.8	24.9	0.141	0.512235	-7.9	176
Southern Victoria Land	Dry Valleys	-77.80	162.27	60745	Bonney Pluton	GHI	127	380	0.97	0.714964	21.7	192. 1	0.068	0.511932	-13.8	176
Southern Victoria Land	Dry Valleys	-77.80	162.27	60746	Bonney Pluton	GHI	114	351	0.94	0.714576	9.8	49.3	0.12	0.512074	-11.0	176
Southern Victoria Land	Dry Valleys	-77.75	162.17	60744	Bonney Pluton	GHI	209	478	1.27	0.716224	7.7	44.7	0.104	0.512030	-11.9	176
Southern Victoria Land	Dry Valleys	-77.74	162.20	60777	Unnamed orthogneiss	GHI	65	274	0.69	0.711885	2.8	18.1	0.095	0.512149	-9.5	176
Southern Victoria Land	Dry Valleys	-77.74	162.18	60509	Felsic porphyry plugs	GHI	267	416	1.86	0.718297	7.1	42.4	0.102	0.512099	-10.5	176
Southern Victoria Land	Dry Valleys	-77.73	162.27	60498	Rhone Pluton	GHI	228	487	1.35	0.715769	7.1	68.0	0.104	0.512092	-10.7	176
Southern Victoria Land	Dry Valleys	-77.72	162.12	60543	Hedley Pluton	GHI	96	573	0.49	0.713096	3.1	22.7	0.083	0.511945	-13.5	176
Southern Victoria Land	Dry Valleys	-77.71	162.27	60464	Felsic porphyry plugs	GHI	371	279	3.87	0.730326	8.6	48.7	0.106	0.512087	-10.7	176
Southern Victoria Land	Dry Valleys	-77.52	161.73	56854	Hedley Pluton	GHI	98	395	0.76	0.714585	2.8	19.5	0.085	0.511911	-14.2	176
Southern Victoria Land	Dry Valleys	-77.52	161.67	56843	Calkin Pluton orthogneiss	GHI	109	435	0.72	0.711817	4.6	27.4	0.103	0.512219	-8.2	176
Southern Victoria Land	Dry Valleys	-77.52	161.87	56875	Dun Pluton Orthogneiss	GHI	62	510	0.35	0.709675	2.8	16.8	0.1	0.512128	-9.9	176
Southern Victoria Land	Dry Valleys	-77.50	162.08	60526	Unnamed granodiorite dike	GHI	161	349	1.34	0.717312				0.511940	-13.6	176
Southern Victoria Land	Dry Valleys	-77.50	162.28	56876	Dun Pluton Orthogneiss	GHI	65	726	0.26	0.708448	2.8	18.8	0.091	0.512154	-9.4	176
Southern Victoria Land	Dry Valleys	-77.46	162.33	60770	Unnamed orthogneiss	GHI	71	253	0.82	0.713764	4.3	23.5	0.111	0.512138	-9.8	176
Southern Victoria Land	Dry Valleys	-77.43	162.63	61178	Brownworth Pluton	GHI	80	249	0.93	0.715074	8.6	28.3	0.098	0.512087	-10.7	176
Southern Victoria Land	Dry Valleys	-77.07	161.93	60492	enclave Bonney Pluton	GHI	162	468	1	0.715454	4.5	49.9	0.054	0.512032	-11.8	176
Southern Victoria Land	Dry Valleys	-77.50	162.00	56811	Pelitic schist	Skelton Group	150	246	1.76	0.721716	3.4	18.8	0.111	0.512055	-11.4	176
Southern Victoria Land	Dry Valleys	-77.50	162.00	56815	Pelitic schist	Skelton Group	75	229	0.95	0.719444	4.7	25.7	0.112	0.512065	-11.2	176
Southern Victoria Land	Dry Valleys	-77.50	162.00	56817	Pelitic schist	Skelton Group	85	100	2.46	0.733454	4.7	22.6	0.125	0.511922	-14.0	176
Southern Victoria Land	Dry Valleys	-77.50	162.00	56880	Psammitic schist	Skelton Group	21	140	0.43	0.710183	2.4	8.9	0.163	0.512491	-2.9	176
Southern Victoria Land	Dry Valleys	-77.50	162.00	60767	Psammitic schist	Skelton Group	82	59	4.05	0.758811	3.6	20.0	0.11	0.511832	-15.7	176
Southern Victoria Land	Dry Valleys	-77.50	162.00	60768	Psammitic schist	Skelton Group	165	97	4.91	0.75915	8.9	45.0	0.12	0.511992	-12.6	176
Southern Victoria Land	Dry Valleys	-77.50	162.00	60789	Psammitic schist	Skelton Group	91	111	2.39	0.729778	12.5	49.5	0.152	0.511961	-13.2	176
Southern Victoria Land	Dry Valleys	-77.50	162.00	60790	Quartzofelds pathic gniess	Skelton Group	108	87	3.61	0.740601	3.7	20.3	0.109	0.512059	-11.3	176
Southern Victoria Land	Dry Valleys	-77.50	162.00	60791	Quartzofelds pathic gniess	Skelton Group	72	135	1.54	0.72814	1.3	7.6	0.102	0.511829	-15.8	176
Central Transantarctic Mnts.		-84.28	169.42	741	Hope Granite	GHI			2.248	0.7237						177
Central Transantarctic Mnts.		-84.17	172.00	672	Hope Granite	GHI			1.775	0.7219						177
Central Transantarctic Mnts.		-83.95	170.10	738	Hope Granite	GHI			9.645	0.7715						177
Central Transantarctic Mnts.		-83.92	173.57	654	Hope Granite	GHI			2.784	0.7292						177
Central Transantarctic Mnts.		-83.82	172.42	647	Hope Granite	GHI			4.45	0.7405						177
Central Transantarctic Mnts.		-83.77	166.10	630	Hope Granite	GHI			1.966	0.721						177

Central Transantarctic Mnts.		-83.60	170.75	576	Ida Granite	GHI			16.41	0.8165						177
Central Transantarctic Mnts.		-83.52	171.27	593	Hope Granite	GHI			2.097	0.7257						177
Central Transantarctic Mnts.		-83.48	170.30	719	Ida Granite	GHI			18.85	0.8337						177
Central Transantarctic Mnts.		-83.38	169.17	605	Hope Granite	GHI			2.816	0.728						177
Central Transantarctic Mnts.		-83.33	157.60	52	Hope Granite	GHI			3.456	0.7594						177
Central Transantarctic Mnts.		-83.33	157.60	54	Hope Granite	GHI			28.37	0.9212						177
Central Transantarctic Mnts.		-83.28	156.50	72	Hope Granite	GHI			6.475	0.7769						177
Central Transantarctic Mnts.		-83.25	157.92	292	Hope Granite	GHI			2.53	0.7518						177
Central Transantarctic Mnts.		-83.25	157.92	297	Hope Granite	GHI			1.178	0.7401						177
Central Transantarctic Mnts.		-83.23	157.95	315	Hope Granite	GHI			2.694	0.7509						177
Central Transantarctic Mnts.		-83.22	157.90	81	Hope Granite	GHI			3.065	0.74585						177
Central Transantarctic Mnts.		-83.22	157.90	314	Hope Granite	GHI			2.769	0.7486						177
Central Transantarctic Mnts.		-83.03	167.58	707	Hope Granite	GHI			69.39	1.16						177
Southern Victoria Land	Mount Discovery	-78.50	166.00	27	Phonolite	McMurdo Volcanic Group	72	420		0.7030						194
Southern Victoria Land	Mount Discovery	-78.37	165.00	23	Phonolite	McMurdo Volcanic Group	30	1440		0.7033						194
Southern Victoria Land	Mount Discovery	-78.10	166.30	12	Basanitoid	McMurdo Volcanic Group	30	640		0.7032						194
Southern Victoria Land	Ross Island	-77.50	168.00	1-11	Basanitoid complex	McMurdo Volcanic Group	34	959		0.7032						194
Southern Victoria Land	Ross Island	-77.50	168.00	24	Phonolite	McMurdo Volcanic Group	36	640		0.7033						194
Southern Victoria Land	Ross Island	-77.50	168.00	20	Anorthoclase Phonolite	McMurdo Volcanic Group	46	840		0.7032						194
Southern Victoria Land	Dredge 4	-76.98	167.49	04DRE4-76	Alkali Basalt	McMurdo Volcanic Group	24	514		0.703200	32.0	6.6		0.512930	5.7	210
Southern Victoria Land	Beaufort Island	-76.93	166.93	AW82-284	Alkali Basalt	McMurdo Volcanic Group	66	1351		0.702930	14.9	74.0		0.512950	6.1	210
Southern Victoria Land	Beaufort Island	-76.93	166.93	NV17A	Alkali Basalt	McMurdo Volcanic Group	42	1236		0.702960	12.0	58.0		0.512920	5.5	210
Southern Victoria Land	Beaufort Island	-76.93	166.93	BFT-1	Alkali Basalt	McMurdo Volcanic Group	129	1316		0.703000	13.0	73.0		0.512930	5.7	210
Southern Victoria Land	Beaufort Island	-76.93	166.93	BFT-2	Alkali Basalt	McMurdo Volcanic Group	112	1378		0.703030	14.7	80.0		0.512950	6.1	210
Southern Victoria Land	Dredge 2	-76.73	168.76	04DRE2-42	Non-vesicular Lava	McMurdo Volcanic Group	62	1407		0.703170	72.0	13.0		0.512880	4.7	210
Southern Victoria Land	Dredge 5	-76.58	166.70	04DRE5-80	Alkali Basalt	McMurdo Volcanic Group	45	874		0.703130	12.7	59.0		0.512920	5.5	210
Southern Victoria Land	Dredge 5	-76.58	166.70	04DRE5-81	Alkali Basalt	McMurdo Volcanic Group	37	798		0.703330	11.2	52.0		0.512940	5.9	210
Southern Victoria Land	Dredge 1	-76.34	168.39	04DRE1-31	Alkali Basalt	McMurdo Volcanic Group	47	1087		0.703440	13.9	71.0		0.513000	7.1	210
Southern Victoria Land	Dredge 1	-76.34	168.39	04DRE1-32	Alkali Basalt	McMurdo Volcanic Group	52	1228		0.702920	14.4	75.0		0.512970	6.5	210
Southern Victoria Land	Franklin Island	-76.17	168.38	04ANT1-6	Alkali Basalt	McMurdo Volcanic Group	50	692		0.702890	40.0	8.0		0.512960	6.3	210
Southern Victoria Land	Dredge 3	-75.98	168.23	04DRE3-73	Alkali Basalt	McMurdo Volcanic Group	50	1005		0.703190	12.4	64.0		0.513010	7.3	210
Southern Victoria Land	Dredge 3	-75.98	168.23	04DRE4-75	Alkali Basalt	McMurdo Volcanic Group	15	1132		0.703380	14.0	73.0		0.512940	5.9	210

Southern Victoria Land	Dredge 6	-75.97	168.62	04DRE6-107	Alkali Basalt	McMurdo Volcanic Group	78	1264		0.703520	16.9	86.0		0.513000	7.1	210
Southern Victoria Land	Ross Island	-77.50	168.00	RI 9373	Kaersutite	McMurdo Volcanic Group				0.703114				0.512931	5.7	211
Southern Victoria Land	Ross Island	-77.50	168.00	RI 5073	Kaersutite	McMurdo Volcanic Group				0.703058				0.512994	6.9	211
Southern Victoria Land	Ferrar Glacier	-77.88	160.73	P62009	Aztec Siltstone	Beacon Supergroup				0.782952				0.511881	-14.8	212
Southern Victoria Land	Ferrar Glacier	-77.87	161.17	P61986	Beacon Heights	Beacon Supergroup				0.72013				0.511742	-17.5	212
Southern Victoria Land	Ferrar Glacier	-77.87	161.17	P62001	New Mountain Sandstone	Beacon Supergroup				0.740301				0.511990	-12.6	212
Southern Victoria Land	Ferrar Glacier	-77.87	161.25	P61740	Terra Cotta Siltstone	Beacon Supergroup				0.772168				0.511858	-15.2	212
Southern Victoria Land	Ferrar Glacier	-77.85	160.28	P61975	Lashly Formation	Beacon Supergroup				0.726078				0.512021	-12	212
Southern Victoria Land	Ferrar Glacier	-77.80	163.58	P21710	Hornfels	Skelton Group				0.730546				0.512114	-10.2	212
Southern Victoria Land	Ferrar Glacier	-77.70	161.91	P83952	Garnetiferous amphibolite	Skelton Group				0.736366				0.512143	-9.7	212
Southern Victoria Land	Ferrar Glacier	-77.62	162.60	P62342	Marl	Skelton Group				0.70721				0.511979	-12.9	212
Southern Victoria Land	Ferrar Glacier	-77.56	162.68	P62345	Greyschist	Skelton Group				0.712175				0.512122	-10.1	212
Central Transantarctic Mnts.	McCrilliss Nunatak	-85.44	-128.93	HM 9A	Graywacke	Beardmore Group	251	65	11.1842	0.791458	6.9	34.2	0.1228	0.512195	-8.6	213
Central Transantarctic Mnts.	McCrilliss Nunatak	-85.44	-128.93	HM 9B	Shale	Beardmore Group	334	39	25.4232	0.83674	9.7	47.7	0.1232	0.512191	-8.7	213
Central Transantarctic Mnts.	Brown Hills	-80.78	159.72	89 BBG 113	Granodiorite	GHI								0.511983	-12.8	213
Central Transantarctic Mnts.	Darnell Nunatak	-80.45	155.91	89 BBG 101A	Granodiorite	GHI								0.511847	-15.4	213
Central Transantarctic Mnts.	Darnell Nunatak	-80.45	155.91	89 BBG 101B	Gniess	GHI								0.511915	-14.1	213
Central Transantarctic Mnts.	Bastion Hill	-79.84	158.27	89 DBG 4	Granodiorite	GHI								0.512033	-11.8	213
Ellsworth-Whitmore Mnts.	Whitmore Mountains	-82.58	-104.50	WM 1		Mesozoic Granites						10.8	0.1228		-4.12	213
Miller Range	Gerard Bluff	-83.62	157.25	86BMR M36A	Greenschist	Nimrod Group	48.36	138.6	1.013	0.736311	3.728	13.373	0.1686	0.512097	-10.6	213
Miller Range	Krieling Mesa	-83.22	157.90	85 DCT M2	Schist (Argosy)	Nimrod Group	135.67	84.16	4.723	0.832213	8.078	45.9908	0.106	0.511828	-15.8	213
Miller Range	Camp Ridge	-83.17	157.00	86BMR M39	Gneiss	Nimrod Group	84.45	351.84	0.697	0.733286	4.39	25.74	0.106	0.510929	-33.3	213
Southern Transantarctic Mnts.	Savage Nunatak	-86.45	-154.90	HM 16	Granite	GHI								0.512469	-3.3	213
Southern Transantarctic Mnts.	S of Gratton Nunatak	-86.17	-127.42	HM 33	Granite	GHI								0.512346	-5.7	213
Southern Transantarctic Mnts.	NW Ford Nunatak	-85.54	-131.73	HM 1	tonalite	GHI								0.512390	-4.8	213
Southern Transantarctic Mnts.	Feeley Peak	-85.45	-126.43	HM 3	monzogranite	GHI								0.512238	-7.8	213
Southern Transantarctic Mnts.	Darling Ridge	-84.75	-115.93	HM 5	monzogranite	GHI								0.512302	-6.6	213
Southern Transantarctic Mnts.	Treves Butte	-84.70	-114.37	HM 4B	monzogranite	GHI								0.512188	-8.8	213
Ford Ranges	Fosdick Mountains	-76.47	-145.30	10CY-039	Fosdick Migmatite	Evolved Granitoids	165	240	1.901	0.723275	0.4	2.0	0.1337	0.512211	-8.3	214
Ford Ranges	Fosdick Mountains	-76.50	-145.81	Y1-IG062	Fosdick Migmatite	Evolved Granitoids	155	226	1.987	0.719905	3.5	15.0	0.1361	0.512259	-7.4	214
Ford Ranges	Fosdick Mountains	-76.46	-145.43	C6-AW86-1	Fosdick Migmatite	Evolved Granitoids	167	329	0.1472	0.713751	5.0	25.8	0.1166	0.512284	-6.9	214
Ford Ranges	Fosdick Mountains	-76.47	-145.23	Y1-AE064	Fosdick Migmatite	Evolved Granitoids	131	211	1.736	0.721116	2.6	13.4	0.1133	0.512221	-8.1	214
Ford Ranges	Fosdick Mountains	-76.49	-146.08	Y1-IG052	Fosdick Migmatite	Evolved Granitoids	131	253	1.532	0.719866	1.1	5.7	0.14	0.512208	-8.4	214
Ford Ranges	Fosdick Mountains	-76.51	-145.81	Y1-IG070	Fosdick Migmatite	Evolved Granitoids	85	219	1.118	0.721597	0.4	3.0	0.0919	0.512183	-8.8	214
Ford Ranges	Fosdick Mountains	-76.46	-145.51	YI-AW038	Fosdick Migmatite	Evolved Granitoids	255	172	4.244	0.726049	0.3	1.1	0.1848	0.512348	-5.6	214
Ford Ranges	Fosdick Mountains	-76.46	-145.36	Y1-AE033	Fosdick Migmatite	Evolved Granitoids	155	195	2.125	0.728855	2.9	12.3	0.144	0.512192	-8.7	214
Ford Ranges	Fosdick Mountains	-76.47	-145.30	10CY-035	Fosdick Migmatite	Palaeozoic Granitoids (W.A.)	196	270	2.105	0.718274	2.5	11.5	0.1309	0.512255	-7.4	214
Ford Ranges	Fosdick Mountains	-76.46	-145.51	Y1-AW039	Fosdick Migmatite	Palaeozoic Granitoids (W.A.)	131	181	2.101	0.721603	6.3	28.8	0.1324	0.511908	-14.2	214

Ford Ranges	Fosdick Mountains	-76.49	-146.08	Y1-IG053	Fosdick Migmatite	Palaeozoic Granitoids (W.A.)	114	286	1.159	0.716186	6.5	34.5	0.1133	0.512254	-7.5	214
Ford Ranges	Fosdick Mountains	-76.46	-145.47	Y1-AW049	Orthogneiss - Fosdick Migmatite	Palaeozoic Granitoids (W.A.)	133	288	1.337	0.714254	6.5	38.4	0.1029	0.512238	-7.8	214
Ford Ranges	Fosdick Mountains	-76.52	-145.65	YI-MJ075	Orthogneiss - Fosdick Migmatite	Palaeozoic Granitoids (W.A.)	225	157	4.164	0.730827	7.0	46.8	0.0904	0.512380	-5.0	214
Ford Ranges	Fosdick Mountains	-76.47	-144.93	10CY-010	Fosdick Migmatite - Paragneiss	Swanson Fm	285	104	7.919	0.739606	13.2	69.9	0.1144	0.512100	-10.5	214
Ford Ranges	Fosdick Mountains	-76.47	-144.93	10CY-015	Fosdick Migmatite - Paragneiss	Swanson Fm	247	64	11.1	0.747548	9.8	51.4	0.1152	0.512089	-10.7	214
Ford Ranges	Fosdick Mountains	-76.44	-146.48	10CY-023	Fosdick Migmatite - Paragneiss	Swanson Fm	232	100	6.762	0.729249	10.5	46.6	0.121	0.512139	-9.7	214
Ford Ranges	Fosdick Mountains	-76.47	-145.30	10CY-033	Fosdick Migmatite - Paragneiss	Swanson Fm	207	98	6.09	0.734213	7.2	35.6	0.1229	0.512134	-9.8	214
Ford Ranges	Fosdick Mountains	-76.49	-144.76	Y1-CB080	Fosdick Migmatite - Paragneiss	Swanson Fm	147	144	2.96	0.731586	7.6	38.6	0.119	0.512073	-11.0	214
Ford Ranges	Fosdick Mountains	-76.49	-146.08	Y1-IG057	Fosdick Migmatite - Paragneiss	Swanson Fm	453	12	111.8	0.876719	12.5	65.7	0.1145	0.512046	-11.6	214
Ford Ranges	Fosdick Mountains	-76.45	-145.15	Y1-LH077	Fosdick Migmatite - Paragneiss	Swanson Fm	165	139	3.429	0.738234	7.5	38.2	0.1187	0.511914	-14.1	214
Central Transantarctic Mnts.	Painted Cliffs	-83.83	162.33	28906		Ferrar Group	12	100	0.35	0.712200						215
Southern Victoria Land	Emmanuel Glacier	-77.90	162.08	4300		Ferrar Group	78	108	2.07	0.715900						215
Southern Victoria Land	New Mountain Sill	-77.87	161.12	4168		Ferrar Group	43	143	0.87	0.715200						215
Southern Victoria Land	New Mountain Sill	-77.87	161.12	4170		Ferrar Group	49	139	1.02	0.715600						215
Southern Victoria Land	New Mountain Sill	-77.87	161.12	4174		Ferrar Group	49	138	1.02	0.715600						215
Southern Victoria Land	Solitary Rocks	-77.78	161.20	4112		Ferrar Group	73	120	1.75	0.718633						215
Southern Victoria Land	Solitary Rocks	-77.78	161.20	GA 1462		Ferrar Group	35	126	0.8	0.714350						215
Southern Victoria Land	Kukri Hills	-77.72	162.80	4266		Ferrar Group	56	136	1.19	0.715100						215
Southern Victoria Land	Lake Vanda	-77.53	161.55	4012		Ferrar Group	30	126	0.69	0.713700						215
Southern Victoria Land	Lake Vanda	-77.53	161.55	4013		Ferrar Group	49	133	1.07	0.713900						215
Southern Victoria Land	Lake Vanda	-77.53	161.55	4017		Ferrar Group	36	127	0.82	0.712233						215
Southern Victoria Land	Lake Vanda	-77.53	161.55	4019		Ferrar Group	20	128	0.45	0.712700						215
Southern Victoria Land	Lake Vanda	-77.53	161.55	4026		Ferrar Group	11	75	0.35	0.712800						215
Southern Victoria Land	Wright Valley	-77.52	161.83	4053		Ferrar Group	118	152	2.24	0.714900						215
Southern Victoria Land	Thumb Point Sill	-75.97	160.47	4342		Ferrar Group	20	98	0.59	0.712200						215
Southern Victoria Land	Thumb Point Sill	-75.97	160.47	26903		Ferrar Group	29	134	0.62	0.712100						215
Central Transantarctic Mnts.	Grosvenor Mountains	-85.67	175.00	85-69-2	Kirkpatrick Basalt	Ferrar Group	67	128	1.528	0.713431	7.3	30.3	0.1455	0.512352	-5.58	216
Central Transantarctic Mnts.	Grosvenor Mountains	-85.67	175.00	85-51-40	Kirkpatrick Basalt	Ferrar Group	67	125	1.56	0.713517	7.3	30.3	0.1454	0.512355	-5.52	216
Central Transantarctic Mnts.	Queen Alexandra Range	-84.00	170.00	85-76-63	Kirkpatrick Basalt	Ferrar Group	61	122	1.445	0.713225	6.7	27.5	0.1463	0.512364	-5.34	216
Central Transantarctic Mnts.	Queen Alexandra Range	-84.00	170.00	85-76-60	Kirkpatrick Basalt	Ferrar Group	67	130	1.498	0.713446	7.4	31.3	0.1435	0.512356	-5.50	216
Central Transantarctic Mnts.	Queen Alexandra Range	-84.00	170.00	33-58	Kirkpatrick Basalt	Ferrar Group	68	127	1.545	0.713500	7.2	29.9	0.1456	0.512361	-5.40	216
Southern Victoria Land	Prince Albert Mountains	-76.00	161.50	78212	Kirkpatrick Basalt	Ferrar Group	74	130	1.647	0.713388	7.3	30.4	0.1455	0.512356	-5.50	216
Southern Victoria Land	Prince Albert Mountains	-76.00	161.50	78208	Kirkpatrick Basalt	Ferrar Group	73	131	1.619	0.713498	7.4	30.5	0.1457	0.512359	-5.44	216
Southern Victoria Land	Prince Albert Mountains	-76.00	161.50	78220	Kirkpatrick Basalt	Ferrar Group	85	130	1.895	0.713948	7.3	30.3	0.1455	0.512354	-5.54	216
Central Transantarctic Mnts.	Storm Peak	-84.58	164.00	27 (Flow 1)	Kirkpatrick Basalt	Ferrar Group	12	129		0.7100						217
Central Transantarctic Mnts.	Storm Peak	-84.58	164.00	27.29 (Flow 10)	Kirkpatrick Basalt	Ferrar Group	43	118		0.7119						217

Central Transantarctic Mnts.	Storm Peak	-84.58	164.00	27.28 (Flow 10)	Kirkpatrick Basalt	Ferrar Group	48	122		0.7129						217
Central Transantarctic Mnts.	Storm Peak	-84.58	164.00	27.41 (Flow 12)	Kirkpatrick Basalt	Ferrar Group	66	128		0.7130						217
Central Transantarctic Mnts.	Storm Peak	-84.58	164.00	27.67 (Flow 9)	Kirkpatrick Basalt	Ferrar Group	53	129		0.7136						217
Central Transantarctic Mnts.	Storm Peak	-84.58	164.00	27.64 (Flow 8)	Kirkpatrick Basalt	Ferrar Group	67	131		0.7140						217
Central Transantarctic Mnts.	Storm Peak	-84.58	164.00	27.56 (Flow 5)	Kirkpatrick Basalt	Ferrar Group	65	135		0.7145						217
Central Transantarctic Mnts.	Storm Peak	-84.58	164.00	27.25 (Flow 7)	Kirkpatrick Basalt	Ferrar Group	52	136		0.7146						217
Central Transantarctic Mnts.	Storm Peak	-84.58	164.00	27.51 (Flow 3)	Kirkpatrick Basalt	Ferrar Group	83	133		0.7148						217
Central Transantarctic Mnts.	Storm Peak	-84.58	164.00	27.4 (Flow 2)	Kirkpatrick Basalt	Ferrar Group	75	134		0.7150						217
Central Transantarctic Mnts.	Storm Peak	-84.58	164.00	27.3 (Flow2)	Kirkpatrick Basalt	Ferrar Group	66	131		0.7154						217
Central Transantarctic Mnts.	Storm Peak	-84.58	164.00	27.18 (Flow 6)	Kirkpatrick Basalt	Ferrar Group	70	137		0.7157						217
Central Transantarctic Mnts.	Storm Peak	-84.58	164.00	27.2 (Flow 2)	Kirkpatrick Basalt	Ferrar Group	69	134		0.7158						217
Central Transantarctic Mnts.	Storm Peak	-84.58	164.00	27.24 (Flow 7)	Kirkpatrick Basalt	Ferrar Group	64	140		0.7160						217
Central Transantarctic Mnts.	Storm Peak	-84.58	164.00	27.36 (Flow 11)	Kirkpatrick Basalt	Ferrar Group	86	135		0.7160						217
Central Transantarctic Mnts.	Storm Peak	-84.58	164.00	27.1 (Flow 2)	Kirkpatrick Basalt	Ferrar Group	65	141		0.7163						217
Central Transantarctic Mnts.	Storm Peak	-84.58	164.00	27.17 (Flow 6)	Kirkpatrick Basalt	Ferrar Group	40	141		0.7163						217
Central Transantarctic Mnts.	Storm Peak	-84.58	164.00	27.13 (Flow 4)	Kirkpatrick Basalt	Ferrar Group	69	95		0.7179						217
Southern Transantarctic Mnts.	Mt Wyatt	-86.77	-152.92	237	Wyatt Fm	Liv Group	144	156	2.686	0.7338						218
Southern Transantarctic Mnts.	Mt Wyatt	-86.77	-152.92	330	Wyatt Fm	Liv Group	133	148	2.597	0.7324						218
Southern Transantarctic Mnts.	Mt Gardiner	-86.32	-150.95	236	Wyatt Fm	Liv Group	139	104	3.875	0.7421						218
Southern Transantarctic Mnts.	Nunataks	?	?	328A	Wyatt Fm	Liv Group	137	127	3.13	0.7351						218
Southern Transantarctic Mnts.	Nunataks	?	?	328B	Wyatt Fm	Liv Group	137	127	3.13	0.7338						218
Southern Transantarctic Mnts.	Nunataks	?	?	329	Wyatt Fm	Liv Group	131	137	2.95	0.7314						218
Central Transantarctic Mnts.	Storm Peak	-84.58	164.00	MR 28-4	Lower Buckley	Beacon Supergroup	56	172	0.9455	0.728984	4.3	24.0	0.109	0.511397	-24.2	219
Central Transantarctic Mnts.	Storm Peak	-84.58	164.00	MR 1-130	Upper Buckley (Carbonate)	Beacon Supergroup	55	792	0.2003	0.708642	3.7	17.8	0.125	0.512596	-0.8	219
Central Transantarctic Mnts.	Storm Peak	-84.58	164.00	85-75-1	Kirkpatrick	Ferrar Group	11	100	0.3044	0.711421	2.9	12.4	0.1432	0.512310	-6.4	219
Central Transantarctic Mnts.	Storm Peak	-84.58	164.00	85-75-4	Kirkpatrick	Ferrar Group	63	137	1.34	0.715863	5.8	25.7	0.1357	0.512272	-7.1	219
Central Transantarctic Mnts.	Storm Peak	-84.58	164.00	85-75-5	Kirkpatrick	Ferrar Group	68	138	1.422	0.716071	5.8	25.8	0.1356	0.512268	-7.2	219
Central Transantarctic Mnts.	Storm Peak	-84.58	164.00	85-75-7	Kirkpatrick	Ferrar Group	68	136	1.438	0.71601	5.8	26.0	0.1355	0.512275	-7.1	219
Central Transantarctic Mnts.	Storm Peak	-84.58	164.00	85-75-9	Kirkpatrick	Ferrar Group	68	137	1.434	0.716096	5.8	26.0	0.1355	0.512271	-7.2	219
Central Transantarctic Mnts.	Storm Peak	-84.58	164.00	85-75-11	Kirkpatrick	Ferrar Group	76	138	1.595	0.71627	5.9	26.2	0.1354	0.512267	-7.2	219
Central Transantarctic Mnts.	Storm Peak	-84.58	164.00	85-75-13	Kirkpatrick	Ferrar Group	70	138	1.456	0.716155	5.9	26.3	0.1357	0.512271	-7.2	219
Central Transantarctic Mnts.	Storm Peak	-84.58	164.00	85-75-14	Kirkpatrick	Ferrar Group	74	139	1.554	0.716255	5.9	26.1	0.1355	0.512273	-7.1	219

Central Transantarctic Mnts.	Storm Peak	-84.58	164.00	85-75-15	Kirkpatrick	Ferrar Group	22	154	0.4101	0.713169	5.7	25.4	0.135	0.512277	-7.0	219
Central Transantarctic Mnts.	Storm Peak	-84.58	164.00	85-75-16	Kirkpatrick	Ferrar Group	42	107	1.142	0.714789	5.7	25.5	0.1359	0.512277	-7.0	219
Central Transantarctic Mnts.	Storm Peak	-84.58	164.00	85-75-17	Kirkpatrick	Ferrar Group	57	64	2.563	0.717934	5.8	26.1	0.1349	0.512284	-6.9	219
Central Transantarctic Mnts.	Storm Peak	-84.58	164.00	85-76-18	Kirkpatrick	Ferrar Group	57	131	1.274	0.715494	5.5	24.5	0.1358	0.512268	-7.2	219
Central Transantarctic Mnts.	Storm Peak	-84.58	164.00	85-76-20	Kirkpatrick	Ferrar Group	74	139	1.543	0.715782	5.8	25.6	0.1367	0.512274	-7.1	219
Central Transantarctic Mnts.	Storm Peak	-84.58	164.00	85-76-23	Kirkpatrick	Ferrar Group	67	143	1.363	0.716161	5.8	26.1	0.1352	0.512265	-7.3	219
Central Transantarctic Mnts.	Storm Peak	-84.58	164.00	85-76-24	Kirkpatrick	Ferrar Group	54	139	1.136	0.715516	5.7	25.3	0.1351	0.512266	-7.3	219
Central Transantarctic Mnts.	Storm Peak	-84.58	164.00	85-76-27	Kirkpatrick	Ferrar Group	61	143	1.237	0.71587	5.8	26.1	0.1352	0.512270	-7.2	219
Central Transantarctic Mnts.	Storm Peak	-84.58	164.00	85-76-29	Kirkpatrick	Ferrar Group	61	132	1.349	0.716273	5.6	25.0	0.135	0.512264	-7.3	219
Central Transantarctic Mnts.	Storm Peak	-84.58	164.00	85-76-30	Kirkpatrick	Ferrar Group	62	132	1.362	0.716152	5.7	25.3	0.1352	0.512266	-7.3	219
Central Transantarctic Mnts.	Storm Peak	-84.58	164.00	85-76-33	Kirkpatrick	Ferrar Group	66	136	1.4	0.715539	5.3	23.5	0.1365	0.512277	-7.0	219
Central Transantarctic Mnts.	Storm Peak	-84.58	164.00	85-76-34A	Kirkpatrick	Ferrar Group	59	130	1.306	0.714912	4.9	21.4	0.1372	0.512282	-6.9	219
Central Transantarctic Mnts.	Storm Peak	-84.58	164.00	85-76-36	Kirkpatrick	Ferrar Group	57	136	1.22	0.714786	5.0	21.8	0.1374	0.512289	-6.8	219
Central Transantarctic Mnts.	Storm Peak	-84.58	164.00	85-76-39	Kirkpatrick	Ferrar Group	45	132	0.9792	0.713053	4.0	17.1	0.1425	0.512317	-6.3	219
Central Transantarctic Mnts.	Storm Peak	-84.58	164.00	85-76-40	Kirkpatrick	Ferrar Group	42	122	0.9929	0.712861	3.9	16.6	0.1418	0.512323	-6.1	219
Central Transantarctic Mnts.	Storm Peak	-84.58	164.00	85-76-42	Kirkpatrick	Ferrar Group	42	123	0.9772	0.712707	3.6	15.4	0.1423	0.512330	-6.0	219
Central Transantarctic Mnts.	Storm Peak	-84.58	164.00	85-76-43	Kirkpatrick	Ferrar Group	35	138	0.7256	0.712323	3.5	14.6	0.143	0.512323	-6.1	219
Central Transantarctic Mnts.	Storm Peak	-84.58	164.00	85-76-44	Kirkpatrick	Ferrar Group	34	130	0.7505	0.712348	3.6	15.1	0.1424	0.512320	-6.2	219
Central Transantarctic Mnts.	Storm Peak	-84.58	164.00	85-76-45	Kirkpatrick	Ferrar Group	38	136	0.8194	0.712516	3.7	15.8	0.1419	0.512323	-6.1	219
Central Transantarctic Mnts.	Storm Peak	-84.58	164.00	85-76-49	Kirkpatrick	Ferrar Group	74	134	1.584	0.71585	6.2	27.5	0.1364	0.512286	-6.9	219
Central Transantarctic Mnts.	Storm Peak	-84.58	164.00	85-76-54	Kirkpatrick	Ferrar Group	77	140	1.606	0.715825	6.3	27.8	0.1364	0.512289	-6.8	219
Central Transantarctic Mnts.	Storm Peak	-84.58	164.00	85-76-60	Kirkpatrick	Ferrar Group	67	130	1.498	0.71346	7.4	31.3	0.1435	0.512353	-5.6	219
Central Transantarctic Mnts.	Storm Peak	-84.58	164.00	85-76-63	Kirkpatrick	Ferrar Group	61	122	1.445	0.713225	6.7	27.5	0.146	0.512364	-5.3	219
Central Transantarctic Mnts.	Dawson Peak	-83.83	162.55	85-72-1	Kirkpatrick	Ferrar Group	8	217	0.1118	0.707966	2.1	9.0	0.1403	0.512382	-5.0	219
Central Transantarctic Mnts.	Dawson Peak	-83.83	162.55	85-72-2	Kirkpatrick	Ferrar Group	6	116	0.1575	0.709173	1.9	7.4	0.151	0.512381	-5.0	219
Central Transantarctic Mnts.	Dawson Peak	-83.83	162.55	85-72-6	Kirkpatrick	Ferrar Group	13	114	0.3184	0.709655	1.6	6.4	0.1513	0.512379	-5.1	219
Central Transantarctic Mnts.	Dawson Peak	-83.83	162.55	85-72-26	Kirkpatrick	Ferrar Group	14	119	0.3459	0.709588	1.8	7.4	0.1508	0.512380	-5.0	219
Marie Byrd Land	Mt Murphy	-75.33	-110.73	62	Alkali Basalt	MBL Volcanic Group	10	548	0.054	0.70288	5.1	22.4	0.1377	0.512880	4.7	220
Marie Byrd Land	Mt Steere	-76.73	-117.82	70	Alkali Basalt	MBL Volcanic Group	33	713	0.1334	0.70271	7.0	37.2	0.1148	0.512980	6.7	220
Marie Byrd Land	Coleman Nunatak	-75.32	-133.65	77-35	Alkali Basalt	MBL Volcanic Group	37	1059	0.0999	0.70273	10.6	56.4	0.115	0.512930	5.7	220
Marie Byrd Land	Mt Cumming	-76.67	-125.80	26A	Alkali Basalt	MBL Volcanic Group	41	771	0.155	0.70286	8.1	40.8	0.1203	0.512980	6.7	220
Marie Byrd Land	Shibuya Peak	-75.17	-133.58	6C	Alkali Basalt	MBL Volcanic Group	24	873	0.0803	0.7028	6.9	34.5	0.1225	0.512950	6.1	220

Marie Byrd Land	Kouperov Pk	-75.10	-133.80	7-47B	Alkali Basalt	MBL Volcanic Group	24	803	0.0853	0.70268	8.0	40.2	0.1217	0.512980	6.7	220
Marie Byrd Land	Holmes Bluff	-74.98	-133.72	77-48B	Alkali Basalt	MBL Volcanic Group	14	558	0.0704	0.70258	5.5	26.6	0.125	0.512960	6.3	220
Marie Byrd Land	Mt Hampton	-76.48	-125.80	22D	Alkali Basalt	MBL Volcanic Group	41	805	0.1488	0.70278	9.4	50.3	0.114	0.512970	6.5	220
Marie Byrd Land	Mt Flint	-75.73	-129.10	9D	Alkali Basalt	MBL Volcanic Group	41	824	0.143	0.7029	8.7	43.0	0.1231	0.512860	4.3	220
Marie Byrd Land	Mt Petras	-75.86	-128.64	PT67D	Alkali Basalt	MBL Volcanic Group	46	791	0.1663	0.70309	9.4	53.2	0.1077	0.512870	4.5	220
Marie Byrd Land	Mt Murphy	-75.33	-110.73	60A	Alkali Basalt	MBL Volcanic Group	11	941	0.034	0.70322	2.9	13.7	0.1297	0.512850	4.1	220
Central Transantarctic Mnts.	Cotton Plateau	-82.90	159.67	98-260	Goldie Fm.	Beardmore Group					2.0	10.3	0.1143	0.511759	-17.1	221
Central Transantarctic Mnts.	Cotton Plateau	-82.90	159.67	99-296	Goldie Fm.	Beardmore Group					2.9	15.0	0.1167	0.511789	-16.6	221
Central Transantarctic Mnts.	Cobham Range	-82.30	159.00	98-229	Cobham Fm.	Beardmore Group					5.5	30.9	0.1082	0.511612	-20.0	221
Central Transantarctic Mnts.	Hobbs Peak	-77.88	163.93	99-279B	Hobbs Fm	Beardmore Group					4.2	22.2	0.1146	0.512019	-12.1	221
Central Transantarctic Mnts.	Dolphin Spur	-84.20	172.80	98-268G	Starshot Fm	Byrd Group	111	111	2.908	0.733884	7.8	40.7	0.1161	0.512071	-11.1	221
Central Transantarctic Mnts.	Softbed Ridges	-83.05	163.75	98-206A	Starshot Fm	Byrd Group	237	148	4.646	0.722846	5.7	29.4	0.1161	0.512019	-12.1	221
Central Transantarctic Mnts.	Cotton Plateau	-82.90	159.67	99-294	Shackleton Limestone	Byrd Group	15	2	17.762	0.824038	0.8	4.5	0.1139	0.511830	-15.8	221
Central Transantarctic Mnts.	Holyoake Range	-82.22	160.00	99-320	Starshot Fm	Byrd Group	93	168	1.612	0.723586	6.0	31.0	0.1174	0.512084	-10.8	221
Central Transantarctic Mnts.	Holyoake Range	-82.22	160.00	99-321	Douglas Conglomerate	Byrd Group	132	52	7.421	0.770611	5.6	29.1	0.1166	0.511830	-15.8	221
Central Transantarctic Mnts.	Mt Ubique	-81.50	160.53	99-282B	Starshot Fm	Byrd Group	61	361	0.485	0.716839	6.0	30.9	0.1175	0.511920	-14.0	221
Central Transantarctic Mnts.	Cape Selbourne	-80.38	160.75	99-314	Dick Fm	Byrd Group	44	91	1.412	0.732914	5.9	30.4	0.1173	0.511949	-13.4	221
Marie Byrd Land	Coleman Nunatak	-75.32	-133.65	46D	Alkali Basalt	MBL Volcanic Group	38	1045	0.104	0.702843	11.7	59.0	0.1200	0.512873	4.6	222
Marie Byrd Land	Coleman Nunatak	-75.32	-133.65	46I	Alkali Basalt	MBL Volcanic Group	37	1047	0.101	0.702809	11.8	58.3	0.1227	0.512919	5.5	222
Marie Byrd Land	Coleman Nunatak	-75.32	-133.65	46B	Alkali Basalt	MBL Volcanic Group	38	1076	0.103	0.702815	11.6	57.3	0.1224	0.512883	4.8	222
Marie Byrd Land	Coleman Nunatak	-75.32	-133.65	35E	Alkali Basalt	MBL Volcanic Group	37	1028	0.103	0.702858	11.9	57.7	0.1247	0.512908	5.3	222
Marie Byrd Land	Coleman Nunatak	-75.32	-133.65	35I	Alkali Basalt	MBL Volcanic Group	37	1046	0.101	0.70283	11.8	58.1	0.1224	0.512894	5.0	222
Marie Byrd Land	Coleman Nunatak	-75.32	-133.65	35M	Alkali Basalt	MBL Volcanic Group	39	1071	0.106	0.702807	11.8	57.9	0.1232	0.512908	5.3	222
Marie Byrd Land	Coleman Nunatak	-75.32	-133.65	35K	Alkali Basalt	MBL Volcanic Group	37	1040	0.103	0.702833	11.3	58.3	0.1176	0.512900	5.1	222
Marie Byrd Land	Cousins Rock	-75.27	-133.52	36B	Alkali Basalt	MBL Volcanic Group	36	953	0.108	0.702883	10.9	57.7	0.1144	0.512892	5.0	222
Marie Byrd Land	Patton Bluff	-75.22	-133.67	37A	Alkali Basalt	MBL Volcanic Group	23	652	0.100	0.702758	7.4	33.8	0.1320	0.512961	6.3	222
Marie Byrd Land	Shibuya Peak	-75.17	-133.58	38A	Alkali Basalt	MBL Volcanic Group	25	829	0.087	0.702831	8.9	42.8	0.1252	0.512911	5.3	222
Marie Byrd Land	Kouperov Peak	-75.10	-133.80	47A	Alkali Basalt	MBL Volcanic Group	24	762	0.090	0.7027	8.9	41.8	0.1289	0.512952	6.1	222
Marie Byrd Land	Holmes Bluff	-74.98	-133.72	48B	Alkali Basalt	MBL Volcanic Group	15	576	0.074	0.702535	6.5	28.5	0.1377	0.513008	7.2	222
Marie Byrd Land	Holmes Bluff	-74.98	-133.72	50A	Alkali Basalt	MBL Volcanic Group	28	900	0.089	0.702716	8.9	42.1	0.1278	0.512945	6.0	222
Marie Byrd Land	Scott Island	-67.38	-179.91	E-27-34c	Alkali Basalt	MBL Volcanic Group				0.702849				0.512989	6.8	222
Marie Byrd Land	Fosdick Mountains	-76.53	-144.75	66-D-91	Alkali Basalt	MBL Volcanic Group				0.703338				0.512859	4.3	222

Marie Byrd Land	Fosdick Mountains	-76.53	-144.75	66-D-30	Alkali Basalt	MBL Volcanic Group				0.703106				0.512948	6.0	222
Marie Byrd Land	Mt Siple	-73.26	-126.67	W83-5C	Alkali Basalt	MBL Volcanic Group				0.703487				0.512847	4.1	222
Marie Byrd Land	Mt Siple	-73.26	-126.67	W83-1	Alkali Basalt	MBL Volcanic Group				0.703723				0.512792	3.0	222
Marie Byrd Land	Mt Murphy	-75.33	-110.73	62	Alkali Basalt	MBL Volcanic Group				0.702917				0.512893	5.0	222
Marie Byrd Land	Mt Murphy	-75.33	-110.73	85-32B	Alkali Basalt	MBL Volcanic Group				0.703165				0.512839	3.9	222
Marie Byrd Land	Hudson Mountains	-74.33	-99.42	24-1-A	Alkali Basalt	MBL Volcanic Group				0.702904				0.512980	6.7	222
Marie Byrd Land	Hudson Mountains	-74.33	-99.42	9-1-C	Alkali Basalt	MBL Volcanic Group				0.703366				0.512859	4.3	222
Marie Byrd Land	Hudson Mountains	-74.33	-99.42	20-2B	Alkali Basalt	MBL Volcanic Group				0.703026				0.512928	5.7	222
Central Transantarctic Mnts.	Portal Peak	-83.83	165.60	87-87	Ferrar sill	Ferrar Group	20	143	0.413	0.71088	3.3	13.9	0.1435	0.511558	-4.2	223
Central Transantarctic Mnts.	Portal Peak	-83.83	165.60	87-93	Ferrar sill	Ferrar Group	30	152	0.562	0.71113	3.1	12.9	0.1433	0.511561	-4.1	223
Central Transantarctic Mnts.	Portal Peak	-83.83	165.60	87-104	Ferrar sill	Ferrar Group	24	166	0.425	0.71016	3.5	14.6	0.1448	0.511578	-3.8	223
Central Transantarctic Mnts.	Portal Peak	-83.83	165.60	87-117	Ferrar sill	Ferrar Group	33	181	0.533	0.71058	2.0	8.7	0.1386	0.511570	-3.8	223
Central Transantarctic Mnts.	Portal Peak	-83.83	165.60	87-122	Ferrar sill	Ferrar Group	30	154	0.569	0.71135	2.8	11.6	0.1446	0.511573	-3.9	223
Central Transantarctic Mnts.	Portal Peak	-83.83	165.60	87-126	Ferrar sill	Ferrar Group	20	161	0.351	0.71173	3.3	14.0	0.1436	0.511542	-4.5	223
Southern Victoria Land	Wright Valley	-77.51	161.83	263	Basalt	McMurdo Volcanic Group				0.704300						224
Southern Victoria Land	Ross Island	-77.50	168.00	257	Trachyte	McMurdo Volcanic Group				0.704500						224
Southern Victoria Land	Ross Island	-77.50	168.00	258	Olivine Basalt	McMurdo Volcanic Group				0.704000						224
Southern Victoria Land	Ross Island	-77.50	168.00	272	Olivine Basalt	McMurdo Volcanic Group				0.704500						224
Southern Victoria Land	Ross Island	-77.83	166.68		Olivine-Augite Basalt	McMurdo Volcanic Group	73	1075	0.1969	0.703370						225
Southern Victoria Land	Ross Island	-77.83	166.68		Trachyte	McMurdo Volcanic Group	159	1041	0.44	0.704210						225
Southern Victoria Land	Ross Island	-77.83	166.68		Titanaugite-hornblende Basalt	McMurdo Volcanic Group	69	1456	0.139	0.703500						225
Southern Victoria Land	Ross Island	-77.83	166.68		Olivine-titanaugite-hornblende Basalt	McMurdo Volcanic Group	104	1014	0.2982	0.703380						225
Southern Victoria Land	Ross Island	-77.83	166.68		Hornblende Trachyandesite	McMurdo Volcanic Group	149	1020	0.4227	0.704030						225
Southern Victoria Land	Ross Island	-77.83	166.68		Titanaugite-olivine Picritic Basalt	McMurdo Volcanic Group	32	681	0.1361	0.703360						225
Southern Victoria Land	Ross Island	-77.83	166.68		Titanaugite-olivine Basalt	McMurdo Volcanic Group	52	917	0.165	0.703440						225
Southern Victoria Land	Ross Island	-77.83	166.68		Titanaugite-hornblende Basalt	McMurdo Volcanic Group	77	1038	0.2142	0.703380						225
Southern Victoria Land	Ross Island	-77.83	166.68		Hornblende-titanaugite Trachybasalt	McMurdo Volcanic Group	133	1783	0.2171	0.703420						225
Southern Victoria Land	Ross Island	-77.83	166.68		Olivine-titanaugite Basalt	McMurdo Volcanic Group	53	851	0.1795	0.703640						225
Southern Victoria Land	Ross Island	-77.83	166.68		Olivine-titanaugite Basalt	McMurdo Volcanic Group	58	816	0.2027	0.703820						225
Southern Victoria Land	Ross Island	-77.83	166.68		Olivine-titanaugite Basalt	McMurdo Volcanic Group	52	760	0.1969	0.703850						225
Southern Victoria Land	Mount Erebus	-77.67	166.78	LAVA	Hawaiite, Nepheline	McMurdo Volcanic Group	62	871		0.703021	85.0	15.1				226
Southern Victoria Land	Mount Erebus	-77.67	166.78	LAVA	Benmoreite, Nepheline	McMurdo Volcanic Group	86	1171		0.703027	96.0	14.4				226

Southern Victoria Land	Mount Erebus	-77.65	167.47	LAVA	Trachyte	McMurdo Volcanic Group	132	81		0.704248	109.0	17.0				226
Southern Victoria Land	Mount Erebus	-77.58	166.27	LAVA	Basanite	McMurdo Volcanic Group	41	1100		0.702958	67.0	12.5				226
Southern Victoria Land	Mount Erebus	-77.57	166.97	LAVA	Phonolite, Anorthoclase	McMurdo Volcanic Group	102	878		0.703029	97.0	15.3				226
Southern Victoria Land	Mount Erebus	-77.50	167.50	LAVA	Mugearite, Nepheline	McMurdo Volcanic Group	77	1270		0.702990	91.0	13.9				226
Southern Victoria Land	Mount Morning	-78.55	164.54	339	Tephrite	McMurdo Volcanic Group	36	999		0.703350	43.4	8.7		0.512852	4.2	227
Southern Victoria Land	Mount Morning	-78.55	164.52	343	Trachyte	McMurdo Volcanic Group	97	34		0.704980	81.0			0.512782	2.8	227
Southern Victoria Land	Mount Morning	-78.49	163.39	151A	Phonolite	McMurdo Volcanic Group	179	297		0.703220	32.3	4.4		0.512846	4.1	227
Southern Victoria Land	Mount Morning	-78.48	163.65	518	Phonolite	McMurdo Volcanic Group	187	320		0.703070	33.2	4.4		0.512882	4.8	227
Southern Victoria Land	Mount Morning	-78.40	163.85	67E	Basanite	McMurdo Volcanic Group	27	673		0.703080	35.6	7.2		0.512874	4.6	227
Southern Victoria Land	Mount Murray	-76.15	161.83	MUR-04	Sills	Ferrar Group	24	125	0.556	0.71278	3.0	10.3	0.172	0.51231	-6.4	228
Southern Victoria Land	Thumb Point	-75.97	160.47	TPS-02	Sills	Ferrar Group	21	107	0.573	0.71316	2.1	7.7	0.164	0.51231	-6.4	228
Southern Victoria Land	Ricker Hills	-75.68	159.17	RIH-02	Sills	Ferrar Group	49	137	1.043	0.71469	4.6	19.9	0.139	0.51230	-6.6	228
Southern Victoria Land	Brimstone Peak	-75.63	158.55	BRI-03	Flows	Ferrar Group	20	138	0.413	0.71122	27.0	11.3	0.145	0.51241	-4.4	228
Southern Victoria Land	Brimstone Peak	-75.63	158.55	BRI-29	Flows	Ferrar Group	64	128	1.444	0.71322	6.9	28.4	0.146	0.51240	-4.6	228
Southern Victoria Land	Mount Joyce	-75.60	160.82	MJY-01	Sills	Ferrar Group	40	137	0.849	0.71377	3.7	15.9	0.14	0.51231	-6.4	228
Southern Victoria Land	Mount Joyce	-75.60	160.82	MJY-02	Sills	Ferrar Group	30	128	0.681	0.71339	3.0	12.5	0.142	0.51231	-6.4	228
Ross Sea	Iselin Bank	-73.68	176.42	P50869	Meta-rhyolite	Unconsolidated sediments	233	58		0.791007	8.7	41.3		0.511987	-12.7	229
Ellsworth-Whitmore Mnts.	Linck Nunataks	-82.68	-104.20	R.2226.4	Linck Nunatak Granite	Mesozoic Granites				0.74592				0.512230	-8.0	230
Ellsworth-Whitmore Mnts.	Linck Nunataks	-82.68	-104.20	R.2227.1	Linck Nunatak Granite	Mesozoic Granites				0.74283				0.512210	-8.3	230
Ellsworth-Whitmore Mnts.	Mount Seelig	-82.47	-103.90	R.2228.1	Mount Seelig Granite	Mesozoic Granites				0.71621				0.511990	-12.6	230
Ellsworth-Whitmore Mnts.	Mount Seelig	-82.47	-103.90	R.2229.1	Mount Seelig Granite	Mesozoic Granites				0.72829				0.512480	-3.1	230
Ellsworth-Whitmore Mnts.	Whitmore Mountains				Mount Seelig Granite	Mesozoic Granites				0.72754						230
Ellsworth-Whitmore Mnts.	Whitmore Mountains				Mount Seelig Granite	Mesozoic Granites				0.72872						230
Ellsworth-Whitmore Mnts.	Whitmore Mountains				Mount Seelig Granite	Mesozoic Granites				0.72659						230
Ellsworth-Whitmore Mnts.	Whitmore Mountains				Mount Seelig Granite	Mesozoic Granites				0.72219						230
Ellsworth-Whitmore Mnts.	Whitmore Mountains				Mount Seelig Granite	Mesozoic Granites				0.78479						230
Ellsworth-Whitmore Mnts.	Whitmore Mountains				Mount Seelig Granite	Mesozoic Granites				0.71886						230
Ellsworth-Whitmore Mnts.	Whitmore Mountains				Mount Seelig Granite	Mesozoic Granites				0.72328						230
Ellsworth-Whitmore Mnts.	Whitmore Mountains			R.2226.5	Linck Nunatak Granite	Mesozoic Granites				0.75405						230
Ellsworth-Whitmore Mnts.	Whitmore Mountains			R.2226.6	Linck Nunatak Granite	Mesozoic Granites				0.75429						230
Ellsworth-Whitmore Mnts.	Whitmore Mountains				Linck Nunatak Granite	Mesozoic Granites				0.78676						230
Ellsworth-Whitmore Mnts.	Whitmore Mountains				Linck Nunatak Granite	Mesozoic Granites				0.77436						230
Ellsworth-Whitmore Mnts.	Whitmore Mountains				Linck Nunatak Granite	Mesozoic Granites				0.80336						230
Ellsworth-Whitmore Mnts.	Whitmore Mountains				Linck Nunatak Granite	Mesozoic Granites				0.74833						230
Ellsworth-Whitmore Mnts.	Whitmore Mountains				Linck Nunatak Granite	Mesozoic Granites				0.74987						230
Marie Byrd Land	Mt Sidley	-77.03	-126.10	MB27.5	Basanite	MBL Volcanic Group	32	877	0.1055	0.702997	7.7	39.3	0.1185	0.512900	5.1	231
Marie Byrd Land	Mt Sidley	-77.03	-126.10	K168	Basanite	MBL Volcanic Group	36	877	0.1187	0.703038	7.76	39.80	0.1179	0.512896	5.0	231

Marie Byrd Land	Mt Sidley	-77.03	-126.10	MB32.11	Mugearite	MBL Volcanic Group	40	492	0.2351	0.703165	7.44	38.13	0.1179	0.512851	4.2	231
Marie Byrd Land	Mt Sidley	-77.03	-126.10	K99	Mugearite	MBL Volcanic Group	56	756	0.2142	0.703055						231
Marie Byrd Land	Mt Sidley	-77.03	-126.10	K134	Benmoreite	MBL Volcanic Group	75	483	0.4468	0.703078						231
Marie Byrd Land	Mt Sidley	-77.03	-126.10	K97	Benmoreite	MBL Volcanic Group	76	491	0.4485	0.703016	11.19	69.14	0.0979	0.512866	4.5	231
Marie Byrd Land	Mt Sidley	-77.03	-126.10	K137	Trachyte	MBL Volcanic Group	218	4	166.1717	0.714708						231
Marie Byrd Land	Mt Sidley	-77.03	-126.10	MB29.4	Trachyte	MBL Volcanic Group	163	7.23	65.2317	0.709201	12.53	66.43	0.1140	0.512879	4.7	231
Marie Byrd Land	Mt Sidley	-77.03	-126.10	K105	Trachyte	MBL Volcanic Group	292	36.88	22.9018	0.704768						231
Marie Byrd Land	Mt Sidley	-77.03	-126.10	K55	Trachyte	MBL Volcanic Group	192	195.54	2.8360	0.703337	13.78	76.08	0.1095	0.512835	3.9	231
Marie Byrd Land	Mt Sidley	-77.03	-126.10	K66	Trachyte	MBL Volcanic Group	124	78.30	4.5917	0.704119	10.23	53.12	0.1164	0.512824	3.6	231
Marie Byrd Land	Mt Sidley	-77.03	-126.10	MB33.3	Trachyte	MBL Volcanic Group					33.01	183.18	0.1089	0.512813	3.4	231
Marie Byrd Land	Mt Sidley	-77.03	-126.10	MB33.8	Trachyte	MBL Volcanic Group					34.51	189.94	0.1098	0.512806	3.3	231
Marie Byrd Land	Mt Sidley	-77.03	-126.10	MB35.5	Phonolite	MBL Volcanic Group	253	4.20	174.2270	0.715455						231
Marie Byrd Land	Mt Sidley	-77.03	-126.10	MB38.3	Trachyte-Phonolite	MBL Volcanic Group	267	41.84	18.4542	0.705332	15.23	84.42	0.1090	0.512816	3.5	231
Marie Byrd Land	Mt Sidley	-77.03	-126.10	MB33.11	Trachyte	MBL Volcanic Group	372	72.99	14.7405	0.704083						231
Marie Byrd Land	Mt Sidley	-77.03	-126.10	MB42.3	Phonolite	MBL Volcanic Group	192	245.03	2.2716	0.703124	13.09	74.46	0.1063	0.512859	4.3	231
Marie Byrd Land	Mt Sidley	-77.03	-126.10	K144	Phonolite	MBL Volcanic Group	208	150.87	3.9853	0.70314	12.62	70.72	0.1078	0.512882	4.8	231
Marie Byrd Land	Mt Sidley	-77.03	-126.10	K115	Phonolite	MBL Volcanic Group	206	153.94	3.8644	0.703107						231
Marie Byrd Land	Mt Sidley	-77.03	-126.10	MB35.2	Phonolite	MBL Volcanic Group	235	47.96	14.1505	0.704044	18.71	102.75	0.1101	0.512863	4.4	231
Marie Byrd Land	Mt Sidley	-77.03	-126.10	K108	Tephriphonolite	MBL Volcanic Group	99	194.77	1.4673	0.703052	17.06	89.40	0.1154	0.512886	4.9	231
Marie Byrd Land	Mt Sidley	-77.03	-126.10	K122	Tephriphonolite	MBL Volcanic Group	106	280	1.0936	0.703019						231
Marie Byrd Land	Mt Waesche	-77.17	-126.90	MB.4.1	Alkali Basalt	MBL Volcanic Group	11	494	0.0644	0.702681						231
Marie Byrd Land	Mt Waesche	-77.17	-126.90	K19	Alkali Basalt	MBL Volcanic Group	25	581	0.1244	0.702732	7.33	37.49	0.1182	0.512877	4.6	231
Marie Byrd Land	Mt Waesche	-77.17	-126.90	K01	Phonotephrite	MBL Volcanic Group	51	589	0.2504	0.702697	11.18	59.48	0.1137	0.512886	4.8	231
Marie Byrd Land	Mt Waesche	-77.17	-126.90	MB.11.2	Tephriphonolite	MBL Volcanic Group	90	201	1.2948	0.702728	13.05	68.61	0.1150	0.512890	4.9	231
Marie Byrd Land	Mt Waesche	-77.17	-126.90	MB.15.1	Trachyte	MBL Volcanic Group	80	221	1.0468	0.70276						231
Marie Byrd Land	Tasch Peak	-76.67	-118.05	TW92-059	Alkali Basalt	MBL Volcanic Group	13	609		0.702761	5.0	23.4		0.512887	4.9	231
Marie Byrd Land	Morrison Rocks	-76.85	-117.65	TW92-130	Alkali Basalt	MBL Volcanic Group	25	611		0.702826	6.2	30.4		0.512907	5.2	231
Marie Byrd Land	Runyon Rock	-76.93	-116.55	TW92-135	Basalt/Hawaiite	MBL Volcanic Group	37	589		0.702735	7.1	40.0		0.512860	4.3	231
Marie Byrd Land	Morrison Rocks	-76.85	-117.65	TW92-142	Alkali Basalt	MBL Volcanic Group	26	404		0.702755	6.0	29.6		0.512883	4.8	231
Marie Byrd Land	English Rock	-76.82	-118.00	TW92-151	Basalt/Hawaiite	MBL Volcanic Group	38	682		0.702757	8.0	40.5		0.512913	5.4	231
Marie Byrd Land	Lie Cliff	-76.70	-117.62	TW92-162	Alkali Basalt	MBL Volcanic Group	23	544		0.702672	5.8	29.0		0.512857	4.3	231
Southern Victoria Land	Hut Point Penisular	-77.85	166.70	22888e		McMurdo Volcanic Group				0.703051				0.512889	4.9	232

Southern Victoria Land	Hut Point Penisular	-77.74	166.77	RI 34		McMurdo Volcanic Group				0.703083				0.512898	5.1	232
Southern Victoria Land	Hut Point Penisular	-77.74	166.87	HP 06		McMurdo Volcanic Group				0.703047				0.512896	5.0	232
Southern Victoria Land	Mt Terror	-77.64	168.57	RI 96		McMurdo Volcanic Group				0.703076				0.512913	5.4	232
Southern Victoria Land	Erebus	-77.58	166.29	RI 61		McMurdo Volcanic Group				0.702935				0.512901	5.1	232
Southern Victoria Land	Mt Terror	-77.58	168.69	RI 109		McMurdo Volcanic Group				0.703079				0.512915	5.4	232
Southern Victoria Land	Mt Terror	-77.52	169.27	22958		McMurdo Volcanic Group				0.703115				0.512911	5.3	232
Southern Victoria Land	Mt Terror	-77.51	167.96	RI 82		McMurdo Volcanic Group				0.702907				0.512959	6.3	232
Southern Victoria Land	Mt Terror	-77.51	169.06	RI 51		McMurdo Volcanic Group				0.702975				0.512943	5.9	232
Southern Victoria Land	Mt Terror	-77.51	169.33	CC 03		McMurdo Volcanic Group				0.703048				0.512920	5.5	232
Southern Victoria Land	Mt Terror	-77.51	168.86	RI 60		McMurdo Volcanic Group				0.702969				0.512940	5.9	232
Southern Victoria Land	Mt Terror	-77.51	168.86	RI 59T		McMurdo Volcanic Group				0.703041				0.512926	5.6	232
Southern Victoria Land	Mt Terror	-77.51	168.75	RI 72		McMurdo Volcanic Group				0.703001				0.512922	5.5	232
Southern Victoria Land	Mt Terror	-77.51	168.97	RI 41T		McMurdo Volcanic Group				0.703029				0.512923	5.6	232
Southern Victoria Land	Mt Terror	-77.50	168.90	RI 37		McMurdo Volcanic Group				0.703097				0.512922	5.5	232
Southern Victoria Land	Mt Terror	-77.50	168.98	RI 40		McMurdo Volcanic Group				0.703055				0.512915	5.4	232
Southern Victoria Land	Mt Terror	-77.50	169.13	RI 22		McMurdo Volcanic Group				0.70309				0.512913	5.4	232
Southern Victoria Land	Mt Terror	-77.50	169.05	RI 25		McMurdo Volcanic Group				0.703119				0.512905	5.2	232
Southern Victoria Land	Mt Terror	-77.50	169.14	RI 14T		McMurdo Volcanic Group				0.703098				0.512901	5.1	232
Southern Victoria Land	Mt Terror	-77.50	168.71	RI 45		McMurdo Volcanic Group				0.703069				0.512919	5.5	232
Southern Victoria Land	Mt Terror	-77.50	169.15	RI 13		McMurdo Volcanic Group				0.703133				0.512906	5.2	232
Southern Victoria Land	Mt Terror	-77.50	168.70	RI 46T		McMurdo Volcanic Group				0.703006				0.512933	5.8	232
Southern Victoria Land	Mt Terror	-77.50	169.23	22962		McMurdo Volcanic Group				0.703088				0.512910	5.3	232
Southern Victoria Land	Mt Terror	-77.48	169.05	RI 17		McMurdo Volcanic Group				0.703032				0.512915	5.4	232
Southern Victoria Land	Mt Terror	-77.47	168.60	RI 79		McMurdo Volcanic Group				0.702993				0.512939	5.9	232
Southern Victoria Land	Erebus	-77.47	167.12	RI 111		McMurdo Volcanic Group				0.702921				0.512907	5.2	232
Southern Victoria Land	Mt Terror	-77.47	168.64	RI 66		McMurdo Volcanic Group				0.702986				0.512950	6.1	232
Southern Victoria Land	Mt Terror	-77.47	169.21	CC 05		McMurdo Volcanic Group				0.703096				0.512911	5.3	232
Southern Victoria Land	Mt Terror	-77.46	169.10	RI 63		McMurdo Volcanic Group				0.702928				0.512960	6.3	232
Southern Victoria Land	Mt Terror	-77.46	169.24	22970		McMurdo Volcanic Group				0.703077				0.512904	5.2	232
Southern Victoria Land	Mt Terror	-77.46	169.20	CC 04		McMurdo Volcanic Group				0.702975				0.512949	6.1	232
Southern Victoria Land	Mt Terror	-77.38	168.10	RI 1		McMurdo Volcanic Group				0.703076				0.512911	5.3	232
Southern Victoria Land	Mt Terror	-77.37	168.33	RI 3		McMurdo Volcanic Group				0.703133				0.512897	5.1	232

Southern Victoria Land	Mt Bird	-77.32	166.54	RI 117		McMurdo Volcanic Group				0.703148				0.512898	5.1	232
Southern Victoria Land	Mt Bird	-77.32	166.54	RI 115		McMurdo Volcanic Group				0.703144				0.512891	4.9	232
Southern Victoria Land	Mt Bird	-77.30	167.10	LB 01		McMurdo Volcanic Group				0.703132				0.512868	4.5	232
Southern Victoria Land	Mt Bird	-77.30	167.10	LB 02		McMurdo Volcanic Group				0.703126				0.512872	4.6	232
Southern Victoria Land	Mt Bird	-77.30	167.10	LB 02I		McMurdo Volcanic Group				0.703124				0.512880	4.7	232
Southern Victoria Land	Mt Bird	-77.29	166.87	RI 98T		McMurdo Volcanic Group				0.703065				0.512858	4.3	232
Southern Victoria Land	Mt Bird	-77.29	166.87	RI 97		McMurdo Volcanic Group				0.703071				0.512859	4.3	232
Southern Victoria Land	Mt Bird	-77.26	166.91	RI 113		McMurdo Volcanic Group				0.702934				0.512917	5.4	232
Southern Victoria Land	Mt Bird	-77.25	166.84	RI 103		McMurdo Volcanic Group				0.702967				0.512911	5.3	232
Southern Victoria Land	Mt Bird	-77.25	166.83	RI 102		McMurdo Volcanic Group				0.702965				0.512913	5.4	232
Southern Victoria Land	Mt Bird	-77.25	166.75	RI 93		McMurdo Volcanic Group				0.702932				0.512896	5.0	232
Southern Victoria Land	Mt Bird	-77.23	166.43	RI 84		McMurdo Volcanic Group				0.703021				0.512874	4.6	232
Southern Victoria Land	Cape Irizar	-75.55	162.95	A13	Irizar Granite	GHI	242	117	6.02	0.749411	8.3	51.5	0.0975	0.512006	-12.3	233
Southern Victoria Land	Cape Irizar	-75.55	162.95	A20	Irizar Granite	GHI	215	120	5.2	0.74433	4.2	26.8	0.0939	0.511967	-13.1	233
Southern Victoria Land	Mount Erebus	-77.53	167.17	ER 83220	Alkali Basalt	McMurdo Volcanic Group				0.703043				0.512905	5.2	234
Southern Victoria Land	Mount Erebus	-77.53	167.17	ER-84505	Alkali Basalt	McMurdo Volcanic Group				0.703133				0.512906	5.2	234
Southern Victoria Land	Mount Erebus	-77.53	167.17	ER 97KS	Alkali Basalt	McMurdo Volcanic Group				0.703039				0.512908	5.3	234
Southern Victoria Land	Mount Erebus	-77.53	167.17	ER 2000	Alkali Basalt	McMurdo Volcanic Group				0.703033				0.512911	5.3	234
Southern Victoria Land	Mount Morning	-78.48	163.54		Basanite	McMurdo Volcanic Group				0.703314				0.512882	4.8	235
Southern Victoria Land	Mount Morning	-78.48	163.54		Basanite	McMurdo Volcanic Group				0.703314				0.512902	5.1	235
Southern Victoria Land	Mount Morning	-77.72	163.75	Basanite	Basanite	McMurdo Volcanic Group				0.703226				0.512840	3.9	235
Southern Victoria Land	Mount Morning	-77.72	163.75	Basanite	Basanite	McMurdo Volcanic Group				0.703314				0.512882	4.8	235
Southern Victoria Land	Mount Morning	-77.72	163.75	Basanite	Basanite	McMurdo Volcanic Group				0.703314				0.512902	5.1	235
Southern Victoria Land	Erebus Flanks	-77.67	166.78	ENRICHED FE-SERIES	Phonolite	McMurdo Volcanic Group				0.703034				0.512912	5.3	235
Southern Victoria Land	Mount Erebus	-77.53	167.15	25724	Phonolite	McMurdo Volcanic Group				0.703058				0.512911	5.3	235
Southern Victoria Land	Erebus Flanks	-77.53	167.15	STAGE 3 EREBUS-LINEAGE LAVA	Phonolite	McMurdo Volcanic Group				0.703088				0.512872	4.6	235
Southern Victoria Land	Erebus Flanks	-77.53	167.15	DVDP-2 LAVA	Phonotephrite	McMurdo Volcanic Group				0.703081				0.512877	4.7	235
Southern Victoria Land	Erebus Flanks	-77.53	167.15	DVDP-2 LAVA	Phonolite	McMurdo Volcanic Group				0.703040				0.512884	4.8	235
Southern Victoria Land	Mount Erebus	-77.53	167.15	BOMB	Phonolite	McMurdo Volcanic Group				0.703019				0.512886	4.8	235
Southern Victoria Land	Erebus Flanks	-77.53	167.15	STAGE 1 EREBUS-LINEAGE LAVA	Basanite	McMurdo Volcanic Group				0.702922				0.512886	4.8	235
Southern Victoria Land	Mount Erebus	-77.53	167.15	BOMB	Phonolite	McMurdo Volcanic Group				0.703031				0.512887	4.9	235
Southern Victoria Land	Mount Erebus	-77.53	167.15	BOMB	Phonolite	McMurdo Volcanic Group								0.512891	4.9	235

Southern Victoria Land	Mount Erebus	-77.53	167.15	BOMB	Phonolite	McMurdo Volcanic Group				0.703010				0.512891	4.9	235
Southern Victoria Land	Erebus Flanks	-77.53	167.15	STAGE 3 EREBUS-LINEAGE LAVA	Phonolite	McMurdo Volcanic Group								0.512894	5.0	235
Southern Victoria Land	Mount Erebus	-77.53	167.15	BOMB	Phonolite	McMurdo Volcanic Group				0.703109				0.512898	5.1	235
Southern Victoria Land	Mount Erebus	-77.53	167.15	25721	Phonolite	McMurdo Volcanic Group				0.703019				0.512900	5.1	235
Southern Victoria Land	Erebus Flanks	-77.53	167.15	STAGE 3 EREBUS-LINEAGE LAVA	Phonolite	McMurdo Volcanic Group								0.512900	5.1	235
Southern Victoria Land	Mount Erebus	-77.53	167.15	BOMB	Phonolite	McMurdo Volcanic Group				0.703018				0.512903	5.2	235
Southern Victoria Land	Mount Erebus	-77.53	167.15	BOMB	Phonolite	McMurdo Volcanic Group				0.703051				0.512903	5.2	235
Southern Victoria Land	Mount Erebus	-77.53	167.15	BOMB	Phonolite	McMurdo Volcanic Group				0.703061				0.512904	5.2	235
Southern Victoria Land	Mount Erebus	-77.53	167.15	BOMB	Phonolite	McMurdo Volcanic Group				0.703036				0.512904	5.2	235
Southern Victoria Land	Erebus Flanks	-77.53	167.15	STAGE 3 EREBUS-LINEAGE LAVA	Phonolite	McMurdo Volcanic Group				0.703005				0.512904	5.2	235
Southern Victoria Land	Erebus Flanks	-77.53	167.15	STAGE 3 EREBUS-LINEAGE LAVA	Phonolite	McMurdo Volcanic Group				0.703008				0.512904	5.2	235
Southern Victoria Land	Mount Erebus	-77.53	167.15	BOMB	Phonolite	McMurdo Volcanic Group				0.703039				0.512905	5.2	235
Southern Victoria Land	Mount Erebus	-77.53	167.15	BOMB	Phonolite	McMurdo Volcanic Group				0.703043				0.512905	5.2	235
Southern Victoria Land	Erebus Flanks	-77.53	167.15	DVDP-2 LAVA	Phonolite	McMurdo Volcanic Group				0.703021				0.512905	5.2	235
Southern Victoria Land	Mount Erebus	-77.53	167.15	BOMB	Phonolite	McMurdo Volcanic Group				0.703024				0.512906	5.2	235
Southern Victoria Land	Mount Erebus	-77.53	167.15	BOMB	Phonolite	McMurdo Volcanic Group				0.703022				0.512906	5.2	235
Southern Victoria Land	Mount Erebus	-77.53	167.15	BOMB	Phonolite	McMurdo Volcanic Group				0.703026				0.512906	5.2	235
Southern Victoria Land	Mount Erebus	-77.53	167.15	BOMB	Phonolite	McMurdo Volcanic Group				0.703039				0.512908	5.3	235
Southern Victoria Land	Erebus Flanks	-77.53	167.15	STAGE 3 EREBUS-LINEAGE LAVA	Phonolite	McMurdo Volcanic Group				0.703085				0.512909	5.3	235
Southern Victoria Land	Mount Erebus	-77.53	167.15	BOMB	Phonolite	McMurdo Volcanic Group				0.703079				0.512910	5.3	235
Southern Victoria Land	Mount Erebus	-77.53	167.15	BOMB	Phonolite	McMurdo Volcanic Group				0.703042				0.512910	5.3	235
Southern Victoria Land	Mount Erebus	-77.53	167.15	BOMB	Phonolite	McMurdo Volcanic Group				0.703033				0.512911	5.3	235
Southern Victoria Land	Mount Erebus	-77.53	167.15	BOMB	Phonolite	McMurdo Volcanic Group				0.703035				0.512912	5.3	235
Southern Victoria Land	Erebus Flanks	-77.53	167.15	STAGE 3 EREBUS-LINEAGE LAVA	Phonolite	McMurdo Volcanic Group				0.703088				0.512912	5.3	235
Southern Victoria Land	Mount Erebus	-77.53	167.15	BOMB	Phonolite	McMurdo Volcanic Group				0.703102				0.512916	5.4	235
Southern Victoria Land	Erebus Flanks	-77.53	167.15	ENRICHED FE-SERIES	TRACHYTE	McMurdo Volcanic Group				0.704251				0.512916	5.4	235
Southern Victoria Land	Erebus Flanks	-77.53	167.15	STAGE 3 EREBUS-LINEAGE LAVA	Phonolite	McMurdo Volcanic Group				0.703017				0.512923	5.6	235
Southern Victoria Land	Mount Erebus	-77.53	167.15	BOMB	Phonolite	McMurdo Volcanic Group				0.703038				0.512924	5.6	235
Southern Victoria Land	Mount Erebus	-77.53	167.15	BOMB	Phonolite	McMurdo Volcanic Group				0.703022				0.512924	5.6	235
Southern Victoria Land	Mount Erebus	-77.53	167.15	BOMB	Phonolite	McMurdo Volcanic Group				0.703033				0.512925	5.6	235

Southern Victoria Land	Erebus Flanks	-77.53	167.15	STAGE 3 EREBUS-LINEAGE LAVA	Phonolite	McMurdo Volcanic Group				0.703077				0.512927	5.6	235
Southern Victoria Land	Erebus Flanks	-77.53	167.15	STAGE 1 EREBUS-LINEAGE LAVA	Basanite	McMurdo Volcanic Group				0.702969				0.512927	5.6	235
Southern Victoria Land	Erebus Flanks	-77.53	167.15	STAGE 3 EREBUS-LINEAGE LAVA	Phonolite	McMurdo Volcanic Group				0.703025				0.512928	5.7	235
Southern Victoria Land	Erebus Flanks	-77.53	167.15	STAGE 3 EREBUS-LINEAGE LAVA	Phonolite	McMurdo Volcanic Group								0.512928	5.7	235
Southern Victoria Land	Mount Erebus	-77.53	167.15	BOMB	Phonolite	McMurdo Volcanic Group				0.703026				0.512929	5.7	235
Southern Victoria Land	Erebus Flanks	-77.53	167.15	DVDP-2 LAVA	Basanite	McMurdo Volcanic Group				0.702991				0.512929	5.7	235
Southern Victoria Land	Mount Erebus	-77.53	167.15	BOMB	Phonolite	McMurdo Volcanic Group				0.703021				0.512930	5.7	235
Southern Victoria Land	Erebus Flanks	-77.53	167.15	STAGE 3 EREBUS-LINEAGE LAVA	Phonolite	McMurdo Volcanic Group				0.703017				0.512931	5.7	235
Southern Victoria Land	Mount Erebus	-77.53	167.15	BOMB	Phonolite	McMurdo Volcanic Group				0.703021						235
Southern Victoria Land	Ross Island	-77.50	168.00	29	Trachyite	McMurdo Volcanic Group	98	48		0.704800						236
Southern Victoria Land	Ross Island	-77.50	168.00	DV-49	Basanitoid	McMurdo Volcanic Group	110	1000		0.703200						236
Southern Victoria Land	Ross Island	-77.50	168.00	MS-41	Basanitoid	McMurdo Volcanic Group	120	1200		0.703100						236
Southern Victoria Land	Ross Island	-77.50	168.00	HMC-35	Trachybasalt	McMurdo Volcanic Group	68	2000		0.703200						236
Southern Victoria Land	Ross Island	-77.50	168.00	DV-32	Trachybasalt	McMurdo Volcanic Group	112	1500		0.703100						236
Southern Victoria Land	Ross Island	-77.50	168.00	DV-17	Trachybasalt	McMurdo Volcanic Group	80	1300		0.703100						236
Southern Victoria Land	Ross Island	-77.50	168.00	DV-8	Trachybasalt	McMurdo Volcanic Group	173	1200		0.703100						236
Southern Victoria Land	Ross Island	-77.50	168.00	DV-5	Trachybasalt	McMurdo Volcanic Group	104	940		0.703100						236
Southern Victoria Land	Ross Island	-77.50	168.00	MS-52	Kaersutite	McMurdo Volcanic Group	11	1000		0.703100						236
Southern Victoria Land	Ross Island	-77.50	168.00	CB-55	Titaniferous augite	McMurdo Volcanic Group	0	135		0.703200						236
Southern Victoria Land	Ross Island	-77.50	168.00	CC-80	Diopside	McMurdo Volcanic Group	0	45		0.703100						236
Southern Victoria Land	Ross Island	-77.50	168.00	ME-104	Anorthoclase	McMurdo Volcanic Group	13	2400		0.703100						236
Ellsworth-Whitmore Mnts.	Whitmore Mnts.	-82.61	-105.76	WM-2G	Metasediment	Whitmore Mountain Metasediments								0.512150	-9.53	This study
Southern Transantarctic Mnts.	Mt. Bjaaland	-86.55	-164.23	PRR-12222	Triassic Sandstone	Beacon Supergroup								0.512275	-7.08	This study
Southern Transantarctic Mnts.	Mt. Schopf	-84.80	-113.25	H3-183	Permian Sandstone	Beacon Supergroup								0.512091	-10.66	This study
Southern Transantarctic Mnts.	Ackerman Ridge	-86.61	-147.14	EAZ	La Gorce Fm.	Liv Group								0.512270	-7.18	This study
Southern Transantarctic Mnts.	Cressey Peak	-85.48	-143.17	CIA	Leverett	Liv Group								0.512362	-5.38	This study
Southern Transantarctic Mnts.	?	-85.01	-166.51	ANI	Duncan Fm.	Liv Group								0.512140	-9.72	This study
Southern Victoria Land	Mt. Ellis	-79.87	156.23	EL-01	Permain white siltsone-mudstone	Beacon Supergroup								0.511761	-17.12	This study

A.3 Changes in Sediment Provenance at IODP Site U1521 during the Miocene Climatic Optimum

The Miocene Climatic Optimum (MCO), spanning approximately 17-15 Ma, saw the warmest deep ocean temperatures in the last 34 Myrs (Zachos et al., 2008). Atmospheric carbon dioxide levels were higher than before and after the event, with variations likely between 300 and 600 ppm (Kürschner et al., 2009; Beerling et al., 2009; Zhang et al., 2013; Breecker and Retallack, 2014; Super et al., 2018; Ji et al., 2018; Steinthorsdottir et al., 2020). These conditions mean that, although not a perfect analogue for the future, the MCO offers an opportunity to better understand the response of Antarctica's ice sheets to conditions warmer than the present. Ice volume was not constant during this interval, with substantial fluctuations occurring on a short eccentricity timescale (Holbourn et al., 2014; 2007; Greenop et al., 2014). During warmer interglacial intervals, ice retreat to positions far inland is probable, with evidence from the AND-2A record suggesting nearby tundra-like vegetation (Warny et al., 2009; Griener et al., 2015). During glacial intervals, ice sheets with an extent similar to the pre-industrial likely existed (Hauptvogel and Passchier, 2011).

However, ice sheet change during the MCO remains highly uncertain, with data from the Antarctic margin required to understand the response of different regions. To improve records of ice sheet history, IODP Expedition 374 drilled Site U1521 on the outer continental shelf in the central Ross Sea. Lithological Unit III dates from approximately 16.7 to 16 Ma, spanning the earliest part of the MCO, with an erosional unconformity spanning ~16-14.6 Ma at the top of the unit (see Chapter 2 Age Model section). Lithologically, the unit is fine-grained mudstone with chert nodules, which is sometimes diatom rich. IRD is notably absent. There are high levels of biogenic silica (30-55%). Palynology reveals high concentrations of brackish water algae, suggesting ice melt is occurring, and groups including *Spiniferites spp.* which require warmer waters. This suggests an ice-distal depositional setting.

Cyclic fluctuations are present in many records throughout Unit III. They are clearest in the natural gamma radiation curve and are consistent with 100 kyr glacial-interglacial cycles (Fig. A.3.1). Over the most pronounced cycle at ~205-190 m CSF-A, radiogenic isotope compositions seem to correlate well with natural gamma radiation (Fig. A.3.1). The peak in the most radiogenic ε_{Nd} sample also coincides well with the highest magnetic susceptibility. However, the biogenic silica curve appears to slightly lag the most radiogenic neodymium isotope values. High levels of biogenic silica likely reflect enhanced nutrient supply,

potentially linked to enhanced silicate weathering. It may therefore be linked to a change in the ice sheet margin; erosion is noted to be faster during transitional periods compared to stable conditions (Golledge et al., 2013). Paleotemperature estimates using the TEX_{86} biomarker suggest sea surface temperatures peaked around the same time as the most radiogenic ε_{Nd} values. However, other biomarkers suggest the opposite trend (Seki, pers. comm.), suggesting the 'saw-tooth' pattern in the NGR cycles is similar to those observed in Pleistocene ice core records, with gradual cooling during a glacial and rapid warming at the termination.

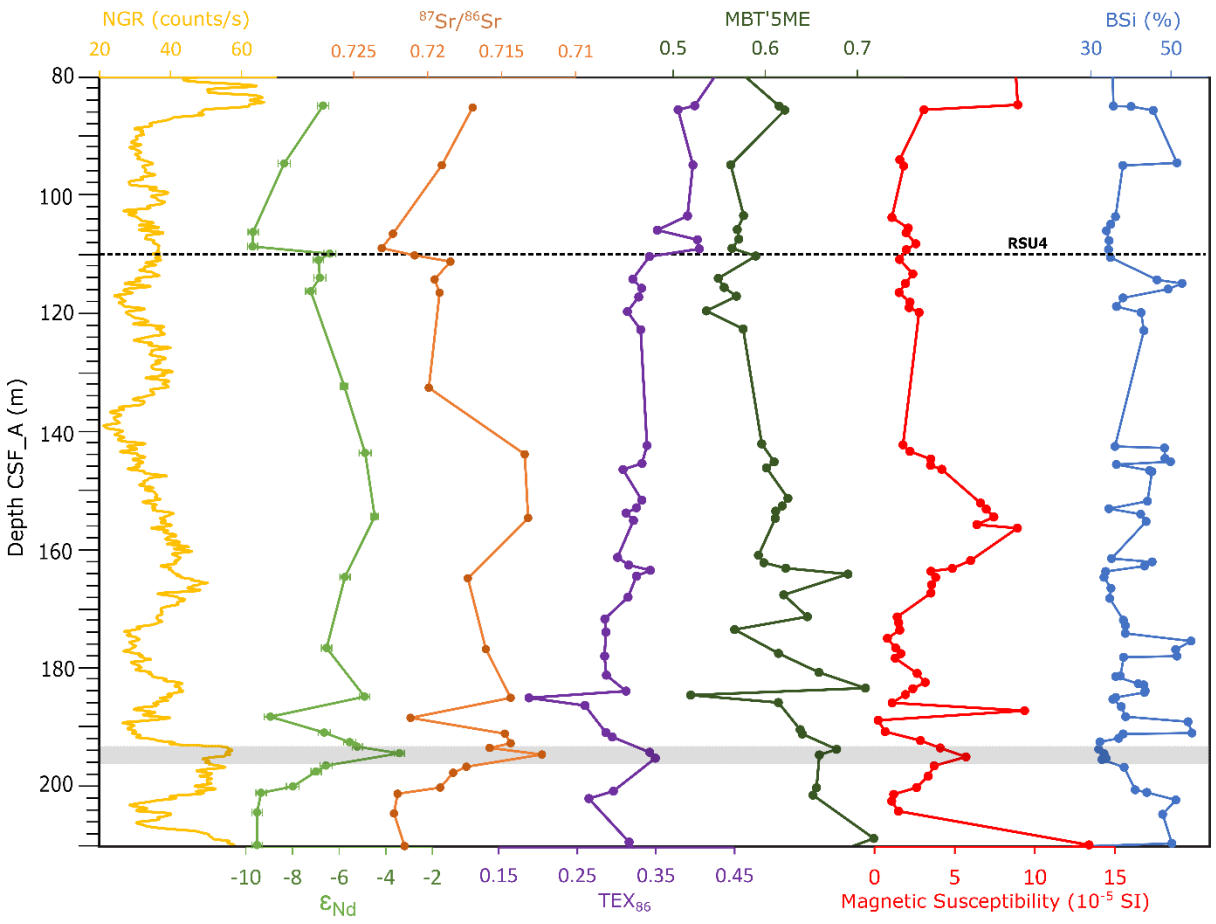


Figure A.3.1. *Comparison of different proxies applied to Unit III. The depth of RSU4 given in Perez et al. (2021) is indicated using a dashed line, and a peak in natural gamma radiation reflected in all other proxies at ~195 mbsf is indicated as a grey shaded region.*

Neodymium and strontium isotope data reveal large variations throughout lithological unit III, indicating changes between very different source lithologies (Fig. A.3.1; A.3.2). The least radiogenic ε_{Nd} values of ~-10 and most radiogenic $^{87}Sr/^{86}Sr$ ratios of ~0.725 are typical of a source from the central Transantarctic Mountains (TAM). Here, they reflect a mixture of the rocks present including the Beacon Supergroup, Ferrar Group, Granite Harbour Intrusive

Series and older metasedimentary rocks. Both isotope ratios are also consistent with moraines (Farmer et al., 2006; Farmer and Licht, 2016) as well as late Quaternary sediments from the Ross Sea thought to have a central TAM provenance (Farmer et al., 2006). We therefore suggest the intervals with ε_{Nd} values of approximately -10 in this MCO succession represent material eroded from the central TAM.

On the other hand, the sediments with more radiogenic values (up to -3.42 ± 0.22) suggest input from a more radiogenic endmember. This is unlikely to be from the central TAM region as measured ε_{Nd} values exceed values from the most radiogenic rocks - the Ferrar Group dolerites (-6 to -4; e.g. Hergt et al., 1989; Molzahn et al., 1996). As the Ferrar Group would almost certainly mix with adjacent, less radiogenic rocks before reaching Site U1521, to reach values as high as -3.42, a more radiogenic source must be contributing.

In the Ross Sea region, Cenozoic volcanic rocks are a likely candidate as these have mean values of +5.23 ± 0.75 (n = 179; see compilation in Marschalek et al., 2021) (e.g. Sims et al., 2008; Phillips et al., 2018). Clay minerology provides further evidence for these geologically young volcanic rocks contributing to the sediments. Smectite is commonly attributed to the breakdown of basalts or volcanic rocks; whilst it is nearly absent from the rest of the unit, it forms 26% of the most radiogenic sample (Table A.2.5). Nd and Sr isotope ratios plotted against each other suggest a simple mixing between a 'typical' central Transantarctic Mountain isotopic composition (ε_{Nd} of ~-10, $^{87}Sr/^{86}Sr$ of ~0.726) and a Cenozoic volcanic rock composition (ε_{Nd} of ~+5.23, $^{87}Sr/^{86}Sr$ of ~0.703) is likely (Fig. A.3.2). The only alternative potential contributor is the most radiogenic widespread rock type in the southern Transantarctic Mountains: the more southerly Granite Harbour Intrusive exposures. In the Gabbro Hills, between Scott and Shackleton Glaciers, these reach ε_{Nd} values of -3.1 to -1.1 and $^{87}Sr/^{86}Sr$ ratios of 0.705 to 0.717 (Borg et al., 1990). These rocks are, however, significantly more distal from Site U1521. They would also have to comprise the majority of the sediment to reach the most radiogenic values, which seems unlikely. I therefore suggest the alkaline Cenozoic volcanic rocks are the most likely endmember. Around the Ross Sea, these rocks outcrop as the McMurdo Volcanic Province and Marie Byrd Land Volcanic province, which are geochemically extremely similar making differentiating them difficult.

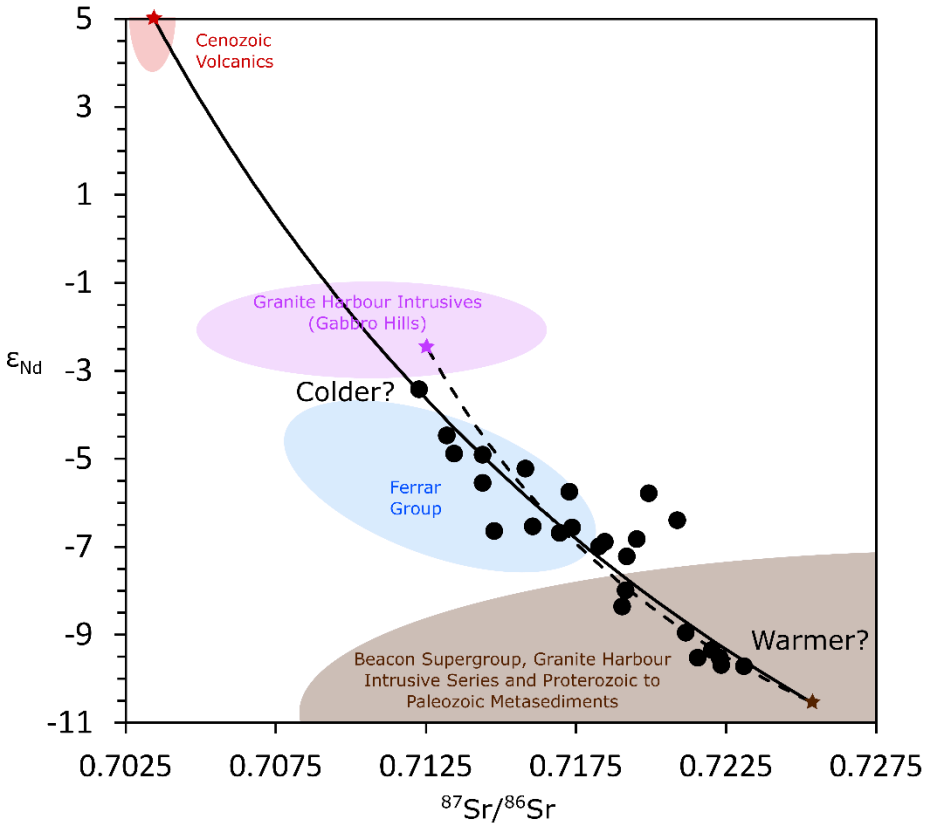


Figure A.3.2. *Nd-Sr crossplot. Coloured bubbles indicate typical values of relevant rock types found across the Ross Sea catchment. Mixing lines between a typical mixture of central TAM rocks (brown star) and Cenozoic volcanic rocks (red star)/GHI from the Gabbro Hills region (pink star) are shown using a solid and dashed line, respectively.*

The regional unconformity referred to as Ross Sea unconformity 4 (RSU4) is crossed at ~110 m CSF-A in Unit III (Perez et al., 2021) and accompanied by a significant change in provenance (Fig. A.3.1). The uppermost sediment preserved below RSU4 has more radiogenic ε_{Nd} values, around -7, whereas immediately above the unconformity, ε_{Nd} values are much more unradiogenic: approximately -10. As mentioned previously, ε_{Nd} values around -10 are consistent with a source from the central Transantarctic Mountains. As this sediment would have been deposited soon after ice retreated from this site, I therefore suggest the RSU4 unconformity was a result of expansion of the EAIS in this part of the Ross Sea.

Table A.3.1. *Nd and Sr isotope data for IODP Expedition 374 Site U1521 Lithological Units I-III.*

Core	Section	Top Offset (cm)	Bottom Offset (cm)	Sample Midpoint Depth (m.b.s.f)	$^{143}Nd/^{144}Nd$	2SE	ε_{Nd}	2SD	$^{87}Sr/^{86}Sr$	2SE
1	1	4	6	0.05	0.512243	0.000009	-7.70	0.26	0.719400	0.000008
1	3	62	91	3.265	0.512169	0.000008	-9.15	0.27	0.728106	0.000007
2	1	85	88	8.265	0.512189	0.000007	-8.76	0.22	0.720287	0.000007
3	1	77	115	17.96	0.512218	0.000009	-8.19	0.24	0.720305	0.000008
4	1	75	78	27.365	0.512205	0.000010	-8.45	0.26	0.722911	0.000008
5	2	66	69	38.375	0.512234	0.000007	-7.87	0.27	0.717806	0.000008
8	1	13	53	65.33	0.512190	0.000009	-8.73	0.24	0.720385	0.000007
9	2	70	73	76.755	0.512303	0.000009	-6.54	0.27	0.716224	0.000008
10	1	81	84	85.025	0.512295	0.000008	-6.69	0.24	0.716965	0.000008
11	1	95	97	94.76	0.512209	0.000007	-8.36	0.26	0.719045	0.000009
12	3	50	53	106.305	0.512141	0.000009	-9.69	0.22	0.722344	0.000007
12	4	145	147	108.76	0.512140	0.000009	-9.72	0.22	0.723105	0.000008
12	5	113	116	109.955	0.512306	0.000007	-6.47	0.26	0.720533	0.000008
Procedural replicate					0.512313	0.000011	-6.33	0.26	0.000011	0.000008
12	6	70	72	111.02	0.512285	0.000008	-6.89	0.22	0.718458	0.000009
13	1	99	102	114.005	0.512268	0.000006	-7.21	0.26	0.720490	0.000010
Procedural replicate					0.512307	0.000007	-6.45	0.22	0.000007	0.000008
13	3	67	69	116.28	0.512272	0.000009	-7.14	0.22	0.719216	0.000009
Procedural replicate					0.512264	0.000007	-7.3	0.22	0.000008	0.000007
15	1	10	13	132.315	0.512342	0.000010	-5.78	0.16	0.719924	0.000009
16	2	60	62	143.53	0.512388	0.000010	-4.89	0.26	0.713446	0.000008
17	3	65	68	154.245	0.512409	0.000008	-4.47	0.16	0.713205	0.000008
18	4	30	33	164.445	0.512343	0.000008	-5.75	0.22	0.717288	0.000007
19	5	63	65	176.4	0.512303	0.000010	-6.54	0.22	0.716062	0.000008
20	4	78	81	184.605	0.512402	0.000009	-4.91	0.22	0.714394	0.000007
20	7	5	7	187.99	0.512179	0.000008	-8.95	0.26	0.721163	0.000009
21	1	84	87	190.655	0.512297	0.000008	-6.64	0.26	0.714803	0.000009
21	2	93	96	192.255	0.512354	0.000007	-5.55	0.26	0.71439	0.000007
21	3	46	49	193.035	0.512370	0.000008	-5.22	0.22	0.715816	0.000009
21	4	7	9	194.15	0.512463	0.000007	-3.42	0.22	0.712278	0.000007
21	5	62	64	196.21	0.512302	0.000006	-6.56	0.26	0.717378	0.000009
21	6	12	14	197.22	0.512280	0.000008	-6.99	0.22	0.71827	0.000007
22	1	32	35	199.735	0.512228	0.000008	-7.99	0.27	0.719153	0.000008
22	2	17	19	200.79	0.512159	0.000007	-9.35	0.22	0.722039	0.000007
22	4	60	62	204.1	0.512150	0.000007	-9.52	0.22	0.722286	0.000007
23	1	60	62	209.61	0.512150	0.000010	-9.52	0.22	0.721559	0.000008

A.4 Nd and Sr Isotope Data for IODP Site U1522

Sediment provenance interpretation of IODP Site U1522 is being led by Kathy Licht and Chris Mallery at Indiana University-Purdue University Indianapolis. However, I here provide a brief summary of the Nd and Sr isotope data I gathered to complement the zircon U-Pb dating done by the afore mentioned collaborators and clast petrography work conducted by Luca Zurli, Franco Talarico and Matteo Perotti at the University of Siena.

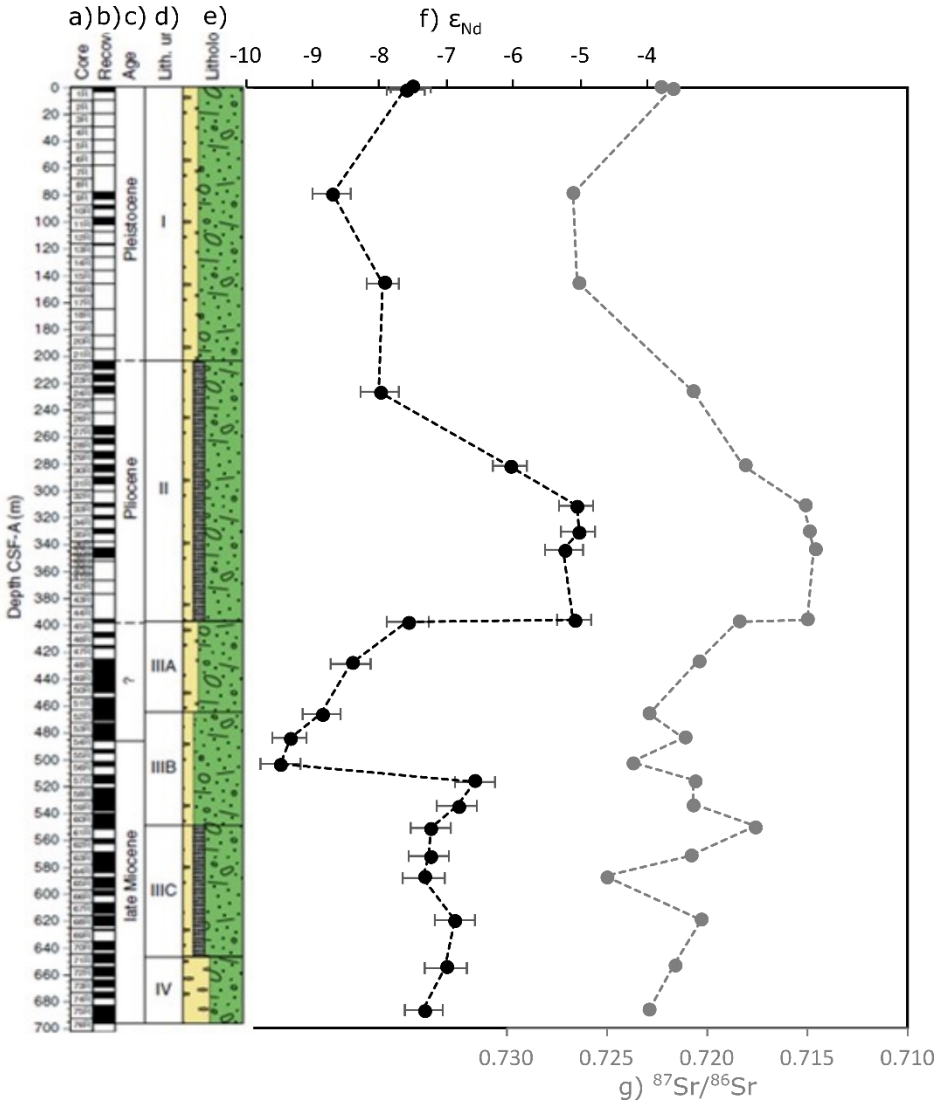


Figure A.4.1. *Site U1522 Nd (f) and Sr (g) isotope data. The left-hand portion of the figure is from McKay et al. (2019). From left to right, this shows depth below sea floor, core number (a), recovery (black = recovered, b), approximate shipboard age (c), lithological unit (d) and lithology (e), where green indicates diamict, grey muds, and yellow diatom-rich muds.*

The lowermost lithological units IV and IIIC in IODP Site U1522 record little provenance change, with consistent ε_{Nd} values of ~-7 suggesting little change to ice flow over time. Such values are similar to the seafloor surface sediment value and would suggest similar ice flow patterns to today. There is, however, a sharp transition at ~520 m bsf in unit IIIB, coinciding with a distinct change in clast lithology (Zurli, pers. comm., 2021) and zircon age populations (Licht and Mallery, pers. comm., 2021). The sediments directly above have much more unradiogenic ε_{Nd} values of ~-9.5 (Fig. A.4.1), which closely resemble sediment samples from the Transantarctic Mountains of East Antarctica (Farmer et al., 2006; Farmer and Licht, 2016). The sharpness of the transition and dominance of diamict may suggest an unconformity created by ice sheet expansion over the site. In this instance, this would be an East Antarctic Ice Sheet (EAIS) reaching remarkably far east over the Ross Sea.

The dominance of East Antarctic derived sediments seems to diminish over the upper part of lithological unit IIIB and IIIA. At the top of this sequence, lithological unit II, dating to the Pliocene, shows a substantial change in provenance. This corresponds to a large regional unconformity, RSU3 (Pérez et al., 2021). The sediments deposited above (in unit II) are muddier and have much more radiogenic ε_{Nd} values (~-6 to -5) mirrored by lower $^{87}Sr/^{86}Sr$ ratios (~0.715). Such data suggest a West Antarctic provenance, although the difference from modern values suggests different ice flow paths compared to the modern ice sheet. RSU3 may therefore reflect an advance of the West Antarctic Ice Sheet (WAIS) over the site. This raises the interesting question of how ice advance in the late Miocene led to the EAIS covering the site, whilst Pliocene ice sheet advance led to the WAIS covering the site.

Pleistocene variations lithological unit I are small, with values of ~-8.5 to -7.5 corresponding to a provenance from Bindschalder Ice Stream or nearby, consistent with modern ice flow trajectories and subglacial till samples (Farmer et al., 2006). This may suggest relative stability of the WAIS at this time.

Table A.4.1. *Nd and Sr isotope data for IODP Expedition 374 Site U1522.*

Core	Section	Top offset (cm)	Bottom offset (cm)	Midpoint depth below seafloor (m)	$^{143}Nd/^{144}Nd$	2SE	ε_{Nd}	2SD	$^{87}Sr/^{86}Sr$	2SE
1	1	2	5	0.04	0.512252	0.000006	-7.53	0.29	0.722357	0.000008
1	2	60	90	2.27	0.512248	0.000010	-7.61	0.29	0.721739	0.000008
9	2	30	70	79.30	0.512191	0.000009	-8.71	0.29	0.726683	0.000009
16	1	44	46	145.65	0.512231	0.000008	-7.95	0.25	0.726418	0.000007
24	3	100	140	226.60	0.512228	0.000009	-8.00	0.29	0.720675	0.000008
30	2	38	41	281.90	0.512328	0.000010	-6.05	0.25	0.718168	0.000006
33	2	110	113	311.29	0.512379	0.000009	-5.06	0.25	0.715151	0.000009
35	2	83	86	330.36	0.512380	0.000010	-5.03	0.25	0.714889	0.000007
37	2	10	60	344.25	0.512369	0.000009	-5.24	0.29	0.714633	0.000009
45	1	56	59	396.08	0.512376	0.000011	-5.10	0.25	0.715022	0.000013
45	2	69	72	397.73	0.512250	0.000011	-7.58	0.31	0.718433	0.000010
48	3	20	60	427.82	0.512206	0.000008	-8.42	0.29	0.720436	0.000007
52	3	40	80	466.33	0.512183	0.000008	-8.87	0.29	0.722914	0.000008
54	2	64	67	484.22	0.512159	0.000011	-9.34	0.25	0.721158	0.000009
56	2	36	39	503.14	0.512152	0.000016	-9.48	0.31	0.723756	0.000008
57	4	82	85	515.88	0.512301	0.000011	-6.57	0.31	0.720646	0.000007
59	4	20	60	534.19	0.512288	0.000010	-6.83	0.29	0.720690	0.000009
61	CC	5	27	550.68	0.512267	0.000009	-7.23	0.29	0.717601	0.000009
63	3	37	77	571.75	0.512266	0.000009	-7.26	0.29	0.720847	0.000009
65	1	0	11	587.36	0.512261	0.000015	-7.35	0.31	0.725058	0.000008
68	3	85	125	619.42	0.512286	0.000010	-6.88	0.29	0.720275	0.000008
72	1	14	25	654.00	0.512278	0.000012	-7.02	0.31	0.721656	0.000008
75	3	65	105	686.31	0.512262	0.000012	-7.34	0.29	0.722906	0.000008

A.5 Modelling Antarctic Erosion and Topographic development in the Early-Middle Miocene

A.5.1 Introduction

Chapter 2 reveals that substantial thicknesses of sediment deposited in the Ross Sea are of Early Miocene age. As well as proving the existence of a large WAIS, the volume of sediment deposited in only 320 kyrs implies a very rapid erosion of the West Antarctic hinterland between ~17.72 and 17.40 Ma, estimated at ~0.275 mm a^{-1} (Marschalek et al., 2021). With assistance from Ed Gasson (University of Exeter), I therefore sought to predict erosion by the WAIS over the Early-Middle Miocene at 23-14 Ma using the Penn State University ice sheet model (Pollard and DeConto, 2012). This allowed us to investigate whether the erosion rates achieved in the sedimentary record can be replicated by current sediment-enabled ice sheet models, and whether the model achieves the West Antarctic sediment provenance signature observed at International Ocean Discovery Program (IODP) Site U1521.

A.5.2 Adjustments to the Ice Sheet and Erosion Model

The Oligocene-Miocene boundary (23 Ma) topography of Paxman et al. (2019a) (hereafter P19) was used as the starting topography and the erosion and ice sheet model used is presented in Pollard and DeConto (2020) (hereafter PD20). To reach the P19 14 Ma topography at the end of the 9 Myr simulation, the quarrying coefficients of different sectors of the ice sheet were iteratively adjusted to match the sediment volumes being deposited by the model to the observed sediment volumes in P19. The quarrying coefficient accounts for processes other than basal shear stress and basal velocity which influence erosion rate, which is calculated as the product of these three variables using Equation 3.2 (DP20).

It was necessary to adapt variables and the model code used in DP20 in several ways. Firstly, the resolution of the model was increased from 160 km to 40 km. This greatly increased model run times, but was necessary to achieve results at a scale with realistic ice trajectories that are useful for comparing to sediment provenance results. It also resolves some Transantarctic Mountain outlet glaciers, which is important for sediment provenance reconstructions in the Ross Sea. The estimated quarrying coefficient proved sensitive to resolution, requiring several iterations at 40 km resolution for model results to converge. We also implemented an updated CO_2 record (Rae et al., 2021).

Furthermore, unlike PD20, who tuned an Eocene starting topography and assumed the final (modern) topography was constant, we used the P19 estimates for both initial and final topographies. We therefore held the initial 23 Ma topography as constant. The sector domains were also adjusted to match those in P19 and the Ross Sea sector split into the eastern and western portions, as the eastern and western Ross Sea sectors have very different sediment provenance signatures and lithologies, meaning a uniform quarrying coefficient seems inappropriate. The method of adapting the quarrying coefficient was also updated.

Our initial simulations resulted in large, unrealistic banks several hundred metres above sea level forming on some outer continental shelves (mainly the Ross and Weddell Seas). To remove these, two changes were implemented. Firstly, the 'CO_2 coefficient', which relates input CO_2 concentrations to warming in the parameterised climate model, was lowered to produce a cooler climate forcing, promoting ice sheet growth and depositing more sediment beyond the palaeo shelf break. This reflects the higher CO_2 concentrations in the Rae et al. (2021) record than in the record used in PD20. The lower CO_2 coefficient was also necessary to achieve a WAIS reaching the outer continental shelf in the Early Miocene, as observed at IODP Site U1521 (Marschalek et al., 2021). Secondly, the transport of sediment beyond the ice sheet margin is crude in PD20, so this was experimented with. Lowering the critical slope angle in the slumping parameterisation was found to be required to prevent large banks forming on the outer continental shelf, even after adjusting the CO_2 coefficient.

A final adaption to PD20 was the use of two basal friction coefficient values, as opposed to the modern inverted friction coefficient map used in PD20. This was viewed as more realistic given that the Miocene Antarctic bed and glacial conditions were likely very different to those today.

A.5.3 Results and Problems

The model can match the volumes of sediment offshore at 14 Ma to the estimate of P19 (Fig. A.5.1), with only minor disagreement in some basins. Inland, the model captures the development of troughs beneath major glaciers and records a lowering of key areas which are below sea level at present, such as the West Antarctic interior and Wilkes Subglacial Basin (Fig. A.5.2). Ice sheet extent and thicknesses are reasonable.

A major problem for studying Ross Sea sedimentation and provenance was the inability of the model to match the relative eastern and western Ross Sea volumes. This is because sediment generated in the western Ross Sea (i.e. Transantarctic Mountains) was typically

deposited in the eastern Ross Sea (i.e. close to the WAIS) due to the ice sheet flow configuration and very simple representation of offshore sediment transport. This meant the quarrying coefficient in the eastern Ross Sea sector tended to zero, as offshore it was receiving western Ross Sea sediment. Conversely, the western Ross Sea quarrying coefficient became very large to attempt to fill the western Ross Sea volume offshore, which was not possible as the bulk of this extra sediment was being deposited in the eastern Ross Sea.

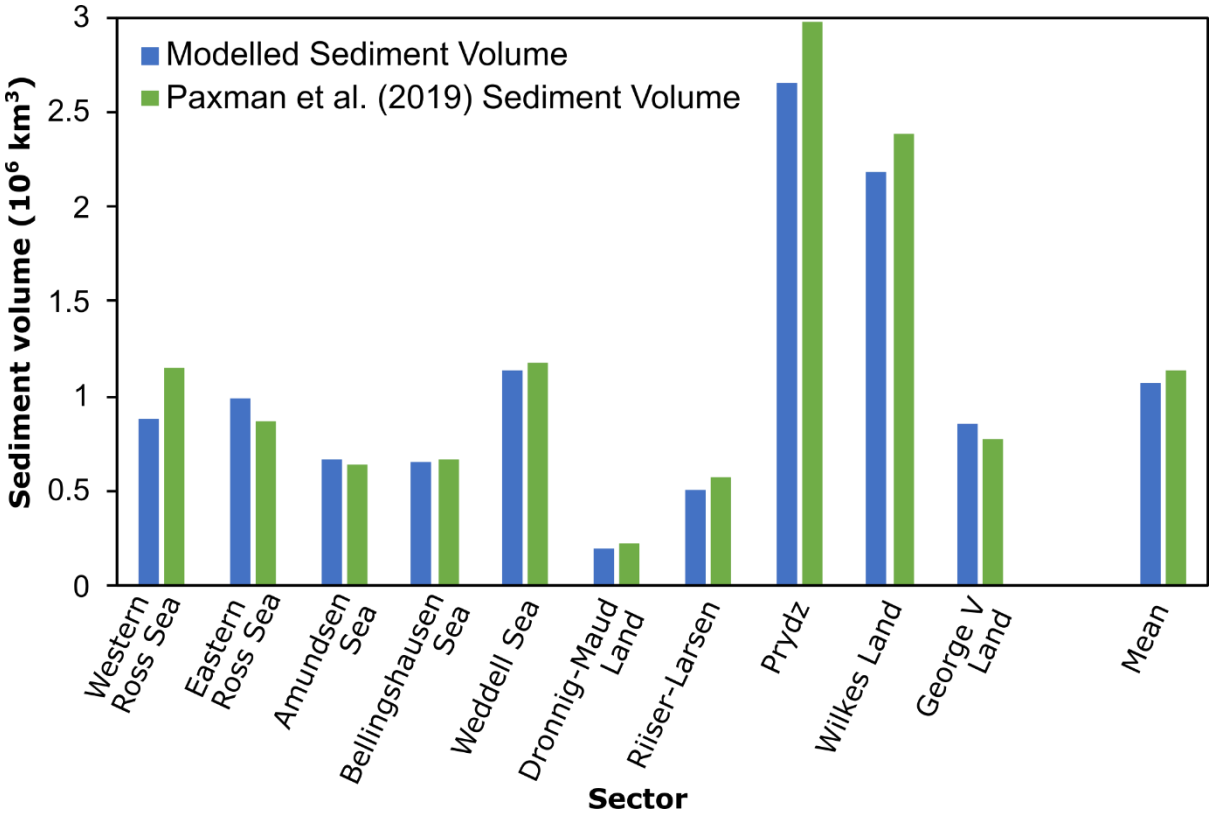


Figure A.5.1. *Sediment volumes for different sectors of Antarctica at 14 Ma for the model (blue) compared to P19 (green).*

The Amundsen Sea sector quarrying coefficient had to be raised to approximately two orders of magnitude higher than most other sectors in order to produce sufficient sediment. This may be due to the climate forcing used not permitting growth of the ice sheet in this sector for sufficiently long, which was being compensated for by increasing the 'erodibility' of the rock.

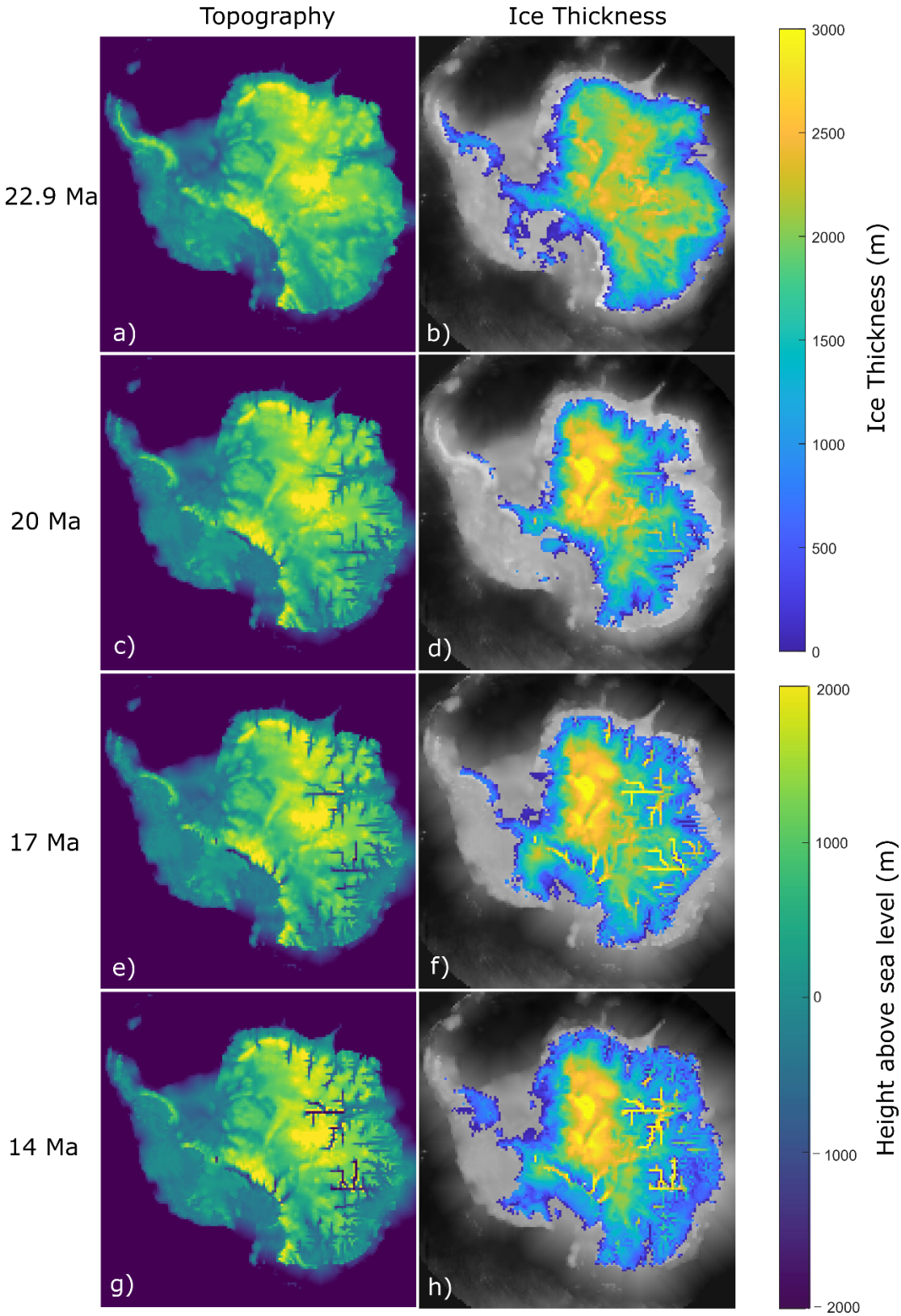


Figure A.5.2. *Modelled bed elevation (a, c, e, g) and ice thickness (b, d, f, h) at three million year intervals between 23 Ma and 14 Ma. Ice thicknesses at a given time slice vary depending on the orbital forcing; those shown are thus only indicative, with larger and smaller ice sheets present at times.*

Further unrealistic results were seen in the Antarctic Peninsula region, as to match sediment volumes in the Bellingshausen Sea sector the quarrying coefficient had to be raised to approximately ten times higher than most other sectors, which had the effect of rapidly removing the entire mountain range. This may suggest that either the sediment packages here are poorly dated, or that there was active uplift of the Antarctic Peninsula during this interval.

A.5.4 Recommendations for Future Work

The issues described and time limitations prevented further exploration of Early-Middle Miocene ice sheet erosion. To overcome many of the problems described, it would be useful to better examine the climate forcing being imposed on the model. The sediment distribution appears to require a larger ice sheet in the Early Miocene than is currently produced. A cooler climate/ocean would allow the ice sheet to expand more frequently into the Amundsen Sea sector, reducing the need for very high quarrying coefficients in this region to produce the observed sediment volumes. Additionally, a larger ice sheet would reach the shelf break and be able to transport sediment to the edge of the palaeo continental shelf, preventing the build-up of a large bank on the outer shelves. This would remove the need to adjust the offshore slumping coefficient, giving more realistic distributions of sediment offshore.

The observed transport of sediment generated in the Transantarctic Mountains being deposited in the eastern Ross Sea would require either a more sophisticated method of inverting for quarrying coefficient, or that the basins be grouped despite the radically different geologies.

A.6 Provenance Tracing of the Last Glacial Maximum Ice Sheet

A.6.1 Introduction

Chapter 3 discusses application of the provenance tracing method developed to the Pliocene. To investigate results using a larger-than-present ice sheet, we use a simulation of Antarctica's ice sheets during the Last Glacial Maximum (LGM). Unlike other palaeo ice sheet configurations, which have been obscured by later ice sheet advances, LGM ice sheet extent and flow direction is well recorded by geological, bathymetric and sediment data (e.g. Farmer et al., 2006; The RAISED Consortium, 2014; Licht et al., 2014; Siegert et al., 2022). This makes the LGM an excellent period to evaluate the accuracy of our model.

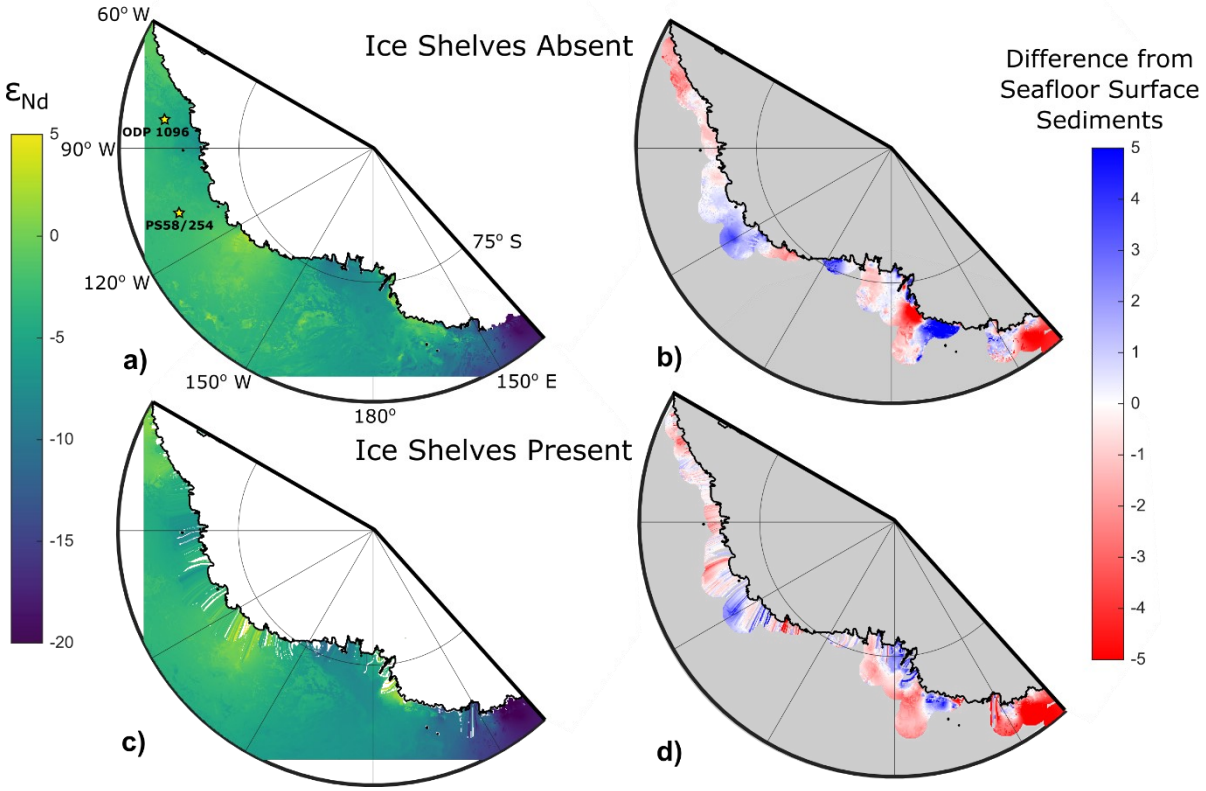


Figure A.6.1 *Predicted ε_{Nd} values around the modelled LGM ice sheet without (a) and with (c) ice shelves. b) and d) show the respective differences from measured seafloor surface sediments.*

There is good evidence that the grounding line of the LGM ice sheet was near the shelf break in many regions (The RAISED Consortium, 2014), but the extent of floating ice shelves is much more difficult to constrain and is poorly represented in numerical models. Factors such as storm waves and upwelling make an ice shelf protruding much beyond the continental slope unstable, evidenced by such ice shelves being rare around the modern ice sheet.

However, the dearth of constraints with which to accurately determine the size of ice shelves means we opt for performing experiments with and without ice shelves, accepting that the 'true' ice shelf extent may lie between these estimates. The extent of ice shelves is a strong control on offshore sediment provenance signatures (Fig. A.6.1).

Further changes made for this larger-than-present ice sheet include our subglacial rock ε_{Nd} value map, which did not extent beyond modern grounded ice. In areas with grounded ice at the LGM but not covered by any ice at present, it was assumed that the modern seafloor surface sediment interpolation, rather than an interpolated subglacial map, is likely to be broadly representative of previous interglacial sediments underlying a glacial period ice sheet.

A.6.2 West Antarctica and Antarctic Peninsula

Although there are small changes to ε_{Nd} values, the model prediction shows relatively little change compared to seafloor surface sediments along much of the Pacific margin of West Antarctica. This suggests ε_{Nd} values in sediments beyond the continental shelf are relatively insensitive to ice sheet growth in the Bellingshausen and Amundsen seas, and along the coast of Marie Byrd Land. This is supported by downcore records in these regions. At the modern seafloor, site PS58/254 in the Amundsen Sea has an ε_{Nd} value of -3.0 (Simões Pereira, 2018), which our model predicts as -4.3. Here, the LGM simulation reaches an ε_{Nd} value of -3.1. This is in close agreement of values measured at ~25 ka (-3.7), or ~31 ka (-3.0) (Simões Pereira, 2018). ODP Site 1096, located on the Pacific side of the Antarctic Peninsula, also displays relatively little change in ε_{Nd} values during the last glacial period (Carlson et al., 2021). Here, measured values are variable but within 1-2 epsilon units of seafloor surface sediments. Consequently, in sediments beyond the continental shelf where Nd isotope compositions represent a more integrated mixture of continental detritus, ε_{Nd} values are likely insensitive to growth of the Antarctic Peninsula Ice Sheet beyond its current position. Our modelling combined with these two records suggest this insensitivity may be applicable for much of the Antarctic Pacific margin.

A.6.3 George V Land Coast

The largest change in ε_{Nd} values is seen at the westernmost end of our study area, offshore of the Wilkes Subglacial Basin. IODP Site U1361, containing the Pliocene record discussed in the main text, also contains sediment from the LGM and earlier Pleistocene glacial periods.

Here, ε_{Nd} values reach ~-15.5 to -12 (Wilson et al., 2018); this is approximately 0.5 to 4 epsilon units less radiogenic than the -11.5 measured for the site's surface sediments (Cook et al., 2013). Our simulation successfully predicts this decrease in ε_{Nd} values, falling from -13.6 for the modern ice sheet to -17.0 (or -19.8 with ice shelves) when the LGM ice sheet is largest. Our magnitude of reduction in ε_{Nd} values (3.4) is therefore comparable to that recorded in the IODP sediment core, particularly in the earlier part of the Pleistocene when the magnitude of observed change is greatest (Wilson et al., 2018). In this region, the drop to unradiogenic values can be attributed to a greater contribution from the Adélie Craton on land. This likely occurred as the ice sheet advanced further onto these rocks and the grounding zone moved closer the Site U1361, reducing the potential for transport of detritus from the east.

The discrepancy with sediment core measurements may be linked to the Antarctic Coastal Current continuing to be shifted further north as described in previous sections, perhaps to a greater extent due to the presence of larger ice shelves. The shift in the coastal current could be caused by grounded icebergs similar to the present day (see Chapter 3), or the presence of an ice shelf close to/over the site. We note that although such a shift may occur in this region and the Ross Sea, in the western Antarctic Peninsula region, the Bellingshausen Sea sector and most of the Amundsen Sea sector, the northern boundary of the coastal current is bathymetrically controlled by the continental slope and would be unlikely to move. Nevertheless, offshore of George V Land a northwards shift in the Antarctic Coastal Current would bias results further towards local detritus, which is highly unradiogenic due to the presence of Precambrian rocks. Alternatively, the decrease to more unradiogenic ε_{Nd} values in the model could be due to a reduction in detritus travelling around the Antarctic Coastal Current due to larger/more ice shelves shedding 'cleaner' icebergs with little or no basal debris, or reduced melting of icebergs due to colder oceans, increasing the fraction of local, more unradiogenic debris. These factors are not simulated in the model.

A.6.4 Ross Sea and Victoria Land

Changes to sediment provenance in the Ross Sea and around the Victoria Land coast are sensitive to the extent of ice shelves, which control whether ice velocities or ocean velocities influence the trajectories of the detritus (Fig. A.6.1). In many places along the Victoria Land coast, the larger LGM ice sheet shifts the focus of erosion to more coastal areas dominated by McMurdo Volcanic Group rocks. This leads to more radiogenic ε_{Nd} values offshore, although

the along-coast transport of this detritus with increased ε_{Nd} values again shows strong dependence in the presence of ice shelves.

Farmer et al. (2006) provide ε_{Nd} data for Late Quaternary sediments at several sites from the Ross Sea, which have been used to reconstruct LGM ice flow and can be compared to the model results. The model simulation provides a close agreement with many of these samples, and modelled ε_{Nd} values in the Ross Sea span the range of the measured data. However, in the central Ross Sea the model often shows only a poor match. In this region, ice draining a cross-sectional area of the ice sheet many hundreds of kilometres wide including a geologically diverse portion of the Transantarctic Mountains and the WAIS interior is funnelled into a comparatively narrow trunk of the Ross Ice Shelf. The mismatch between our modelling and the Farmer et al. (2006) data can thus be explained by small variations in ice flux not captured in ice sheet models, which shifted the flow trajectories of ice in the Ross Ice Shelf, thus the provenance of entrained detritus, by distances sufficient to significantly impact the signature of LGM marine sediments.

A.6.5 Summary

The modelled LGM ice sheet reveals that ice sheet expansion along the Pacific coast of West Antarctica likely produces only small changes to ε_{Nd} values, as reflected in sediment core records (Simões Pereira, 2018). The provenance signature of sediment in the Ross Sea appears sensitive to the uncertain extent of ice shelves. Offshore the WSB, the model reproduces a change to more unradiogenic ε_{Nd} values, similar those that measured at IODP Site U1361.

A.7 BEAMISH Drilling - Foundation Ice Stream

Samples of the BEAMISH sediment core were provided by C.-D. Hillenbrand.

A.7.1 Site and Geological Setting

Recent hot water drilling as part of the BEAMISH programme penetrated 2154 m of ice to reach the bed of Rutford Ice Stream, which drains into the Ronne Ice Shelf (Anker et al., 2021; Smith et al., 2021). A short, ~10 cm, sediment core was retrieved from the bed.

Rutford Ice Stream is flanked on the southern side by the Ellsworth Mountains, and its catchment mainly covers this side of the main glacier trunk. There is significant rock exposure, recording continuous Cambrian to Permian sediment deposition in a 13 km thick sequence (Webers and Sporli, 1983). Isotopic measurements have not been performed on these sedimentary rocks. However, some inferences can be made based on their contemporary counterparts in the Transantarctic Mountains. Cambrian rocks of similar age have ε_{Nd} values of ~-9.5 around the Whitmore Mountains, -9.7 to -5.4 in the non-volcanic beds of the Liv Group, and -15.8 to -10.0 in the Byrd Group (Borg et al., 1990; Goodge et al., 2008; Marschalek et al., 2021). The Swanson Formation of Marie Byrd Land, although geographically distant, is also metasedimentary and of a comparative age and formed in a similar tectonic setting; here ε_{Nd} values span -14.1 to -9.7 (Korhonen et al., 2010; Yakymchuk et al., 2015; Brown et al., 2016). Between these extremes, these rock types typically range between -12 and -10. Epsilon Nd values with a mean of approximately -12 therefore seem likely for most Ellsworth Mountain sediments, and fit with ε_{Nd} values in Weddell Sea sediments (Williams, pers. comm.). However, significant variability is expected in sedimentary rocks such as these, which may have very different precursor rocks both spatially and stratigraphically.

The other side of the glacier, the bedrock is not exposed. This limits knowledge of the geology to geophysical data. However, magnetic anomalies on this side of Rutford Ice Stream are consistent with the outcropping Haag Nunataks (Jordan et al., 2020). These rocks formed in the Mesoproterozoic (Millar and Pankhurst, 1987), but are juvenile, meaning they have relatively radiogenic ε_{Nd} values for their age (~-7.4; Storey et al., 1994). It is possible that Haag rocks are overlain by younger sediments, but these probably comprise a mixture of local rocks so are likely to have a similar range of ε_{Nd} values. As Rutford Ice Stream flows over both these rocks and the Ellsworth Mountain sediments discussed above, a mixture of these rock types would be expected beneath it.

A.7.2 Results and Discussion

Methods used in the isotopic analyses were identical to those throughout this thesis, without the leaching step.

Table A.7.1 *Neodymium and strontium isotope data collected from the BEAMISH core. The 2 standard deviation errors reported for the ε_{Nd} values are based on the JNdi-1 measurements during the sessions.*

Upper depth (cm bsf)	Lower depth (cm bsf)	Midpoint depth (cm bsf)	$^{143}Nd/^{144}Nd$	2SE	ε_{Nd}	2SD	$^{87}Sr/^{86}Sr$	2SE
englacial	englacial	englacial	0.512171	0.000011	-9.11	0.27	0.719798	0.000008
1	4	2.5	0.512175	0.000010	-9.03	0.25	0.720388	0.000008
4	5	4.5	0.512172	0.000009	-9.08	0.21	0.720972	0.000008
5	9	7	0.512178	0.000009	-8.96	0.25	0.719236	0.000007

Three samples spanning the length of the core, plus sediment entrained in the lowermost ice, gave ε_{Nd} values within error of each other, with a mean of -9.05 (Table A.7.1). These ε_{Nd} values fall between the two major rock geological provinces discussed above, and likely reflect a mixture of Ellsworth Mountains and Haag sediment sources. $^{87}Sr/^{86}Sr$ ratios are also relatively homogenous, with a mean of 0.720098 (Table A.7.1). Clay mineralogy is also similar throughout the length of the core and is dominated by illite (~68-70%) and chlorite (~20-24%), consistent with a physical, glacial weathering regime (Hillenbrand and Ehrmann, pers. comm.). Smectite (2-7%) and kaolinite (4-6%) comprise only a small fraction of the sediment. The kaolinite may be recycled from the Palaeozoic sedimentary strata.

The lack of stratigraphic variation suggests the sediment has a homogenous provenance, which is unsurprising given the short length of the core. The close agreement of the debris entrained in the basal ice and the sediment core samples suggests the englacial sediment may have been incorporated locally and not transported far. Alternatively, if the sediment has been transported from where it was entrained, the basal till must have a uniform provenance signature down the ice stream flow line. This would match the new data presented here for the Siple Coast ice streams, which show fairly homogenous radiogenic isotope ratios at more upstream and downstream sites. Indeed, deforming till is present beneath Rutford Ice Stream similar to that beneath the Siple Coast ice streams discussed above (Smith, 1997; Smith et al., 2021). Mixing of sediment may therefore occur further upstream, with little generation of new sediment towards the grounding zone, similar to the Siple Coast ice streams. An additional drill site upstream or downstream would be required to ascertain whether this hypothesis is correct.

Appendix References

Anker, P. G., Makinson, K., Nicholls, K. W., & Smith, A. M. (2021). The BEAMISH hot water drill system and its use on the Rutford Ice Stream, Antarctica. *Annals of Glaciology*, *62*(85-86), 233-249.

Beerling, D. J., Fox, A., & Anderson, C. W. (2009). Quantitative uncertainty analyses of ancient atmospheric CO2 estimates from fossil leaves. *American Journal of Science*, *309*(9), 775-787.

Breecker, D. O., & Retallack, G. J. (2014). Refining the pedogenic carbonate atmospheric CO2 proxy and application to Miocene CO2. *Palaeogeography, Palaeoclimatology, Palaeoecology*, *406*, 1-8.

Greenop, R., Foster, G. L., Wilson, P. A., & Lear, C. H. (2014). Middle Miocene climate instability associated with high-amplitude CO2 variability. *Paleoceanography*, *29*(9), 845-853.

Griener, K. W., Warny, S., Askin, R., & Acton, G. (2015). Early to middle Miocene vegetation history of Antarctica supports eccentricity-paced warming intervals during the Antarctic icehouse phase. *Global and Planetary Change*, *127*, 67-78.

Hillenbrand, C.-D. & Ehrmann W. (Personal Communication, September 2021).

Holbourn, A., Kuhnt, W., Lyle, M., Schneider, L., Romero, O., & Andersen, N. (2014). Middle Miocene climate cooling linked to intensification of eastern equatorial Pacific upwelling. *Geology*, *42*(1), 19-22.

Holbourn, A., Kuhnt, W., Schulz, M., Flores, J. A., & Andersen, N. (2007). Orbitally-paced climate evolution during the middle Miocene "Monterey" carbon-isotope excursion. *Earth and Planetary Science Letters*, *261*(3-4), 534-550.

Ji, S., Nie, J., Lechler, A., Huntington, K. W., Heitmann, E. O., & Breecker, D. O. (2018). A symmetrical CO2 peak and asymmetrical climate change during the middle Miocene. *Earth and Planetary Science Letters*, *499*, 134-144.

Kürschner, W. M., & Kvacek, Z. (2009). Oligocene-Miocene CO2 fluctuations, climatic and palaeofloristic trends inferred from fossil plant assemblages in central Europe. *Bulletin of Geosciences*, *84*(2), 189-202.

Molzahn, M., Reisberg, L., & Wörner, G. (1996). Os, Sr, Nd, Pb, O isotope and trace element data from the Ferrar flood basalts, Antarctica: evidence for an enriched subcontinental lithospheric source. Earth and Planetary Science Letters, 144(3-4), 529-545.

Pollard, D., & DeConto, R. M. (2012). Description of a hybrid ice sheet-shelf model, and application to Antarctica. *Geoscientific Model Development*, *5*(5), 1273-1295.

Smith, A. M. (1997). Basal conditions on Rutford ice stream, West Antarctica, from seismic observations. *Journal of Geophysical Research: Solid Earth*, *102*(B1), 543-552.

Smith, A. M., Anker, P. G. D., Nicholls, K. W., Makinson, K., Murray, T., Rios-Costas, S., ... & Anandakrishnan, S. (2021). Ice stream subglacial access for ice-sheet history and fast ice flow: the BEAMISH Project on Rutford Ice Stream, West Antarctica and initial results on basal conditions. *Annals of Glaciology*, *62*(85-86), 203-211.

Steinthorsdottir, M., Jardine, P. E., & Rember, W. C. (2020). Near-Future pCO2 during the hot Mid Miocene Climatic Optimum. *Paleoceanography and Paleoclimatology*, e2020PA003900.

Super, J. R., Thomas, E., Pagani, M., Huber, M., O'Brien, C., & Hull, P. M. (2018). North Atlantic temperature and pCO2 coupling in the early-middle Miocene. *Geology*, *46*(6), 519-522.

Webers, G. F., & Sporli, K. B. (1983). Palaeontological and stratigraphic investigations in the Ellsworth Mountains, West Antarctica. *Antarctic Earth Science. Australian Academy of Science, Canberra*, 261-264.

Zhang, Y. G., Pagani, M., Liu, Z., Bohaty, S. M., & DeConto, R. (2013). A 40-million-year history of atmospheric CO2. *Philosophical Transactions of the Royal Society A: Mathematical, Physical and Engineering Sciences*, *371*(2001), 20130096.